Screw Extrusion Additive Manufacturing of Elastomers and High-Performance Thermoplastics

Department of Industrial and Manufacturing Engineering

Faculty of Engineering

A dissertation submitted to the University of Malta in partial fulfilment of the award of Doctor of Philosophy

Albert Curmi

2024

L-Università ta' Malta

FACULTY/INSTITUTE/CENTRE/SCHOOL Engineering

DECLARATION OF AUTHENTICITY FOR DOCTORAL STUDENTS

(a) Authenticity of Thesis/Dissertation

I hereby declare that I am the legitimate author of this Thesis/Dissertation and that it is my original work.

No portion of this work has been submitted in support of an application for another degree or qualification of this or any other university or institution of higher education.

I hold the University of Malta harmless against any third party claims with regard to copyright violation, breach of confidentiality, defamation and any other third party right infringement.

(b) Research Code of Practice and Ethics Review Procedure

I declare that I have abided by the University's Research Ethics Review Procedures. Research Ethics & Data Protection form code 6271_25082020_Albert Curmi.

☒ As a Ph.D. student, as per Regulation 66 of the Doctor of Philosophy Regulations, I accept that my thesis be made publicly available on the University of Malta Institutional Repository.

□ As a Doctor of Sacred Theology student, as per Regulation 17 (3) of the Doctor of Sacred Theology Regulations, I accept that my thesis be made publicly available on the University of Malta Institutional Repository.

□ As a Doctor of Music student, as per Regulation 26 (2) of the Doctor of Music Regulations, I accept that my dissertation be made publicly available on the University of Malta Institutional Repository.

□ As a Professional Doctorate student, as per Regulation 55 of the Professional Doctorate Regulations, I accept that my dissertation be made publicly available on the University of Malta Institutional Repository.

Copyright Notice

Abstract

Fused granulate fabrication (FGF) is an emerging material extrusion technology for additive manufacturing which offers a lower cost and more versatile solution over the established fused filament fabrication (FFF) techniques. FGF uses granulates instead of filament which area cheaper and enable the use of softer materials which would not be processable with FFF. Despite this, no small-scale FGF systems exist which are capable of reliably extruding high-performance thermoplastics and research on very soft TPEs remains limited. The aim of this thesis was to address this gap by developing a lightweight, simple, and small-scale screw granulate extrusion system intended for additive manufacturing of niche elastomeric and high-performance thermoplastic materials. Extruder development involved four iterations with Extruder 1 successfully 3D printing ABS and then subsequent iterations optimised extruder performance to 3D print thermoplastic polyolefin (TPO), TF3ZG0-LCNT, polyetherimide (PEI), and polyether ether ketone (PEEK) (Extruders 2-4). The research also aimed to establish optimal processing parameters to additively manufacture products using these materials and then to test and investigate the resulting material properties and case study part's performance. The methodologies used in this study involved material characterization using multiple spectroscopy techniques, thermal analysis, mechanical testing, and imaging. Results showed that TPO is a good alternative to the popular thermoplastic polyurethane (TPU) as it does not require pre-drying which simplifies material handling for 3D printing. TF3ZG0-LCNT, a super soft TPE was successfully 3D printed, setting a record as the softest TPE yet, with uniaxial strains exceeding 3365% and biaxial strains up to 590%. PEI, an amorphous high-performance polymer demonstrated viability for rapid tooling, producing injection molding (IM) inserts capable of 14 IM cycles, albeit part complexity influenced performance. The mechanical properties of PEEK products obtained via FGF were improved by using high molecular weight grades and elevated processing temperatures. This achieved improved layer bonding including a stress at failure of 72.4 MPa in the XY plane. The system's effectiveness was also validated by producing specialized parts including a child orthotic insole (TPO), elastic inflatable actuators (TF3ZG0-LCNT), injection mould inserts (PEI), and mechanical components (PEEK). This research advances FGF technology, enabling the additive manufacturing of specialized materials using a small-scale system, thus reducing associated costs and making the technology available to a wider user base and application field.

Acknowledgements

I would like to begin by expressing my gratitude to Prof. Arif Rochman for his unwavering support throughout every stage of my PhD journey. His guidance and encouragement have been invaluable. I will happily remember all the travels we had together over the past years. I am equally grateful to Prof. Joseph Buhagiar and Prof. Alfred Gatt for sharing their expertise and insights in their respective fields, which greatly enriched my work.

A special thanks goes to the technical staff of the Department of Industrial and Manufacturing Engineering and the Department of Metallurgy and Materials Engineering. Their skill and assistance with the advanced equipment in their labs were crucial for conducting the studies that underpinned this research. I am also deeply appreciative of the support from the Biomedical Engineering Lab team, who generously allowed me to use their thermal cameras numerous times over the years.

This PhD would not have been possible without the financial support provided by Xjenza Malta. I am thankful for the funding of two pivotal projects: the MALTI3D research project, funded by the Malta Council for Science and Technology (MCST) through the FUSION: R&I Technology Development Programme (R&I-2018-009T), and REO3D which was funded by the Fusion R&I Research Excellence Programme (REP-2023-025). Their backing made this journey a reality.

My deepest appreciation also goes to my fellow PhD students at the research suites. Too many to name individually, they created a vibrant and supportive community that made the highs higher and the lows more bearable. Sharing this journey with them has been a privilege.

Finally, to my friends and family, thank you for being my rock. To my amazing fiancé, Martina whose patience in listening to my endless complaints and your constant encouragement through every struggle over these past four years have meant the world to me. To my mother Georgina and father Paul, thank you for supporting me through all these years. Your consistent patience and love are what gives me spirit to move on whenever I falter. And, of course, a special shoutout to Duke, the family dog, who kept me company during many writing sessions, often stealing food but always lifting my spirits.

Publications and Patents

1. **Curmi A.**, Rochman A. (2022) From Theory to Practice: Development and Calibration of Micro Pellet Extruder for Additive Manufacturing. Key Engineering Materials 926:34–45. https://doi.org/10.4028/p-b22a9a

2. **Curmi A.**, Rochman A. (2023) Miniaturized fused granulate fabrication of polyether ether ketone (PEEK). Progress in Additive Manufacturing. https://doi.org/10.1007/s40964-023-00518-4

3. **Curmi A.**, Rochman A., Buhagiar J. (2024) Influence of polyether ether ketone (PEEK) viscosity on interlayer shear strength in screw extrusion additive manufacturing. Additive Manufacturing 84:104086. https://doi.org/10.1016/j.addma.2024.104086

4. **Curmi A.**, Rochman A. (2024) Fused granulate fabrication of injection molding inserts from high-performance ULTEM 9085TM thermoplastic for cosmetic packaging industry. Progress in Additive Manufacturing. https://doi.org/10.1007/s40964-024-00630-z

5. **Curmi A.**, Rochman A., Gatt A. (2024) Screw extrusion additive manufacturing of thermoplastic polyolefin elastomer. Progress in Additive Manufacturing. https://doi.org/10.1007/s40964-024-00696-9

6. **Curmi A.**, Rochman A. (2025) Screw Material Extrusion of Super Soft Thermoplastic Elastomer for Additive Manufacturing of Inflatables. Virtual and Physical Prototyping. DOI: 10.1080/17452759.2024.2408658

7. **Curmi A.**, Rochman A. (2025) Screw extrusion fused granulate Fabrication: Trends, materials, extruder classification and future development. Polymer. https://doi.org/10.1016/j.polymer.2025.128459

8. EXTRUDER SYSTEM FOR 3D PRINTING, L-UNIVERSITÀ TA' MALTA, *Patent application in PCT stage*, PCT/EP2024/068855.

Conference Attended

1. Curmi A., Rochman A., "From theory to practice: development and calibration of micro pellet extruder for additive manufacturing", Presentation given at the European Scientific Association for material FORMing - ESAFORM 2022, 27 – 29 April, Braga, Portugal.
2. Curmi A., Rochman A., "Miniaturized fused granulate fabrication of polyether ether ketone (PEEK)", Presentation given at the 15th International conference on computational engineering and experimenting – ACEX 2022, 3 – 7 July, Florence, Italy.
3. Curmi A., Rochman A., "Fused Granulate Fabrication of Injection Molding Inserts from High-Performance ULTEM 9085 Thermoplastic, for Cosmetic Packaging Industry", Presentation given at the 16th International conference on computational engineering and experimenting – ACEX 2023, 3 – 7 July, Heraklion, Crete, Greece.
4. Curmi A., Rochman A., "Screw-based Material Extrusion Additive Manufacturing of Inflatables Using Ultra Soft Thermoplastic Elastomer", Presentation given at the 39th International Conference of the Polymer Processing Society, PPS 39, 2024, 19 – 23 May, Cartagena de Indias, Colombia.

Academic and Industrial Visits

1. Attendance at Formnext 2022 Tradeshow on additive manufacturing technologies – 16th to 19th November 2022.
2. Visit to Cracow University of Technology, Warszawska 24, 31-155 Krakow as part of an international scholarship exchange of PhD candidates and academic staff – PROM NAWA project – 6th to 20th March 2023.

Contents

List of Figures

List of Tables

Glossary

Acrylonitrile butadiene styrene	ABS
American Iron and Steel Institute	AISI
Additive manufacturing	AM
American Society for Testing and Materials	ASTM
Attenuated total reflection	ATR
Big area additive manufacturing	BAAM
Binder jetting	BJT
Brickman number	Br
Computer aided design	CAD
Compound annual growth rate	CAGR
Carbon fibre	CF
Computational fluid dynamics	CFD
Computer numerically controlled	CNC
Cyclic olefin copolymer	COC
Compression shear testing	CST
Discrete element method	DEM
German Institute for Standardization	DIN
Direct ink writing	DIW
Dynamic mechanical analysis	DMA
Differential scanning calorimetry	DSC
Energy dispersive spectroscopy	EDS
Elastic inflatable actuator	EIA
Ethylene Propylene Diene Terpolymer	EPDM
European Union	EU
Ethylene-vinyl acetate	EVA
Fused deposition modelling	FDM
Fused filament fabrication	FFF
Fused granulate fabrication	FGF
Fourier transform infrared spectroscopy	FTIR
Glass fibre	GF
Graphene nanoplatelet	GNP
High density polyethylene	HDPE

Heat deflection temperature	HDT
High impact poly styrene	HIPS
Injection Molding	IM
Infrared	IR
International Organization for Standardization	ISO
Material jetting	MJ
Material extrusion	MEX
Melt flow rate	MFR
Metal injection molding	MIM
Melt volume flow rate	MVR
Max volumetric speed	MVS
National Electrical Manufacturers Association	NEMA
Polyamide	PA
Pellet additive manufacturing	PAM
Polybutylene adipate succinate	PBAS
Polybutylene adipate-co-terephthalate	PBAT
Powder bed fusion	PBF
Polycarbonate	PC
Polycaprolactone	PCL
Poly(D, L-lactic acid)	PDLLA
Polyethylene	PE
Polyether ether ketone	PEEK
Polyethylene glycol	PEG
Polyethylene graft maleic anhydride	PE-g-MAH
Polyetherimide	PEI
Personal protective equipment	PPE
Polyethylene terephthalate	PET
Polyethylene terephthalate glycol	PETG
Polyhydroxyalkanoates	PHA
Proportional–integral–derivative	PID
Polyketone	PK
Polylactic acid	PLA
Poly(lactic-co-glycolic) acid	PLGA
Poly(L-lactide)	PLLA

Polymethyl methacrylate	PMMA
Polypropylene	PP
Polyphenylene sulfide	PPS
Polystyrene	PS
Polytetrafluoroethylene	PTFE
Polyvinyl alcohol	PVA
Polyvinyl chloride	PVC
Polyvinyl alcohol	PVOH
Rapid prototyping	RP
Rotation per minute	RPM
Rapid tooling	RT
Rapid tooling injection moulding	RTIM
Sodium alginate	SA
Styrene-Ethylene-Butylene-Styrene	SEBS
Scanning electron microscopy	SEM
Sheet laminations	SHL
Stereolithography	SLA
Shape memory polymer	SMP
Single screw extruder	SSE
Tricalcium phosphate powder	TCP
Thermoplastic elastomer	TPE
Thermoplastic polyolefin	TPO
Thermoplastic polyurethane	TPU
United states of America	USA
Ultraviolet	UV
Volatile organic compounds	VOC
Vat photopolymerization	VPP
Vinyl-functionalized graphene oxide	VGO
X-ray diffraction	XRD

PEEK pellets

1 Introduction

1.1 Additive Manufacturing

Additive manufacturing (AM) is defined by the ISO 52900 of 2021 as the *process of joining materials to make parts from 3D model data, usually layer upon layer as opposed to subtractive manufacturing and formative manufacturing methodologies* [1]. The establishment of this innovative method of fabrication ushered in new manufacturing possibilities which were previously impossible using conventional techniques.

Additive manufacturing utilizes a wide array of materials, including metals, ceramics, polymers, and composite variations, enabling applications across diverse industries. Additively manufactured metals and ceramics are often preferred for demanding applications due to their strength, thermal resistance and biocompatibility, though they remain costly. Conversely, polymers ranging from commodity to engineering and high-performance grades like polyether ether ketone (PEEK), as well as soft elastomers, offer a more affordable, versatile, and widely accessible option. The accessible nature of polymer AM extends the geometric flexibility of 3D printing to a broader range of users and market sectors. AM supports intricate designs, such as lattice structures and organic geometries, optimizing strength-to-weight ratios in aerospace parts and providing patient-specific implants in the biomedical field. Examples include spinal implants, dentures, and a variety of porous implants 3D printed out of multiple materials such as PEEK [2]. AM is also used to produce lightweight structures tailored to challenging operational environments and complex engine components such as turbopumps and heat exchangers [3]. At the same time, it also enables the production of one-off replacement parts or bespoke components in-situ or simple aesthetic objects meant for decoration or as toys.

The wide material range available to AM is achievable through a plethora of techniques each with its strength and weaknesses across a range of materials. The family of techniques encompassing AM, specifically concerning polymers and composites thereof, is shown in Figure 1.1, as defined in ISO 52900 *Additive manufacturing - General principles - Fundamentals and vocabulary* of 2021 [1]. The principal polymer AM techniques are material extrusion (MEX), material jetting (MJ), powder bed fusion (PBF), binder jetting (BJT), vat photopolymerization (VPP) and sheet laminations (SHL). Out of these techniques, the most widely used are MEX, MJ, VPP and PBF. BJT techniques principally use polymers as the binder material when 3D printing metals or ceramics. This polymer material is removed as a second step in order to sinter the green particles,

hence BJT will not be considered in this discussion. SHL has been in decline over the years due to its lack of significant advantages compared to other techniques. Similar to BJT, it is not primarily developed for polymer additive manufacturing.

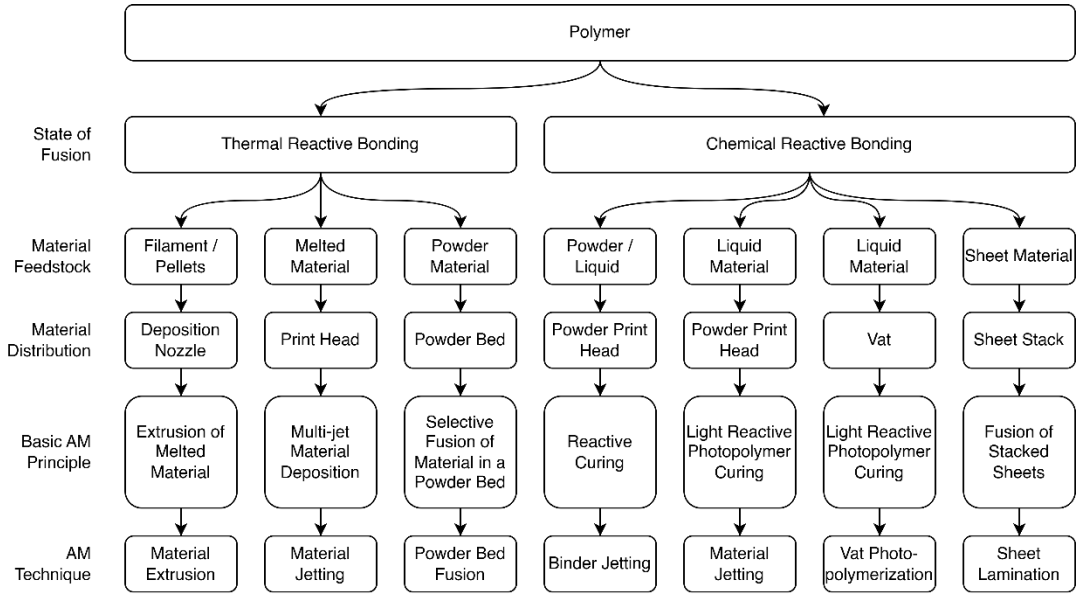

Figure 1.1 – Polymer AM processing principles adapted from ISO 52900 of 2021 [1]

Of the four main techniques listed, MEX is the most widely used polymer AM technology [4] due to its relatively low cost and material versatility [5]. It involves the selective deposition of material by extrusion through a nozzle to generate the desired geometry, layer by layer. This process is generally conducted in atmosphere or in a heated chamber in the case of high-performance polymers [6]. This simple setup facilitates multi material 3D printing along with any in-process alterations of the object being 3D printed. Other popular techniques such as VPP are not as flexible or easy to use. VPP is the oldest AM technology [7] which works by selectively curing a light-activated, liquid photopolymer, to generate the desired geometry [1]. The necessity to use photosensitive resins limits the material variety available to VPP, mostly to select methacrylate- and epoxy-based resins [8]. Nevertheless, material modifications led to development of tough, elastomeric and even biocompatible resins [7, 8]. Yet, the technology is fundamentally limited to thermoset resins which cannot be remelted. Recycling of these materials is therefore limited to chemical methods to convert the material back to monomers or by mechanical methods through which the physically broken down thermoset polymers are used as a filler in other materials [9]. This is a critical limitation considering the drive towards a circular economy [10] driven by the contemporary global sustainability goals [10, 11]. The same issue pervades MJ techniques which

predominantly use thermoset polymers as their raw material, in the form of monomer liquids. MJ is similar to conventional inkjet printing whereby liquid material is selectively deposited either by drop on demand or in a continuous approach by an inkjet head [1, 5]. This technique is capable of very small resolutions, down to the nanometric range [5], but it comes at much higher equipment and consumable cost compared with both MEX and VPP but is on a similar cost level to PBF [12].

PBF is another common polymer AM technique, characterized by its selective fusion of powder particles to generate the desired geometry [1]. A primary advantage of PBF is the self-supporting nature of powder beds which negate the necessity for material wasteful and time-consuming support structures, as opposed to all other techniques mentioned. PBF employs thermoplastics which make its 3D printed products easily remelted for reproduction. Furthermore PBF can make use of high performance thermoplastics, just like MEX and unlike all the other techniques mentioned [13]. The biggest limiting factor of PBF is the high equipment, personnel and material costs which limit its wider adoption. The materials used necessarily have to be in powder form which increases costs and requires trained personnel with appropriate personal protective equipment (PPE) [14]. This process complexity is part and parcel of MJ and PBF. To some extent even VPP is complex to handle due to its use of liquid resins which tend to produce volatile organic compounds (VOC). The post-cleaning and curing processes often necessary with these resins is also convoluted, as it involves the use of PPE especially for engineering grade resins [15].

This wide technology field that makes up polymer AM, with its distinct needs and limitations as well as its growing capabilities, has been the subject of numerous research efforts trending towards further growth. This is best illustrated by the number of published research articles per year, as shown in Figure 1.2. This graph was generated using web of science by searching for the terms indicated in the legend, in title or abstract. The dip in 2024 occurred because the data was collected during that same year, resulting in a shorter effective duration for data accumulation. According to this analysis 23% of the published articles concern polymer AM. Of these MEX, shown as the dotted bottom curve, takes up to 45%. Both values are the average results over the past 5 years. These statistics demonstrate the importance of MEX as a 3D printing technology, as a research tool or as a research area in itself.

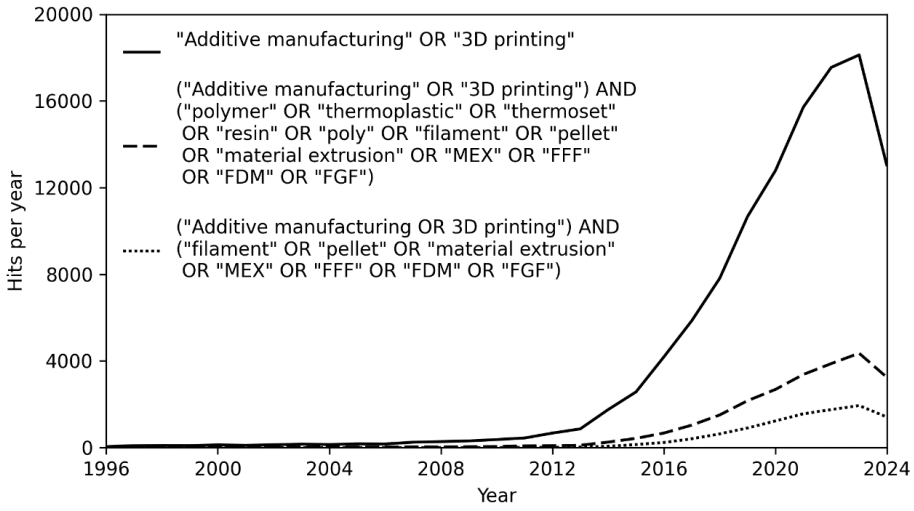

Figure 1.2 - Number of hits in web of science on the 15th of September 2024 when searching in title or abstract.

1.1.1 Material Extrusion (MEX)

MEX is predominantly used with thermoplastics yet there is a growing body of research delving into thermoset MEX. This thesis is primarily interested in elastomers and high-performance thermoplastics. The most common MEX techniques are shown in Figure 1.3 which branch out based on technique's core concept and with its intended material family [16]. The thermosets family of polymers are predominantly held together using covalent bonds. Breaking covalent bonds is non-reversible except through chemical recycling and therefore unlike thermoplastics, recycling of thermosets with the aim of gaining back the raw material for reuse, is more expensive and generally less sustainable [9]. As shown in in Figure 1.3, thermoset MEX is possible, but it is not a common process. Thermoset MEX is most commonly carried out in a direct ink writing (DIW) process whereby extrusion is caused by pumping viscoelastic ink through an orifice. This contrasts with thermoplastic MEX which melts the material by heating it up to a liquid like state [16]. The most common thermoplastic MEX techniques are fused filament fabrication (FFF) and fused granulate fabrication (FGF).

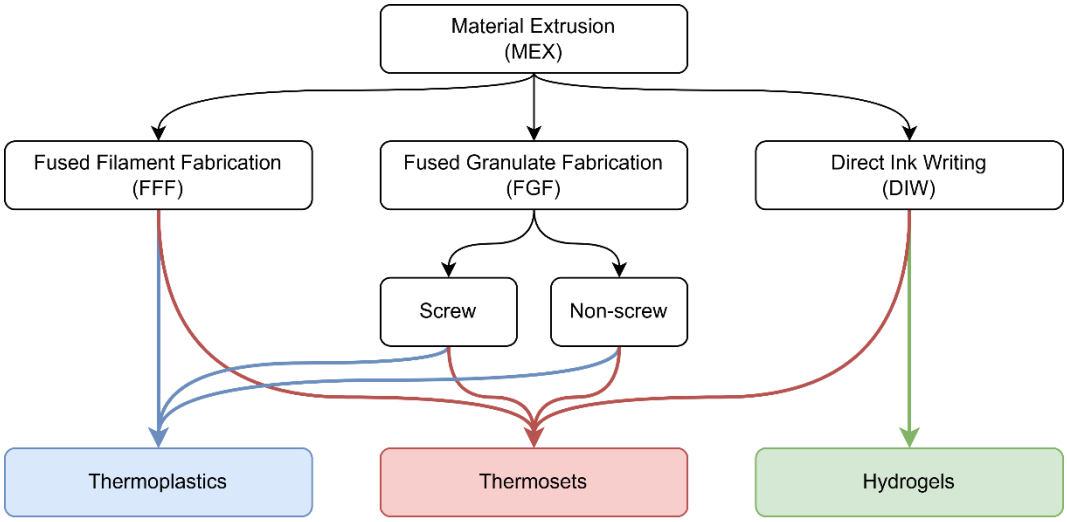

Figure 1.3 – Relationship between material extrusion techniques and their sub-types leading into processable material families.

The raw material source of both FFF and FGF are granulates, also known as pellets. FFF requires a further filament making step as illustrated in Figure 1.4. This step necessitates a high degree of accuracy over a long continuous length, which can be achieved by using specialised filament making systems. Such systems require significant financial investment along with maintenance and personnel to run and therefore impart a cost to the process. Packaging and distribution of said filament is also a wasteful process as the filament is usually wound on plastic or cardboard reels, sealed in a plastic bag and packed inside a cardboard box for delivery. This process is more costly and requires more material and energy than a comparable granulate value chain. Granules, also known as pellets, are generally the raw material used to produce filament. FGF systems can directly use this raw material which is generally simply shipped in recyclable plastic or multi-ply, paper sack. This efficient process is a direct consequence of the wide utilization of thermoplastic granules as the raw material of major industrial processes such as injection molding.

To convert the raw polymer into the desired final product, the MEX process requires accurate extrudate dosage control and accurate positioning, as the part is being constructed layer by layer [1]. Ideally, the extrusion mechanism would be fundamentally a volumetric process whereby a volumetric command for extrusion is directly converted to a volumetric output. For example, an ideal, lossless piston extruder is volumetric as the motion of the piston is directly related to the change in volume in the piston chamber which is equivalent to the amount extruded. In this ideal scenario the correct volume of material is deposited in the requisite position. A practical example of this concept is FFF

in which case the filament enables the volumetric extrusion. Likewise, DIW can also be volumetric as the volumetric dosage of liquids is a well-honed technology. Screw extrusion, FGF on the other hand is not a volumetric process, whereby the extrusion rate is related with screw speed and a host of other process parameters [17]. Non-screw FGF techniques are also emerging such as pneumatic systems [18] and piston driven [19], albeit not all are volumetric, depending on the distinct process being used.

Figure 1.4 – Production process from raw material to 3D printing for FFF and FGF

The MEX process is further removed from the ideal volumetric model when considering the complex viscoelastic behavior of thermoplastics. This is determined by their rheological properties, often demonstrating different degrees of shear thinning and thixotropic (time dependent shear thinning) behavior [16]. These features mean that extrusion start and stop is not instantaneous as would be necessary in an ideal volumetric system. This non ideal nature of thermoplastic extrusion becomes relevant when recalling the definition of FFF which mentions the *layer by layer* nature of MEX. Each layer is not necessarily continuous and may involve a number of island features as shown in Figure 1.5 (a). In such a scenario, the extrusion process has to start and stop whilst accounting for any delay in either case. These kinds of nuance considerations are

part and parcel of contemporary, open-source, 3D slicing software and firmware intended for MEX, often specifically for FFF. Slicing software convert a 3D object into a collection of layers, where each layer is a list of toolpaths, coordinates and commands. Other considerations include accounting for accelerations and decelerations at corners and the corresponding extruder motor speed control. As well as controlling over-extrusion at the first layer; seam position referring to the start and stop of extrusion even within a layer; mapping of infill structure of 3D objects, like as shown in Figure 1.5 (b, c), along with a slew of other features that have been ironed out over the years. These features were developed in tandem with FFF's market growth, as the technology adoption increased with time.

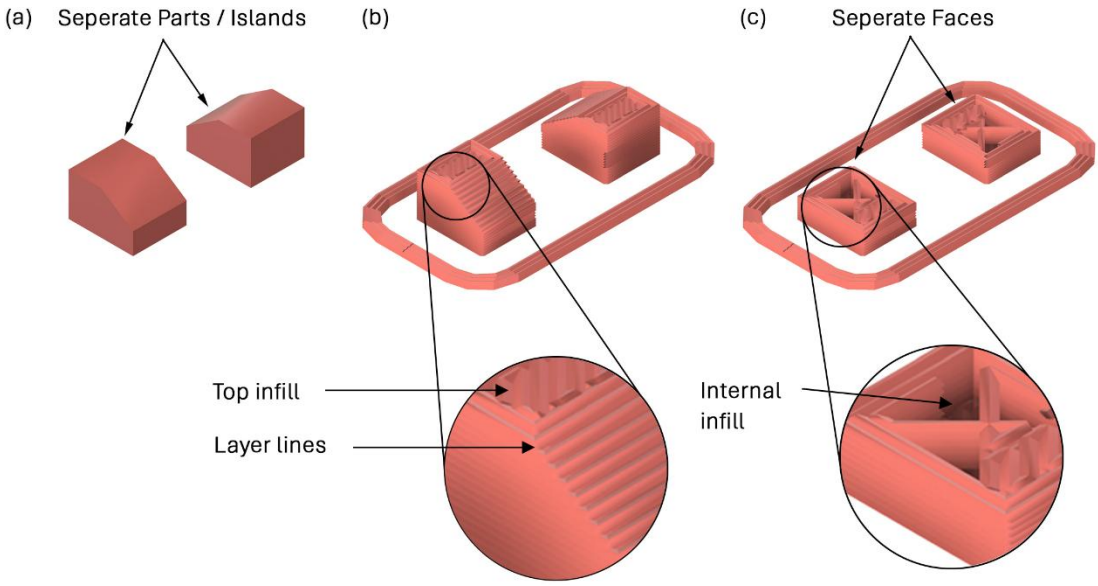

Figure 1.5 – Two part to be printed simultaneously (a), sliced (b) with multiple features in a layer with separate faces or islands in a layer (c).[1]

1.1.2 Fused Filament Fabrication

FFF is arguably the most well-known and applied AM technology due to its simple nature and low cost. A classic FFF extruder cross-section is shown in Figure 1.6. In FFF, the filament is pushed through a channel through to a hot-end. The hot end melts the filament which is then pushed through a nozzle. The pushing force is generated by an extruder mechanism on the solid, un-molten filament which is still being pushed to the hot-end. To maintain the correct length of unmolten filament, the hot-end is separated

[1] This and other 3D figures throughout the document which have no adaption or reference note, were produced by the author using a combination of software packages, primary amongst which is Autodesk Fusion 360.

from the extruder mechanism by a cold-end. In general, the extruder mechanism of FFF comprises of a drive and idler gear. The filament lies between the two whilst the idler gear compresses the filament on the drive gear. The length of filament extruded is directly related to the volume extruded provided that the diameter of the filament is constant and known.

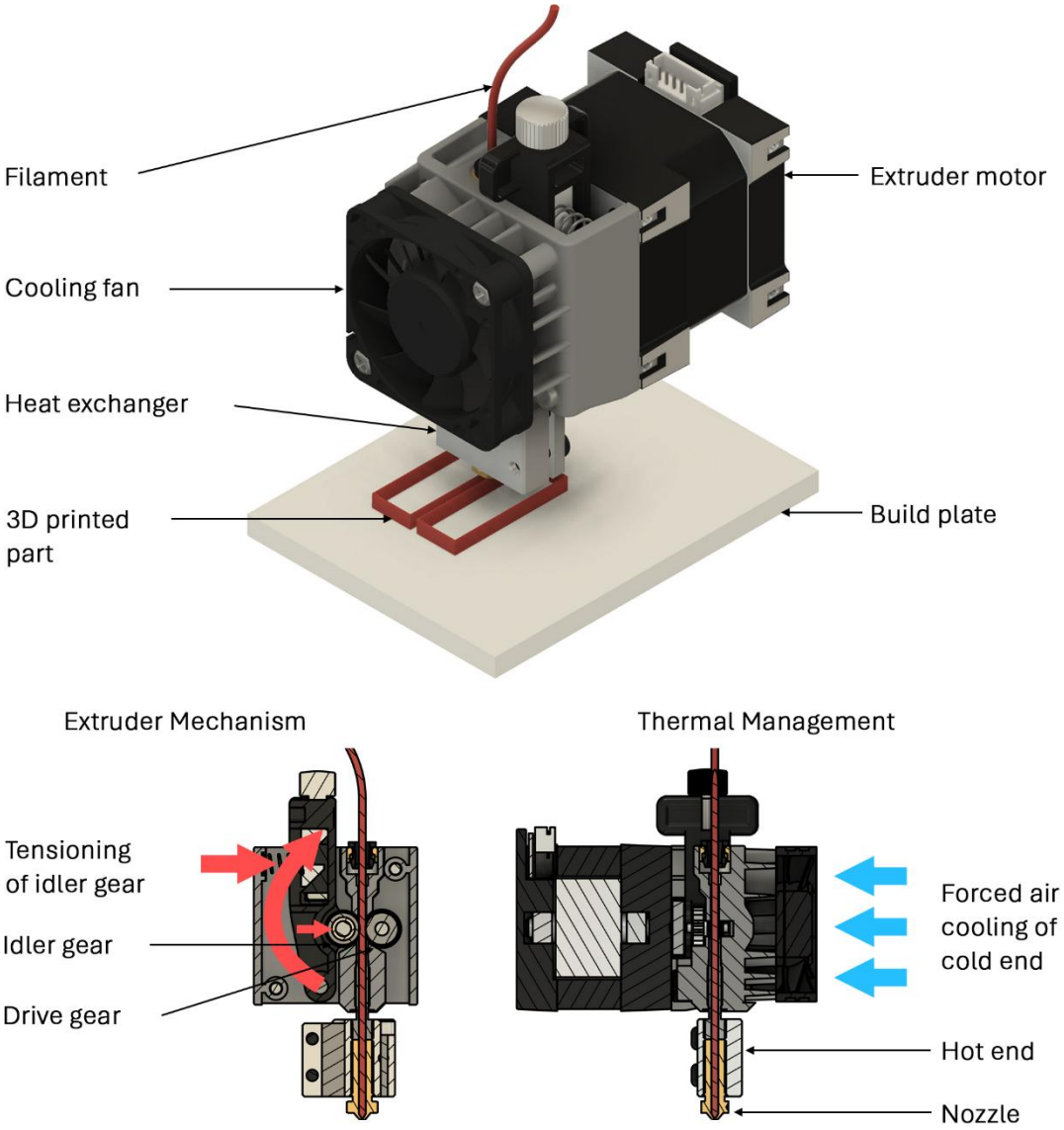

Figure 1.6 - The fused filament fabrication process

Filament is a crucial part of the process, especially its consistency, homogeneity and more importantly, its low diametric variance. By assuming that filament diameter is consistent, then the process becomes directly volumetric. The number of turns rotated by the drive gear is related to the length of filament pushed, which is directly related to the volume of material extruded. This is an assumption, as there will be some slippage between the filament and gear which results in inaccuracies in the 3D printed part,

unless accounted for through an extra, extrudate measuring step. This allows FFF to employ a simple and cheap extrusion setup which can accurately dispense the material needed. The rotation of the extrusion screw in FGF is also related to the extrusion rate, but it is not the only significant variable, as will be discussed in the next section.

1.1.3 Fused Granulate Fabrication

The most common form of FGF is screw extrusion whereby a screw residing in a barrel is rotated in reverse creating a force that acts on the granulates. The granulates are molten and subsequently extruded, as shown in Figure 1.7. This process is non-volumetric and somewhat complex, involving an interplay between screw and barrel geometry, temperatures of barrel, screw and material being processed, and the resulting friction coefficients between material and screw, and material and barrel respectively. Other variables may also have a significant effect on the extrusion rate, such as pellet morphology, pellet melting range, atmospheric humidity, the pellets solid conveying gravitational pressure and others [17, 20]. Further details on the subject will be provided in chapter 2, specifically section 2.1, page 22. The multitude of variables that influence the extrusion rate means that the process is not volumetric but nonetheless it still may be usable for AM provided calibration.

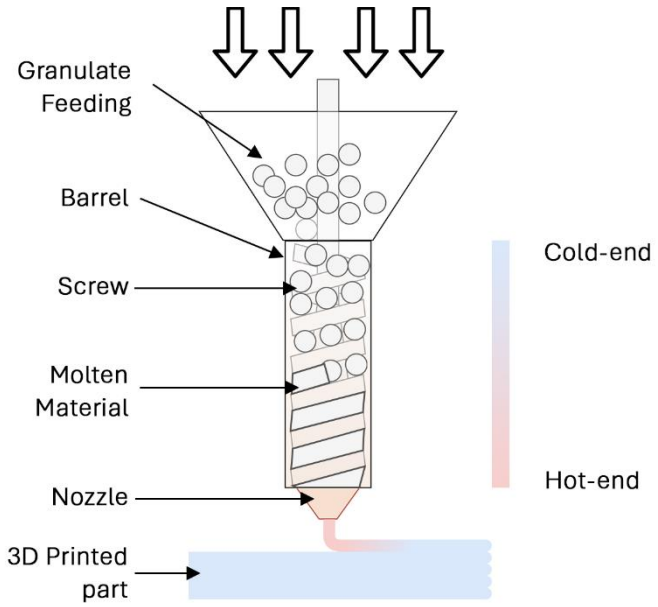

Figure 1.7 – Fused granulate fabrication schematic

If all process parameters are constant, then a screw extrusion, FGF process can be calibrated in order to determine the change in extrusion rate for a selected change in a process parameter. The most relevant process parameters are screw speed and

temperature. Other parameters are often fixed such as the screw geometry that can be altered but this usually requires an involved screw disassembly, servicing, and reassembly procedure. Such modifications are not usually possible during the 3D printing process itself and therefore are considered constant. With all other parameters constant, screw speed is analogues to filament push rate in FFF. Nonetheless, the non-volumetric nature of screw extrusion means that doubling the screw speed does not necessarily ensure doubling of the extrusion rate as occurs in FFF [21]. Hence, calibration in the case of FGF involves the determination of the extrusion rate for different screw speeds and extruder temperatures. Using this information, the same slicing software developed for FFF can be used for FGF systems. This scenario is only possible given that the other process parameters mentioned remain constant.

Provided a consistent extrusion process, following the calibration routine as described, screw extrusion FGF then becomes a viable MEX AM technique. FGF allows 3D printing which is unconstrained by the filament production process, providing greater flexibility and lower operational costs. On the matter of material flexibility, the first screw extrusion FGF system in a published study, shown in Figure 1.8, was part of the PhD thesis of Anna Bellini, which concerned the 3D printing of biocompatible ceramics for tissue engineering [22]. Such ceramic 3D printing would not be possible with FFF as it is not practical to convert the ceramic into a filament form. The fact that the first FGF study back in 2002 involved the use of a new material for AM demonstrates that material flexibility was one of the first drivers for FGF technology development.

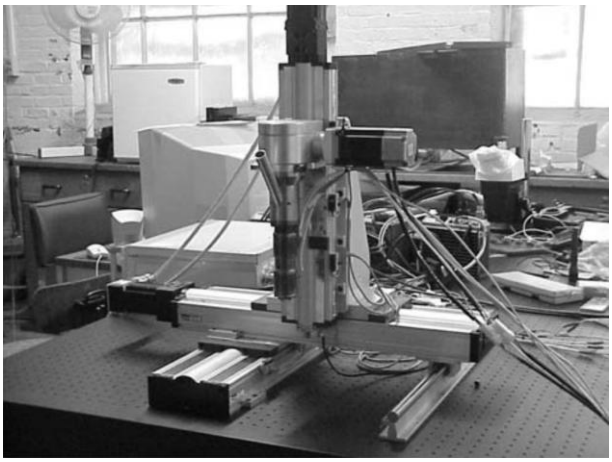

Figure 1.8 - First screw extrusion, FGF system, found in published literature [23].

Nowadays, material feedstock versatility remains an important driver for FGF development. Contemporary environmental concerns demand the need for a circular

economy which necessitates techniques which can revalorize waste. Thermoplastic FGF can be one such technique whereby thermoplastic reground waste is directly converted into a 3D printed object. This makes FGF an important tool towards fulfillment of the European green deal [10] and the United Nations sustainability goals [11]. In contrast, as described in section 1.1.1, the filament making value chain is not sustainable due to its wasteful nature. The energy required to remelt the granulates, the material necessary to package the filament and the space required to ship said filament, all contribute to make the FFF process rather unsustainable compared to FGF [24].

Cost is another important consideration for any production process. Cost comparisons between filament and granules can be difficult to make as prices fluctuate but in 2020, Alexandre *et al*. reported that granulates are at least 3 times cheaper than filament and shredded regrind thermoplastic waste was 600 times cheaper [25]. Another advantage of screw extrusion FGF is scalability. If a greater extrusion rate is desired, increasing extruder size will inherently increase the extrusion rate [17, 20]. Increasing extruder size will usually imply a necessary scale up in motion system capability. Any 3D printer requires an apposite motion system, which will be discussed briefly in the following section.

1.1.4 Motion System

A classic example of a MEX cartesian motion system is illustrated in Figure 1.9. This style of motion system is often referred to as a *bed slinger* since the heated build plate moves in the Y direction. In effect it is being slinged around during 3D printing. The extruder head is then driven in the X and Z directions. A desktop size motion system usually drives the 3 axis by using NEMA 17 stepper motors which are controlled by a specialized, albeit usually low cost digital controller. Most motion systems make use of a heated build plate along with a bed levelling system. In practice, the first layer quality of a 3D printed object has a significant impact on the final part quality. For this reason, a working build plate levelling system coupled with a capable motion system are necessary for good quality 3D printing.

Arguably the biggest disadvantage of FGF over FFF is the larger extruder size and weight. This requires a more complex motion system which is generally more expensive. For this reason, the small, desktop scale segment of the MEX market remains dominated by FFF. The poor scalability of FFF extruders coupled with the larger acceptable costs of big area

additive manufacturing (BAAM), allowed FGF to dominate that market instead of FFF [21].

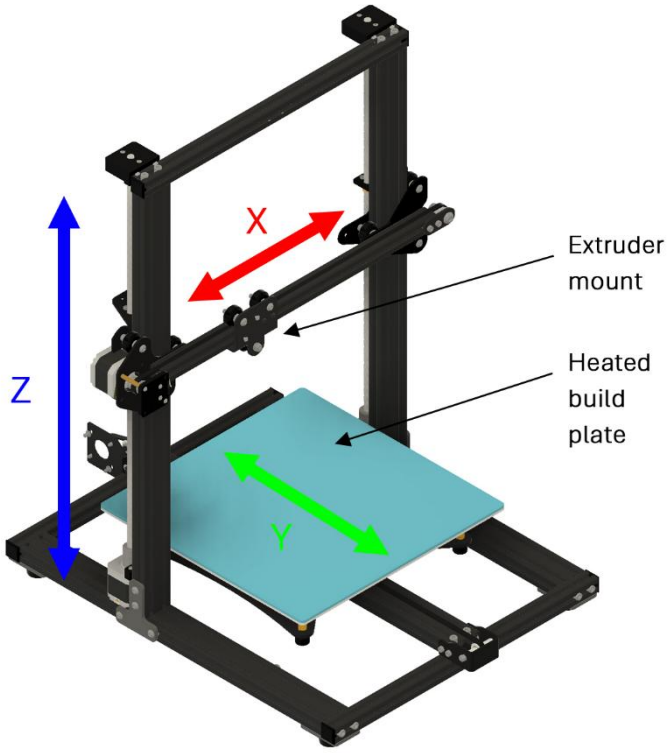

Figure 1.9 – Cartesian motion system.

1.2 Materials

A substantial part of this thesis concerns the materials used with FGF. A wide range of materials have been studied in the context of MEX AM, as suggested by the large number of published articles on the subjects as shown in Figure 1.2. More specifically, the number of studies on materials used with screw extrusion FGF is rather limited, as will be discussed in greater detail in the systematic review of section 2.2, page 41. The most significant knowledge gaps concern material extremes. This is despite the fact that the original study which spurned FGF development was itself driven by a desire for greater material choice flexibility for AM [22].

The two stiffness extremes of polymers are elastomers and rigid high-performance polymers. Thermoplastic elastomers (TPEs) are materials which can recover size and shape after deformation [26]. The most common TPE with MEX AM is thermoplastic polyurethane (TPU), in a relatively stiff and hard blend [27]. This stiffness is necessary as a fundamental limitation of FFF is that the filament acts as a piston and therefore if it is

not stiff enough, the FFF extrusion process does not work as the filament buckles [28]. In the hardness range necessary for FFF, there are other TPEs other than TPU, with divergent, ulterior properties and attributes which are underrepresented if at all present in the available research literature. Thermoplastic polyolefin (TPO) is such a TPE, providing improved chemical resistance to polar solvents, lower density, non-hygroscopic [29], and has high impact strength [30]. Such TPEs also merit study both to determine their 3D printability and method thereof but also to demonstrate the capacity of FGF to employ relatively novel materials successfully. The study will also delve into the softer TPEs which are not available to FFF systems. To push the current AM capabilities concerning elastomer softness and stretchability, this study will employ TF3ZG0-LCNT which is a super soft, 32 Shore 00 hardness TPE [31]. The high stretchability of this material, if successful 3D printed, may open new applications in the realm of inflatables, damping systems, packing and biomedical sectors.

MEX of rigid high-performance thermoplastics have been studied by multiple research groups as these materials have desirable properties and attributes for specialized and demanding applications. Amongst the most used high-performance thermoplastics are polyetherimide (PEI) and PEEK [32]. These materials have been successfully 3D printed using FFF and have found uses in aerospace, electronics, and medical sectors amongst others. Yet, FFF of high-performance thermoplastics comes at a high filament cost and is limited to the grades that are available in filament form. Each grade of polymer can have different molecular weights and may include additives, both of which may significantly alter the end material properties. This kind of material versatility is not available to FFF users unless they also have apposite filament making systems. The issue of cost, is also considerable as the filament version is usually at least 3 times more expensive than the granulate original. Another contrast between screw extrusion FGF and FFF is the melting process. The more complex screw extrusion process is more sensitive to the melting behavior of the thermoplastic being processed [20]. Such differences may be significant when considering amorphous and semi-crystalline high-performance thermoplastics. Any changes may also extend to the 3D printing domain with an impact on the finished part's quality. For these reasons, the study of two distinct high-performance thermoplastics with different crystallization kinetics is an important contribution to the field of FGF AM. Furthermore, the important applications possibly using high performance thermoplastics ensure that any studies conducted on the

subject will provide a meaningful contribution to this topical field, which is still rife with multiple technical challenges.

Further details on the material challenges and the possible applications thereof will be covered in section 2.3, page 79. These materials merit study both to determine their 3D printability and method thereof but also to demonstrate the capacity of FGF to employ relatively novel materials successfully. Finally, the determination of a technique that is capable of 3D printing such novel materials will open the way to new applications that can take advantage of the increased material choice available.

1.3 Motivation

Is additive manufacturing sufficiently capable, beneficial, and essential to warrant substantial research interest for wider adoption? Recent market analyses by Frost & Sullivan highlight the sector's rapid growth, evidencing a sustained interest from both academia and private industry [33]. In 2021, the AM market was valued at USD 14.7 billion, with a projected compound annual growth rate (CAGR) of 20.4% [33]. By 2023, the market had grown to USD 19.8 billion, with a projected CAGR of 21.7% from 2024 to 2036 [34]. This steady expansion underscores AM's significant role in various sectors, becoming part of industrial, commercial, and domestic applications, meeting market demands. Desktop-scale FFF has notably contributed to this growth [35]. Screw extrusion FGF has also driven AM growth, but its primary impact has been in big area additive manufacturing, with limited contributions at the desktop scale [36].

Desktop scale screw extrusion FGF has the potential to substitute FFF if it achieves comparable printing quality, equipment cost, and ease of use. FGF's use of pellet-based feedstock offers cost and sustainability advantages, along with greater theoretic, material versatility, including flexibility in material grades and elastomer hardness. However, the limits of this versatility, especially for desktop-scale FGF, remain undefined. For instance, while FGF has successfully printed progressively softer TPEs [37], yet it is unclear how soft a TPE can be for effective screw extrusion. Additionally, the capacity of small-scale screw extrusion FGF to print high-performance thermoplastics remains unexplored. As detailed in section 2.2.4, page 51, no existing research addresses this topic. If high-performance thermoplastics could be extruded and printed via small-scale FGF, it would expand the user base, particularly for applications requiring lightweight aerospace structures or biocompatible biomedical

implants. The smaller size and simpler motion systems in desktop FGF setups reduce costs and complexity, making high-performance 3D printing economically feasible for a broader range of commercial and research applications

This thesis is therefore motivated by:

- the growing market for AM,
- the benefits of desktop FGF if it's quality (surface quality, geometric accuracy and mechanical properties) is improved to within similar capability levels of FFF systems, and
- the need to expand the material library available to small-scale FGF to increase its application scope.

These motivations led to the aim outlined in the next section.

1.4 Aim and Scope

The aim of this study is to develop a lightweight, modular, screw, granulate extrusion system for additive manufacturing and apply that system to niche elastomeric and high-performance thermoplastic materials.

This study will in a first part develop a small scale, screw extrusion, FGF system. In the second part this system will be applied to elastomeric and high-performance thermoplastics. The application process will guide extruder development by refining prototypes and validating the functionality of the developed system.

This research endeavor will only consider thermoplastic polymers as these materials are the most sustainable amongst polymers and topical at the time of writing. The application of the extruder through 3D printing of four specified thermoplastics will make up a significant part of the contribution brought forward by this study. The study will employ two elastomers to evaluate the extrusion and 3D printing performance at different ends of the shore hardness spectrum. The hard TPE was set to be TPO whereas the softer TPE was set to TF3ZG0-LCNT. Regarding high performance thermoplastics, two materials will also be tested, one amorphous, PEI, and the other semi-crystalline, PEEK. In this manner the different mechanisms related to 3D printing of amorphous and semi-crystalline thermoplastics will be evaluated in the context of FGF.

The study will not aim to optimize the extrusion process itself, rather it is limited to the achievement of a functioning system capable of 3D printing using the materials set out with sufficient quality for the identified applications. The study also does not purport to define the minimum hardness of TPE or to identify which grades of high-performance thermoplastics can be 3D printed by FGF. These are beyond the scope of this thesis as the range of materials available is too vast and is constantly changing. These limitations in scope are justified by the relative novelty of the subject. There is a lack of published literature that can guide extruder development both due to its size as well as the material combination set out.

1.5 Thesis Structure

This thesis is structured as follows. Chapter 2 is divided into three parts the first of which is concerned with the basic process of single screw extrusion along with related relevant theory. The second part of this chapter then carries out a systematic review of FGF extruders available in literature followed by a classification process. In the last part, a literature review of the four materials selected for this thesis is carried out covering our current understating of their behaviour during MEX.

In Chapter 3 the aim of the study is refined further to better suit the existing research gap following the literature review carried out in the previous chapter. The research gap, objective and scope are likewise defined as instructed by the refined aim. Extruder development is then set out in Chapter 4, including extruder design, theoretical analysis, prototyping and preliminary extrusion tests.

The next chapters from Chapter 5 to Chapter 8 will apply the developed extrusion system to the four materials set out in section 1.4. Each chapter is self-contained, including distinct method and results sections. This structure was deemed necessary due to the divergent nature of the topics that will be covered by this thesis.

- **Chapter 5 Hard Elastomer,** will apply a hard elastomer, TPO, for extrusion and 3D printing using FGF. TPO is novel TPE for material extrusion AM but it is within the scale of hardness usually available to FFF systems.
- **Chapter 6 Soft Elastomer,** will push the boundary further by employing TF3ZG0-LCNT with FGF. This is an ultra-soft TPE which is impossible to 3D print using FFF

and may be difficult to 3D print even with FGF. The goal of using this TPE is to fabricate ultra-soft products, including inflatables, directly using FGF.

- **Chapter 7 High Performance – Amorphous,** then evaluates the other spectrum of thermoplastic materials i.e., high performance thermoplastics. This chapter will employ amorphous PEI for FGF of injection molding inserts.
- **Chapter 8 High Performance – Semi-crystalline,** is the last experimental chapter in which the FGF extruder will be used to extrude and 3D print using PEEK. This high-performance polymer is a semi-crystalline material which makes it difficult to accurately 3D print with. PEEK is a topical material due to its myriad of applications. Successful 3D printing PEEK directly from granulates using a small scale FGF system would demonstrate the flexibility of the technology whilst also highlighting its wide application portfolio.

Finally, Chapter 9 will make conclusions on the combined findings of all the subjects covered by Chapter 2 and Chapter 5 to 8. Any future work identified will also be listed in this chapter.

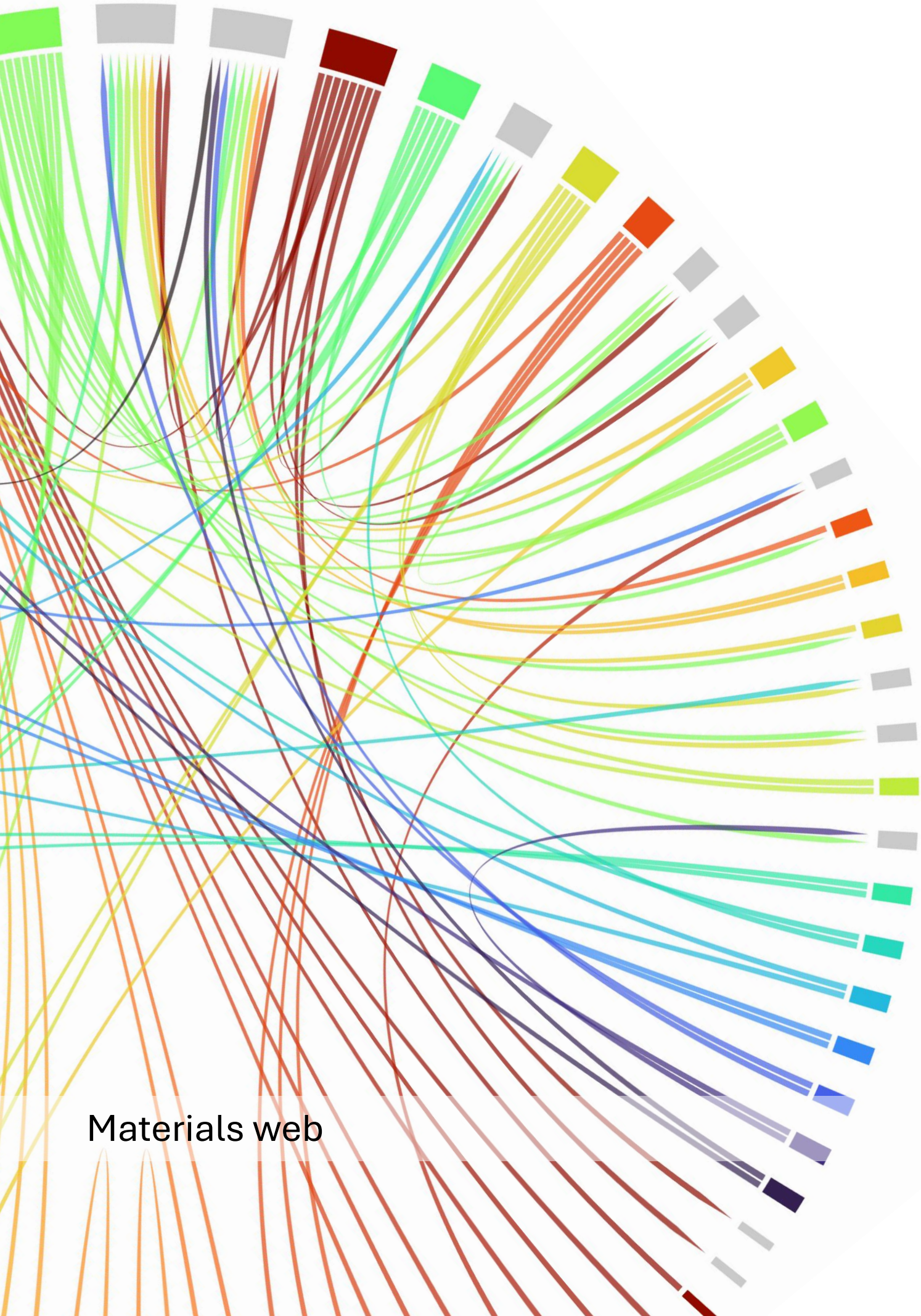

Materials web

2 State of the Art

2.1 Single Screw Extrusion

2.1.1 General Process

Polymer processing was defined by Bernhardt and McKelvey back in 1958 as an engineering activity which involves operations conducted on polymeric materials or systems to increase their utility [38]. Screw extrusion is amongst the most used techniques of polymer processing. What makes screw extruders attractive is their simple design, continuous extrusion capability, reliability and performance to cost ratio [17]. A schematic of a single screw extruder is shown in Figure 2.1. This technique not only can shape the raw polymeric material into a desired product but it can also impart additional functionality. A common example is the alteration of mechanical properties via the inclusion of modifiers such as reinforcing fibres. Other modifications are more visual, such as the addition of colourants to impart a desired colour on the product [20]. These two examples should indicate how versatile screw extrusion technology is and why it is so widely applied to industrial and mass production processes, such as profile extrusion. Its wide application has made it the subject of study of multiple research groups, intent on improving its understanding and optimising the process. Before delving further in this subject, it is first better to understand the core concepts.

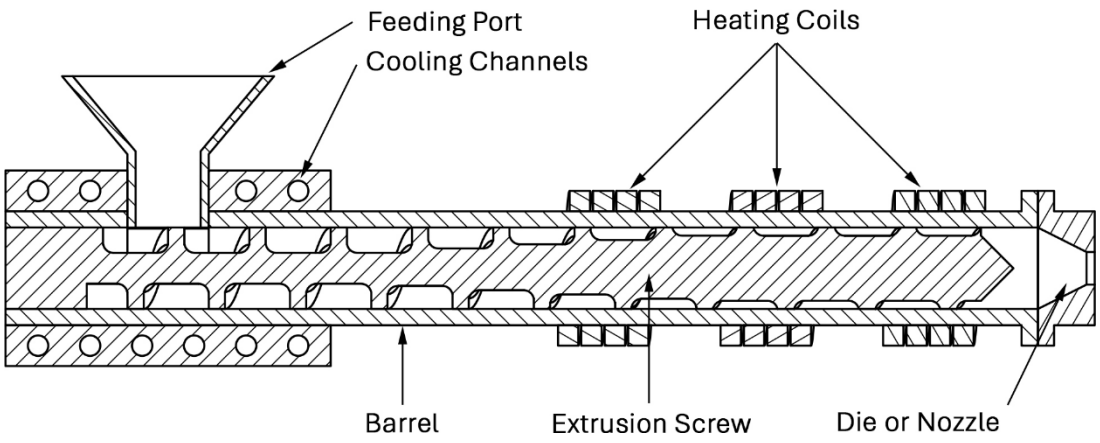

Figure 2.1 - Schematic diagram of an empty single screw extruder with basic sub-assemblies.

In its simplest definition, an extruder is a device that melts and forces material through a die or nozzle. The extruder product is then referred to as the extrudate. A screw extruder, rotates an extrusion screw to pressurise the material, melt, and then extrude it. A general representation of a single screw extruder which is often used in mass production and industrial processes, is shown in Figure 2.1. The screw extruder comprises of a feeding end (left), where the solid and raw material is fed, and an

extrusion end, where the molten material is extruded through a die (right). The feeding end including the hopper and the initial length of the screw, is kept cooled, usually using a liquid cooling system. The rest of the extrusion screw is then heated by multiple band heaters, each with independent temperature control. These heaters are mounted on the barrel that encases the extrusion screw. The die, located at the hot end of the extruder, serves as the outlet through which material is forced. The shape of the extrudate replicates the shape of the die orifice [17].

The main tasks of a screw extruder are solid conveying, plasticating, melt conveying and extrusion. Solid conveying, as the name implies, refers to the movement and packing of the solid granules inside the screw. This process generates a high amount of pressure by two means namely, gravity and drag induced solid conveying. It occurs at the cold end of the screw, as shown in Figure 2.2. Gravity solid conveying is often limited to the hopper whereby the weight of the granules induces a pressure component. The other pressure component is derived from the rotation of the screw. As the granules are conveyed around the barrel by the screw, the friction between the granules and the barrel should be higher than that between granules and screw. In this manner, a drag induced pressure component is generated on the granules [17, 20].

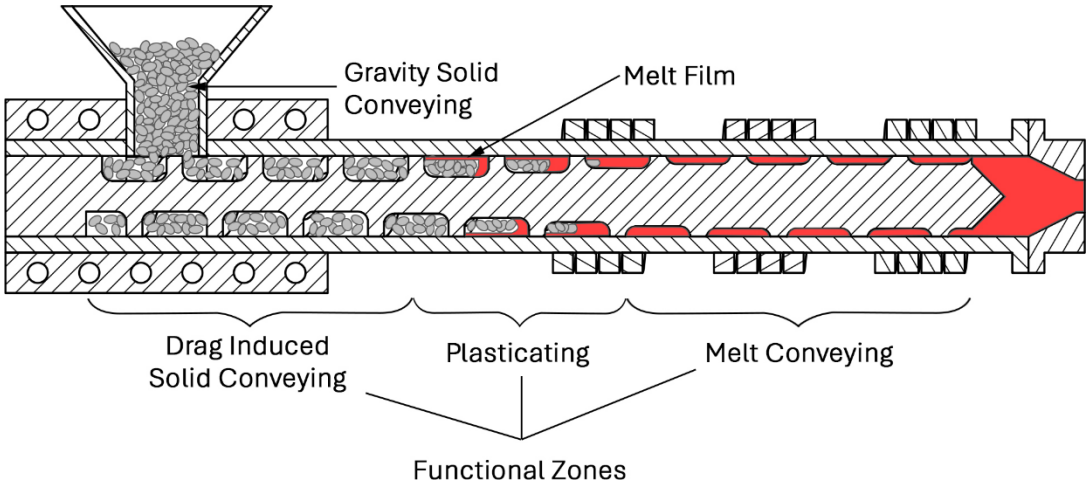

Figure 2.2 – Schematic diagram of shift from solid conveying to melting and melt conveying in operational single screw extruder.

The transition from solid conveying to melt conveying functional zones is the plasticating stage. In this functional zone, a melt film is created at the barrel surface which marks a change in the behavior of the material. This is also the start of the melting process as the solid granules are molten and eventually extruded. The last functional zone is the melt conveying section which generates part of the pressure necessary to extrude the

material through the die. To achieve proper plastication, the screw extrusion process must ensure near complete melting of the material before being extruded through the die. This can be ensured through process parameter optimisation and correct screw and barrel design [17, 20]. Such design optimisations have been the subject of a number of studies, as will be seen in the following sections.

2.1.2 Screw Geometry

Although a screw extruder comprises of multiple components, the most important is the extrusion screw itself. The design of the screw has a significant impact on the operation of the screw extruder. All other sub-assemblies will be discussed in later sections.

An example extrusion screw, with the most relevant geometric features, is shown in Figure 2.3. The classic extrusion screw is divided into three geometric sections namely, feeding, compression and metering sections. These geometric sections are similar to the functional zones described in the previous sections but functional zones are process and not geometry dependent. The feeding section is cooled to prevent premature melting, ensuring that it functions as a solid-conveying zone. Without this cooling, the extrusion screw's pressure generation capability could be compromised as part of the feeding section would be acting as a plasticating functional zone instead of solid conveying. Furthermore, cooling is necessary to protect the motor and bearing system which is used to drive the extrusion screw. The next section is the compression section at which point the material is being plasticated. The degree of melting achieved depends on the screw geometry, material and process parameters used. In this section, any voids in the bulk are removed by linearly decreasing the channel cross sectional area along the length of compression section. By the start of the last section i.e., the metering section, all the material must be molten and compressed. The metering section should predominantly act as a melt conveying zone to meter the flow of material and so ensure a consistent throughput [17, 20].

The length of each section has an effect on the extrusion performance. Extrusion screw design must take into consideration the optimal section lengths for an effective extrusion process. Lengthening the feeding section may increase pressure generation. Shortening the compression section will increase the compression gradient i.e., how rapidly the channel cross-sectional area is decreasing from the feeding section to the metering section. The steeper the compression gradient the greater the pressure loss in

this section, caused by the compression process. More pressure is necessary to compress the material in a shorter length. Similar to the feeding section, lengthening the metering section will increase the back pressure acting on the die. Any alterations in the lengths of these three sections will have significant effects on the extrusion performance. In general lengthening each section will create a positive effect to some extent, beyond which the effect becomes negligible or even deleterious [17, 20].

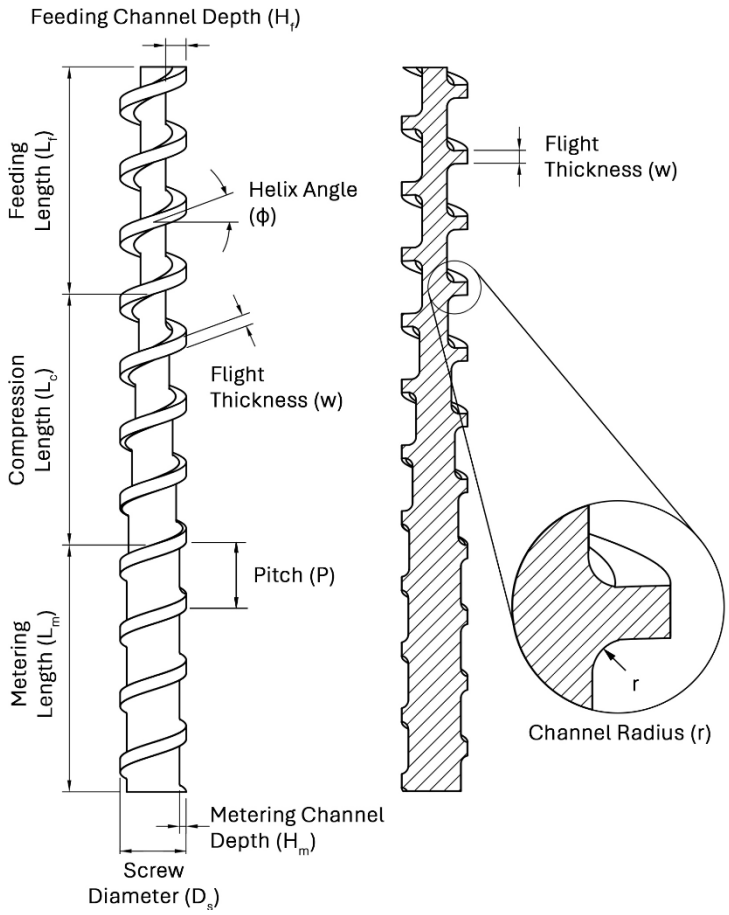

Figure 2.3 – Key geometric features of extrusion screws.

The channel depth of the feeding (H_f) and metering (H_m) sections is also relevant. Decreasing the channel depth will decrease the channel cross-sectional area, as shown in Figure 2.4. At a minimum, the channel depth of the feeding section has to be deep enough to accommodate the material granulates. The ratio of the feeding section channel depth to the metering section channel depth is known as the compression ratio. This value is widely used as one of the key specifications of the screw and in polymer processing guidelines. Generally, the value ranges from 1.5:1 to 4:1, with the most commonly used ratios being 2:1 or 3:1. Despite its popularity, the compression ratio on its own is not relevant as it is the taper of the compression section that governs the

process. This is defined in Equation 2.1, where L_c is the compression length [20, 39]. A large taper may result in pressure surges which have negative effects on screw wear and extrudate throughput [17].

$$A = \frac{dH}{dz} = \frac{H_f - H_m}{L_c} \qquad \textit{Equation 2.1}$$

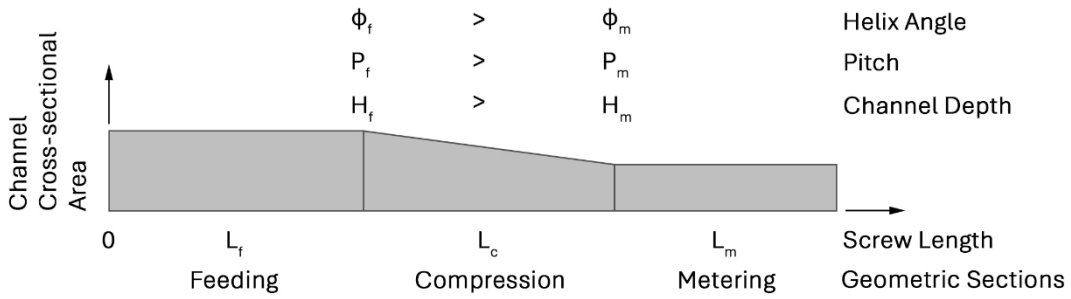

Figure 2.4 - Effect of varying helix angle, pitch and channel depth on the channel cross-sectional area along screw length.

Helix angle (φ) and screw pitch (P) are related geometric features, as defined by Equation 2.2, where D_s is the screw outer diameter. The traditional extrusion screw uses the so called square pitch where the pitch is equal to the screw diameter, which results in a helix angle of 17.66°. Multiple studies have demonstrated that whilst such a helix angle was proven to work, it is often not the optimal value to maximise throughput or energy efficiency [17]. Furthermore, in most optimisation scenarios, the helix angle also varies along the length of the screw in a similar fashion to channel depth [17]. In turn, it also has an effect on the channel cross sectional area as illustrated in Figure 2.4.

$$\tan(\varphi) = \frac{P}{\pi D_s} \qquad \textit{Equation 2.2}$$

The last two geometric features, namely the flight width and channel radius, are critical features for a mechanically sound screw. A flight width which is too thin and a channel radius which is too small, will not have enough strength to take up the load produced during screw extrusion. This is especially true for large extrusion screws intended for mass production of large products. A flight radius, in the range of 0.5 to 1.0 of the channel depth, will not only provide good mechanical support to the flight, but it will also improve pressure generation. On the other hand, a large flight radius for a small channel size can significantly decrease the overall channel area which results in a decreased throughput. It should be noted this statement was derived from a study conducted on a 63.5 mm diameter screw with a channel depth of 11.1 mm [40]. Provided that the largest dimension of a generic thermoplastic granule is of 4 mm, the channel depth of 11.1 mm

is more than double this value. It is therefore difficult to conclude whether the conclusion that increasing channel radius decreases throughput is transferable to smaller sized extrusion screws intended for AM. With regard to flight width, increasing its size will increase strength but it will also make the extrusion process less efficient. This effect is related to flight clearance and the ensuing leakage flow it creates [17].

Flight clearance is a hidden but crucial geometric feature of screw and barrel assemblies. The standard clearance is of 0.001 the barrel internal diameter which is large enough for molten polymer to flow through. This flow is called leakage flow which is one of the three flows that occur during polymer extrusion as shown in Figure 2.5. Its direction depends on several factors including the magnitude of pressure flow and drag flow which are the other two major flows that occur. The greater the screw to barrel clearance, the greater the leakage flow, which in turn can decrease the melting rate of the material [17].

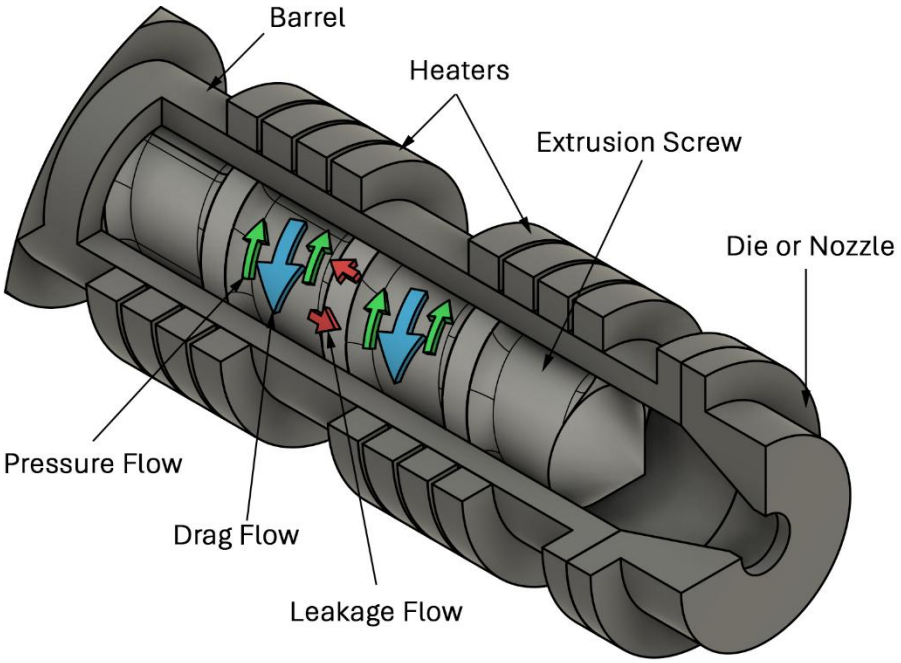

Figure 2.5 - Schematic diagram of polymer flow during screw extrusion.

Leakage flow has a strong relationship with flight thickness. A thicker flight results in a larger squeeze area through which the polymer must leak. This results in increased power consumption due to an overall increase in screw resistance to rotation. The thin nature of the cross-section through which leakage flow occurs, leads to high localised shear stresses which will induce shear heating. This in turn leads to high localised temperatures with the possibility of undesired polymer degradation. Decreasing flight

width and increasing the channel width will increase extrusion power efficiency at the cost of decreased screw flight strength. Leakage flow is not an issue at the feeding end as it is a solid conveying functional zone. In this screw section, increasing flight width will provide the necessary strength to sustain the higher pressures in this region without compromising extrusion power efficiency [17].

In order to decide the correct values for each of the geometric features just discussed, a theoretical background is necessary. In this manner the governing principles are quantified and an extrusion screw may be designed.

2.1.3 Theory

The first research published which studied the melting behaviour in a screw extruder can be attributed to Maddock [41]. His work involved performing screw-freezing experiments where a screw was pulled-out when operating steadily to investigate the actual melting behaviour of the thermoplastic therein. From his observations, Maddock noted that the polymer first melts as a thin film at the interface between the solid pellets (solid bed) in the screw channel and the heated barrel. This thin film is actively dragged by the rotating screw and pushed downwards towards the leading flight of the screw, as shown in Figure 2.6. A melt pool is formed in this region which builds up pressure and in turn compresses the solid bed, thus actively decreasing its width. The height of the solid bed remains relatively constant throughout the whole process. The material movement is defined by the cross-channel barrel velocity V_{bx} (m/s) and the cross-channel velocity V_{sy} (m/s) of the solid bed. The geometric nomenclature is delimited by the melt film thickness δ (mm), solid bed width X (m), channel width W (m) and channel depth H (m).

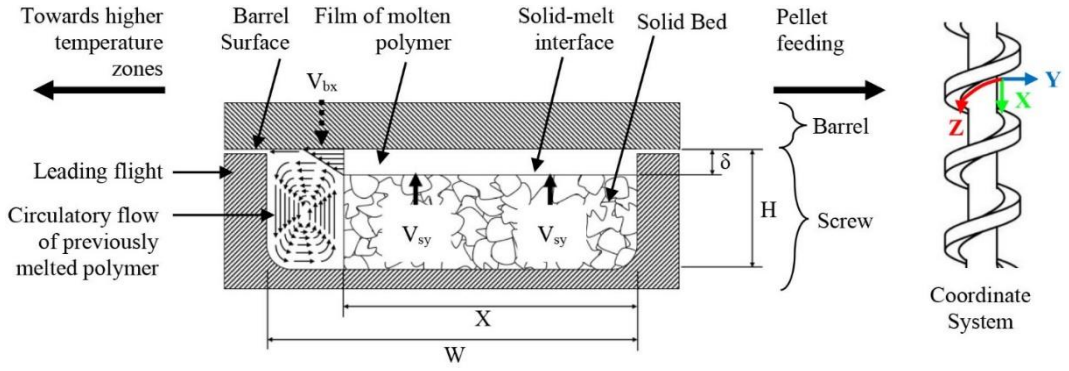

Figure 2.6 - Model diagram of the drag induced melting mechanism in screw channel cross-section with coordinate system.

The Maddock melting mechanism just described is not the only possible melting mechanism that can occur during extrusion albeit, it is the most common. Another two

models were identified, one by Klenk when extruding polyvinyl chloride (PVC) [42] and another by Lindt which was observed first when extruding polypropylene (PP) [43]. All the three melting mechanisms are shown in Figure 2.7. The Klenk model is similar to the Maddock model with the key difference being that the melt pool collects on the passive flight rather than the active flight. The Lindt model differs from the other two as it does not consider a melt pool but instead the solid, unmolten material is encased within a volume of molten material. To predict the melting performance of an extrusion process, the first step is to identify the dominant melting mechanism. Next the correct theoretical model which simulates that type of melting should be applied to predict the melting performance of the extrusion process. Given the relative rarity of the Klenk and Lindt mechanisms in most material extrusion processes, these mechanisms will not be considered further as they probably do not represent a major fraction of the extrusion processes in FGF. For the same reason, the vast majority of studies found in literature are dedicated to the Maddock melting mechanism [44].

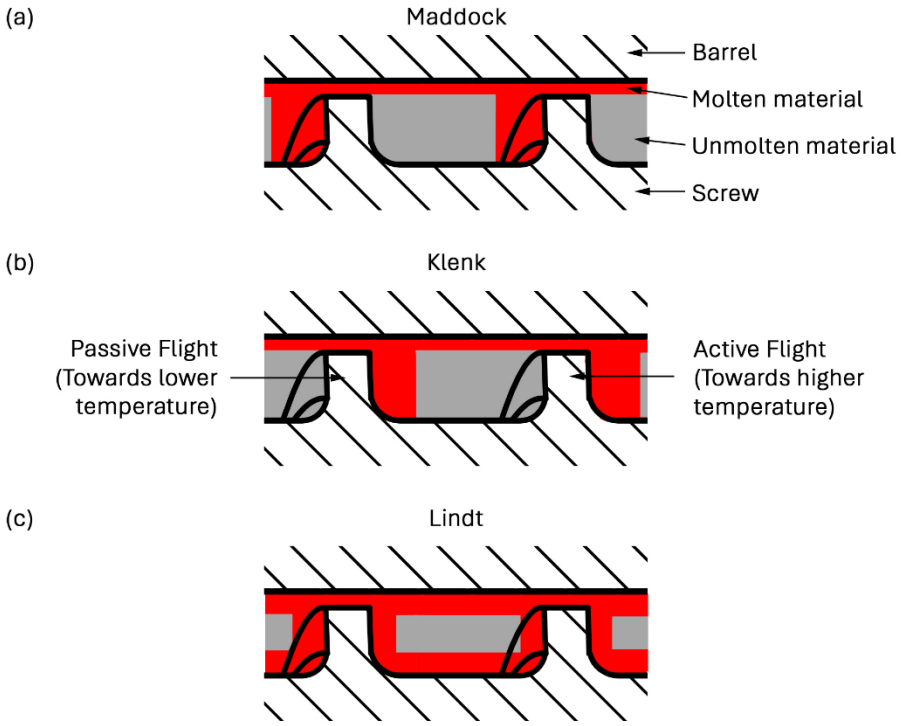

Figure 2.7 – Melting mechanism of (a) Maddock, (b) Klenk and (c) Lindt in single screw extrusion.

Using the screw freezing experimental results provided by Maddock, an analytical model was developed years later by Tadmor. The model use material, geometric and process parameters data to predict the melting rate of the material inside the screw. The original model had a number of assumptions and some of which had a strong, incorrect contribution to the end result. Tadmor further refined and validated his work with

multiple successive publications [45–47]. Subsequent researchers that continued to develop the original model aimed to decrease its main simplifying assumptions. These works led Mount et al. to argue that in general, the Tadmor model erroneously predicted the melting rate and only by coincidence it could predict the solid-bed profile [48]. The profile prediction is significantly related to the calculations used to determine the solid bed velocity [49]. The crux of the problem was that the Tadmor model assumes a constant solid-bed velocity along the length of the screw which is known to be incorrect. In practice, the velocity will change due to tapering screw sections, changes in barrel temperature, and the decreasing depth of the screw channel towards the metering section.

The validity of the Tadmor model remains a contentious subject. A study brought forward by Altinkaynak *et al*. demonstrated that the Tadmor model predictions of the melting rate were similar to those produced using numerical simulation and to those observed using empirical testing of the same extrusion setup [49]. These results nonetheless have to be taken in context. The study made use of a 63.5 mm diameter screw with a length of 1333.5 mm which ensures a large channel depth to screw diameter ratio. In contrast, an FGF extrusion screw generally has a low depth to screw diameter ratio. This makes the assumption taken by the Tadmor model inadequate as it defines the extruder channel as a rectangle without curvature [44].

It is not just analytical models that have limitations, computational models also come with their own challenges. Arguably the most advanced techniques available at the time of writing are modelling of the solid conveying zone using discrete element method (DEM) coupled with computational fluid dynamics (CFD). DEM is best suited for solid conveying and plasticating functional zones as it simulates interactions between single granulates [44]. This allows for an accurate representation of the solid conveying process but it suffers from two principal drawbacks. On a first note, DEM is a time consuming and computational heavy process as it requires a short time step to be able to accurately simulate the momentum exchange between granulates. The other issue is that to obtain accurate results, accurate material properties and attributes are necessary [50].

The most significant defect which is common to both analytical and computational techniques is the determination of key material and equipment attributes that have a significant impact on the simulation result. Probably the most important and difficult to

obtain values are the screw and barrel coefficients of friction with granules [17]. Variations in these values will cause significant changes in results. Part of the challenge is obtaining accurate values for the coefficients of friction, which is rather complicated given the high temperature environment involving complex curved surfaces. The matter is further complicated by the nature of these values. If in practice, an extruder was first used with a material e.g., ABS and then switched over to PP, then the previous material will leave residue on the screw and barrel, leading to altered coefficients of friction which may in turn change with time as subsequent extrusion runs wear away old residue. This is all to argue that despite the best effort to predict the melting rate in an extrusion screw, the nature of the subject at hand makes accurate predictions difficult even when using computational modelling.

Despite its short comings, the Tadmor model remains useful as it provides an approachable method to predict the melting performance of a screw design. It makes use of simple equations which have to be evaluated over section of the screw length. This simplifies the prediction of material melting during the extrusion process, without having to deal with the extra cost and complexity of computational modelling [49]. For these reasons it may be useful to delve further in the non-isothermal drag flow of a power law fluid model described by Tadmor and Gogos in their latest known publication which dealt with the most poignant issues of the original model [20].

The equations listed from Equation 2.3 to Equation 2.19 describe the Tadmor analytical model for the melting rate and solid bed profile in a single screw extruder [20]. This model assumes that there exists a steady state in which the velocity and temperature of the thermoplastic at any given cross-section of the extruder screw are constant with time. The solid bed is assumed to be homogenous and continuous. The cross-section of the screw channel is assumed to be a rectangle, i.e. the channel is not filleted and has sharp corners. Melting is assumed to take place solely at the surface in contact with the barrel which is taking part in a drag-induced melt removal mechanism. This model does not take note of the non-linear temperature profile in the melt film nor the effect of flight clearance between the screw and barrel. The latter assumption is generally the most significant [20].

The rate of melting is defined by Equation 2.3 where V_b is the barrel speed (m/s), ρ_m is the melt density (kg/m^3), k_m is the thermal conductivity of the polymer (W/m°C), T_b is the barrel temperature, T_m is the melting temperature of the polymer, X is the solid bed width,

λ is heat of fusion (J/kg), C_s and C_m are the polymer's heat capacity in solid and molten form respectively (J/kg°C). By removing the root of the solid bed width ($\sqrt{X}$) from Equation 2.3, the term Φ can be defined by Equation 2.4 which is a useful simplification for later calculations.

$$w_L(x) = \sqrt{\frac{V_{bx}\rho_m U_2\left[k_m(T_b - T_m) + \frac{U_1}{2}\right]X}{2[\lambda + C_s(T_m - T_{s0}) + C_m\bar{\Theta}(T_b - T_m)]}} = \Phi\sqrt{X} \qquad \textit{Equation 2.3}$$

$$\Phi = \sqrt{\frac{V_{bx}\rho_m U_2\left[k_m(T_b - T_m) + \frac{U_1}{2}\right]}{2[\lambda + C_s(T_m - T_{s0}) + C_m\bar{\Theta}(T_b - T_m)]}} \qquad \textit{Equation 2.4}$$

The melt film thickness δ (mm) is found using Equation 2.5. The terms U_1 (N/s) and U_2 are defined in Equation 2.6 and Equation 2.7 respectively. U_2 represents the reduction of the rate of melt removal by drag flow. This may be caused by the change in viscosity brought about by a change in temperature along with the shear thinning behaviour of a given material. $U_1/2$ represents the rate of viscous dissipation per unit width in the melt film. The $k_m(T_b - T_m)$ term in Equation 2.4 represents the heating by conduction in the material. Therefore, by comparing the former and latter terms just described, one would compare the viscous dissipation and heat conduction also known as the Brickman Number (Br) as shown in Equation 2.8.

$$\delta = \sqrt{\frac{[2k_m(T_b - T_m) + U_1]X}{\rho_m V_{bx} U_2[\lambda + C_s(T_m - T_{s0}) + \lambda + C_m\bar{\Theta}(T_b - T_m)]}} \qquad \textit{Equation 2.5}$$

$$U_1 = 2m_0 V_j^{n+1}\bar{\delta}^{1-n}\left(\frac{e^{-b\prime} + b\prime - 1}{(b\prime)^2}\right)\left(\frac{b\prime}{1 - e^{-b\prime}}\right)^{n+1} \qquad \textit{Equation 2.6}$$

$$U_2 = \frac{2\left(1 - b\prime - e^{-b\prime}\right)}{b\prime(e^{-b\prime} - 1)} \qquad \textit{Equation 2.7}$$

$$Br = \frac{U_1}{2k_m(T_b - T_m)} \qquad \textit{Equation 2.8}$$

The term b' may be found using Equation 2.9 where a and n are terms which make part of the viscosity for a power-law fluid model as shown in Equation 2.10, where T (K) is the temperature of the material, $\dot{\gamma}$ is the shear rate (1/s), n is the power law index and a and m_0 are both co-efficient of viscosity. The b' term is also required to calculate the mean temperature $\bar{\Theta}$ of the melt film as shown in Equation 2.11.

$$b' = \frac{-a(T_b - T_m)}{n} \quad \text{Equation 2.9}$$

$$\eta = m_0 e^{-a(T-T_m)} \dot{\gamma}^{n-1} \quad \text{Equation 2.10}$$

$$\bar{\Theta} = \frac{\frac{b'}{2} + e^{-b'}\left(1 + \frac{1}{b'}\right) - \frac{1}{b'}}{e^{-b'} + b' - 1} \quad \text{Equation 2.11}$$

The down channel velocity V_{sz} (m/s) of the solid bed may be found with Equation 2.12, where G is the solid mass flow rate (kg/s) and ρ_s is the material solid density (kg/m^3). This is the weakest aspect of the Tadmor model as discussed previously. The barrel velocity V_b (m/s) is found using Equation 2.13, where N is the rotational speed of the screw (RPM) and D_b is the barrel diameter (mm). The more useful cross-channel barrel velocity V_{bx} (m/s) is found using Equation 2.14 where ϕ is the helix angle of the screw. The absolute difference between the barrel velocity and the velocity of the solid bed is V_j and is found using Equation 2.15.

$$V_{sz} = \frac{G}{\rho_S H W} \quad \text{Equation 2.12}$$

$$V_b = \pi N D_b \quad \text{Equation 2.13}$$

$$V_{bx} = V_b \sin\varphi = \pi N D_b \sin\varphi \quad \text{Equation 2.14}$$

$$V_j = \overrightarrow{V_b} - \overrightarrow{V_{sz}} = \sqrt{{V_b}^2 + {V_{sz}}^2 - 2V_b V_{sz}\cos\varphi} \quad \text{Equation 2.15}$$

For the feeding and metering sections, both of which have a constant depth, Equation 2.16 may be used to calculate the solid bed profile (*X/W)*, where X_1 (mm) is the previous solid bed width at Z_1 (mm), z (mm) is the current coordinate and ψ is a dimensionless number calculated using Equation 2.18. Similarly, the solid bed profile (*X/W)* of the compression section may be found using Equation 2.17, where A is the taper co-efficient calculated using Equation 2.19 and H_1 is the previous channel depth.

$$\frac{X}{W} = \frac{X_1}{W}\left[1 - \frac{\psi(z - Z_1)}{2H}\right]^2 \quad \text{Equation 2.16}$$

$$\frac{X}{W} = \frac{X_1}{W}\left\{\frac{\psi}{A} - \left[\left(\frac{\psi}{A} - 1\right)\sqrt{\frac{H_1}{H}}\right]\right\}^2 \quad \text{Equation 2.17}$$

$$\psi = \frac{\Phi}{V_{sz}\rho_s\sqrt{X_1}} \quad \text{Equation 2.18}$$

$$A = \frac{dH}{dZ} = \frac{H_1 - H_2}{N_{turns}\left(\frac{D_b}{\sin\varphi}\right)}$$ *Equation 2.19*

The model as presented predicts the melting rate in a screw extruder but to be able to do so it requires the throughput value *G* for a given set of parameters. For this reason, the Tadmor model may be a good tool to predict the behaviour of a screw for certain processing conditions. For example, whether extrusion will fail at lower barrel temperatures due to insufficient melting of the material. The model is not a good tool to obtain optimal values for pertinent screw geometric features such as channel depth. Nonetheless, it may assist in the design process by allowing estimation of melting rate at different feature values. In so doing it highlights any expected issue with a theoretical screw geometry. A better approach for screw design is to seek theoretical solutions for specific geometrical elements which optimise for throughput or energy savings. These types of results will be delved into, in the following section.

2.1.4 Theoretical Results

This section will report a number of important results originating from multiple studies that can guide screw geometric design. Some of these results are derived from theoretical models such as the Tadmor model described in the previous section, as well as numerical simulation models.

The only application of the Tadmor model to an FGF screw extruder was provided by La Gala *et al*. when using a conically shaped screw [51]. The study modelled ABS extrusion using the Tadmor model combined with a non-Newtonian fluid model with a Cross-like rheological material model, as shown in Equation 2.20, where τ^* is the critical cross model stress and $\dot{\gamma}_{cr}$ is the critical cross model shear rate both at the transition to shear thinning. The zero-shear viscosity is represented by η_0 [51].

$$\eta = \frac{\widehat{\eta_0}}{1 + \left(\frac{\eta_0 \dot{\gamma}}{\tau^*}\right)^{1-n}}$$ *Equation 2.20*

$$\widehat{\eta_0} = \eta_0 \left(1 + \left(\frac{\eta_0 \dot{\gamma}_{cr}}{\tau^*}\right)^{1-n}\right)$$ *Equation 2.21*

This contrasts with the classic Tadmor model which utilises the power law fluid model, shown in Equation 2.10. The power law model does not take into account the zero-shear viscosity experienced by a polymer but rather assumes shear thinning for all shear rates,

as shown in Figure 2.8. The switch towards the more complex cross model may be necessary due to the lower screw speeds generally used during FGF as opposed to conventional extrusion and injection moulding. This results in a lower shear rate that may be lower than that of the shear thinning zone and may instead be part of the zero-shear viscosity zone. In such a case, by using the power-law model the viscosity would be overvalued.

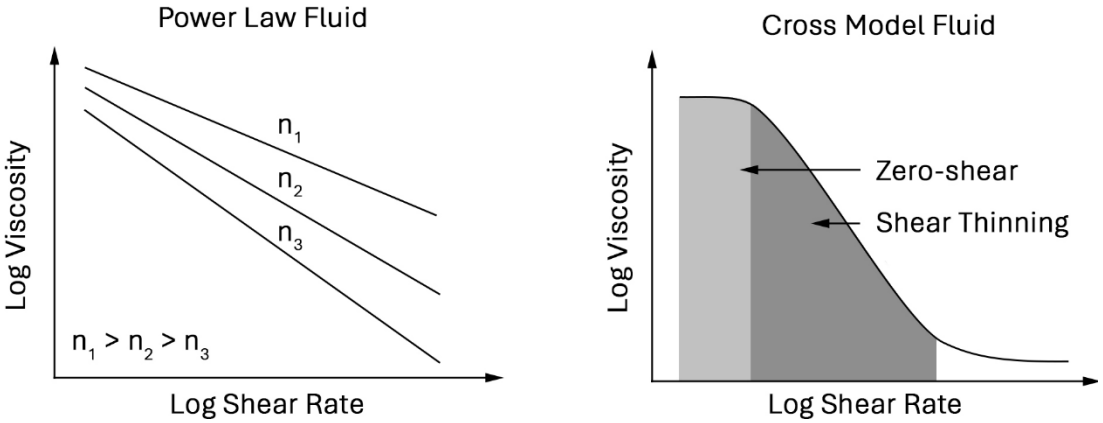

Figure 2.8 - Power law model vs cross model of a fluid.

The results presented by La Gala *et al.* were theorised using a 662 mm long screw with a diameter decreasing from 28 mm at the feeding end to 16 mm at the metering end. Such a screw is significantly smaller than a standard extruder which, for comparison, can have a length of 1333 mm and a diameter of 63.5 mm. Nevertheless, at 662 mm long, the FGF extruder presented by La Gala *et al.* is a large-scale extruder usually intended for large part production [51]. In such a scenario, the research team concluded that the FGF extruder had a higher share of polymer heating being produced by the extruder heaters rather than by viscous heating.

This same effect means that increasing screw speeds should increase throughput which in turn decreases the melting rate. This is a necessary result as the polymer has a lower residency time leading to a lower period of conduction heating. Increasing the compression ratio and helix angle resulted in an increase in melting rate. On the other hand, increasing channel width resulted in a decrease in melting rate. The material being processed also has a strong effect on the process. Material with a higher power law index will results in a better melting performance. This is expected as higher power law index values mean that the material is more viscous and will therefore generate a greater amount of viscous heating which explains the improved melting rate [51].

The results just discussed concern the plasticating region i.e., that region where the polymer granulates are being molten. Similar studies on conventional, large scale, single screw extruders were also conducted by Rauwendaal with important results shown in Figure 2.9. When it comes to helix angle, increasing helix angle increases the melting rate but little improvement is obtained if it is increased beyond 30°. For improved melting rate, it would be better to decrease the radial clearance instead. Doubling the standard clearance of 0.001D would result in a 25% reduction in melting rate, underscoring the importance of minimising this clearance value. Another important factor is flight width, the wider the flight the lower the melting rate [17].

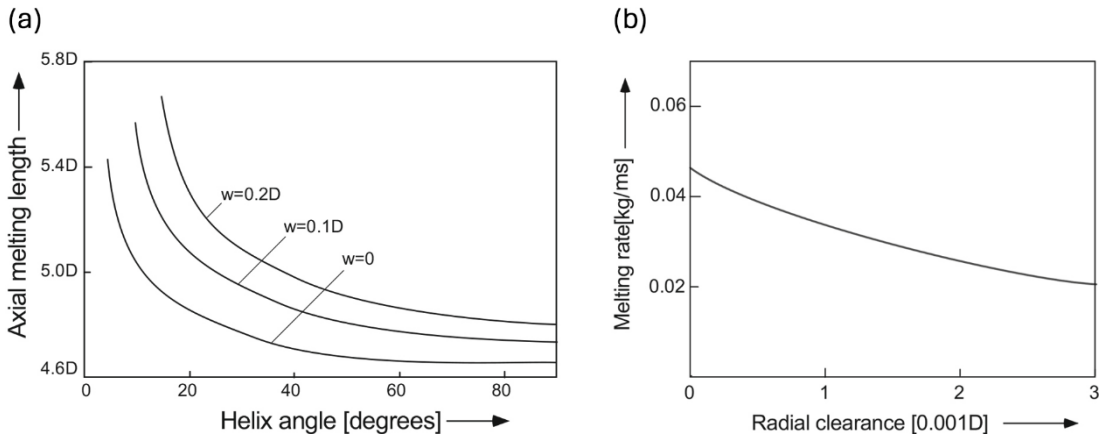

Figure 2.9 – (a) Axial melting length vs helix angle and (b) melting rate vs radial clearance for a large extruder setup [17].

The next step following plasticating is melt conveying. Simultaneous optimisation of helix angle and channel depth for either pressure generation or throughput yields the same results. The optimal helix angle is described by Equation 2.22, where $\widehat{w}$ is the reduced flight width defined by Equation 2.23, with result as shown in Figure 2.10 (a). This solution assumes a non-Newtonian fluid described using the power law, as shown in Equation 2.24 which assumes that the representative shear rate in the channel is the Couette shear rate.

$$\sin(\varphi) = \left(\frac{n}{2n+2}\right)^{1/2} + \widehat{w}\left(\frac{n+2}{4n}\right) \qquad \textit{Equation 2.22}$$

$$\widehat{w} = \frac{w}{\pi D} \qquad \textit{Equation 2.23}$$

$$\eta = m\left(\frac{\pi D N}{H}\right)^{n-1} \qquad \textit{Equation 2.24}$$

The optimal channel depth does not have a simple solution as it depends on screw speed, screw diameter, consistency index (m) and pressure gradient. A two dimensional

power law, numerical simulation result was proposed by Rauwendaal and is shown in Figure 2.10 (b) but the actual process parameters used are not available as open access [52]. The numerical results indicate that the analytical solution possibly overvalues the optimal helix angle.

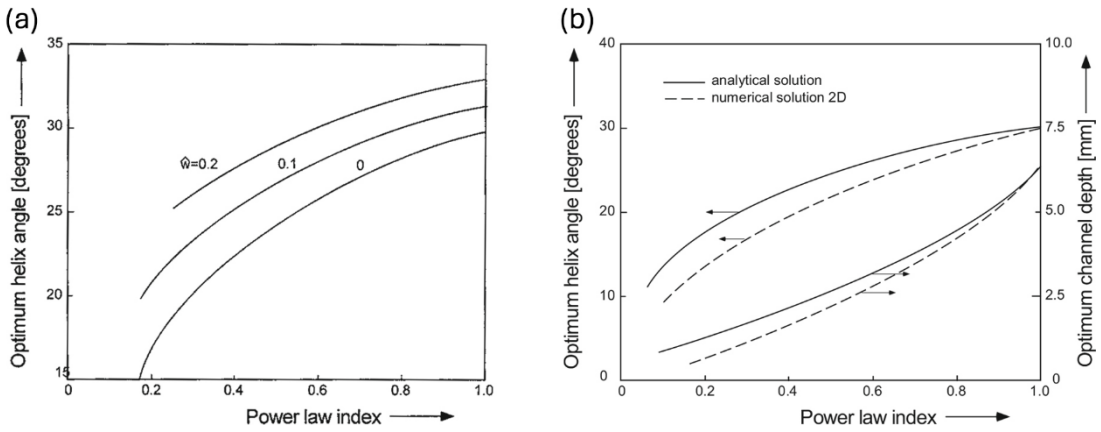

Figure 2.10 – Optimal helix angle for various values of reduced flight width vs power law index, using an analytical theory (a) and optimal helix angle and optimal channel depth vs power law index using analytical and 2D numerical solution [17].

The previous results focused on optimising for throughput. In the case of FGF, especially for small scale, optimising for power consumption may also be beneficial. Determining the optimal helix angle and channel depth in this case becomes related to the pressure being generated in the extruder [17]. All results available in literature were produced with large extruders in mind, such as those with a 50 mm diameter screw. For this reason, there are no theories which can be used to guide small scale extruder design for optimal power consumption.

To optimise for power consumption, apart from helix angle and channel depth, a major contributor is flight width. The wider the flight width, the greater the volume through which there is leakage flow. This kind of flow requires a lot of power to go through the thin gap, which would be otherwise used to generate throughput. The flight width contribution to power consumption depends on the ratio of flight width to the sum of flight width and channel width. If the ratio is 0.1, leakage flow would cause 40% of the power consumption produced by the extruder, as shown in Figure 2.11 [17]. It is therefore clear that the flight width should be minimised as much as possible whilst maintaining structural integrity.

The results presented in this section provide some guidance towards optimal design of an extrusion screw for a given application. These revolved around the selection of helix

angle, channel depth, flight width and flight clearance. There are other fundamental design decisions which have not been covered as they are of a basic mechanical nature. A prime example being the determination of the shaft size that has sufficient torsional strength. These design decisions may not necessarily be decided using complex extrusion prediction theories but rather by more a practical approach. For example, it is more sensible to select the screw shaft size that can sustain the max torque generated by the driving motor, in order to minimise risk of damage. The other option would be to consider the maximum torque resistance created by the extrusion process but that would not take into account unexpected issues, such as screw stalling by contact with barrel. These topics will be covered further in Chapter 4. The next section will lightly discuss other extrusion systems and components that are important to general polymer processing.

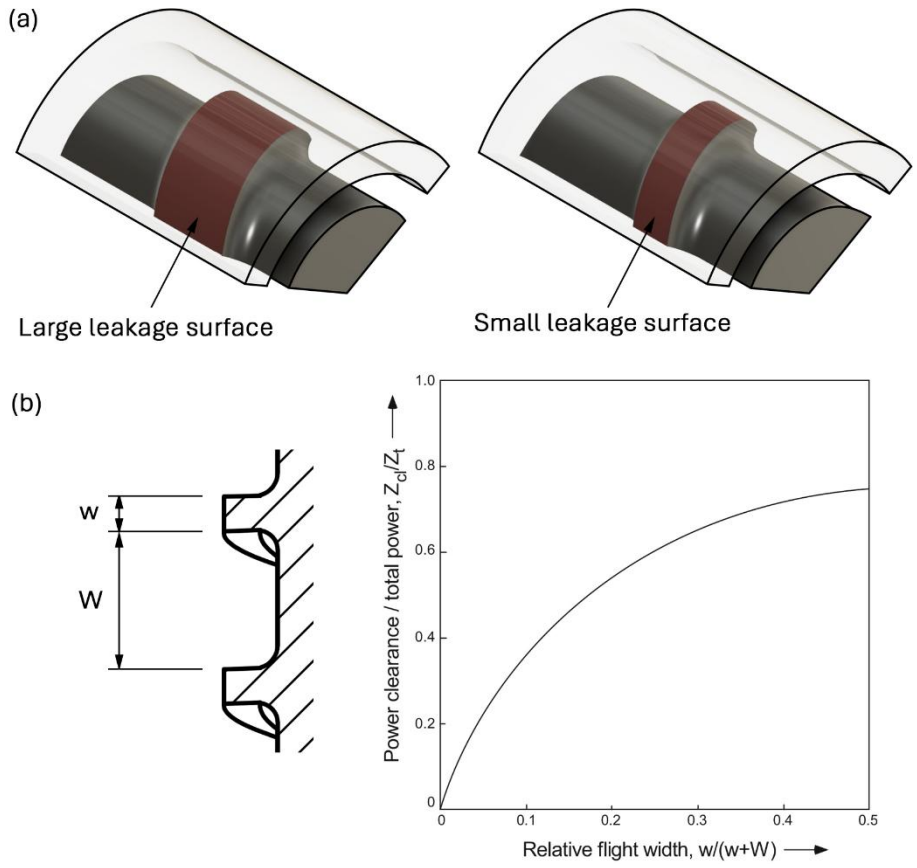

Figure 2.11 – Comparison between large and small leakage surfaces (a) and the ratio of power consumption taken up by flight clearance (b) [17].

2.1.5 Other Systems

The single screw extruder, as shown in Figure 2.1 is arguable the simplest setup currently available for extruding granulate material. This kind of setup can deal with most

common thermoplastics but only for plasticating and extrusion. If instead, the polymer has to be blended or reinforced with some additive, then modifications are necessary to the core extrusion concept. Common additives include fibre reinforcement, colouring agents, bulk fillers, flame retardants and UV stabilisers. These additives need to be dispersed and distributed in the polymer matrix for correct use [17].

Dispersive mixing involves the break-up of the minor component of a mixture into smaller size particles or droplets, whereas distributive mixing leads to a homogeneous spatial distribution of the minor component into the polymer matrix, as shown in Figure 2.12 (a) [53]. Not all additives require both distributive and dispersive mixing but in general it is preferable to have both in order to achieve complete mixing. One method available for achieving this level of mixing is by using a single screw extruder with a mixing section included. There are multiple designs of mixing sections available each with different levels of distributive and dispersive mixing. Furthermore, different section designs have different pressure drop levels, barrel wiping effectiveness and instances of dead spots. Some examples of mixing sections are shown in Figure 2.12 (b). These mixing sections are generally added as the last part of the extrusion screw, right after the metering section.

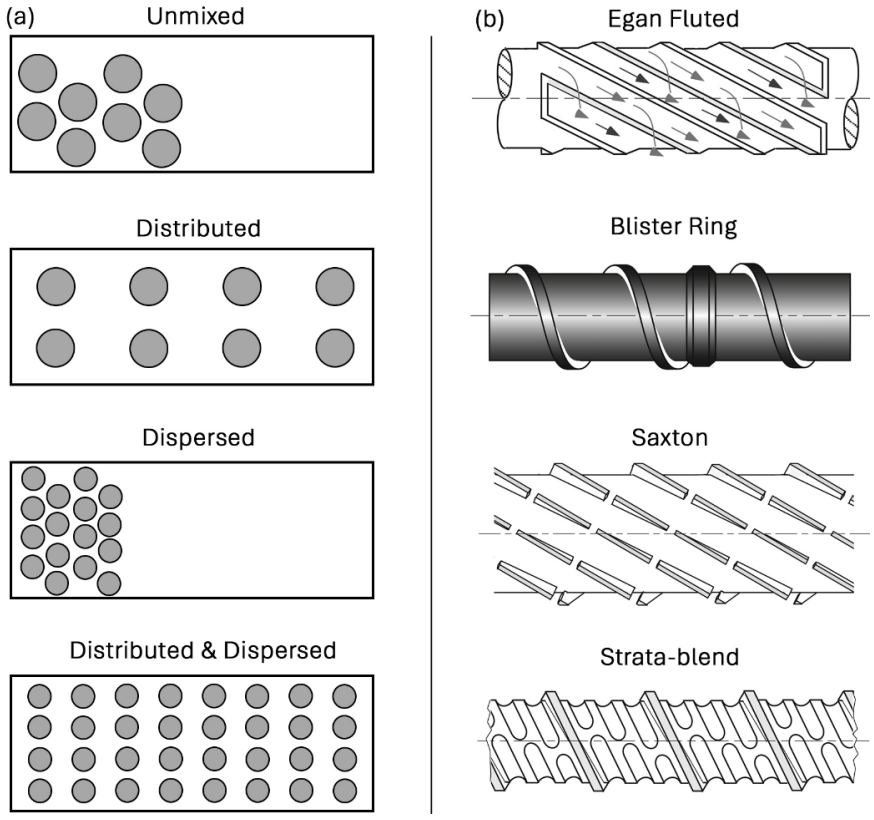

Figure 2.12 - Distributive and dispersive mixing demonstration (a) and examples of mixing sections (b) [17].

Apart from screw mixing sections, mixing can be achieved by including static mixers. A static mixer is a stationary device, often placed right after the screw and before the extruder die, whose main purpose is to divert the polymer flow and thus create a mixing effect. An example of such a mixer is shown in Figure 2.13. Static mixing section cause significant pressure drops in the melt but have the advantage of being modular i.e., they can be added to existing extruder systems without changing the screw. For this type of mixing sections, the design of the extrusion screw may require modification to ensure sufficient pressure generation to extrude properly [17].

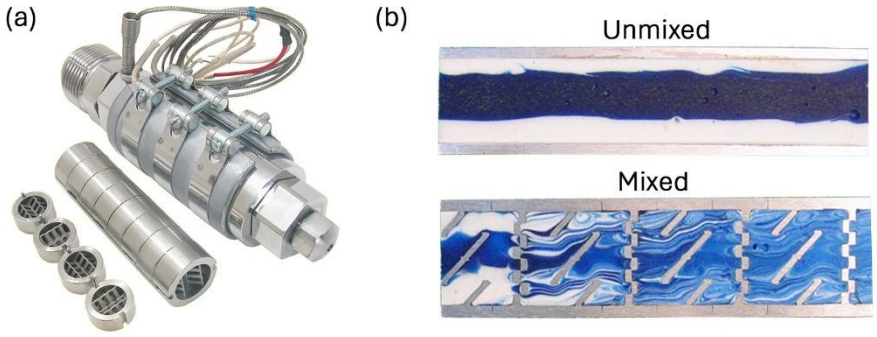

Figure 2.13 - Example of static mixers (a) with cross-section view of bi-coloured flows with and without its operation (b) [54].

Even higher quality mixing can be achieved with the used of twin-screw extruders, an example of which is shown in Figure 2.14 (a). Twin-screw extruders have two principle established applications namely, extrusion of thermally sensitive materials and speciality polymer processing such as compounding, devolatilization and chemical reactions. The subject of twin-screw extruders is rather involved as multiple design variations exist. These including different screw rotating mechanisms and various screw sections, as shown in Figure 2.14 (b). It suffices to note that twin screw extruders offer a greater control over the extrusion process by utilising various screw geometries to modify the material as necessary. Twin screw extruders are generally considered as significantly more complex than single screw extruders, a fact which is also reflected in their cost [17].

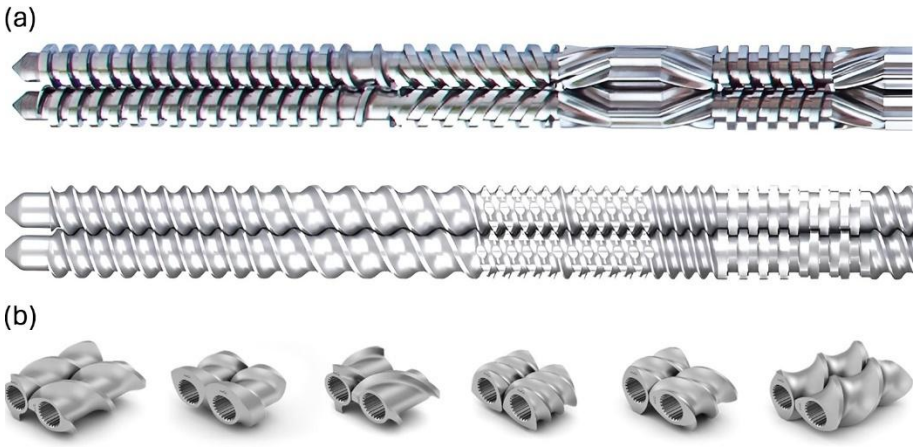

Figure 2.14 - Example of twin screws (a) and separate sections (b) [55, 56].

This section does not purport to report all aspects of screw extrusion and in multiple occasions it mentions aspects of complex subjects. The latest two topics i.e., mixing and twin-screw extruders, are perfect examples of vast subjects which were barely introduced in this section. This choice was necessary as the subject of FGF screw extrusion is still in its infancy and has not yet even tested all the geometries and methods available to the general extrusion subject. Often the biggest challenge is to miniaturise existing technologies and, in the process, carry out the necessary modifications. The next section will delve in FGF additive manufacturing to better understand its history along with the most recent developments in this research field.

2.2 Fused Granulate Fabrication

2.2.1 Introduction

Additive Manufacturing (AM) continues to grow rapidly, with techniques making up a substantial part of this industry. Among these polymer-based techniques, material extrusion (MEX) AM is one of the most widely used processes. While Fused Filament Fabrication (FFF) is the dominant MEX method, Fused Granulate Fabrication (FGF) presents notable advantages [24]. By eliminating the need for filament production, FGF expands significantly material choices, lowers energy consumption, and enhances sustainability. It also reduces costs, increases 3D printing speeds, and facilitates easier experimentation with new materials [21]. Furthermore, FGF aligns with circular economy principles, supporting key United Nations sustainability goals [11].

Since the last systematic review of FGF, published in 2021, the field has experienced rapid growth, with the volume of published literature more than doubling. This increase

in research output has led to a need for a more recent understanding of current FGF technology. For this reason, an updated literature review that determines both the latest developments as well as changes in research trends, is necessary.

The origin of recent research developments in the field may have a significant correlation with the type of research being conducted. A research group with multiple published articles along the years would highlight a consistent effort towards FGF development. Understanding these aspects along with the geographic distribution of research activity could facilitate future collaborations and enhance knowledge sharing within this research field. In this manner, the development of FGF could be enhanced and accelerated.

One prominent trend in FGF research is the expanding variety of materials used. Although FGF system manufacturers often claim a broad range of compatible materials, users have reported otherwise, particularly when using materials other than standard options such as polylactic acid (PLA) and acrylonitrile butadiene styrene (ABS) [21]. This issue is particularly pertinent for high-performance thermoplastics, such as polyether ether ketone (PEEK), where FGF systems present a cost-effective alternative to FFF. Similarly, FGF demonstrates superior capabilities in 3D printing elastomers as opposed to FFF [37]. Therefore, it may be interesting to evaluate what was achieved with this improved technology and which materials in general have been used with FGF.

The large variety of thermoplastics and their composites that may be 3D printed using MEX techniques has contributed to the development of a number of FGF screw extruder designs. Previous classifications may no longer adequately capture the nuances of recent innovations, which highlights the importance of a systematic review to provide a more accurate and up-to-date framework.

This study aims to provide a comprehensive overview of the current state of FGF research by identifying key research groups and geographical regions involved in FGF research, analysing past and recent trends driving the field, examining the subjects and applications covered by studies utilizing FGF, as well as compiling and evaluating the materials and composites applied in FGF systems. Furthermore, this study will classify the types of FGF extruders available, focusing on key dimensions such as screw length and diameter, and identify trends that may indicate future developments. Lastly, it will also highlight new extruder designs that push the boundaries of FGF development and offer new capabilities. In this manner, this review will offer valuable insights for both

researchers and industrial stakeholders in the field, contributing to the further advancement and adoption of FGF technology.

2.2.2 Systematic Literature Review Methodology

The system review was carried out following the guidelines of the PRISMA process [57]. A pictorial summary of the systematic review process is shown in Figure 2.15. The identification of the research articles was carried out on the 7th March of 2024, using the search term shown in Table 2.1. The exclusion criteria were as follows: review articles, non-English articles, articles older than 2004 which was the date of the oldest article found by previous systematic reviews, and document types which are neither a conference paper neither a journal research article. Articles, part of which are presented in this thesis, were also excluded. The search terms and exclusion criteria were used with the Web of Science and Scopus databases. The results were 623 and 8257 respectively, which required further filtering before screening. To refine the dataset for effective screening, the first 500 of each database, sorted by relevance, were selected for review. Of these 1000 articles, 98 were found to be duplicates and where removed. The remaining articles were screened by title and abstract and selected based on their relevance with the research aims. This screening process yielded 112 research articles which were then combined with another 51 articles originally reviewed by the Justino Netto *et al.* [21]. The combined lists had a total of 35 duplicates, which left the final list of 128 unique articles.

Table 2.1 - Search terms used for research article identification.

Field	Operator	Search Term
All fields	AND	"additive manufacturing"
All fields	AND	pellet OR granule OR granulate OR granular OR screw
All fields	AND NOT	metal OR sinter OR sintering OR wire OR arc OR blow OR "powder deposition" OR binder

Each article was screened to determine the use or otherwise of an FGF system in its methodology. At this stage, those articles which included FGF were screened in more detail to determine, when available, the design of the extruder used. The screw length and diameter as well as the nozzle diameter used in the study, were also tabulated. This data is of an objective nature and therefore does not require multiple reviewers to

counter for bias. In certain cases, the screw length and diameter were not provided in the text, but rather as part of figures. In some cases, the figures had a scale and so the data required was collected. In other cases, the text only provided either the diameter or the length of the screw and then supplied an image without scale. In such situations, a scale was created using the information provided, and the necessary data was calculated. Another scenario occurred when research articles used commercially available extrudes to conduct their studies. Often, the length and diameter of the screw were neglected. When possible, the data was collected from the official website and information documents provided by the company supplying the commercial extruder.

Those articles which did not have any information available using the process described, where noted as "N/A" meaning *not available*. For all data metrics collected, any lack of data for that analysis would lead to an omission of the concerned article from the analysis. Extruders for which no information was available regarding screw length and dimensions were not classified using a numerical metric. In order not to neglect these valuable contributions, the studies were classified separately by comparing with similar extruders of known size. This classification process is not deterministic as it does not use a quantified metric and relied primarily on the non-numeric description provided by the authors of the respective studies. Although this approach is not ideal, but given the lack of available information, it was considered the most appropriate option.

Apart from extruder geometry, the materials, composite mix, extruder design and extruder type were tabulated. Extruder design refers to the setup of the physical screw extruder. Most extruders involved variations of the conventional single screw extruder, often altering the screw geometric features such as channel depth, screw length and diameter. These dimensions are shown in Figure 2.3. All such extruders were classified as single screw extruders (SSE). In the case of novel or divergent designs, these were classified using the naming scheme provided by the original authors, wherever possible. A distinction was also made to describe whether the extruder was static or was part of the translation motion. Whilst this aspect is not directly related to the extruder design, having a static extruder implies a heavy extruder and therefore was deemed a separate design type. In contrast, extruder type refers to the research group or company used to provide a specific extruder. The extruder type field is concerned with linking studies which used the same FGF systems. Those studies which used a one-off FGF systems and were custom made by the research group, were marked as "Custom". In the case of

materials and composites, all types of mixtures were recorded except for co-polymerised blends.

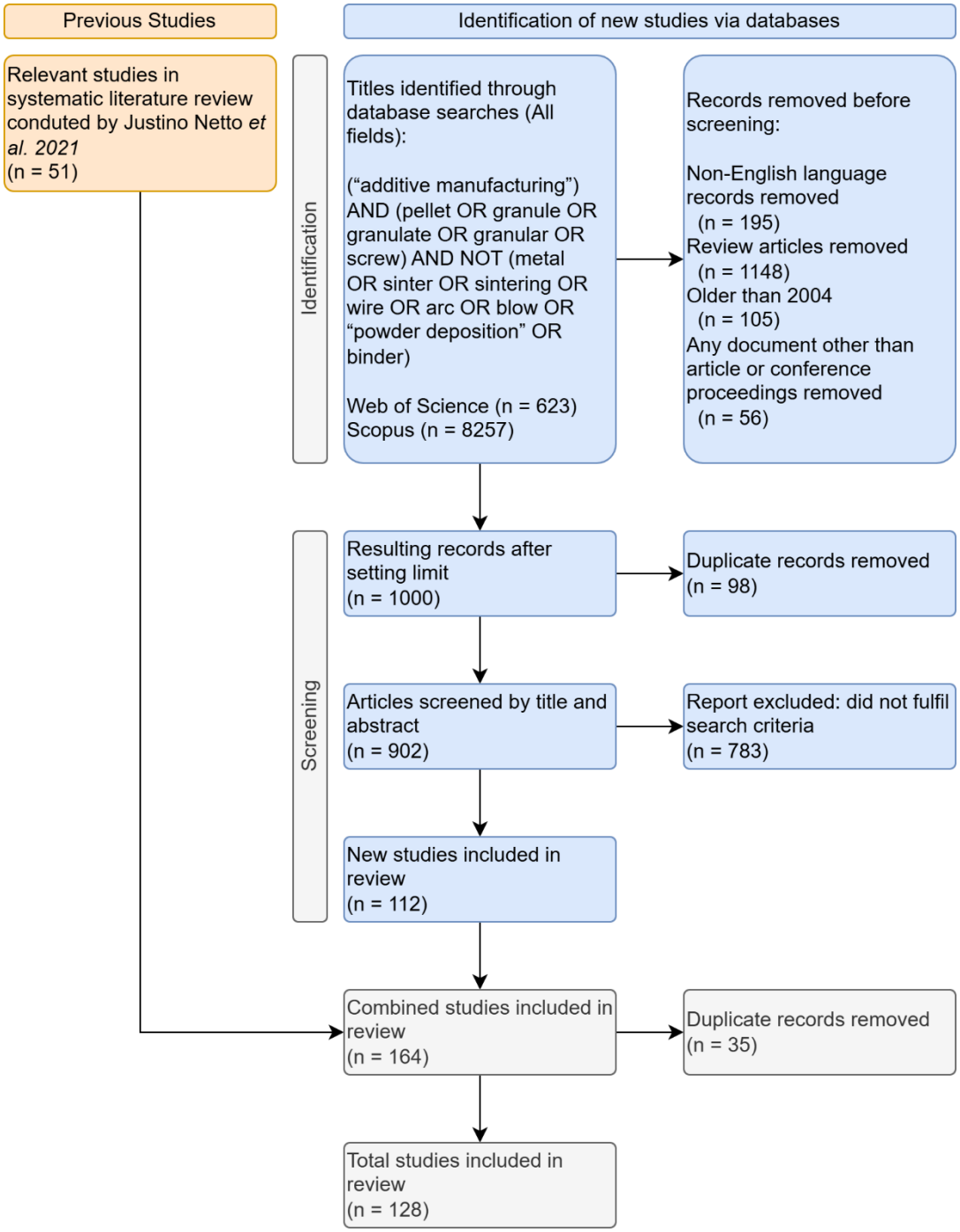

Figure 2.15 - Flow diagram summary of the PRISMA process adapted for this systematic literature review.

The data collected was analysed with the aim of highlighting changes in extruder features with time, classify extruder types and the amount of research conducted on each. The relationship between extruder size, nozzle diameter and how these changed with time, was also evaluated. This analysis should help to generate a comprehensive overview of what studies were conducted on FGF and what is the general path research

is taking at this point. The analysis should also highlight any factual extruder design classes present in literature, but that are still undefined up till now. A class here is used to refer to a collection of extruder designs which all share common, prevalent traits. Beyond the extruder design, the materials that were 3D printed up till now were also analysed. The aim of this exercise is to demonstrate which materials have been applied to FGF the most and what are those materials that may merit further attention or that have never been publicly studied with FGF.

Apart from technical data, the data collection process also looked at the author address provided. The aim of this data collection was to understand from which countries are FGF studies originating. Those articles which were produced by researchers from multiple countries were noted. In such cases, each country involved was noted as having a published research article. No preference was given to authorship order. Furthermore relationships between authors and keywords were also evaluated using VOSviewer [58, 59]. A co-authorship co-occurrence map was generated, using full counting with 3 minimum documents per author. The same software was also used to evaluate co-occurrence of keywords in the title and abstract of all the articles selected. Binary counting was used with a minimum of 10 occurrences per term. The relevant terms were selected and then generic terms such as “paper”, “lament” and “need” were removed. Spelling differences were corrected, and synonyms terms merged. This form of analysis allowed the determination of principal research groups working in the field of FGF and highlights the main topics being studied.

All of the data collected along with the relevant article details were then tabulated. The table was sorted by publication year and is provided in appendix 1, page 331

2.2.3 Research Trends and Classification

Before delving in more detail about the FGF extruders, it is useful to provide a background of where the research is being conducted and which fields are related to it. The location and application of a technology often directs its development and by extension any research conducted.

2.2.3.1 Geographic Distribution of FGF Research

The largest body of published research articles originated from the United States of America (USA), with 25 articles. This was followed by China and Spain with 17 and 15

articles respectively. Due to the nature of the European research and related research funding, it is reasonable to combine all European Union (EU) countries into one group, which would yield the largest research output with 65 articles. This number was corrected to count articles which were published by multiple EU countries as one article. The top European countries with the highest article number are Spain, Italy, United Kingdom, Germany and then France. India with 15 articles is the fourth most prolific publisher on this subject.

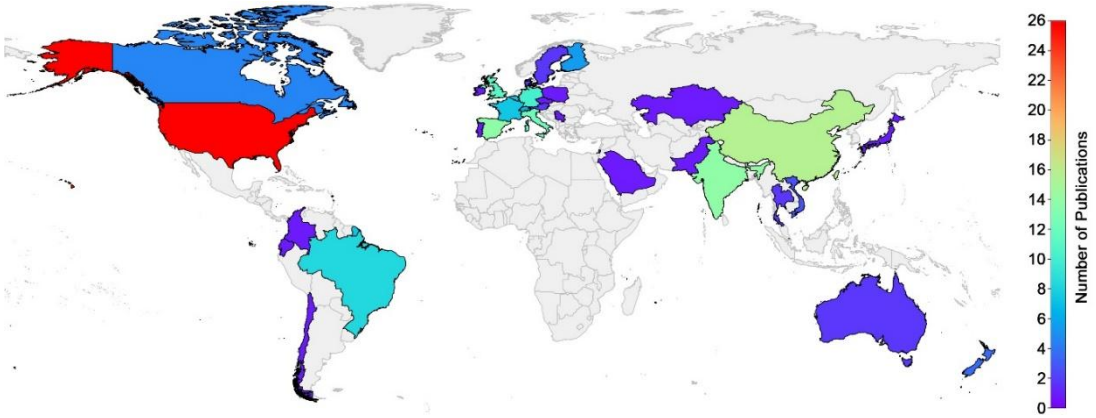

Figure 2.16 – Geographic mapping of origin of authors that contributed towards publication of FGF research articles.

Considering only the extruder found in this literature review, countries with high research output also tend to have locally grown companies supplying FGF extruders. The literature reviewed used extruders from companies listed in Table 2.2. This does not include those studies which developed their own custom FGF system. Whereas the USA tops both publication and company list, only 2 companies from China have been mentioned. Considering that only English-language articles were considered in this review, the results may be biased towards English-speaking countries and overlook significant contributions from non-English-speaking countries such as China.

As shown in Figure 2.17, only five research groups have published more than three papers on FGF and have collaborative links with other similar researchers. These groups are geographically spread apart throughout the world. This result demonstrates how most researchers working in FGF only have a limited exposure to the field before changing subject or shifting completely out of research publication entirely. This aspect is confirmed by the omission of major contributing countries to the FGF research field, from Figure 2.17. Studies conducted in China, Spain, Italy, Germany, and France, which were numerous, did not make it in co-occurrence web of authorship, indicating multiple independent studies.

Table 2.2 - Companies per country that provide FGF extruders, as mentioned in literature.

Country	No. of Companies	Companies
USA	7	Cincinatti Massive Dimension Brinter Hybrid Manufacturing Technologies Strangpresse Cosine Additive 3D Cultures
Spain	3	Discovery 3D Printer Mahor IT3D
Italy	3	Wasp 3D Direct 3D CMS
Switzerland	2	RegenHU SAEKI Robotics
Germany	2	AIM3D Herz
People's Republic of China	2	Creality Yizumi
France	1	Pollen AM
United Kingdom	1	FabRx
Colombia	1	Fused Form

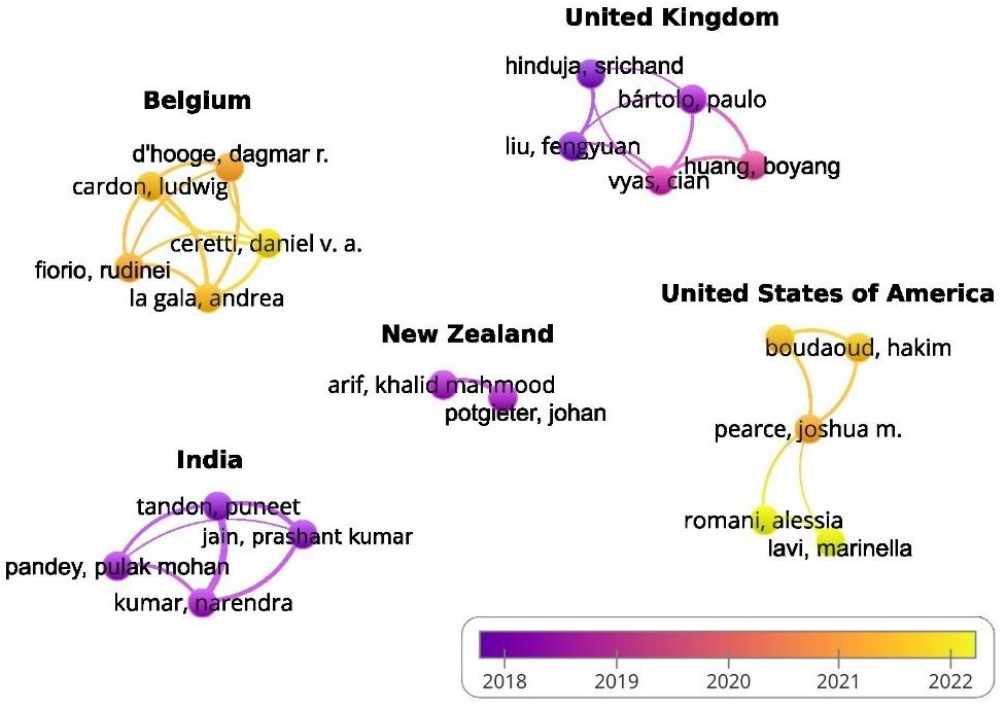

Figure 2.17 - Co-occurrence web of authorship, colour graded by average publication year.

2.2.3.2 Overview of FGF Research Field

The research field of FGF currently focuses on recycling and performance. This statement is demonstrated by the keyword co-occurrence analysis of title and abstract as illustrated in Figure 2.18, where both terms are marked in yellow which indicates their prominence in recent literature. The subject of recycling including its aim at a more sustainable future is well linked with FGF's ability to directly use virgin granules or reground waste material in form of regrinds or flakes. Thus, FGF is being perceived as a key technology towards the goal of creating a circular economy. Multiple research efforts have been dedicated to the subject, one such example is the work conducted by Byard *et al.* with the Gigabot X [60] and similar other studies by the research group of Joshua M. Pearce [60, 61], shown in Figure 2.17. Other popular terms that surfaced are effect, processes parameter, property, and speed. These terms are linked with efforts to improve the FGF process and the quality of the products manufactured using FGF process. Another separate term of interest is *cost* since FGF is often proposed as a more affordable alternative to filament systems due to the significantly lower price of granules compared to filaments.

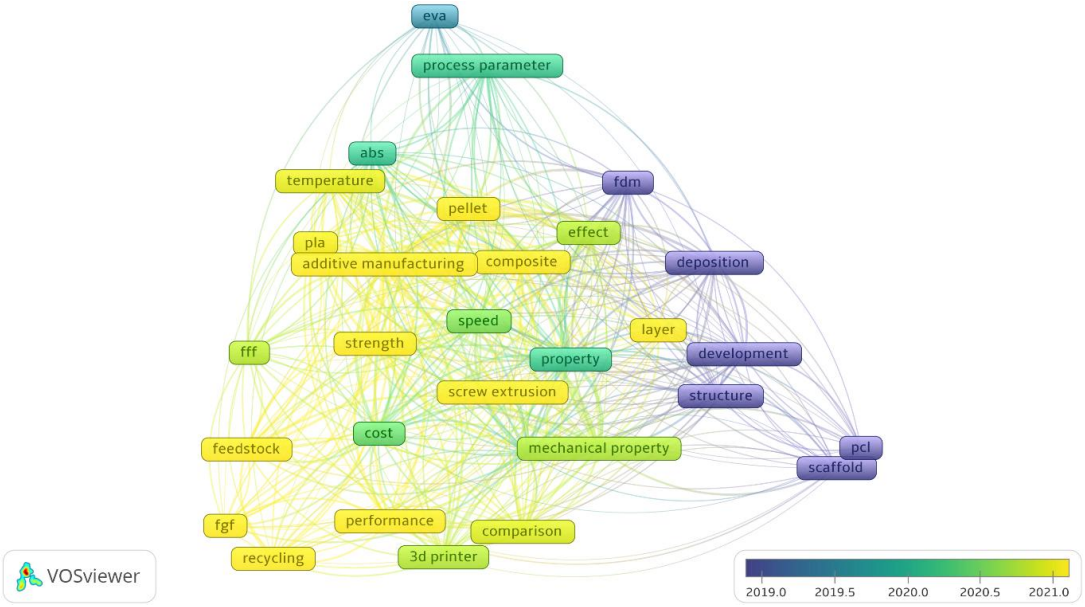

Figure 2.18 - Co-occurrence web of keywords in the title and abstract, colour graded by average publication year.

The co-occurrence web also highlighted the term strength in yellow indicating the recent interest in this subject. It is generally useless to produce products out of any material from any source if it has inadequate properties and performance. Therefore, it is the driving goal of multiple studies conducted using FGF systems often involved an

evaluation of strength. In fact, the term strength often accompanies other terms such as of recycling, performance, composite, feedstock and pellet. All of these terms have a recent, average, publication age which highlights their popularity. Feedstock and pellet are innately linked with FGF and therefore are bound to be prominent. The inclusion of *composite* is indicative of the significant interest towards composite additive manufacturing (AM) even when using FGF. For example, composite materials have been formulated to improve strength via reinforcement, such as done by Hu *et al*. [62] but also for multiple other objectives, such as controlling the burning process of the material [63]. Such flexibility increases the range of possible applications of FGF.

As indicated by the co-occurrence web, the initial development of FGF was spurned by scaffold fabrication using polycaprolactone (PCL), marked in blue in Figure 2.18 which indicates its popularity in earlier years. The authorship map, shown in Figure 2.17, demonstrate that a significant contribution to this field was provided by the research group of Liu *et al*. [64–69] as they led the development of plasma treated, screw extrusion fabricated, PCL scaffolds. At the time, the deposition rate and the structure were of interest as these controlled the quality of the scaffolds produced. The low average publication year value of this term indicates that the research interest has shifted away from PCL and scaffolds over the years.

The acronym FDM also lost its popularity with time. This was in part fuelled by the trademarking [70] of the term by Stratasys which led to the counter popularisation of FFF. The term FGF is analogous to FFF and creates a cohesive terminology. It is also notable that other terms such as pellet additive manufacturing (PAM) [44] which are sometimes used to describe FGF systems, were not as widely used as FGF and did not gain enough usages in literature to be present in the web of Figure 2.18. Neither FFF or FGF are present in the ISO/ASTM 52900:2021 standard of *Additive manufacturing – General principles – Fundamentals and vocabulary* [1]. Both technologies are grouped under material extrusion (MEX) along with other techniques that are beyond the scope of this review. The lack of popularity of this term is emphasised by its omission in Figure 2.18. It is possible that this may change in future publications but the low uptake in MEX term usage since publication of the standard indicates a lack of willingness to adopt this term in the research field. One possible cause may be that the term is too generic as opposed to most studies which tend to be specialised and therefore prefer a more accurate term.

The next development shift was towards additive manufacturing of EVA. A number of research articles were published on auger screw FGF of ethylene-vinyl acetate (EVA) by the research group led by Kumar *et al*. [71–76]. Fabrication of thermoplastic elastomers is not simple when using a filament fed system. Not only is the quality that FFF can achieve with elastomers inferior to that using rigid thermoplastics but the level of softness usable with FFF is often limited to around 70 shore A [77]. At lower shore hardness, the filament feeding system tends to buckle the filament, leading to incorrect extrusion. This issue does not exist within FGF, and therefore, the first research works using FGF systems focused on elastomers.

Regarding materials, the first thermoplastic to be extruded using FGF was PCL, followed by ABS, and then PLA. The latter two are cornerstones of thermoplastic material extrusion (MEX) AM. The flexibility of FGF lends itself well to the study of highly specialised and experimental materials. In contrast with FFF, FGF eliminates the need for filament production, a step with its own challenges leading to a poor-quality filament and inconsistent extrusion. This simplifies the whole AM process, which allows for studies focusing mainly on material properties and applications. Although FGF has been used to study a diverse range of materials, this cannot be seen in Figure 2.18 since many of these studies are one-off experiments. While the mainstream AM thermoplastics such as PLA and ABS have been more extensively investigated, only a few non-mainstream thermoplastics such as EVA and polypropylene (PP) have been explored in multiple studies.

2.2.4 Materials

Figure 2.19 shows all the materials along with any mixtures thereof that were used in the literature and reviewed in this study. The most used thermoplastic was PLA, followed by ABS, both of which are widely used in FFF systems. Notably polyethylene terephthalate glycol (PETG) is not as widely applied in FGF studies as in FFF. In total, 53 different matrix materials have been studied whilst using FGF. Most research involved 3D printed composites, with the most tested fillers being carbon fibre and glass fibre. Wood and

cellulose fibre have also been tested as fillers for multiple thermoplastics due to their desirable properties and aesthetic [78–81].

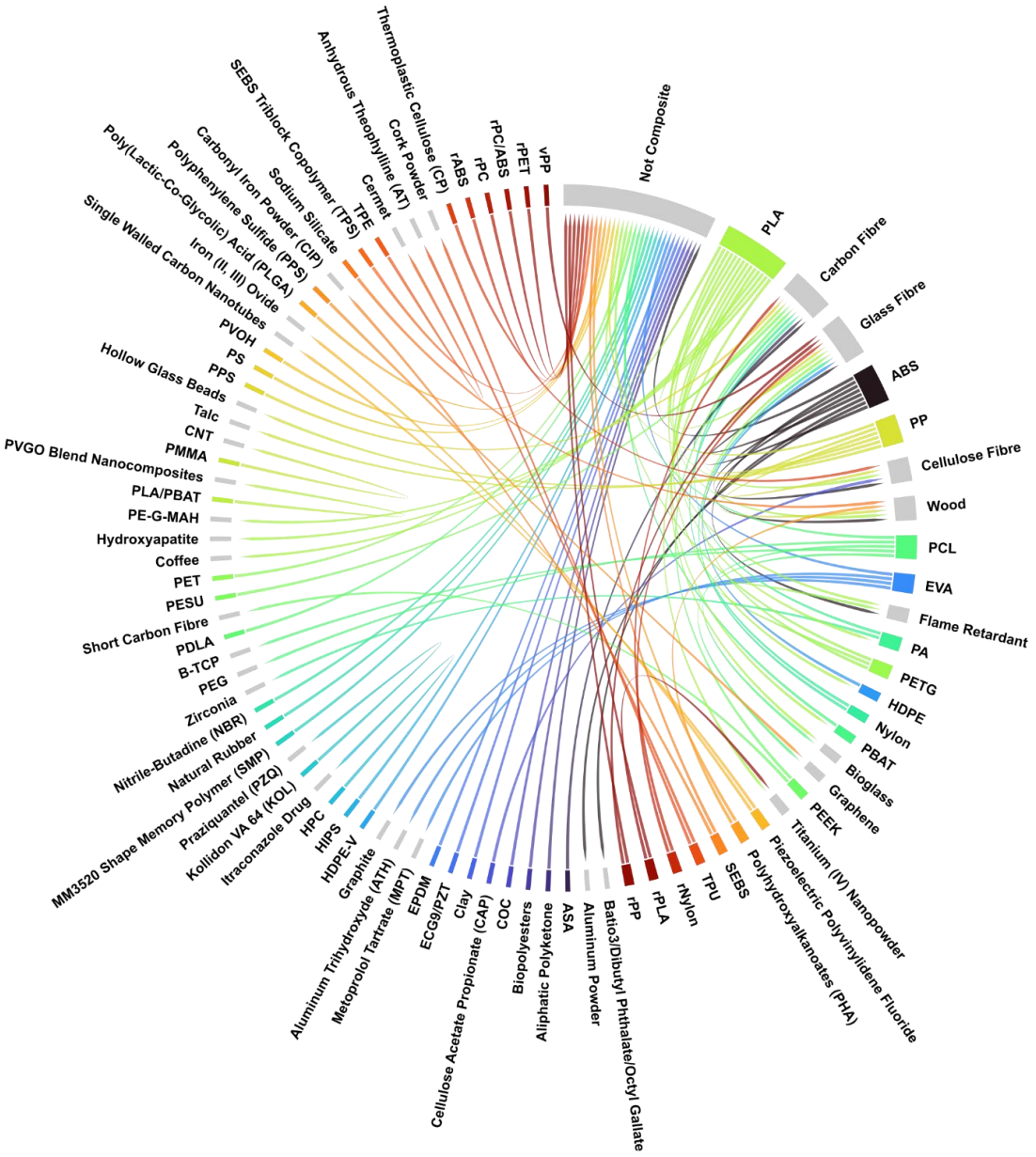

Figure 2.19 - Chord diagram ordered clockwise by count showing material to fillers and additive links.

Flame retardant additive [63], graphene [82–84], bioglass [85] and titanium nano powder [86] have also been used with multiple thermoplastics. Graphene and bioglass were utilised in order to improve cell viability and proliferation in biomedical scaffolds [82, 85]. The addition of graphene nanoplatelets was also found to improve mechanical properties [87], where graphene oxide nanosheets allowed the compatibilization of PLA/PBAT blends [84]. The addition of titanium dioxide nanoparticle to recycled PLA was found to improve thermal stability and degree of crystallinity along with tensile strength. In this manner the loss in mechanical and thermal properties brought about by remelting

of PLA were counteracted by the nano powder addition [86]. Apart from the fillers and additives just mentioned, another 23 have been used in conjunction with only one other base thermoplastic. The necessity to 3D print so many different materials led to the development of numerous extruder designs, some of which specifically intended for inline mixing of composites [88] and others meant to be used with continuous fibres [89].

2.2.5 FGF Extruder Classification

The number of published articles that either makes use off or develop FGF systems for MEX has been increasing yearly. Last year i.e., 2023 was the most prolific as shown in Figure 2.20. Out of the 128 research articles selected, 69 used custom developed FGF systems. Multiple designs exist, some intended for specific applications or materials.

2.2.5.1 Screw Design

The most popular configuration and the one which will be considered first, is the simple single screw extruder. This design has been popular since the very beginning and most other designs can be considered as variations from the original concept. The most significant variation was to use of a Moineau pump [90] and the application of a flexible heated hose [37]. Given the large number of single screw extruder studies, it may be useful to determine a metric to classify the different extruders, as done in the following sections.

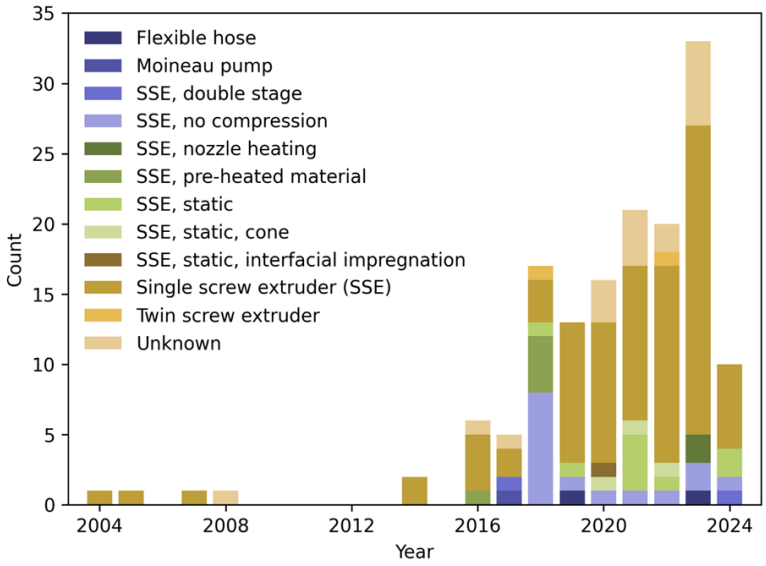

Figure 2.20 - Histogram of published research articles based on extruder type used.

2.2.5.2 Screw Diameter

The classic single screw extruder has multiple parameters that can be varied to produce a different system. The two most important parameters are the screw diameter and screw length. The diameter can be used to classify what kind of material can be fed. Most thermoplastic granulates or pellets have the smallest dimension of around 3 mm which means that the screw feeding channel depth has to be the same or higher than this value. Screw channel depth is rarely provided in literature and therefore cannot be used as a classifier. Comparing the studies that used small diameter screws, the smallest diameter system that managed to properly extrude using pellet feedstock was the V4 commercial extruder by Mahor, which has an 8 mm diameter screw [91]. A version of the Mahor extruder is also used in FGF systems by Tumaker [92]. The next smaller diameter system used a powder feedstock with a screw diameter of 7 mm, developed by Silveira *et al.* [93]. Larger diameter screws can progressively make use of larger pellets or granulates. Using these observations, the screw diameter classification was divided into two classes: *powder extruders* ($Ø \leq 7$ mm) and *pellet or granulate extruders* ($Ø > 7$ mm), as plotted in Figure 2.21.

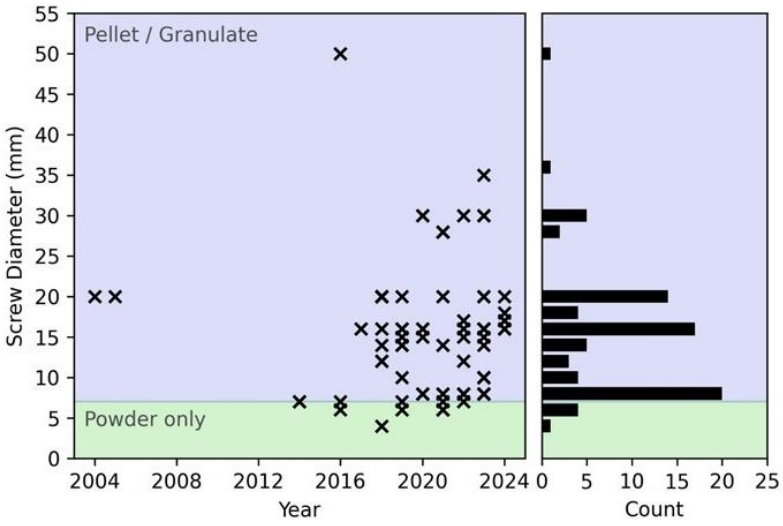

Figure 2.21 - Screw diameter vs research article publication year with histogram of screw diameters.

There are significant differences between powders and pellet feedstock. Powder feedstock is usually more expensive than classic pellets from which it is generally produced. The production process to create powder also requires equipment as well as energy and labour, reducing the overall sustainability of the FGF process. Availability is another key factor. Pellets are easily accessible due to their widespread use in mass production and industrial processes, making them easier to source and offering greater

material versatility. These aspects could contribute to the relatively low amount of published literature on powder extruders as compared with pellet / granulate extruders.

Compared to powder extruders, pellet extruders offer a much wider spectrum, with a range of tested screw diameters. As the histogram shows, most extruders used in the reviewed literature had a diameter of 8, 16 or 20 mm. Only a small number of systems used different screw diameters. A screw diameter of 8 mm is a natural size limit due to the typical dimensions of pellets. A smaller screw diameter would require an even smaller screw root, which could impair the screw's torsional strength. Increasing the screw diameter to 16 mm makes it large enough to sustain easier granulate feeding and to generate a higher torque. At this diameter the channel depth can reach 6 mm with a screw root of 4 mm diameter. Increasing further the screw diameter to 20 mm allows for a thicker screw root diameter leading to higher sustainable torques which can be used to extrude a higher sustainable throughput [17]. The 16 mm and 20 mm diameter are also widely used in large, stationary, industrial extrusion and injection moulding processes, making them easier to procure and adapt to FGF. Furthermore, most of the screw extrusion theory available has been developed using extruders of this diameter [20]. Therefore, it is simpler to study the phenomena occurring during FGF processing when using a system with such a screw diameter. Increasing the screw diameter further than 20 mm is rather rare. All the studies that used such extruders made use of composite feedstock. These large systems are usually more adept at handling a higher percentage of reinforcement without clogging. They can also sustain the extra resistance caused by the increase viscosity of the thermoplastic melt with reinforcing fibres. The two main companies that provide extruders of these sizes and that were found in the literature review are Cincinatti (USA) [94–97] and Massive Dimension (USA) [98, 99].

2.2.5.3 Screw Length

The overall size of an extruder is best characterised by the screw length. In practice, weight is the most important specification of an extruder but often this is hard to come by, especially for custom made systems. As noted earlier, custom systems make up nearly 55% of all extruders found in the review. However, none of these provided the weight of the extruder. For this reason, the screw length was deemed the most reasonable parameter to classify the bulkiness or size of the extruders. Only a small number of commercial systems reported the extruder weight, making screw length a more reliable metric for a comprehensive review of the literature due to the greater

availability of data. The screw length (l) classification was divided into three classes: small ($l \leq 100\ mm$), medium ($100 < l \leq 200\ mm$) and large ($l > 200\ mm$), as plotted in Figure 2.22.

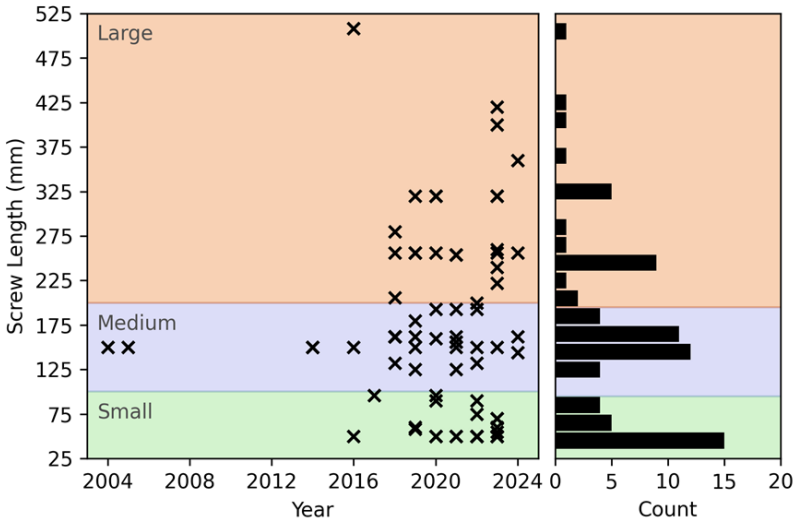

Figure 2.22 - Screw length vs research article publication year with histogram of screw lengths.

The small extruder classification is based on the idea that if the screw length is smaller than or equal to 100 mm, it may be used in desktop 3D printing systems. Such systems are the most widely used in FFF 3D printing that have dominated the domestic market. These small sized 3D printing systems are also amongst the first forms of 3D printers that users tend to purchase when they are still learning about 3D printing. Popular examples are the Prusa MK4 3D printer [100] and Bambu Lab 3D printers [101]. Therefore, the small type FGF extruders are critical drivers towards a wider adoption of FGF in commercial, industrial and domestic sectors. The histogram in Figure 2.22 also shows a clear distinction in extruder screw lengths dividing the small and medium categories. This suggests a common design intent amongst various research groups and companies. The first published study using a small extruder appeared in 2016, after which its popularity began to rise [102].

The earliest FGF extruders were developed using medium-sized extruders. At this scale, the motion system can remain similar to that of smaller extruders, with some modifications to handle the increased weight. At the longer length limit of medium scale extruders, the size increase becomes significant enough to warrant a major redesign of the motion system. Such extruders are at the edge between medium and large classifications. Unlike with small extruders, the further increase in the extruder size diminishes the possibility and therefore the need for integration with existing motion

systems. In fact, the distinction between medium and large extruders, as shown in the histogram of Figure 2.22, is less pronounced than the division between small and medium ones. The medium class is arguably the most adaptable, making it an ideal test bed for advancing FGF technology. At this scale, engineering designs are easier to produce, as they avoid the challenges of miniaturization faced by small-class extruders and the heavy load requirements and material handling typical of large-class extruders. From a technical standpoint, medium FGF systems can still be relatively simple, making them cost-effective and accessible compared with large scale FGF.

Aside from size, the main differentiator between medium and large extruders is what they can produce. Large systems, often referred to as big area additive manufacturing (BAAM) have an application profile that includes large products such as life-size furniture and boats amongst others [103]. Producing such items with small or medium-sized FGF extruders would be highly challenging, and even if it is possible, the production time would be prohibitively long. In essence medium class extruders are more akin to small extruders with greater throughput capacity, feedstock morphology variety and are generally more robust, albeit with an increase in weight. In contrast, large extruders stand out as a class of their own, requiring different process considerations and offering capabilities beyond those of their smaller counterparts.

2.2.5.4 Nozzle Size

Another differentiator of MEX 3D printing processes is the nozzle size. The smaller the nozzle size, the smaller the parts that can be reasonably produced. From a MEX perspective, the smaller the nozzle, the greater the resistance to flow and therefore the smaller the maximum throughput. The effect of nozzle size on the FGF process as well as on the 3D printed parts themselves, makes it an important process parameter. For this reason, the nozzle sizes found in the literature review are plotted against screw diameter and length, with colour grading for publication year, as shown in Figure 2.23.

As shown in the plot, there is a trend of larger extruders using larger nozzle sizes. Nonetheless, small style extruders sometimes also made use of large nozzle sizes, e.g. when extruding clay as done by Pitayachaval *et al.* [104] and when using composite ABS with glass fibres by Liu *et al.* [105]. The reverse is also true as exemplified by the work of Romani *et al.* when 3D printing using recycled polycarbonate (rPC) and rPC/ABS blends with a 0.8 mm nozzle on the Gigabot X [61] and by Mi *et al.* when testing a novel application of a sheering feature in the form of a blister ring, at the metering section

[106]. These incongruencies demonstrate that the use of the nozzle size is flexible amongst FGF classes.

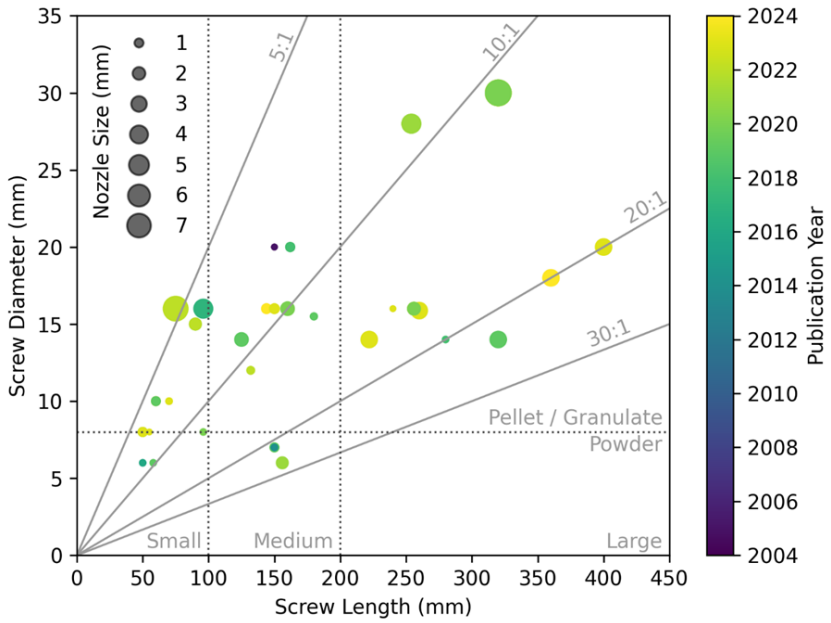

Figure 2.23 – Extrusion screw diameter vs length, with nozzle size and publication year. Grey line denotes the L:D ratios of studies in that region. Dotted line demarcates the classes based on screw length and diameter.

Screw length and diameter can be used separately as these parameters are independent of each other, as can be seen in Figure 2.23. By convention, most industrial extruders, not meant for additive manufacturing, make use of a 20:1 or 30:1 length to diameter (L:D) ratios. This is often not the case in FGF as can be seen in Figure 2.23. Most extruders feature an L:D ratio of 20:1 or lower, with only a small number exceeding this ratio. As the L:D ratio increases, the screw lengthens, resulting in a longer, heavier, and more cumbersome extruder. Consequently, this increase in size adds complexity and cost to the required motion system. A number of extruders opted for L:D ratios smaller than 20:1. This design decision was necessary to miniaturise FGF systems as much as possible and in so doing decrease the complexity and cost of the related motion system. The reviewed research articles reveals that 44 out of the 75 known L:D ratios (58.7%) fall within the range of 10:1 or smaller. This indicates that the conventional design guidelines used for static, classic, shop floor-type screw extruders are not applicable to MEX AM, despite both being a form of screw extrusion process. The distribution of publication year also shows a trend towards smaller extruder with a smaller L:D ratios and larger extruders with an L:D ratio not more than 20:1. Nevertheless, the interest towards powder extruders seems to have decreased, with recent publications focusing more on

granulate extruders. This was probably caused by the smaller application spectrum of such systems.

2.2.6 FGF Extruder Studies

The following section is meant to briefly outline the major findings of the studies being reviewed. The classification system presented in sections 2.2.5.2 and 2.2.5.3 has been used to structure this section.

2.2.6.1 Powder Extruders

Powder-only extruders have been successfully developed for specialized applications, particularly in the biomedical field. Initial studies conducted by Tian *et al.* [78], Boyle *et al.* [107], Samiul *et al.* [108] and Drotman *et al.* [102] developed four distinct powder extruder systems. These studies concluded that a compression section is necessary in screw extruders to allow for consistent extrusion [107, 108], while a fast screw compression ratio results in a decreased extrusion rate [78, 79].

Powder-only extruders, particularly the M3DIMAKER 3D printer from FABRX [109], have emerged as valuable tools for biomedical applications, especially in scaffold production for cell growth and personalized medicine. This system allows direct 3D printing of multi-component blends, as demonstrated by Aguilar-de-Leyva's *et al.* [110] that worked on thermoplastic polyurethane (TPU) tablets blended with theophylline drug and as a ternary blend with magnesium stearate. Silveira et al.'s pioneering research in 2013 laid the groundwork for using powder-only extrusion in scaffold production, using materials such as PCL [93, 111] , PCL/b-TCP [112], and PCL with Bioglass [85]. This early-stage research employed a near 20:1, L:D ratio screw with a single heated zone [113]. Both pre-compounded and dry mixed PCL with bioglass were used but extrusion quality of the latter was inferior. This is an indicator that in such cases a mixing section may be necessary [17].

For thermoplastics with a low melting point, Phung *et al.* [114] and Nguyen *et al.* [115] suggested the use of a PTFE extrusion screw as opposed to a conventional metal screw. The PTFE screw required a larger screw root diameter whilst using a shallow channel depth. The latter decreases the molten material residence time, which potentially decreases the degradation of heat sensitive materials. This aspect was studied further by Zhou *et al.* [116] which used a 1.5 mm deep screw channel and multiple feeding ports

along its length, as shown in Figure 2.24 (a). As needed, this feature can effectively decrease the working screw length, thereby decreasing material residency time.

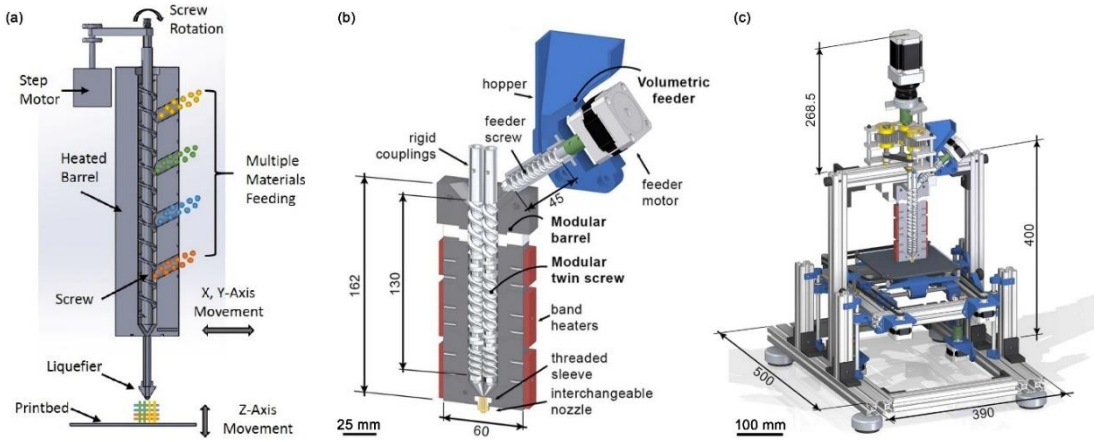

Figure 2.24 – Schematic of multiple feeding port extruder (a), co-rotating twin screw extrusion head (b), and twin screw 3D printer (c) adapted from [117].

Mixing components in a controlled manner during the 3D printing process can be particularly advantageous as it allows for the creation of components with functional gradients. This was the objective of the twin screw extruder developed by Justino Netto et al [117, 118], shown in Figure 2.24 (b and c). Further research is required to fully develop this technology, but its successful implementation could extend the applications of powder screw extruders beyond the biomedical field.

2.2.6.2 Small Scale

Extruders with a screw length of 100 mm or less, excluding powder extruder, were classified as small-scale extruders, totalling 21 separate studies. Out of the studies, 6 used in-house developed extruders, while 2 utilized commercial extruders [91, 92].

The Mahor extruder, an unmounted example of which is shown in Figure 2.25, is the most widely used commercial small-scale FGF extruder [91]. A modified version of this extruder is implemented in the Tumaker (IT3D) 3D printers [92]. It employs an 8 mm diameter and 50 mm long screw, resulting in an L:D ratio of 6.25:1. This extruder, positioned at the bottom left corner of Figure 2.23, is capable of 3D printing complex geometries [119] and can be used with minimal modifications on existing FFF motion systems [120]. It was employed by multiple research groups for 3D printing of elastomers such as vulcanised rubber [121], TPU with cork powder [122] and EVA blended with a medical compound [123]. The Tumaker 3D printer was similarly applied by Georgopoulou *et al.* [77, 124] for 3D printing of unfilled styrene-ethylene-butylene-

styrene (SEBS) grades of 25, 50 and 75 shore A even with the addition of 50% carbon black filler. These materials were then applied to 3D print inflatable actuators and soft compliant robotic grippers. Extrusion and 3D printing of composite materials performed best when using pre-blended feedstock. This is a common shortfall of small scale FGF caused by the short screw being used which was not capable of distributing and dispersing the composite material. Nevertheless, this aspect should not understate the capability of the Mahor FGF extruder to 3D print using thermoplastics of various viscosities, to a greater extent than FFF systems [123].

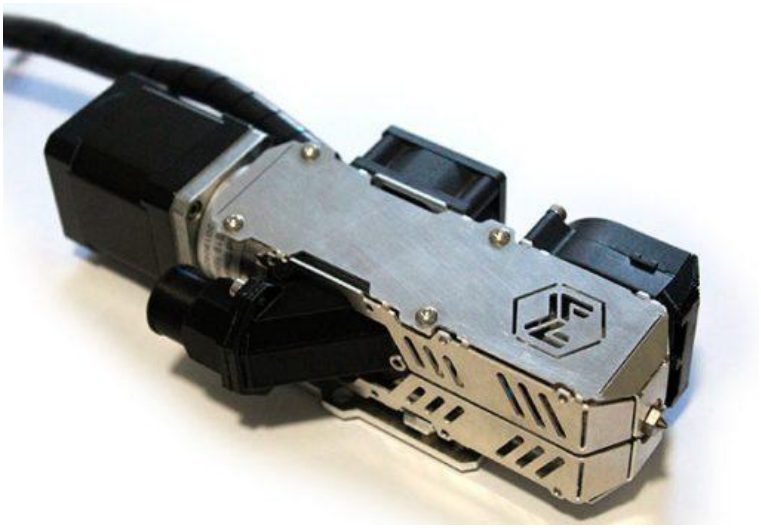

Figure 2.25 - Mahor v4 Pellet Extruder [91].

The Mahor extruder was found to be able to directly extrude reground INGEO 4043D PLA and another unknown grade of PLA, whilst achieving similar mechanical properties to virgin PLA [25, 125]. However, it was reported that the reground PLA was more difficult to extrude and prone to clogging, even when the feeding section temperature was decreased. On the other hand, 3D printing using recycled PLA with FGF decreases material degradation compared to FFF [125]. This was attribute to the extra thermal cycling necessary to produce the filament for FFF [125]. On another occasion, the study by Pagés-Llobet *et al.* [126] using a Tumaker FGF system concluded that FGF 3D printed parts had improved mechanical properties over FFF. This went against previous studies [25, 125], which is most probably caused by the unusually low density of the FFF parts which indicates abnormal printing conditions.

The Tumaker 3D printer was also successfully employed for 3D printing of biopolymer thermoplastic including heat sensitive material such as polyhydroxyalkanoates (PHA) [127]. The research group led by Martinez also successfully 3D printed PLA pre-blended

with micro-fibrillated BioPA to improve fracture toughness and strain at failure [128]. These kinds of studies demonstrate the material extrusion versatility of small-scale FGF extruders which allows the technology to be applied to various fields, ranging from consumer, automation, and even to biomedical.

The quality of small-scale FGF achievable today can be partly attributed to the pioneering studies by Whyman *et al.* [129, 130] back in 2018 which were then applied further by Harris *et al.* [131]. The initial extruder designs used aluminium alloy barrels which suffered from rapid wear which contaminated the extrudate. Nonetheless the system was capable of 3D printing complex geometries, despite issues with clogging caused by the aluminium wear particles. In contrast, the small-scale FGF extruder developed by the research team of Liu *et al.* [89] could 3D print polyamide (PA12) with continuous carbon fibre reinforcement through co-deposition, as shown in Figure 2.26. In this investigation, screw extrusion was employed to generate the requisite pressure which was essential for achieving near complete impregnation of the 1 K carbon fibre tows, resulting in a porosity level of 0.15%. Such systems allow the fabrication of load bearing components for specialised applications.

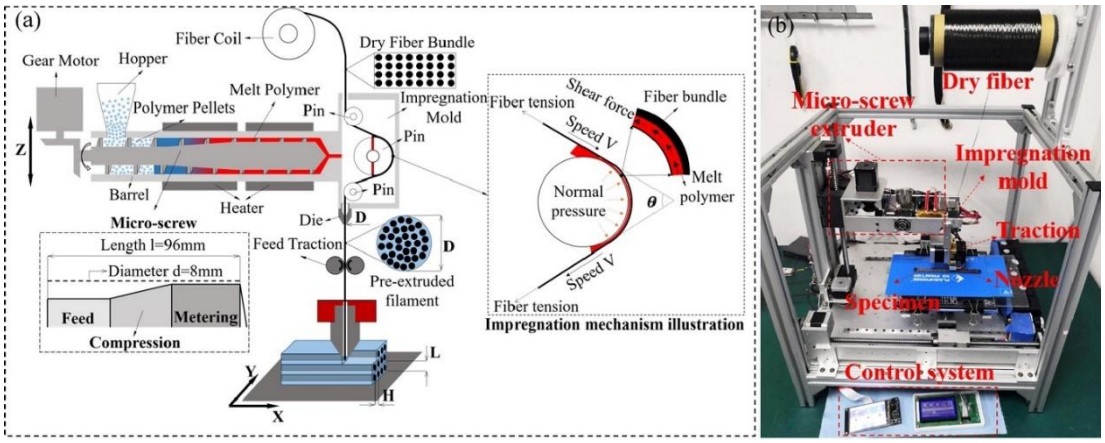

Figure 2.26 - Schematic (a) and equipment (b) of micro-screw in-situ extrusion based 3D printed continuous fibre reinforced composites adapted from [89].

In conclusion, small-scale FGF extruders have shown capabilities comparable to those of FFF for all thermoplastics groups including high performance polymers. The success of these extruders is now prompting studies into 3D printing of high-performance composites. Research on small-scale FGF has also highlighted its potential for elastomer 3D printing. Further investigations are required to enhance the capabilities in this domain and to explore novel applications of this technology.

2.2.6.3 Medium Scale

The medium class includes 32 individual studies and all of which utilized custom-developed extruders. These extruders feature screw lengths longer than 100 mm but no more than 200 mm, excluding powder extruders

The first published journal article on FGF was a medium class extruder which pioneered PCL scaffold fabrication using FGF. It was published in 2004 by Wang *et al.* [132] using a system developed by Anna Bellini in 2002 [22]. This system utilised a custom screw with a compression and metering section, unlike the later studies published by Kumar *et al.* which employed an auger screw extruder setup [71–76, 133–136]. This compression less system worked adequately when using elastomers, namely EVA [73, 75, 76] even when blended with additives such as graphite powder [72, 134]. On the other hand, rigid polymer failed to extrude consistently, indicating that such polymers may require a compression and metering section in the extrusion screw for consistent extrusion [135–137].

Apart from elastomers, custom FGF extruders were also employed for testing of biopolymers including PLA and PBAT [138, 139] as well novel applications of conventional thermoplastics, such as PP [140]. Two of the biggest barriers to 3D printability using MEX processes are shrinkage and poor self-adhesion, such as experienced during the studies of Singamneni *et al.* [138, 139]. This aspect is equally critical for both FGF and FFF processes.

The flexibility and ease of implementation of medium scale class extruders is further exemplified by the study of Hertle *et al.* The extruder was mounted on 6 axis robotic arm to 3D print PP strands sheet on an aluminium substrate [140]. This innovative study evaluated the bond strength between these two materials and demonstrated the applicability of FGF beyond conventional 3D printing.

The reduction of weight and size was a common goal that drove the studies of La Gala *et al.* [141, 142] and Khondoker and Sameoto [37]. These teams developed two radically different solutions for the same problem. The research team of La Gala *et al.* [141, 142] proposed a conical extruder, shown in Figure 2.27, which allows for a longer screw path in a more compact extruder configuration. The system managed to extrude ABS and polystyrene (PS) with less material degradation than in FFF, the same result as reported by Liu *et al.* [125] with small-scale extruders. Degradation is a process that involves the

scissoring of polymer macromolecules caused by thermal cycling, resulting in the reduction in material molecular weight. The main limitation is the increased manufacturing complexity especially when it comes to the critical barrel to screw clearance. Furthermore, the use of a large diameter at the feeding end, may limit the extruder's capability in generating pressure. The other solution developed by Khondoker and Sameoto [37] involved the use of a static screw extruder with a flexible heated hose to deliver the melt to the deposition head during 3D printing. This setup was used to successfully 3D print elastic inflatable actuator (EIA) using SEBS and shape memory polymers [143]. The most significant issues that may hinder this setup is the extended residency time of the material which may lead to undesired degradation along with the added energy consumption of the heated hose.

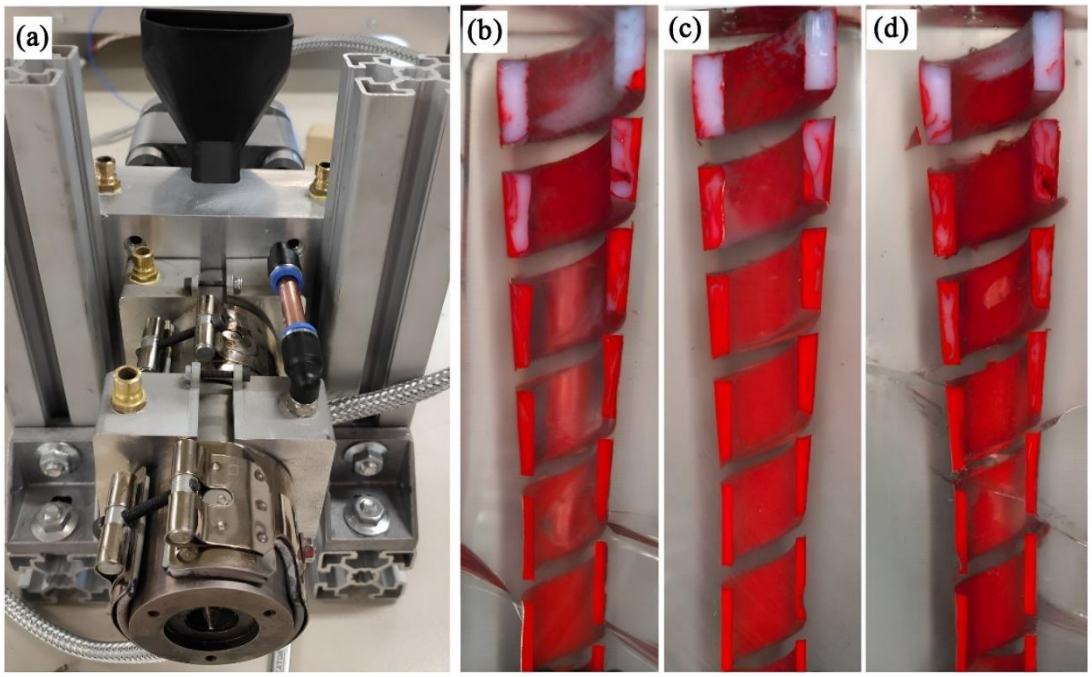

Figure 2.27 - Micro-extruder cooling setup for screw-freezing experiments and (b to d) embedded samples for ABS at screw frequency of 2, 5, and 8 rpm, adapted from [141].

A more recent study brought forward by Lu *et al*. [88] has further advanced the research area by enabling online mixing of high performance thermoplastics with fibre reinforcement. The extruder comprised of two horizonal feeding screws and one main vertical mixing and plasticating screw, as shown in Figure 2.28. The study used PEEK powder and carbon fibre (CF) 50 wt.% / PEEK 50 wt.% powder as the two feedstock materials. Whilst the system successfully 3D printed at different concentrations, increasing CF concentration led to an increase in porosity caused by an increase in viscosity. This indicates that further studies possibly with longer screws may be

necessary to improve compression and thus decrease undesired porosity of the composite extrudate.

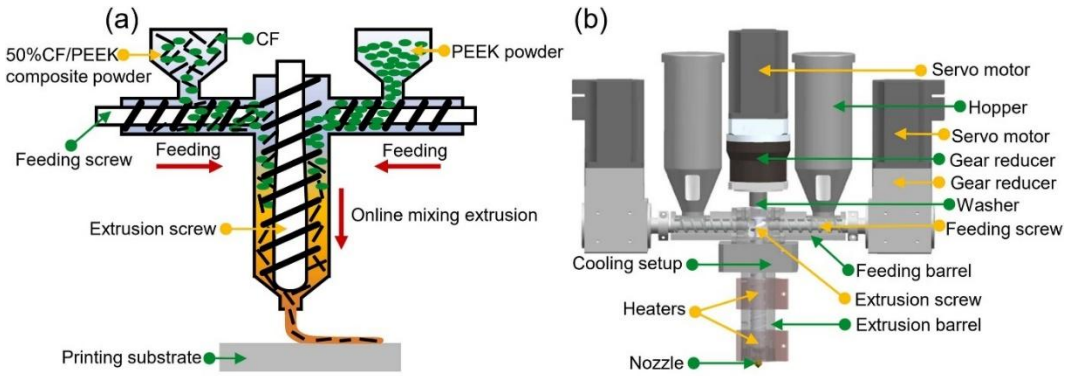

Figure 2.28 - Schematic of the screw-extruded online mixing 3D printhead (a) and the resulting 3D model (b) [88].

This section demonstrated various novel medium-scale FGF extruder designs, all of which involved modifications to the single screw extruder configuration. With sufficient research, these innovative designs could potentially be miniaturized to the small-scale class. Miniaturizing the technology enhances accessibility, while scaling up increases throughput and enables the fabrication of larger objects.

2.2.6.4 Large Scale

Large-scale extruders make use of extrusion screws which are longer than 200 mm. These extruders employ stronger motors which, combined with the longer screws, can drive a greater throughput with a greater degree of plasticating and mixing. These aspects make large-scale extruders critically different than the other classes, with their own benefits and trade-offs.

A classic example of a large scale FGF 3D printer is the Fused Form FF600+ [144] which uses a single screw extruder mounted in a closed chamber. Mazzei Capote et al. [145] used this system to 3D print ABS with barium titanate ceramic and a plasticizer to reduce its complex viscosity. A distinctive extruder is the Massive Dimensions MDPH2, which operates at speeds between 25 and 200 RPM [146], unlike most extruders that stay below 25 RPM [79]. This extruder was successfully used to produce PLA reinforced with continuous CFs [98, 99]. Optimal CF deposition occurred at a 25° tilt, enabling higher printing speeds and better impregnation quality. However, the study did not show the CF's cross-sectional position in the extrudate, indicating the need for further research to improve understanding of fibre co-deposition.

The Gigabot X, shown in Figure 2.29, is another classic large-scale system which has been used predominantly for studies involving recycled or regrind thermoplastic [60, 61, 147–150]. Byard et al. demonstrated that direct 3D printing with shredded polymer waste can yield cost savings compared to mass-produced products [60]. Another study by Little *et al.* [149] highlighted the difficulty of 3D printing using recycled polyethylene terephthalate (rPET) flakes on the Gigabot X printer with a 16 mm diameter screw. This required an extra feedstock crammer for rPET flakes, unlike when pelletized rPET was used. However, this result is inconclusive as flaky rPC [51, 99] did not exhibit the same extrusion inconsistencies as flaky rPET [149]. The research team of Reich et al. managed to achieve similar properties to FFF PC [99]. This indicates that the problems associated with 3D printing of flaky rPET may not have been caused by the feedstock morphology but rather by the material itself. Larger extruders than the Gigabot X, such as the BAAM-100 by Cincinatti (USA), were more successful when 3D printing reground feedstock.

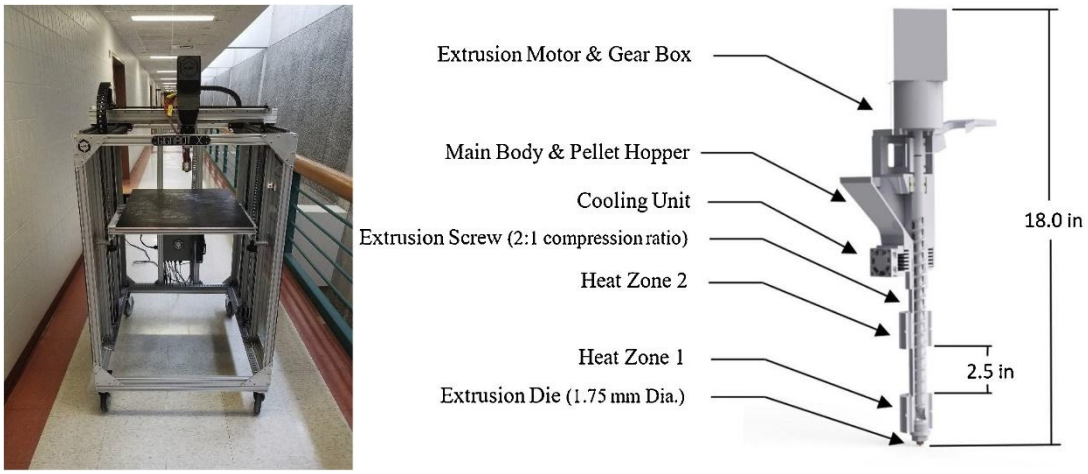

Figure 2.29 - Gigabot X extruder with pellet/granules/particles and regrind feeder [60].

BAAM-100 by Cincinatti (USA) with a screw of 30 mm in diameter and 320 mm in length was found to be the extruder with the largest screw diameter applied for FGF. The larger screw diameter allowed for easy feeding and processing of regrind thermoplastics even when mixed with fillers such as CFs [97] and wood flour [96] without necessitating pre-compounding before 3D printing. When using the recycled granulates, the extrusion was consistent without any clogging [96, 97], unlike when using a small-scale extruder as done by Alexandre *et al.* [25].

Large extruders are capable of large extrusion rates especially when using large nozzle diameters. The use of large nozzle diameters leads to a small surface area to volume ratio which in turn means that the extrudate takes a long time to cool down. A slow to

cool extrudate coupled with a fast deposition rate often leads to warpage. This is a common issue with systems like the BAAM-100, caused by the high heat energy present in the large volume of extrudate, as shown in Figure 2.30. Reinforcement using CF or glass fibre (GF) was found to improve thermal stability and decrease this warpage issue [95]. Studies conducted by Leander Schmidt *et al.* [151] and Merez Trejo *et al.* [94] aimed to minimise this warpage issue through modelling and thus account for the temperature build-up in the slicing process and by determining the max allowable extruder temperature respectively.

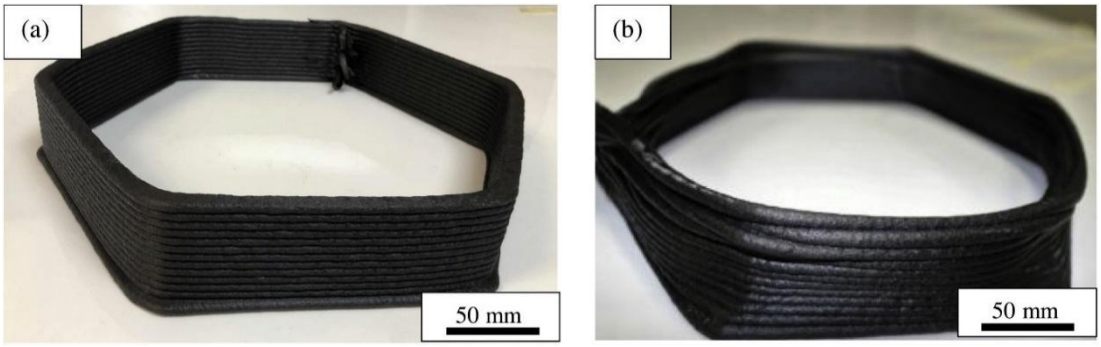

Figure 2.30 - Hexagon geometries printed with a BAAM machine. Frame (a) depicts a hexagon printed with a 90 s delay between layers, while frame (b) depicts a hexagon geometry printed with no added layer time. Notice the difference in print quality where the part shown in (b) is defective, adapted from [94].

The research group of Brackett *et al.* [152] took fibre reinforcement a step further and studied 3D printing with functional gradient by transitioning from unfilled ABS to ABS with 20 wt.% CF during print. The system was also employed to 3D print a high performance polymer polyphenylene sulfide (PPS) with 50% CF [153]. Only 10% of the data sheet strength was achieved. This was partly attributed to porosity but probably the largest contribution is the lack of heated chamber as observed when 3D printing PEEK [88, 154–156]. The same chamber heating issue was noted by Barera et al. [157] when 3D printing polyamide 6 (PA6) compounded with 40 wt.% CF using the CMS Kreator Ares. This underscores a gap in literature, as there is a lack of published studies developing layer or chamber heating system for large-format FGF 3D printing. This is necessary to improve the layer bond strength with similar materials. A different solution was proposed by Wang *et al.* [158] which would use specifically designed nozzle geometries that aimed to decrease the 3D printing porosity to then improve strength.

Beyond application of commercial large-scale extruders, a number of advancements have been made in the development of novel systems. Mi *et al.* [106] evaluated the effects on extrusion by adding an elongated blister ring at the end of the extrusion screw,

as shown in Figure 2.31. This extra section replaced part of the metering section with a shaft section instead of the extrusion screw thread. The new shaft section had a smaller diameter than the overall screw outer diameter. The thin gap created between screw shaft and barrel allowed for only a thin sliver of molten material to flow through, effectively shearing it. This resulted in an increase in extrusion consistency and blending but also an increase in polymer degradation possibility. The shearing screw also caused a higher degree of orientation of the molecule chains which increased tensile modulus and decreased elongation at break for rPP. The flow resistance caused by the shearing section led to a significant increase in the necessary screw speed for the same extrusion rate, increasing from 11.7 to 39 RPM respectively.

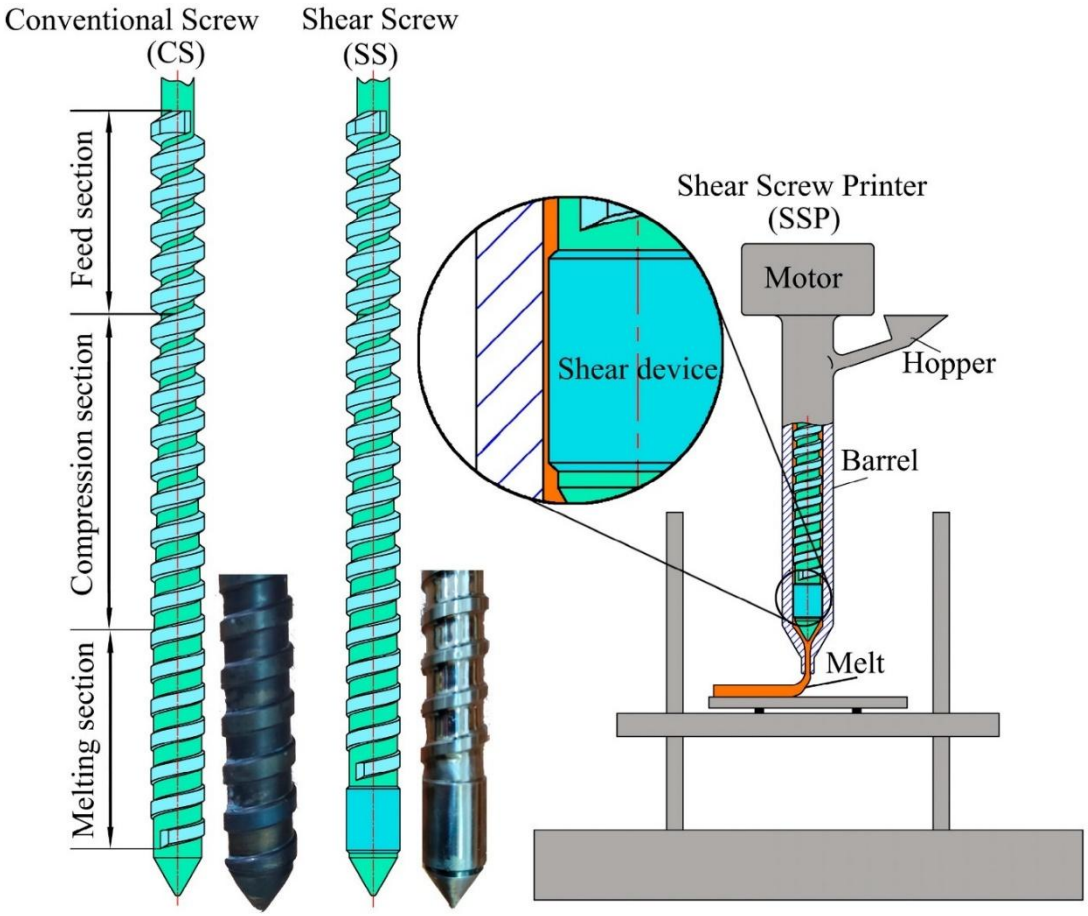

Figure 2.31 – Schematic representation of conventional screw (CS), shear screw (SS), and shear screw printer (SSP) [106].

Extruder designs for large format 3D printing do not necessarily have to be heavy neither require a bulky motion system. One solution to this problem was provided by Rattan *et al*. [159] which implemented the Hangprinter system by Tobben [160], as shown in Figure 2.32. A hangprinter is a cable driven motion system, allowing large volume printing., It was originally designed for lightweight extruders but this development by Rattan *et al*.

has brought about this low-cost motion system for FGF, at about €2000. The accuracy achieved was less than that of a conventional desktop system, reaching at best ~ 0.1 to 0.3 mm absolute error. This value can be improved by implement an already existing optical positioning system called the hp-mark developed by Tobben [161]. Even if the accuracy and reliability of the system never reaches the same level as that of a rigid motion system, the cost savings are significant enough to make the product worthwhile.

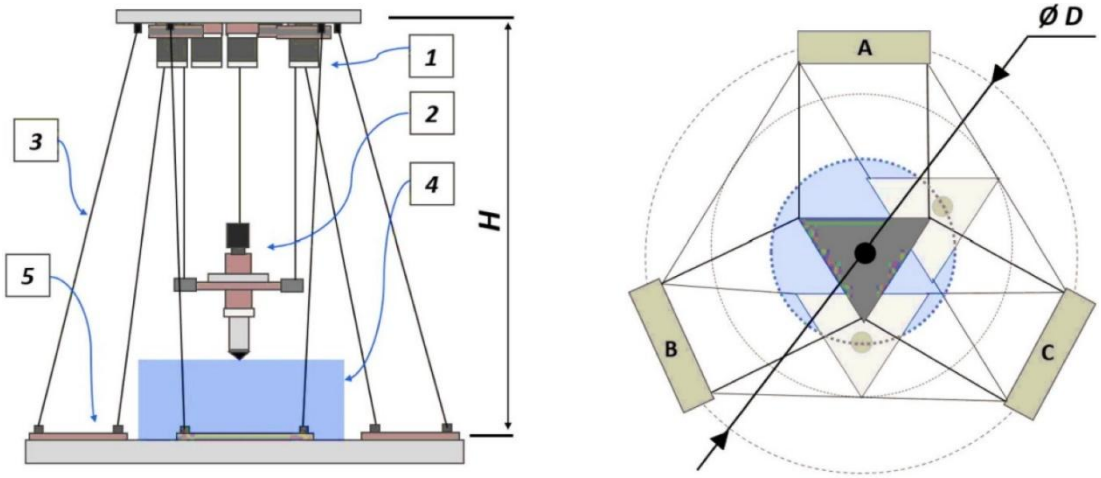

Figure 2.32 - Waste plastic FGF/FPF Hangprinter schematic where (1) ceiling unit housing controls and 4 motors for A, B, C and D axes; (2) end effector with FGF/FPF extruder; (3) A, B, C, and D lines/cables; (4) scalable, conical build volume and (5) print bed and ground anchors, adapted from [159].

High-performance polymers like PEEK are among the most challenging thermoplastics to 3D print. Tseng et al. [155], Hu et al. [62], and Li et al. [162] studied unfilled PEEK [155], PEEK with up to 30 wt.% CF [62], unfilled PA6, and PA6 with up to 33.6 wt.% CF [162]. Tseng et al. utilized infrared (IR) lamps, while Hu et al. employed an enclosed heated chamber reaching 200°C and a heated bed at 250°C to improve mechanical properties. Both studies with CF reported lower extrudate density and increased porosity with higher CF content, attributed to the higher viscosity preventing trapped air bubble release. Despite underperforming compared to injection molded specimens, the filled specimens achieved higher strength than all the previous MEX studies [62, 162]. However, all tests were conducted in the XY plane, ignoring expected material anisotropy. Future research work is necessary to elucidate this important aspect of the 3D printed product's mechanical properties.

2.2.6.5 Unclassified

2.2.6.5.1 Commercial extruders

All the journal articles covered till to date included information about the extruder design, which eases the classification of extruders. The remaining 57 articles did not have any information openly available and therefore were classified based on common traits with other similar extruders with known dimensions. Out of these articles, 19 of them used custom developed FGF systems, whereas the rest employed commercially available systems of various sizes.

Of the small FGF commercial systems there are 5 namely Direct 3D [163], Creality G5 [164], Brinter [165], 3D Cultures [166] and 3D Discovery by RegenHU [167]. Daniele *et al*. [168] employed the Direct 3D [163] system to demonstrate that recycled high density polyethylene (rHDPE) can be 3D printed and that the addition of 15% wt.% GF countered degradation by doubling the elastic modulus and increased yield strength. Another study by Wang *et al*. [83] used the Creality G5 [164] to successfully 3D print polyphenylene sulphide (PPS) with graphene nanoplatelets (GNPs). Immonen *et al*. [81] also studied composites 3D printing using the Brinter [165] and showed that the addition of plasticiser to cellulose acetate propionate was necessary to enable self-adhesion. Further studies on composite 3D printing were carried out with the 3D Discovery by RegenHU [167] to produce scaffolds made out of PCL with graphene [169] and with carbon nanotubes and nanohydroxyapatite [170]. In the same year, Huang *et al*. [171] published another study using unfilled PCL to produce scaffolds and subsequently laying down fibrils using electrospinning. The research team of Lee *et al*. [172] pushed the research boundary of small scale FGF by 3D printing hybrid piezo-magnetic self-sensing actuators (HPSMA) using the Pellet Extrusion Bioprinter by 3D Cultures. Despite this positive result the study reported that immersion precipitation 3D printing was found to be a superior solution than FGF to produce HPSMA. Immersion precipitation 3D printing is a method in which a polymer solution is extruded into a coagulation bath (typically a nonsolvent like water), where phase separation occurs, causing the polymer to solidify rapidly into a porous or dense structure. The result of this article is a reminder that whilst FGF is a versatile technique, it is not always the best tool for a given application.

The medium scale is more difficult to identify especially for those systems which are close to either end of the spectrum. Out of the remaining FGF systems, 3 commercial

systems were found namely, PAM series P and Lx [173], Ambit extruder [174] and the Cosine AM1 3D printer [175]. The PAM series offer off the shelf FGF 3D printers that can produce multi-material parts through multiple extruders. This feature was used by Yousfi *et al.* [176] and Andreu *et al.* [177] to study polymethyl methacrylate (PMMA)/PLA layered structures and poly(d,l lactide) (PDLLA) with different combinations of hydroxyapatite and bioactive glass respectively, as shown in Figure 2.33. These functionally graded materials were found to have transitional mechanical properties of each material's distinct properties.

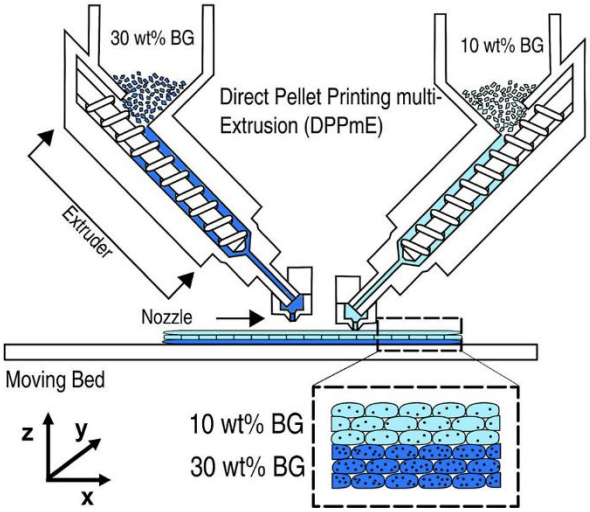

Figure 2.33 - Schematic representation of direct pellet printing multi-extrusion process with 10 and 30 wt. % of bioglass, adapted from [177].

The PAM series 3D printers were also used in single extrusion mode using polylactic-co-glycolic acid (PLGA) [178], EVA with fire-retardant [63], rPP and PP with glass fibres and mineral fill [179], and 85 wt.% of zirconia powder with 15 wt.% PA [180]. Similar to as reported by Andreu *et al.* [177] that used PDLLA, Gradwohl *et al.* [180] also reported thermal degradation of PLGA when using FGF. On the other hand, 3D printing the same material using FFF resulted in less degradation due to shorter residence time and less shearing involved. Degradation studies using powder and small-scale extruders with a smaller screw have shown the opposite effect i.e., the FFF products degraded more [25, 125]. High filler content materials such as produced by Spitaels *et al.* [180] where the PAM series MC was used to 3D print 85 wt.% of zirconia powder with 15 wt.% PA produced poor 3D printing quality, but this was expected due to the low thermoplastic content.

Montoya-Ospinai *et al.* [181] also studied novel additives. The research team employed the Cosine AM1 to 3D print HDPE with vitrimers. This resulted in decreased part warpage

and improved self-adhesion during the 3D printing process, compared to virgin HDPE. The vitrimers also decreased anisotropy when the parts are heat-treated after 3D printing. A diverse 3D printing approach was studied by Northup *et al.* [182] using the Ambit extruder in a milling machine [174]. The system was used to 3D printed a mold which was then post-machined to improve surface finish.

The remaining large-scale commercial FGF systems are presented in this section. Of these, there are 15 different studies, with 8 distinct 3D printing systems. The Super Discovery 3D Granza, shown in Figure 2.34, was used by Moreno Nieto *et al.* to 3D print furniture for naval applications using PLA/ABS blend with fire retardant [183]. This study demonstrated the capacity of large scale FGF to 3D print large objects, but it also highlighted the necessity for post-processing, especially when a smooth surface finish is necessary. The same system was used to 3D print using acrylonitrile styrene acrylate (ASA) with 20 wt.% CF [184], PLA and rPLA with titanium dioxide (IV) nanopowder [86], and ABS with 20 wt.% CF [185]. The addition of titanium (IV) nanopowder to recycled PLA increased thermal stability and crystallinity and countered the loss of mechanical properties brought about by thermoplastic degradation caused by the remelting process necessary for recycling [86].

Figure 2.34 - Super Discovery 3D Granza, large scale FGF system [186].

The researchers at Politecnico di Milano delved further into large format 3D printing by using unfilled regrind PLA [187] and with the addition of spent coffee grounds [103]. These studies were conducted with the Delta Wasp 3MT. Romani *et al.* [187]

demonstrated that after six 3D print and regrind cycles, each time using the same batch of material, there was a decrease in mechanical properties and only minor variations in thermal properties. The addition of spent coffee grounds by Paramatti *et al*. [103] to PLA led to an increase in flowability and layer adhesion, whilst achieving good 3D printability. Another important filler is GF which, as shown by previous studies, can improve thermal stability. Winter *et al*. [188] using the Delta Wasp 3MT and Austermann *et al*. [189] with the Extruder 500-CU-D by Yizumi, also used this filler to reduce the warpage of PP. Globular or powder fillers, namely talcum powder and glass bubbles did not demonstrate a similar improvement in warpage behaviour [188]. To minimise the occurrence of pores brought about by the addition of fibre reinforcement, Sayah and Smith [190] proposed compressing the extrudate by using a roller to decrease porosity.

More studies with novel materials were published by Lengauer *et al*. [191] which used an ExAM 255 printer by AIM3D to produce hardmetal and cermet bodies and by Zlatanovic *et al*. [192] with the ExOn10 using aliphatic polyketones (PK). The former study demonstrated the material flexibility of FGF by adding metal injection molding pellets as another possible 3D printing material. The latter study also opened further the material's library by introducing aliphatic PK which have good chemical resistance and better mechanical properties than PA12. This could be done at a lower cost and with 61% lower environmentally harmful emission created during its production process.

Finally, the study by Leschok et al. [193] developed an innovative 3D printing approach, using a well-known device, the annular die. The research group used a SAEKI robotics FGF system to deposit hollow tube extrudates in different patterns, as shown in Figure 2.35. This novel printing technique allowed for light weight 3D printing of large objects, using PETG, PLA, cyclic olefin copolymer (COC) and PP. To produce hollow tube extrudates, the extrudate was pressurised with an internal stream of air, otherwise it would flatten out. Studies such as by Leschok et al. [143] greatly expand the capabilities of AM, demonstrating that the subject merits further research as there are still novel techniques that may be developed.

Figure 2.35 - (a): Hollow-Core 3D printing nozzle with a 24 mm orifice and a 2 mm wall thickness. (b): Extruded PETG bead. (c): 3D printed sample, cut, with a hand to represent scale and transparency, adapted from [193].

2.2.6.5.2 Custom

In some cases, even published research articles that made use of custom developed FGF systems, failed to report the dimensions of the extruder. These studies all used FGF extruders purely as tool and did not try to optimise or otherwise improve the technology itself.

When it comes to small-scale FGF, three studies were found, all of which used novel material combinations. The study by Yu *et al.* [84] demonstrated that reactive compatibilization of PLA with up to 3 wt.% polybutylene adipate-co-terephthalate (PBAT) blends using vinyl-functionalized graphene oxide (VGO) nanosheets had higher impact strength and increased the crystallinity of PLA. A separate study by Mondal *et al.* [194] produced magnetorheological elastomers using SEBS thermoplastic elastomer (TPE). This study determined that the infill density can be used to tune the magnetorheological stiffening effect when using a hexagonal infill structure. Another study by Brooks *et al.* [195] produced biopolymer thin shells on a curved, hemispherical mandrel. Another novel configuration, 4 axis, 3D printing system was developed by the research team of Wang *et al.* [196] that used a medium scale extruder for the production of poly(L-lactide) (PLLA) and PCL cardiovascular stents with zero Poisson's ratio in longitudinal deformation. The 4th axis comprises of a rotating mandrel upon which the cylindrical stent was 3D printed.

When it comes to large-scale FGF extruders, one of the first studies on the subject was brought forward by Reddy *et al.* [197], back in 2007. The study used ABS to optimise nozzle temperature, chamber temperature and strand to strand gap for improved bond strength and surface finish. A layer study by Akbari *et al.* [198, 198] developed a thermal simulation strategy using finite element analysis to reduce the occurrence of thermal

warpage. This approach was justified due to the long extrudate cooling time which was found to be around two orders of magnitude longer than that of small scale FGF. Another challenge of large scale FGF which is in common with all MEX scales is the capability of the system to produce overhangs. This issue was studied by Krčma and Paloušek [199] using a 5 axis robotic arm to control the movements of the extruder. The study achieved a greater overhang angle of 75° when using a 5 axis, non-planar 3D printing methodology. In contrast, the classic 3 axis planar only managed to print features with a 30° overhang.

An interesting study by Romeijn *et al.* [200] evaluated instantaneous and time-dependent mechanical properties on PETG specimens 3D printed using a 5 mm nozzle. The results that used time temperature superposition technique for creep were rather limited as the creep experiments conducted at 65 °C did not superimpose on the lower temperature experiments. This is the only published study on long-time dependent mechanical properties concerning FGF. This kind of research is necessary if products are to be made with intention to last.

The last article of interest is different from all the rest as it concerns the implementation of a pump to FGF systems. This study, presented by Canessa *et al.* [90], aimed to create a known volumetric extrusion rate by employing the use of a Moineau pump using the design shown in Figure 2.36. The system was only used with chocolate and wax and managed a consistent extrusion rate. Further work on this type of design is necessary if such a system would ever be usable for thermoplastic polymer FGF. The added manufacturing complexity brought about by the Moineau pump geometry may also make this extruder design undesirable.

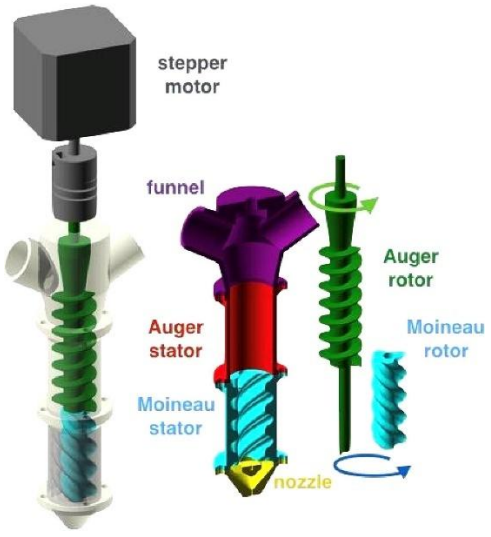

Figure 2.36 - Schematics of a pellet extruder, combining together Auger and Moineau screws [90].

2.2.7 Summary

Fused Granulate Fabrication (FGF) has shifted from traditional applications like PCL scaffold fabrication to a contemporary focus on recycling and performance. This growing interest is evident in the increasing number of published studies and innovations in extruder design in the last decade.

A new classification system for FGF extruders was proposed, categorizing them by screw diameter and length into three classes: small-scale extruders with screws up to 100 mm in length, medium-scale extruders with a screw length from 100 to 200 mm, and large-scale extruders with a screw length of over 200 mm. Additionally, powder extruders are classified separately, defined by a screw diameter of 7 mm or smaller. While this classification provides a useful framework, there are outliers in each class, which is typical in a rapidly evolving field like FGF.

Each class of extruders demonstrated specific advantages, limitations and research gaps, which became evident upon reviewing the relevant literature. In order to summarise the findings, seven metrics concerning FGF systems were identified which were of interest across multiple studies. Each extruder class was adjudicated a grade for each metric to signify its strength in that particular area, as shown in Figure 2.37. Grade adjudication was not empirical but rather followed an estimation approach based on the results of the systematic literature review. The metrics used were ease of 3D printing, motion system complexity, material degradation, material mixing without pre-compounding, material handling from powder to pellets to reground feedstock, material viscosity from conventional thermoplastics to high performance thermoplastics with fibre reinforcement, and throughput referring to the extrusion rate. Medium extruders were set as the base type as in general they stand in between small and large extruder. The graphlol clearly demonstrate the polarised nature of FGF, whereby large extruders have better throughput, ability to process viscous materials, can easily handle various feedstock morphologies, and can even provide a modicum of material handling. On the other hand, powder-based and small-scale extruders offer more accessible 3D printing capabilities with reduced material degradation, that are cost-effective and have low-maintenance motion systems.

In the case of powder only extruders, their small size made them suitable for 3D printing of heat sensitive materials due to their short material residency time. This feature contributed to the adoption of small-scale extruders, including off-the-shelf FGF

systems, for producing biomedical scaffolds. To achieve good quality extrusion, it was shown that even at this scale, the extrusion screw must include a compression and metering section, especially for rigid thermoplastics. Despite the use of powder which would imply easier mixing, studies highlighted the need for pre-compounding multi-component feedstock to achieve proper extrusion. Research efforts to resolve this issue have involved the use of miniaturised twin screw extrusion, but the system is still at an early stage of development. Further advancement of powder extruders is necessary, especially when it comes to high performance polymers of which there are no published studies at this scale.

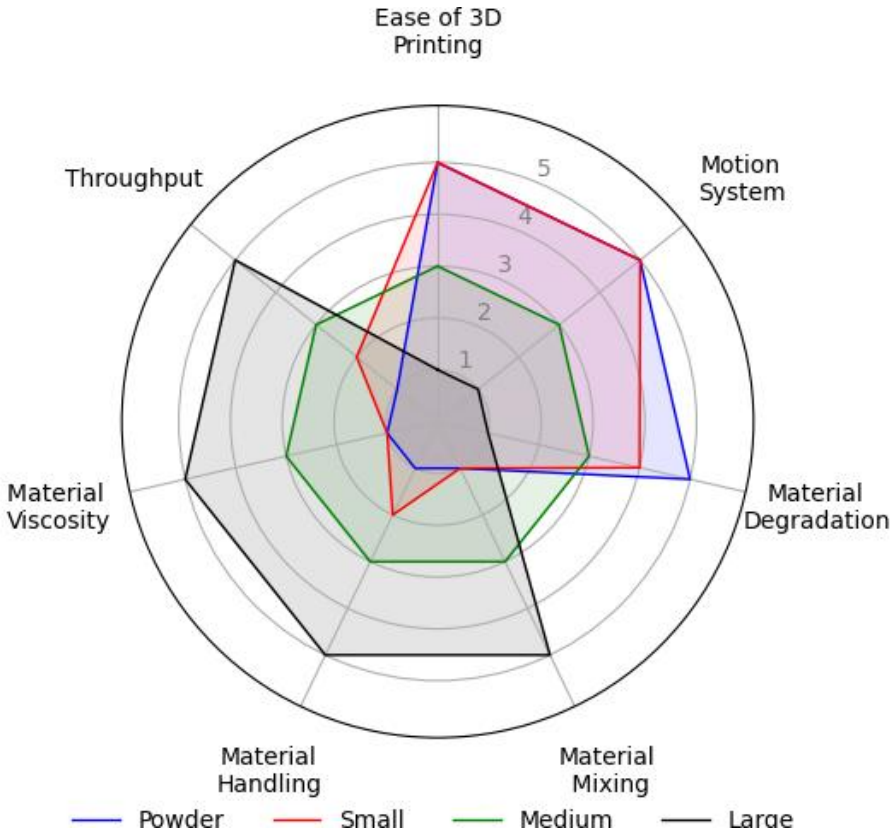

Figure 2.37 - Radar plot of key FGF metrics where: Ease of 3D Printing (1, Hard to 5, Easy); Motion System (1, Complex to 5, Simple); Material Degradation (1, High to 5, Low); Material Mixing (1, Low to 5, High); Material Handling (1, Powder to Pellets to 5, Regrind); Material Viscosity (1, Low to 5, High); Throughput (1, Low to 5, High).

Small scale extruders are a direct competitor to desktop MEX systems which are currently dominated by FFF systems. Small scale extruders were found to be capable of 3D printing softer TPEs than FFF and with better quality. These extruders have been used with a variety of materials including in continuous fibre reinforcement setups. Small scale FGF material costs are significantly cheaper than that of FFF. On the other hand, the equipment cost of FGF is higher than FFF, even at the small scale. At this scale, the

extruders may still be small enough to adequately extrude heat sensitive polymers. One study also evaluated the extrusion of regrind thermoplastic flakes, but the extrusion quality was inconsistent. Similarly, dry mixed, multi-component feedstock can be extruded but with poor quality, indicating the need for pre-compounding. Further research in this class of extruders is necessary to improve the capability and reliability of theses extruders for a wider range of polymers, including high-performance polymers. The high cost and greater complexity of FGF extruders compared to FFF remain significant barriers to the broader adoption of this technology.

Medium class extruders are ideal for advancing FGF technology as any successful development can then be upscaled or downscaled to large or small systems, respectively. Several innovative solutions were developed in this class, including conical extruders and systems with in-process, controlled material mixing. The longer screws in medium-class extruders allow for processing more viscous thermoplastics, such as high-performance polymers and fibre-reinforced materials. Like smaller systems, these extruders demonstrate consistent TPE extrusion. Like in powder extruders, medium class FGF extruders were shown to extrude poorly when using extrusion screws that lack a compression and metering section. This is probably the case for all extruder classes. In contrast to powder and small class extruders, material thermal degradation may become significant at the medium scale for certain materials extruded at a low rate, due to the longer material residency time. Thermal degradation was evaluated using different methodologies by various studies, with the principal methods including measurement of the molecular weight or determination of changes in mechanical performance. Despite their greater versatility in handling a wider material range, there are no studies yet on the extrusion of regrind or flaky thermoplastics in this class. This is an important next step for this class of extruders given the greater extrusion screw size flexibility compared to powder and small scales.

The large class of FGF extruder systems demonstrates greater extrusion capability than medium scale extruders. Large scale FGF is primarily used in large-format 3D printing including amongst others furniture, and large scale models. These FGF extruders have been used to achieve the best mechanical properties available to MEX AM by using high performance thermoplastics with a high degree of fibre reinforcement. These kind of materials, such as PEEK with 30% CF reinforcement [62], have a high level viscosity and to date, can only be extruded by high power extruders, generally available only to large scale FGF. The elevated viscosity was found to induce porosity in the extrudate which

decreased the attainable mechanical properties. Further extrusion improvement is necessary to decrease this induced porosity.

Multiple studies have successfully employed large-scale FGF for direct 3D printing with regrind thermoplastics, achieving high-quality results, particularly when utilizing large-diameter extrusion screws. Further studies are required to assess whether there is any relation between extrusion capability and consistency with increasing screw diameters when using regrind and other inhomogeneous feedstock types. The high flow rates common in large scale FGF contribute to thermal warpage. This common issue can be abated by using fibre reinforcement. The heavy nature of large scale FGF extruders requires a complex and generally expensive motion system to run. This places a heavy initial investment barrier which may be the most significant reason limiting a greater adoption of this technology in industry. Efforts towards simpler and cheaper motion systems, even for large scale FGF are ongoing, with the Hangprinter style system leading the way.

The systematic review has demonstrated the diverse nature of FGF, involving four distinct classes, each with their different research gaps and trends. The FGF research field is expanding with each class of FGF extruders becoming more defined as research advances. Its commercialization is progressing as it is driven by the growing interest in FGF across different applications. Despite this, each class continues to face specific challenges that require further research to fully realize the technology's potential and ensure broader adoption in both industrial and academic settings.

2.3 Materials

As discussed in section 2.2.4, page 51, a large number of thermoplastics have been applied to FGF, summarised by Figure 2.19. However, most materials have been studied once, with the exception of PETG, EVA, PCL, PP, ABS and PLA which have been investigated more than 3 times in an FGF context. This thesis demonstrated the applicability and potential of FGF, particularly through the development of an improved FGF system along with its application towards the study of four thermoplastics. The study will evaluate two TPEs and two high performance polymers. These represent thermoplastic families at extreme ends of the spectrum, having completely different properties and extrusion behaviours. Successfully 3D printing using all materials would

be a further demonstration of the capabilities of FGF and a step forward towards its broader adoption.

2.3.1 Thermoplastic Elastomers

Thermoplastic elastomers (TPEs) are a family of polymers which often stand apart from other thermoplastics due to their unique properties and attributes. Elastomers generally have a low hardness and allow for large elongations. These properties make elastomers part of several industrial applications such as automotive [28], medical [201], electronics, footwear and construction industries [202]. Elastomers are used for sports applications [203] as well as textile and protective equipment for comfort and flexibility, such as knee and back protectors [28, 204]. Elastomers have also found an array of uses in the biomedical sector, for drug delivery, orthopaedics, dental, and soft and hard tissue implants [201] and prosthesis [205]. Beyond the biomedical sector, elastomers are also found in a number of applications such as microfluidics [206], insoles [207], wearable flexible sensors [87] and inflatables, including elastic inflatable actuators (EIAs).

EIAs are particularly interesting as they relate with collaborative robotics which is a growing research field. Elastomers allow for the production of compliant robots which are safer for a human to work around compared with a rigid robotic system. Otherwise, an impact between a machine operator and a robot involving rigid materials can result in serious injury [208]. Furthermore, EIAs do no rely on electricity, magnetism or high temperature to operate which may be undesirable for robotic orthotics or robotic surgery tools [209]. The wide applications field just discussed illustrates the usefulness of elastomers which prompted the development of a number of AM techniques that can produce elastomeric products.

Arguably the most applied technique for extrusion AM is FFF [28]. Material extrusion of elastomers can also be carried out using direct ink writing [210] and FGF. Other techniques involve vat polymerisation systems including Stereolithography (SLA), Digital Light Processing (DLP), [201] and Tomographic Volumetric Printing (TVP) [211, 212]. As well as material jetting (MJ) systems such as drop on demand (DOD) [205] and powder based systems such as selective laser sintering (SLS) [27]. Each technique just mentioned has its own advantages and disadvantages but the most accessible is probably FFF followed by SLA. As outlined in section 2.2.3.2, page 49, FFF of elastomer has a significant limitation known as filament buckling, shown in Figure 2.38. This limits

the softness of elastomers suitable for FFF-based 3D printing to approximately 70 Shore A [77]. In contrast, FGF avoids this issue by utilizing granulates, which offer a more affordable and diverse material source. Consequently, FGF has the potential to surpass FFF as the leading elastomer additive manufacturing technology, provided it becomes equally accessible.

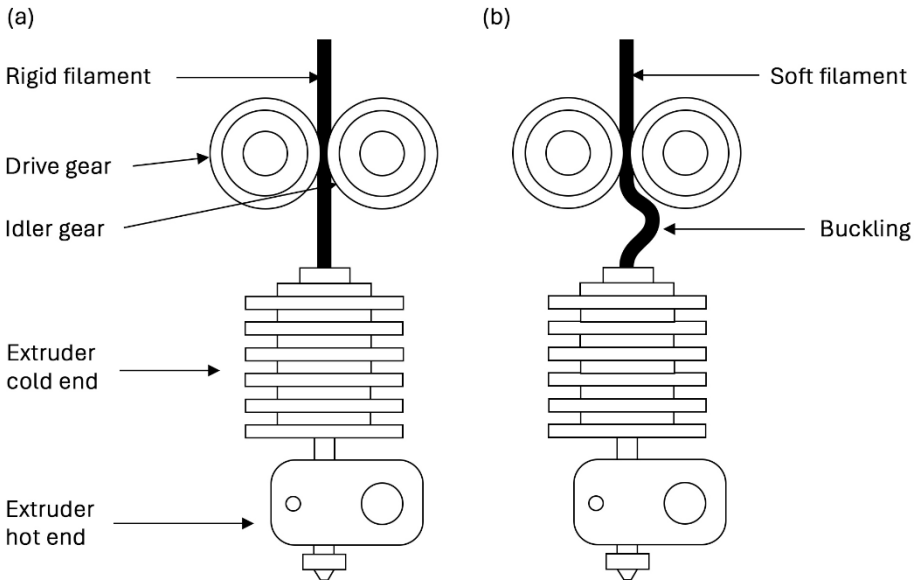

Figure 2.38 – Schematic diagram of normal filament extrusion using rigid filament and filament buckling when using soft materials.

The most commonly used TPE for material extrusion AM is TPU [27] partly due to its tuneable mechanical properties and partly due to its relatively stiff nature which makes it amenable for 3D printing using FFF. Amongst the materials discussed in section 2.2.4, page 51 that have been applied to FGF in published studies, only four are elastomeric: TPU, SEBS, EPDM, and EVA. This study proposes TPO as an additional material for FGF, intended as a potential alternative to TPU. TPO is a relatively stiff elastomer with a hardness of approximately 30 Shore D, as depicted in Figure 2.39. Additionally, a softer and potentially more challenging-to-print TPE, specifically TF3ZG0-LCNT, will be investigated. The aim is to produce extremely soft components with a Shore hardness of 30 Shore 00. To aid comprehension, Figure 2.39 includes a scale illustrating Shore hardness levels with examples of materials, helping to highlight the differences in hardness targeted by this 3D printing system.

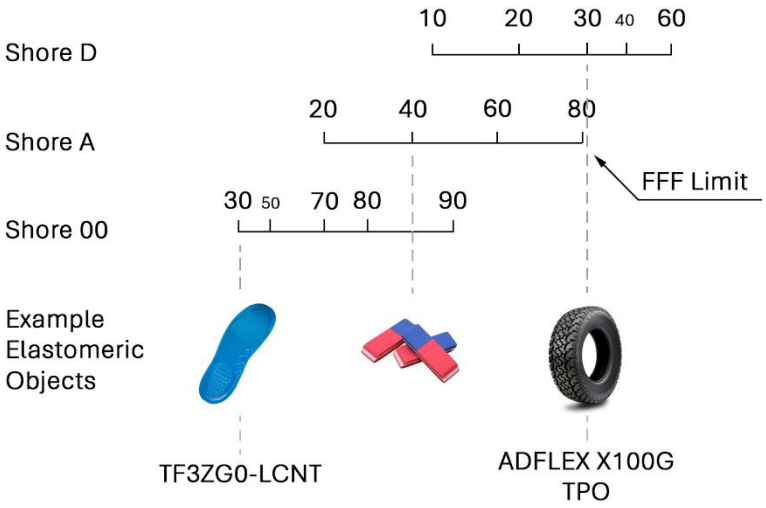

Figure 2.39 - Range of shore hardness and conversion with FFF limit and example elastomeric objects, as well as an indication of the hardness of the elastomers that were later applied to FGF.

2.3.1.1 Hard Elastomers

Thermoplastic polyolefin (TPO) is the second most used thermoplastic elastomer (TPE), just after styrenic TPE, taking up 26% of the share. It is used in automotive, consumer goods, asphalt, roofing, adhesives, sealants and coatings [213]. TPO is also inexpensive, in fact its largest market is the automotive sector. It is often selected for its low cost, low temperature toughness, weatherability, and low specific gravity [214]. Despite its wide application, TPO has not been widely studied for MEX AM, especially with screw extrusion, FGF

The first study that employed TPO for MEX AM using FFF was published by Laoutid *et al.* which managed to 3D print TPO-rubber blends using FFF. The group achieved good quality 3D prints, however the 3D printed geometries were not complex [215]. Another study using FFF was carried out by Lv *et al.* which 3D printed TPO with graphene nanoplatelets. This nanocomposite was used to 3D print products with improved electromagnetic shielding performance [216]. The first study involving FFF 3D printing of unfilled TPO grades was conducted by Adrover-Monserrat *et al.* which evaluated the mechanical properties achievable using this material. The study reported a yield strength of 3.4 MPa and a maximum stress of 4.5 MPa at a strain at failure of 350%, when tensile testing along the extrudate direction [217]. None of the published studies have optimised the 3D printing process in order to improve quality and mechanical properties. In fact, there is a lack of complex geometries that were 3D printed using TPO. Finally, all studies used FFF meaning that TPO was never 3D printed using an FGF setup.

The principal advantage of TPO over thermoplastic polyurethane (TPU), which is the current dominant MEX elastomer, is TPO's non-hygroscopic nature. No pre-drying should be necessary prior to 3D printing using TPO pellets or even filament [29]. Humidity absorption in TPU causes bubbles in the 3D printed parts which in turn decreases the aesthetic value and mechanical performance of the product [218]. This advantage alone provides ample reason to study the application of TPO to material extrusion AM as it could significantly decrease the running costs and complexity of elastomer MEX AM. Decreasing the need for preparation along with the necessary equipment required for pre-drying would make elastomer MEX AM simpler, more reliable, and less time consuming. This in turn would make it more approachable for a wider user base.

Apart from the principal advantage of being non-hygroscopic, TPO also has a high impact strength and is light weight [30]. The density of TPO is reported to be 0.88 g/cm^3 [219], whereas the density of TPU varies from 1.18 g/cm^3 up to 1.42 g/cm^3 [220]. TPO also has good chemical resistance, similar to that of polypropylene (PP) and is easy to recycle [30]. The properties of TPO can vary as it is a tunable elastomer composed out of two main components: a polyolefin semi-crystalline thermoplastic and an amorphous elastomeric component. Commonly, TPO is a mixture of isotactic PP and ethylene-propylene random copolymer (EPM). Depending on the ratio of these two components, the hardness and stiffness of the TPO can be altered as desired, customarily ranging from 70 shore A to 70 shore D. The mixture may be made by either mechanically blending the two components or else by dynamic vulcanization [29].

TPO may also be produced via a reactor process which produces an alloy rather than a simple blend [221]. An alloy is a blend between two or more immiscible components which have been compatibilized. In this context, compatibilization means to modify the interfacial properties of one or more components of the blend to stabilize the dispersed components [222]. Reactor processes produce a cheaper TPO than mechanical blending processes, making TPO more affordable [223]. Reactor TPOs also have an improved weldability [221], melt flow, a finer dispersion and an often more homogenous mixture of the components which stabilizes the properties of the material, when compared with TPO produced using the previously mentioned processes [29]. All the aforementioned attributes make reactor TPO the most amenable version for MEX AM.

2.3.1.2 Soft Elastomers

The softest elastomer manufactured using FGF that could be found in literature were produced by Georgopoulou *et al*. The study successfully 3D printed styrene-based tri-block copolymers (SEBS) by Kraidburg TPE (Germany) of three different grades with three Shore hardnesses, namely 25, 50 and 70 Shore A [77]. Another noteworthy study was published by Khondoker and Sameoto that utilized a fixed screw extruder coupled with a flexible heated hose to produce SEBS inflatables with a 47 Shore A, achieving a high maximum elongation at break of around 870 % [37].

The softness and elongation achieved by TPEs produced through screw-based MEX additive manufacturing remain limited compared to those attainable with polydimethylsiloxanes (PDMS), commonly known as silicone rubbers. PDMS can be 3D printed using alternative MEX techniques such as DIW [224]. These thermoset polymers are however less sustainable and often achieve lower print quality compared to equivalent TPEs. Nevertheless, the elongation at break of PDMSs outstrip that of TPE parts produced using screw MEX AM. Amongst the highest strains at break was achieved by using DragonSkin 10 with hardness of 10 Shore A which managed to reach 1000% elongation at break [225]. Nevertheless, these high elongations at break are still low compared to those of molded resins such as acrylamide-alignate materials which surpass 2000% elongation at break [226]. This research field is growing at a rapid pace, with developments involving novel materials for EIA productions. Some examples include photo-responsive liquid crystal elastomer composites [227] and multi-material 3D printing of multifunctional heterogeneous objects [228]. This highlights the importance of further development in this field.

There are no studies conducted on 3D printing of TF3ZG0-LCNT with any AM technology. Furthermore, there are no other AM materials which can achieve the same level of softness and stretchability as the base material properties of TF3ZG0-LCNT. The material has also never been applied to EIA production and at the moment used only for applications involving cushioning. This is a clear indication of the lack of research conducted in this area despite the clear applications that may be possible. Examples include in automation, such as EIAs and as cushioning in general and as inflatables, which would be applicable in multiple sectors such as aerospace, naval and again in automation.

2.3.2 High Performance Thermoplastics

The early polymers which were developed had linear or branched aliphatic backbones. Some of these polymers are still in use today, such as polyethylene. An aliphatic backbone is flexible and can rotate which in turn makes the polymer less stiff. The necessity for stiffer thermoplastics, higher glass transition temperatures and better solvent resistance, led to the development of high-performance polymers. These polymers generally have an aromatic backbone which have increased intermolecular forces, thus restricting the movement of the backbone chain. This effect improves thermal and mechanical properties as well as solvent resistance [229]. Some examples of high-performance thermoplastic families are polyketones, polyarylene sulfides, polyamides, polyimides, and polyesters. The repeat units of the macromolecular chains of PEI and PEEK are shown in Figure 2.40, demonstrating the prevalence of aromatic rings [230].

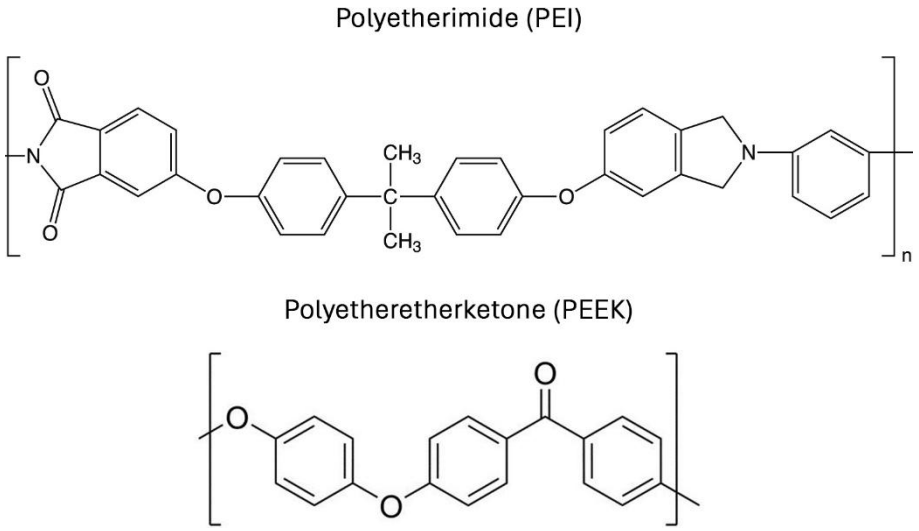

Figure 2.40 - Repeat unit of polyetherimide (PEI) and polyether ether ketone (PEEK) [231].

This necessity for better thermoplastic properties was driven by more rigorous component conditions such as in aerospace. In this sector, the strength to weight ratio coupled with simple processing of certain high-performance thermoplastics, such as PEEK, makes these material competitive with metals. It should be noted that whilst processing of high-performance polymers is often simpler and hence cheaper than that of metallic materials, it is still more challenging than commodity and engineering grade thermoplastics. In general, the higher glass transition temperature of high-performance polymers is associated with elevated melt viscosity and processing temperature [229].

The challenges associated with processing are arguably one of the primary reasons why some high-performance polymers have gained wider application than others. In particular, the size and weight limitations of AM systems make it difficult to utilize thermoplastics that are hard to extrude. Among the most commonly used high-performance thermoplastics for additive manufacturing are PEEK and PEI [32]. These polymers have similar mechanical and thermal properties, with PEEK demonstrating superior mechanical strength and toughness whereas PEI has a higher heat deflection resistance [232, 233]. The tensile strength of various MEX 3D printed high performance polymers is shown in Figure 2.41. Arguably the most critical difference between these two materials is their crystallinity. PEI is an amorphous material whereas PEEK is a semi-crystalline thermoplastic whose degree of crystalline is closely linked to the cooling rate during processing [6]. Crystallinity is in turn linked with the material's properties, especially its mechanical strength. The higher the crystallinity the stronger and stiffer the material. Nevertheless, crystallinity in AM parts can be deleterious as it often leads to shrinkage and warpage which are undesirable as they compromise the parts geometric tolerances and introduce significant internal stresses [6, 234].

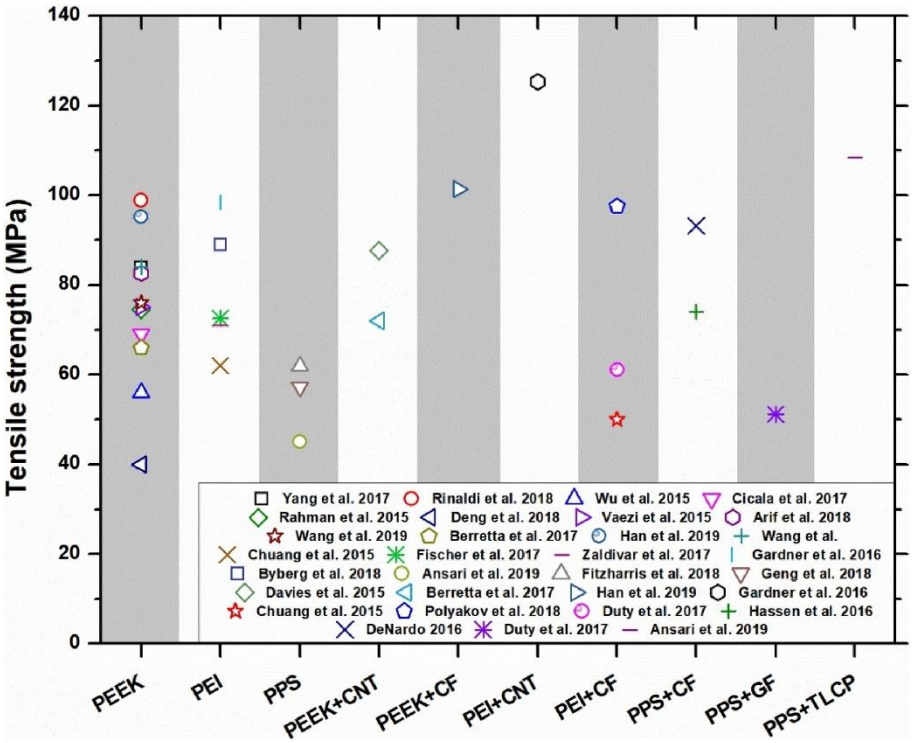

Figure 2.41 - Tensile strength of high temperature thermoplastics and their composites printed using material extrusion. All tests were carried out at room temperature [32].

2.3.2.1 Amorphous Polyetherimide

The amorphous nature of PEI makes this high-performance thermoplastic generally easier to print than PEEK. Both PEEK and PEI necessitate a heated chamber for high strength 3D printing but not completely for the same reason. In the case of PEI, the material is extruded at nozzle temperatures between 330°C and 405°C. This leads to a large temperature difference between extrudate and ambient temperature which causes a sharp drop in extrudate temperature. This rapid cooling decreases the energy available for layer bonding and thus can decrease the mechanical properties of the printed parts. This effect is less strong in PEI than PEEK simply due to the semi-crystalline nature of PEEK. Printing PEI in open air or lower chamber temperature will not cause warpage and therefore dimensional tolerances are preserved [32].

There are 3 grades which have widely applied for extrusion 3D printing namely, ULTEM 9085, 1000, and 1010. ULTEM 9085 is the weakest grade with a glass transition temperature of 170°C compared with that of ULTEM 1000 and 1010 which occurs at 217°C for both grades. Similarly, the heat deflection temperature of ULTEM 9085 is lower than that of the other grades. What makes ULTEM 9085 interesting for 3D printing is its low processing temperature of 330 to 350°C compared with 345 to 405°C of ULTEM 1000 and 1010. This aspect makes it simpler to 3D print and therefore has led to a greater focus on ULTEM 9085 as opposed to the other grades. NASA employed ULTEM 9085 and ULTEM 1000 with 10 wt.% CF for the production of aircraft engine components by FFF [235]. A number of studies were conducted to evaluate the mechanical and thermal properties of 3D printed ULTEM 9085 when using various printing orientations [236–238]. The results showed that for the XY orientation, also known as along the layer, the FFF ULTEM 9085 achieved 85 % of the respective injection moulding properties. In Z orientation i.e., perpendicular to the layer, the properties were found to be weaker, achieving only 46 % of the respective injection moulding values [237]. A number of research groups carried out further studies of various PEI grades to evaluate creep behaviour [239], flexural properties [240] and fracture toughness [241]. Chemical smoothing of 3D printed parts improved tensile strength and ultimate strain by 16 % and 24 % respectively in the Z orientation [238]. Another research group led by Han, developed a laser layer pre-heating system which also managed to improve mechanical performance in a 90°C chamber [242]. Multiple studies have also been conducted which altered PEI's properties by using reinforcing fibres [235, 243] and additives [244, 245] or by blending [246] with other polymers.

The demanding applications which make use of PEI components drive the further improvement of mechanical and thermal properties of 3D printed PEI. PEI is meant for demanding applications such as replacing metallic components in military aircrafts to avoid detection. It is an aerospace grade material whose solvent resistant nature makes it adequate for contact with various fuels coolant and lubricants [247]. PEI is also used as an electrical and thermal insulator due to its high flame resistance and low smoke generation [233, 247]. Despite its important application there is only one published study that has printed PEI using FGF with examples of high-quality prints shown in Figure 2.42. The study, conducted by Fabrizio et al., successfully demonstrated the FGF of PEI, achieving mechanical properties comparable to those obtained with FFF while utilizing a more cost-effective material source, namely pellets [248]. It should be noted that this study utilised an innovative, medium to large scale extruder which combined a probably screw driven plasticating unit coupled with a piston injector to extrude the material being used, in this case PEI, with high pressure and control. The details regarding the extruder setup were not fully disclosed but it is clear that it was a rather complex FGF system was used [249].

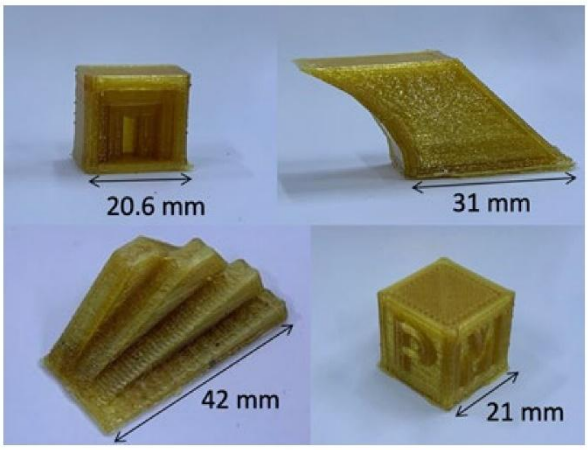

Figure 2.42 - Example FGF PEI objects [248].

2.3.2.2 Semi-crystalline Polyether Ether Ketone

PEEK is a high-performance polymer with advanced mechanical, thermal and electrical properties along with good chemical resistance [250]. These desirable properties have made it applicable in high end industrial fields namely aerospace, electrical, chemical, and biomedical industries [250, 251]. The combination of biocompatibility and similar mechanical properties to cortical bone, make PEEK an adequate material for load bearing implants with complex geometries [251, 252]. Additive manufacturing (AM) is an

ideal technology to produce bespoke PEEK implants given its great flexibility prompting multiple studies along the years [253, 254]. Beyond its established use in implants, PEEK offers properties comparable to metallic components whilst being easily producible using a versatile technique such as AM. This opens up broader scope of applications, including everyday mechanical components like gears and even more demanding usages such as ablation shields [255].

The amount of studies conducted on PEEK 3D printing is significant, making it arguable the most studied high performance polymer for MEX and probably AM in general [32]. The reason behind this is partly the challenging nature of its 3D printing process. Improving the tensile strength of MEX PEEK has been the main endeavour of multiple studies. The solutions evaluated included controlling printing parameter [254, 256–276], using various PEEK molecular weighs [268], using additives [277–280] such as fibres [281–284], post-processing [272, 283–289], and various chamber or layer heating methods [267, 290–292]. The reason behind these efforts to improve mechanical properties lies in the generally poor quality of 3D printed PEEK as compared to injection moulding parts.

PEEK, unlike PEI, is semi-crystalline which in turn makes the 3D printing process more complicated. PEEK has two crystal structures, both of which have a higher density than amorphous PEEK [293]. This also means that PEEK shrinks upon crystallisation. This, combined with the layer-by-layer additive nature of MEX, means that different regions of a print may crystallize at varying rates. As a result, inhomogeneous shrinkage can occur, leading to internal stresses, part cracking, and warping. The principal method used in 3D printing to deal with this issue is to introduce a heated chamber. Increasing chamber temperature to 130°C reduced warpage [294] and improved strength [263].

The other method available to improve PEEK's 3D printability is to modify its chemistry. This comes at a cost of altered mechanical and thermal properties. The crux of the matter is the crystallisation temperature. A patent application by STRATASYS Inc., proposed a method to control the crystallisation kinetics of PEEK [295]. In order to minimise shrinkage effects, PEI can be added to PEEK to slow down crystallisation kinetics to a point where the material does not crystallise fully. Without the addition of PEI, PEEK crystallises to a high degree. It is theorised that a subsequent layer of deposited PEEK does not provide sufficient thermal energy to melt the previously deposited PEEK crystallite to create a meaningful interpenetration of the

macromolecular chains through reptation, as summarised in Figure 2.43. Reptation is the process that occurs when two thermoplastic surfaces are heated above their glass transition, polymer chains become mobile. Chains from one layer "reptate" into the adjacent layer, gradually entangling across the interface. For this to happen, both thermoplastic surface have to be hot enough which may not be the case when using high softening temperature thermoplastics. Chamber heating remedies this problem by minimising thermal losses in two ways. Firstly, the extrudate cools at a slower rate as it cooling to the higher chamber temperature rather than the lower room temperature. This reduces the thermal gradient and therefore the cooling rate of the extrudate. Secondly, the part being printed stays at the chamber temperature. Upon deposition of the subsequent layer, there is less energy required to heat the previous layer in order to melt the crystallites and create an interpenetration effect.

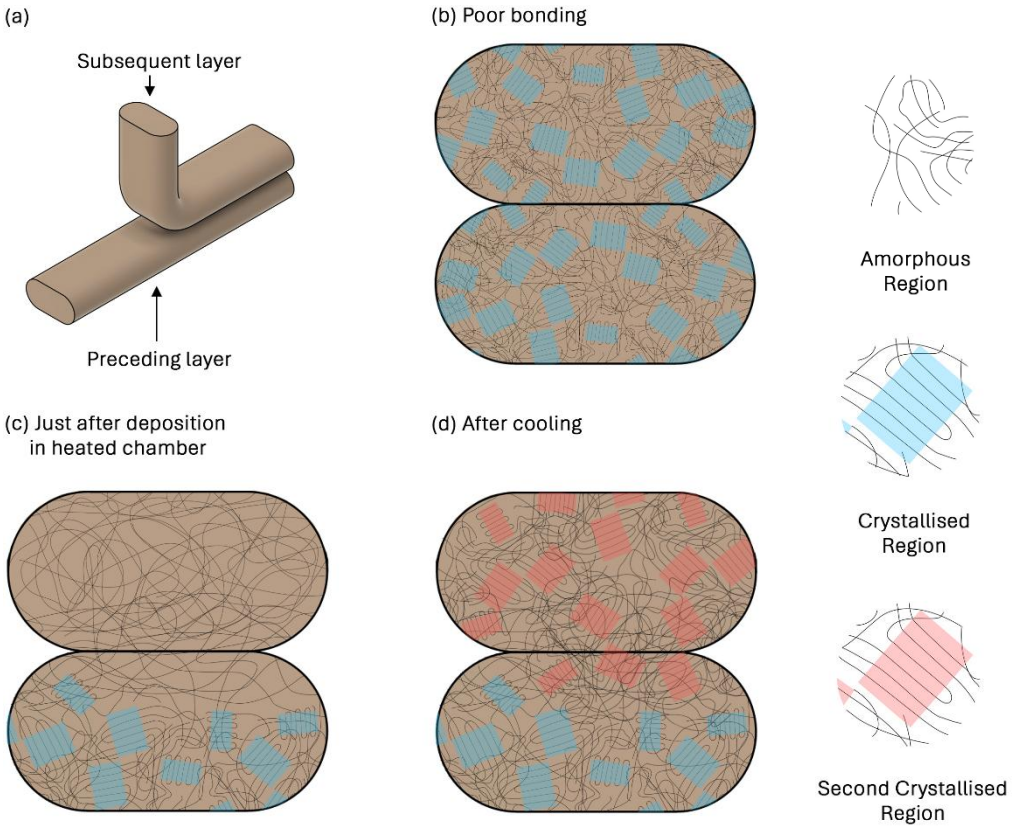

Figure 2.43 – Reptation mechanism.

As discussed in section 2.2.6.3, page 63 and section 2.2.6.4, page 65, the only PEEK FGF extrusion studies conducted were undergone using medium and large scale screw extruders. The first study on the subject was conducted by Tseng et al. [155] using a large-scale extruder. In contrast, another system introduced by Lu et al. [88] deviates from Tseng et al.'s conventional setup by incorporating three screws working in unison.

This innovative design enables in-process extrudate composition control during the 3D printing of PEEK composites. The extruder system was nonetheless rather bulky and must have used a complex motion system to drive the 3D printing setup. The other major study on large scale FGF of PEEK and pre-compounded PEEK-CF composite granulates was published by Hu *et al.* [62]. In all published cases, PEEK FGF necessitated the use of large, bulky extruder, with equally complex motion systems to counter the heavy extruder weight. It is therefore clear, that a research effort may be necessary to simplify and miniaturise PEEK FGF extrusion.

2.3.3 Conclusion

Of the materials selected for elastomer FGF, none were previously used in an additive manufacturing screw extrusion setup. TPO has been 3D printed on a number of occasions, using FFF but each time it was limited to simple geometries, with no optimisation efforts towards improved 3D printing quality and mechanical properties. Both TPEs selected namely, TPO and TF3ZG0-LCNT, were never applied to FGF or MEX AM in any published literature. TF3ZG0-LCNT should exhibit a level of softness and stretchability which was never previously studied with any AM technique and material combination currently known.

Regarding high performance polymers, in the case of PEI, only one study managed to 3D print this material using FGF. In the case of PEEK, a more concerted effort was undergone, with 3 separate studies, all involving unfilled and filled PEEK grades. In all cases, medium or large-scale extruders were used coupled with complex motion systems. There is also a lack of studies involving the layer bond strength which is the weakest orientation of most 3D printed objects. Most studies focus on the along layer orientation (XY) which is comparatively, significantly easier to improve but not as important to improve the overall part strength.

For the reasons outlined above, all of the materials selected require further study, especially in an FGF context. These materials also have a clear use case, summarised as follows: TPO is a cheaper, lighter and easier to handle and store, “hard” TPE for MEX, compared to TPU. TF3ZG0-LCNT, as a novel material in AM, enhances design flexibility by enabling the production of softer, stretchable parts, surpassing previous capabilities. The high-temperature strength of PEI and PEEK allows these thermoplastics to replace metals and ceramics, unlocking opportunities in fields that can benefit from a more

accessible and cost-effective AM technology capable of 3D printing these advanced materials.

TPO curly vase

3 Research Problem

3.1 Aim and Scope

The refined aim of this study is to develop a light-weight, simple, modular, small scale, screw, granulate extrusion system for additive manufacturing of niche elastomeric and high-performance thermoplastic materials.

Following the literature review presented in Chapter 2 of this thesis, the aim was adapted slightly by confining the study to small scale extruders. The extruder developed should also minimise complexity to improve ease of use, lower the cost, and make the system more reproducible and accessible to a wider audience. Modularity is a necessary aspect to ensure extrudability of different thermoplastics each having distinct process characteristics. The latter part of the aim was kept the same as there are few to no existing studies which employed the materials selected especially in the context of FGF on a small scale.

Apart from the scope described in section 1.4, the study will also endeavor to use low cost and open-source solutions wherever possible. In this manner, the system developed becomes easier to reproduce whilst also decreasing the associated costs. This research endeavor will not delve in the extrusion and 3D printing of regrind thermoplastic waste, despite its advantages and desirability towards the current sustainability needs. The literature reviewed demonstrated that the subject of direct recycling is challenging even for medium and large-scale extruders. It was deemed necessary to first build up knowledge on the subject of small-scale extrusion before delving into such a complicated topic as regrind extrusion and 3D printing. This topic may be covered in future work but was excluded from this thesis.

3.2 Research Gap and Objectives

In view of the literature reviewed in Chapter 2, specifically as summarised in section 2.2.7, page 76, and in section 2.3.3, page 91 and in line with the aim and scope, the following research gaps were addressed.

1. *There is no existing small class FGF extruders capable of processing high performance thermoplastics as well as TPEs.*

   There are no published articles that managed to extrude and 3D print high performance thermoplastics using small scale FGF extruders. The higher

processing temperature required along with the higher melt viscosity of these materials make extrusion and 3D printing using small scale FGF extruders challenging, as discussed in section 2.3.2 of this thesis.

Elastomers have different necessities as these are not usually highly viscous and generally require low processing temperatures. On the other hand, elastomers usually require careful process control to ensure consistent extrusion as they may be sensitive to temperature gradients inside the barrel especially if the particular TPE being extruded has a wide melting range.

2. *Unknown processing parameter that are necessary to extrude and 3D print the materials selected using small-scale FGF extruders.*

   FGF 3D printing relies on at least two key aspects: extrusion and motion capability. Both aspects necessitate precise control of process parameters. Determining these parameters is crucial for improving the likelihood of 3D print success and achieving the desired material properties. Since none of the materials selected for this thesis are conventional, each one requires optimization of its processing conditions. Only then can the performance of the developed FGF extruder be properly evaluated.

3. *Unknown level of 3D printing quality achievable using small-scale FGF coupled with the materials selected.*

   The FGF system to be developed should be capable of 3D printing with all four specified materials. In practice, this means producing objects with high geometric fidelity and acceptable mechanical properties. Each material presents unique challenges. The TPEs identified are novel application for MEX, requiring the determination of appropriate process parameters. Each material may have its own unique limitations in 3D printing. For instance, super-soft TPE might be so flexible that achieving precise geometric accuracy becomes challenging. Likewise, both high performance thermoplastics require high processing temperatures and are highly viscous, making it difficult to maintain consistent extrusion rates and achieve desirable mechanical properties.

   Additive manufacturing is often promoted as a versatile technology capable of producing almost any geometry or product. However, this is often far from reality, whether for 3D printing seemingly straightforward items such as inflatables or

specialized tools like injection molding inserts. One way to validate the capabilities of the FGF system would be to successfully produce these typically challenging objects.

To address the identified research gaps, the following objectives need to be tackled.

1. *To develop a small, lightweight, granulate screw extruder which can extrude and 3D print using high temperature, high performance thermoplastics as well as TPEs.*

In order to achieve this objective a number of considerations need to be dealt with:

- The screw extruder needs to be designed within the work volume of a conventional desktop scale, 3D printing motion system. This includes size and weight considerations.
- The development of the extruder should include modelling of the melting rate to ascertain good extrusion quality.
- The extruder should be able to interface with existing 3D printer control systems to make integration easier.
- The extruder should be easy to use, involving similar sub-systems to an FFF setup. In this manner, interfacing both on a technical level as well as on a user level becomes simpler. More specifically, the extruder should use a single heated zone and a single cooling zone, same as in FFF. This simplifies temperature tuning, system control, maintenance and fault finding, and reduces associated costs.
- The extruder must be able to at least reach high processing temperatures of 400°C for prolonged periods. This is necessary to be able to extrude and 3D print using high performance thermoplastics.
- The extruder should be modular; as it is improbable that the exact same setup that is used to extrude high performance thermoplastics is ideal for all the other materials, especially TPEs.

2. *To determine the optimal processing parameters for correct extrusion and 3D printing using the FGF system developed with the materials selected*.

This objective can be divided as follows:

- The system should be able to extrude and 3D print a wide material range including elastomers and high performance and high temperature thermoplastics. This involves determining the correct process parameters such as extruder temperature, extrusion multiplier, heated build plate temperature, build plate material and coating as well as motion control parameters.
- Following the achievement of 3D printability, the process should be optimised in order to improve mechanical properties. This is especially important for those materials which are completely new to AM or which are not yet optimised for this method of production. The achievement of high bond strength is especially important for high performance thermoplastics which are known to suffer from weak layer bond strength. It is also important for TPEs meant for applications requiring high strains.
- Material viscosity is another process parameter which is often not discussed. The weak layer bond strength of high-performance thermoplastics invites further optimisation even in the realm of the material itself.

3. To verify FGF 3D printing quality when using all the materials selected and to validate the system by producing case study parts of a specialized nature.

The verification and validation required by this objective can be achieved by:

- Verification of 3D printing quality by visual analysis of benchmark 3D printed objects such as the commonly used Benchy [296] or general feature measurement and by evaluating the mechanical properties of 3D printed objects.
- Validation of FGF system by 3D printing of speciality case study parts.

14 mm extrusion screw

4 Development of Screw Extrusion System

4.1 Introduction

As discussed in section 3.2, page 96, one of the objectives of this study is to develop a small, lightweight, granulate screw extruder which can extrude and 3D print using high temperature, high performance thermoplastics as well as TPEs. Extruder development must follow the target specifications set out in a specification list which will be discussed in the section size. The development of an FGF extruder must also consider the control and motion system it will interface with, to ensure proper integration for 3D printing. In this context, interfacing refers to both the electrical and software connections, as well as the mechanical mounting of the extruder to the motion system. Successful interfacing goes beyond enabling the extruder to work with the motion system; it must ensure consistent and high-quality operation. This is critical for optimizing the 3D printing process and achieving repeatable results.

4.2 Extruder Specifications

The specifications list for the development of a small scale, screw extruder, is shown in Table 4.1. The screw length was limited to 100 mm as the extruder must fit within the small category. The screw diameter was not specified as it does not have a significant effect on the overall extruder size. Changing screw diameter has nonetheless a significant impact of on the screw geometry and extrusion process. One such example is the maximum channel depth which can be limited when using a small screw diameter. Since there is no good reason to specify a maximum screw diameter than there is therefore no basis upon which to limit the maximum channel depth. The minimum channel depth was set to 4 mm to be able to accommodate most common granulates. A deeper channel depth would accommodate even non-conventional pellet sizes.

The overall extruder envelope, i.e. the bounding dimensions of the overall extruder, shown in Figure 4.1 (a), were set by comparing with a standard desktop FFF systems such as Creality CR-10s [297], the Prusa MK3 and MK4 [298] and an E3D extruder V6 Hemera [299]. This figure and other similar 3D model figures were produced using Fusion 360 by the author. Two values were provided for height, one with motor and one without. The *no motor* height was set by using double the largest of the aforementioned FFF extruder. The doubling was justified due to the extra complexity of FGF extrusion system compared with FFF. The *with motor* height was determined by checking the

maximum available Z height in a generic FFF machine, which for the CR-10s is 300 mm. A larger value than 300 mm would make the extruder far too large and bulky for such a desktop setup. The *no motor* height value is relevant as the actual height of an FGF extruder depends on the configuration of the motor and the extrusion screw and its concomitant components. If the extruder is configured as shown in Figure 4.1 (a) the *no motor* height would be the actual extruder height whereas a configuration as shown in Figure 4.1 (b) would be better represented by *motor* height. An angled extruder, as shown in Figure 4.1 (c), would not necessarily comply with the objectives set out in section 3.2, page 96, as it complicates the mechanical interfacing of the extruder with various desktop motion systems. This goes against the objective of keeping the extruder design as simple as possible.

Table 4.1 - Product development specifications for small class FGF extruder.

Extrusion Screw		
	Length	*< 100 mm*
	Channel depth	*> 4 mm*
Extruder		
	Envelope	
	Depth	*< 75 mm*
	Width	*< 75 mm*
	Height (no motor)	*< 200 mm*
	Height (with motor)	*< 300 mm*
	Weight	*< 2 kg*
	Barrel temperature	*> 400°C*
	Materials for extrusion	*Commodity thermoplastics;* *TPEs;* *High-performance thermoplastics;*
	Simple design	*1 heating zone;* *1 cooling zone;*
	Modular structure	*Screw;* *Barrel;*
	Feeding	*Flood feeding*
Electronics		
	Control board	*Open hardware*
	Power	*12 V / 24 V*
Software		
	Firmware	*Open source*
	Slicer	*Open source*

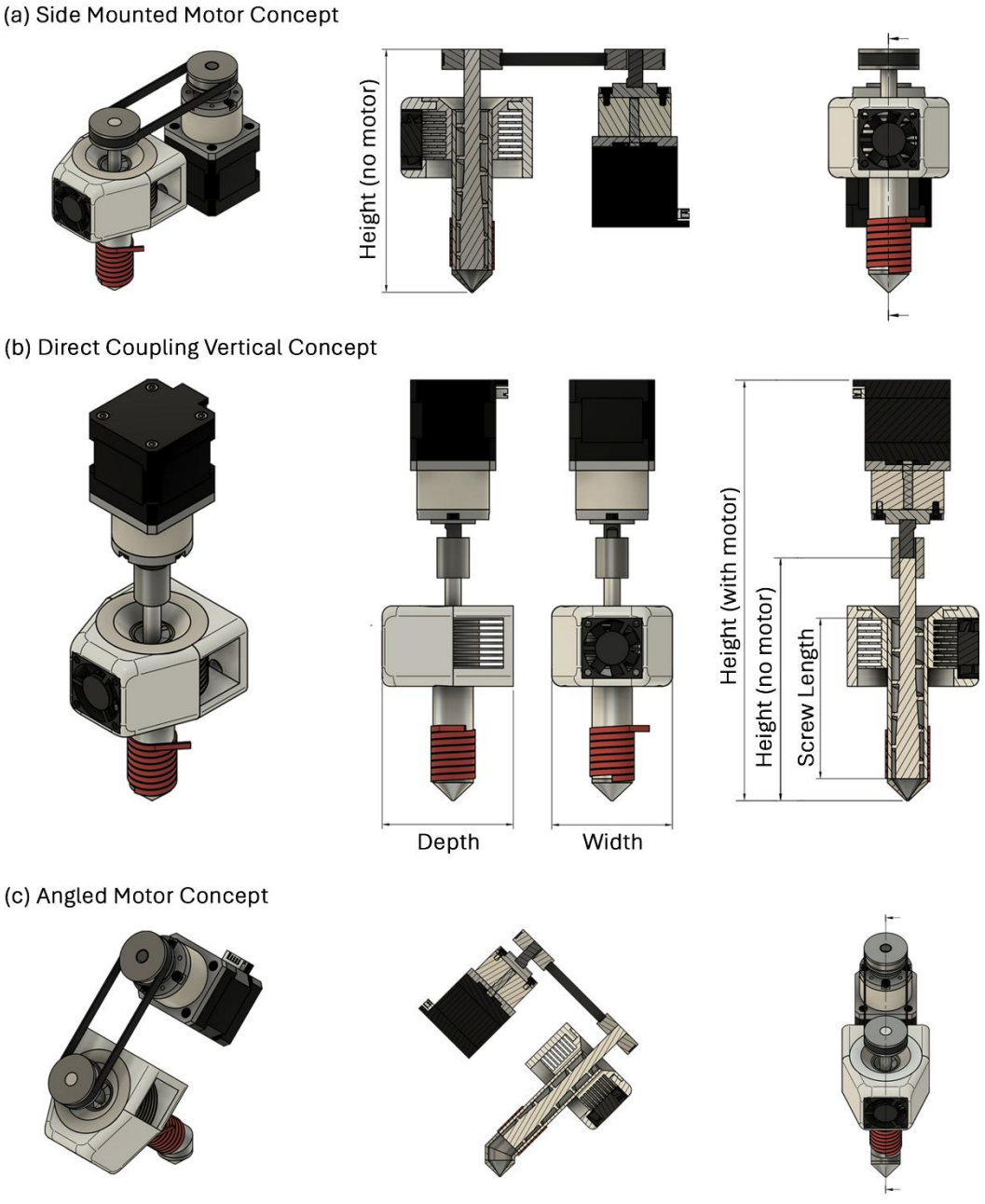

Figure 4.1 - Extruder envelope dimensions when using side mounted motor (a), directly coupled vertical (b) and angled extruder motor (c) configuration concepts.

Most FFF extruders weight less than 1 kg. similar weight was achieved by the Mahor extruder which weighs about 1 kg [300]. The Mahor extruder is limited to commodity and possibly engineering grade thermoplastics which generally have a lower viscosity than high-performance thermoplastics. For this reason, a stronger driving motor may be necessary which in turn will make the extruder heavier. Given this design constraint, the acceptable weight was doubled to 2 kg. As shown in Figure 4.2 the stepper motors of the Z-axis in a bed-slinger setup as used in the CR-10s are usually rather short NEMA 17 motors. These can normally be easily upgraded to longer and stronger NEMA 17 motors

that would allow for the use of a 2 kg FGF extruder. Other motion system configuration, such as core XY do not lift the extruder but rather move the build plate in the Z axis. In such a case, the extruder weight is not as critical. The heavier extruder will nonetheless decrease the overall printing speed as slower accelerations will be necessary due to the increased momentum generated by the heavier extruder.

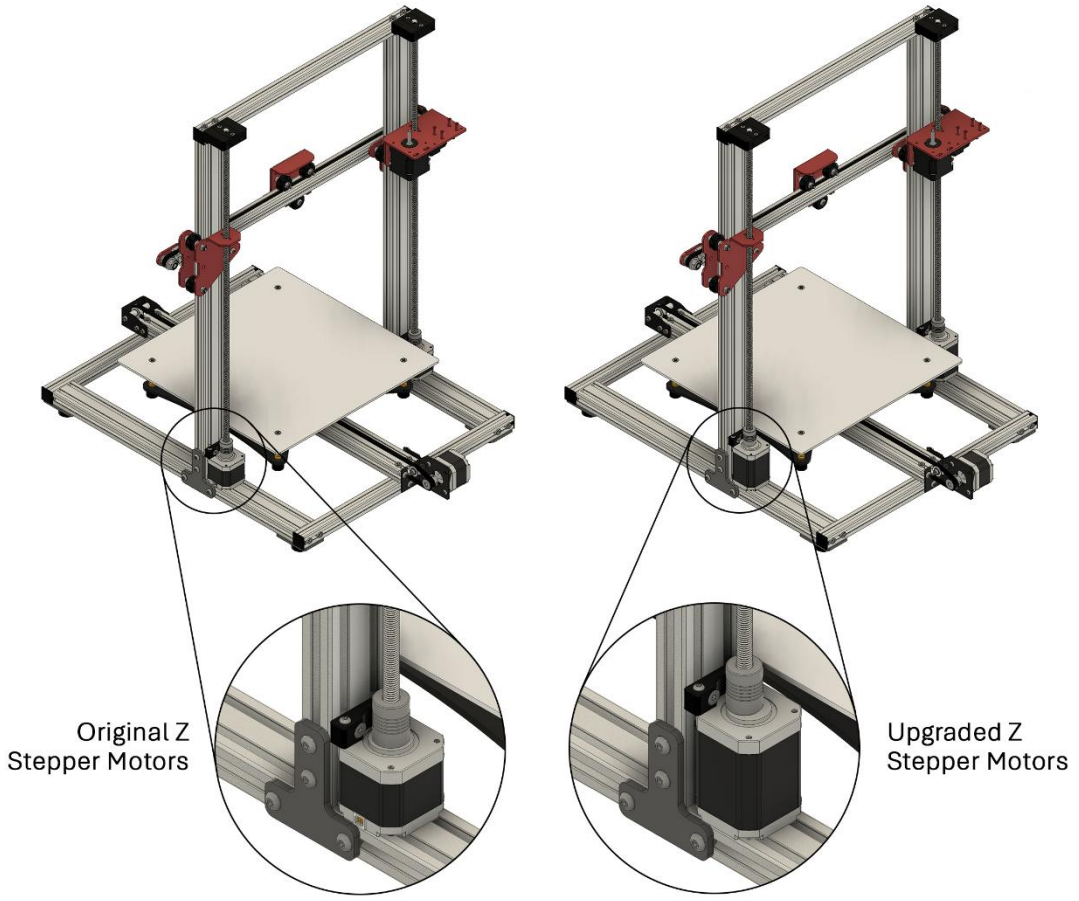

Figure 4.2 – Bed-slinger desktop 3D printer motion system with highlighted Z axis stepper motors.

The barrel material has to sustain operating conditions in which the heating system maintains a temperature high enough to process PEEK whilst providing sufficient thermal energy for layer bonding during 3D printing. This specification limits which materials may be used to manufacture the screw and barrel as these would need to maintain their material properties at temperatures upwards of 400°C.

The extruder should be able to extrude commodity thermoplastics such as ABS as well as the materials set-out in section 1.4, page 16. As stated previously, the extruder should be simple and modular. It should utilise a single heated zone and cooling zone. A modular approach is preferred to allow the use of different sub-component configurations depending on the material being used. The lack of information available

on the materials selected means that a flexible setup is necessary to counteract any issues encountered during application of the extruder. The extruder should also use a flood feeding setup in which case the raw material is let to flood the extrusion screw. A starve feeding setup, which would control the amount of material being delivered to the extruder would further complicate the extruder design, with minimal expected improvement give the envisaged short extrusion screw length.

The electronics and software used should be open source. This is necessary to enable interfacing with multiple existing system if necessary. The electrical power used with the 3D printed should be of 12 V or 24 V to remove any risk of electrocution during operation. One final hidden objective is to minimise cost. Whilst it is not a direct necessity of this study to minimize cost, it is still practical up to a certain point to ensure that the extruder is not prohibitively expensive to make and operate.

4.3 Extruder Development 1

The first extruder iteration was meant as an experimental setup, with allowance for further changes depending on issues and possibilities of improvement, encountered during use. This extruder served as a starting point for the development of Extruder 2 and both the following amendments.

4.3.1 Concept

The FGF extruder was first split into its main components and sub-systems namely, barrel and screw, heating system, cooling system, mounting system, pellet feeding, drive train and extruder die (nozzle). These components and sub-systems were laid out in the concept extruder shown in Figure 4.3 which shows an FGF concept extruder with a directly coupled drive train. The concept extruder is highly simplified and does not include components that are ancillary but not critical to extrusion such as fastening elements and bearings. For this reason, most sub-systems are visible as single components. This study will make use of a directly coupled setup to keep the system simple and easily interfaceable with multiple desktop motion systems. Conversion to a side mounted driver would not be a complicated affair as it is a simple matter of either using a belt or chain link or a gear train to transmit power, as shown in Figure 4.1 (a).

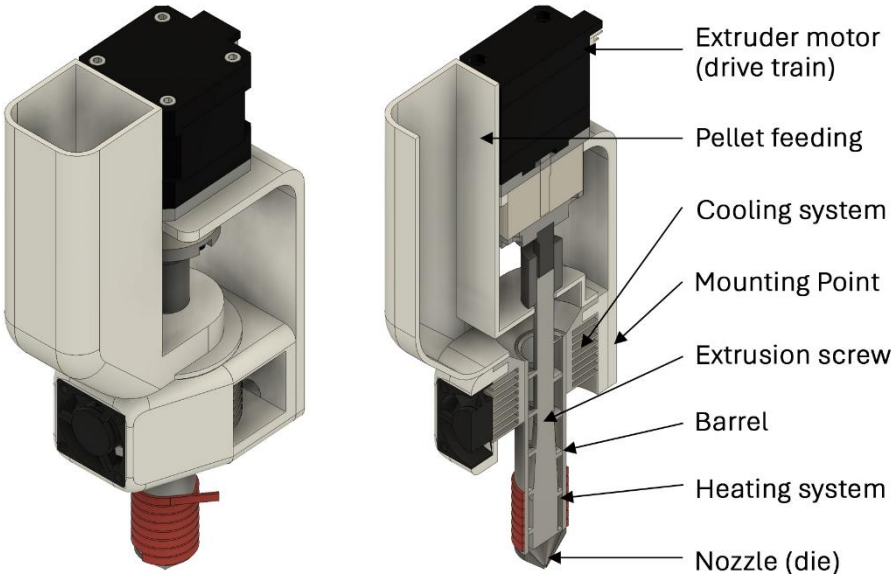

Figure 4.3 – Sub-assemblies of concept FGF extruder.

The barrel and the extrusion screw were configured in to be parallel with the Z axis of the motion system. A horizontal configuration would limit the Z movement, as shown in Figure 4.4 (a). This kind of configuration is common with stationary extruders used for large, high throughput, industrial processes and are not usually meant for AM. This effect is caused by the structural element which is necessary to ensure stiffness of the motion system frame which close of the Z axis "columns" at the top. A vertical setup would not conflict with these structural members, as shown Figure 4.4 (b), allowing for a greater Z free length, with the same motion system setup. Even in the case of a core XY style motion system, a horizontal setup may conflict with the drive train mechanism lying on the top of the XY frame. In both motion systems, special design consideration may be used to alleviate these issues. Such specialised modification would make the extruder tailor-made for each specific motion system which is undesirable as a general solution is preferred. For the above reasons, a vertical setup was chosen.

A vertical setup also has an adverse effect, that of promoting drooling, caused by the weight of the molten material itself. Drooling refers to the unintended oozing or dripping of molten material out of the nozzle, even when the screw is not rotating. This effect is common with all FFF setups and can be mitigated by adjusting process parameters, such as extruder temperature and retraction. This is also possible for FGF but instead of retraction the screw is rotated in reverse to decrease the amount of molten material at the nozzle. Further details on this topic will be covered in section 4.3.2.1 and section 5.3.4, page 178.

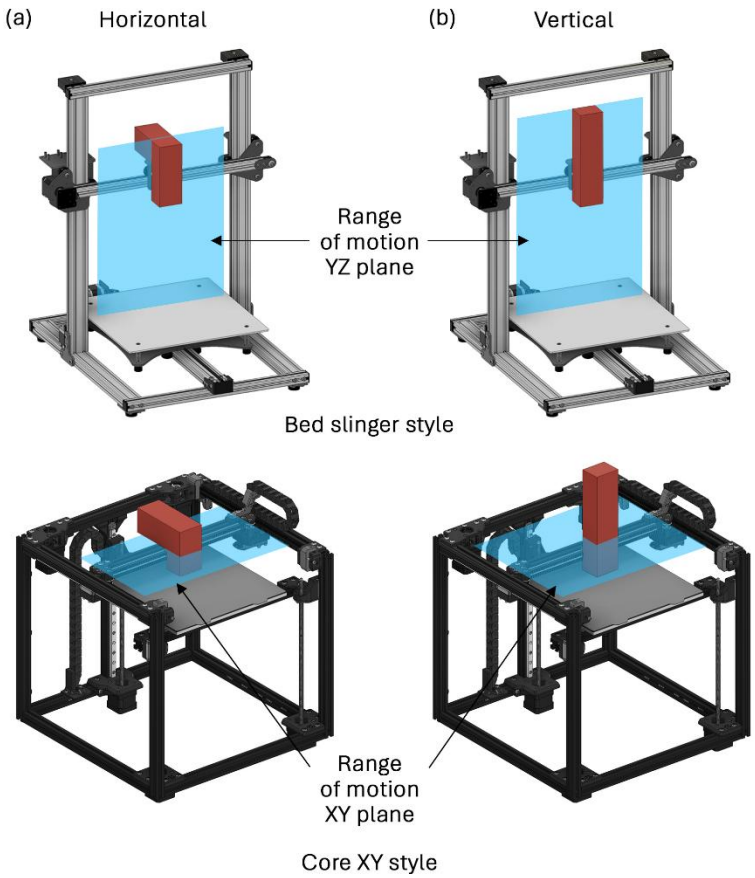

Figure 4.4 – Horizontal (a) vs vertical (b) barrel and screw setup for a bed slinger motion system and a core XY style motion system.

The heating and cooling sub-system are to be placed similar to as described in section 2.1.1, Figure 2.1, page 22. The cooling system should cover the extrusion screw bearing and a portion of the feeding end. The heating system will be made up of a single source and will cover the metering section and possibly part of the compression section of the extrusion screw, as shown in Figure 4.3. The extruder will be mounted to the motion system at the cold end, to ensure no unintended heating of the motions system by heat transfer from the extruder. The extruder motor was then linked with the extrusion screw by using a solid coupler. The two sub-assemblies remaining for further discussion are the pellet feeding system and nozzles.

Despite the simplicity of flood feeding as opposed to starve feeding, the setup of flood feeding in an FGF screw extruder is different from the traditional approach. The traditional setup feeds pellets to the side of the extrusion, as shown in Figure 4.5 (a). In a side feeding setup as used with larger, stationary extruders, the high power of the extruder motors ensures that if any pellets gets stuck between the extrusion screw flight and the barrel wall edge, then the pellet is either broken or at least forced away. The use of high-power motors implies the use of larger motors which in turn means that the

extruder becomes significantly heavier. A more efficient approach for FGF would be end-feeding, as used in the Mahor extruder, discussed in section 2.2.6.2, page 60, and as shown in Figure 4.5 (b). The only disadvantage of this kind setup is that the screw shaft needs to be elongated to create a chamber area where the pellets can accumulate and flood feed the extrusion screw. This in turn will increase the effective length of the extruder.

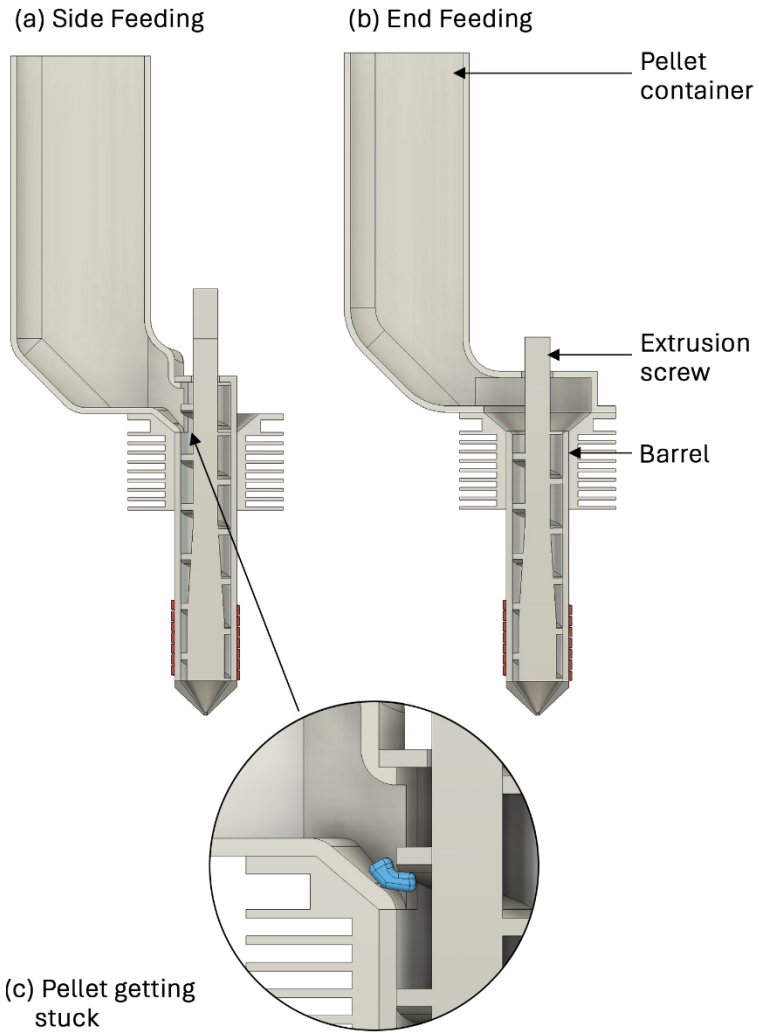

Figure 4.5 – Side (a) and end (b) pellet feeding in vertical, FGF screw extruder and pellet getting with side feeding.

The last sub-system or component of note is the nozzle or die. This extruder feature may be simplified sufficiently to be produced in a single object whereas in a different configuration it may have to be considered as a sub-assembly. The nozzle must be designed in such as manner as to transition from the relatively large diameter of the barrel to the small diameter of the nozzle orifice, as shown in Figure 4.6 (a). The longer the transition (x), the less the resistance caused by the viscous thermoplastic melt. On the other hand, a long transition would result in a larger melt chamber in front of the

screw. This melt chamber would increase the effective residence time of the melt which would increase the probability of material degradation. Furthermore, a larger melt pool is more prone to drooling as there is a greater mass of unhindered melt which is being forced down by gravity. In contrast, the melt in the metering section experiences some resistance to gravitational flow due to the screw flights, which create friction and limit the free flow of material. The nozzle also needs to have a leakage proof connection to the barrel. This can be achieved best by ensuring that once the barrel and nozzle are attached together, there are two flat faces along all the leakage front, which are pressing together completely, as shown in Figure 4.6 (b). If both faces are pressed flush against each other, even if they are only milled and not ground faces, the combination of low melt pressure and the relatively viscous thermoplastic melt ensure that there is no leakage at the interface. In this manner, leakage can be prevented due to the low pressures expected to be generated by this short FGF extruder.

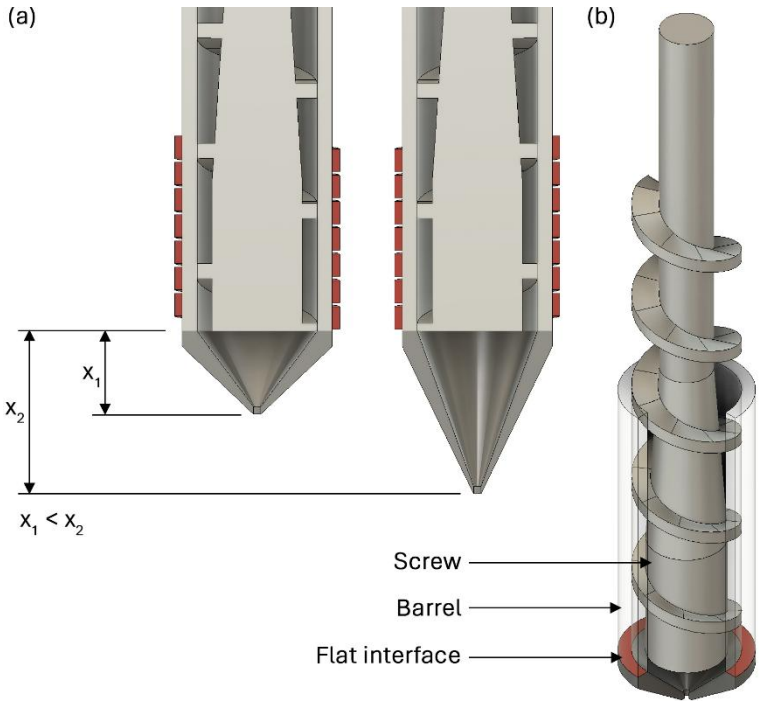

Figure 4.6 – FGF extruder nozzle (a) with different sizes x and leakage interface (b).

4.3.2 Embodiment

The concept extruder outlined the main challenges of a small scale FGF extruder. The next step was to design each sub-system of the extruder, using the theory and results laid out in section 2.1, page 22.

This first extruder development involved initial calculations necessary to design or select the extrusion screw, extruder driver, barrel, screw fixturing, heating and cooling systems, nozzle and electronics. The process was guided by the results published in literature, general theories and existing small scale extruder designs. As discussed in section 2.1.4, most screw extrusion theoretical models and results are intended for large diameter and long extrusion screws. These kinds of screws are fundamentally different from those being dealt with by this study and therefore some allowance has to be taken during extruder design which takes note of this discrepancy.

The results obtained through the development of Extruder 1 provided the basis upon which the common extruder concept of extruders 2 to 4, was derived. For this reason, the design decision taken in subsequent extruder developments can not be properly understood without knowledge on the initial choices laid out in the development process of Extruder 1.

4.3.2.1 Extrusion Screw and Driver

The hearth of an extruder are its screw and barrel. The former is arguably the most complex of the two as it requires careful design of the multiple different aspects, all of which were covered in section 2.1.2, page 24. The screw developed for Extruder 1 is shown in Figure 4.7. The screw has a diameter of 20 mm with a threaded length of 85 mm. This screw was developed by taking note of the resources discussed in sections 2.1.3 and 2.1.4, through a calculation and decision process, as will be outlined in the following text.

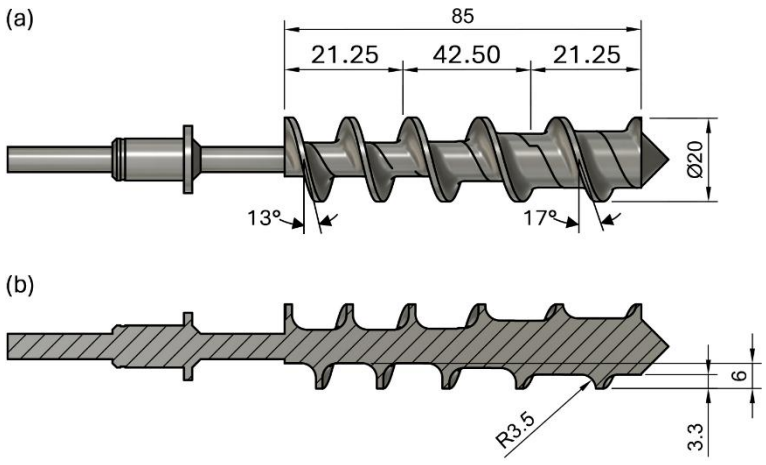

Figure 4.7 – Extrusion screw 1 with key geometric specifications.

The large 20 mm diameter allows the use of a deeper feeding channel, as listed in Table 4.2 which in turn ensures that even unconventional pellet sizes can be employed. Large scale extruders have suggested that a large screw diameter allows for consistent extrusion of non-uniform feedstock, such as regrind thermoplastics, as discussed in section 2.2.6.4, page 65. This thesis will not employ such feedstock in its study, but successful 3D printing using conventional pellets with a 20 mm, small scale FGF system, would demonstrate that large screw diameter may be used with short screws. This result would in turn provide an important first step for future research concerning 3D printing of regrind material using small scale FGF extruders.

Table 4.2 – Geometric specifications of extrusion screw 1, with a 20 mm diameter.

Section	Length [mm]	Turns	Helix Angle [°]	Pitch [mm]	Depth [mm]	Flight thickness [mm]
Feeding	21.25	1.46	13	14.5	6.0	
Compression	42.50	-	-	-	-	1.5
Metering	21.25	1.11	17	18.5	3.3	

The next crucial specification of an extrusion screw is the helix angle. The helix angle was set to a relatively shallow 13° at the feeding end with a linear transition to 17°. A shallow helix angle was selected to ensure that there are enough turns to create an actual screw shape in the available length. With a helix angle of 13°, the feeding section has about 1.5 turns in the allocated length of the screw. A square pitch of 20 mm would provide a little more than a single turn for the feeding section.

The variable helix angle also meant that the compression ratio is not related solely with the change in channel depth, but also with the change in helix angle. In order to calculate the effective compression ratio instead of using the change in channel depth, the change in cross-sectional area was used by calculating Equation 4.1, following the schematic of Figure 4.8, using nomenclature shown in Figure 2.3 and where the subscripts *f* and *m* refer to the feeding and metering sections. The compression ratio was set to 1.4:1 instead of the conventional 2:1 or 3:1. This value was set as low to minimise pressure losses. In contrast to a conventional extruder, the nozzle pressure loss is expected to be high due to the small orifice sizes used, the most common being 0.4 mm. This in turn leads to a further compression of the melt before leaving the nozzle. The low compression ratio may also increase the probability of drooling, due to the expected

higher-pressure generation. By changing the subject of Equation 4.1, the channel depth of the metering section was set to 3.3 mm given a feeding channel depth of 6 mm.

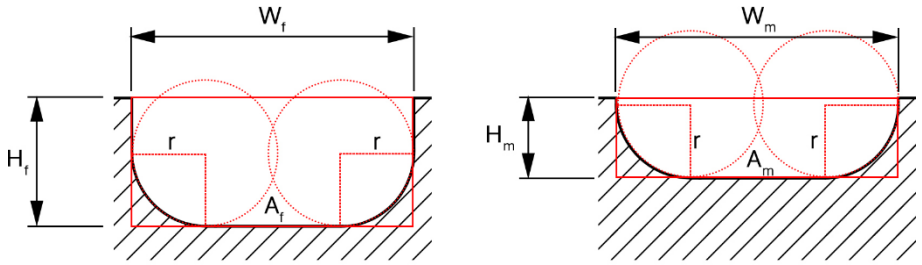

Figure 4.8 – Schematic of channel cross section.

$$Compression\ Ratio = \frac{A_f}{A_m} = \frac{2\big(P_f - w\big)\big(H_f\big) - r^2(4-\pi)}{2(P_m - w)(H_m) - r^2(4-\pi)}$$
$$= \frac{2\big(\tan(\emptyset_f)\pi D - w\big)\big(H_f\big) - r^2(4-\pi)}{2(\tan(\emptyset_m)\pi D - w)(H_m) - r^2(4-\pi)} \qquad \textit{Equation 4.1}$$

The feeding channel depth was set to 6 mm in order to create a minimum screw root diameter of 8 mm. This shaft diameter has to sustain the torque generated by the extrusion screw driver. For the reason, the driver has to be selected in order to determine the maximum continuous torque acting on the extrusion screw during operation. Stepper motors are the most popular desktop MEX 3D printer motors. All other alternatives require using encoders to achieve position accuracy. This in turn greatly increases the motion system cost. On the other hand, not only do stepper motors have innate, open loop position information, but they are also significantly cheaper and easier to control than servo motors. To fulfil the specifications outlined, including simplicity, ease of interfacing and low cost, a stepper motor driver was selected for this application. Stepper motors are available in standard sizes of which the NEMA 17 is generally used in most popular FFF motion systems. The next size, i.e. NEMA 23, comes at a significant increase in weight which can heavily impact the usability of the extruder, as discussed previously. For this reason, a NEMA 17 stepper motor was selected to drive the extrusion screw.

The standard speed range of stepper motors is of up to about 1200 RPM. The torque producible reaches a maximum at low speed and decreases as a rectangular hyperbola whereby torque decreases rapidly with increasing rotational speed. Despite the high low speed torque nature of stepper motor, controlling these motors at such low speeds is suboptimal and may lead to stuttering and loss of torque, as shown in the torque curve of Figure 4.9 (a). This is relevant to screw extrusion as the extruder is expected to operate in the range of 0 to 10 RPM as is often the case with small class FGF extruders. The

optimal configuration to make use of a greater component of the actual power deliverable by a stepper motor at very low speeds is to use a gear box. The optimal gear ratio was found to be 1:30, to be able to achieve an effective speed of 10 RPM, with a real stepper motor speed of 300 RPM which is within the high torque operating region of stepper motors. By using a gear box, the effective torque producible is multiplied by the gear ratio, minus losses in efficiency.

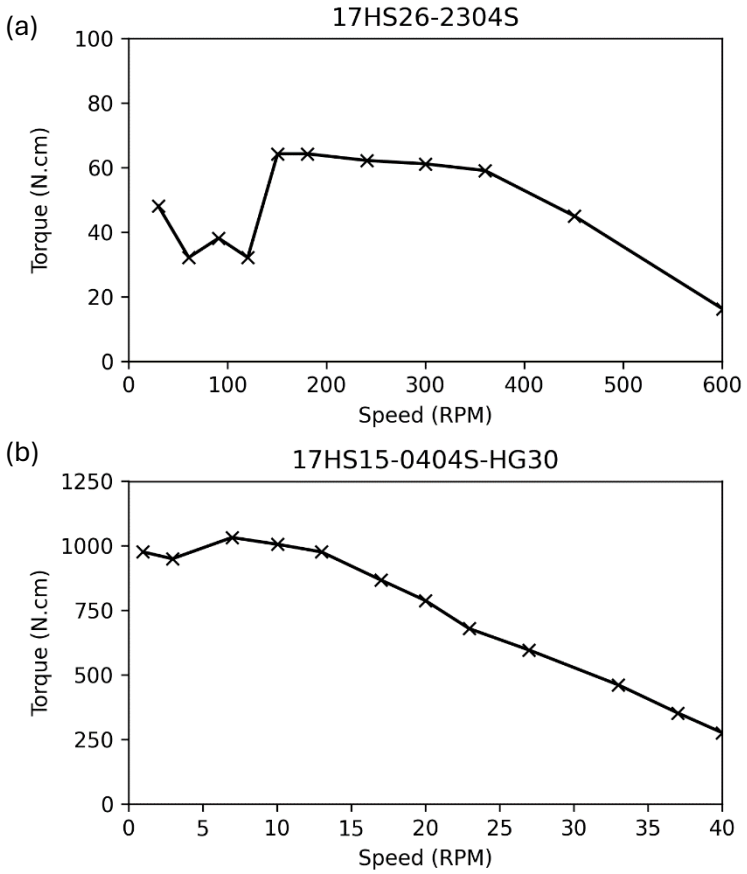

Figure 4.9 – Torque curve of NEMA 17, 17HS26-2304S (a) and of 1:30 geared NEMA 17, 17HS15-0404S-HG30 (b) by stepper online [301, 302].

The introduction of gear boxes also led to generation of undesirable backlash caused by the gearbox. Backlash is the imperfect meshing of gears which have gaps in between them. These gaps cause positional inaccuracy when changing motor rotation. In FGF extruders, this inaccuracy would occur when reversing the extrusion screw to cut the flow of extrudate and reduce the internal pressure. This is analogous to retraction in FFF in which the filament is pulled or retracted to stop or minimise the undesired drooling caused by pressure in the nozzle, as shown in Figure 4.10. In principle, the positional accuracy loss caused by retractions does not have a significant impact on 3D printing quality. In effect, if motion is reversed twice, as occurs when first retracting and then re-

extruding, the backlash error is cancelled and therefore would not affect the 3D printing quality. The only issue is that a set value used for retractions will innately have included an amount caused by backlash. Given that it was deemed that there was no need to use high precision gear boxes, that would minimise backlash, a normal geared stepper motor was used, specifically the 17HS15-1684S-HG30 by Stepper Online (China). The torque curve, provided by the supplier for this geared stepper motor is shown in Figure 4.9 (b), with a maximum torque of 10.5 Nm.

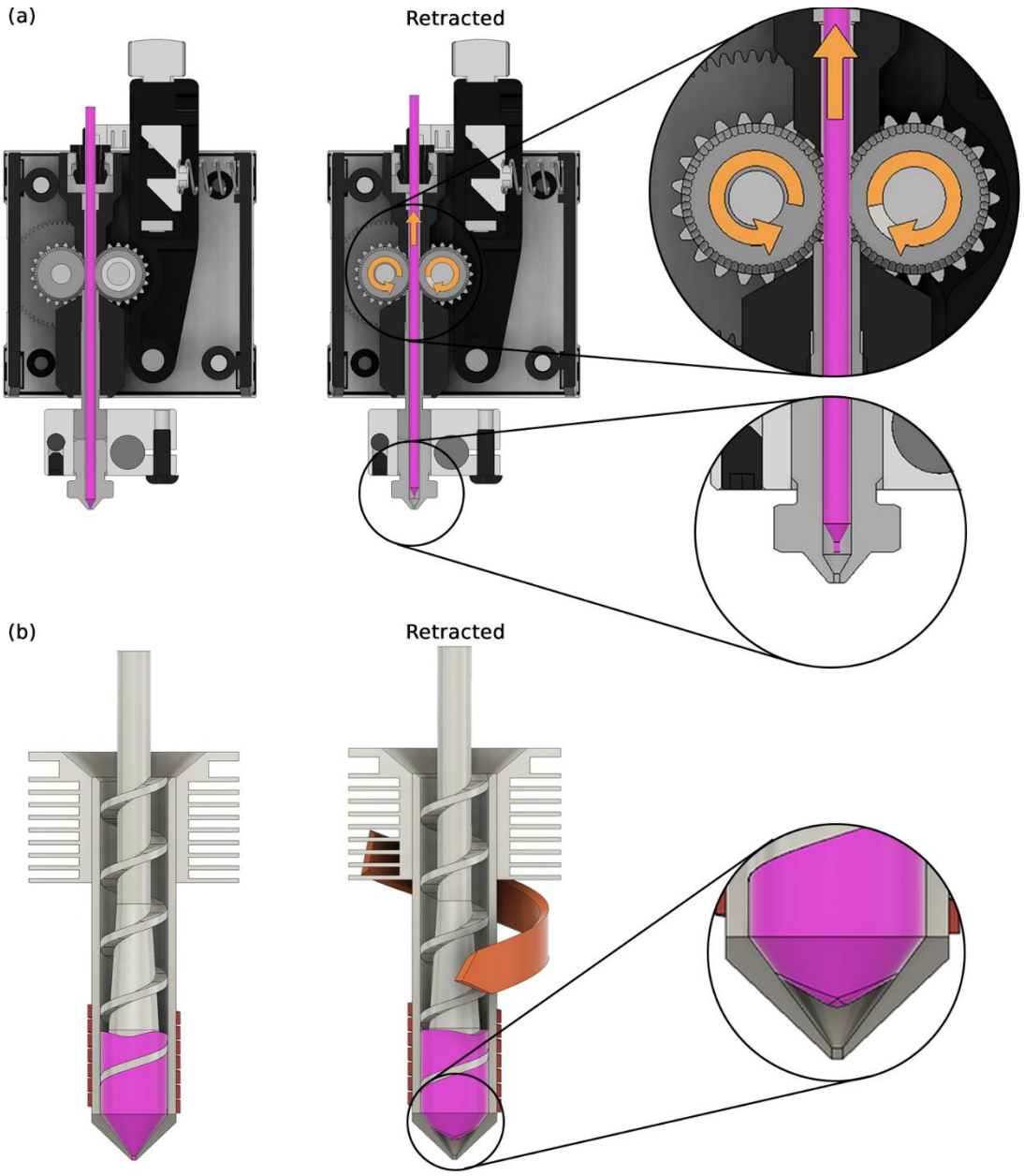

Figure 4.10 – Retraction in FFF (a) and FGF (b)

To calculate the minimum shaft size, the motor maximum torque value, and the screw material properties are necessary. Extrusion screws conventionally use AISI 4140

medium carbon steel with surface hardening and polishing [17]. However, this low-cost steel was not suitable for this FGF extruder as a service temperature greater than 400°C is required. At this temperature, AISI 4140 steel loses nearly half of its yield strength, from 665 MPa at room temperature to 350 MPa at 400°C [303, 304]. To achieve the high service temperature necessary, AISI H13 tool steel was selected instead. This steel is another commonly used material for extrusion screws, but it is usually limited to high temperature extrusion such as done with PEI and PEEK which this FGF extruder is meant to process [17]. The material was procured from Meusburger and Uddeholm with trade names of 1.2344 and Orvar Supreme respectively. At 400°C, quenched and tempered AISI H13 tool steel has a yield strength of 1000 MPa and a shear strength of about 570 MPa [305]. The barrel was machined using the austenitic version of the tool steel, to make the machining process easier. The system was tested using this state of material and it was found that a quench and temper heat treatment step was unnecessary.

The minimum shaft diameter *D* may be calculated using Equation 4.2 where *T [Nm]* is torque acting on the shaft, *S* is the safety factor and τ *[MPa]* is the allowable shear stress. By using a safety factor of 3, the minimum theoretical shaft diameter becomes 6.6 mm. With a safety factor set to 1, the minimum shaft diameter is of 4.5 mm. Both values are below the maximum possible screw shaft diameter of 8 mm, imposed by the channel depth selected at the feeding end (6 mm) and the extrusion screw outer diameter (20 mm). This demonstrates that in this setup, the extrusion screw should be mechanically sound. Taking into consideration the minimum feeding channel set out in the specifications, the minimum screw diameter is then between 12.5 mm and 14.6 mm, for a safety factor of 3 or 1 respectively. The short length of the screw ensures that there is no need to consider bending or buckling of the screw during normal operation.

$$D > 2\left(\frac{2TS}{\pi\tau}\right)^{\frac{1}{3}} \qquad \textit{Equation 4.2}$$

The remaining specifications of the extrusion screw are flight thickness and channel radius. The flight thickness was set to 1.5 mm as opposed to the conventional approach which would use a flight of 2 mm. This convention is empirical and simply takes 10% of the screw diameter. The 25% reduction was selected to account for the lower pressure generated in this due to the low power of the motor and short length of the extruder. A thinner flight could improve efficiency further but may also lead to difficulties in machining such as warpage or bending of the flight during machining.

The screw was machined from a stock 20 mm rod using a CNC mill-lathe. A CNC grinder would have achieved a better finish with lower probability of bending the screw during machining. On the other hand, CNC grinding is a more expensive process which would therefore increase the fabrication cost of the extrusion screw. Since a mill-turn process was used, the channel radius was set to 3.5 mm to accommodate a 6 mm diameter, ball nose cutter for machining. A smaller radius would require a smaller cutter which would slow down machining and increase machining complexity due to the short cutter length.

As discussed in this section, screw design for FGF was guided by mechanical considerations, results found in literature but also by limitations of machining equipment available. The next section will cover barrel design along with co-axial fixturing of the screw with the barrel.

4.3.2.2 Barrel, Screw Fixturing, and Temperature Control

The barrel is a simple tube which encases the extrusion screw. Its thermal co-efficient of expansion must be the same or very similar to that of the extrusion screw. When heated up, a screw with a larger coefficient would expand more than the barrel possibly leading to seizure of the screw inside the barrel due to lack of clearance. For this reason, the barrel and screw were manufactured from the same material, i.e. AISI H13 tool steel. The final geometry of the barrel is shown in Figure 4.11. The internal part of the barrel was drilled, bored and then reamed in that order to obtain an H7 “bore” which has a tolerance of +16 µm. As stated earlier, the screw was machined from a 20 mm diameter cold rolled round bars giving an outer radial tolerance of -200/-50 µm. The effective screw to barrel clearance, in a perfectly concentric system would be between 34 µm and 184 µm. This provide a clearance of about 0.0017D to 0.0092D which is higher than the target 0.001D. This looser tolerance was justified by the lower associated manufacturing complexity and cost. Furthermore, the low pressure expected in this small FGF extruder may not intrinsically necessitate such tight screw to barrel tolerances to minimise leakage flow.

A bearing is necessary to join the screw with the barrel to allow screw rotation inside the barrel. Certain designs, such as the Mahor extruder and the Tumaker FGF extruders do not have such a bearing but instead use the bearing included inside the stepper motor. In this manner, most of the load generated by the extrusion goes along the screw length, into the motor bearing. The low load generation expected by Mahor style, FGF extruders allows for this kind of space and cost saving configuration. In high power, large

throughput stationary extruders, a thrust bearing between driver and extrusion screw is critical for correct operation. A conventional bearing is not always necessary as the screw should be well constrained axially by the barrel.

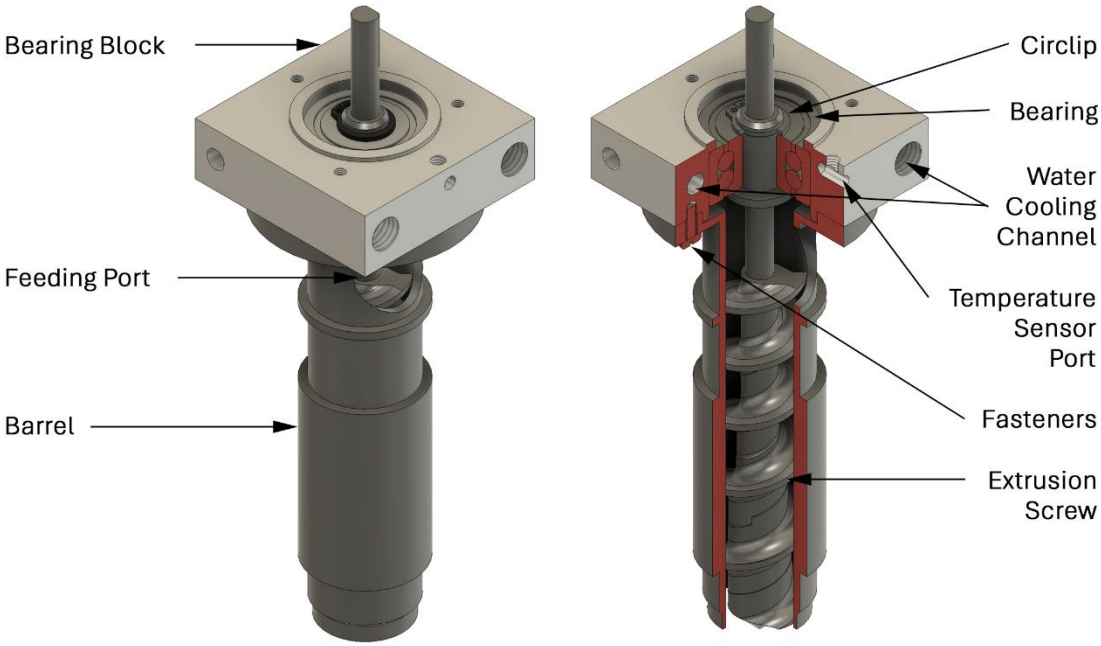

Figure 4.11 – Barrel with extrusion screw assembly.

Just like the Mahor extruder, this FGF extruder is not expected to produce a such a strong counter force that a thrust bearing would be necessary. The specifications then diverge on the processing temperature used. This FGF extruder must be able to sustain working temperature higher than 400°C which means that thermal separation between screw and stepper motor is especially important to minimise heat-up and subsequent damage of the motor. To create this thermal separation, three methods exist. The one selected for this extruder design is the simplest and cheapest in order to comply with the set specifications. The extrusion screw was joined to the barrel via a double row bearing housed in a water-cooled aluminium block as shown in Figure 4.11. The cooled bearing would limit heat transfer from the screw to the driver as the bearing would absorb the excess heat energy. In contrast, direct extrusion screw cooling, achieved by inserting a cooled core inside the extrusion screw, would increase extruder complexity and costs whilst achieving a similar effect. Direct stepper motor cooling would not be as expensive to achieve but its efficacy is not as direct as the other two techniques which directly block the source of undesired heat from reaching the motor.

The bearing was mounted in the bearing block by using a milled pocket with an interference fit. The bearing block itself joined with the barrel by using a milled cylindrical

hole for positioning co-axially with the screw axis and a flat milled faced for perpendicular positioning. The bearing block was then secured with screws, fixing it to the barrel, as shown in Figure 4.12. The screw then maintained its positional accuracy using a shoulder and circlip at either end of the bearing.

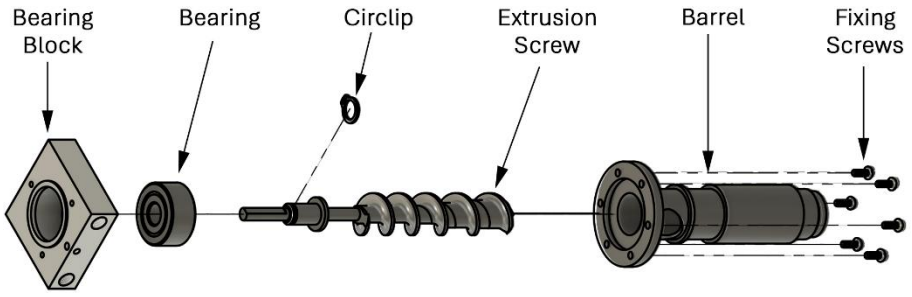

Figure 4.12 – Fixturing of bearing block to barrel and screw fixturing to bearing.

The barrel also had another cooling block, just under the feeding hole in the barrel, covering the feeding section of the extrusion screw. Both the bearing block and feed section cooling block were water cooled. Water cooling was selected instead of the generally simpler and cheaper forced air-cooling setup, popular with most FFF extruders, due to the high temperature requirements set out in the specifications. As discussed in the literature review of section 2.3.2, page 85, PEEK and PEI 3D printing is best carried in a heated chamber. This study will not make use of heated chamber nonetheless it would be unrealistic to design an extruder intended for high performance thermoplastics 3D printing that does not take into account the environment that it could be used in. A forced air cooling system residing in a heated chamber is not feasible.

The heating and cooling system was designed with the assumption that the cooling system is over sized to ensure that the heating rate can never be higher the cooling rate and so minimise the probability of a related incident. The water flow rate was set to constant speed of 5 l/min. It should be noted that the hotter the barrel and screw get, the greater is the effective cooling power of the water-cooling system. This occurs as there is greater temperature difference between the cooling block and the barrel and screw which increases the cooling rate. The power of the heating system was modulated in order to maintain the target temperature at the barrel. Furthermore, the water-cooling system is a low-cost component and therefore it was deemed sensible to take an empirical approach to size the cooling setup. To this end, the cooling channels were set at 6 mm to maintain a similar channel cross-sectional area as the common 8 mm outer diameter pipes used to deliver the cooling water. A common aquarium water pump (OptiMax 3000) with a desktop personal computer grade heat exchanger (EK-

CoolStream PE 360, triple with cooling fans) was used in conjunction with a 10 L water tank. Both the bearing block and the barrel cooling block used an internal u-shaped cooling channel, surrounding the bearing and barrel respectively. This cooling setup was never optimised in the design process as it was found to work adequately for all barrel temperatures used. If further weight savings are necessary, future work may focus on optimising this aspect of the extrude.

The heating system employed used a 28 mm inner diameter, 25 mm long, 300 W spring coil heater. This was selected as it was the lightest, most power dense and cheapest alternative from the rest, which are shown in Figure 4.13. Both brass encased heaters and band heaters would have provided better mounting on the barrel, creating a better heat transfer leading to improved heating efficiency and speed. On the other hand, these types of heaters were significantly heavier than spring heaters and were not available at the small diameters necessary for an FGF extruder.

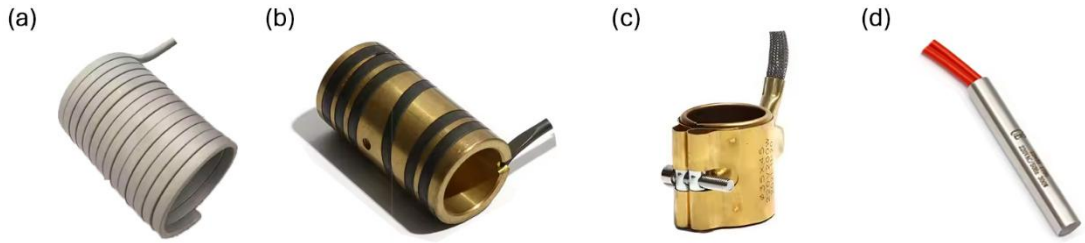

Figure 4.13 – Spring style heater (a), brass encased heater (b), band heater (c) and cartridge heater (d).

The heater was controlled directly by the 3D printer controller by using as PID loop. The temperature of the barrel was read by PT100 temperature sensor mounted in a collar, attached at the of the barrel or on the nozzle. This setup allowed direct measurement of the temperature at the very tip of the FGF extruder. The use of PT100 temperature sensor as opposed to a thermistor as generally done in FFF was necessary due to the higher processing temperature necessary for extrusion of high-performance thermoplastics.

4.3.2.3 Nozzle

The only extruder component remaining for discussion is the nozzle of which the final geometry is shown in Figure 4.14. Two nozzles were manufactured and used with an opening of 1 mm and 0.4 mm respectively, where the 1 mm nozzle size was expected to be the easiest to extrude given the lower resistance to polymer flow. On the other hand, the 0.4 mm nozzle should be able to obtain better results given the smaller 3D printing resolution it may achieve. In each case, a 90° internal cone was used. The melt chamber

inside the nozzle was reduced by adding a conical tip at the end of the extrusion screw. In this manner, the propensity for drooling is expected to decrease due to the decreased free volume and increased frictional resistance. The sealing effect necessary to ensure no undesired melt leakage at the interface during extrusion was achieved by including a flat milled interface, highlighted in Figure 4.14. A hex pattern on the outside of the screw allowed for mounting and unmounting using conventional hex sockets.

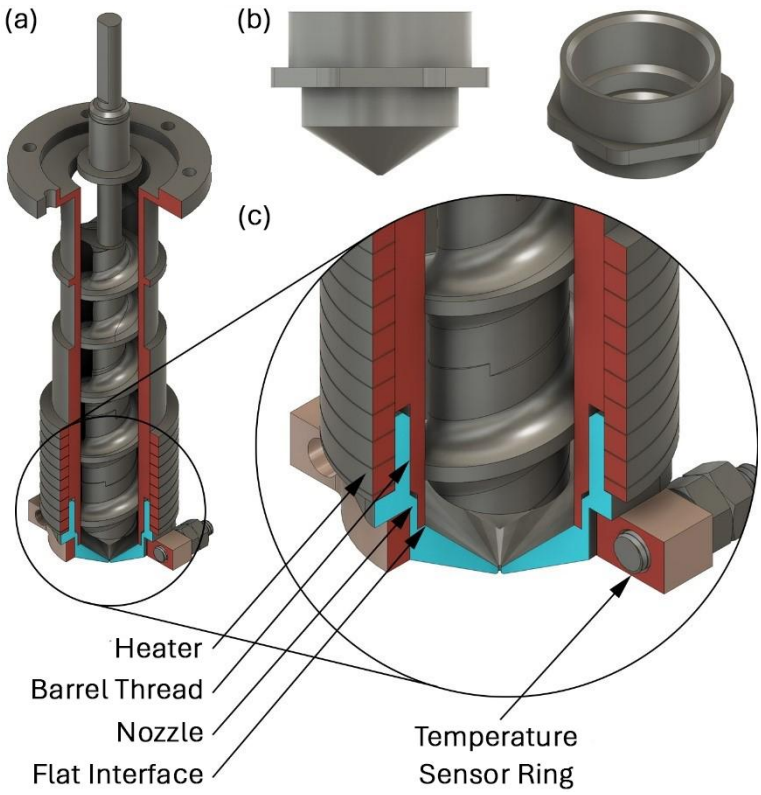

Figure 4.14 – Cross-section of nozzle with concomitant components (a), nozzle outer geometry (b) and detail view of cross-section with interface (c).

4.3.2.4 Manufactured Extruder 1

The assembled extruder is shown in Figure 4.15 including the mounting system meant for the CR-10s 3D printer and a pellet feeding tube. With all sub-assemblies included, Extruder 1 weighted 1.7 kg, including the stepper motor with gear box which accounted for about half the total weight. The extruder was 274 mm long, 64 mm wide and 100 mm deep, were the stepper motor itself was 110 mm long. If the stepper is mounted laterally rather than coaxially with the extruder, then the extruder would shorten to a more reasonable 160 mm. The complete list of engineering drawings is shown in appendix 2, page 355. The next section will discuss remaining aspect of this FGF 3D printing system i.e., the software and electronics which control it.

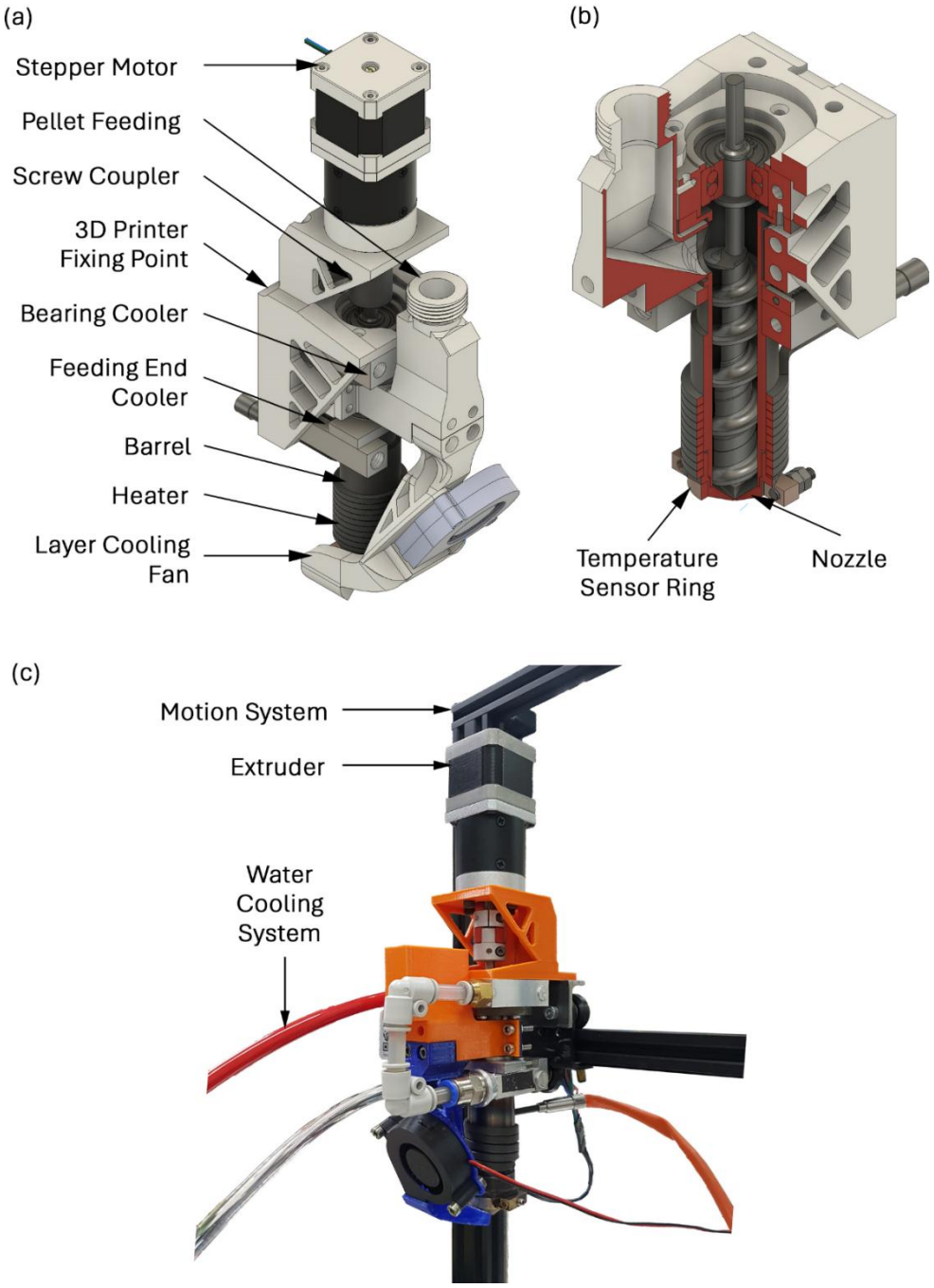

Figure 4.15 – Schematic of assembled Extruder 1 (a) with cross section (b) and real-life extruder (c).

4.3.2.5 Electronics and Software

The extruder was mounted on a CR-10s by Creality (China) which had upgraded Z axis motors to take the extra weight. The Z stepper motors were changed from two BJ45D14-26V02 with a rated torque of 0.4 Nm each to two 17HS19-2004S1 stepper motors from Stepper Online (Jiangning Nanjing, China) with a rated torque of 0.59 Nm each using independent stepper drivers. The 3D printer was controlled using a BTT SKR V1.4 Turbo

(China) controller board with Marlin Firmware using GCODE created with PrusaSlicer by Prusa Research (Prague, Czech Republic).

The extruder stepper motor was driven using a TB6560 stepper driver with micro-stepping set to 1/8. The stepper motor is geared with a 30:1 gearbox, which means that in effect 48000 microsteps are required to cause one full screw rotation. The controller was set at 800 steps per mm and therefore, 60 mm of travel were equivalent to one full screw rotation. The value of 60 ensures that the value of steps per mm is a round number, in this case 800 steps/mm as it divides 360, which is one full rotation, cleanly. It is the author's opinion, that it is impractical to set a conversion which would match the same volume calculated in an FFF system, since, as discussed in section 2.1.2, page 24, the extrusion rate per screw rotation is dependent on multiple factors, unlike in FFF where it is purely volumetric and only dependent on the amount driven by the stepper motor.

The next step is to evaluate the capabilities of the extruder and to determine what are the necessary improvements for the next extruder iteration.

4.3.3 Evaluation

To evaluate the performance of Extruder 1, the system was set to extruder using a number of materials and eventually for 3D printing with the 0.4 mm and 1.0 mm nozzles. The aim of this evaluation was to identify critical performance limitations inherent in the Extruder 1 design. The evaluation was also necessary to attain a datum upon which further iterations may be compared against. The melting behaviour of the extruder was also compared with the Tadmor model [20] to evaluate the applicability of this model to this kind of specialised FGF screw extruders.

4.3.3.1 Material and Method

4.3.3.1.1 Materials

The mass flow rate, glass transition temperature and melting temperature of each material tested are listed in Table 4.3. The main material used for testing was ABS pellets (P2H-AT) from ELIX POLYMERS, La Canonja, Spain, which is an easy flowing, high gloss, and injection moulding grade ABS. The ABS did not have any added colorants and had a natural ivory colour. The Magnum 3453 pellets by Trinseo, Heok, Netherlands which is an extrusion grade ABS with a white color, the INGEO 4043D PLA pellets by NatureWorks, Minnetonka, Minnesota, USA and the Ellastolan 1995 thermoplastic polyurethane (TPU)

by BASF, Germany, were all used for general testing and light 3D printing were appropriate. PLA is the lowest viscosity material tested at processing temperature, as shown by the MFR value. For this extruder, PEEK was used in a limited capacity, as given the difficulty to clean the extruder after using it, it was deemed more sensible to work with PEEK on the next extruder iteration which would implement new design features intended to make extruder maintenance simpler. The table shows that the glass transition temperature is not related with the MFR and therefore will not have an appreciable effect on the extrusion process.

Table 4.3 – Mass flow rate of the materials tested, adapted from datasheets [220, 306–308] and journal articles [309, 310] .

Thermoplastic Grade	Mass Flow Rate	T_g (°C)	T_m (°C)
P2H-AT ABS	37 cm^3/10 min (10 kg, 220°C)	110[309]	Amorphous
The Magnum 3453 ABS	14.3 cm^3/10 min (10 kg, 220°C)	100[310]	Amorphous
INGEO 4043D PLA	4.84 cm^3/10 min (2.16 kg, 210°C)	55-60	145-160
Ellastolan 1995 TPU	N/A	-28	Amorphous

4.3.3.1.2 Melting and Extrusion Performance

The extruder was tested out using all the polymers listed in section 4.3.3.1.1. In each case the extruder temperature was set at 20°C below the supplier's suggested processing temperature and incremented at 5°C steps until the stepper motor was capable to rotate the screw. Each test was done using a 1 mm nozzle, as it provided less resistance to extrusion flow which increased the probability of success. An operation test was deemed a success if the extruder kept extruding without any significant changes after 4 hours of intermittent extrusion. For each material, given the geometry of the extruder, a screw warm-push test was carried out similar to the conventional pull tests popularised by Maddock [41].

The screw warm-push test involved the screw being pushed out of the barrel for disassembly. The system was let to extrude until the material output, if any, was continuous. This was considered as the extruder steady state and then it was let to cool

to room temperature. Next the barrel was heated slowly whilst periodically trying to push the screw out. Eventually the screw was dislodged and pushed out gently. The temperature was set lower than the usual processing temperature. Using this technique decreases the smearing of molten material from the metering and compression section onto the feeding section. Doing so would decrease the usefulness of the result as the start of melting would be less clear. After the extrusion screw cooled down, the thermoplastic being processed was dislodged and separated from the extrusion screw. The remaining material was split in 5 cross sections per turn. Each cross section was sliced using a Diamond WireTec DWS175 (Germany) Diamond Wire Saw and the sections were viewed using a Remet Nikon SMZ-2T Stereomicroscope (Japan) with a Leica DFC295 (Germany) digital colour camera.

The P2H-AT Elix ABS was selected for further studies dealing with extrusion rate, melting performance and 3D printing. The material sectioning and analysis carried out only on ABS. ABS is a popular 3D printing material and therefore may be used as a comparative material to conventional FFF setups. The extruder was set at the desired temperature and left to stabilize. Next, two extrusion regimes were carried out with three repeats, first at 5 RPM for 5 screw turns and then at 10 RPM for 10 screw turns. This test was done using temperatures between 225°C and 245°C with 5°C increments. For each repeat, the extruded material was weighted on a PS 1000.3Y, Radwag (Poland) precision balance.

4.3.3.1.3 Comparing Practical and Theoretical Melting rates

The screw was modelled using a modified Tadmor model implemented in Python, which allows for a variable helix angle. The easy flow Ivory, P2H-AT, ABS was used for both the theoretical model and the practical test. The ABS rheological behaviour was modelled according to the power law model used by Tadmor [20] supported by the material data provided by the manufacturer.

The model was coded using Python 3 programming language with Jupyter Lab and Jupyter Notebook programming environments. The Tadmor model was calculated using the order shown in Figure 4.16, which follows the general indications set by Tadmor with the exception that the helix angle ϕ may be altered along the length of the screw. A change in ϕ leads to a change in velocity of both the barrel and the solid bed and

therefore these parameters have to be recalculated every iteration down the length of the screw along with the usual parameters (U1, Φ, ϕ, δ, X/W).

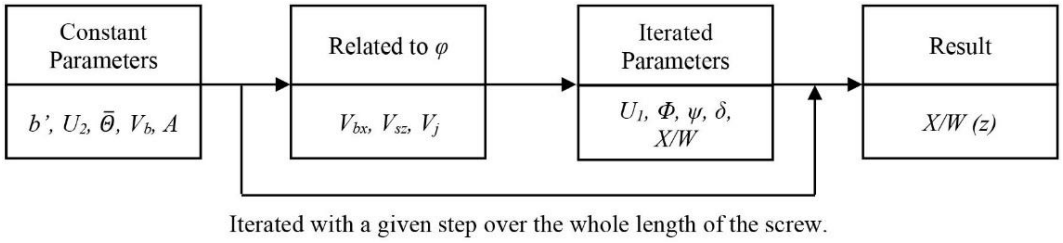

Figure 4.16 - Calculation flow of Tadmor model with consideration for variable helix angle.

All of the process parameters are listed in Table 4.4. The screw speed *N* and mass flow rate *G* were determined by experimentation on the working extruder. The material feeding temperature T_{s0} was set at a common room temperature value of 25°C. The thermal conductivity k_m, solid heat capacity C_s and molten heat capacity C_m were found from literature, given that the supplier did not provide this information. The melt density ρ_m was assumed to be 1170 kg/m^3 at any point in the process. The value is ballpark figure taken from literature [20]. The heat of fusion was set to 0 as it does not apply in the case of ABS, which is amorphous and therefore does not have a clear solidification phase change. The melting process was assumed to start 1 turn down the extrusion screw. The model was increment with a step of 0.1 turns.

Table 4.4 - Processing parameters for modelling using material properties taken from [20] in appendix Table A.3.

Symbol	Unit	Value	Symbol	Unit	Value
T_b	°C	235	k_m	W/m.°C	0.205
N	RPM	10	C_s	kJ/kg°C	1.189
G	kg/hr	0.28	C_m	kJ/kg°C	1.863
T_{s0}	°C	25	ρ_m	kg/m3	1170

In one modelling session, the barrel temperature was varied in between 225°C and 245°C with 5°C steps. In another study, the barrel temperature was kept constant, but the screw speed was decreased to 5 RPM and the solid mass flow rate G was decreased to 0.164 kg/s to reflect the change in speed. The practical data was produced via screw warm-push test, with the same method described previously. The pellets and initial solidified material in the feeding section and start of compression section were difficult

to preserve and study given that they were very fragile. These were disregarded in the present study.

4.3.3.1.4 Calibration and 3D Printing

When adapting filament extruder slicers for use with pellet extrusion, the extrusion multiplier is the most critical parameter. It is used to control how much material is extruded for a given movement. The extrusion multiplier may be set to an equivalent value so that a certain material flow rate is obtained for a given rotation of the screw extruder. To determine the correct extrusion multiplier, PrusaSlicer was used to generate a simple GCODE which printed a single outer wall perimeter of a 30 mm square, 3 layers high. The width of the third track was measure using Remet Nikon SMZ-2T Stereomicroscope (Japan) with a Leica DFC295 (Germany) digital colour camera, on each side and the average was taken. This value was then compared to the target width and the extrusion multiplier was adjusted accordingly. The process may have to be repeated if the extrusion multiplier was significantly off or the extrusion process was not stable enough. This test was carried out using both 0.4 mm and 1 mm nozzle, with 40 mm/s printing speed and at a barrel temperature of 235°C.

The Benchy [23] was 3D printed to verify the capabilities of the extruder but also as a reference for further tuning. This model is popular within the 3D printing community and therefore it is simple to compare and troubleshoot. The slicing parameters were left similar to those set on a Creality CR-10 3D printer, except for the extrusion multiplier as discussed previously. The speeds were also increased to 80 mm/s for perimeters and infill whereas for external perimeters and top solid infill, it was set to 40 mm/s. The layer cooling was set to high, and a 1 mm and 0.4 mm nozzles were used for 3D printing, with a layer height of 0.5 and 0.2 mm respectively.

4.3.3.2 Results

4.3.3.2.1 Warm Push Test

The white extrusion grade Magnum 3453 ABS did not extrude reliably and had a markedly lower extrusion rate than the P2H-AT Elix ABS. On the other hand, the P2H-AT Elix ABS extruded consistently and therefore allowed for further work to be carried out with it. The respective screw warm-push tests are shown in Figure 4.17 (a) and (b). In the case of the Magnum 3453 screw push, the extruder was extruding poorly with its extrusion rate

decreasing with time. The Magnum 3453 screw push is the only screw which has molten material in the feeding section whilst there is little to no material left in the compression section. This was caused by premature melting of the pellets in the feeding section, which stopped the material from filling the rest of the screw. This indicated that the feeding section cooling system should be improved, and the length of the extruder heater should be decreased.

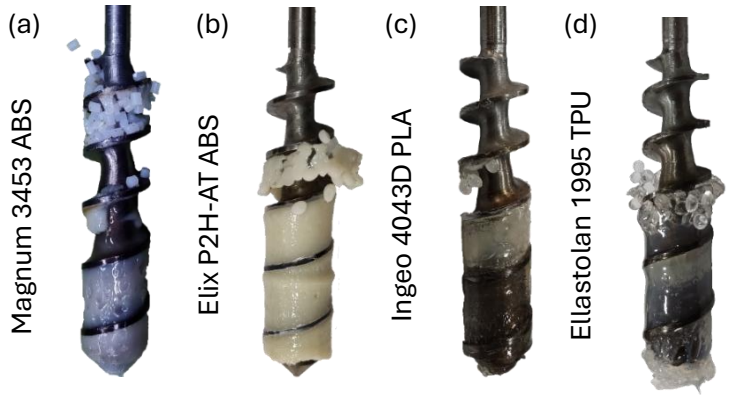

Figure 4.17 - Screw warm-push tests conducted on: (a) Magnum 3453 ABS; (b) P2H-AT ABS; (c) INGEO 4043D PLA; (d) Ellastolan 1995 TPU using Screw 1.

The screw push results of the injection moulding grade materials, namely, P2H-AT ABS and INGEO 4043D PLA are shown in Figure 4.17 (b) and (c), both of which were extruded consistently and without issues. Both screw pushes showed a clear feeding section, signifying that whilst the screw was in the barrel, it was filled with unmolten and therefore discrete pellets.

The injection moulding grade Ellastolan 1995 TPU elastomer behaved differently than both the P2H-AT ABS and the INGEO 4043D PLA albeit the screw push shown in Figure 4.17 (c) is rather similar. When extruding Ellastolan 1995 TPU, the material shows a low viscosity which causes drooling of the molten TPU. This drooling makes it difficult to use the extruder for 3D printing as the movements of the 3D printing head would have to be very fast to deal with the fast extrusion/drooling rate.

4.3.3.2.2 Extrusion Rate

The extruder was capable of extruding P2H-AT ABS continuously at temperatures above 235°C. Temperatures below this value led to two forms of failure, either by excessive polymer viscosity which would lead to insufficient stepper motor power to drive the screw or else plugging of the polymer in the screw, making the extruder rotate without

extrusion. Going sufficiently beyond 245°C increased the propensity for polymer degradation.

The best operating temperature was found to be 235°C, given that it is the lowest temperature which does not have any issues associated with excessive viscosity, nor is there any visible burning or degradation in some form of the ABS. As shown in Table 4.5, increasing the temperature and the rotational speed of the screw leads to an increase in extrusion rate. In both cases, the increase is seemingly linear but not one to one, which is expected given that the change in viscosity with temperature is not necessarily linear. The multiplier value refers to the result obtained when dividing the extrusion rate at 10 RPM with that at 5 RPM. In a one-to-one linear relationship, the value would be expected to be 2 or thereabouts.

Table 4.5 - Extrusion rate results using a 1 mm nozzle, for different temperatures and screw speeds with sample standard deviation (n = 3).

Temperature	**Extrusion Rate [g/s]**		**Multiplier**
[°C]	***5 RPM***	***10 RPM***	
235	0.0441 ± 0.0023	0.0762 ± 0.0026	1.73 ± 0.15
240	0.0455 ± 0.0025	0.0776 ± 0.0054	1.70 ± 0.21
245	0.0477 ± 0.0015	0.0846 ± 0.0038	1.77 ± 0.13

4.3.3.2.3 Screw Melting Rate

The material model for ABS is shown in Figure 4.18 which presents the data provided by the supplier compared with the power law model. The power law fitting shown in Figure 4.18 was made using points in the shear rate region generally employed in an extrusion process, i.e. from 100 to 1000 (1/s). The power law model should be applied to the injection molding shear rate range, i.e. from 1000 to 10000 (1/s) where the exponential decrease in viscosity is correctly modelled using power law. This approach would be incorrect as it would make the model overestimate the actual viscosity present in the process.

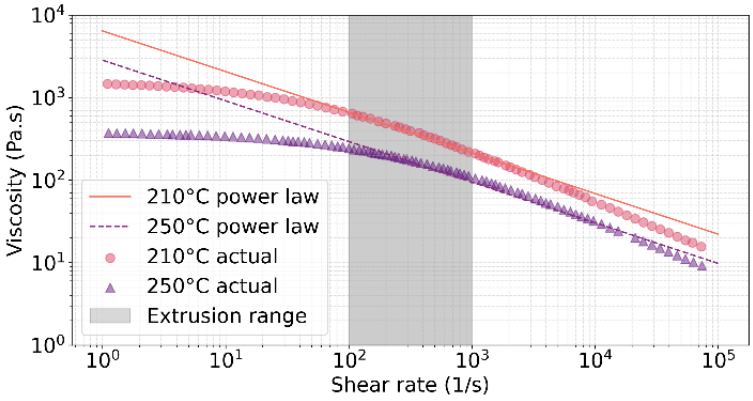

Parameter	Value
m_0	6417
n	0.51
a	0.0204
T_m	210°C

Figure 4.18 - Viscosity vs Shear rate graph of ABS P2H-AT with manufacturer data and power law model along with the numerical value of the power law model parameters. Values for a shear rate range of conventional extrusion between 100 s^{-1} and 1000 s^{-1}.

The most relevant results of the analytical model are shown in Figure 4.19. The solid lines shown in (a) and (b), show the same result given that it follows the parameters listed in Table 4.4 and may be considered as the reference. The vertical lines labelled as section change mark the transition points from feeding to compression section and from compression to metering section. An X/W value of 0 would signify that the pellets have completely melted at that point. The shear rate increases at the metering section because theoretically the melt film thickness decreases significantly. In practice, at that point the screw section would be mostly melted and therefore the shear rate value presented in inconsequential. The Br number is relatively constant and set at very low value, throughout the whole extrusion process. This indicates that most of the melting is being achieved by direct, conduction heating of the material rather than by shearing as is done in most extruders.

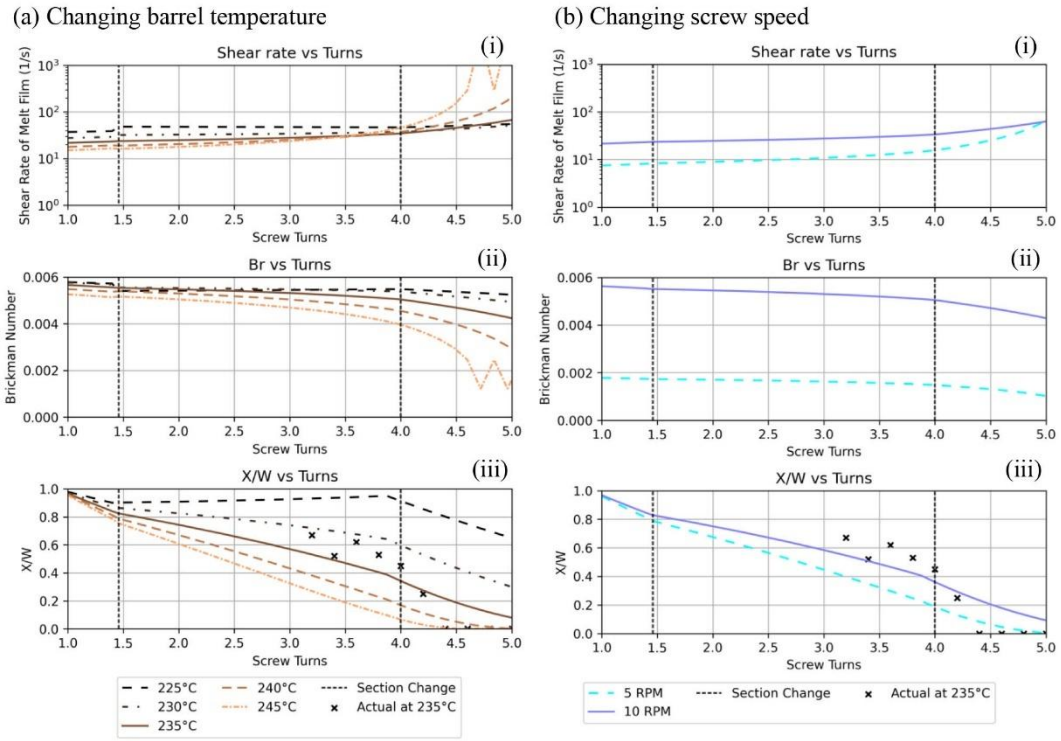

Figure 4.19 - Plots of shear rate of melt film (i), Brickman number (ii) and solid bed profile (X/W) (iii) vs the screw turns from feeding section to metering section, with: (a) varying barrel temperature and (b) varying screw rotational speed, using 100 to 1000 s-1 shear rate power law model, using the Tadmor analytical model with ABS P2H-AT.

The actual melting profile (X/W), measured at 235°C at 10 RPM, is superimposed on the analytical predictions of in Figure 4.19 (a) and (b), and shows a moderate agreement in the compression section. The solidified polymer cross-sections are shown in Figure 4.20. The sections between turns 4.4 to 5 are not shown as they would show a fully molten polymer just like turns 4.4 and 5. The whitening, outlined with a dashed line, predominantly visible in the cross-section of turn 4.4 and to a lesser extent in cross-sections of turns 3.6 and 5 are due to bending of the ABS caused during removal from screw and cutting, which elongates it and causes the marks. Incompletely molten material is ivory-white in colour and does not show as parallel lines, whereas molten material is a dark ivory colour.

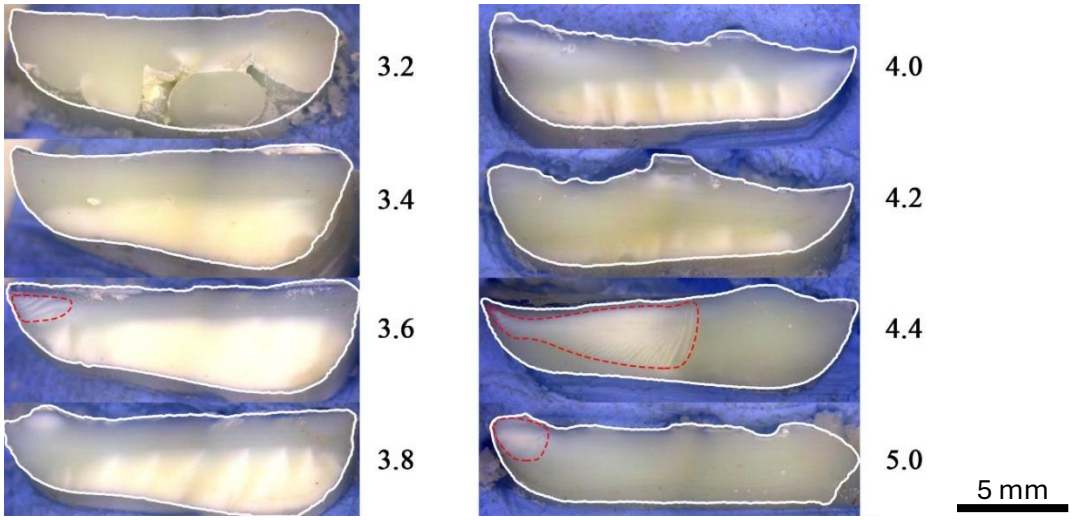

Figure 4.20 - Cross-section of solidified P2H-AT ABS derived from screw warm push-out test, sliced face outlined in white and each is annoted with screw turn position.

4.3.3.2.4 Calibration and 3D Printing

The extrusion multiplier for the 1 mm nozzle was found to be 0.27 whereas the 0.4 mm nozzle was 0.37, with the slicer being set with a pseudo filament diameter of 1.75 mm. Using this value, the parts produced were found to be dimensionally correct. The calibration test had to be carried out three times to get a correct result. 3D printing was successful using both the 1 mm nozzle and 0.4 mm nozzle. Two respective examples are shown in Figure 4.21. The Benchy 3D printed using the 1 mm nozzle suffered from poor layer cooling. The clearest marker of this defect is the indistinguishable chimney shown in Figure 4.21 (a) which is caused by a series of short extrudes in one location which deposit a great amount of heat which has no time to dissipate or otherwise cool down. Apart from the insufficient cooling, the Benchy printed adequately given the low resolution provided by a 0.5 mm layer height whilst using a 1 mm nozzle.

The 0.4 mm nozzle Benchy printed with greater detail and has a similar finish and quality as a conventionally printed FFF Benchy. The only issues found in the 3D printed part were minor surface defects which were easy to remove by hand. These defects may be seen in Figure 4.21 (b), especially near the top of the entryway of the cabin. Another minor issue is stringing which refers to undesirable, thin strings which follow the movements of the printing head whilst travelling. These are a common occurrence with FFF extruders and are easily resolvable by increasing the retraction of the extruder or by simple post-processing.

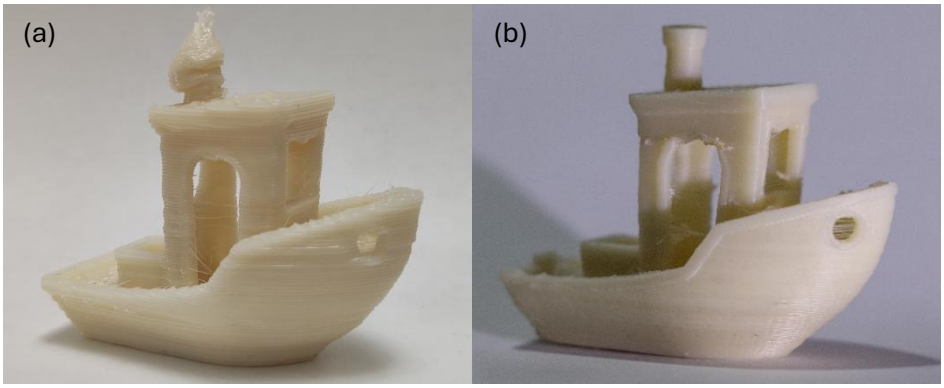

Figure 4.21 – Pellet 3D printed Benchies using (a) 1 mm nozzle and (b) 0.4 mm nozzle.

4.3.3.3 Discussion

4.3.3.3.1 Relevance of the Modified Tadmor Model.

The results shown Figure 4.19 are useful in a number of ways. At a preface value, these results provide an indication of the sensitivity of the extrusion process to changes in temperature and screw rotational speed. On the other hand, the result was not completely representative of what was actually observed in practice. The model failed to predict the early complete melting observed in the metering zone but the melting rate of the compression section was very similar to the experimental result. This problem agrees to some degree with the observations of Mount et al. stated earlier, in the sense that the Tadmor model is not best suited to accurately predict the solid bed-profile [16].

Nonetheless, the value of the model, especially when applied to unusually low L:D ratio screws for additive manufacturing, lies in its ability to pre-emptively showcase possible issues with a given design. For example, for the given screw geometry, the model predicted that operating at 225°C and 230°C would likely mean that the extruder would not sufficiently melt the ABS, as shown in Figure 4.19 (a)(iii) and therefore extrusion would fail. The extrusion study confirmed this prediction as it showed that extrusion was not possible at that temperature as the stepper motor could not turn the screw continuously due to the excessive resistance caused by the high melt viscosity.

The experimental results provided also have an inherent error. The early melting observed in the metering section may have been caused by the method used to extract the screw from the barrel. Given that the barrel had to be heated slightly to push out the screw so as not to damage the equipment, it is expected that the material may have melted some more, even beyond the outer shell of the screw and thus distorted the results. This effect would be more prevalent in the metering section as it is usually the

most heated as the cooling applied to feeding end creates a thermal gradient to the metering end. Nonetheless, it is the author's opinion, that this effect is improbable given that the barrel temperature was kept at about 140°C and for a very short period of time.

The model also gave an indication of the effect of decreasing screw speed, predicting a higher melting rate. In most conventional extruders, increasing speed would increase melting rate due to greater shearing. In this case, it is expected that due to the higher residency time of the thermoplastic in the extruder, the material would be more molten.

The result of the model also indicates that the Br number is low, close to 0, as shown in Figure 4.19 (a)(ii) and (b)(ii). A low Br number indicates that heating is mostly done conductively by the resistance heaters rather than by shearing. This is as expected given that the rotational speed is very low and therefore shearing is limited. The shear rate is set within the 1 s-1 to 100 s-1 range which is well below the conventional extrusion range. Nonetheless, it is not unusual as most extrusion processes operate at much larger throughputs and speeds than those applied in this process. The study conducted by La Gala *et al*. using an adaptation of the same analytical model but for conical, medium scale extruders, recorded higher Br numbers, even up to 3.5 which is close to what is observed in larger extruders [51]. It is probable that the slow speed used by small scale extruders caused the lower Br value. In turn, the slow speeds were necessary as weight is often a critical aspect of small-scale extruders which limits motor power available. Small scale extruder therefore may operate using a different fundamental process then larger extruders, one which is powered by conduction heating and not viscous heating. This difference from larger extruders was also seen in the melting behaviour of the solid bed profile.

The solid bed profile observed was not the same as that observed by Maddock, as shown in Figure 2.7 (a), upon which the whole model is built. The cross-sections shown in Figure 4.20 do not have a clear melt pool as observed by Maddock on his significantly larger screw extruders. The solid bed profile is apparently compressed by an ever-thickening top layer of molten material. The heat transferred from the barrel, melts the solid bed from the top and then the heat keeps travelling down towards the root of the channel until it melts all of the material therein. For this reason, the Tadmor model may not be the correct modelling approach necessary for small scale FGF, despite the close results.

4.3.3.3.2 Extrusion Consistency and 3D Printing

A consistent and predictable extrusion rate is necessary for good quality 3D printing. The melting rate and the extrusion test results shown in Table 4.5 tell of a relatively consistent extrusion but which changes non-linearly with temperature and screw rotational speed.

During normal 3D printing, the temperature is kept relatively constant, with maximum possible fluctuations of about 1°C ever so often. Shifting the temperature by 5°C did show a change in extrusion rate, but even at 5°C the change was not that significant therefore it is expected that a 1°C change would only show as a minor imperfection in the surface quality of most 3D prints. More importantly, the presence of this effect indicates that any tuning done to determine the extrusion multiplier should be carried out at the desired printing temperature.

The issue becomes more relevant when dealing with screw speed whilst extruding and 3D printing. Usually, the slicer is set to print outer layers slowly, for better positional accuracy, whereas the internal structures would be printed faster to reduce the overall production time. In such a scenario the internal structure would invariably be over extruded relative to the external structure. Oftentimes this issue is not significant as the material being deposited has ample empty space where it can be shifted to. Therefore, extrusion multiplier tuning should be carried out using outer perimeters rather than any internal features, as done in this study, if dimensional accuracy and aesthetics are valued.

The best 3D printing quality was achieved when using a 0.4 mm nozzle. This is expected due to the greater 3D printing resolution available and the more effective layer cooling possible. The smaller extrudate flow rate employed when using small nozzles means that there is less heat energy to dissipate and thus cool down the extrudate. This makes it easier to retain the shape desired during 3D printing as the material becomes more viscous at a faster rate, the faster it is cooled down. This is a perfect example whereby even though extrusion control may be up to par, for correct 3D printing all the other process parameters must also be correctly set.

4.3.4 Improvement

The evaluation results highlighted takeaways which are necessary to improve the design of the extruder, and thus develop Extruder 2. The initial extrusion tests shown in section 4.3.3.2.1 indicated that the there was a deleterious temperature gradient acting on the barrel which caused premature melting at the feeding end of the barrel. This led to a transient pre-mature material melting which eventually would block the feeding end screw channel and cause an inconsistent extrusion rate. To solve this issue, either the barrel heater should be shorter, the cooling end may be longer or a combination of both. This issue was more prevalent with low flow rate materials, namely the Magnum 3453 ABS. High flow rate materials, such as P2H-AT ABS and Ingeo 4043D PLA extruded consistently. The vertical setup of the extruder means that those material with a high flow rate may still be unprintable as the level of drooling would be excessive, impeding 3D printing.

Regarding extruder cooling, Extruder 1 used two separate water-cooling blocks at the feeding end of the extruder. The system may be simplified by integrating both extruders in a single component. Another simplification improvement is necessary to improve screw changeover. As designed, the temperature sensor ring can only be placed on the nozzle and cannot be mounted on the barrel. In this manner, removing the screw when the material is molten becomes time constrained. In Extruder 1, upon removing the nozzle, heating must be stopped as there is no active temperature sensing. The screw then has to be pushed in the short time frame during which the extrusion screw is cooling down. This is not an adequate setup and is a critical improvement necessary for correct operation of the extruder.

With regard to theoretical modelling, these results were useful to predict the melting rate. In the next extruder iteration, the extrusion screw may be improved to increase extruder throughput especially of viscous thermoplastics. This is necessary especially when considering high-performance polymers which are known to have a low flowability. Such improvements may be carried out by using known theoretical results, presented in section 2.1.4, page 34 and do not need further theoretical modelling.

4.4 Extruder Development 2

The main objectives of the development of Extruder 2 were to improve ease of use and make the extruder more modular and versatile. This development exercise also focused on component combination and simplification, with the aim of reducing the production time and complexity. Component with critical dimensions such as the barrel and the extrusion screw mounting point were designed with machinability and ease of use in mind. Ease of use was an important aspect of this development process, with the aim of improving general operation, simplify extruder maintenance and make testing procedures, namely the extrusion screw warm push tests, easier and safer. Lastly, the extrusion throughput should be improved. This is necessary in order to enable the extrusion of more viscous thermoplastics compared with ABS, which has already been confirmed as extrudable and 3D printable with Extruder 1. An improved extrusion throughout would allow for extrusion of high performance polymers, such as PEEK, which is part of the aim of this thesis. The extruder should be sufficiently reliable, especially when extruding and 3D printing high performance polymers, to be used for a more detailed analysis of both its performance and that of the products it may produce.

4.4.1 Concept

The aim set out of this extruder development required the alteration of most sub-system designs of Extruder 1. The extrusion screw was redesigned with the aim of increasing the extrusion rate especially with more viscous thermoplastics, such as high-performance polymers. The barrel was simplified to make machining of this precise component easier and cheaper. This change involved the implementation of a faster barrel fastening mechanism than as used in Extruder 1. The integrated barrel feeding port was also removed whilst shortening the whole barrel. The bearing end and feeding end water coolers were combined into one block, serving as a feed end cooling system, pellet feeding port as well as a fixing point of barrel, screw, stepper motor with the rest of the 3D printer. The temperature sensor ring was also altered in order to be able to slide it across nozzle and barrel as desired during use. These conceptual changes were then applied in a new embodiment which will be described in the following section.

4.4.2 Embodiment

The most visually striking change in Extruder 2 is the new feeding block which has multiple functions all integrated in one component. This led to a simplification of the barrel, as described in the following section. Despite these crucial changes, the hearth of the extruder remains the extrusion screw which will be discussed in the next section.

4.4.2.1 Extrusion Screw

The extrusion screw maintained the same length and diameter as in the previous embodiment. This was a necessary decision in order to make comparisons between the two extruders simpler. The main changes in the extrusion screw are a change in bearing shaft size and a different helix angle specification. The lengths of each screw zone i.e., feeding, compression and metering, where also marginally altered compared with extrusion screw 1, as shown in the geometric specification shown in Figure 4.22 and Table 4.6. This was done to simplify extrusion screw inspection during machining. In this manner, the feeding end is 20 mm in length with one turn, which is easier to inspect compared to measuring the helix angle. The feeding end is also the deepest screw section which makes it the most susceptible to machining inaccuracies especially those caused by tool sliding.

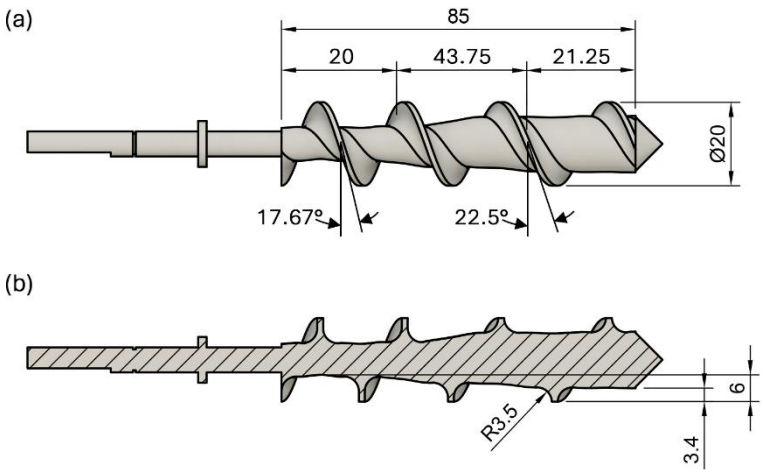

Figure 4.22 – Extrusion screw 2 with key geometric features.

Table 4.6 – Geometric dimensions of extrusion screw 2, with a 20 mm diameter.

Section	Length [mm]	Turns	Helix Angle [°]	Pitch [mm]	Depth [mm]	Flight thickness [mm]
Feeding	20	1.00	17.67	20	6.0	
Compression	43.75	-	-	-	-	1.5
Metering	21.25	0.82	22.5	26	3.4	

The most significant change is the increase in helix angle which now changes from a square pitch at the feeding end and increases linearly to a 22.5° helix angle or a 26 mm pitch at the metering section. This change was driven by theoretical results from literature, specifically the optimal helix angle for maximising throughput. This result was shown in Figure 2.10 (b), page 37, using both analytical and numerical methods. To obtain the optimal helix angle, a target material needs to be set for the specified application of the extrusion screw and its power law index needs to be obtained. In this case, the material was set to VESTAKEEP L3300G PEEK, whose power law index is 0.66, as derived by fitting from the viscosity-shear rate curve, provided by the supplier, shown in Figure 4.23. The suggested helix angle for PEEK is of 25.5° or 27.3° according to the numerical and analytical study respectively. The results also proposed that the optimal metering channel depth would be 3.3 mm or 3.6 mm for the analytical and numerical results respectively [17]. In view that the compression ratio had to be kept at 1.4 using channel area, the channel depth was therefore set to 3.4 mm with a pitch of 26 mm i.e., a helix angle of 22.5°.

This kind of optimisation, despite using the available literature, is also flawed as the process parameters used to derive these results are unknown. Furthermore, most theoretical results available were calculated with large extruders in mind and whose assumptions may not be correct for small scale system. One example is the assumption that channel curvature is negligible which may be correct for large diameter extruders. For small diameters, curvature may instead have a significant role. Another example is the Brickman number results shown in section 4.3.3.2.3 which highlights the lack of shear heating present during the process. This means that the extrusion process is rather different than what is conventionally undergone in large, static, continuous

extrusion processes. For this reason, theoretical results can only be used as a guide and may not provide a definite answer.

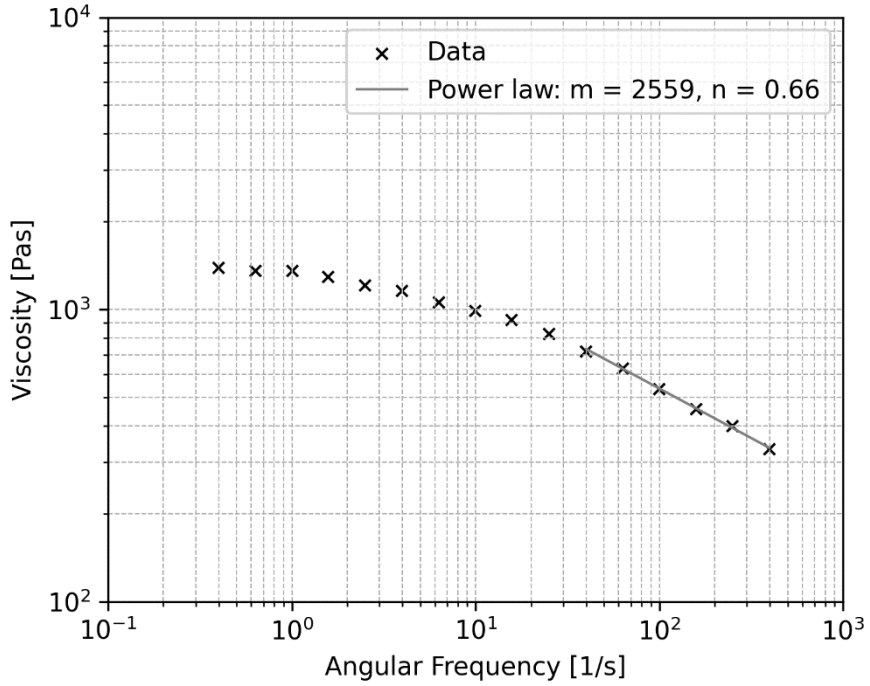

Figure 4.23 – VESTAKEEP L3300G viscosity-shear rate curve with power-law fitting.

The new extrusion screw also has a smaller shaft diameter at the bearing end. This is part of the improvements undergone to the general assembly of the extruder. This will be discussed in further detail in the following section, starting with the new barrel design.

4.4.2.2 Barrel, Nozzle and Cold Feeding Block

The barrel of this second extruder configuration was shortened and simplified significantly, as shown in Figure 4.24. The barrel outer surface was made to be flush with that of the nozzle in order to allow a seamless shifting of the temperature sensor ring from nozzle onto the barrel when necessary. This was especially useful for removing the nozzle and screw for servicing or testing purposes. The nozzle is still fastened using a hex socket, but this time a smaller size is used to fit within the diameter of the barrel. A flat interface was integrated inside the nozzle to seal off the polymer flow and prevent leakages.

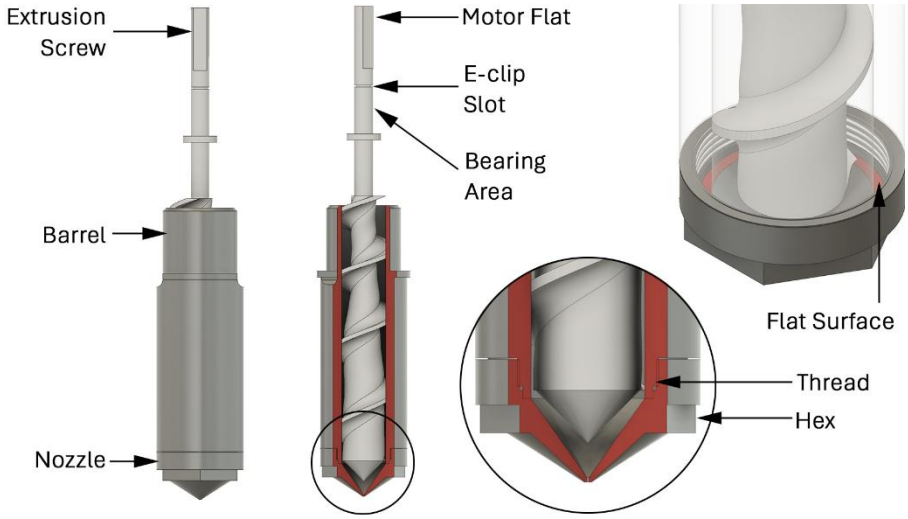

Figure 4.24 – Extruder 2 barrel with screw and nozzle, with side, isometric and section views.

The next and arguably the most visible change in this extruder iteration is the feeding block, shown in Figure 4.25. The feeding block as designed has four main functions namely: cooling of barrel and feeding end, pellet feeding, location fixturing of barrel with extrusion screw and fixturing of feeding block to the driver mount and the 3D printer motion system. This compact, multi-functional component was fabricated using CNC milling, out of any 2000 series aluminium grade and temper. Aluminium has a high thermal conductivity which is ideal for thermal management along with a low density which decreases the overall weight. In order to achieve further weight savings a series of pockets on the side faces were made to remove excess material.

Of the four functions of the feeding block, the most convoluted is the water-cooling system. A detailed view of the water channels is shown in Figure 4.26. These channels were fabricated by drilling through and then closing off the necessary section by using plugs. These channels cool two levels of the feeding block i.e., at the top, close to the bearings and the bottom, close to the barrel. The top level is necessary to ensure that the top part of the screw remains cool and does not transfer heat to the driver or the rest of the 3D printer. Bottom level cooling is necessary for correct extrusion by ensuring that the feeding end of the extrusion screw remains in a solid feeding scenario. The water-cooling channels were then connected via push fits located at the top of the feeding block.

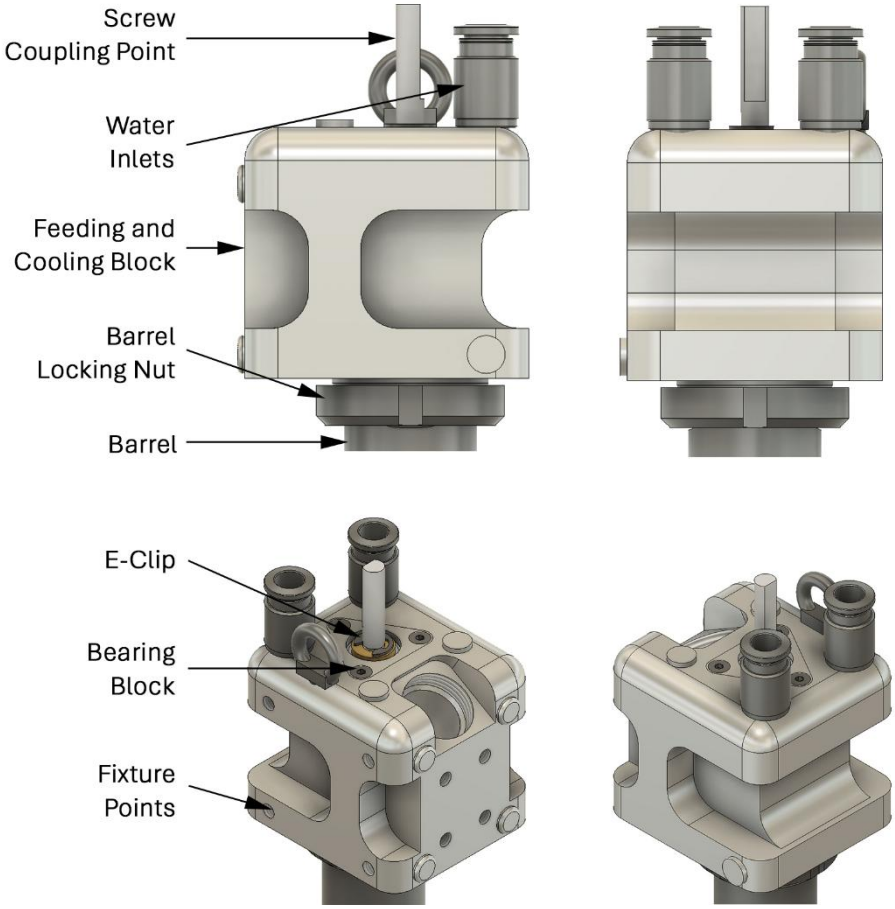

Figure 4.25 – Feeding block, viewed from multiple angles.

Pellet feeding was achieved via a sloped channel passing between the back fixturing points and the bearing chamber. The feeding port has a threaded end to which a flexible pipe for pellet delivery may be fixed to. The fixturing points at the two sides of the block allow for a flexible setup of the extruder with different motions systems. The bearing chamber, shown in detail with bearings in Figure 4.27, can be reached from the top side of the feeding block where it is closed off using a triangular lid. The bearings are to be press fit or glued in, in such a manner the bearing lid does not take the load of the extrusion screw. The main purpose of the bearing chamber lid is to minimise dust and debris from reaching the bearings and to act as a slow indicator of failure if the bearings get loose. For these reasons, the bearing lid was also fabricated out of 2000 series aluminium which is highly ductile and will bend before failure. A spacer was also added so that an e-clip could be fitting, flush with the top of the feeding block surface to retain the extrusion screw. As shown previously in Figure 4.22, the extrusion screw also has a shoulder at the bottom of the bearings. In this manner, it is constrained vertically but can rotate with the bearings.

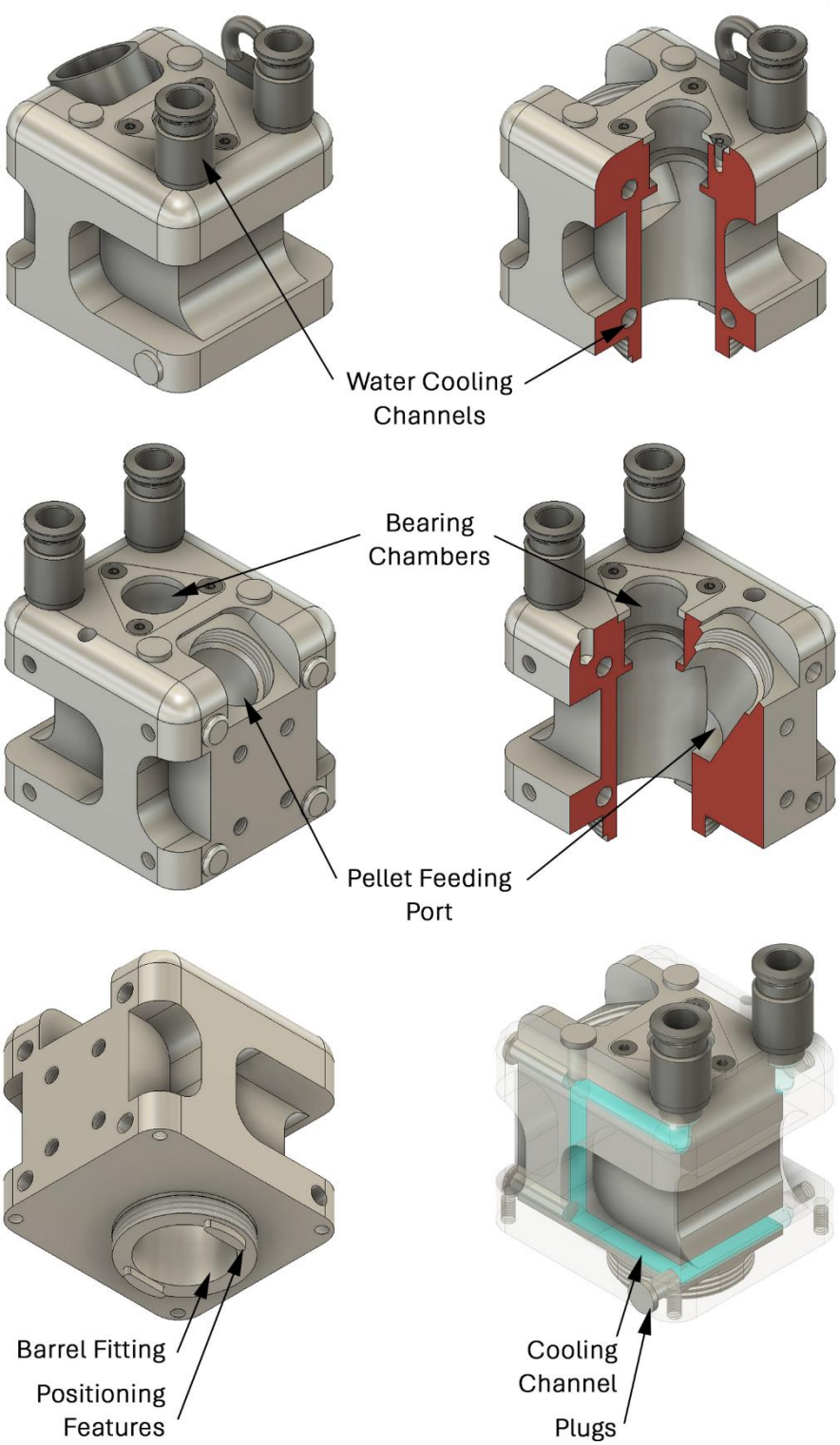

Figure 4.26 – Sectioned feeding block with views of the pellet feeding port, barrel fitting and internal cooling channels. Sectioned areas are marked in red and cooling channels are marked in light blue.

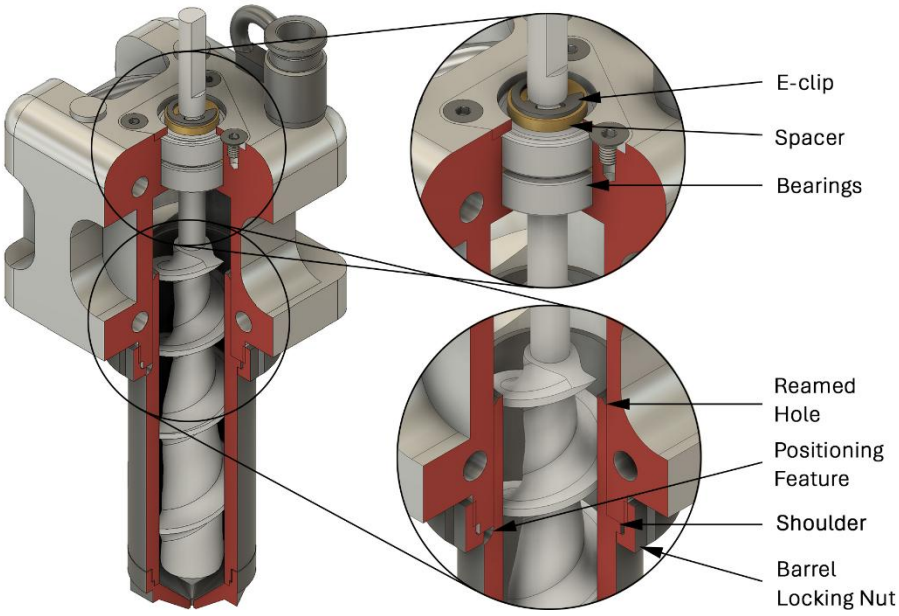

Figure 4.27 – Section view of assembly including feeding block, barrel and extrusion screw with detail of bearing chamber and barrel locking including guiding feature.

The connections between the barrel and the feeding block were done by using a reamed hole in the feeding block and fine turned barrel shaft. The barrel was fastened to the feeding block by a nut which pressed the shoulder of the barrel onto the flat of the feeding block. This method of fastening the barrel to the feeding block only constrains the system vertically and does not constrain rotation except by the friction acting in between the faces. To stop the barrel from rotating during the extrusion, two positioning features, best shown in Figure 4.26 bottom left, were added that slide in appositely milled faces on the barrel, shown in Figure 4.24 left.

4.4.2.3 Ease of Use

Another significant advantage brought about by the new feeding block, is the improvement in ease of use of the extruder. By implementing the use of a barrel locking nut, removing the barrel now involves loosening just that barrel locking nut, as opposed to unscrewing the 6 small screws used in the flanged barrel of Extruder 1, shown in Figure 4.12 right. If the barrel is filled with solid polymer and cannot be removed without the screw, the next step would be to remove the e-clip holding the barrel, as shown in Figure 4.28. In this manner the barrel and screw together, can be easily unassembled from the extruder for maintenance and cleaning.

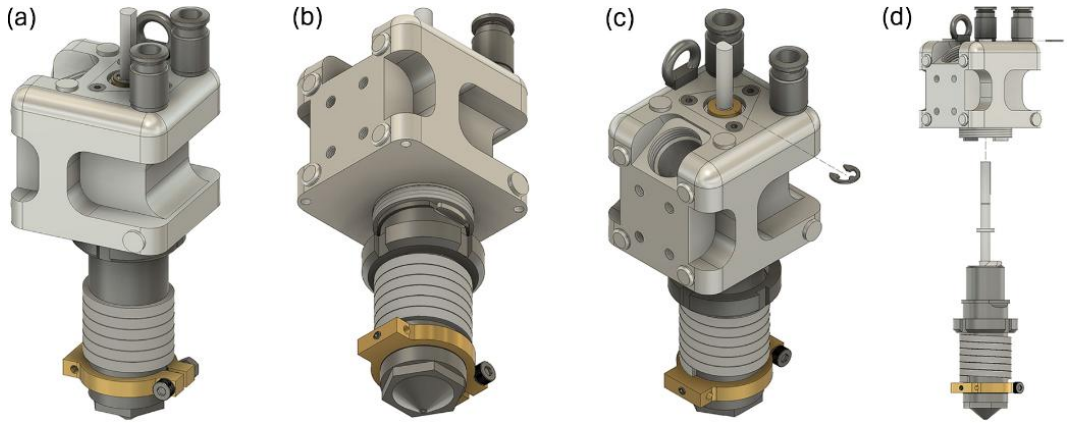

Figure 4.28 –Extruder (a), loosening of the barrel lock nut (b), removal of e-clip (c) and un-assembly of barrel and screw (d).

The screw can also be unmounted whilst leaving the barrel with the heater and temperature sensor still attached to the feeding block. This is necessary when conducting a warm-push test as described in section 4.3.3.1.3. In such a case, the nozzle must be unscrewed using a common socket wrench, and the e-clip holding the screw should be removed. The stepper motor with coupler should also be loosened and disassembled during the procedure. The screw can then be slid down the barrel by pushing the screw from the top end by levering against the apposite ring as shown in Figure 4.29. A c-spanner which is used to unscrew the barrel lock nut can also be used to lever out the extrusion screw.

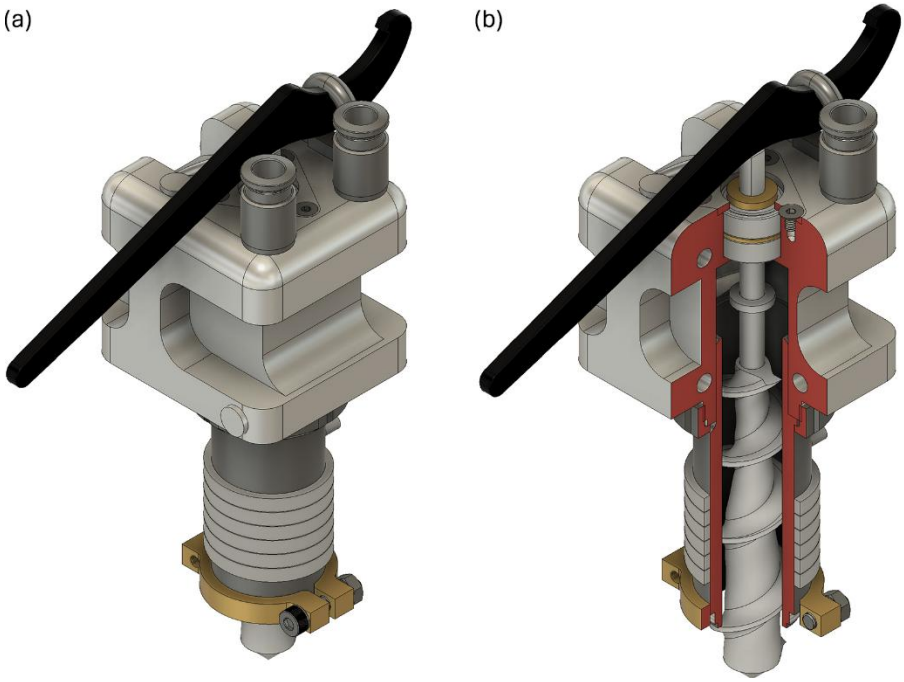

Figure 4.29 –Extruder with a c-spanner acting as a lever (a) and sectioned (b).

The ease-of-use improvements included in this extruder development allowed for easier testing, 3D printing and general maintenance. In this manner, the FGF extruder developed by this study already has features which are not yet available in commercial systems, such as the Mahor FGF extruder. In practice, these improvements are especially important for testing and maintaining the extruder when using high temperature materials, such as PEI and PEEK.

4.4.2.4 Manufactured Extruder 2

Extruder 2 is shown in Figure 4.30 with an extruder width of 54 mm and a depth of 60 mm. By adding the 3D printer fixing point and layer cooling fan, the width becomes 75 mm and the depth is 74 mm. Extruder height from nozzle tip to screw end is of ~ 160 mm and the full extruder height including stepper motor is of ~ 270 mm. The extruder is expected to be an improvement over the previous iteration when it comes to ease of use and possibly extrusion capability especially of high-performance polymers. The complete list of engineering drawings is shown in appendix 3, page 371. The next step is to evaluate the capabilities of the extruder and to determine what are the necessary improvements for the next extruder iteration.

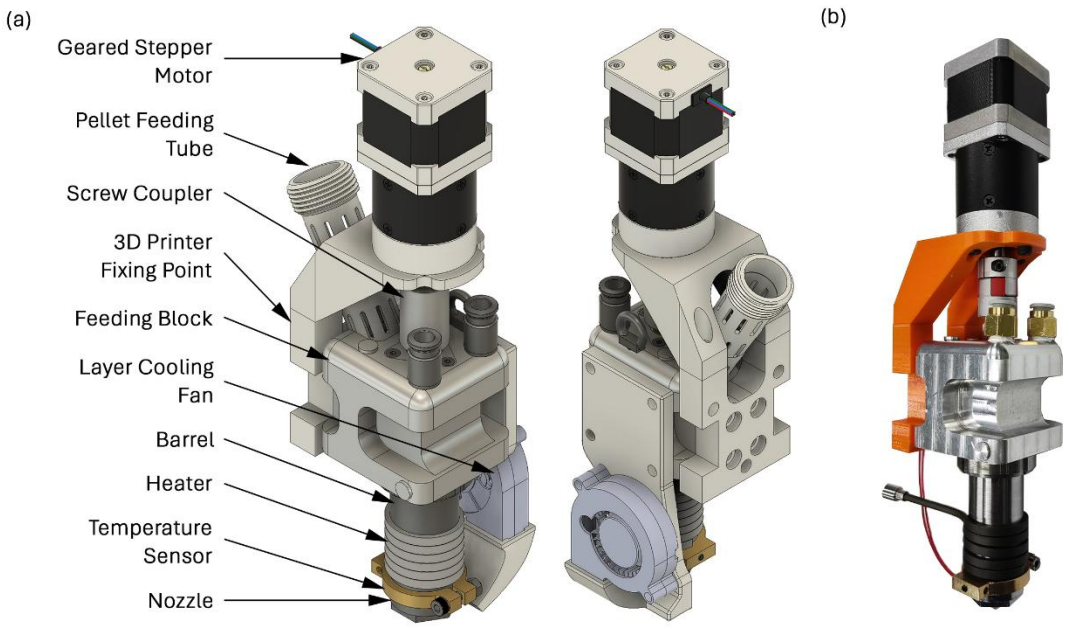

Figure 4.30 – Schematic of assembled Extruder 2 (a) and real-life Extruder 2.

4.4.3 Evaluation and Application

The extruder was assembled on the same motion system used with the previous extruder. Given that Extruder 2 is an upgrade over Extruder 1 and yet it maintained the same key concepts, it was deemed plausible to move on to the main materials intended for this study. Extruder was used for extruding and 3D printing TPO elastomer and PEEK which is a high-performance polymer. In each case the material had to be calibrated before undergoing a more involved analysis. During the calibration process, the extruder was used with the material for a long duration, evaluating the extrusion rate and its consistency, amongst others. In this manner, during this calibration process of new materials the extruder was also being evaluated in practice. This evaluation process confirmed the functionality of the extruder, but it also highlighted certain limitations especially when it comes to 3D printing of the super soft TPE and high performance polymers. A more detailed application of Extruder 2 with TPO and PEEK will be covered in Chapter 5, page 165 and Chapter 8.2, page 240 respectively.

4.4.4 Improvement

The general extruder design was found to be satisfactory, especially the ease-of-use systems implemented. TPO extrusion and 3D printing was flawless which indicated that the system is ready to study more challenging elastomers namely, TF3ZG0-LCNT super soft elastomer. PEEK extrusion, whilst satisfactory using Extruder 2, indicated that more extrusion force would be desirable especially if using higher molecular weight grades of PEEK. Such grades tend to be more viscous and therefore more difficult to process. In order to achieve this, without having to increase motor size and weight, the screw diameter has to be decreased. In this manner for the same torque, there is a greater force acting on the melt. This change requires a new screw and barrel design. Likewise, the temperature sensor ring and the spring heater have to be adapted for the smaller barrel. The nozzle requires improvement towards better ease-of-use and a reduction in production complexity.

As currently setup, the nozzle has an internal thread which is necessary to screw the nozzle onto the barrel. This setup is convention when the barrel does not have any material loaded and is clean. On the other hand, when the extruder is in use, any material leakage either in process or caused during a screw warm-push would lead to smearing of molten thermoplastic onto the threaded section of the nozzle. Another issue

is machinability. The threaded section forces the tapered section of the nozzle deeper into the part. This extra depth makes machining of the taper more difficult leading to poorer control of machined surface quality. By removing the internal thread, nozzle ease-of-use would be improved along with a reduction in part complexity.

The next extruder development section will deal with the aspects just discussed. In effect the new extruder will be a variant of the existing extruder as the conceptual jump in the next development will be minimal compared to that between extruder development 1 and 2.

4.5 Extruder Development 3

This extruder development was intended to optimise the extruder for 3D printing of high-performance thermoplastics. The objectives of this extruder development were to improve nozzle geometry for better ease-of-use and decreased complexity, to decrease screw diameter in order to improve the force acting on the thermoplastic being processed and to adapt the concomitant extruder components to the new screw diameter and nozzle geometry. The barrel, extrusion screw, temperature sensor ring, spring heater and nozzle components were all modified to account for the new changes necessary for this extruder development.

4.5.1 Concept

By decreasing the screw diameter, the force acting on the material becomes larger. This follows the fundamental torque to force relationship described by Equation 4.3, where T is the toque, F is the force and x is the distance which in this case is equivalent to the radius of the screw. Re-arranging the equation allows for the calculation of the maximum theoretical increase in acting force on the material, as shown in Equation 4.4, where the subscripts *1* and *2* refer to the 20 mm and 14 mm diameter screws respectively. The variable r refers to the radius of the screw, whereby r_1 is 10 mm and r_2 is 7 mm. This results in a percentage increase in force of 42.9 %. This change is also accompanied by a marginal decrease in extruder weight due to diametric shrinking of barrel, screw and concomitant components. The principal disadvantage is the decrease allowable channel depth which in turn means that the allowable pellet size is also decreased. Given that this specific modification is meant to ensure better processing of high-

performance polymers, specifically PEI and PEEK which are known to have conventional pellet sizes, it was deemed an acceptable trade-off.

$$T = Fx \qquad \textit{Equation 4.3}$$

$$\%\ increase = \frac{F_2 - F_1}{F_1} = \frac{\frac{T}{r_2} - \frac{T}{r_1}}{\frac{T}{r_1}} = \frac{\frac{T(r_1 - r_2)}{r_2 r_1}}{\frac{T}{r_1}} = \frac{r_1 - r_2}{r_2} \qquad \textit{Equation 4.4}$$

Implementing the new screw diameter size requires a new barrel size which in turn has a cascade effect on multiple smaller components. By design, the feeding block is not similarly affected. This component is used as a joining element for multiple parts of the extruder as well as the extruder itself to the rest of the 3D printing motion system. It is therefore sensible for it to be as modular and versatile as possible. To maintain modularity, the barrel interface with the feeding block, highlighted in Figure 4.31, must maintain the same diameter and features. This allows for modularity in screw size depending on the material being extruded with minimal mechanical difficulty to affect the changeover.

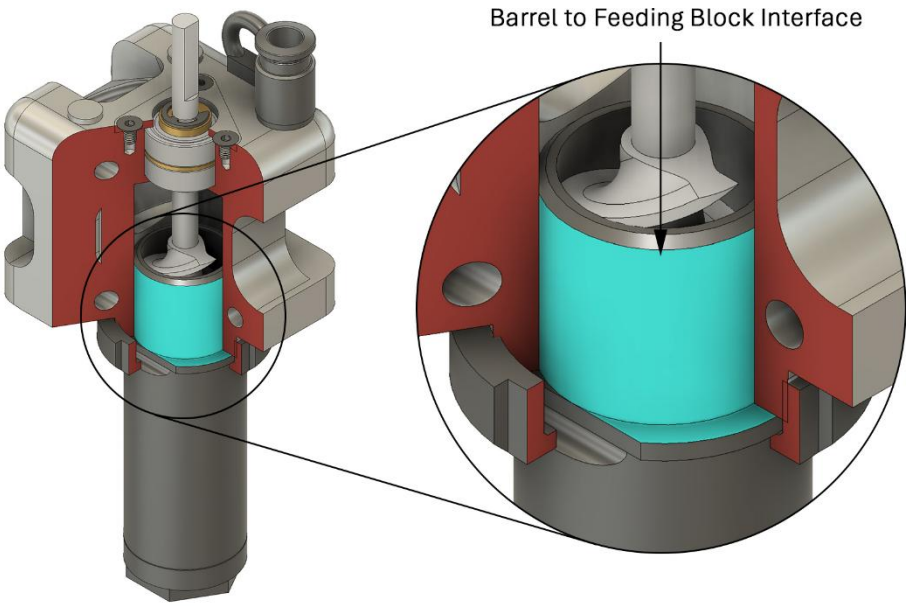

Figure 4.31 – Barrel to feeding block interface in Extruder 2, light blue indicating the interface and red indicating the section.

The last change necessary for this extruder development concerns the nozzle. In the current configuration, shown in Figure 4.24, there is an internal thread used to screw the nozzle onto the barrel, which now must be removed. The new concept divides the nozzle in two components, one is just the tapered section of the nozzle with the actual orifice, as shown in Figure 4.32. The tightening mechanism is now similar to the barrel nut,

whereby a new nozzle nut is used to tighten the nozzle onto the barrel. With this concept, if the nozzle tapered inner surface has a sufficient smooth surface, the nozzle may be removed even if there is cold, solid thermoplastic in the extruder. This may be possible due to the lack of protrusions or similar features that may get filled with thermoplastic.

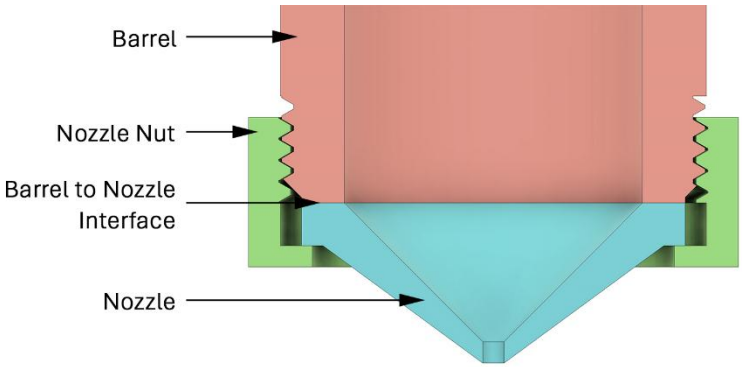

Figure 4.32 – Nozzle 3 concept with nozzle to barrel interface.

The new concept to be implemented in this extruder version should make it easier to extrude and 3D print high performance polymers. The next section will cover in the details the actual changes that were made to the extruder that was developed in the previous section.

4.5.2 Embodiment

The principal changes involve the extrusion screw, barrel and nozzle. The next section will delve into the new extrusion screw design and will analyse the changes made.

4.5.2.1 Extrusion Screw

The third extrusion screw maintained the same screw length but shrunk the diameter down to 14 mm. The helix angle remained unchanged except for a marginal increase in the metering section. The latter was only done in order to have a round pitch number which makes machining inspection simpler. The compression ratio using cross-sectional area was likewise unchanged at 1.4:1. To maintain this compression ratio, the feeding channel depth was set to 4 mm with a meter channel depth of 2.1 mm, as shown in Figure 4.33 and Table 4.7. Another alteration is the increase in feeding section length coupled with a decrease in compression section length. The longer feeding section promotes greater pressure generation by solids conveying which should promote a higher extrusion rate. Furthermore, since the compression section now starts further out

from the cold end and closer to the hot end, the material is expected to be more molten when it reaches the compression section. This in turn should decrease the probability of material plugging at the compression section due to excessive material viscosity.

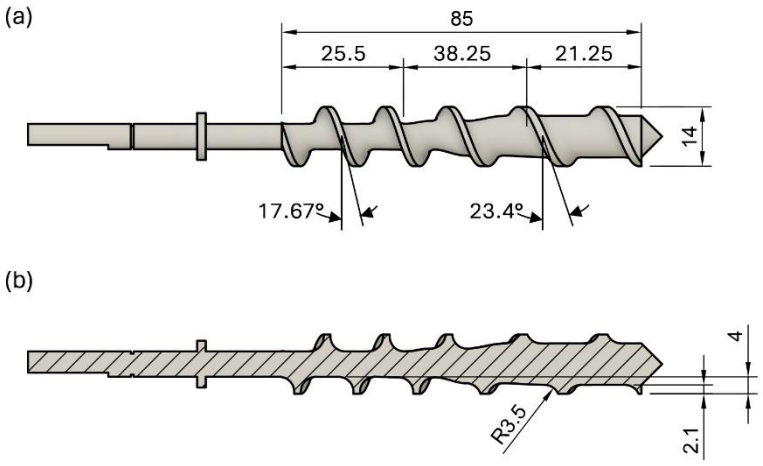

Figure 4.33 – Extrusion screw 3 with key geometric features.

Table 4.7 – Geometric dimensions of extrusion screw 3, with a 14 mm diameter.

Section	Length [mm]	Turns	Helix Angle [°]	Pitch [mm]	Depth [mm]	Flight thickness [mm]
Feeding	25.5	1.82	17.67	14	4	
Compression	38.25	-	-	-	-	1.5
Metering	21.25	1.12	23.36	19	2.1	

The changes outlined for the extrusion screw 3 are not major except for the decrease in screw diameter. As calculated in section 4.5.1, the decrease in screw diameter should result in a theoretical maximum of 42.9 % increase in force compared with the previous 20 mm diameter screw design. Likewise, the increase feeding length should also increase pressure generation and decrease susceptibility to clogging especially for wide melting temperature range materials such as certain elastomers. The following section will discuss the changes necessary to the extruder design to accommodate the new screw diameter.

4.5.2.2 Barrel and Nozzle

The barrel internal diameter was shrunken down to 14 mm. The same drill, bore and ream technique was used to achieve a low clearance fit in between barrel and screw.

The feeding block interface, as labelled in Figure 4.34, was kept with the same diameter and same shoulder feature as done in Extruder 2. This allowed for a direct modular connection between the 14 mm barrel and the previous 20 mm barrel system.

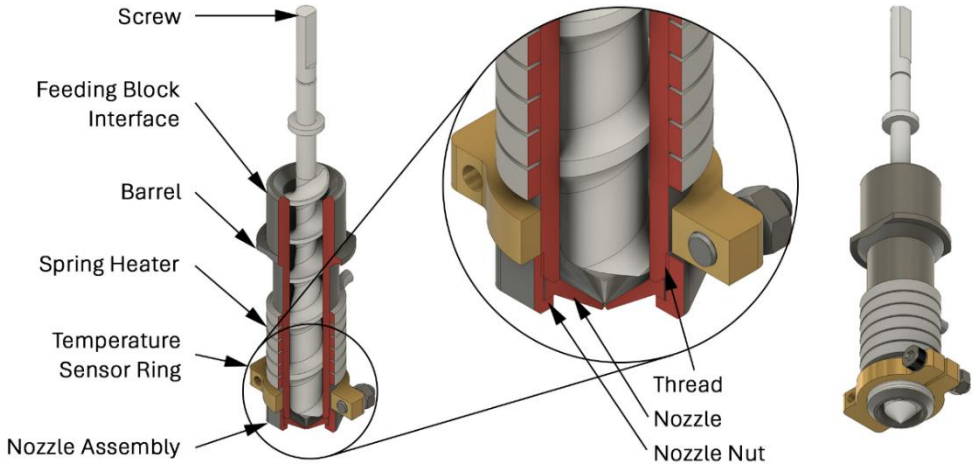

Figure 4.34 - Extruder 3, 14 mm barrel with nozzle assembly, temperature sensor ring and spring heater.

A significant change in barrel design is the new nozzle interface. The setup, shown in Figure 4.34 and Figure 4.35, is simpler to machine repeatably, and is easier to use in practice. The new system makes melt leakage less probable as the nut presses evenly on the nozzle, creating a better nozzle to barrel seal. The threaded section is also further away from the nozzle, decreasing the probability of material getting stuck in the small threads. Since the new system effectively allows removing the force acting on the nozzle i.e., by unscrewing the nut, without rotating the nozzle. This allows the removal of the nozzle even when there is solid material in it. This is possible as it is easier to unplug a filled nozzle using a vertical force rather than a rotational force. The nozzle of Extruder 2 was limited to a rotational movement due to the integrated thread in the nozzle. This ease-of-use improvement is critical for extruding and 3D printing high performance polymers. Any such material getting stuck in the threaded section becomes very difficult to removal without damaging the threads.

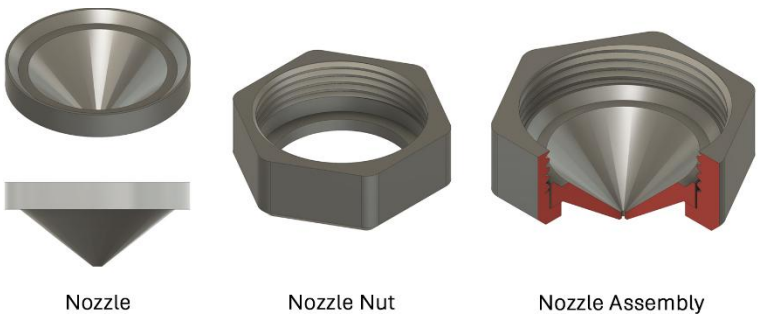

Figure 4.35 - Nozzle system for Extruder 3.

4.5.2.3 Manufactured Extruder 3

The manufactured extruder of the third development is shown in Figure 4.36. This iteration retains the same external dimensions as the previous version but features a higher force applied to the material and enhanced ease of use. The primary focus of this development was to improve the extrusion of high-performance polymers. A complete set of engineering drawings can be found in appendix 4, page 388. The next step is to assess whether these modifications effectively enhance the extrusion and 3D printing of high-performance polymers in small-scale FGF applications.

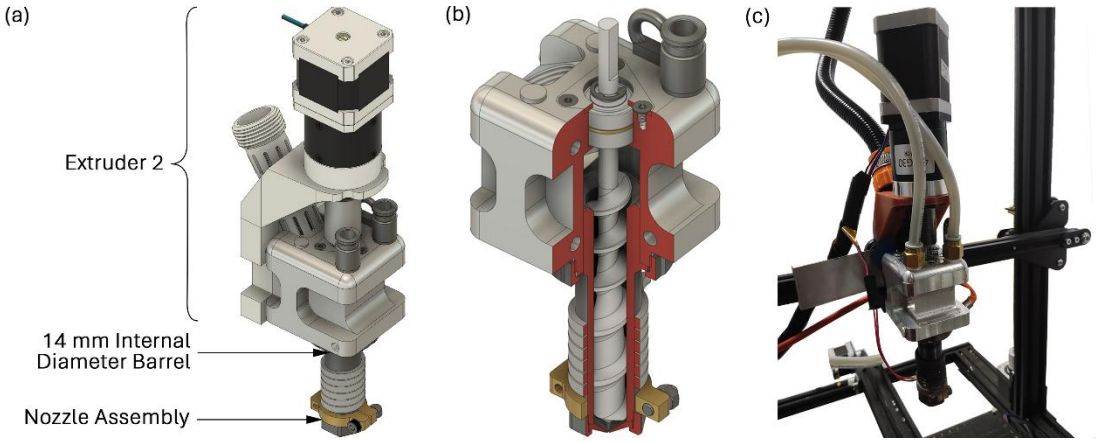

Figure 4.36 - Extrude 3 (a) with cross-section of feeding block, barrel and concomitant components (b) and manufactured and mounted Extruder 3 (c).

4.5.3 Evaluation and Application

As with previous extruder developments, the extruder was mounted on the CR-10s motion system. Its extrusion quality and 3D printing performance were evaluated using two high-performance thermoplastics, PEI and PEEK. A case study was conducted using PEI to produce injection molding inserts. Additionally, the extruder's capability was tested with various grades of PEEK, each differing in molecular weight and viscosity. The impact of viscosity on 3D printing quality was also assessed. The extruder performed adequately when it comes to extrusion and 3D printing of high-performance thermoplastics. Upon using the same setup for extrusion of TF3ZGO-LCNT, the extrusion rate was not consistent which in turn meant that the extruder could not be used for 3D printing of this elastomer. Further application of Extruder 3 with high performance polymers will be presented in Chapter 7, page 217 and Chapter 8.3, page 256, using PEI and PEEK respectively.

4.5.4 Improvement

The biggest issue of Extruder 3 was the limited extrudability of TF3ZG0-LCNT. The main cause behind this failure was deemed to be the wide melting range of this amorphous, blended TPE. To enable the extrusion and 3D printing of this material, the last extruder development for this thesis will endeavour to shorten the hot end and lengthen the cold end. In this manner, a greater portion of the screw is dedicated to pressure generation. More importantly, the pellets should still be mostly discrete whilst in the feeding section of the screw, i.e. there are not partially molten pellets which bond to each other and start to plug the extruder flow. This was the main cause behind the extrusion inconsistency. The next section will deal with the issue just outlined.

4.6 Extruder Development 4

The fourth extruder development dealt with another incremental modification over extruder development 3. This fourth development concerns a modification of the cooling and heating system of the extruder. This was necessary to allow for extrusion and 3D printing of wide melting range materials, such as TF3ZG0-LCNT which is a blended TPE.

4.6.1 Concept

The problem at hand involves the premature melting of the TPE pellets that eventually block feedstock flow to the extrusion screw. This was caused by an extruder temperature gradient which was too hot at the feed end. As shown in Figure 4.37 (a), in Extruder 3, the feeding end of the barrel is directly being cooled by the feeding block and yet this is insufficient for TF3ZGO-LCNT. This effect may be due to the screw becoming overheated. In practice, the screw is primarily cooled through conduction, with heat dissipated by the processed material, the barrel via a thin polymer layer filling the clearance between the two, and the bearings at the screw root. As a result, the screw at the feeding end may not be as cool as the barrel, potentially causing the pellets to heat up. The most direct method to resolve this issue would be to cool down the screw itself but this would greatly increase complexity and size constraints making it difficult and possibly inefficient to internally cool the screw at that point. The simplest solution is to further cool down the feed end section of the screw by adding an extra cooler. Furthermore, the hot end section may be shortened by using a heater which directly covers a smaller length of the barrel. This meant using a custom manufactured heater

assembly to obtain the desired height of heater. In this manner the thermal gradient is pushed downwards, as shown in Figure 4.37 (b).

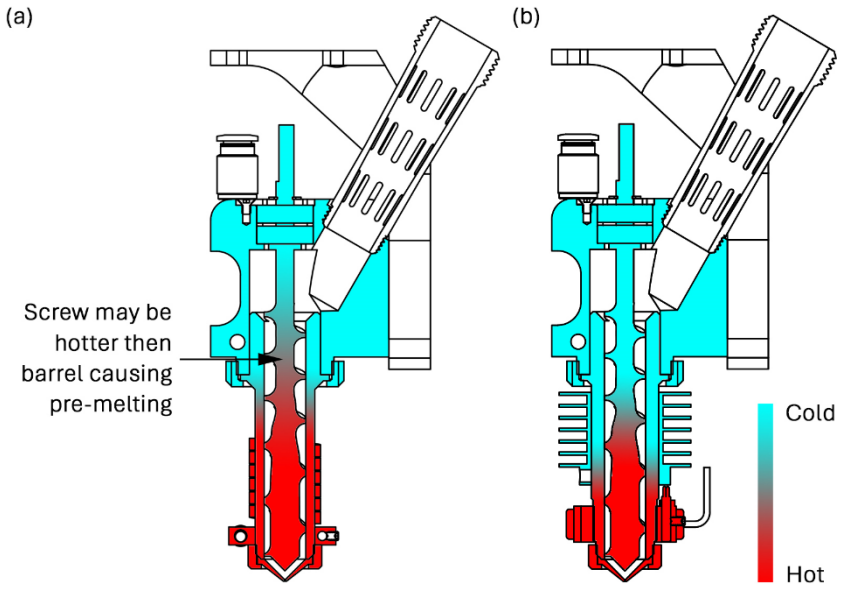

Figure 4.37 – Schematic diagram of probable temperature gradients in Extruder 3 (a) and Extruder 4 (b).

This concept just described is the only change deemed necessary to enable 3D printing of TF3ZG0-LCNT in a consistent manner. The next section will delve into more detail on how the concept proposed was achieved.

4.6.2 Embodiment

To achieve the concept set out, the spring heater that was used in all the previous extruder developments was removed and instead two cartridge heaters mounted in a custom heater block were used. Likewise, the temperature sensor ring was integrated in the new heater block. This was done to further reduce the Z-height of the heater and simplify assembly. To ensure good contact between heater block and barrel, the interface was threaded, and thermal paste was included to further improve heat transfer. This also meant that the barrel surface in contact with the heater should also be threaded, necessitating a design change to the barrel, as shown in Figure 4.38.

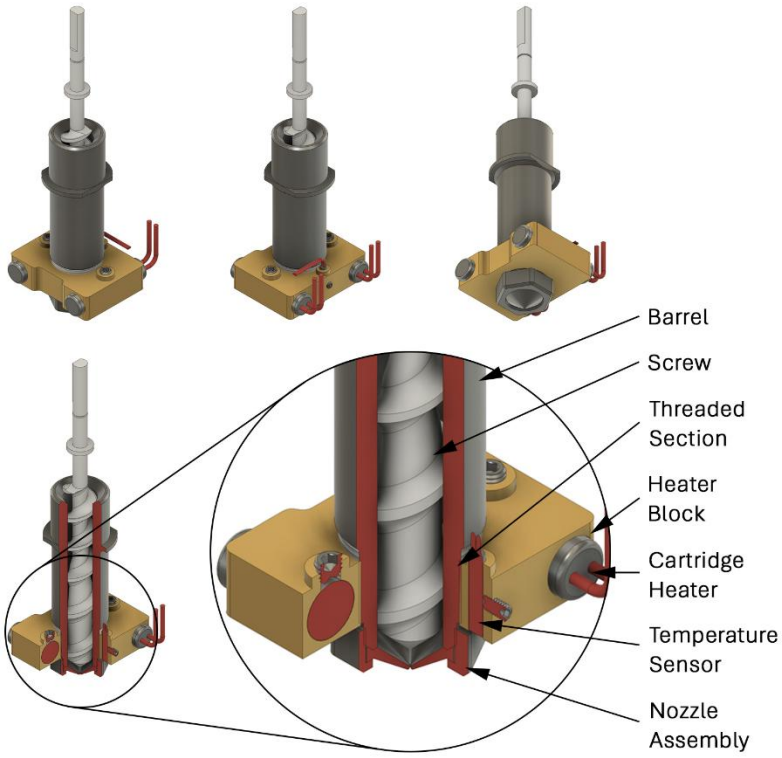

Figure 4.38 – Barrel and cartridge heater with temperature sensor block, isometric view with cross-section marked in red.

The cold section also had to be lengthened to cover a longer section of the extrusion screw. To achieve this, an extra, forced air, finned cooler, shown in Figure 4.39 was used just under the feeding block. Sizing of the both the cartridge heaters and the cooler was carried out as following. The original spring style heater had a power of 300 W which was adequate for high temperatures required for high performance polymers but overpowered for lower temperatures. In practice, the spring heater was capable of maintaining any set temperature, but at low temperatures there was a tendency to overshoot the target temperature. This behaviour could not be easily remedied by modifying PID values as the initial heating rate was too high and the temperature sensor lag too slow to allow for correction using classic PID. Nonetheless, it should be made clear that this overshoot did not in any way harm the extrusion and 3D printing process, due to its brevity. It is only an annoyance to the user as it does not conform to normal FFF practice where overshoot is minimal.

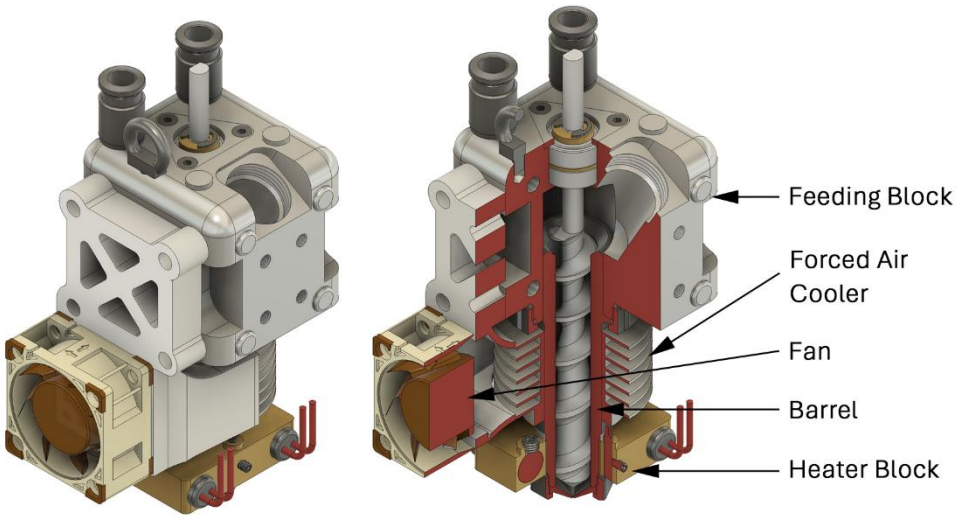

Figure 4.39 – Extruder with heater block and cooler, isometric view and cross-section.

Instead of a 300 W heater, two 100 W, cartridge heaters, 10 mm diameter and 40 mm in length were used to provide 200 W of power. A higher heater power may be necessary for PEI or PEEK due to the higher temperature. The heater block itself was manufactured out of OT58N (EN 12614) brass due to its low cost and good heat conductivity. Pure copper was also an acceptable choice for its higher thermal conductivity, but the elevated cost and loss of mechanical properties made the switch unwarranted. Another alternative was aluminium, but it has an even lower service temperature than brass for a similar cost. Using this heating block style for higher temperature would require using a different block material such as copper-tungsten alloys to sustain the higher working temperatures whilst maintaining good thermal conductivity.

The geometry of the chiller was designed by size constraints and cooling power estimation. Assuming a cylindrical heat exchange for simple machinability, the maximum diameter of the heat exchanger, including space allowance for a fan duct, was of 45 mm. The barrel diameter is of 23 mm and the acceptable height i.e., the space left in between feeding and heating block is of 31 mm. The height dedicated solely to cooling fins is shorter as a fastening element needs to be included to hold the heat exchanger onto the barrel. To simplify PID tuning of the heating system, from a control perspective, it is easiest to set the cooler at full power whilst controlling the heater power only. The maximum cooling power can be less than that of the heater as there is another cooler backing the heat exchanger, i.e. the water-cooled feeding block. Another important point is that the hotter the heaters, the more effectively the heat exchanger operates, as the greater temperature difference between the air and the metal enhances the cooling effect. [311].

From a machinability and space availability perspective the heat exchanger would have 7 fins (*n*) that are 9.5 mm long (*L*), 1 mm thick (*t*) to ensure sufficient strength for handling and spaced at 3 mm (*s*). The heat exchange would be machined out of 2000 series aluminium which has a thermal conductivity (*k*) of 200 W/mK. The cooling fan was selected to be Noctua NF-A4x20 fan [312] which has an airflow speed of 2 m/s (*v*). This generates a convective heat transfer (*h*) of 26.2 W/m^2°C on the aluminium surface, which was determined using the empirical solution of Figure 4.5 [311]. The fin efficiency of the heat exchanger was derived from Holman whereby using geometric value specified, the fin efficiency is estimated to be 100%. Assuming an ambient temperature (T_a) of 20°C and barrel temperature (T_b) of 250°C, the fin heat transfer (q_{fin}) was calculated using Equation 4.6 where r_0 is the outer radius of the fin and r_b is the fin base radius as shown in Figure 4.40. Likewise, the base heat transfer (q_b) was calculated using Equation 4.7. Calculating and summing the two values gives a total cooling power of 105.8 W [311].

$$h = 12.12 - (1.16)v + (11.6)\sqrt{v} \qquad \textit{Equation 4.5}$$

$$q_{fin} = 2\pi\left(r_o^2 - r_b^2\right)h(T_b - T_a) \qquad \textit{Equation 4.6}$$

$$q_b = 2\pi r_b hns(T_b - T_a) \qquad \textit{Equation 4.7}$$

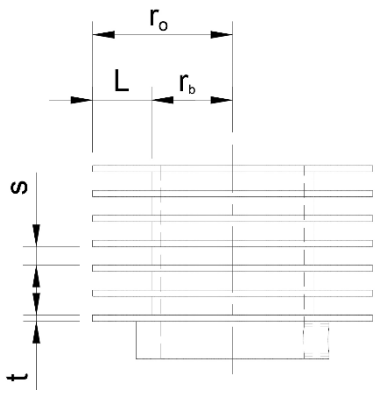

Figure 4.40 – Geometric features of heat exchanger.

The total cooling power is at half of the power of the heater. Considering that the heaters are usually never at max power except on startup and considering that the water-cooled feeding block will still provide the main cooling necessary, this heat exchanger was deemed adequate. In case of excessive cooling effect, despite the estimation made, the fan may be downsized or reduced in speed.

The final extruder assembly, shown in Figure 4.41, had the same height and depth of Extruder 2 and 3. The only dimensional changes was the increased width of 86 mm

caused by the addition of the side cooling fan. This dimension now goes against the initial specifications set out in section 4.2 but in practice the location of this extra component does not conflict with the motions of the CR-10 3D printer. In case of any volumetric conflicts, the fan can be relocated to the direction of the extruder as necessary. The engineering drawings of the components changed in this development are shown in appendix 5, page 401. The next step will be to evaluate whether the changes made effectively improved the consistency of TF3ZG0-LCNT extrusion and 3D printing when using small scale FGF.

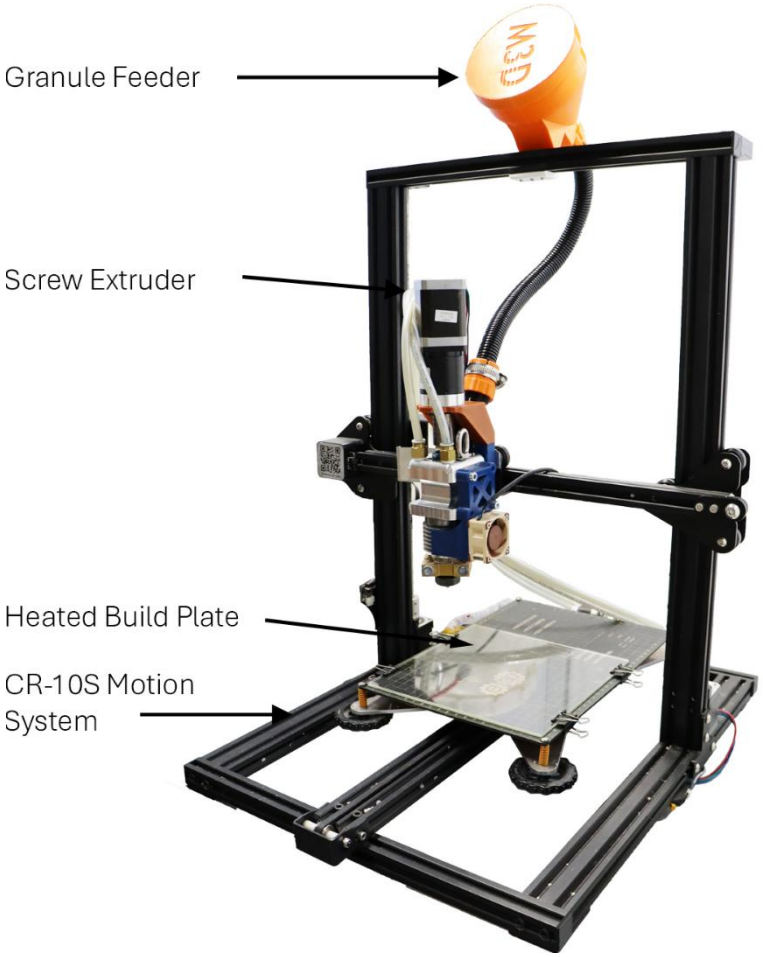

Figure 4.41 - Assembled Extruder 4, mounted on CR-10s 3D printer.

4.6.3 Evaluation and Application

Extruder 3 was updated with the outlined in the previous section. The extruder was then used for extrusion and 3D printing of TF3ZG0-LCNT parts. The full study related to this is shown in Chapter 6, page 189. This last extruder development concludes the cycle for this thesis. Further studies on FGF extruder development are beyond the scope of this current work. Multiple research paths are available for future work, the most poignant of

which being: direct regrind thermoplastics extrusion, closed-loop FGF extruder, further miniaturisation of extruder and testing and application of more materials especially of a high melting temperature nature. The next section will summarise all extruder developments made throughout this chapter.

4.7 Summary and Classification

The application of the extruder development cycles described in this chapter, are summarised in Table 4.8. All the extrusion screws developed are shown in Figure 4.42. Extruder 1 was the first-generation extruder and due to its unrefined nature was not used to study any of the four principal materials specified in section 1.4, page 16. On the same note, extrusion screw 1 was not reproduced in the next extruder developments and served only as a starting point of the development process. The lessons learnt from Extruder 1 instructed the development of extrude 2 which formed the backbone of the material studies carried out in the following chapters. As shown in Table 4.9, extrusion screw 2 had a larger helix angle whilst maintaining similar screw section lengths. This update was intended to improve processing of high-performance thermoplastics.

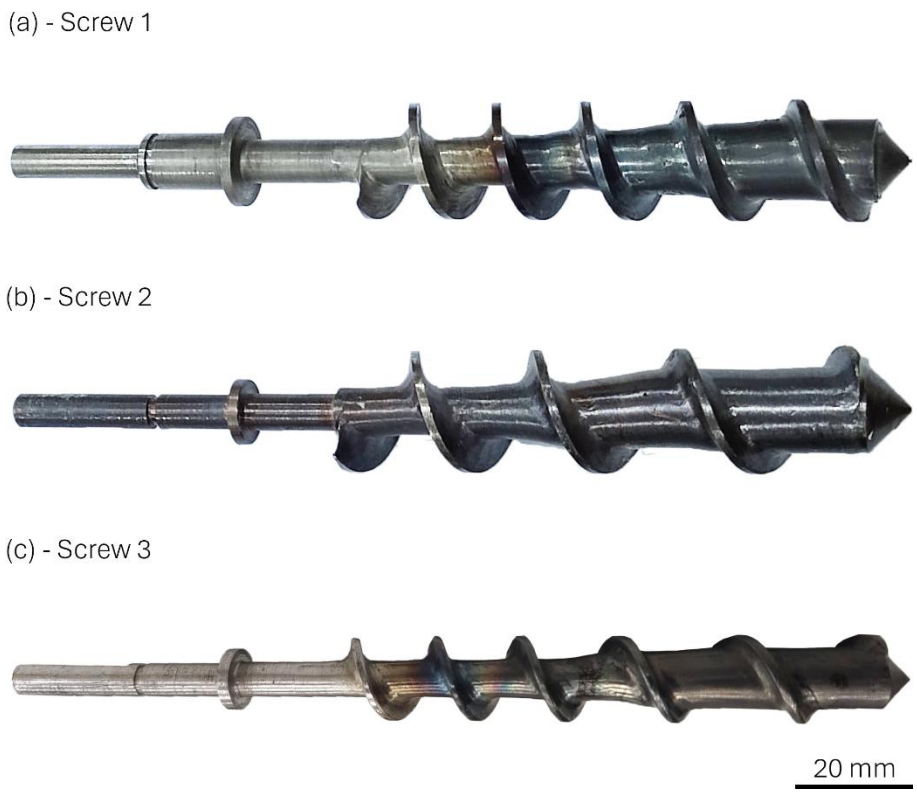

Figure 4.42 - Extrusion screw 1 (a), 2 (b) and 3 (c).

Table 4.8 - Extruder and extrusion combinations with screw diameter, materials tested and respective chapter/s in which they are utilised.

Extruder	Screw	Diameter (mm)	Material	Chapter/s
1	1	20	Magnum 3453 *ABS* Elix P2H-AT *ABS* Ingeo 4043D *PLA* Ellastolan 1995 *TPU*	4
2	2	20	Adflex X 100 G *TPO* VESTAKEEP L3300G *PEEK*	5 8.2
3	3	14	ULTEM 9085 *PEI + PC* VESTAKEEP L2000G *PEEK* VESTAKEEP L3300G *PEEK* VESTAKEEP L4000G *PEEK*	7 8.3
4	3	14	TF3ZG0-LCNT *TPE*	6

To further improve the force acting on the material being processed; the screw diameter was shrunk down to 14 mm in extrusion screw 3 for Extruder 3. The helix angle was mostly unchanged, but the feeding section length was increased to minimise probability of pre-mature melting in the feeding section of the screw. Extruder 3 was used for extensive testing on FGF of high-performance polymers. Another update to the extruder was necessary to 3D print TF3ZG0-LCNT, using the same extrusion screw. In this case the heating setup was altered to further ensure no premature material melting in the feeding section, even when using wide melting range materials such as TPE blends.

Extruder 2 to 4 all used the same feeding block concept which allowed for a modular setup of the extruder. With such a setup, the same system can easily adapt to materials which, from a processing perspective, are at extreme ends. In this manner, the first research gap identified in section 3.2, page 96, and its related objective was addressed in this chapter.

Table 4.9 – Extrusion screw geometric specifications of the 3 screws in feeding, compression and metering sections.

Specification	Screw	Feeding	Compression	Metering
Length [mm]	1	21.25	42.50	21.25
	2	20.00	43.75	21.25
	3	25.50	38.25	21.25
Helix Angle [°]	1	13.00	-	17.00
	2	17.67	-	22.50
	3	17.67	-	23.36
Depth [mm]	1	6.00	-	3.30
	2	6.00	-	3.40
	3	4.00	-	2.10

4.8 Conclusion

This chapter presents the development of a modular extruder, allowing for efficient extrusion and 3D printing of both hard and soft elastomers, as well as high-performance thermoplastics such as PEI and PEEK. Several contributions to knowledge were derived from this development process. From an extrusion perspective, traditional experimental studies on screw extrusion often assume that a significant amount of heat generated during extrusion is due to viscous heating. However, the Tadmor model, adapted for small scale FGF, showed that conduction heating was found to dominate. This suggests that many empirical results for static, large scale screw extrusion which use high power motors, should be treated cautiously, as the underlying processes differ.

Another contribution to knowledge is the extruder development itself. It demonstrated that various screw geometries are suitable for 3D printing. Using a 20 mm diameter, short 4.25:1 length to diameter ratio screw is possible. This also opens up the possibility of using small scale extruder for regrind thermoplastics which would benefit from the larger screw diameter. Increasing the helix angle and reducing the screw diameter improved processing of highly viscous materials. In addition to the screw design, the temperature gradient across the screw and barrel was found to significantly impact extrusion consistency, particularly when processing TF3ZG0-LCNT TPE, a material with a wide melting range due to its multi-component blend.

TPO gyroid egg

5 Hard Elastomer

5.1 Introduction

This chapter focuses on thermoplastic polyolefin (TPO) as the first of the two TPEs that will be studied in this thesis. Achieving high-quality 3D-printed elastomeric components requires careful optimization of process parameters, which in the case of FGF with TPO are yet indeterminate. Key aspects which are still lacking sufficient data including the build plate configuration, extrusion rate calibration, extruder temperature control, retraction settings, and information on material storage conditions. Additionally, the mechanical properties of 3D-printed TPO, especially when using FGF with varying nozzle sizes were still unknown.

This study determined whether TPO is a suitable material for screw extrusion, FGF. As a first step, the FGF process parameters had to be obtained, and the 3D printed quality was optimized. The next step was to determine the mechanical properties achievable using this process, even along the layer bond. To satisfy the former step, the optimal extruder temperature, build plate surface type and temperature and extrusion rate control were all established. Using the optimized process settings, a set of complex geometries were 3D printed to analyse the quality achievable with FGF of TPO. The mechanical properties of these prints were also evaluated with the aim of understanding the elastomeric temperature range of TPO and its strength. Finally, the principal advantage of TPO, i.e. its non-hygroscopic nature, was also studied to assess its effect on AM. This study provides an overview of the performance of TPO as an FGF material, defines a set of process parameters that can achieve good quality 3D printing and attained an understanding of the product strength possible.

5.2 Material and Methods

5.2.1 Material and Equipment

The TPO used in this study is a reactor TPO produced by Lyondellbasel, Netherlands with tradename Adflex X 100 G which was delivered in granulate form. TPO has been previously discussed in greater depth in section 2.3.1.1. The material was 3D printed using Extruder 2, screw 2, which was described in section 4.4, page 137. Extruder 2 was easier and safer to use then the original Extruder 1 due to the ease-of-use improvements that were implemented in it. The longer heated barrel range, as opposed to Extruder 4, provided a higher melting rate, enabling a higher extrusion rate when using TPO. Unlike

the other TPE, TPO also has a rather narrow melting temperature range, since as discussed in section 2.3.1.1, Adflex X 100 G TPO is an alloy grade rather than a simple blend. TPE alloys are compatibilized therefore the melting range becomes narrower as compared with simply blended TPE mixtures. This enabled the preferential use of Extruder 2 as opposed to the more controlled heating system but possibly lower extrusion throughput of Extruder 4. As discussed in section 4.3.3.3.1, page 133, small scale extruders melt the material primarily through conduction heating and therefore, a longer heating range will probably increase the melting rate which is related with extruder throughput. Two nozzles with diameters of 1 mm and 0.4 mm respectively were used throughout this study.

5.2.2 Differential Scanning Calorimetry (DSC)

A differential scanning calorimetry (DSC) test was conducted on the TPO granules to determine whether the thermoplastic is amorphous or semi-crystalline, along with the glass transition temperature (T_g), melting temperature (T_m) and the crystallization temperature (T_c). This information is useful both to initially determine an acceptable processing temperature as well as aid in the selection of the temperature for the heated bed [313]. The DSC test was carried out using the raw pellets on a STAR System DSC 3+ by Mettler Toledo (Ohio, USA). The specimen was first heated from room temperature to 200°C, then cooled to -100°C and heated again to 200°C, each time at 10 K/min heating and cooling rate respectively. The test was carried out twice and in each case the specimen was kept in a nitrogen atmosphere.

5.2.3 Determination of FGF Process Parameters

Unlike filament extruders, screw extruders are not volumetric. Filament extruders assume that the filament being fed has a consistent diameter and therefore can compute the volume being extruder based solely on the length of filament being pushed. Screw extruders on the other hand are not volumetric and therefore the extrusion rate profile of a given extruder must be determined to maintain a consistent output.

To determine the extrusion rate behaviour of TPO within this study's setup, an extrusion rate test was conducted. The extruder was gravity-fed TPO pellets and set to extrude. The barrel temperature was first tested at the melting temperature as determined by the DSC test. Subsequently, the temperature was increased in steps of 10°C until the stepper motor could drive the extruder screw. The extrusion rate was then tested from 160°C to

190°C, in steps of 10°C. In each case the extruder speed was varied in between 1 RPM and 9 RPM in steps of 2. The extrusion rate was determined by extruding for 1 minute, with 5 repeats, for each testing condition. The extrudates were then weighted on a MYA 11.4Y Plus micro balance, by RADWAG Balances and Scales (Poland).

The calibration of the extruder was carried out by 3D printing 25 mm sided cubes using different extrusion multipliers. The extrusion multiplier (EM), also known as flow rate multiplier, was used to account for the non-volumetric nature of screw extrusion 3D printing. The EM was increased or decreased if the cube's dimension were under or over the nominal value. The process was repeated a number of times, until the dimensional accuracy was within 0.1 mm range. The EM was determined for 30 mm/s 3D printing, at the selected 3D printing temperature, using both 0.4 mm and 1 mm nozzles. This speed was selected as it assures a good 3D printing quality even though the 3D part itself may be too soft to maintain its shape during 3D printing, as the nozzle deposits a subsequent layer.

There is no published method that describes what build plate configuration to use with TPO. Build plate adhesion is a combination of build plate material, coating, and its temperature. To determine a suitable configuration, aluminum sheets, galvanized sheet metal and glass were tested out using different finishes and temperatures. Both aluminum and galvanized sheet metal were tested out using both a smooth and roughened surface. In the case of glass, this was tested using multiple surface modifications, namely: clean glass; with PEI tape; with PEI tape and PVA glue; with PVA glue; with Magigoo Flex glue and finally with Magigoo PP glue. In each case, the bed was tested once at room temperature and once heated. The heated bed temperature was to be just a bit higher than the T_g of TPO, which was determined by the DSC test. This was done to obtain a good bed adhesion as suggested by Spoerk *et al.* when studying how to improve PLA and ABS bed adhesion. When the bed temperature is higher than the T_g, the surface tension between the bed and part is reduced and the contact surface area is increased thus improving the bond strength [313].

5.2.4 3D Printing of Complex Geometries

The calibrated FGF system was used to 3D print a set of complex geometries. These parts are meant to demonstrate what level of part complexity and quality can be achieved by FGF using TPO. For the purposes of this study, a complex geometry is any

model which can be 3D printed without using supports, except for simple, extruded 2D profile. A set of complex models, shown in Figure 5.1, were used to both demonstrate the capabilities of the system as well as improve the GCODE slicer 3D printing profile. For this study, the open-source Prusa Slicer (v2.5.0) by Prusa Research was used to generate the GCODE to 3D print the models. All models were printed using the 0.4 mm nozzle.

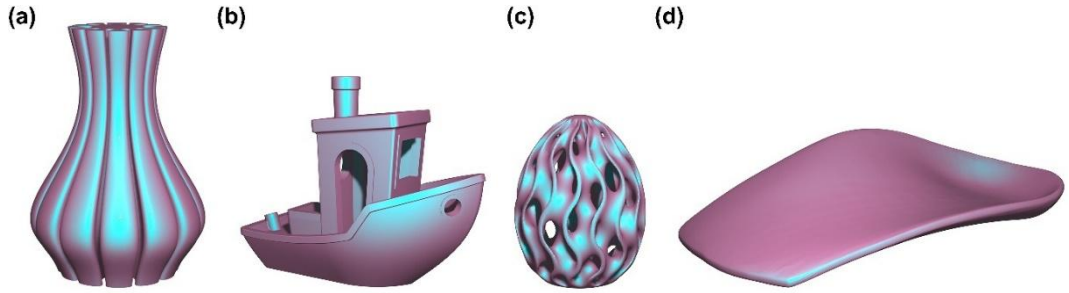

Figure 5.1 - 3D models of: (a) curly vase; (b) Benchy [296]; (c) gyroid egg and (d) orthothic insole

The objectives behind each chosen model are listed summarily in Table 2. The curly vase, shown in Figure 5.1 (a), printed in vase mode which disregards the internal volume of the part and prints the outer walls in one continuous spiral. During this process, there are no retractions or otherwise any stops in flow therefore any discontinuities should be easily visible as defects. The iterated curls of the vase are useful to judge if any defects present are caused by the incorrect motion rather than extrusion. A defect which is related to the motion system should be visible as a gradual change across the rotation of the part.

Table 5.1 - Models for 3D printing and related objective

Model	**Objective**
Curly vase	Extrusion rate consistency
Benchy	Retraction testing, lengths: 0 mm; 0.2 mm; 0.5 mm; 1 mm; , which is equivalent to: 0°; 1.2°; 3°; 6°; of screw rotation.
Gyroid egg	Retractions demonstration
Orthotic insole	Application demonstration

The curly vase served as a steppingstone to then follow up with more complex models, such as the Benchy torture test, shown in Figure 5.1 (b) [296]. This model checks for

surface, overhangs and bridging quality as well as dimensional accuracy and propensity for stringing. All of these tests are presented in an aesthetic model, representative of a conventional 3D printing process. A feature of note are the four corner walls which are supporting the roof. The positioning of these walls causes a stringing and retraction test. Stringing refers to the cobweb of extra, unintended extrudate left on a 3D printed part. In filament systems, retractions are used to stop the flow of material by pulling the filament and thus depressurizing the hot end. In screw extruders, the same retraction effect can be achieved by simply reversing the extruder screw rotation by some angle. Since Prusa Slicer is meant for filament, the software uses retractions in millimetres. Therefore, an equivalent value is given for the desired rotation, to achieve the same effect. The Benchy was printed multiple times to calibrate the retraction settings. The retraction angle was tested at 0°, 1.2°, 3° and 6° of screw rotation.

An even more challenging retraction test then the Benchy, is the gyroid egg [314]. This model is in effect a combination of ordered, twisting columns, which makes for multiple retractions per layer. Therefore, the gyroid egg was printed with optimal settings, using the results of the Benchy torture test to demonstrate the capabilities of the system during an aesthetic 3D print. This model was selected for this study, not just for its value as a retraction test but also as a demonstration of the aesthetic quality achievable by an FGF TPO part.

The optimized pellet 3D printing system was finally applied to 3D print an orthotic insole. Insoles often need to be customized to a patients form and therefore can make use of the flexibility provided by 3D printing. The elastomeric nature of TPO makes it a good candidate process for orthotic insole production. Another convenient feature of TPO is its non-hygroscopic nature which may be a useful feature when applied to sweaty environments such as in shoes.

5.2.5 Characterization of 3D Printed TPO

5.2.5.1 Water Uptake Analysis

One of the most notable purported advantages of TPO is its non-hygroscopic nature. A water uptake test was conducted following the *Plastics - Determination of water absorption* DIN EN ISO 62 standard, to determine the water absorption of this grade of TPO. The test was carried out using three 25 mm long strands of extruded TPO, using the 1 mm nozzle. The strands were produced out of TPO pellets which were dried in a pellet

drier for 4 hours at 70°C. The test strands were placed in an airtight container filled with deionized water, and left at a temperature of 23°C. The test was carried over a period of 16 days, as outlined by the standard. On allocated days, the test strands were collected out of the water, dried using paper towels and then weighted on a MYA 11.4Y Plus micro balance, by RADWAG Balances and Scales (Poland).

The result of the mass measurements was then fitted using the ideal model of Fick's second law, assuming constant water absorption properties over the diameter of the strands. The model defines the time-dependent water content as shown in Equation 5.1, where c_s is the water absorption at saturation (mass %), D is the water diffusion coefficient at the surface normal direction (mm^2/s), d is the strand diameter, t is the duration of immersion time in water (s) and k is index of summation.

$$c(t) = c_s\left(1 - \frac{8}{\pi^2}\right)\sum_{k=1}^{20}\frac{1}{(2k-1)^2}e^{\left[-\frac{(2k-1)^2 D\pi^2 t}{d^2}\right]} \qquad \textit{Equation 5.1}$$

The water diffusion coefficient was estimated using Equation 5.2, where t_{70} is the time at which the strand reached 70% saturation.

$$D = \frac{d^2}{\pi^2 t_{70}} \qquad \textit{Equation 5.2}$$

5.2.5.2 Tensile Testing

Tensile testing was carried out to determine the strain as well as the stress at yield and stress at break of FGF TPO, at room temperature. These properties allow for informed mechanical design of simple loading scenarios of any component to be 3D printed out of TPO. The specimens were designed using the *Standard Test Methods for Vulcanized Rubber and Thermoplastic Elastomers-Tension*, ASTM D412-06A standard, type C shape and printed 2 mm thick. Since such a standard is not intended for 3D printing, it does not account for any possible anisotropy in the printed specimens. Therefore, three orientations were used to study this possible property when applied to TPO, as shown in 3D representation of Figure 5.2 (a), produced using Fusion 360. Two nozzles were used to print the specimens, namely 0.4 mm and 1 mm nozzles. The comparison of the tensile testing results will highlight any discrepancies in print strength of the specimens printed using different nozzle sizes and printing orientations. All the specimens were tested on a M350 20CT tensile tester by Testometric, United Kingdom using an LC50, 490 N load

cell. The test was conducted at 500 mm/min. Each condition was tested using 10 specimens.

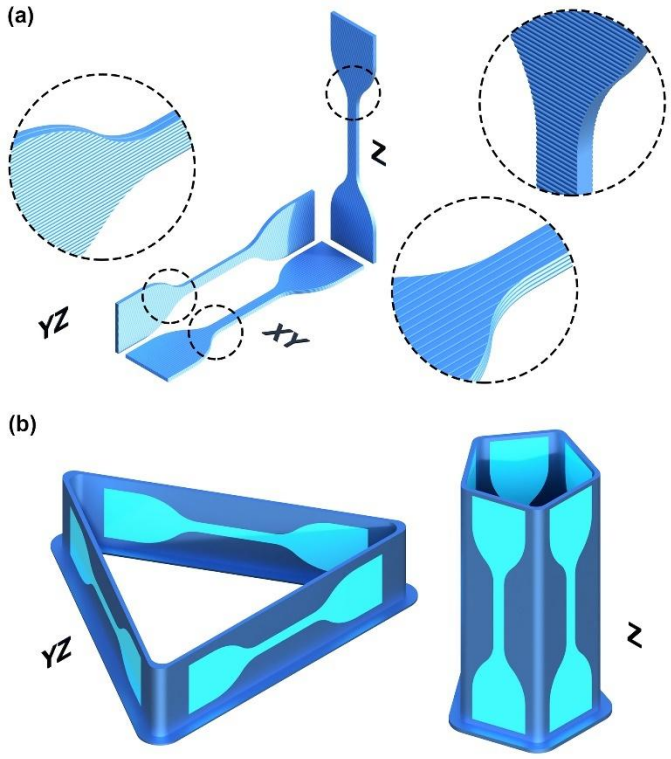

Figure 5.2 – (a) Tensile testing orientations for XY, YZ and Z specimens and (b) geometry of 3D printed blanks for YZ and Z orientations.

The specimens were all printed using a printing speed of 30 mm/s for all 3D printing features including the first layer speed. For each nozzle size used, 10 specimens were printed. The layer height was set to 0.2 mm and 0.5 mm for the 0.4 mm and 1 mm nozzles respectively. All specimens were printed without layer cooling to attain the best experiment repeatability and to ensure good layer bonding [315]. The XY specimens were printed flat on the printing bed, using 100% aligned rectilinear infill, and without perimeters. The YZ specimens for the 0.4 mm nozzle were printed directly using supports to bridge the gap. On the other hand, for the 1 mm nozzle, the printed YZ specimens were still too hot to maintain their shape adequately during printing. In light of this issue a triangular prism blank, as shown in Figure 5.2 (b), left was 3D printed. Similarly, both 0.4 mm and 1 mm nozzles, Z specimens were punched out of an appositely printed pentagonal prism blank, as shown Figure 5.2 (b), right. Since TPO is an elastomer and rather soft during its solidification, it is not sufficiently stiff to provide support to directly 3D print the long and thin Z orientation specimens as these would bend during 3D

printing resulting in a poor-quality part. A summary of the preparation method used per case to produce the tensile specimens, is shown in Table 5.2.

Table 5.2 - Preparation method for tensile testing specimens

Nozzle Diameter (mm)	Orientation		
	XY	YZ	Z
0.4	As printed	As printed	Printed blanks and die cut
1.0	As printed	Printed blanks & die cut	Printed blanks and die cut

5.2.5.3 Dynamic Mechanical Analysis (DMA)

In many applications, one example being in automotive, elastomers are expected to maintain their properties in a set temperature envelope. The tensile testing experiment described above does not take this aspect into account. To remedy this deficiency, a temperature sweep, dynamic mechanical analysis (DMA) test was carried out.

The DMA test was conducted on a STAR System DMA 1 by Mettler Toledo (Ohio, USA). It was carried out in tension with the load being applied in the 3D printing direction, i.e., perpendicular to the cross-section of the deposited strands, as shown in Figure 5.3. The DMA results include the change in storage modulus (M') and Tan (δ) with temperature. The storage modulus is a measure of the energy required to distort a sample. Conversely, the loss modulus (M'') is a measure of the energy lost (dissipated) during a cycle of strain on the sample. Tan (δ) is a ratio between the loss and storage modulus, i.e. the higher the value, the more viscous the material. By assessing the change in storage modulus and Tan (δ), one can also find the T_g along with any perturbations in mechanical properties experienced and an indication of possible phase changes.

The temperature sweep DMA tests were carried out using a 10 μm amplitude, as suggested by an amplitude sweep test carried out beforehand. The temperature sweep test was set to cover a temperature range between -100°C and 125°C, changing at a rate of 10 K/min and was carried out in a nitrogen atmosphere. The test was carried out twice and in each case 25 mm by 5 mm by 2 mm cuboids specimens were used. These specimens were printed flat on the print bed at 30 mm/s, using the 1 mm nozzle with perimeters only. The test was conducted by first cooling to -100°C and then reheating to 125°C.

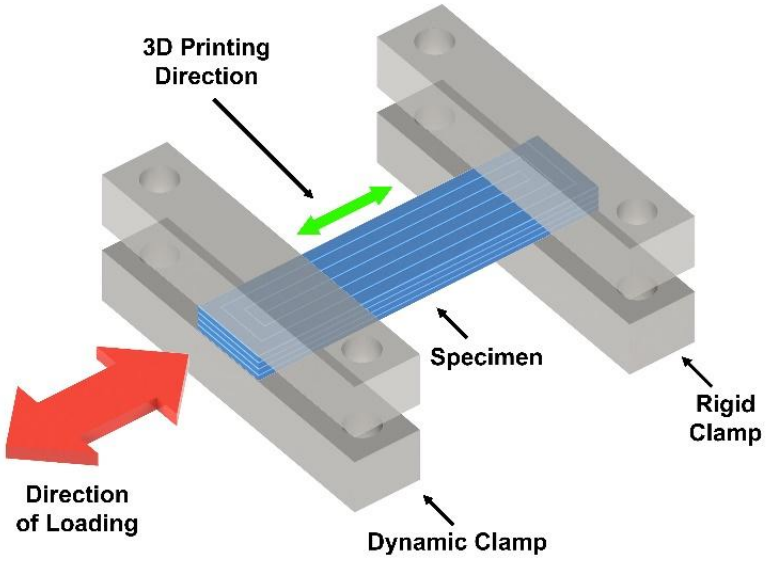

Figure 5.3 - Schematic diagram of DMA test with 3D printing direction.

5.3 Results and Discussion

5.3.1 Differential Scanning Calorimetry (DSC)

The DSC results presented in Figure 5.4 show a typical curve of a semi-crystalline thermoplastic. The most pertinent results are summarized in Table 5.3. Both shoulders at -35°C and 79°C refer to the secondary T_{g1} and primary T_{g2} glass transitions of TPO. The peak at 143°C indicates the melting temperature T_m at which point the main crystal structure of the polymer is molten. The crystallization temperature T_c, when cooling at 10 K/min, occurs at about 99°C, which marks the point at which molten material cools sufficiently to crystallize and solidify. The second heating curve presented a larger peak at the T_m region suggesting that after the first heat and cooling cycle, the crystallinity achieved was higher than in the initial pellet. This result also suggests that any melt processing using this grade of TPO should be conducted beyond 143°C and ideally higher than about 165°C to ensure that the crystal structure is fully molten and the viscosity gets lower, which makes it easier to process. Given that the T_{g2} was found to be 79°C, the build plate temperature should be set at around 80°C.

Table 5.3 - Summary of DSC results for Adflex X 100 G TPO

Property	Symbol	Value
Secondary glass transition temperature	T_{g1}	-35°C
Primary glass transition temperature	T_{g2}	79°C
Melting temperature	T_m	143°C
Crystallization temperature	T_c	99°C

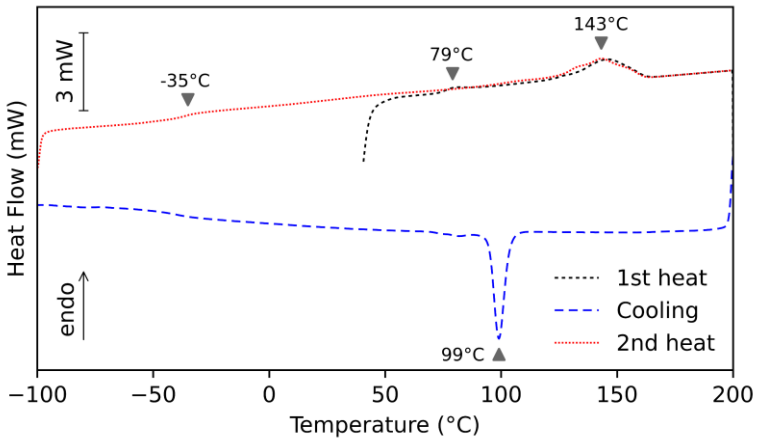

Figure 5.4 - DSC graph of TPO pellet samples

The results of the DSC indicate that TPO could be used as an elastomer even in cold, sub-zero environments. It is impractical to compare the performance of TPO to TPU in this regard as TPU is really an agglomeration of wide variety of formulations. This point is well illustrated by the work of León-Calero *et al.* who studied different TPU formulations and identified the relevant monomers [316]. The lower and upper glass transition temperatures vary wildly and were found to be as low as -60°C and as high as 165°C for different, discrete TPU formulations [316–320].

5.3.2 Extrusion Rate Analysis and Calibration

The results of the extrusion rate tests are plotted in Figure 5.5. As expected, the 1 mm nozzle achieved a higher extrusion rate than the 0.4 mm nozzle. There is a nearly linear relationship but not one to one between the screw speed and extrusion rate. Therefore, the FGF process requires different extrusion multipliers for different printing speeds. The extrusion rate was also significantly influenced by the barrel temperature. Increasing the barrel temperature beyond 170°C reduced the extrusion rate. At 160°C the extrudate

was broken and had a staggered appearance since the melt temperature was too low for consistent and homogenous extrusion. Therefore, 170°C was deemed the most suitable temperature for 3D printing with the current setup as it provided the best extrusion rate combined with a good melt flow consistency. The effects of both temperature and screw speed were the same for the 0.4 mm and 1 mm nozzles. Given that extrusion rate is influenced by screw speed, and the relationship is not one to one, any calibration done has to be carried out at constant speed. Otherwise, the extrusion rate will vary whilst printing and the calibration will be incorrect. The cube calibration was carried out at 30 mm/s using both nozzle sizes separately. For the 1 mm and 0.4 mm nozzles, the EM was found to be 0.85 and 5.5 respectively, both at 170°C.

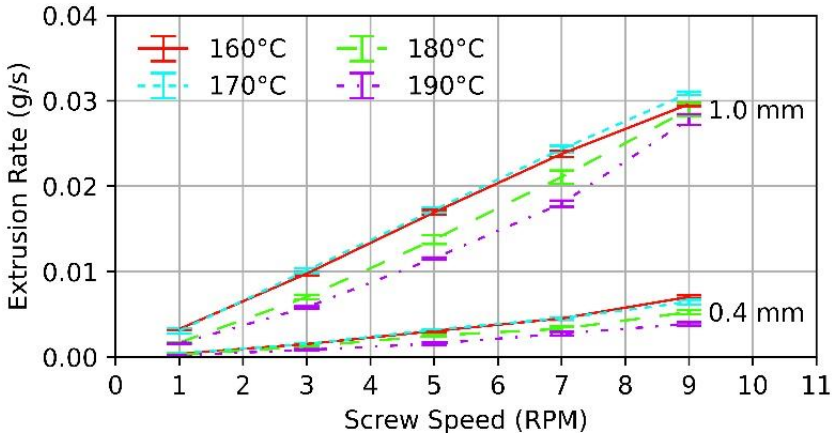

Figure 5.5 - Extrusion rate at varying screw speed, temperature, and nozzle size

The extrusion rate result also allows for the determination of the maximum 3D printing speed. By using the TPO density of 0.88 g/cm^3 as per data sheet [219] and the extrusion rate results at 9 RPM, the max volumetric speed (MVS) was calculated for both the 1 mm and 0.4 mm nozzles. The MVS is an industrial metric which defines the max volumetric speed of material being extruded by the extruder. The MVS was calculated to be 34.1 mm^3/s and 8.5 mm^3/s for the 1 mm and 0.4 mm nozzles respectively. For comparison, the widely used E3D V6 filament extruder reported an MVR of about 15 mm^3/s and 2.5 mm^3/s for polylactic acid (PLA) and TPU/TPE respectively, using the 0.4 mm nozzle [321]. Therefore, the extrusion rate of the setup provided is not only sufficient for conventional desktop 3D printing but can reach even higher speeds if provided with sufficient cooling and an adequate motion system.

5.3.3 Build Plate Adhesion

TPO did not adhere well to most common 3D printing build surfaces. The build plate temperature was set at 80°C for optimal adhesion, as indicated by the DSC results. The results of the build plate adhesion test are shown in Table 5.4, with the best performing being glass with Magigoo PP glue at 80°C. Using this build plate setup, the 3D printed parts adhered very well and printed without warpage. All the other build plate setups provided an inadequate bond.

Table 5.4 - Classification of TPO adhesion to different build surfaces

Build Plate Surfaces	**Adhesion**	
	Build Plate Temperature	
	RT	**80°C**
Smooth Aluminum	None	Very Poor
Brushed Aluminum	Very Poor	Poor
Smooth Galvanized Steel	None	Very Poor
Brushed Galvanized Steel	Very Poor	Poor
Glass	Poor	Poor
Glass with PVA glue	None	None
Glass with PEI tape	Poor	Poor
Glass with PEI tape and PVA glue	Poor	Poor
Glass with Magigoo Flex	Poor	Good
Glass with Magigoo PP	Good	Very Good

Legend: None: No adhesion at all; Very Poor: Inconsistent bonding and poor first layer quality; Poor: Initial bonds weakly but as 3D print progresses the adhesion is insufficient; Good: Better adhesion than poor but still insufficient, long parts detach; Very Good: Part has to be pulled off the bed to be able to remove, or else the bed is left to cool.

The PVA glue acted as a release layer, i.e. rather than promoting a better adhesion between the part and build plate, it ensured that the extruded TPO would not adhere at all. In contrast, ABS build plate adhesion improves when using PVA glue. The Magigoo Flex surface did improve adhesion unlike with the PVA glue but nevertheless the bond was insufficient for 3D printing. Magigoo Flex is marketed as a glue for TPUs and TPEs, which should make it adequate for TPO as it belongs to the latter polymer group. It is concluded that the most suitable glue for TPO is Magigoo PP. PP is a major component

of TPO and therefore it makes sense that such a combination would work well and is the reason why this glue was selected for testing in the first place. The other non-adhesive methods fared rather poorly.

5.3.4 3D Printing of Complex Geometries

Successful production of the curly vase model demonstrated sufficient extrusion rate consistency for AM. The 3D printed vase is shown in Figure 5.6 (a) and its flexibility is demonstrated in Figure 5.6 (b). This result empirically proves that granulate extrusion of TPO using a screw with a low length to diameter (L/D) ratio as previously described is adequate for 3D printing, even when challenged with a highly flexible object such as the vase shown. The vase had no unexpected blemishes or under extrusions that would be caused by an inconsistent extrusion rate. Each curl of the vase had the same surface and pattern, which indicates that the motion system does not have any noticeable defects.

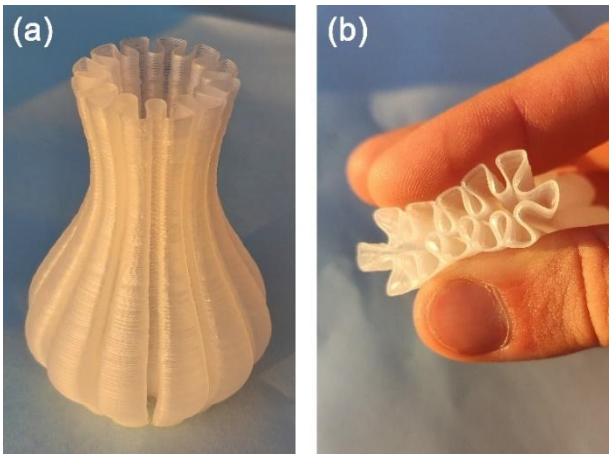

Figure 5.6 – Curly case, 3D printed out of TPO (a) and shown squashed (b).

The Benchy was a more challenging model to 3D print compared to the previous case study parts. This model has multiple retraction points, as shown by the red dots in Figure 5.7 (a). Each retraction point can either be a point of stringing caused by a lower retraction value or a point of under extrusion caused by excessive flow inhibition. Insufficient retraction leads to stringing which, in this case, would follow the green lines illustrated in Figure 5.7 (b). Stringing which is easy to remove by hand leaves a minor blemish on the 3D printed part and is often acceptable. Without retraction, the stringing was severe, as shown in Figure 5.7 (c), nonetheless the Benchy could be cleaned well and its overall quality was adequate. The best result was achieved at 3° reverse angle as the Benchy printed with good fidelity to the digital model and the amount of stringing

was quite low, as shown in Figure 5.7 (e). Increasing the reverse angle further led to under extrusion as can be seen in Figure 5.7 (f). Notably, the under extruded regions were mostly clustered in regions with a high density of retraction points. Therefore, a high retraction value was observed to cause under extrusion in the subsequent lines.

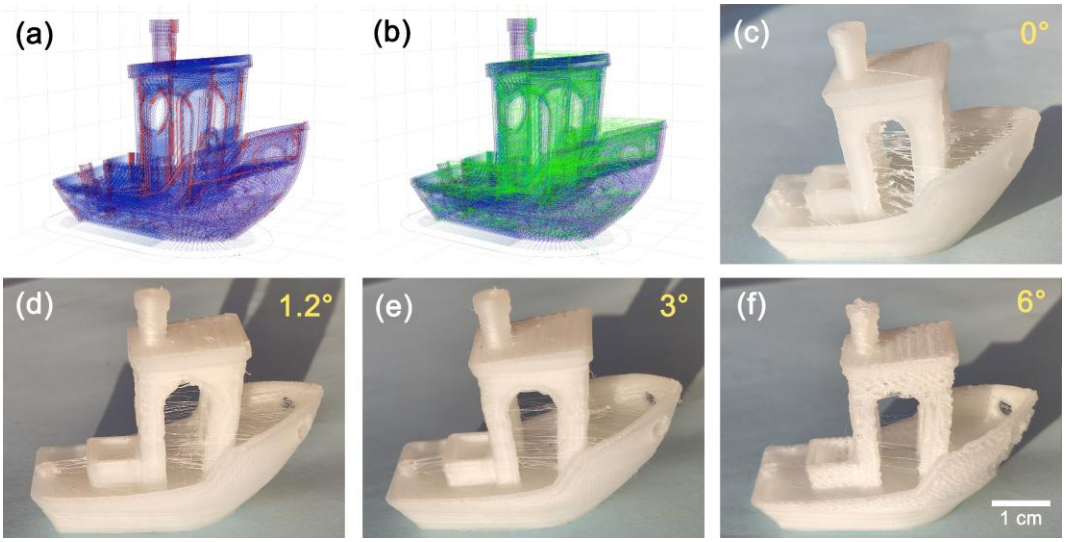

Figure 5.7 - Retraction diagram of Benchy where in (a) the red dots represent the retraction points and in (b) the green lines are the travel movements after retraction. The 3D printed Benchys using 0° (c), 1.2° (d), 3° (e) and 6° (f) reverse screw rotation on retraction. Stringing artefacts in 3D printed Benchys match travel movements. All Benchys 3D printed using Adflex X 100 G TPO.

The reverse angle of 3° was used when printing the gyroid egg model. The egg printed without any stringing, as shown in Figure 5.8 (b) and (c). The retraction point diagram of the gyroid egg, shown in Figure 5.8 (a) indicated that the model is widely populated with retraction points but that these are well distributed throughout the model. In fact, the edges of the gyroid egg were found to be rather rough as they were dotted with seemingly random, tiny blobs of over extruded TPO. When select zones were compared with the retraction point diagram, it was confirmed that these blobs were located at the ends of discrete perimeters. To remedy this issue, the extruder should have been set with a marginally higher reverse angle to account for this blobbing.

The last 3D printed model was the orthotic insole shown in Figure 5.8 (d). The insole was printed rather small, more adequate for a child's size. The surface was printed smooth and without blemishes. The insole was pliable but required some effort to bend in the fashion shown in Figure 5.8 (e) and (f). Upon bending, the insole did not crack or tear, nonetheless further studies would be required for a practical application to determine the longevity of the layer bond when bent repeatedly.

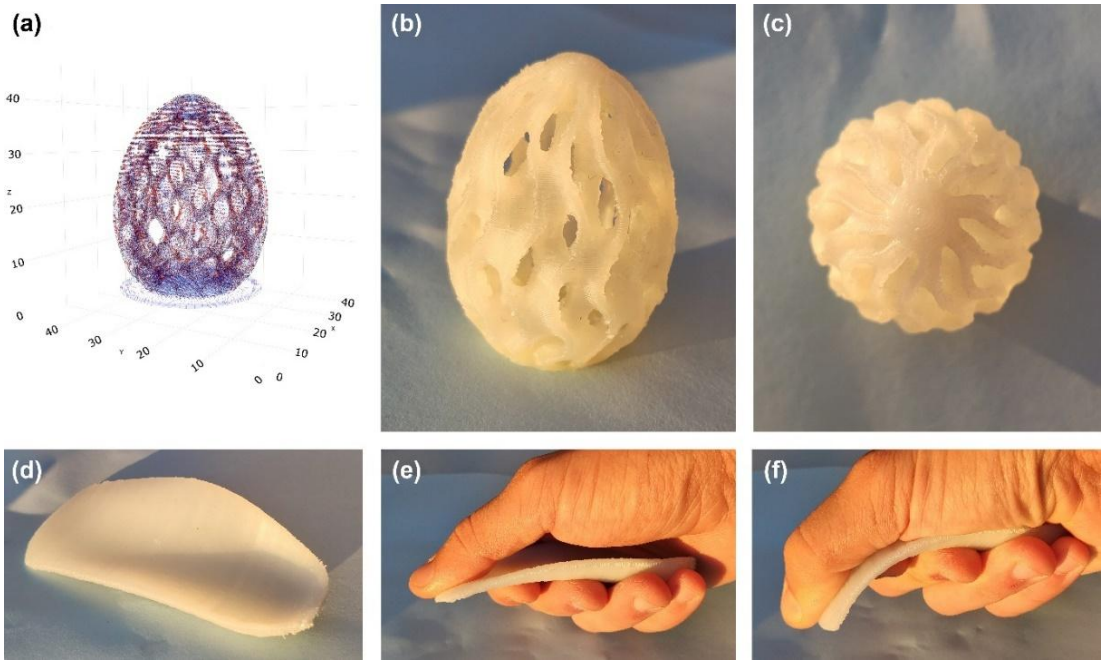

Figure 5.8 - Retraction diagram of gyroid egg where in (a) the red dots represent the retraction points and blue lines are the 3D printing path. The 3D printed gyroid egg out of TPO from side (b) and top (c). Rough zones were found to match the retraction points. Orthotic insole 3D printed out of TPO (d) shown straight (e) and bent (f). All Benchys 3D printed using Adflex X 100 G TPO.

5.3.5 Water Uptake

The results of the water absorption test are shown in Figure 5.9 along with the Fick's Law fitted curve. The water content at saturation, c_s, was found to be 0.25% mass gain. The diffusion coefficient, D, was calculated to be 1.79×10^{-6} cm^2/s. The results fitted well with Fick's law, indicating that Fickian diffusion applies. The overall level of water uptake was lower than that gained by most TPU filaments used in 3D printing. Bruère *et al.* reported a water uptake of almost 2% [218] which is about eight times that reached by TPO. Some TPO manufacturers, such as The Plastic Group of America, recommend that pre-drying is not required for TPO [322]. During the use of the 3D printing system, the extruder did not have any perceivable difference in extrusion rate, aesthetic and dimensional accuracy when using undried TPO granules.

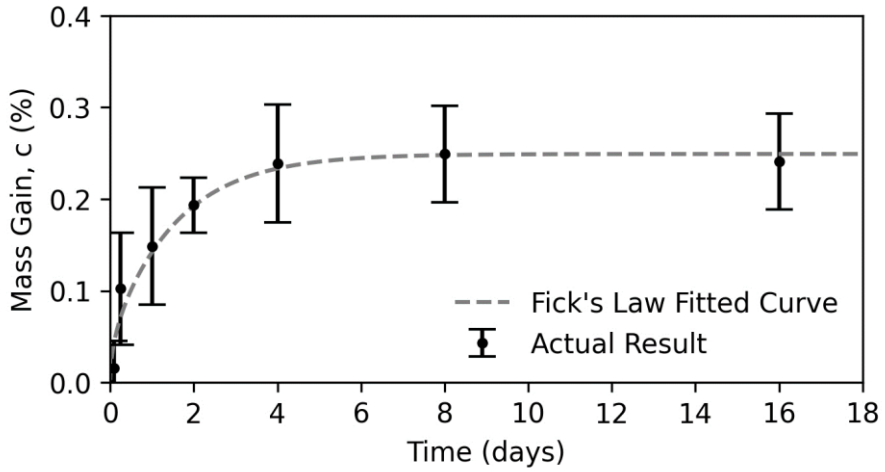

Figure 5.9 - Measured water absorption and Fick's Law fitted result for extruder Adflex X 100 G TPO strands.

5.3.6 Tensile Testing

The tensile testing results are listed summarily in Figure 5.10, with representative curves of each specimen type in Figure 5.10 (a). The results were represented as box plots with average lines in Figure 5.10 (b) to (d) with dots representing statistical outliers. An independent sample t-test was also conducted to determine whether the average result of the same orientation but with different nozzle sizes, are equivalent. The p-value of each result is shown in Figure 5.10 (b) to (d), where a value under 0.05 means that with a 95% confidence, the averages are not equivalent. The properties of the same material when injection molded, as taken from its material data sheet [219] are represented as a dashed line in Figure 5.10 (b) to (d). In the case of the strain at break value, the data sheet provides a lower limit rather than a definite value. The following comparisons are made with the datasheet as it is the only source which uses the exact same grade as 3D printed in this study. Such a comparisons highlight the strengths and weakness of this rather new process i.e., FGF as opposed to the well-established and highly utilized injection molding process. The only other similar source available is the research work published by Adrover-Monserrat *et al.* [217] but even in that case, the material grade is not the same, therefore a comparison is not warranted.

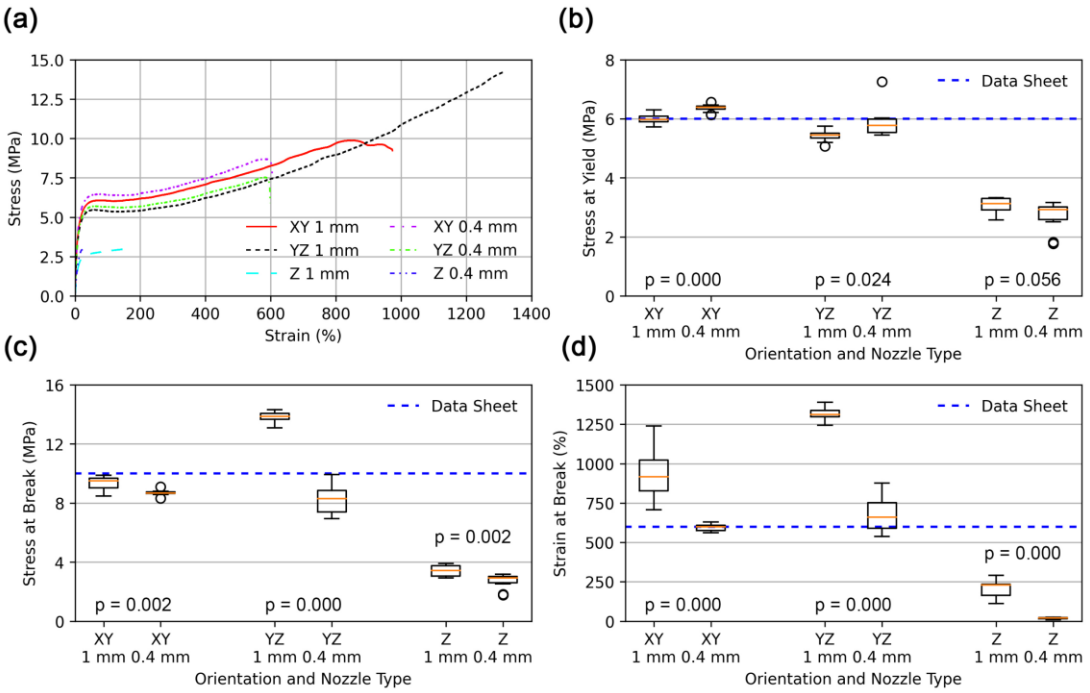

Figure 5.10 - Representative results of tensile test (a), stress at yield (b), stress at break (c) and strain at break (d) with average result line and data sheet value line for comparison (n = 10). The circles represent statistical outliers in the results. The p value is the result of an independent sample t-test, $p < 0.05$ confirms the hypothesis that the averages are not the same with a 95% confidence.

Across both 1 mm and 0.4 mm nozzle specimen types, the Z orientation specimens were the weakest in all metrics studied. The XY orientation test results for both 1 mm and 0.4 mm nozzles achieved the highest average stress at yield. The best average result was achieved by 0.4 mm nozzle, XY orientation, coming at 6.36 MPa. When it comes to stress and strain at break, the results of the XY and YZ orientations are rather similar except for the YZ orientation, 1 mm results. This orientation and nozzle size topped the chart, with an average stress at break of 13.8 MPa and strain at break of 1300%.

The YZ specimens, 3D printed using the 1 mm nozzle were a clear outlier when considering stress and strain at break. This was most probably caused by the die cutter used to cut the shape of the tensile specimens rather than printing them directly. In contrast to directly printed specimens, the edges and shape of the die cut specimens did not have any discontinuities or blemishes. The directly 3D printed specimens, i.e., those using the 0.4 mm nozzle, YZ orientation, inherently have edge discontinuities. These discontinues are caused by the bridging and support structure required to 3D print such specimens. Any imperfection in the specimen then acts as tear initiator during the tensile testing process, leading to a lower attainable stress and strain at break. Going back to the die cut, 1 mm nozzle specimens, the observed high stress and strain at break

can be attributed to their compressed edges, which lacked the defects characteristic of 3D printed edges. Consequently, these robust edges did not provide tear initiation sites.

Both the stress at break and strain at break results of the 1 mm nozzles were always higher than their 0.4 mm counterpart. All specimens were printed with a half nozzle diameter layer height, i.e. 0.2 mm and 0.5 mm for the 0.4 mm and 1 mm nozzles respectively, therefore the discrepancy should not be accounted towards that. The discrepancy is also non-trivial, as attested by the low p-value of the sample t-test carried out between the 1 mm and 0.4 mm nozzle results. The difference is often stark, especially when considering strain at break, where specimens printed using the 1 mm nozzle reached significantly higher values, often around double their 0.4 mm nozzle counterparts.

It was postulated that the changes in mechanical properties observed were caused by the differences in bond strength. This could be attributed to the higher energy content in 1 mm strands as opposed to 0.4 mm strands. All specimens were 3D printed without cooling to ensure that the experiment is easily reproducible given that there is no standard airflow rating. This decision may have exacerbated the energy level difference between the two nozzle sizes. If the cross-sectional area of the two is considered, the area of the 1 mm extruded strand is more than 6 times higher than that of the 0.4 mm strand. Therefore, the 1 mm strand has a greater amount of energy available for material diffusion with the underlying layer, thus leading to a stronger bond. This effect might explain the improved stress at break and elongation of the 1 mm nozzle, specimens. This improvement was not reported when it comes to yield strength results, rather, the 0.4 mm nozzle specimens had a slightly higher yield strength for XY and YZ specimens.

Unlike the stress and strain at break, the stress at yield is rather similar for all orientations and is not affected as much by any defects in the specimens. Nonetheless, the Z orientation specimens fared poorly in all 3 properties, as is generally the case with MEX AM [323]. The nozzle diameters did not affect the stress at yield as the p-value indicates that the average result of the two nozzle sizes is equivalent. The Z orientation strength is lower than that of the other orientations since these have a higher void volume resulting in a lower contact area. The 3D printed strand orientation also contributes to the Z specimen strength. For both XY and YZ orientations, the load is parallel with the 3D printing direction, thus ensuring maximal strength. Finally, Z orientation specimens, by design, are susceptible to under-extrusion event. An under-

extrusion event can be either a slight dip in extrusion rate over a period of time or a sudden, significant decrease in extrusion rate for a short period of time. In either case, for XY and YZ orientation specimens, the weakened zone would always be parallel with the load, whereas for Z orientation specimens, it would be perpendicular, as shown in Figure 5.11 and it could affect all the cross-sectional area under load or a significant amount of it. This indicates that not only is the Z orientation weaker it may also be more prone to defects caused by under extrusion or any similar extrusion deficiencies.

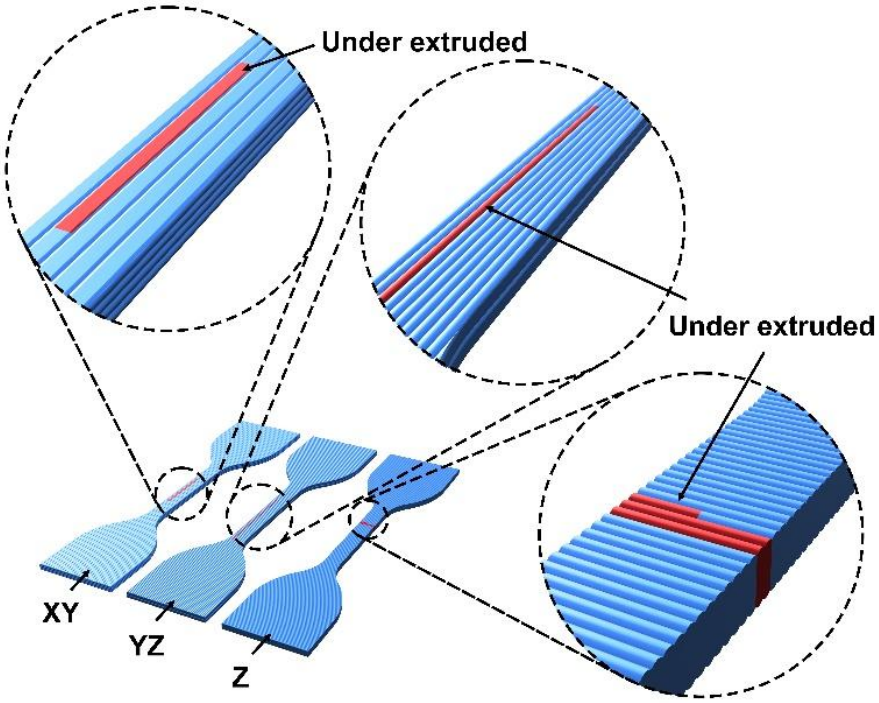

Figure 5.11 - Schematic diagram of possible location of under extruded strand / zone.

5.3.7 Dynamic Mechanical Analysis (DMA)

The DMA conducted on the TPO specimens, shown in Figure 5.12, demonstrated how glassy the material becomes at sub-zero temperatures. At -100°C, TPO becomes somewhat stiffer than ABS at room temperature [324, 325], reaching an M' of nearly 2500 MPa. At temperatures higher than about -23°C most of the stiffness is lost and the material becomes elastomeric. This observation is supported by the low storage modulus and the peaking Tan (δ). Heating beyond 70°C softens the material further and makes it act more viscous rather than elastic. At this point, the TPO was found to have a very low stiffness. Therefore, TPO may be used as an elastomer with a temperature range between -23°C and 70°C.

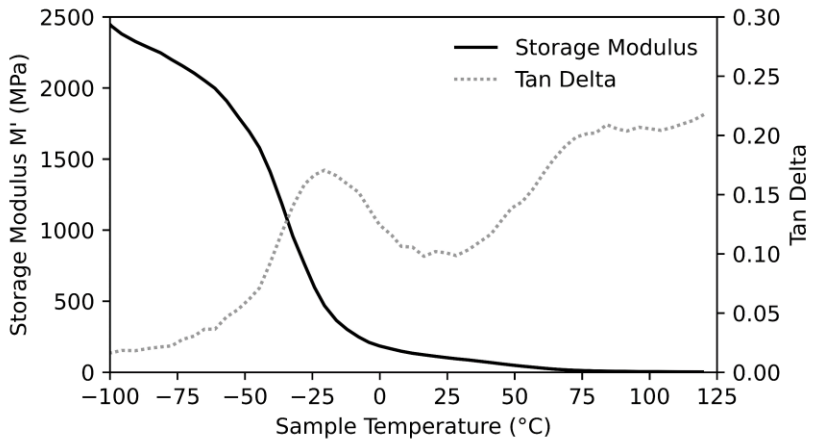

Figure 5.12 - DMA results of TPO showing storage modulus M' and Tan(δ) against temperature.

The DMA results of TPO are difficult to compare with those of TPU for the same reason as when trying to compare DSC results. TPU is a varied material with tunable properties depending on the composition used. Even when it comes to how stable the storage modulus is within a set temperature range, some TPU formulations such as that studied by Beloshenko *et al.* and Harynska *et al.* are rather stable, seemingly more so that the TPO results presented here [319, 326]. Others, such as the formulations studied by Shin et al and Maldonado *et al.* were rather unstable, with a decreasing storage modulus with temperature [327, 328].

5.4 Conclusion

TPO was proven to be suitable as a thermoplastic elastomer (TPE) for screw-based material extrusion (MEX) additive manufacturing (AM). Fused granulate fabrication (FGF) using TPO achieved satisfactory results to generate complex parts of high quality such as the Benchy and child orthotic insole. The measured water content saturation (c_s) of around 0.25% is considered as low and is eight times lower than the one of TPU. This suggests that TPO most likely does not require drying before use. This is a crucial advantage over the dominant MEX elastomer TPU.

The DSC and extrusion rate results revealed that TPO extrudes best at 170°C barrel temperature. The extrusion rate and screw speed did not have a one-to-one relationship; therefore, the speed must be kept constant throughout. For the 1 mm and 0.4 mm nozzles, both at printing speed and temperature of 30 mm/s and 170°C, the optimal extrusion multiplier was found to be 0.85 and 5.5 respectively. TPO was found to adhere best to glass at 80°C when using Magigoo PP glue.

Additively manufactured TPO was found to be anisotropic, with the XY and YZ orientations achieving superior stress at yield as well as stress and strain at break than the Z orientation. The best average stress at yield of 6.36 MPa was achieved when using the 0.4 mm nozzle and XY orientation, whereas the best average stress and strain at break of 13.8 MPa and 1300% respectively were reached by the specimens printed in the YZ orientation using the 1 mm nozzle. The DSC results of TPO indicated a glass transition temperatures (T_{g1}) occurs at -35°C and the (T_{g2}) at 79°C, with melting (T_m) at 143°C and crystallization (T_c) at 99°C. The DMA experiments confirmed these results and reported that the working elastomeric temperature range of FGF TPO is -23°C and 70°C.

The results of this study attest to the applicability of TPO as a thermoplastic elastomer for material extrusion 3D printing. Furthermore, the small scale FGF extruder developed by this work has been shown to be more then capable of 3D printing TPEs, even those which are not usually encountered in MEX AM. The next elastomer for FGF is TF3ZG0-LCNT which is a blended TPE and therefore required a different extruder configuration to be able to manage the wider temperature melting range of this material.

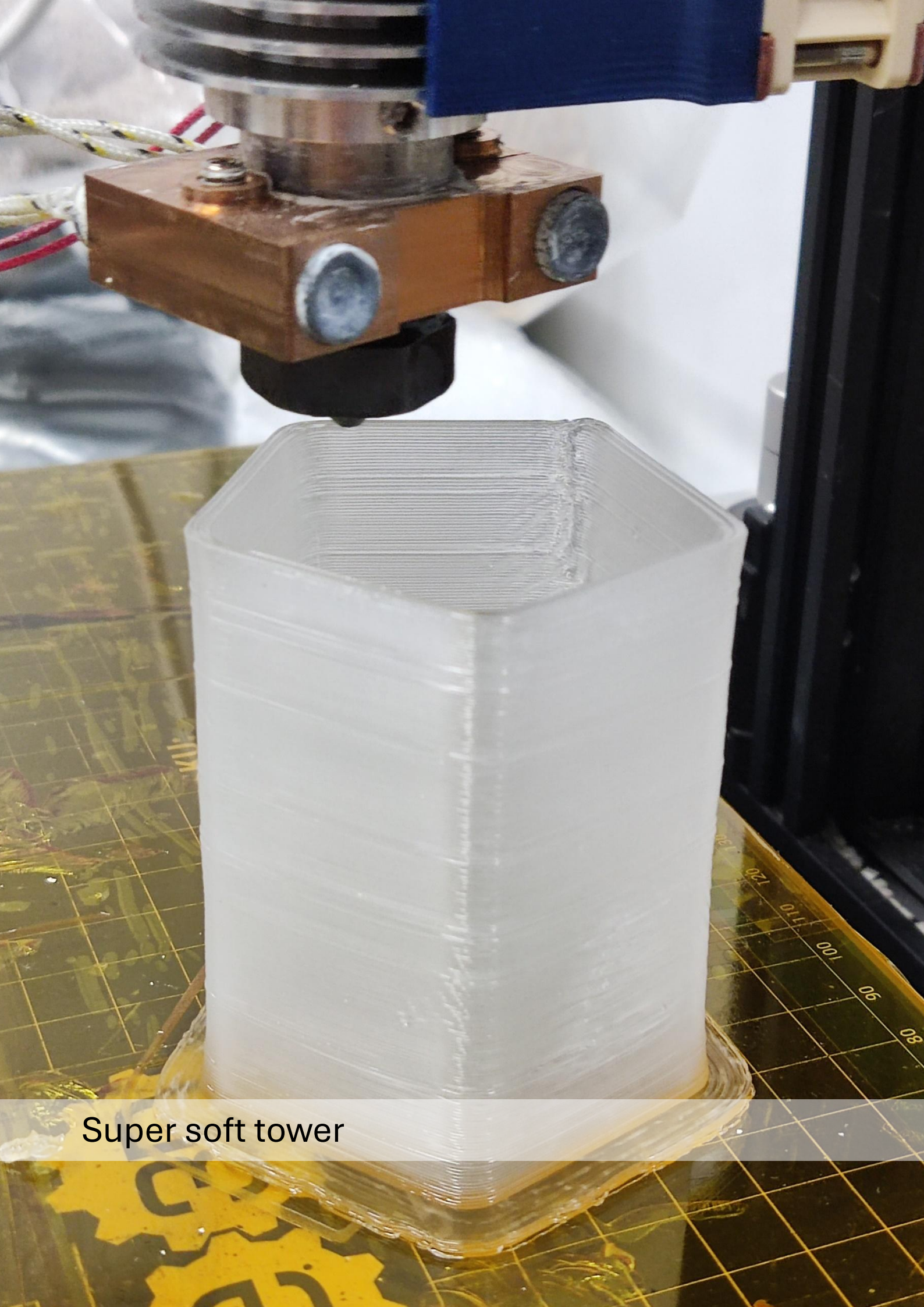

Super soft tower

6 Soft Elastomer

6.1 Introduction

Soft robotic solutions, particularly inflatables, are transforming various industrial sectors. They offer a more flexible approach to the well-established pick-and-place task of industrial production lines, as can be seen by the flex-shape gripper which was recently commercialised by Festo Ltd. [329]. Apart from automation solutions, inflatables have found numerous applications in marine, defence [330], and aerospace sectors [331]. One of the most impactful inflatable applications in industry are the elastic inflatable actuators (EIAs). These actuators are increasingly replacing the conventional, rigid pick-and-place actuators mainly due to their high design flexibility and overall safer nature of operation [208]. EIAs are a form of soft robotics, a technological sector which endeavours to bridge the gap between machines and people [332]. MEX AM, specifically fused filament fabrication (FFF) [225] is one of the most accessible and cost-effective option for EIA production. It's cheap and simple to use and has a large available material library. Furthermore, FFF uses thermoplastic materials which are generally recyclable.

The primary thermoplastic elastomers (TPEs) used for FFF are formulation variations of thermoplastic polyurethane (TPU) as well as TPU and olefin elastomer blends. For instance, Ninjaflex TPU filament has been widely used for the production of various EIAs [333–338], while other TPU grades such as Filaflex [339], eSUN eFlex [340], and Ultimaker TPU [341] have also been used for this application. The properties of these TPUs are listed in Table 6.1. The lowest hardness and highest elongation at break can be achieved by using Filaflex 60A. There is no published work that used this TPE for inflatable production. While ideal materials for inflatables prioritize high elongation and softness for greater flexibility and actuation, tensile strength remains important to enable sufficient inflation. Finding the right balance between these properties is crucial for withstanding inflation pressures.

Using softer materials for inflatables offers significant advantages since they require lower initial inflation pressure, leading to gentler operation. Additionally, softer materials create a more compliant inflatable surface. Following the trend of using even softer materials, researchers have explored alternative materials to the commonly used TPE filaments.

The literature search of section 2.3.1.2, page 84 highlights the need for further exploration in three key areas of screw MEX AM for soft TPE inflatables. Firstly, achieving higher elongations in the printed material is crucial since it will allow for inflatables with even greater flexibility and range of motion. Secondly, a deeper understanding of the tensile properties, particularly in the direction perpendicular to the printing layers (often 30% weaker), is crucial. This weaker direction can limit the overall elongation achievable. Finally, it also requires research on the lower limit for TPE softness that remains processable using screw MEX AM.

Table 6.1 - Mechanical properties of principal TPUs used for EIA production.

	Tensile Strength (MPa)	Hardness (Shore A)	Elongation at break (%)
NinjaFlex [342]	12	85	660
Filaflex 70 A [343]	32	70	900
Filaflex 60 A [343]	26	63	950
eSUN eFlex [344]	52	87	500
TPU 95 A [345]	23.7	95	560

This study pushed the boundaries of 3D printing large expansion inflatables by exploring the use of the softest TPE available (32 Shore 00) via screw MEX AM. Such ultra-soft TPE enables novel EIA designs with a gentler grip and exceptional expandability. To achieve this, this study investigated the 3D printability of such a super-soft TPE, optimizing extrusion temperature and build plate setup. It also evaluated the necessity or otherwise of pre-drying. Furthermore, the tensile strength was analysed across and along the layer directions. Finally, the strain behaviour under inflation (biaxial straining condition) was evaluated and compared with uniaxial loading, tensile test results to understand the impact of biaxial stress.

6.2 Method

6.2.1 Raw Material and Characterisation

The TPE used for this study was TF3ZGO-LCNT Thermolast® S granulates (Kraiburg TPE GmbH, Germany) which, as discussed in section 2.3.1.2, has a low hardness of 32 Shore 00. Other soft grades, such as TF5ZG0-LCNT, did not demonstrate the same autohesion as TF3ZGO-LCNT. Therefore, it could not be used for AM using FGF and will not be

covered in this study. This also demonstrates the importance of TF3ZGO-LCNT for material extrusion AM of soft, high elongation elastomeric components.

The TF3ZGO-LCNT granulates were characterised using Raman spectroscopy, Fourier transform infrared spectroscopy (FTIR), energy dispersive spectroscopy (EDS), and differential scanning calorimetry (DSC). The data gathered was used to determine the initial 3D printing process parameters. Raman spectroscopy was conducted on Xplora Plus by Horiba (Kyoto, Japan) using a 532 nm laser with a 1200 grating (750 nm), 500 µm hole, 100 µm slit, a 10% filter and an acquisition time of 5s. FTIR analysis was carried out on an IRAffinity-1, by Shimadzu (Kyoto, Japan), set in transmittance measurement mode with 20 scans taken per sample at a resolution of 4 cm^{-1}. EDS analysis was carried out using a Carl Zeiss FE-SEM Merlin Gemini II column (Germany) equipped with an Ametek EDAX energy dispersive X-ray detector (USA). The working voltage was set at 8 kV with a resolution of 125.8 eV. A higher voltage of 15 kV was previously used to determine whether heavier elements were present in the sample. The DSC test was carried out using the raw granulates on a STAR System DSC 3+ by Mettler Toledo (Ohio, USA). The sample was first heated from room temperature to 220°C, then cooled to -100°C and heated again to 220°C, each time at 10 K/min heating and cooling rate respectively whilst being held in a Nitrogen atmosphere. Each test was carried out twice to evaluate the result's repeatability. The DSC test was also conducted on tensile specimens 3D printed at 290°C, 300°C and 310°C, using the same testing parameters for granule.

6.2.2 Fused Granulate Fabrication System

The 3D printer was setup with a heated, glass build plate to hold the deposited material during 3D printing. To ensure accurate deposition of the material, the 3D printing speed was kept constant at 20 mm/s. The granulates were extruded using Extruder 4, with screw 3, which was discussed in section 4.6, page 154. The extra cooling system of this extruder configuration was a necessary addition to counter premature melting of the granules at the feeding zone of the screw. Due to the high softness of the material, the pellets were often more prone to compression than to movement along the screw channel, especially if softened by a high barrel temperature at the feeding end. This effect would not occur right at the start but rather after sufficient time has passed for the barrel to heat up enough to prematurely melt the granules at the feeding zone. Without the addition of the heat exchanger, the extrusion rate was inconsistent and inadequate for AM.

6.2.3 Extrusion Calibration and Limit Testing

Generally, the extruder or heater temperature is not necessarily equal to the extrudate temperature so that it is difficult to predict whether the actual melt or extrudate temperature is comparable to the material temperature in the DSC measurement. Therefore, the extrudate temperature was measured by placing a type K thermocouple just at the exit of the nozzle, approximately 1 mm away, as shown in Figure 6.1. At this distance, it is assumed that extrudate cooling is negligible. Extrudate was let flow on the thermocouple and a reading was taken once the temperature stabilised. The heater cartridge temperature was varied from 240°C to 310°C, in steps of 10°C.

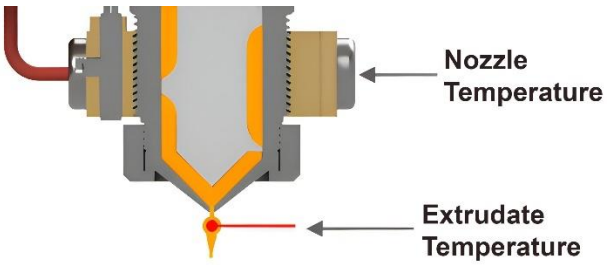

Figure 6.1 - Extrudate temperature and nozzle temperature measurement point.

When using granulate extruders, the extrusion rate may change with screw speed and extruder temperature. If the change in extrusion rate is excessive, the 3D printing slicing process would require compensation at different printing speeds. Determining the extrusion rate at different temperatures and screw speeds ensures that the extrusion is consistent at those specific processing condition. The extrusion screw speed was tested at 2.5, 5, 7.5, and 10 RPM, whereas the temperature was set to 290°C, 300°C, and 310°C as suggested by the DSC result. The test involved setting the extruder at the desired, constant extrusion speed and temperature and then cutting a strand of extrudate every minute. For each condition, 5 extrudates were cut and weighed on a MYA 11.4Y Plus micro balance, by RADWAG Balances and Scales (Poland).

The extruder was then calibrated to use with PrusaSlicer software, for each extruder temperature used. This slicing software is an open-source program, but it is meant for filament systems and not for screw or granulate extruder. Therefore, to accommodate this distinction, the pseudo filament diameter was set to 1.75 mm. The extrusion rate was then calibrated by altering the extrusion multiplier value in the slicing software. Several 20 mm sided cubes were 3D printed at different extrusion multipliers which were

changed if the cube sides were over or under extruded. This process was repeated until the sides of the cuboid where within a tolerance of ± 0.1 mm.

Inflatables must have internal, air-tight chambers to be able to contain the pressure build up required for inflation. To create internal chambers, a bridge has to be created between two walls where the material is being deposited in mid-air. The longest bridge possible is determined by a combination of speed, extrudate temperature, layer cooling, and the material's own rheological behaviour. For the purposes of this study, a practical bridging test was conducted. A specimen that included bridges starting from 2 mm, going up to 22 mm was designed and 3D printed. The specimen was then analysed to determine the maximum allowable bridge length.

6.2.4 Mechanical Testing

To determine the optimal extruder temperature for improved layer bonding, a tensile testing study was conducted for specimens printed at 290°C, 300°C, and 310°C. The test also studied the orientation effect, with XY specimens 3D printed flat on the build plate and the Z specimens with the longest section printed perpendicular to the build plate, as shown in Figure 6.2 (a). XY specimens were printed using aligned rectilinear paths, whereas Z specimens were printed using perimeters only. Unlike the XY specimens, the Z specimens could not be 3D printed directly in shape as the material was too soft to sustain such a long, unsupported structure. To remedy this issue, a pentagonal prism was 3D printed as shown in Figure 6.2 (b) and 5 specimens were stamped out using an appositely made punch die. Tensile testing was conducted according to the standard for *Determination of tensile stress-strain properties of rubber, vulcanized or thermoplastic* elastomers, ISO 37 [346]. Type 3 specimens were used with a 4 mm thickness, as shown in Figure 6.2 (c). All the specimens were tested on a M350 20CT tensile tester by Testometric (United Kingdom), using a 490 N load cell. Prior to testing, the cross-sectional dimensions of each tensile specimen were measured using an Infinite Focus optical measuring system by Bruker Alicona (Austria). Optical measurement was necessary as the material was too soft for conventional contact methods such as using callipers.

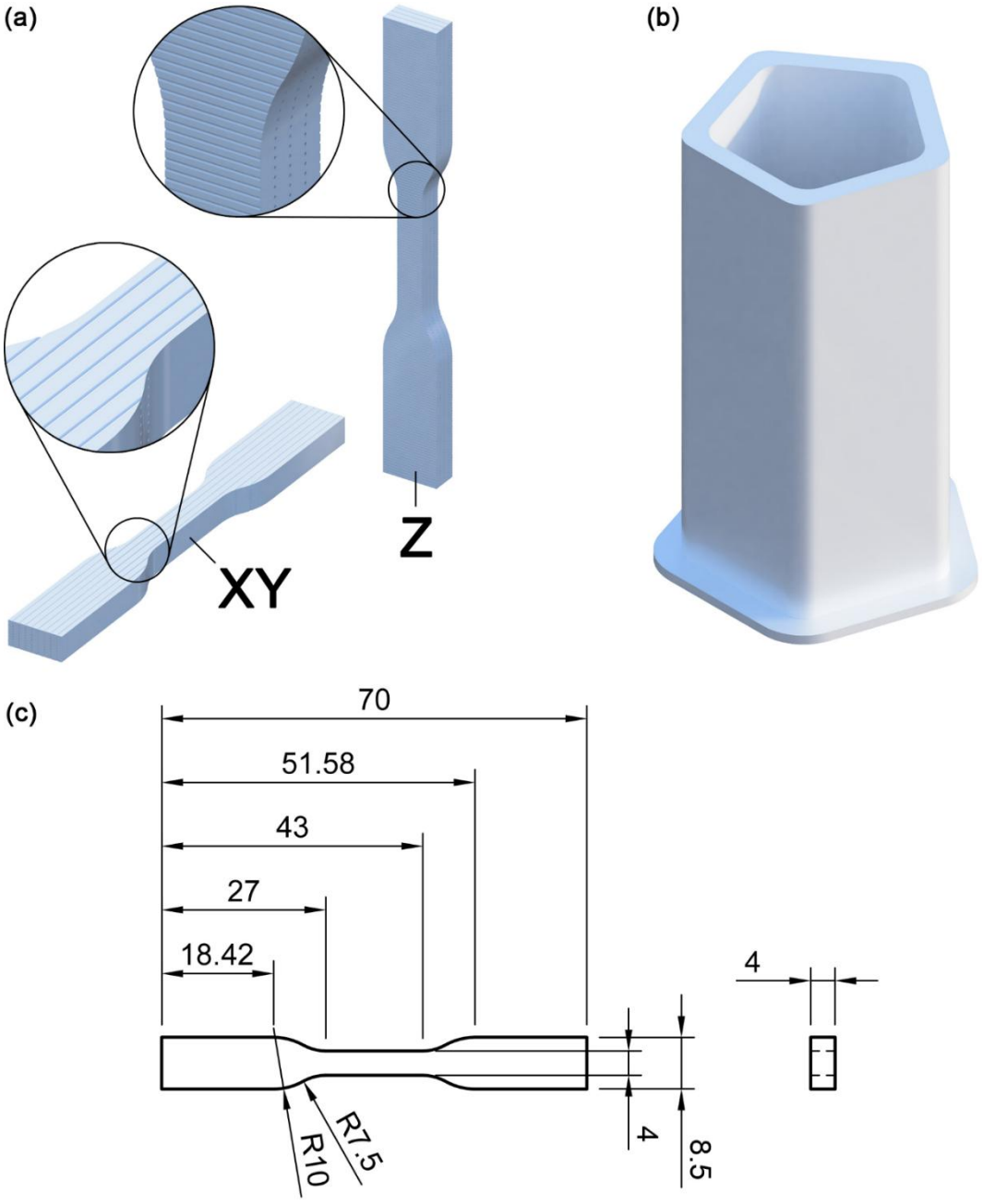

Figure 6.2 - (a) Build orientation of tensile testing specimens, (b) Z orientation pentagonal prism and (c) tensile specimen dimensions.

6.2.5 Water-Uptake Analysis

To determine the water absorption rate of TF3ZGO-LCNT, a water absorption test was conducted using extrudate processed at 310°C, 5 RPM following the standard for *Determination of water absorption of Plastics*, ISO 62 [347]. The granulates were pre-dried for 4 hours at 70°C before extrusion. For the study, 5 strands were used, each around 25 mm long. The strands were immersed in deionized water in an airtight container and kept at a constant room temperature of 23°C. The strands were kept

immersed for a total of 128 days, with periodic agitation. On allocated days, the test strands were collected out of the water, dried using paper towels and then weighed using the micro balance.

The result of the percentage change in mass was then fitted using the ideal model of Fick's second law, assuming constant water absorption properties over the diameter of the strands. The model defines the time-dependent water content as shown in Equation 5.1. The water diffusion coefficient was estimated using Equation 5.2 [347], as discussed in more detail in section 5.2.5.1.

6.2.6 Inflatables Case Study

The relatively soft nature of TF3ZG0-LCTN combined with the results of mechanical testing indicated that this TPE could be suitable for large extensions, such as required by inflatables. Successful production of inflatables would allow for the design and fabrication of EIAs. To this end, the bi-axial properties of the 3D printed TPE need to be understood. In such a scenario, the hoop and axial loading directions are the strongest components. To study the suitability of TF3ZG0-LCTN for this application a set of prisms with varying shape and wall thickness were 3D printed. The results of the prism inflatables promoted the development of mostly 3D printed gripper for a pick and place application.

The prism inflatables were printed with extruder temperature of 310°C, with dimension as shown in Figure 6.3 (a). Cube and hexagon prisms were used to check whether the initial shape influenced the maximum inflation of the prisms. Three wall thickness were studied, namely 2 mm, 3 mm, and 4 mm. The specimens were inflated with an inflation rate of 5 l/min using compressed air regulated at 5 bar.

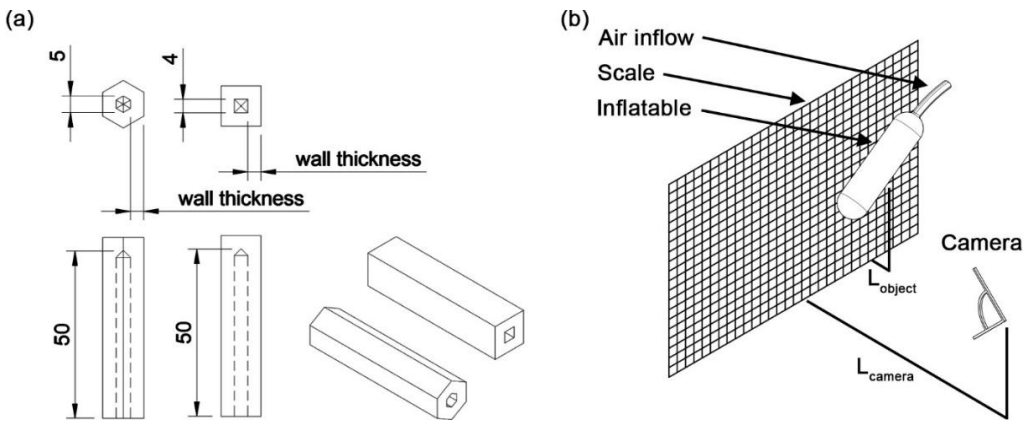

Figure 6.3 - (a) Dimensions of inflatable and (b) filming setup consisting of camera, scale, and inflatable.

The strain measurement and evaluation of expanding inflatables is complex, and no standard exists. One technique is photogrammetry as conducted by Blandino *et al*. when studying biaxial strain in an inflated cylinder [348]. Another approach is to use digital image correlation, as in a study by Yang *et al*. [349]. Both approaches are challenging especially when the inflatable is transparent. One solution would be to paint over the inflatable. However, due to the high softness and expandability of this TPE it was unclear how well this approach would work and how the end results would be affected. A simpler approach was demonstrated by Bustos *et al*. which used a video feed of the inflation process which was then fitted to an ellipse by image processing [350]. This study adopted a non-contact the approach similar to the one used by Bustos *et al*. so that no modifications of the inflatable were necessary.

All specimens were inflated till failure and the whole process was filmed using a Sony IMX 582 Quad-Bayer 1/2" sensor with 0.8 µm pixels, 25 mm f/1.8 lens, with a setup as shown in Figure 6.3 (b). The resulting video was split into an image sequence and processed digitally, using a purpose made python program. The most relevant scripts of this program are shown summarily in appendix 6, page 408. A breakdown of the procedure used is shown in Figure 6.4.

The first frame of the video was set as a reference image and the remaining frames were the respective working images. The general working area relevant to inflation process was selected and the rest cropped away. The scale was set for both the x and y axis by using the 5 mm square scales behind the inflatable. The starting point of the inflatable was then selected to be used later to find the correct contour. Any undesired regions were removed at this stage as well from all frames. Each frame was then processed as follows. All frames were turned to greyscale, including the reference frame. Each frame was then subtracted from a copy of the reference frame, as shown in Equation 6.1, where F_s is the subtracted frame, F_0 is the background frame and F_n is the current frame. All frames are a matrix of x and y dimension containing a value denoting the intensity of the greyscale, with a max value of 256.

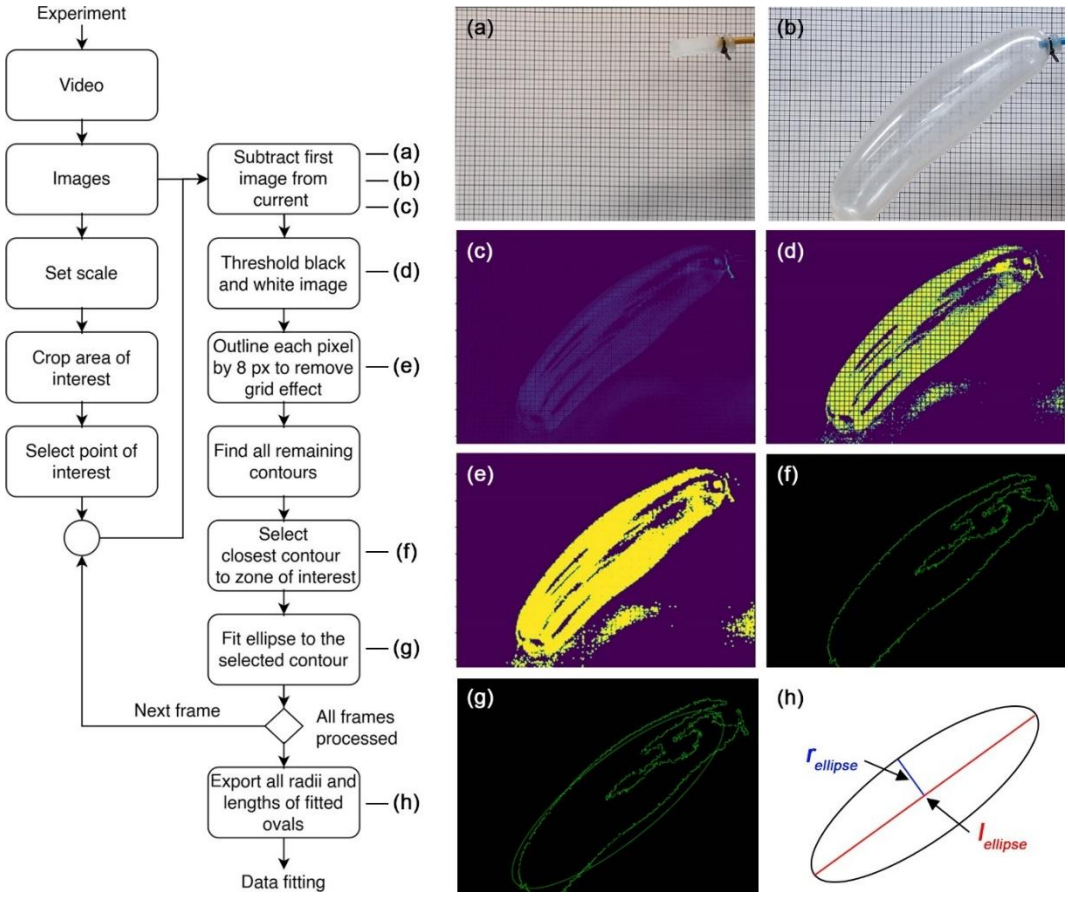

Figure 6.4 - Video processing to obtain radii and length of inflatable with time, where (a) reference, (b) cropped, (c) subtracted, (d) threshold, (e) outlined, (f) contour select, (g) fitted ellipse images and (h) is the radius and length of the fitted ellipse.

$$F_s = F_0 - F_n \qquad \text{Equation 6.1}$$

A threshold was then set on a scale of 5 out of 256 on the subtracted image to leave visible only the change in inflatable. The transparent nature of the stretched TF3ZGO-LCNT allowed the background scale to be visible which in turn created an undesired gridding effect that limits contouring. To remedy this defect, all regions in the image were selected and then outlined by 8 pixels. All the remaining regions were identified again and the largest region which was closest to the reference point was selected. An ellipse was fitted to the selected region and its radius $r_{ellipse}$ and length $l_{ellipse}$ were recorded, as shown in Figure 6.5. The radius $r_{ellipse}$ and length $l_{ellipse}$ were corrected using the distortion correction factor *C,* calculated using the distance from camera to scale L_{scale} and the distance from object to scale L_{obejct}, as shown in Figure 6.3 (b) using Equation 6.2.

$$C = 1 - \frac{L_{object}}{L_{camera}}$$

$$r_c = Cr_{ellipse} \qquad \text{Equation 6.2}$$

$$l_c = Cl_{ellipse}$$

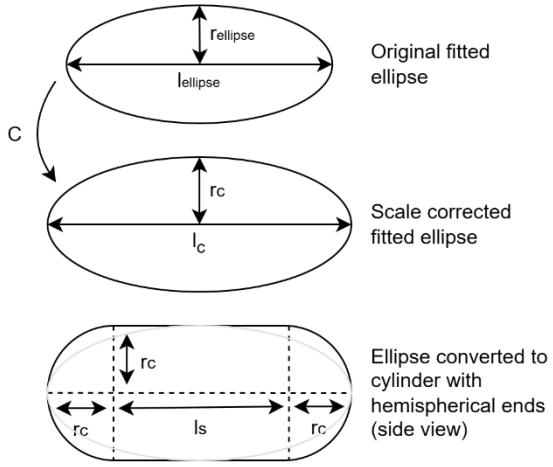

Figure 6.5 – Schematic diagram of original fitted ellipse, corrected using correction factor (C) and fitting of cylinder with hemispherical ends using fitted and scaled ellipse.

The inflatable was then assumed to be a cylinder with hemispherical ends, where r_s is the cylinder radius which is equal r_c, and l_s is the cylinder length calculated using Equation 6.3.

$$l_s = l_c - 2r_c \qquad \text{Equation 6.3}$$

The data was filtered using rolling maximum per 10 frames for r_c and l_s. The data was fitted to produce r_f and l_f using a 2nd order polynomial in the case of l_s and a combined logarithmic and 2nd order polynomial curve for r_c, as shown in Equation 6.4.

$$f(x) = (a)log(x) + bx^2 + cx + d \qquad \text{Equation 6.4}$$

The hemispherical ended cylinder volume $V_p(t)$ was then calculated using Equation 6.5. The rate of change of $V_p(t)$ with time, assuming a linear relationship, was then compared with the known inflation rate of 5 l/min. A similar value validates the assumption of hemispherical ended cylinder and the scaling solution used.

$$V_p(t) = \frac{4}{3}\pi\left(r_f(t)\right)^3 + \pi\left(r_f(t)\right)^2 l_f(t) \qquad \text{Equation 6.5}$$

The perimetric and longitudinal strain with time ε_P and ε_L, as shown in Figure 6.6, were calculated using r_f, and l_f using Equation 6.6 and Equation 6.7, where r_0 and l_0 are the original radius and length.

$$\varepsilon_P(t) = \frac{r_f(t) - r_0}{r_0} \qquad \text{Equation 6.6}$$

$$\varepsilon_L(t) = \frac{l_f(t) - l_0}{l_0} \qquad \text{Equation 6.7}$$

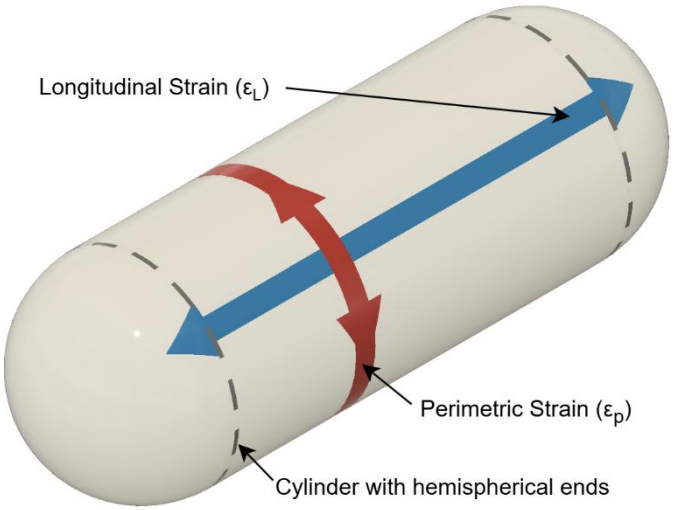

Figure 6.6 - Schematic diagram of longitudinal and perimetric strain in cylinder with hemispherical ends model.

6.3 Results and Discussion

6.3.1 Material Characterisation

TF3ZGO-LCNT granulates were analysed using both Raman, FTIR, and EDS spectroscopy without any prior modification. The Raman and FTIR spectroscopy results are shown in Figure 6.7 (a).

Conducting a negative correlation analysis using the results provided by George Socrates [351] demonstrated that the TPE possibly contains an alkane, amide, and ether blend. The major distinct bands were assigned as shown in Table 6.2, where the bands at 1014 cm^{-1} and 1643 cm^{-1} are representative of an amide component. The EDS results shown in Figure 6.7 (b) confirm the presence of Nitrogen which is a key element of the amide polymer chain. This confirms the presence of amides which indicates that TF3ZGO-LCNT may work well with adhesion promoters meant for polyamides. For this reason, Magigoo PA adhesive was applied on a heated glass build plate and used throughout the study. This adhesive enabled 3D printing with TF3ZGO-LCNT as the material was otherwise unable to bond as necessary to heated or cooled build plates made from glass, Polyetherimide or polyimide.

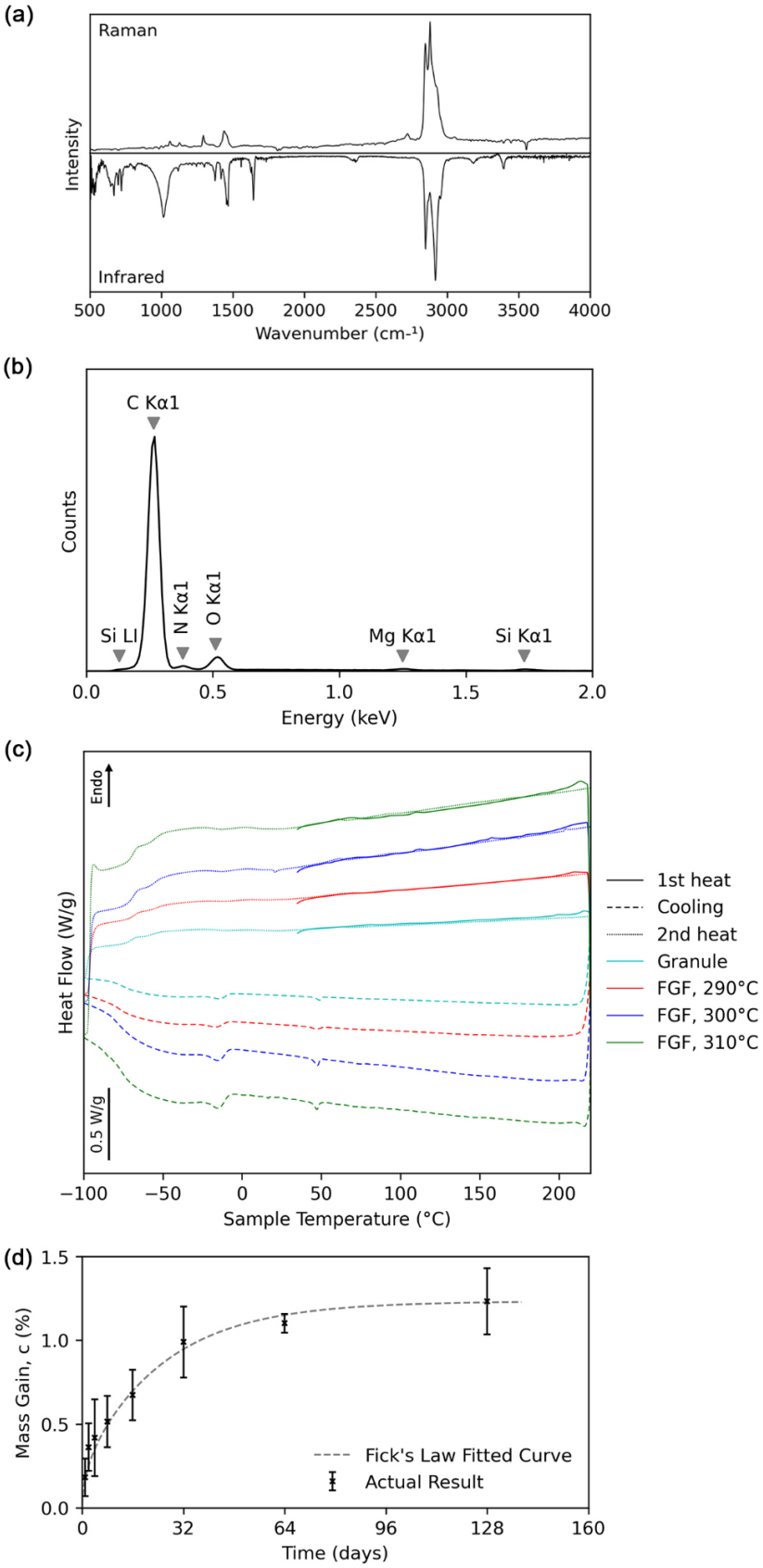

Figure 6.7 – Characterisation results of (a) Raman and infrared spectroscopy, (c) EDS of TF3ZGO-LCNT granulates, (c) DSC with y axis shifted results and (d) water absorption test of extrudate.

Table 6.2 - FTIR and Raman band labels.

Wavenumber (cm^{-1})		Assignment
FTIR	**Raman**	
3393 (w)		C=O str, overtone
2954 (m)		C-H asym str. CH_3
2920 (vs)		C-H asym str. CH_3-Ar, -CH_2-alkanes
	2881 (vs)	C-H sym str, CH_3
2847 (s)	2847 (s)	C-H sym str, CH_2-alkanes
1643 (m)		N-H def, primary amides solids amide II band
1647 (m)		-CH_2- scissoring, alkanes
	1446 (m)	CH_3 asym (bending) def
1375 (w)		C-O str and OH def, carbonxylic acids
	1294 (w)	C-O str, carboxylic acids dimers
1014 (s)		Thioamides

w – weak, m – medium, s – strong and vs – very strong

The first heating curves of the DSC analysis, as shown in Figure 6.7 (c), revealed a predominantly amorphous structure of the granule and 3D printed specimens. This is due to the multiple endothermic peaks observed at around 213°C are tiny, thus insignificant. It can be assumed that these endothermic peaks are related to the formation of pseudo crystallinity in this blended grade of TPE. Such pseudo crystallinity was not formed during the DSC cooling cycle since the respective exothermic peaks could not be observed. Consequently, the second heating curves did not show endothermic peaks. The DSC analysis also revealed two glass transition temperatures: -15°C and 49°C from the cooling curves or 7°C and 65°C from the heating curves. Based on these findings, the heated build plate temperature was set to 70°C, slightly above the secondary glass transition as suggested by Spoerk *et al.* [313]. The result also suggests that the optimum service temperature range of this TPE between 7°C and 65°C.

Figure 6.7 (d) shows the water absorption test result and the water absorption at saturation c_s was reached at 1.23%. The stand diameter d was measured to be 0.51 mm on average in between the 5 specimens and the time at 70% saturation was met after 25.6 days. This resulted in a water diffusion coefficient D of 1.19E-8 mm^2/s. This test indicates that drying may be required only after months of storage. It should be noted that in this study the granulates were immersed in water and even in such a scenario,

the water uptake was rather low. This is contrary to the mostly used TPE for filament printing i.e., TPU, which is known to require pre-drying after a few days left in open air. A similar water absorption test, but on TPU, conducted by Boubakri *et al*. reached saturation at around 1.5 % mass gain after only 5 hours [352].

6.3.2 Screw Material Extrusion and 3D Printing Calibration

The measured extrudate temperature significantly differs from the respective, set nozzle temperature, as shown in Figure 6.8 (a). The relationship was linear, with a coefficient of determination (R^2) of 0.992. The extrudate temperature was measured directly when it leaves the nozzle, as shown in Figure 6.1. The DSC results did not indicate a melt temperature as the material is predominantly amorphous. Nonetheless the peak at 213°C was set as the target temperature which is equivalent to about 315°C. This was done with the aim of obtaining a sufficiently molten polymer. In order to account for temperature measurement inaccuracies and to minimise possibility of unexpected degradation, the set point temperature was decreased to 280°C, and then increased progressively with 10°C steps. A consistent extrusion rate was achieved at 290°C. Below 290°C nozzle temperature, extrusion became poor and discontinuous. A higher nozzle temperature then 290°C could possibly provide a better layer bond and, therefore, it was also set at 300°C and 310°C. The extrusion rate analysis, shown in Figure 6.8 (b), demonstrated that the extrusion rate increased consistently with screw speed at 300°C and 310°C. At 290°C, the extrusion rate started to increase with screw speed at a higher rate than the other temperatures, but then decreased at 10 RPM. This discrepancy may be caused by insufficient heating of the melt which could lead to a lower melt temperature at higher screw speeds, increasing viscosity and therefore decreasing extrusion rate. This is possible as the melt is principally being heated by conduction. At higher screw speeds there might not be enough time to heat the melt before it is extruded, when using a 290°C nozzle temperature. The similar extrusion rates meant that the same extrusion multiplier could be used at different nozzle temperatures. The extrusion multiplier was found to be 0.45 at 20 mm/s printing speed.

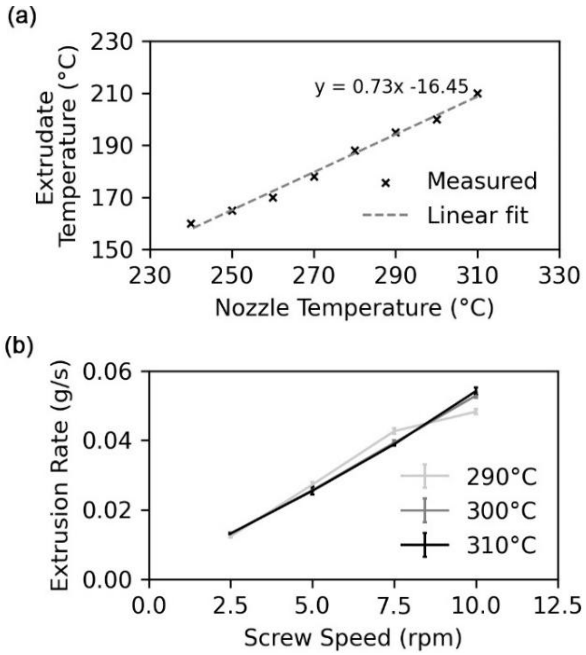

Figure 6.8 - (a) Relationship between set nozzle temperature and measured extrudate temperature (R^2 = 0.992) and (b) relationship between extrusion rate screw speed and nozzle temperature.

6.3.3 Optimisation of 3D Printing Process

For optimal 3D printing of inflatables, it is critical to identify the maximum bridge length, i.e. the longest span that can be deposited in midair without leaving defects. The bridging test demonstrated that the maximum bridging distance is of 7 mm, as shown in Figure 6.9. Following this result, the inflatables case study used a 5 mm bridge to ensure that there would be no unintentional gaps which could affect adversely the printing and inflation testing results. The bridging test demonstrated that any inflatables designed to be produced by this system would require a supporting structure at least for each 7 mm span. An even shorter span such as 5 mm would ensure consistent quality.

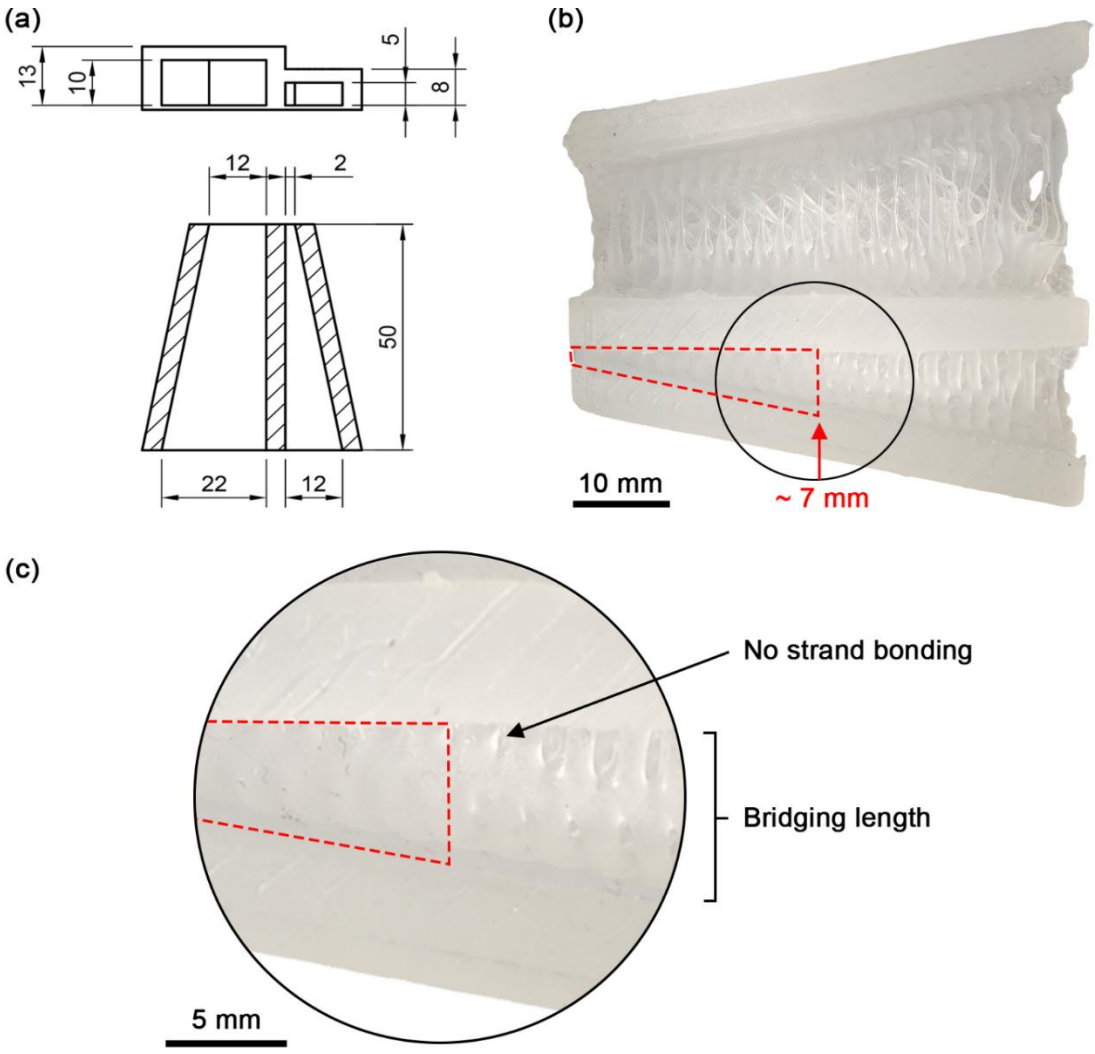

Figure 6.9 - (a) Bridging test geometry and (b) result with the dashed outlined region indicating the possible bridging length with (c) zoom in.

The quality of an inflatable also depends on the material's mechanical strength. In most material extrusion, the 3D printed parts tend to be anisotropic, whereby the Z orientation is the weakest. This trend was evaluated by tensile testing using specimens and die shown in Figure 6.10. It can be confirmed that the Z orientation is the weakest for all nozzle temperatures used during tensile testing, as shown in Figure 6.11 and Table 6.3. All uncertainty values are provided with a 95% confidence interval. The strongest layer bond, i.e. Z orientation strength, was achieved at a nozzle temperature of 290°C, reaching a maximum average stress of 0.74 ± 0.09 MPa and a strain of 2328 ± 138 %. Increasing the nozzle temperature reduced the layer bond strength by decreasing the maximum loading stress and strain achievable. The nozzle temperature increases at 310°C results in the decrease of layer bond stress and strain at failure by 78.4 % and 45.9 % respectively. It was concluded that for optimal layer bond strength, the nozzle temperature for this TPE should be set to 290°C.

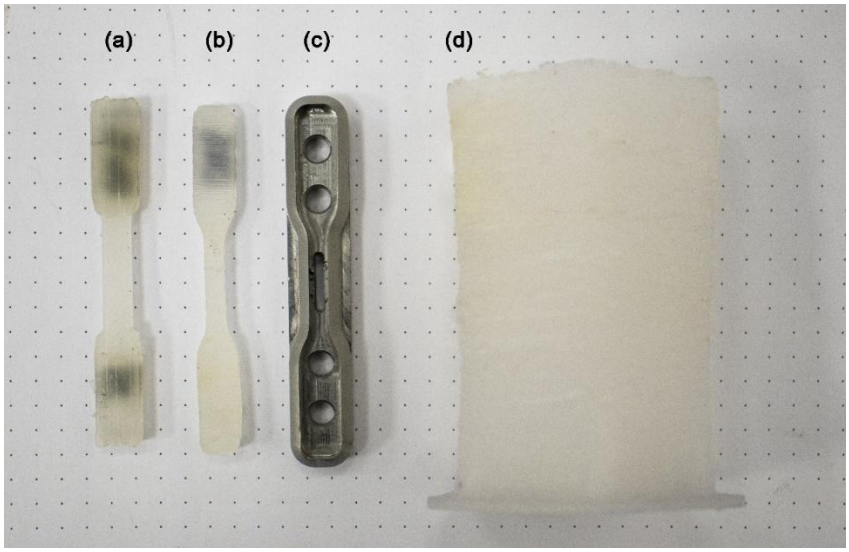

Figure 6.10 - 3D printed XY specimen (a) and Z specimen (b) which was punched out using a custom machined die (c), out of vertically printed pentagonal prism blank (d). Background dots with 5 mm spacing.

The XY specimens never failed upon testing for specimens printed at 300°C and 310°C since their elongation could reach the machine limits which is the 3365% strain, as can be seen in Figure 6.11. The highest maximum stress in the XY orientation of 1.01 ± 0.09 MPa was achieved by the specimens printed at 300°C. The 290°C XY specimens showed a decrease in the maximum average strength of 8.9% at a strain at failure of 2815 ± 224 % as opposed to their layer bond strength which increased. The opposite effect was observed for Z orientation specimens, whereby the strength increased at higher nozzle temperatures at the same strains. The effect becomes most significant at strains higher than 500 %. At this strain, Z oriented specimens with nozzle temperature of 290°C and 300°C were 11 % stronger than those printed at 310°C. The discrepancy became larger at 1000% strain where the 290°C specimens were 16 % and 19 % stronger than those printed at 300°C and 310°C respectively.

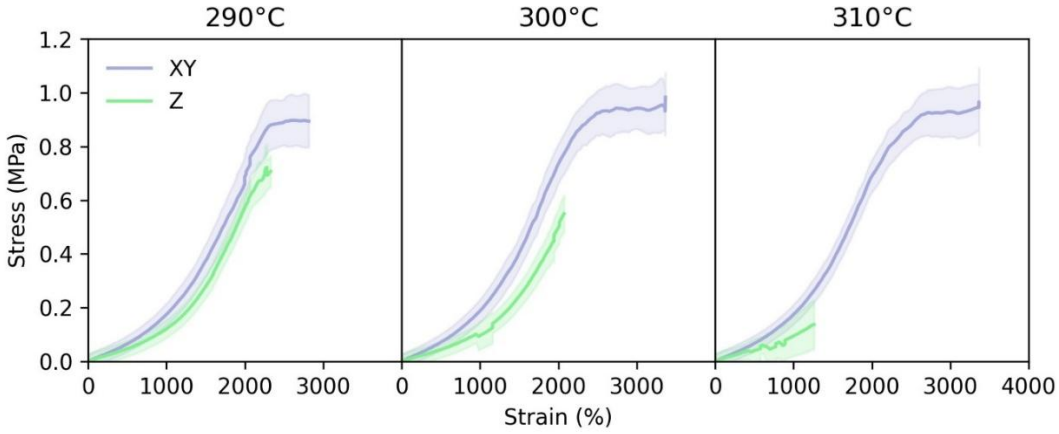

Figure 6.11 - Stress-strain curves of tensile testing at different nozzle temperatures and orientations.

No other published research works presented such long elongations achieved by a 3D printed specimen. The closest available result was published by Khondoker and Sameoto which achieved 875 % thermoplastic extrudate elongation [37]. 3D printed TF3ZGO-LCNT surpassed this result even in its weakest orientation, reaching higher than 2000 %. On the other hand, the stress at failure of TF3ZGO-LCNT was significantly lower, reaching at its highest 1.01 ± 0.09 MPa as contrasted with the 12.5 ± 2.2 MPa achieved using SEBS [37]. This result indicates that TF3ZGO-LCNT TPE achieved the highest extensibility and lowest hardness currently available for AM technologies. This combination of properties makes it a good fit for fabrication of inflatables and impact dampers amongst others.

Table 6.3 - Measured stress for discrete strains.

		Stress [kPa] at Build Orientation and Extruder Temperature [C°]		
		XY 290	**XY 300**	**XY 310**
Strain [%]	**250**	55.8 ± 27.6	56.0 ± 25.3	56.5 ± 26.4
	500	90.2 ± 29.8	98.2 ± 28.4	91.5 ± 27.3
	1000	200 ± 41.1	215 ± 41	200 ± 35
	1500	400 ± 61	432 ± 58	398 ± 49
	2000	714 ± 84	763 ± 72	715 ± 59
	3000	885 ± 69	969 ± 76	953 ± 91
		Z 290	**Z 300**	**Z 310**
Strain [%]	**250**	44.3 ± 27.3	45.4 ± 25.4	43.9 ± 24.2
	500	68.7 ± 28	67.4 ± 26.9	61.0 ± 39.6
	1000	142 ± 33	120 ± 49	116 ± 71
	1500	300 ± 42	267 ± 42	235 ± 56
	2000	596 ± 57	522 ± 62	N/A

6.3.4 Inflatables Case Study

6.3.4.1 Inflation Till Failure

Although the inflation of the prisms was successful, the assumption that the inflatable would take the shape of a cylinder with hemispherical ends, was not always correct. For example, at the start of inflation, as shown in Figure 6.12 (a), the prisms were not similar to a hemispherical ended cylinder and therefore at the very beginning the assumption is incorrect. As the inflatables increase in volume, their shape became similar to the assumed cylinder but even then, the shape could vary from the ideal. An example outline progression is shown in Figure 6.12 (b), whereby each green outline shows the processed

perimeter of the inflatable. The inflatables tended to be either centre expanded, ideal or bent, as seen in Figure 6.12 (c to d). By ideal, it is meant that the inflatable is most like the assumed geometry of hemispherical ended cylinder. Centre expanded and bent inflatables led to incorrectly exaggerated radius and undervalued length of the fitted ellipse, respectively. The former case tended to occur close to inflatable failure by rupture whereas the bent inflatables varied and at times started from the very beginning of inflation.

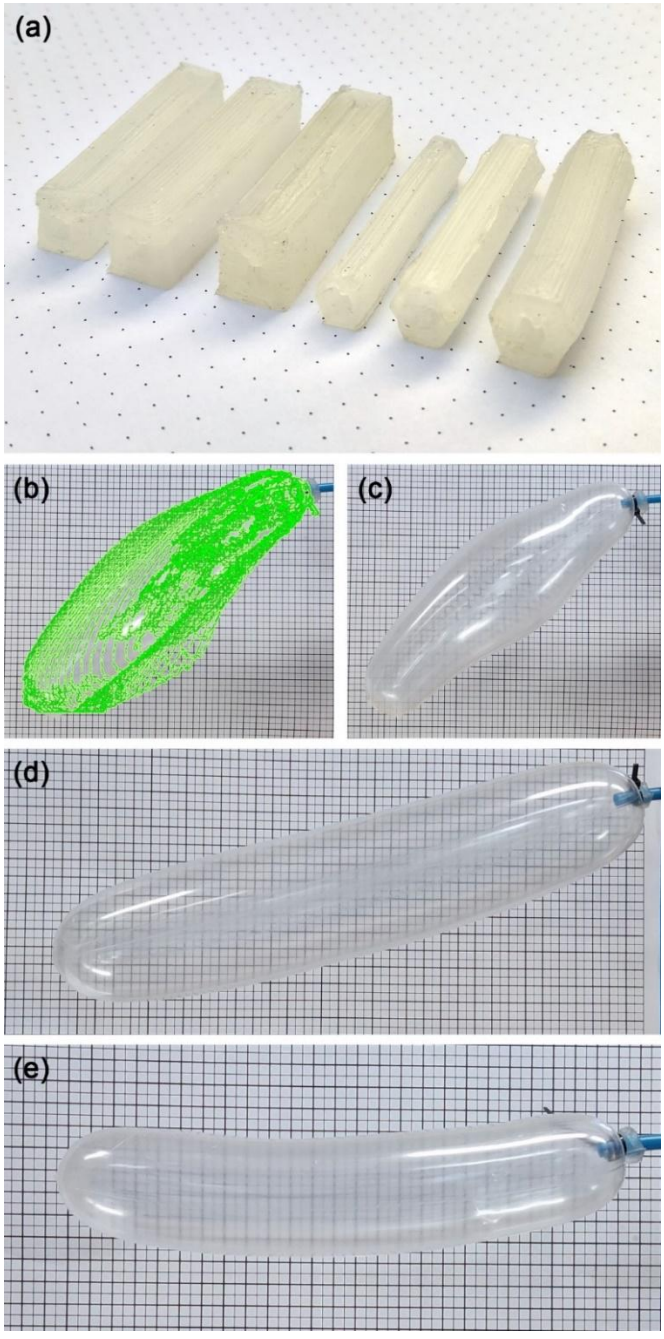

Figure 6.12 – (a) Uninflated prisms and inflated prisms: (b) large hexagon with green contours indicating inflatable expansion with time; (c) centre expanding inflatable; (d) ideal hemispherical end cylinder and (e) bent inflatable.

The results of the video processing are shown in Figure 6.13, using a correction factor *C* of 0.8. In each case, the best video for a given set of parameters was selected for processing. This was necessary as most specimens tended to expand off-camera or orient incorrectly which would have resulted in incorrect readings. The increase in radius and length with time followed a similar pattern for each process condition. Volume increase was close to a linear rate of 5 l/min, with overall average rate of 4.85 ± 0.21 l/min, 95% confidence. The curves were not perfectly linear but had inconsistencies which may be attribute to inflatable off axis shifts or poor image processing, leading to incorrect ellipse sizing.

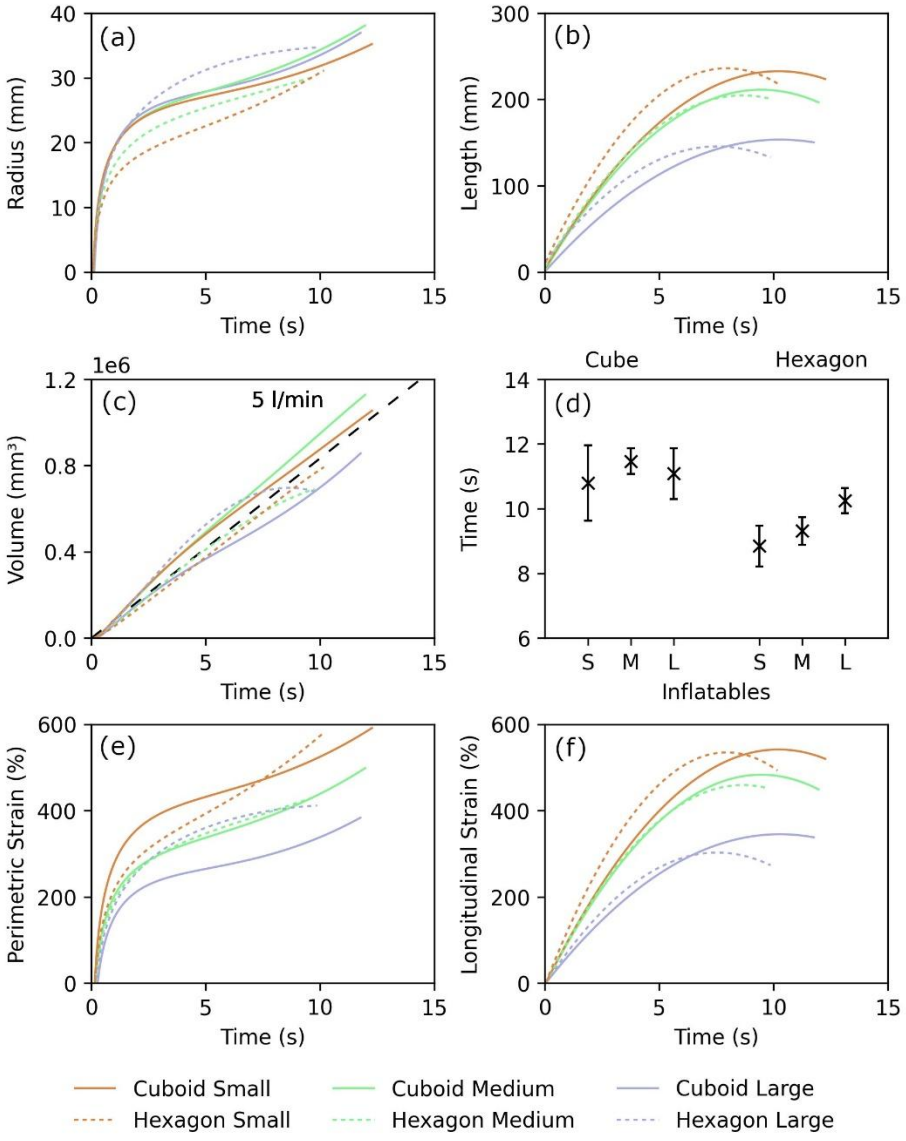

Figure 6.13 - Inflation image sequence analysis for (a) radius, (b) length, (c) volume, (e) perimetric strain, (f) longitudinal strain with time (n=1) and (d) time to failure for specimen type where S is small, M is medium and L is large (n=3).

For both geometries used, the thinner the inflatables walls, the greater the increase in perimetric and longitudinal strain. The thinner wall specimens are expected to experience higher strains as these have lower strength due to the smaller cross-sectional area, whilst experiencing the same pressure. Despite the different wall thicknesses, each geometry achieved a similar time to failure and maximum volume. Cuboid inflatables expanded 40 ± 12% more than their hexagonal counterparts. The inflation time to failure of all specimens' tests, shown in Figure 6.13 (d) further confirmed that cuboid specimens can sustain a larger expansion compared to hexagonal prism inflatables. The difference could be caused by defects in the angled walls of the hexagon, during the 3D printing process. Hexagonal prism inflatables also demonstrated an expected increase in inflation time with thicker walls, as shown in Figure 6.13 (d). This was not observed when using cuboid specimens which had a similar inflation time throughout. The discrepancy may be caused by defects in the geometries imparted during 3D printing or poor ellipse fitting towards the end of inflation. The latter issue may be caused by large deviations from the assumed geometry of hemispherical ended cylinder, as discussed previously.

The highest strain was reported at the perimeter which agrees with the general solution of hoop stresses in cylindrical pressure vessels. This also explains the faster increase in perimetric strain compared to longitudinal strain at the start of inflation. Failure occurred at a maximum of 590% strain, significantly lower than that achieved during uniaxial tensile testing. In a scenario similar to bi-axial stress load, the strain at failure is lower. In all cases, longitudinal strain tended to decrease with time as it approached failure. This was attributed to the centre expanded or bent inflatables as previously described and as shown in Figure 6.12 (c, e) respectively. This effect may be the reason behind the increase in perimetric strain of cuboid specimens before rupture, i.e. exaggerated radius fitting.

6.3.4.2 Failure Mode Analysis

All inflatables failed in a similar manner with a curved C shape tear line, as shown in Figure 6.14 (a to d), generally at the centre of the inflatable. Microscopic evaluation of the failure front indicated that rupture started at the centre point of the tear, as shown in Figure 6.14 (a), marked with a dashed line box. For all specimen type, this region was characterised by a rough failure surface, as shown in Figure 6.14 (b, d). As the tear progressed to either side of the burst point, the failure front become smooth. Such a

failure front is typical of a thinly stretched material under load, suddenly tearing up. The burst point always occurred at a strand-to-strand bond region at the mid length point of the prims for both cube and hexagon inflatables. Some failures started at bottom of the inflatable, i.e. where material was deposited on the build plate, as shown in Figure 6.14 (a) whereas others started at the side walls, as in Figure 6.14 (c). This indicates that 3D printed TF3ZGO-LCNT has equal strength on all faces, irrespective if it is deposited, pressed down on the build plate or built freely as a sidewall is.

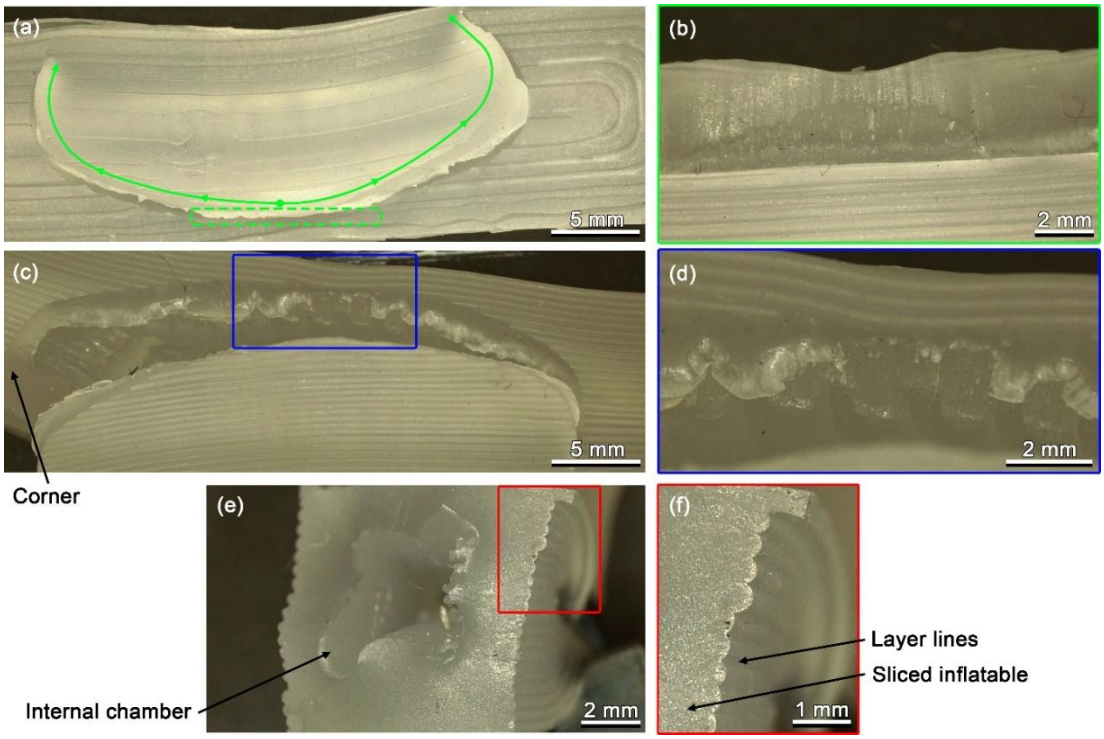

Figure 6.14 – Microscopic images of (a) large cuboid with bottom failure and (c) medium cuboid with side failure with magnified (b,d) image of rough surface at expected start of failure,(e) sliced section of small cuboid with magnified (f) wall cross-section.

The cross-section of a small cuboid specimen, shown in Figure 6.14 (e, f), shows an apparently homogenous, bulk material, with no layer line indications except at the outer layer. The start of failure at the layer-to-layer region is a combination of the reduced amount of material in this region which creates the visible layer line feature and the lower tensile strength of the bond compared to bulk, as shown by the tensile testing results. At this point the actual inflatable is slightly thinner and acts as a stress and tear initiator point. The rest of the tear probably occurred whilst the material was deflating as evidenced by the c-shaped tear on hexagonal prims that spans seamlessly across multiple faces of the hexagon. In conclusion, TF3GO-LCNT is amenable to inflatable additive manufacturing using material extrusion (MEX). Similar to most thermoplastics

used with MEX technology, the Z axis is the weakest and therefore for the application of inflatables, it controls the overall expandability of a given design.

6.3.4.3 Gripper Demonstration

The tensile and inflation test results demonstrated that TF3ZGO-LCNT MEX AM behaviour is rather different than other TPEs. The low hardness of 32 Shore 00 led to large elongations, higher than 2000 %, coupled with low stress, below the 1 MPa upper limit. Therefore, any application derived from this material-process combination should be focused on a soft design concept, even softer than what is generally done with EIAs. This TPE cannot sustain large inflation pressures but is able to expand significantly more than alternative TPEs used in literature. Using this concept, a side expanding inflatable was created that makes use of the preferential expansion of thinner walls compared to the thicker section. To use this EIA design, the inflatable can be expanded well below the failure level, ensuring longevity of device. This also creates a cushioning effect upon contact, making this system ideally suited for a pick and place system of fragile artefacts. Such an EIA type can be considered as a novel form of the expanding type of EIAs, as defined by Gorissen *et al*. [208]. This type of EIA also has the advantage of working straight off the 3D printer without any intervention. Furthermore, the inflatable does not require a bonded second material or structure to act as a constraint, such as a fibre mesh to limit expansion except were desired.

Using this concept, a side inflating geometry was modelled and used to create an inflatable gripping system, as shown in Figure 6.15. All walls were set to 4 mm or thicker except for the thin wall which was set to 2 mm. The assembly included an adjustable holder that could be moved up to alter the allowable gripping volume. Upon inflation, the geometry repeatedly expanded preferentially at the wall of least thickness, as shown in Figure 6.15 (d, e). Three such inflatables were produced and then arranged in a triangular manner with the inflating part aimed towards the centroid of the triangle. Upon simultaneous inflation, the system could grip a 100 g weighed object as shown in Figure 6.15 (f, g). This simple gripper design was meant purely as a demonstration of one application where low-cost, custom inflatables could be used for production purposes.

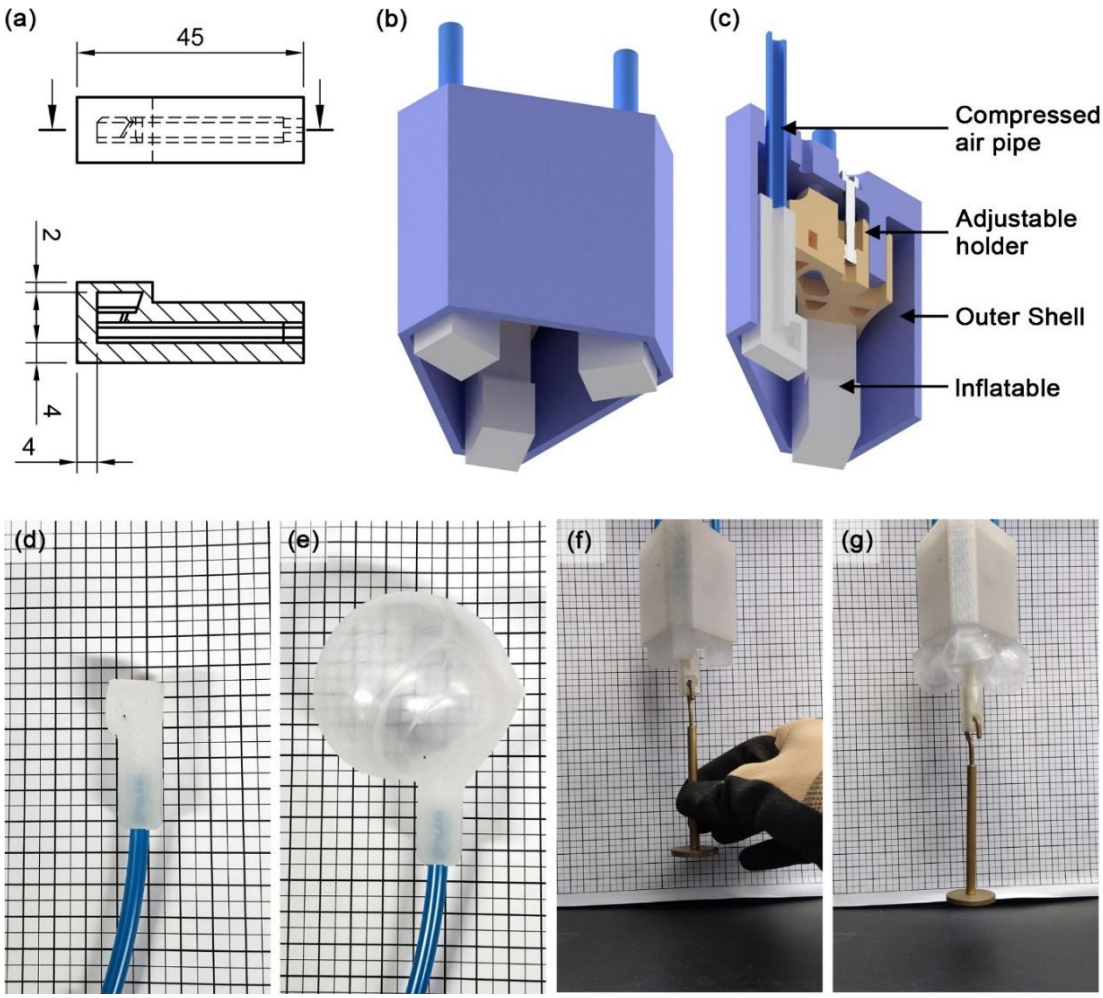

Figure 6.15 – Schematic diagram of (a) side inflatable gripper drawing with cross-section, (b) render of gripper assembly with (c) cross-section and images of (d) uninflated and (e) inflated specimen and demonstration of (f) uninflated and (g) inflated system gripping a 100g weight.

6.4 Conclusion

In conclusion, this study demonstrated that FGF can 3D print a 32 Shore 00 TPE making it the softest 3D printed elastomer in scientific literature up till now. This process was then successfully used to produce elastic inflatable actuators (EIAs). To achieve these results, FGF screw Extruder 4, fitted with an 85 mm short screw was used to consistently extrude TF3ZG0-LCNT TPE granulates.

Uniaxial tensile testing showed that in the XY orientation this 3D printed TPE could surpass 3365% strain at 300°C and 310°C nozzle temperatures. In the Z orientation, which represented the layer bond strength, decreasing the nozzle temperature to 290°C, increased the stress and strain at failure. This is contrary to what was observed for the XY orientation which were strongest at 300°C and 310°C nozzle temperatures. At 290°C, the Z orientation strained to failure at 2328 ± 138 % with a stress of 0.74 ± 0.09 MPa. Such

a large strain in the layer bond orientation is a clear indication that the material may be used for inflatable production.

Inflation tests of 3D printed cuboid and hexagonal prisms of various thicknesses demonstrated that in a biaxial strain condition as done during inflation, the maximum strain at failure reached 590%. This value was recorded using a custom developed video processing software which tracked the change in volume of the inflatable with time. The large strains reported in both uniaxial and biaxial strain conditions, coupled with the soft nature of TF3ZG0-LCNT prompted the development of novel elastic inflatable actuator. This EIA used low pressures expansion to grip objects with low forces.

These results were made possible by the production of an FGF system capable of processing TF3ZG0-LCNT granulates and the determination of process parameters that ensure a consistent and versatile 3D printing process. The ideal extruder nozzle temperature was found to be between 290°C and 310°C. The 3D printed objects were controllably bonded to a glass build plate which was coated with Magigoo PA adhesive and heated to 70°C. No prior material drying is necessary except after long periods in storage.

The combined results of the studies presented in chapters 5 and 6 demonstrate the propensity of the FGF extruders developed, to extrude and 3D print TPEs. The sharp difference in shore hardnesses used highlight how versatile FGF technology is. It also demonstrates its greater material versatility possible with FGF as compared to FFF systems, when it come to AM of TPEs. The system developed, paves the way for upgrades of existing products or completely new products that only now have become possible following the introduction of these new FGF technologies. These extruders also provide new prototyping possibilities which were previously impossible and necessitated the use of molding techniques to generate the required geometry, especially when dealing with super soft TPEs. These improvements will allow for the development of new applications in multiple sectors such as biomedical and packaging, allowing designers to better cater for society's needs.

RTIM specimens

7 High Performance – Amorphous Thermoplastic

7.1 Introduction

AM can be used for rapid prototyping (RP), rapid tooling (RT), and rapid manufacturing (RM) [353]. The raw material versatility provided by FGF allows for a more cost-effective and discerning material choice. In the case of RT for injection molding (IM), often referred to as RTIM, high-performance polymers may be used to produce bespoke mold inserts for prototype production or low-batch production of end products with typical injection molding quality. In contrast to RP using RT, direct RP using an AM technology even using the same desired grade of material will create prototypes with incongruent mechanical properties due to the disparate processing conditions [236, 354].

Vat polymerization AM techniques for RTIM have been studied by multiple research groups [355–361]. This group of technologies has a high level of surface finish control, capable of obtaining smooth or textured surfaces by design. Such surface quality is important for RTIM inserts but material properties also play a crucial role. Studies by Davoudinejad et al. and Moritz et al. showed that the higher the mold temperature, the lower the service life of the insert and the produced part quality [355–357]. MEX 3D printed inserts are not capable of reaching the same surface quality as vat polymerized inserts [362] but can achieved better mechanical performance. MEX systems are capable of 3D printing using high performance thermoplastics such as PEEK and PEI which can have even better thermal resistance and strength than their resin counterparts for Vat polymerization AM. PEEK filled with carbon fiber was used for FFF to produce mold inserts by Rodzeń et al. which showed encouraging results. The combination of high temperature resistance, strength, and toughness and the use of a simple insert with no features resulted in the reported production of 100 inserts by IM with no apparent damage to the insert [363]. ABS [364, 365], PLA [366], and PA [364, 365, 367] have also been applied for RTIM with good success but with a lower performance and part quality compared to PEEK-CF inserts.

A common issue amongst all MEX research works is the large presence of flash on the molded parts. All polymeric RTIM inserts also suffer from a low thermal conductivity compared to metallic molds. Better cooling of injected parts is often necessary and can be achieved by using conformal cooling channels [368], improved heat conductivity [369] or resorting to the basic solution of simple increasing cooling time [368, 370].

Apart from PEEK, PEI (e.g. ULTEM 9085) is another high-performance polymer with a wide usage in FFF 3D printing. ULTEM 9085 is PEI blended with polycarbonate (PC) [371], having a heat deflection temperature of 153°C [233], which makes it applicable as an RTIM material. The only published study involving PEI AM for RTIM, was presented by Farioli et al. but using ULTEM 1010 and FFF 3D printing [372]. Similar to most studies carried out on RTIM, this study used a simple part geometry which results in a simple insert design and print. This simplification neglects the real-life complexity of common day objects, where RTIM process would be applied. Apart from empirically testing more complex applications of RTIM, simulation may also be viable route. The issue with such techniques is to ensure that the anisotropic properties and internal porosity, both micro and macro, are reflected in the simulation process. When it comes to thermal behavior during IM, the discrepancies could be substantial. Another issue is the level of detail captured by thermal measurement in the available, published research works. This lack of detail limits understanding of the effects of low heat dissipation of polymeric RTIM inserts.

The aim of this study was to investigate PEI ULTEM 9085 for RTIM using an in-house built FGF 3D printing system. This novel application of ULTEM 9085 for RTIM could provide greater insert longevity whilst maintaining acceptable insert quality. The reduction in costs associated with insert production, brought about by FGF, would make RTIM even more cost-effective and applicable to industry. A packaging case study from the cosmetic industry, is used to investigate the challenges caused by complexity. The accuracy of the FGF process will be evaluated for dimensional fidelity, by comparing the inserts to the original 3D CAD model. The RTIM process will also be studied, with special focus on the thermal behavior to determine the cooling rate and the severity of hot spots in the inserts. The produced parts will also be analyzed for dimensional accuracy and quality achieved. Apart from empirical testing, the IM process will be simulated to predict the expected part deflection and to verify the applicability of such a simulation to an RTIM process.

7.2 Materials and Method

7.2.1 Case Studies

A cosmetic compact studied by Vella et al. [362] will be used as the case study part for this work as shown in Figure 7.1. This case study originates from the cosmetic packaging

industry which often requires multiple prototyping steps in its design cycle [373]. The original part was simplified to as shown in Figure 7.2 (a), similarly done by Vella et al. [362].

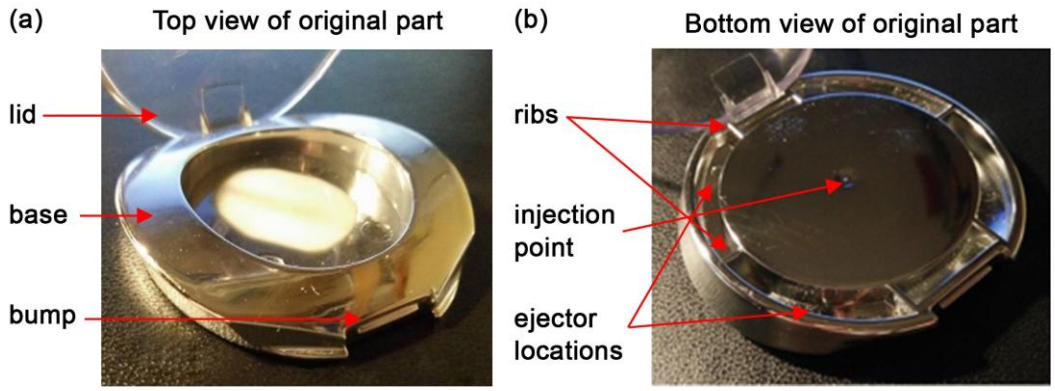

Figure 7.1 - Original cosmetic compound upon which the case studies were inspired, specifically the base part of the compound. The original part has ribs and uses ejector pins.

Case study 1 had a complex geometry which can be challenging to 3D print using MEX additive manufacturing processes. Both injection and ejection side inserts had shallow curved surfaces as highlighted and magnified in the 3D render of Figure 7.2 (a). It is relatively difficult to achieve a high quality of such shallow curved surfaces when using MEX systems especially if the inserts are printed horizontally, i.e. flat on the build plate. Such shallow curves lead to a terraced face where the layer height used for the 3D printing process limits how well the 3D printer can resolve the surface curves, as shown in Figure 7.2 (b). The issue may be remedied by using 5 axis or non-planar 3D printing process which in practice can follow the ideal 3D model surface. Future studies could employ one or both technologies to improve the insert geometry fidelity. Another relevant issue is poor z strength i.e. interlayer bond strength which can lead to premature part failure. Case study 1 has a good example for such a feature, highlighted in the right, magnified region of Figure 7.2 (a). As illustrated in Figure 7.2 (c), the pressure generated by the molten polymer starting to fill the insert will leverage on the weak layer-to-layer bond, possibly leading to breakage [374]. The aforementioned issues led to drafting of another case study with a simpler geometry, better suited to MEX processes.

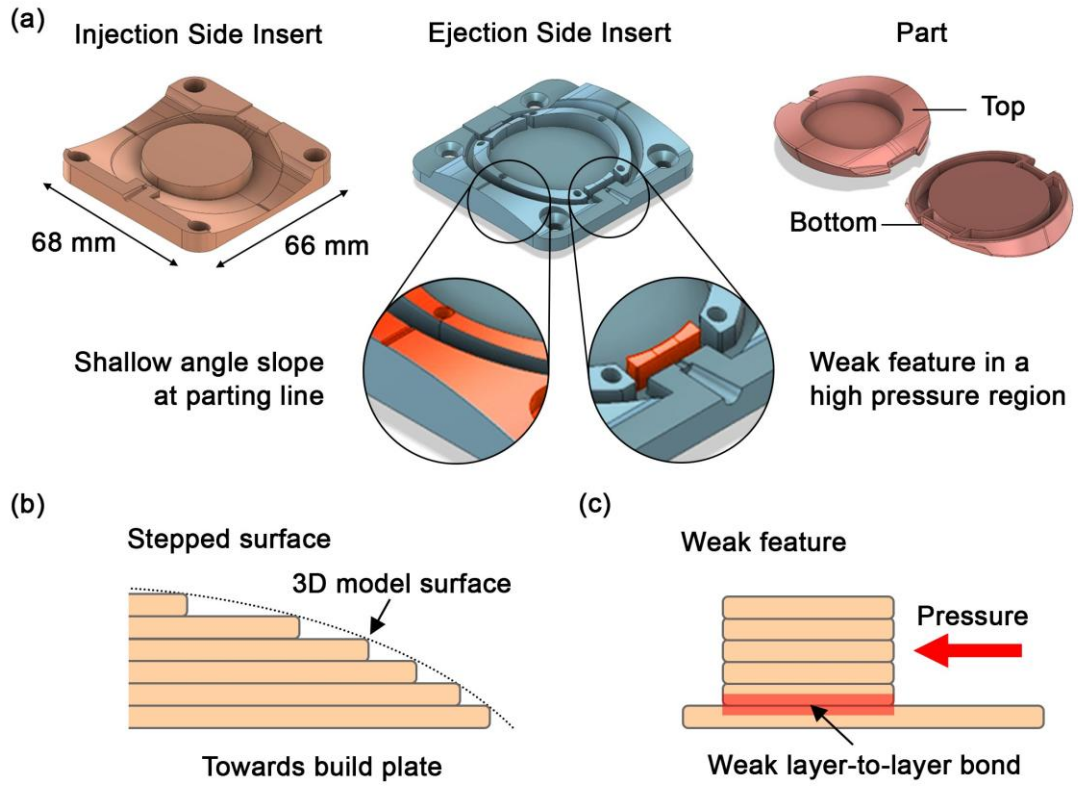

Figure 7.2 - Case study 1 inserts and part (a) with detail of stepped surface (b) and weak features (c).

The second case study, as shown in the 3D render of Figure 7.3, has a flat contact surface instead of the shallow curved surface that existed in case study 1. The change is illustrated further in the 3D render of Figure 7.4 where both case studies are compared side by side. The part itself, nevertheless, still has a shallow curved surface which will be 3D printed as stepped terraces. A flat contact surface should improve the watertightness of the mold which in turn would improve the quality of the parts produced. The part ribbing was also altered to remove the occurrence of weak features, especially in front of the injection point [374]. Finally, the insert was also widened to increase the distance between the fasteners holding the insert to the mold. Both inserts were FGF 3D printed and subsequently tested using injection molding.

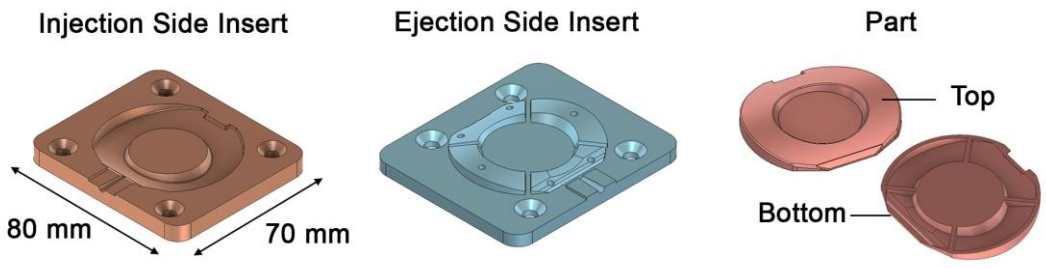

Figure 7.3 - Case study 2 inserts and part

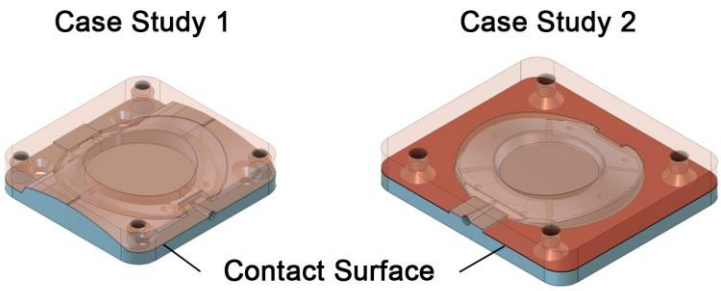

Figure 7.4 - The contact surface for case studies 1 and 2, a crucial factor affecting both the parting line of the injected part and the risk of material leakage.

7.2.2 Material, Equipment and Insert Production

The inserts were 3D printed out of ULTEM 9085 in granulate form, supplied by Ensinger Plastics (Germany). The granules were dried at 140°C for 4 hours prior to 3D printing. Extruder 3 with screw 3 was used to 3D print the inserts. The smaller screw diameter of Extruder 3 compared with that of Extruder 2, provided the higher torque necessary to extrude the more viscous high-performance thermoplastics. The improved nozzle system of Extruder 3 also made general use and testing of this extruder easier and more reliable. ULTEM 9085 has a high processing temperature which makes ease of use considerations all the more important to ensure safety during operation and maintenance.

The inserts were 3D printed flat on a high temperature heated build plate (E3D, United Kingdom), as shown in Figure 7.5. The borosilicate glass build plate was cleaned using acetone and heated to 200°C before each insert was 3D printed. The insert was 3D printed in series i.e. from start to finish before moving on to the next insert. This method ensured the best repeatability for insert production. Two insert pairs were produced per case study as the mold itself has two insert cavities.

The most pertinent process parameters used for 3D printing are listed in Table 7.1. The nozzle and build plate temperature were selected by following the data provided by Sabic technical datasheet [233]. The printing speed was set to 30 mm/s to improve the extruder positional accuracy. At this speed, the corners were well-defined and calibration cubes were found to 3D print accurately. The infill was set to 20% gyroid to minimize production times with 4 outer perimeter, 8 top layers and 5 bottom layers [375]. These settings are commonly used to obtain high printing speeds whilst still maintaining good surface quality and strength. The layer height was set to 0.2 mm which is half of the nozzle diameter of 0.4 mm, to further minimize production time.

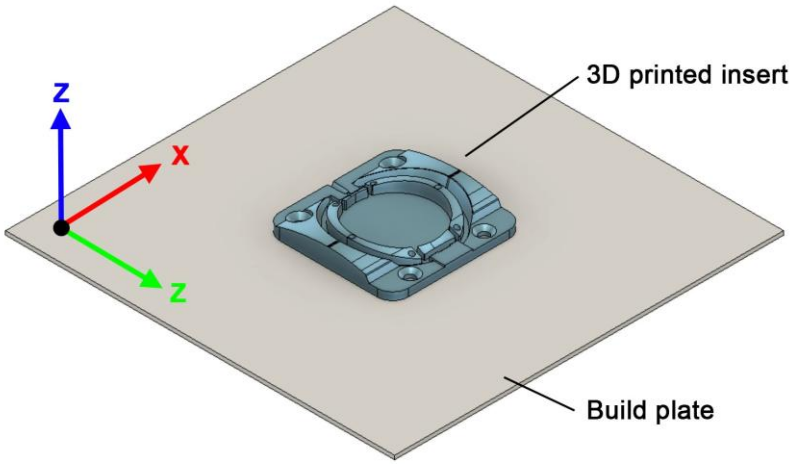

Figure 7.5 – Insert orientation on build plats as set up for 3D printing.

A dynamic mechanical analysis (DMA) using a Mettler Toledo (USA) DMA 1 in a 3-point bending mode was conducted on parallel and perpendicular FGF 3D printed specimens, as shown in Figure 7.6. The 30 x 5 x 2.5 mm specimens were heated from 25°C to 150°C, at 10 µm amplitude at a frequency of 1 Hz, with a 1 N preload, whilst recording the storage modulus (M').

Table 7.1 - FGF 3D printing process parameters.

Parameter	**Value**
Nozzle Temperature	310°C
Build Plate Temperature	200°C
Speed	30 mm/s
Infill Type	Gyroid
Infill Percentage	20%
Perimeter Count	4
Number of Top Layers	8
Number of Bottom Layers	5
Layer Height	0.2 mm
Nozzle Size	0.4 mm

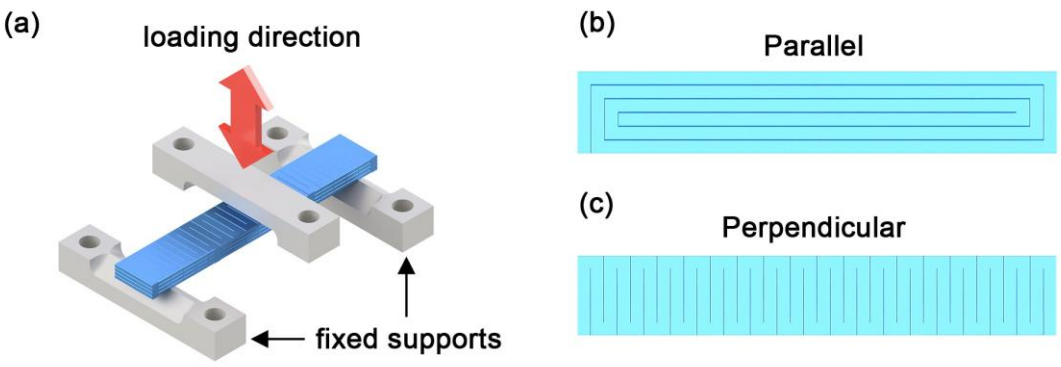

Figure 7.6 - 3-point bending DMA setup (a) with parallel (b) and perpendicular (c) orientation.

7.2.3 Insert and Part Dimensional Analysis

Inserts and subsequent parts produced by the injection molding process had some level of unwanted warpage and geometric inaccuracy imparted to them. The dimensional accuracy of both inserts and parts produced was analyzed by optical profilometry using a Bruker Alicona G5 Infinite Focus (Austria) measurement system. In each case, the surface of a representative specimen was 3D scanned and then the resulting data was compared with the original 3D surface model, as illustrated in the 3D illustration of Figure 7.7. Cloud Compare open-source software [376] was used to carry out the comparison. The ideal and surface models were 3D registered and the difference in between the two models was calculated using the mesh to cloud program available in Cloud Compare.

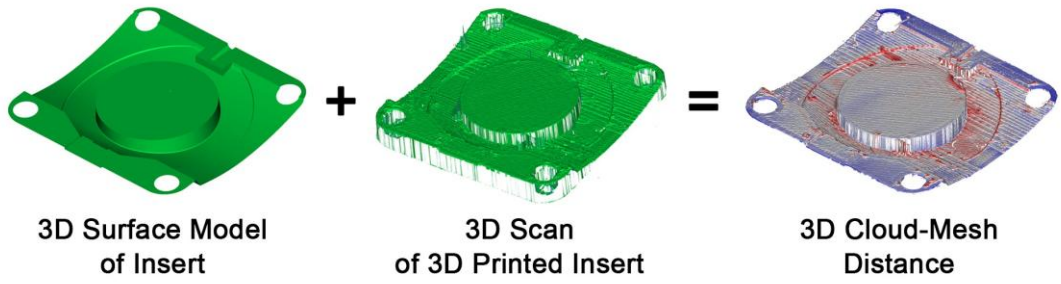

Figure 7.7 - 3D ideal vs scan comparison method.

7.2.4 Simulation and Experimental Injection Molding

The injection molding process was simulated using Autodesk Moldflow Insight 2023 with a standard fill and pack strategy. The simulation predicted the warpage of the molded part after its ejection/demolding from the mold inserts. The simulations results were then compared with the optical profilometry results of the produced parts. The

simulation mold material properties used the values listed in Table 7.2. The cooling time was set to 300s with an isothermal mold temperature of 25°C. Moldflow Insight does not have built-in additive manufacturing functionality for molds nor does it have a dedicated library for AM produced inserts. The values selected were the closest approximation available to the expected properties and attributes of 3D printed UTLEM 9085. This is a limitation of the study whereby future works may focus further on the simulation aspect.

Table 7.2 - Mold material parameters for simulation [233, 377, 378].

Mold	**Value**
Density [233]	1.34 g/cm^3
Specific Heat [377]	50 J/kg.K
Thermal Conductivity [378]	0.25 W/m. K
Coefficient of Thermal Expansion [233]	6.5e-5 1/K
Elastic Modulus [233]	3000 MPa
Poisson Ratio [233]	0.4

The inserts and mold were mounted on a BOY 22E injection molding machine with a 22 mm diameter screw and maximum clamping force of 220 kN. The mold temperature was controlled using a Singer temperature control unit and was kept at 25°C to allow for faster mold cooling. The parts were injection molded using MOPLEN HP501L homopolymer polypropylene (PP) by LyondellBasel (Netherlands) [379] with a barrel temperature set to 190°C. Since the inserts were printed using a low thermal conductive polymer, a long cooling time of about 265 s was used. The injection molding cycles was repeated until the insert failed.

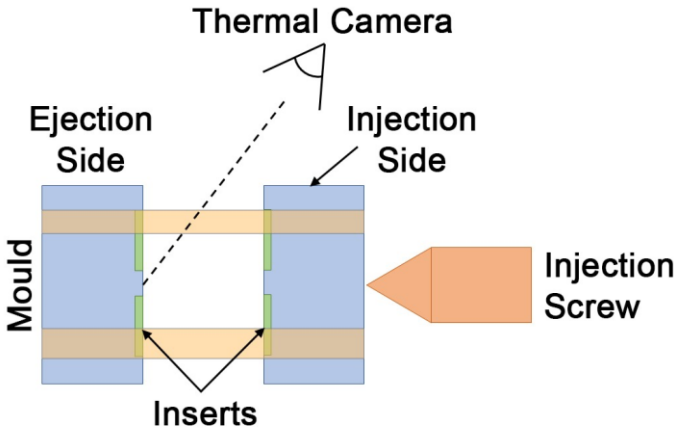

Figure 7.8 - Schematic diagram of thermal camera location with injection molding setup.

The injection molding process was recorded using an E95 thermal camera by Teledyne FLIR LLC (USA) with setup shown in Figure 7.8. The emissivity (ε) of ULTEM 9085 was determined to be 0.85 by heating a specimen in a furnace to 100°C and then measuring the surface temperature using an E95 thermal camera. Temperature measurement was started when the mold began to open after the set cooling time was reached. The thermal camera recorded the mold insert's temperature of the ejection side as they cooled. FLIR Research IR Max was used to process the recorded video and extract the cooling rate at different locations on the inserts.

7.3 Results and Discussion

7.3.1 Insert Production and Evaluation

Production of inserts using FGF was similar to that using a filament system, except for one key aspect, the raw material. ULTEM 9085 as granules poses the same physical properties as its filament counterpart, unless modified. The costs, on the other hand, were not the same. ULTEM 9085 granules costs around 140 €/kg [380], nearly half the price of their filament counterpart (260 €/kg) [381], nearly twice as much as the granulate counterpart. This positions ULTEM9085 granules similarly to the standard gray resin provided by Formlabs (130 €/kg) [382] and even to the high-temperature version (200 €/kg), which are for a Vat polymerization process and would be more suitable for this application [383]. Therefore, FGF using granules offers a cost-effective alternative since the cost of ULTEM 9085 is similar to the cost of the basic resins' materials used for the Vat polymerization process. However, a trade-off exists between the cost and inserts properties. While the Vat polymerization generally boasts a smoother surface finish, FGF excels in material strength and, consequently, inserts' longevity. Production time compared to Vat polymerization might be slower, but the time difference is often negligible.

The inserts produced via FGF were of good apparent quality as shown in Figure 7.9. As expected, the shallow curved surfaces were printed as terraced sections. The terracing effect could have been mitigated by using a smaller layer height or a completely different AM processes such as vat polymerization which could achieve even smaller layer heights, as shown by Vella et al. [362].

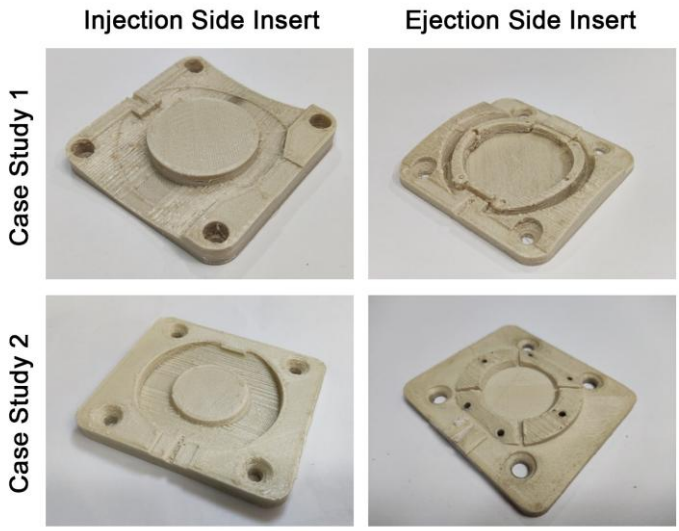

Figure 7.9 - FGF 3D printed ULTEM 9085 inserts for case study 1 and 2, showing injection and ejection side inserts.

The results of the more detailed optical profilometry inspection of case study 1 inserts are shown in Figure 7.10 (a). All inserts were printed with a dimensional difference smaller than ± 0.5 mm. These values were determined using Chebyshev's theorem using a 95% range. This range is intended to remove any trivial strands and artefacts which in practice are easy to remove and are not relevant for the analysis. The range between ± 0.5 and ± 1 mm was greyed out as only strands and other easily removable artefacts are present in this range.

All results showed in Figure 7.10 suggest that the inserts were convexly warped i.e., the internal region is higher than the external region of the inserts. This dimensional study also confirmed that the terraced and shallow curved surfaces were 3D printed with the outer edge following the 3D model surface, as illustrated in Figure 7.2 (b). Therefore, this is a clear indication that case study 1 is not watertight. Similarly, case study 2 is also not watertight since the flat contact/clamping surface area has micro paths which leave gaps in the order of 10^{-1} mm, as shown in the representative profilometry results in Figure 7.11. Such gaps are sufficient to leak polymer melt during injection. This is supported by the work of Menges et al. which defined a recommended vent thickness of 0.015 mm to ensure no leakages for low viscosity materials [384]. It should be noted that during actual injection molding, the inserts were compressed on each other which may cause a certain amount of crushing. Therefore, once the inserts are compressed, the effective gap between the faces might be of a smaller order than as discussed.

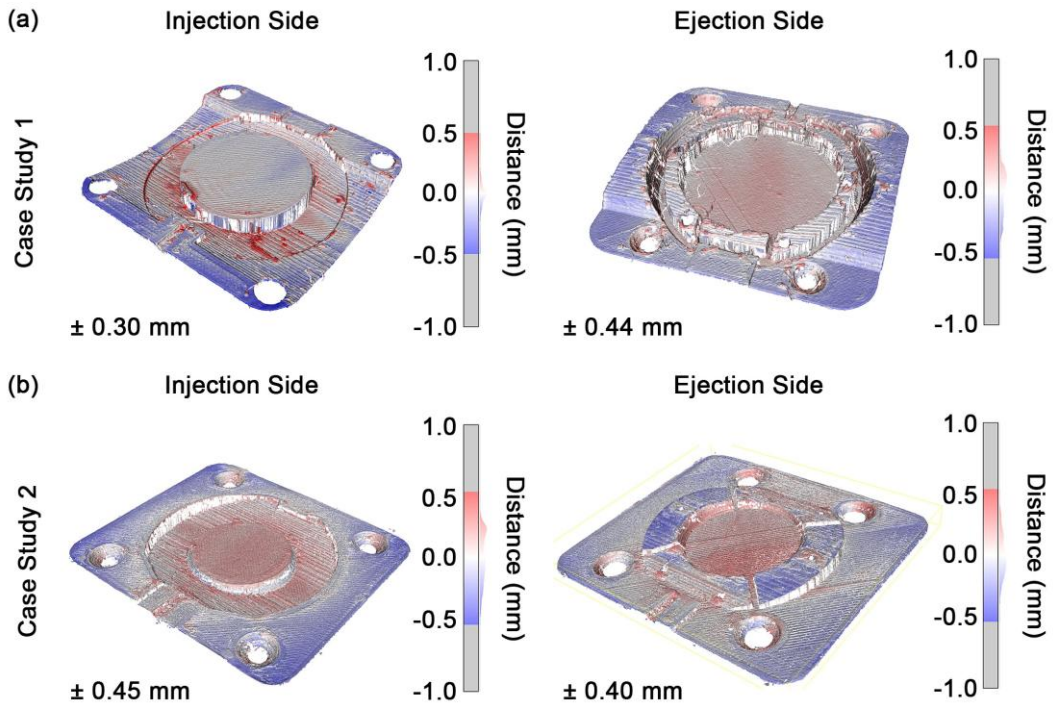

Figure 7.10 - Dimensional fidelity analysis for case study 1 and 2 with 95% displacement value range using Chebyshev's theorem

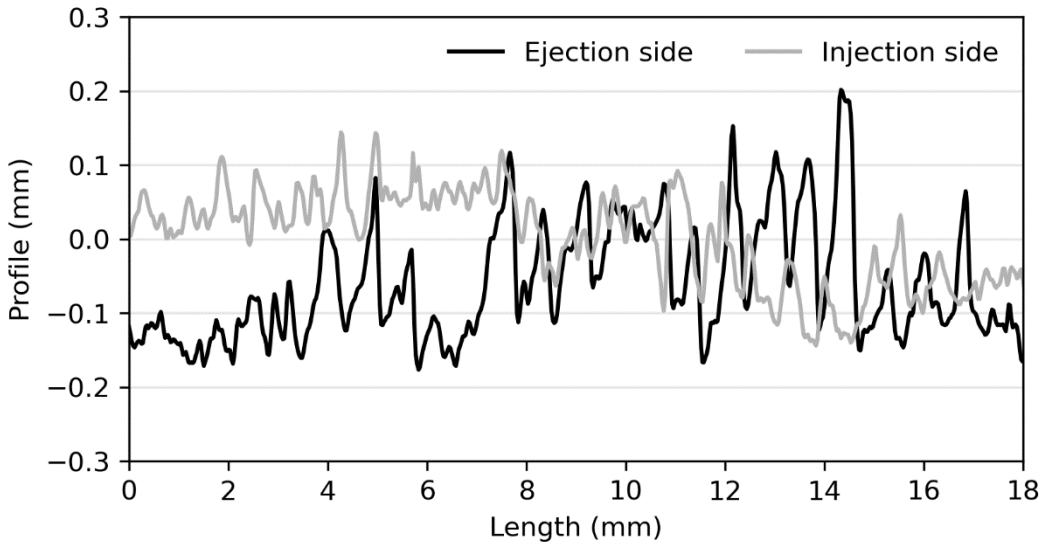

Figure 7.11 - Representative profile of ejection and injection contact surface obtained by optical profilometry.

Apart from the warpage and general lack of watertightness, the 3D printed inserts had areas of over-extrusion and blobbing. Such regions are marked with sharp reds in Figure 7.10, with the most prominent example being the injection side insert of the case study 1. These artefacts are easily removable by hand but leave a blemish upon removal. A

high retraction or screw reversing value of the FGF system may decrease the occurrence of such defects given that they are commonly caused by drooling.

7.3.2 Part Production and Failure Analysis

The case study 1 inserts failed at the first injection molding run. The ejector pins were unable to push out the molded part from the insert. This caused the insert to rip out from the mold as shown in Figure 7.12 with the parts still attached. Since the case study 1 inserts had a large surface area with a rough surface finish, the molten polymer could get ingrained within the layer lines. This led to a strong bond between the molded part and the insert so that the ejector pins failed to demold the molded parts without damaging them and/or the inserts. The large amount of flashes formed, as shown in Figure 7.12, was caused by the blockage of the other cavity which led to an overflow of material.

Figure 7.12 - Ejection side, case study 1, insert failure at first injection run.

In contrast to the case study 1 inserts, the case study 2 inserts did not fail. They were used for 18 molding cycles of which the first 5 cycles were only partially filled, as listed in Table 7.3. These first shots were underfilled to avoid premature insert failure. The shot volume had to be increased beyond the theoretical target part volume, to be able to completely fill the cavity and account for the flashing. This flash formation was attributed to the poor water tightness of the inserts as described previously. The extra material also filled the thin space between the insert and metal cavity plate, which in turn partially stuck the parts to the mold. It was also noted that during injection molding, there was a slow but progressive removal of material from weak points in the ULTEM

9085 inserts, such as at corners or sharp edges. This gradually decreased the structural integrity of the inserts and led to failure.

Table 7.3 - Case study 2 injection molding detailed run description

Trial	Shot volume (c.cm)	Fill rate (estimate)	Damage to Insert
1	10	Partial	None
2	10	Partial	None
3	11.1	Partial	Material removal at outer edge
4	12.4	Partial	Material removal at outer edge
5	14.5	Partial	Material removal at outer edge
6	15.5	Filled	Material removal at outer edge
7	15.5	Filled	Material removal at outer edge
8	15.5	Filled	None
⋮	⋮	⋮	⋮
18	15.5	Filled	None

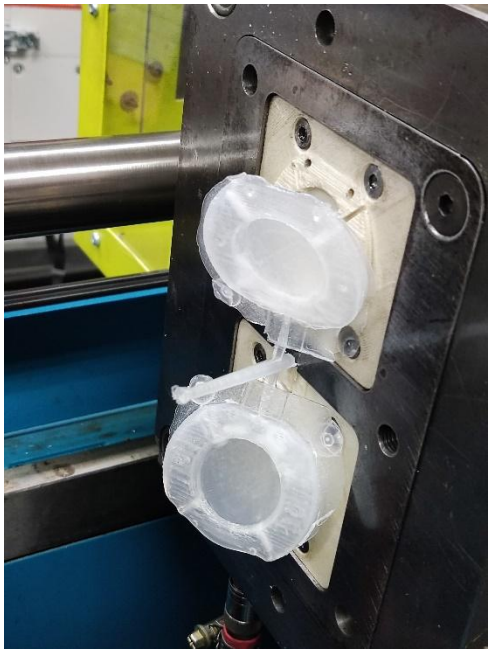

Figure 7.13 - Parts of case study 2 as produced during injection molding. The parts were stuck to the sides of the inserts due to flash, even after ejection

Two types of failures were noted. The first one involves the molten PP being stuck in the features of the inserts, as shown in Figure 7.14 (a). This occurrence did not create any

direct part defects or any instabilities in the molding process. The second type of failure is more relevant as it led to the insert failure. In this case, one of the two injection side inserts failed through interlaminar cracking, as shown in Figure 7.14 (b). Failure was caused by the action of pulling the part out of the injection side insert. This motion created a perpendicular stress on the insert which, as shown by Zaldivar *et al.* and Shelton *at al.,* acts on the weakest direction of FGF 3D printed parts i.e., the inter-layer bond [236, 354].

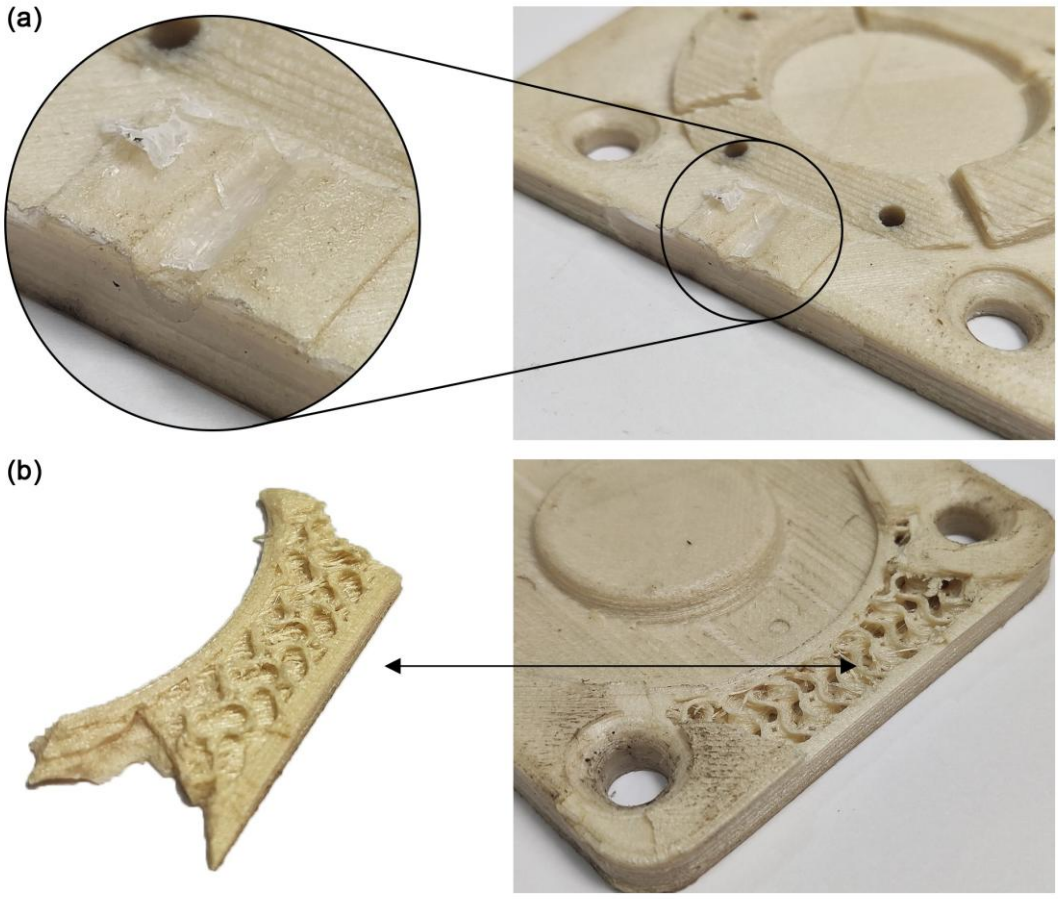

Figure 7.14 - Failure modes of case study 2 inserts

Another contributing factor to the inserts' failure is temperature. The thermal images of the mold are shown in Figure 7.15 with detailed cooling curves illustrated in Figure 7.16. After mold opening, the maximum insert/part temperature was around 130°C which is lower than the heat deflection temperature (HDT) as listed in the material datasheet [233]. Nonetheless, the barrel temperature was set to 190°C and therefore during the initial stages of injection, the inserts could be hotter than the HDT tested at 1.82 MPa and 153°C. This could partly be the cause behind the gradual removal of material from the insert edges after multiple runs in contact with the hot melt. The thermal imaging

also confirmed that when injecting PP in ULTEM 9085 inserts, a long cooling time with an open mold of about 170 s is necessary to get the mold back to room temperature. Without this extra cooling process, the heat accumulation in the inserts could lead to an accelerated degradation.

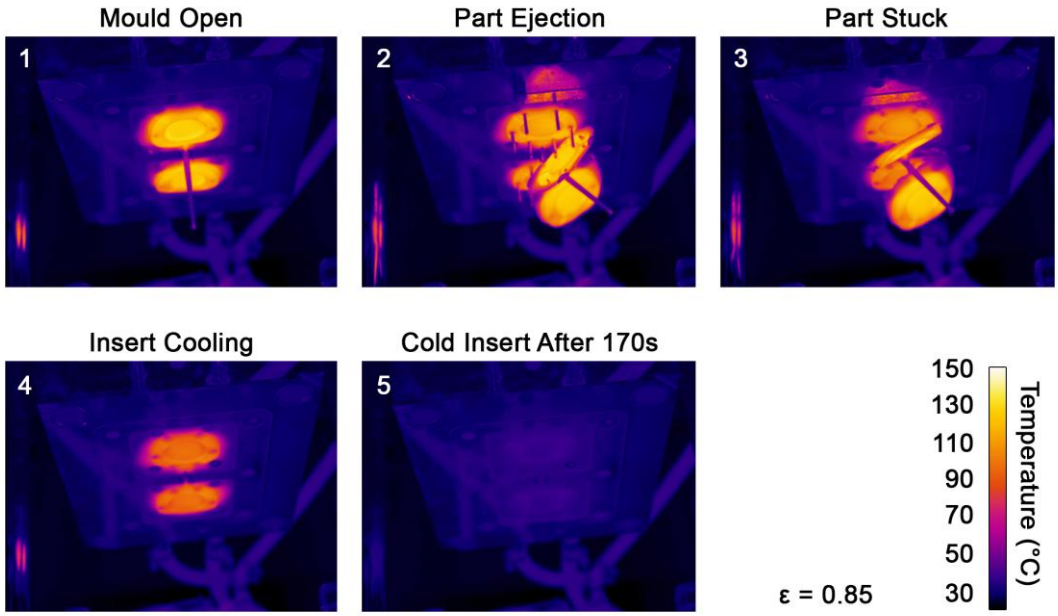

Figure 7.15 – Thermal images of injection molding cycle

The detailed cooling curves shown in Figure 7.16 demonstrate the change in temperature along the ejection side insert. It should be noted that the disturbance seen around the 50 s mark was caused during the removal of the stuck part. The insert heating and cooling process seemed inhomogeneous being highest at the center (1) of the insert and at the rib (4) sections. The part regions adjacent to the ejector pins (3) and insert's edge (5) cooled at a similar rate. Any simulation carried out in future work should therefore account for the cooling effect of ejector pins. The outer region of the insert was completely cool with barely any change registered during the whole cooling cycle. At mold opening, the difference in temperature between the center of the mold and outer regions was about 80°C. Such a large temperature difference may lead to the generation of internal stresses and insert warpage caused by the thermally expanded center of the insert. In this case, ULTEM 9085 is a rather ductile material [233] and can absorb the extra load caused by the constrained, localized thermal expansion. A brittle material could fail prematurely because of differential thermal expansion. Vat polymerization resins tend to be brittle and therefore, when it comes to RTIM, grades which are modified for increased toughness should be used.

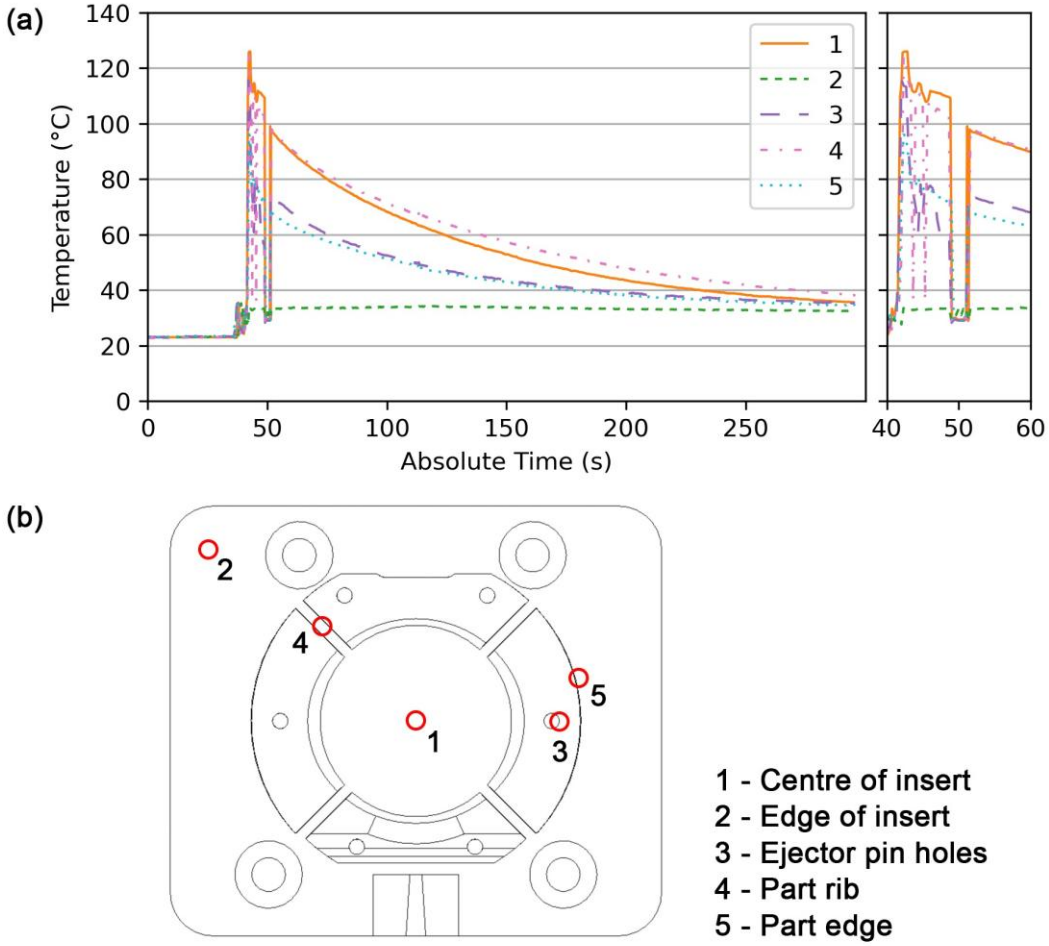

Figure 7.16 - Cooling curves (a) of discrete points on the ejection side insert (b)

The highest temperature recorded by thermal imaging was less than 130°C. In contrast, the DMA results shown in Figure 7.17 indicated that FGF 3D printed ULTEM 9085 maintained a high M' until about 140°C. This compares favorably with vat polymerization material, such as Rigid 10k and HighTemp by Formlabs. The DMA conducted by Moritz et al. demonstrated that whilst these materials tend to have a higher M' at room temperature, it is not maintained over the whole molding temperature range [357]. By 100°C, the resins would have softened significantly whereas the 3D printed ULTEM 9085 maintained similar M' until about 140°C. The DMA results also demonstrate that the perpendicularly printed specimens, representing the strand-to-strand bond, had half the storage modulus of parallelly printed specimens. This further confirms the weak interlayer bond created by the respective printing parameters and setup used in this study, leading to the failure shown in Figure 7.14 (b). Future studies may use a heated chamber coupled with a higher extrusion temperature, to improve the layer-to-layer bond strength and thus improve insert longevity.

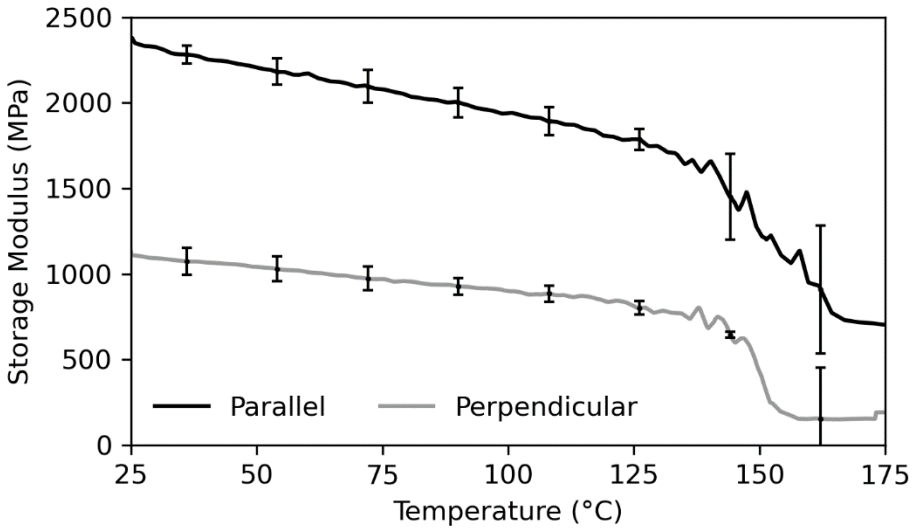

Figure 7.17 - DMA of parallelly and perpendicularly 3D printed ULTEM 9085 (n=3)

7.3.3 Part Quality

A molded part is shown in Figure 7.18, with the extra flash removed as a representative molding result. Most of the PP molded part is slightly transparent which indicates that a large share of PP part was amorphous. Transparency decreased at the ribbed sections of the parts and at the injection point, creating whited-out regions. Such regions are caused by hot spots created by the poor thermal conductivity of ULTEM 9085, which limited heat dissipation. These hotter regions led to a prolonged period of high temperature which allowed for crystallization of the PP that lent the parts a whited-out color at those hot spots only. Apart from changes in color, crystallization also changes mechanical properties and density. In the latter case, the result is a densification of the PP leading to a decrease in volume at the crystallized region, creating differential shrinkage thus warping the part. In general, shrinkage at the crystallized area pulls in the surrounding region causing a bending effect along with localized stresses in the part. Any dimensional tolerances required of the part are therefore compromised unless crystallization is accounted for in the design [385]. Furthermore, the mechanical behavior of the part becomes a complex mix of amorphous and crystalline PP properties further complicated by localized, internal stresses. In this manner the part is inhomogeneous which is undesirable in most application. Localized hot spots may also lead to other undesirable features such as sink marks which are more prevalent for thicker parts [386]. The end result is a part which is not as originally desired and which therefore may not be correct for the intended application.

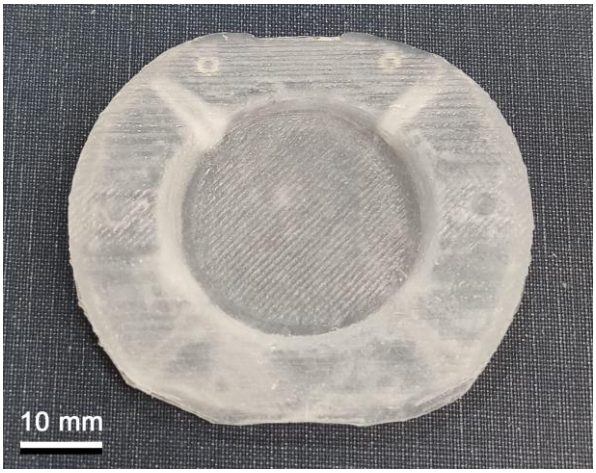

Figure 7.18 - Representative injection molded part with flash removed

All parts produced had a rough surface with a clear imprint of the FGF 3D printed insert strand lines and terraced shallow curves. Optical profilometry results, shown in Figure 7.19 (a), demonstrated that the parts warped with a deviation from the ideal geometry of ± 0.60 mm for 95% of the top surface. The simulated deflection is shown in Figure 7.19 (b). There is a significant discrepancy between the two results as the simulation results grossly underestimating the deflection to about ± 0.2 mm. Furthermore, as seen from top view of actual part deflection in Figure 7.19 (a), the side portions of the part are deflected outwards as opposed to the top and bottom portions. Therefore, the simulated deflection shape did not agree with the actual part deflection.

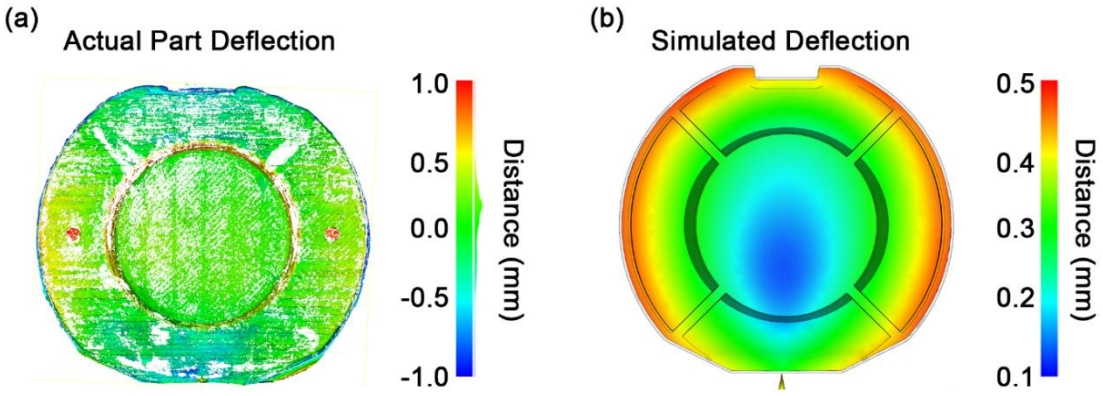

Figure 7.19 - Part warpage as observed using optical profilometry (a) and as predicted by simulation (b)

The discrepancy between these two results may be caused by two aspects. The first concerns the ejection process. Upon mold opening and ejection, the part temperature was the same as that of the insert, reaching 130°C, as shown in Figure 7.15. At that temperature, PP is beyond its softening temperature [379] and therefore the ejection process was conducted on a soft part, with poor shape retention. This effect is expected to increase the part's warpage, beyond what was directly caused by differential

shrinkage. The second is related to insert temperature and the discrepancy in temperature between different points on the insert, as observed by the thermal imaging results of Figure 7.16. The Moldflow simulation with pack and fill strategy may not be optimized for such slow heat transfer and may assume that the insert is at a stable 25°C, leading to the lower deflection. Even if the simulation had correctly calculated the cooling rate, the ejector pin issue would have nullified the warpage results anyway as the simulation can not take that kind of action into account. Therefore, due to the high, undesired but unavoidable flashing of the parts and the related anchorage of part with insert, simulating warpage is not deemed feasible for FGF printed inserts.

7.4 Conclusion

This study demonstrated for the first time that rapid tooling of injection mold inserts manufactured using ULTEM 9085 with an open chamber FGF system are amenable to produce small quantities of molded parts intended for prototyping purposes. In one case, a total of 28 parts were produced until the insert failed. The Moldflow simulation undervalued the amount of part deflection and even the general warpage shape. This was attributed to the slow cooling speed of the inserts and the action of the ejector pins pushing on the molded parts. The part geometry complexity was found to affect the viability of the rapid tooling process. Simpler geometries with a lower amount of anchorage points that are unintentionally created by the layered nature of MEX 3D printing system are better suited for rapid tooling of injection mold inserts. FGF 3D printed inserts are expected to produce parts with flash. A flat surface 3D printed using a 0.4 mm nozzle, will have surface perturbations large enough to allow polymer melt to flow. ULTEM 9085 demonstrated its applicability for RTIM as it maintained a high storage modulus up to 140°C.

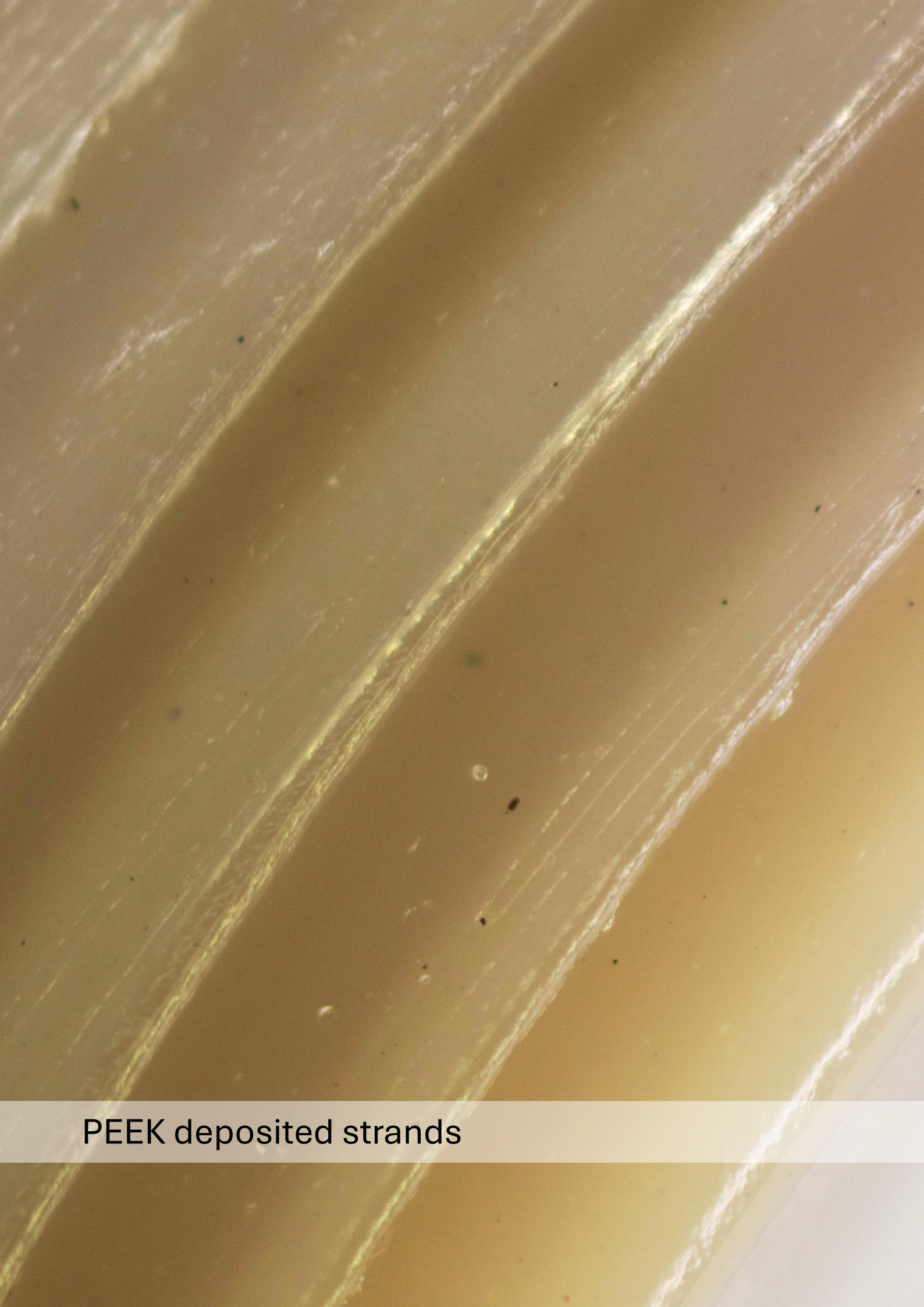

PEEK deposited strands

8 High Performance – Semi-crystalline Thermoplastic

8.1 Introduction

The attractive properties of PEEK have made this material adequate for multiple niche applications despite its high cost. Being able to reliably 3D print such a high performance polymer would allow for affordable low volume, production thus decreasing cost and increasing manufacturing versatility. Apart from conventional product geometries, MEX AM enables the production of components with internal cavities and other such features which are usually impossible or at least very difficult to achieve using traditional manufacturing process. Such possibilities and advantages make PEEK AM attractive despite weaker mechanical properties achieved by MEX compared with extruded and injection moulded PEEK components. As discussed in section 2.3.2.2, page 88, multiple studies have been conducted on PEEK MEX using FFF systems and even a few using FGF systems. However, as determined in section 2.2, small scale FGF 3D printing using PEEK or any other high-performance thermoplastic, has never been achieved before. The purpose of this chapter was to address this research gap whilst also endeavouring to improve the mechanical properties achievable by MEX 3D printing of PEEK.

8.2 Small Class FGF

8.2.1 Introduction

The current literature available on FGF of PEEK is limited to three separate studies conducted by Reddy et al., Tseng et al., and Zhou et al. All of which have developed different FGF 3D printing systems all of which were relatively bulky compared to conventional FFF systems [116, 155, 197]. Each research group has used different screw lengths and diameters. Tseng et al. employed a 14 mm diameter and 280 mm long screw, whereas Zhou et al. used a 12 mm diameter and 206.4 mm long screw. Thus, the screw length to diameter ratio is of 20:1 and 17.2:1 respectively [116, 155]. These long screws ensure that the granulates are well molten and plasticized in the extruder whilst providing enough pressure to push material out of the nozzle.

The main challenge when using large extruders such as done in the available literature is that these systems are relatively bulky so that they may not be applied to a common FFF desktop motion system. In this present work, a small L:D ratio granulate, screw extruder, was used to extrude and eventually 3D print PEEK. The novel screw geometry

made the extruder small enough to mount on a conventional desktop 3D printer. In this manner, the technology was rendered more cost-effective and accessible due to its lower complexity compared to larger FGF systems. To apply the extruder for 3D printing, a calibration process was required, which in this case used a modelling phase to estimate the calibration before using a practical approach. The capabilities of the system were then evaluated to determine the quality and strength of the parts produced using surface roughness, tensile testing and dynamic mechanical analysis (DMA).

8.2.2 Materials and Methods

8.2.2.1 Raw Material

VESTAKEEP L4000G PEEK grade by Evonik, Essen, Germany was provided by Ensinger, Nufringen, Germany and used throughout this study. It is an unfilled PEEK granulate grade [387] with a relatively high viscosity compared to other unfilled PEEK grades.

The raw granulates were characterised using a differential scanning calorimetry (DSC) on a DSC 3+ by Mettler Toledo (Ohio, USA). The DSC was used to obtain the glass transition temperature T_g, melting temperature T_m, and crystallization temperature T_c. The PEEK samples were first heated from room temperature to 400°C, then cooled back to 30°C, and finally heated again to 400°C, with a heating and cooling rate of 10 K/min. The test was carried out twice, and in each case, the sample was kept in a nitrogen atmosphere.

8.2.2.2 Calibration Technique

The study was conducted using Extruder 2, with screw 2 with a 1 mm nozzle. This extruder and screw combination used a 20 mm screw diameter system. Successful extrusion and 3D printing of PEEK using this setup would demonstrate that there is no need to use a large and bulky extruder to 3D printing high performance thermoplastics. The lessons learnt from the results achieved by using this extruder were then critical for the development of Extruder 3 which was primarily intended for AM of high-performance thermoplastics. Extruder 2 was used instead of Extruder 1 due to the ease-of-use improvements that were implemented in Extruder 2. These were critical to enable safe handling of the extruder during use and maintenance.

An extrusion rate test was conducted to evaluate the relationship between screw speed, barrel temperature and extrusion rate for the PEEK grade being used. Apart from the

aforementioned test, the extrusion consistency was also evaluated through extrusion tests at a certain extrusion temperature for a relatively long, cumulative, extrusion period. If the extrusion behaviour did not change by the end of the test, generally the extruder with the current setup is considered as suitable for extrusion and possibly for 3D printing of PEEK.

PEEK was tested from 360°C to 400°C with 10°C increment, using screw speeds of 1, 3, 5, 7 and 9 RPM. For each condition, five specimens as an extrudate were produced each of which was taken at an extrusion time of 1 minute. The specimens were then weighed using an MYA 11.4Y Plus (Poland) micro balance.

The results of the extrusion test were then used to create a linear best fit curve, whose equation was used as part of the process to predict the extrusion multiplier for a given printing speed. To predict the extrusion multiplier, first the theoretical mass flow rate $\dot{M}_t$ is calculated which is required to 3D print a track of material. A 3D printing track is a strand of extruded/deposited material to print a 3D object as shown in Figure 8.1. The theoretical mass flow rate $\dot{M}_t$ is related to the density ρ (g/cm^3), width w (mm), height h (mm), and movement speed v_{xy} (mm/s) as described by Equation 8.1.

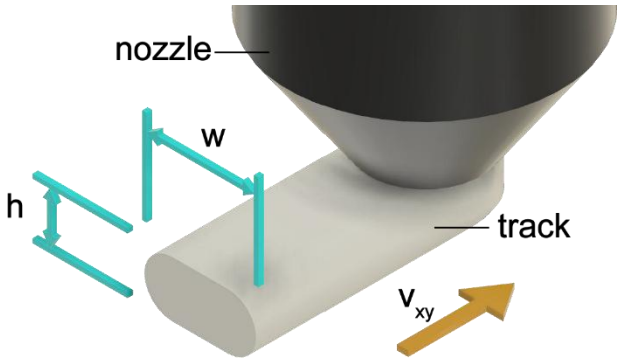

Figure 8.1 - Schematic of track being 3D printed.

$$\dot{M}_t = v_{xy}\left((w-h)h + \pi\left(\frac{h}{2}\right)^2\right)\left(\frac{\rho}{1000}\right) \qquad \textit{Equation 8.1}$$

For an ideal filament extrusion setup with an extrusion multiplier of unity, the rate of extruded material is related to the pseudo extruder speed v_e (mm/s), the theoretical filament diameter d (mm), and density ρ as shown in Equation 8.2. The pseudo extruder speed v_e (mm/s) is then equivalent to the screw rotational speed n_e (RPM) as shown in Equation 8.3.

$$v_e = \frac{4000\dot{M}_t}{\pi d^2 \rho} \qquad \textit{Equation 8.2}$$

$$n_e\ [RPM] = \frac{60v_e}{60} = v_e\ [mm/s]$$ *Equation 8.3*

Therefore, the extrusion multiplier E_m may be predicted by using the results of the extrusion rate testing. The relationship is shown in Equation 8.4, where n_p (RPM) is the screw speed required to provide the extrusion rate necessary to support the required mass flow rate $\dot{M}_t$. The extrusion multiplier was predicted for 3D printing at movement speed v_{xy} of 5 mm/s to 20 mm/s at steps of 5. The predicted extrusion multiplier values were then compared with the actual extrusion multipliers found in practice.

$$E_m = \frac{n_p}{n_e}$$ *Equation 8.4*

To determine the extrusion multiplier empirically, 25 mm sided squares and 10 mm high with a simple internal cross were printed, as shown in the slicing simulation of Figure 8.2. The track width and layer height were set to 1 mm and 0.5 mm respectively. The printing speed was varied from 5 to 20 mm/s with an increment of 5 mm/s. For each speed, 12 calibration cubes were printed with a different extrusion multiplier. The latter was varied between 1 and 3 with an increment of 0.2. Using a digital calliper, the track width at the top layer was measured and 3 readings were taken per sample.

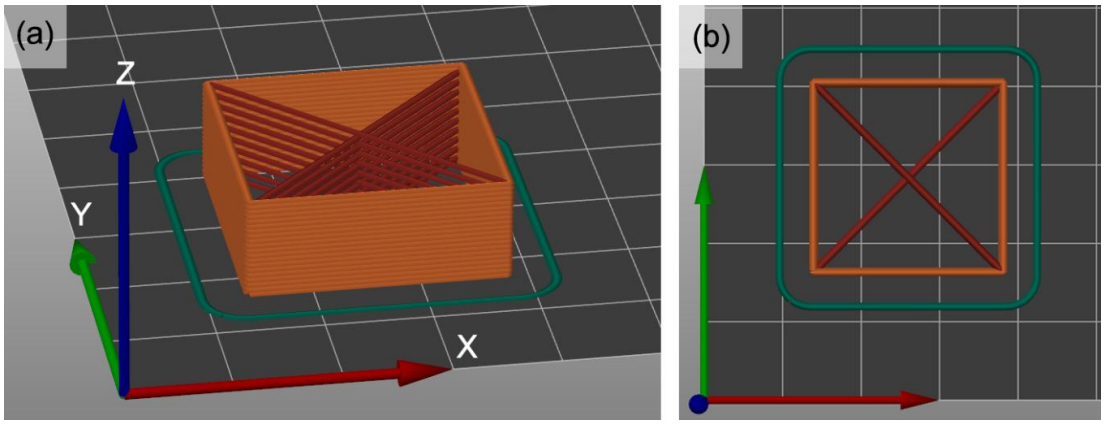

Figure 8.2 - G-CODE simulation of calibration squares with isometric (a) and top (b) views where one grid box is equal to 10 mm

8.2.2.3 3D Printing Method

A simple gear and backup ring were printed to demonstrate the practical capability of the 3D printing setup. The printing speed was set to 15 mm/s throughout with an extrusion multiplier of 2.4, as suggested by the practical calibration results. A 1 mm nozzle was used and the slicer was set with a layer height of 0.5 mm. The top surface of both specimens was analysed using an Infinite Focus by Bruker Alicona and the resulting scan was compared to the ideal, CAD 3D model profile of each specimen.

8.2.2.4 Characterisation of 3D Printed Parts

Optical profilometry using Infinite Focus by Bruker Alicona was used to study the effect of extrusion multiplier and printing speed on the surface roughness of 3D printed PEEK objects. For this test a cuboid with 25 mm sided base and 10 mm height, was printed using different process parameters. The printing speeds were 5, 10 and 15 mm/s, whereas the extrusion multiplier was decreased and increased by 20% for each speed iteration. Cuboids were also printed using the correct extrusion multiplier to compare with the over and under extruded prints. The top surface of the 3D printed parts was analysed using ten roughness paths taken perpendicular to the 3D printed tracks so as to analyse the highest roughness. The cuboids were printed with a 20% gyroid fill, 3 top layers, and 2 bottom layers, using a 0.5 mm layer height.

A dynamic mechanical analysis (DMA) and tensile tests were carried out on the respective specimens printed out of the VESTAKEEP L4000G. In the DMA test, the specimens are subjected to a sinusoidal deformation to characterize the material's mechanical properties such as storage modulus (E') and tan (δ) as a function of time, temperature, and frequency. The storage modulus is the dynamic equivalent of young's modulus as it is a measure of the energy required to distort a specimen. Conversely, the loss modulus (E") is a measure of the energy lost (dissipated) during the sinusoidal deformation of the specimen. Tan (δ) is the ratio between the loss and storage modulus, i.e. the higher the value, the more viscous the material. The glass transition T_g can be determined by the sudden change in storage and loss modulus or at the peak of tan (δ), which indicates the material transition from a brittle glassy to flexible rubbery state.

The DMA tests were conducted using a frequency of 1 Hz. The suitable amplitude of 5 µm was determined in preliminary tests by using an amplitude sweep test at 25°C. Two DMA samples with dimensions of 5x2x15 mm (WxHxL) were printed flat on the build plate at 15 mm/s printing speed and using the empirical correct extrusion multiplier.

The tensile test was conducted on 3D printed specimens with the goal of evaluating the basic behaviour of the 3D printed PEEK. The test was carried out using a M350 20CT tensile tester by Testometric, United Kingdom using an LC50, 500 N load cell. Five specimens were printed horizontally using rectilinear strands as shown in Figure 8.3. The tensile test geometry follows the ASTM D 412-06a standard, similar to type C. However, this standard is not meant for rigid 3D printed polymers but given the warpage often experienced with open chamber PEEK 3D printing, it was deemed that a smaller

specimen would be easier to print. The test was conducted using a testing speed of 5 mm/min with a 1 N preload.

Figure 8.3 - Tensile test specimen (a) G-code simulation and (b) 3D printed.

All specimens were printed at 360°C using 10 mm/s printing speed, a 1 mm nozzle, and a 3.5 extrusion multiplier which is intentionally set for over-extrusion. This was done with the aim of minimizing pores and improving mechanical properties. A rectilinear infill was used without any perimeter walls as this allowed for straight strands to be deposited with minimal time interval between subsequent strands. In this manner the strands would retain as much heat energy as possible till the next strand would be deposited, aiming at improvement of the inter-layer bonding strength. If a perimetric approach had been chosen, the cooling time would have been higher, leading to a poorer inter-layer strength.

8.2.3 Results

8.2.3.1 Differential Scanning Calorimetry (DSC)

The VESTAKEEP L4000G PEEK was found to have a Tm of about 340°C, a Tg of about 146°C and a Tc of 290°C, as shown in Figure 8.4 which are common with most PEEK grades. The high crystallization temperature Tc of 290°C may cause issues with poor crystallization behaviour during 3D printing due to the low ambient temperature in an open chamber 3D printing.

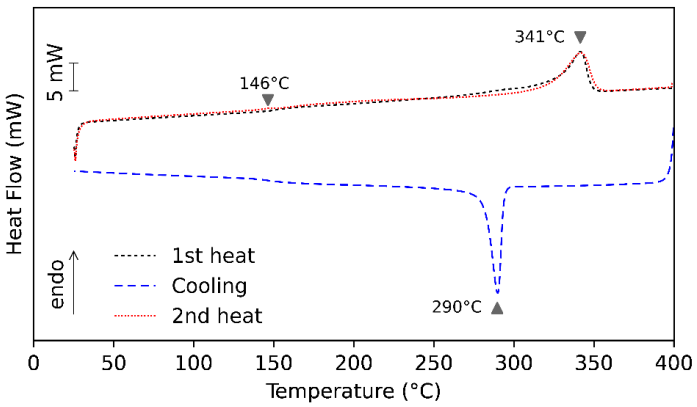

Figure 8.4 - DSC graph of PEEK granulate (VESTAKEEP L4000G).

8.2.3.2 Extrusion Process Analysis

The FGF system extruded reliably even at the lowest temperature (360°C). Increasing the barrel temperature did not have any clear effect on the extrusion rate, as shown in Figure 8.5. On the other hand, it was noticed that the extrusion rate started to decrease with time when the extruder was tested at 370°C and 380°C. The effect was significantly faster when the barrel temperature was set to 390°C and 400°C. For this reason, performing an extrusion rate test at these temperatures was deemed erroneous. Increasing the screw speed beyond 9 RPM would require higher torques which exceed the maximum torque of the stepper motor and cause lost steps. The recorded extrusion rate for a given screw speed when extruding at 360°C was fitted using a linear fit which produced Equation 8.5.

$$\dot{M}_f = \frac{1}{10000}(9n_p + 20) \quad \rightarrow \quad n_p = \frac{10000\dot{M}_f - 20}{9}$$

Equation 8.5

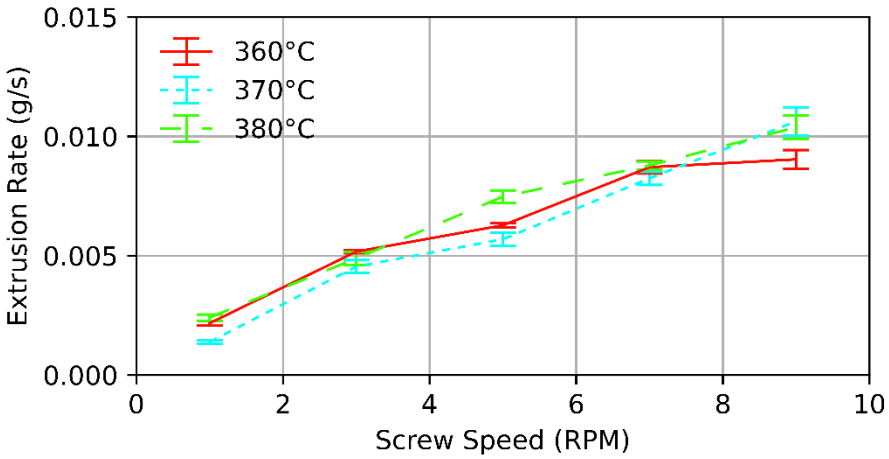

Figure 8.5 - Extrusion rate vs screw speed and printing temperature of VESTAKEEP L4000G using a 1 mm nozzle.

8.2.3.3 Extruder Calibration

The measured calibration results are shown in the top graph of Figure 8.6, whereas the bottom graph shows the screw speed required to achieve the correct extrusion multiplier for a given 3D printing speed. Both the measured and predicted results showed an exponential relationship between the increase in extrusion multiplier and printing speed. The predicted extrusion multiplier shifted towards higher values, compared to the measured one, with the exception of 5 mm/s printing speed. At 20 mm/s speed, the correct extrusion multiplier is above the ideal operation range of the stepper motor.

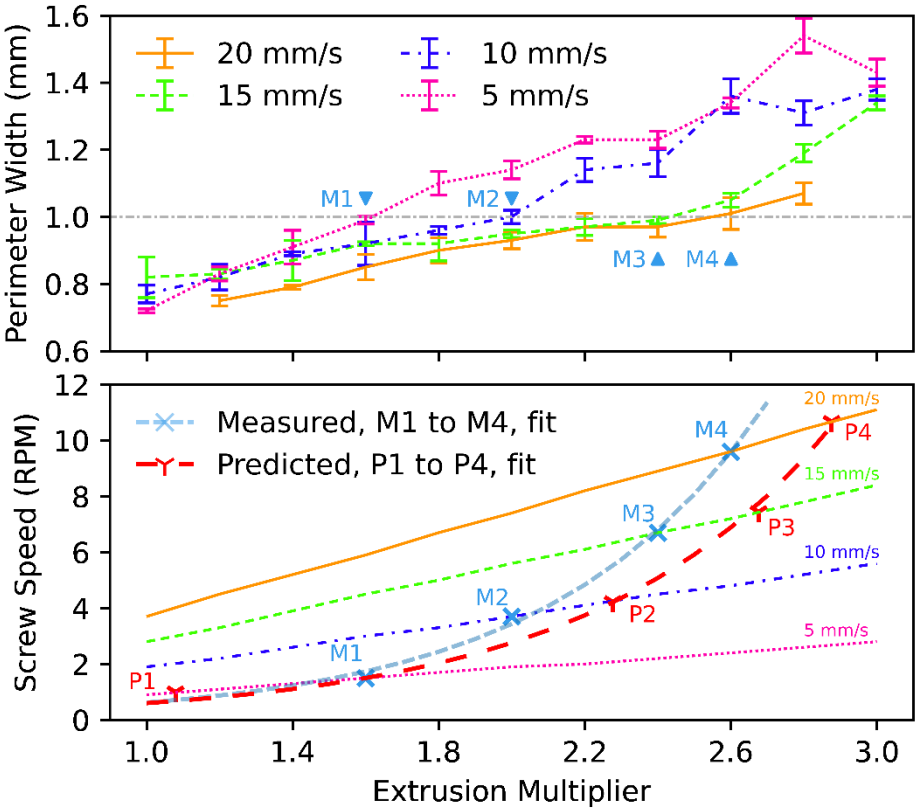

Figure 8.6 - Top plots measured extruded perimeter width for a given extrusion multiplier with target width of 1 mm, using different printing speeds. Bottom plots the predicted (P1 to P4) and measured (M1 to M4) extrusion multiplier for each printing speed vs the screw speed along with the required screw speed for a given printing speed and extrusion multiplier

8.2.3.4 Surface Roughness

The optical analysis focused on three features as shown in Figure 8.7: the average roughness (Ra), maximum profile height (Pz), and Waviness average (Wa). The values of Ra, Pz and Wa for the side of the specimen did not show any clear trend, neither for changes in speed nor for over and under extrusion. The top side showed a greater

tendency of increased roughness at high values when over- or under-extruding. The printing speed did not show any clear relationship with changes in Ra, Pz, and Wa.

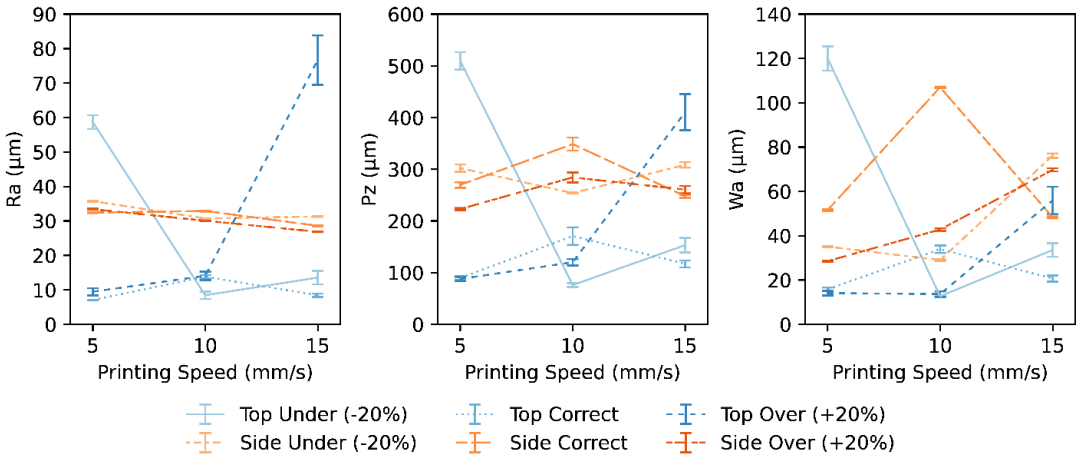

Figure 8.7 - Roughness average (Ra), maximum profile height (Pz) and waviness average (Wa) of top and side faces for under-, correct-, and over-extruded cuboid specimens (n=5). Error bars illustrate the standard error.

As shown in Figure 8.8, the specimens printed with the calibrated extrusion multiplier had a lower surface height range, i.e. overall a better roughness and more uniform surface. At higher printing speeds, the difference between under- and over-extruded specimens becomes more distinct. Under-extruded specimens tend to have gaps in the top layer, which in Figure 8.8 can be seen as sharp changes in colour. Over-extruded specimens create a wavy surface as the nozzle ploughs through the deposited material.

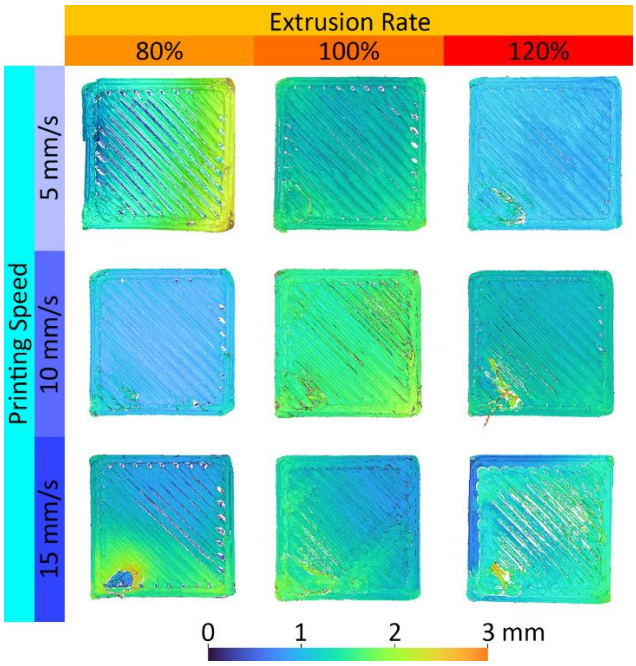

Figure 8.8 - Top view with colour height map of 3D printed samples, using different print speeds for 80% under-, 120% over-, and correct-extrusion multiplier.

8.2.3.5 3D Printed Objects

The 3D printed gear and back-up ring are shown in Figure 8.9. The 3D printed parts were similar to the sliced simulation. As seen in Figure 8.9 (c) and (d), both parts were very similar to the 3D model profile. The gear had extra rounded roots, compared to the 3D model, which was attributed to the low printing resolution of a 1 mm nozzle. The crystallinity of the PEEK decreased towards the top of the printed gear, as shown in the semi-transparent teeth of the gear in Figure 8.9 (b) [388]. Nonetheless the centre of the gear becomes crystalline indicated by the light beige colour. The back-up ring printed rather smooth and was somewhat pliable.

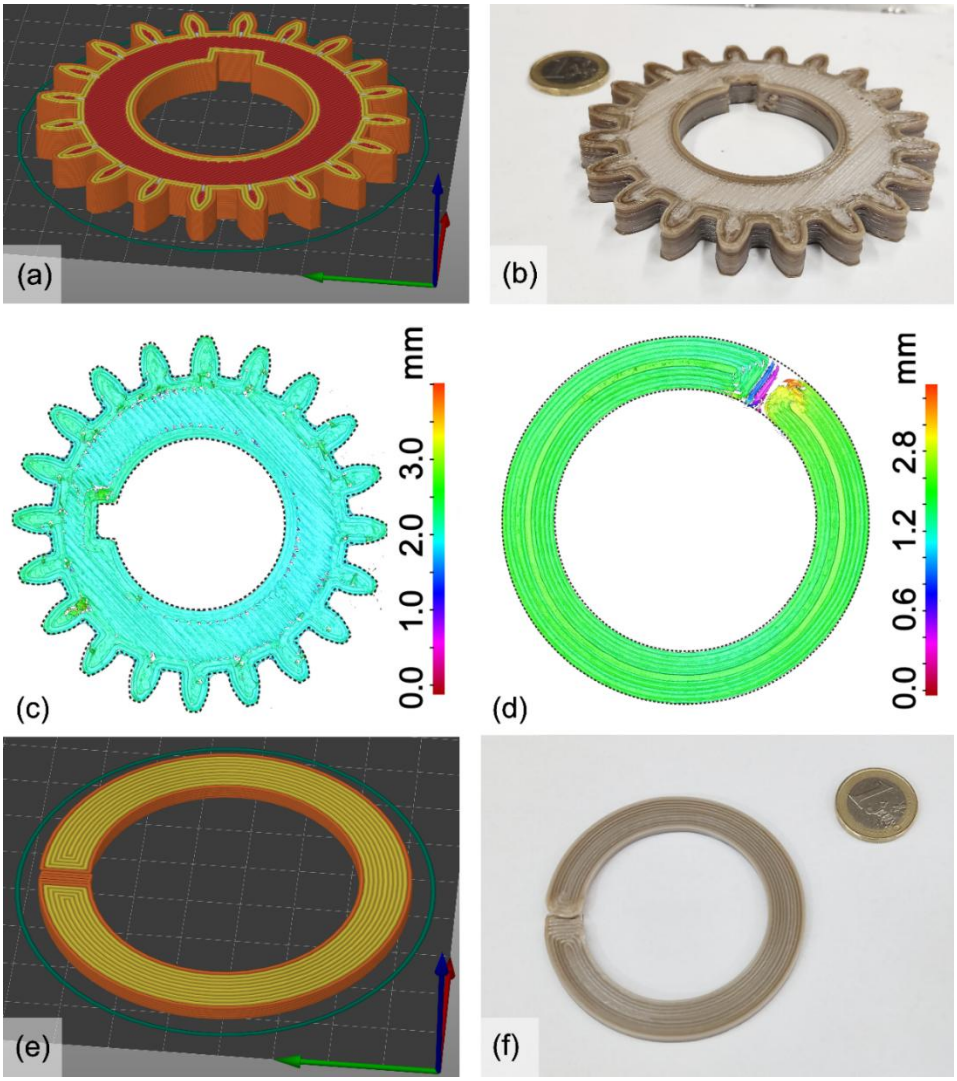

Figure 8.9 – Simulation using Prusa Slicer (a, e), 3D printed part (b, f), and top view with colour height map and contour of ideal profile using black dashed line (c, d) of gear (a – c) and back-up ring (d – f).

8.2.3.6 Mechanical Properties

Visual inspection of the FGF specimens indicated a good print quality. However, the surface finish and the tensile testing results are akin to FFF printed objects. All of the samples tested started to crack at the onset of pulling. The initial cracking predominantly occurred between the extruded strands (inter-strand cracking), which is continued with the inter-layer cracking. As shown in the engineering stress-strain curve in Figure 8.10 the result is jagged with multiple sawtooth peaks as a result of inter-strand cracking, whereby the PEEK strands with the weakest inter-strand bonding failed first. Subsequently the isolated strands failed separately leading to sharp changes in stress-strain behaviour. For example, the first failure occurs at 9.2% strain at which there is a sharp decrease in stress. At higher strains, the specimens would be loaded on few strands therefore the actual area under load is decreased. These strands would stretch, neck and fail independently leading to high strain, low stress, and jagged curves as seen in Figure 8.10 from 12% strain onwards. This phenomenon is not normally encounter with injection moulded or extruder specimens and therefore the tensile modulus and stress at yield are expected to be different.

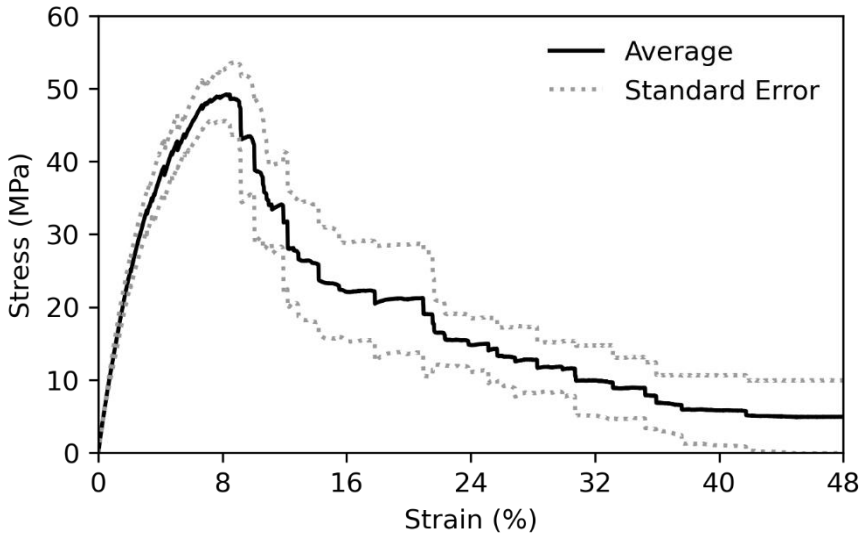

Figure 8.10 - Average tensile test result with standard error of 3D printed VESTAKEEP L4000G PEEK (n=5).

The tensile modulus reached a value of 15.5 MPa which is less than 1% of the datasheet value of 3600 MPa [1]. The ultimate yield stress and strain were found to be 49.2 ± 3.7 MPa and 8.3% respectively. When compared to the values from the datasheets, the ultimate tensile strength (at yield) reached around 48% (of 93.8 MPa), whereas the strain at yield is 66% higher than the one of injection moulded PEEK (5%) [1].

Apart from the tensile properties at room temperature, the dynamics stiffness results obtained from the DMA tests are shown in Figure 8.11. The 3D printed PEEK maintains a stable storage modulus, starting at 2.3 GPa at 25°C and ending at 2.0 GPa at 150°C which is the start of the glass transition temperature (T_g). Beyond T_g, the material consequently transitioned from a stiff to elastic state, which is indicated by the significant drop of the storage modulus (E').

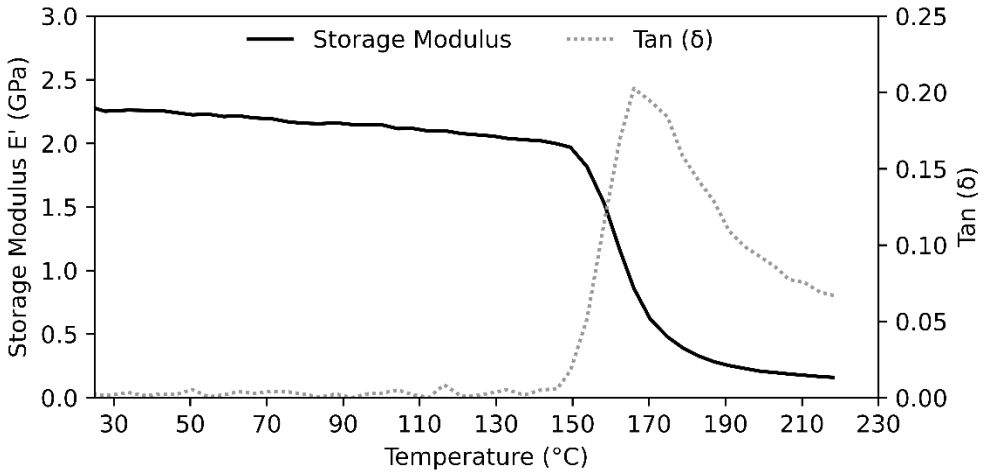

Figure 8.11 - Representative results of DMA of VESTAKEEP L4000G PEEK showing storage modulus E' and tan (δ) against temperature.

8.2.4 Discussion

8.2.4.1 A Non-Linear Process

Screw/granulate additive manufacturing is not a linear process **[155, 389]**. This means that the slicing software designed for filament-fed (FFF) systems are technically not ideal for screw/granulate extruders as the FFF slicing software assume a linear, one-to-one relationship between filament feed rate and extrusion rate. The two calibration methods presented in this work concur that not only does the screw speed increase with printing speed, but also that the increase is non-linear. As shown in Figure 8.6 increasing the printing speed would involve an exponential increase in extrusion multiplier. The reason behind this exponential relationship was not studied in this work, nonetheless, the authors speculates that it is related to the change in viscosity with relation to temperature and shear rate of the molten material (VESTAKEEP L4000G). With a higher screw speed (RPM), the extrusion rate should be higher since a greater pressure is generated in front of the screw tip and more material is pushed through the 1 mm nozzle orifice. However, in this case, the greater the pressure, the greater the amount of energy

is absorbed in the material due to its high viscous component, rather than causing extrusion. This effect is expected to be more pronounced with smaller nozzles and higher extrusion rates.

FFF slicing software do not have the option to relate printing with extrusion multiplier. Implementing such a feature would allow the use of an equation describing the necessary change in extrusion multiplier with speed for the specific FGF setup used, such as Equation 8.6. This equation was obtained by fitting the exponential data shown in Figure 8.6, to attain the relationship between the printing speed and extrusion multiplier.

$$v_{xy} = (0.716)e^{1.28E_m} \quad \rightarrow \quad E_m = (0.782)ln(1.40v_{xy}) \qquad \textit{Equation 8.6}$$

The discrepancy noted between the predicted and measured results shown in Figure 8.6 may be attributed to errors in extrusion rate testing as shown in Figure 8.5. It seems that the extrusion rate tests were under valuing the sample weight which caused the higher values of the predicted extrusion multiplier (P2-P4). On the other hand, the predicted extrusion multiplier for the printing speed of 5 mm/s (P1) was lower than the actual value (M1). This may occur only when printing is carried out at the low screw speed regions as it is also evident from in Figure 8.6. These low printing speeds could increase the actual error of the extrusion rate test due to the small amount of extruded material. It is assumed that the extrusion time of 1 minute per test result was likely too low. A more practical approach would be to take only two different screw speeds but the extrusion time is increased by a magnitude.

8.2.4.2 3D Printed Part Quality

Using a 1 mm nozzle has its positives and negatives. On one hand, using such a nozzle significantly decreases the printing time due to the larger volume of material being deposited compared to smaller nozzles, by virtue of size alone. On the other hand, the 3D printing resolution suffers dramatically, e.g. even the relatively large gear as shown in Figure 8.9 (b-c) had rounded roots since the inner corners were too sharp to properly resolve.

Apart from the poor resolution, another relevant issue is the surface roughness, the results of which are shown in Figure 8.7. The surface roughness provided by a 1 mm nozzle was expected to be inferior to that provided by smaller nozzles, especially when combined with a high layer height of 0.5 mm. The average top surface roughness of the

printed specimen with a correct extrusion multiplier was of 9.77 ± 1.01 µm Ra which was in agreement with ones found in similar studies [390–394] when using a large nozzle diameter and layer height. On the other hand, the side surface roughness was significantly higher, namely 31.31 ± 0.63 µm Ra. Although this is the first study to use a 1 mm nozzle, the results were however rather similar to those of the 0.8 mm nozzle reported by Wang et al. of about 8 µm and 20 µm for top and side surfaces respectively [257]. The lower values reported by Wang et al. were expected considering the lower nozzle size which allows for an improved 3D printing resolution.

Referring back to the 3D printed gear and back-up ring, the surface z height map, shown in Figure 8.9 (c) and (f), were similar to those of correctly extruded samples shown in Figure 8.8. The parts obtained the common surface texture of filament 3D printed parts. This study showed that using a small screw with a novel and low L:D ratio of 4.25:1, and thus, a relatively low weight, one can achieve a good quality of 3D printed parts using PEEK in granulate form.

8.2.4.3 Mechanical Properties and Crystallinity

The 3D printed gear shown in Figure 8.9 (b) was not crystalline throughout, as some regions had a semi-transparent dark brown colour, characteristic of amorphous PEEK. This is caused by the quenching or rapid cooling of the extruded strands, which inhibits the formation of crystals. This phenomenon is part of the underlying cause behind the poor mechanical performance of the 3D printed specimens PEEK parts.

The rapid cooling rate and the ensuing crystallinity or lack thereof is related to crystallisation temperature T_c. As shown in Figure 8.4, the DSC recorded a T_c of 290°C which is higher than the 170°C reported by Collinson et al. using Ketaspire PEEK which was specially formulated for 3D printing [395]. This higher T_c of VESTAKEEP L4000G makes it more difficult to print parts with a crystallinity degree since a heating chamber with a much higher heating temperature is required. A good example for this is the 3D printed gear as shown in Figure 8.9 (b) is a good example. As the 3D print gets further away from the bed, the strength of the radiated heated created by the heated bed starts to decrease. This leads to an increase in extrudate quenching and the crystallinity of the PEEK starts to decrease.

Despite the poor chamber temperature the DMA results obtained are comparable to those in a study conducted by Wu et al. in which the DMA test was conducted on

extruded VESTAKEEP L4000G sheets [387]. The specimens started to soften at 148°C and by 179°C the storage modulus decreased from 100 to 19.8 GPa. The storage modulus of the FGF specimens is about 14% lower which may be attributed to inter-strand porosity within the 3D printed specimen. The discrepancy in DMA results between 3D printed and extruded sheet PEEK [387] is relatively low and expected given the porous nature of MEX 3D printing processes.

When comparing the tensile test results between FGF printed and injection moulded PEEK parts (PEEK datasheet), the discrepancy is more significant. This indicates a fundamental difference in the inter-strand bonding behaviour that occurred whilst 3D printing the DMA and tensile specimens. In the case of the DMA specimens, the previously deposited strands would be at a higher temperature and therefore the new strands being bonded to them are quenched less and a better bond may be formed.

The PEEK tensile testing results were characterised by poor inter-strand and inter-layer bonding, which is caused by the rapid cooling of the strands. The discrepancy in tensile properties can be attributed to the early onsets of inter-strand cracking leading to an uneven tensile force loading of the cracked or separated strands. In this manner, the loaded surface area became lower, i.e. decreasing the effective area and thus weakening the material. A stronger inter-strand bonding would improve the mechanical properties. Future work may consider the effects of higher extrusion temperature and the application of different grades of PEEK with possibly different molecular weight, aiming at the improvement of the inter-strand bonding strength.

The work by Tseng et al. on a granulate extruder for PEEK obtained relatively similar results with a slightly higher maximum stress achieved [155]. There are two major differences worth to mention that are the screw size and the heated printing chamber. Tseng et al. used a 280 mm long screw which is about 3.3 times longer than used in this work. The screw extruder was held fixed due to its high weight, and instead, the printing bed was moved. Secondly, the system also had two infrared lamps to heat up the 3D printing environment. This is intended to improve the inter-layer bonding strength, nevertheless, the ultimate tensile strength achieved was around 60 MPa which is still significantly lower than the datasheet value. Similar to this study, the authors also reported a poor inter-layer bonding strength. Therefore, it may be concluded that the results achieved by this work are a clear improvement over the similar studies in spite of the smaller and lighter extruder.

Involving any method to heat the printing chamber would be useful for future studies on attaining a higher inter-strand and inter-layer bonding strength and thus higher mechanical properties of FGF PEEK parts. A higher strength would allow for wider applicability of 3D printed PEEK, especially in load bearing applications at relatively high service temperatures.

8.2.5 Conclusion

This study demonstrated that PEEK can be extruded, and 3D printed using a 4.25:1 L:D ratio screw extruder system. The observed extrusion multiplier required for a correct extrusion rate increased exponentially with higher printing speeds. When assessing the quality of the FGF 3D printed parts, the roughness produced using a 1 mm nozzle and a 0.5 mm layer height was in accordance with recent studies on FFF PEEK 3D printing using 0.8 mm nozzles. Therefore, with adequate calibration, an FGF system performs similar to an FFF system even when it comes to PEEK 3D printing. When using the correct extrusion multiplier for speeds of 5 mm/s to 15 mm/s, there was no significant relationship between the printing speed and surface Ra, Pz, and Wa results. Over- and under-extrusion resulted in an inferior quality of the top surface but it did not significantly affect the side wall quality of the 3D printed parts. Apart from surface evaluation, the DSC and DMA results showed that VESTAKEEP L4000G has a T_c of 290°C which leads to the creation of amorphous regions when 3D printing at 360°C. Furthermore, the PEEK started to soften at 148°C and by 179°C the storage modulus decreased from 100 to 19.8 GPa. The ultimate tensile strength achieved (49 MPa) is similar to the ones found in literature on FFF 3D printing of PEEK in an open chamber.

8.3 Improving Layer Bond Strength

8.3.1 Introduction

The previous study managed to achieve only 50 MPa ultimate tensile strength in an open chamber, whereas Tseng *et al.* achieved 98 MPa when printing at 390°C in an infrared irradiated workspace. When using a lower extruder temperature of 370°C, the group achieved an ultimate tensile strength of about 65 MPa [155]. Decreasing extruder temperature led to a decrease in ultimate tensile strength. This may be part of the reason behind the low 50 MPa ultimate tensile strength achieved in the study presented in section 8.2 as in that case the extruder temperature was even lower at 360°C. Another contributing factor is the material grade used and its associated molecular weight. It is possible that using a high molecular weight grade may lead to a stiffer material. This aspect will be analysed in the present study.

To better understand the changes in 3D printed part strength, it is best to evaluate the weakest point i.e., the interlayer bond strength. Neither the study presented in section 8.2 or the study by Tseng *et al.* [155] evaluated the interlayer strength. Interlayer and along layer mechanical properties are generally tested in tensile mode. Using this technique, only a small cross-sectional area is used to represent the general 3D printing geometry. This is an undesirable simplification of all the deposition techniques available to the MEX 3D printing world. Some shear testing techniques do not suffer from this problem but there are only a few studies concerning shear properties of MEX 3D printed PEEK [396–401], and none for those obtained by FGF. This gap limits mechanical modelling of PEEK components, fabricated by MEX AM systems. The studies by Zhou et al. and Luo et al. showed that shear strength is improved by the same methods which improve tensile strength. Specifically, increasing nozzle and build plate temperature [396] and applying layer heating [397, 400], increased shear strength. Alteration in the extrudate cooling rate are known to alter the crystallinity of PEEK [287, 402–404]. Crystallinity is also related to molecular weight, as shown by Chivers et al., a lower molecular weight leads to a higher degree of crystallinity [405]. Therefore, both processing conditions and PEEK grade are important contributors toward the final AM part strength. Using shear testing could not only simplify the testing procedure but also provide more representative results than tensile testing.

The objective of this research work is to improve the strength of FGF 3D printed PEEK by studying the interlayer region and its relation to material grade and extruder temperature, when using a 1 mm nozzle. No heating chamber will be used, to ensure that the difference in layer strength in between each condition is more pronounced. Furthermore, determining the correct parameters and PEEK grades that can achieve a strong layer despite the lack of heated chamber, would greatly simplify the equipment required for AM of PEEK components. The relationships between PEEK grade, extruder temperature, interlayer strength, fracture type, crystal structure and crystallinity are evaluated. To achieve these objectives, novel techniques are applied to AM, such as the determination of interlayer strength over relatively large representative areas using shear testing. Crystallinity is evaluated using Raman spectroscopy, differential scanning calorimetry (DSC) and X-ray diffraction (XRD) whilst the actual crystal structure is imaged using scanning electron microscopy (SEM). Finally, the tensile strength of XY plane 3D printed specimens is obtained to set a comparable standard with available literature. This is deemed necessary due to the lack of studies on shear strength.

8.3.2 Method

8.3.2.1 Materials

Three grades of PEEK were used in this study, namely VESTAKEEP L2000G, L3300G and L4000G by Evonik Industries, provided by both Evonik Industries (Germany) and Ensinger (Germany). Unfilled PEEK grades were used throughout the study with the main distinguishing factor being their respective molecular weight or viscosity which, in this study, is represented by their melt volume-flow rate (MVR). The VESTAKEEP L2000G, L3300G and L4000G grades had an MVR of 70 cm^3/10 min, 20 cm^3/10 min and 12 cm^3/10 min respectively, tested at 380°C with 5 kg load. The lower the molecular weight, the higher is the MVR value due to the shorter macromolecules. Prior to the 3D printing experiments, the pellets of all grades were subject to the same pre-drying conditions at 150°C for 4 hours.

8.3.2.2 FGF Setup

The specimens used in this study were all fabricated using Extruder 3, with screw 3. This extruder made use of a smaller screw diameter which provided a greater force on the material being processed. This enabled the extrusion of more viscous thermoplastics.

This advantage was important for this study as in this case 3 PEEK grades were used, each with a different viscosity profile. In general, if the extruder is capable of extruding using the most viscous thermoplastic, then it can handle the other less viscous grades. The ease-of-use improvements implemented in Extruder 3, especially the easily removable screw, barrel and nozzle, were of critical importance to enable easy and safe maintenance and testing when using PEEK.

A 1 mm nozzle was used to partially mitigate the lack of a heated chamber, which is well documented to lead to inferior 3D printing performance due to rapid cooling of the extrudate [287, 402]. The extruder did not make use of a layer cooling system as this was directly against the scope of the study.

8.3.2.3 FGF Process Parameters

The open-source Prusa Slicer (v2.5.0) by Prusa Research (Czech Republic) was used to generate the G-code required for each 3D printed specimen. The nozzle diameter of 1 mm was used with a strand width set at 1 mm. All specimens were 3D printed on a glass build plate which was heated at 150°C. The bed was coated with a layer of Magigoo (Malta) High Temperature glue to promote part adhesion during 3D printing. The layer height was set to 0.4 mm for all layers except for the first, which was printed at 0.3 mm to enhance bed adhesion. The speed was kept at 20 mm/s for all 3D printing features including the first layer to account for the extrusion rate with speed relationship of screw-driven FGF systems [154]. By keeping the printing speed relatively slow and constant throughout, the geometric accuracy of the parts was maximised, at the cost of the printing time. Each specimen was 3D printed at 380°C, 400°C and 420°C to study the effect of temperature on the shear and tensile strength of the AM-part. Temperature also influences the extrusion rate and therefore the extrusion multiplier was altered to account for this discrepancy, as shown in Table 8.1. The extrusion multiplier was determining using a trial and improvement method. For each grade and extrusion temperature, a 25 mm sided cube was 3D printed using an extrusion multiplier of 1. The cube was observed and measured to determine whether it was under or over extruded. The extrusion was then increased or decreased respectively. The procedure was repeated for all cases, until the cube side dimensions were within 0.1 mm accuracy.

Table 8.1 - Extrusion multiplier used for each discrete extrusion temperature and PEEK grade combination. Each grade's melt volume-flow rate [232, 406, 407] included form comparison.

Grade (VESTAKEEP)	MVR (380°C, 5 kg) [cm^3/10 min]	Temperature 380°C	400°C	420°C
L2000G	70	1.9	1.6	1.4
L3300G	20	1.2	1.1	0.9
L4000G	12	1.8	1.7	1.6

The different temperatures used in this study for each of the PEEK grades, as listed in Table 8.1, change the material viscosity and will lead to differences in printing performance. Both an excessively low or high processing viscosity can hamper the MEX process [16]. A simple geometry lacking any overhangs, bridges, or large, negative, draft angle walls, can be 3D printed even using material with undesirable rheological characteristics. To create an equal scenario for all specimens, the geometry was kept as simple as possible i.e., without any of the aforementioned complex features. In this manner, the specimen geometry would be similarly reproducible for all the different process parameters.

8.3.2.4 Tensile Testing

The aim of tensile testing for this study is solely to compare this setup with other available literature which utilise a heated chamber. The necessity for this experiment comes out of a lack of available literature on shear strength of 3D printed PEEK, which limits comparison. Tensile testing was carried out using a M350 20CT tensile tester by Testometric, United Kingdom using a Testometric 1000 kg F load cell (S/N 31440). The test was conducted on each grade at each extrusion temperature, using the 1B geometry as described by the ISO 527-2 standard using a 5 mm/min strain rate [408], printed in the XY plane i.e., flat on the build plate. The geometry of tensile test specimens, as described by ISO 527-2 standard, is a simple dumb-bell shape for specimens printed in the XY plane. The complexity increases when considering which 3D printing path generation methodology should be used to account for the lack of layer heating. A solely perimetric approach was discarded due to the propensity to create and undesired void close to the tab region of the specimens [409]. More importantly, a perimetric approach would lead to the generation of long strands being deposit adjacent to relatively cool pre-deposited strands. A common approach for 3D printing is to use several perimeters, generally 2 or more, surrounding a rectilinear infill. This approach was selected as it allows the deposition of a new strand concomitant to a still hot strand. In this manner,

the bond created is expected to be superior as compared to a perimetric bond. Each result metric was then analysed to establish statistically significant differences between means using a one-way ANOVA test with Tukey post-hoc. To verify that the data is normally distributed, a Shapiro-Wilk test was conducted on each group *a priori*.

8.3.2.5 Shear Strength

In contrast to tensile testing, all shear testing methods invariably have a component of bending [410] so that the experiment validity is often down to the actual severity of the bending involved. Like for other testing methods including tensile testing, there is no standard shear test for 3D printed specimens. The available shear testing standards use a lap pull technique [411], a compression technique [412] or a v-notched specimen [413]. There are also short and long beam bending tests [414, 415] which acknowledge and include the bending moment as part of the final result. The shear lap testing (SLT) technique, is commonly applied to adhesive joints, a condition similar to components produced via AM. This technique has an elevated bending component for tough specimens with high shear strength which in severe cases, bend the tabs upon loading, creating an undesirable combined tensile and shear failure. For such cases, compression shear testing is the preferred solution [410]. Compression shear testing (CST) specimen geometry comprises of a simple cube, at times with a guiding notch, making it easy to produce using MEX AM.

8.3.2.5.1 Shear Lap Testing (SLT)

The shear strength was preliminary tested using a simplified version of the shear lap test based on ASTM D 3163 (2023) *Standard Test Method for Determining Strength of Adhesively Bonded Rigid Plastic Lap-Shear Joints in Shear by Tension Loading*, as shown in Figure 8.12. The simplification was necessary to ensure easy, reliable, and comparable 3D printing for all processing conditions. The simplified geometry used a single tab with a short tab on top instead of two tabs bonded together. This removed the occurrence of an overhang in the specimen geometry. Each tab is 6 mm thick with the larger tab being 75 mm by 25 mm whereas the small tab was a 25 mm sided square. The test was conducted on a Testometric, (United Kingdom) universal testing machine using a Testometric 1000 kg F load cell (S/N 31440) in which the specimens were griped by jaws using 25 mm out of 75 mm total length. The specimen was printed in one piece, flat on the build plate. The slicer was set to use 2 wall perimeters with a full rectilinear infill

pattern at 45°, changing direction each layer. Shear testing was carried out on each grade of PEEK and extrusion temperature selected for this study.

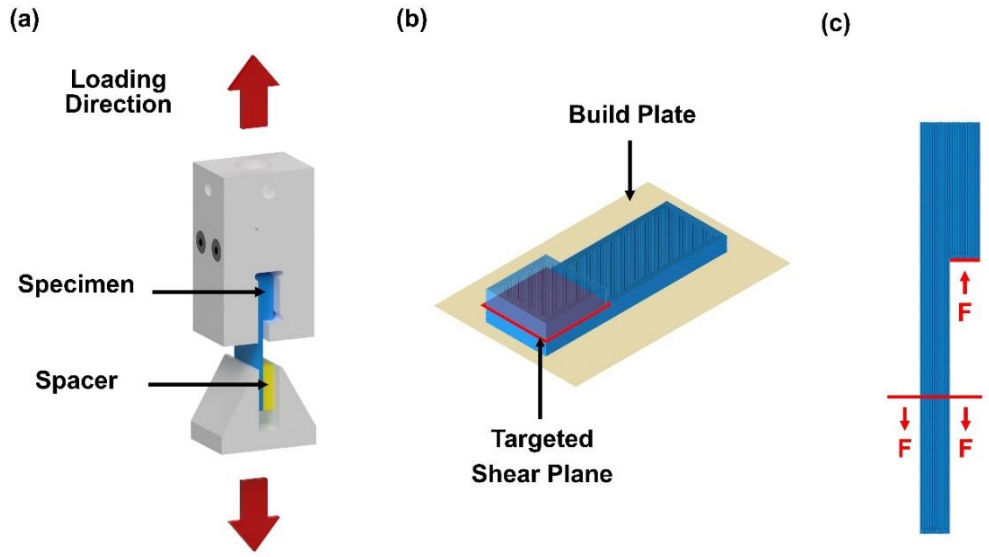

Figure 8.12 - Shear lap testing method adapted for 3D printed specimens: (a) 3D diagram of jig and setup, (b) specimen as oriented during 3D printing and (b) force diagram of specimen during testing.

The experiment was limited to shear testing of the XY plane, as shown in Figure 8.12 (b) with the aim of loading what is generally the weakest section of a 3D print i.e., the interfacial, layer-to-layer bond [260, 287, 398, 404]. The geometry of the specimen, the targeted shear plane, and the 3D printing orientation are all shown in Figure 8.12 (b). A jig, shown in Figure 8.12 (a) was fabricated to pull on the tab without supporting the specimen on any other surface. An ideal representation of the forces acting on the specimen is shown in Figure 8.12 (c). The simplifications of the shear lap test geometry led some specimens to fail at the pull tab under normal load instead of the shear plane. This undesirable scenario led to a simulation exercise to better understand the stresses occurring in the specimens during testing. Compression shear testing is inherently less prone to bending moments which should increase testing reliability. Further shear tests were conducting using this technique.

8.3.2.5.2 Compression Shear Testing (CST)

Compression shear testing (CST) required a simpler geometry than shear lap testing, comprising simply of a stepped cuboid block, as shown in Figure 8.13. The size of the 3D printed stepped cuboid is non-trivial as it should be representative of a general infill structure. To this end a 25 mm sided, stepped cuboid, 12 mm thick was selected for this

study. A smaller size would create hot spots in the part, decreasing the part quality and reproducibility of the specimens. The specimen also included a 6 mm thick alignment step (5 mm by 25 mm) on one side meant to make testing setup faster and reduce experimental error. All specimens were 3D printed flat on the build plate as shown in Figure 8.13 (a), using 2 wall perimeters with a full rectilinear infill pattern at 45°, changing direction each layer, same as with the tensile testing specimens. Each grade and extrusion temperature combination were used in the production of the specimens.

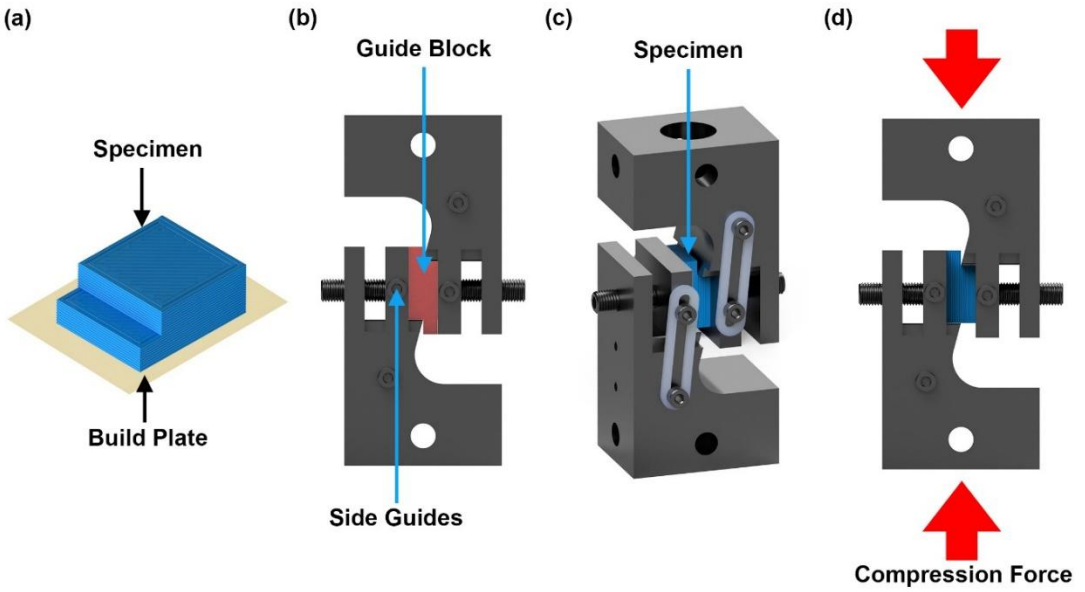

Figure 8.13 – 3D model schematic diagram of specimen as oriented during 3D printing (a), front diagram of compression shear tester jig with alignment guide block (b), tester with specimen (c) and front diagram of jig during testing with loading direction(d).

The 3D printed CST specimens were tested using a novel testing jig adapted for larger sized specimens, shown in Figure 8.13 (b) to (d). Conventional CST jigs are employed for rather small specimens making them impractical to adapt the already developed equipment to the specimen size required by this experiment. The novel CST jig design is shown in Figure 8.13 (a) to (c). A guide block, setup as shown in Figure 8.13 (b) is required as a first step during setting up of the Testometric universal testing machine to ensure that the jig aligned correctly. The specimen alignment tab is then used to ensure that the shear load is applied primarily at the central layer of the specimen. All test results were statistically analysed using the same procedure as used for tensile testing results.

8.3.2.5.3 Shear Test Simulation

Both the SLT and CST were simulated to evaluate their shear stress and equivalent stress distributions upon loading. In so doing, any strong, localised, bending moments, pealing or other such undesired features are noted. Simulations were carried out using ANSYS Workbench 2022 R2 (USA), static structural setup with the aim of generating the shear stress and equivalent stress distributions. Each simulation model along with the loading scenarios, are shown in Figure 8.14. The compression shear model also incorporated frictionless sliding constraints at the bottom and top faces as is in the case of the experiment. In each case the load was set to 1 N and the material was kept as default. The complex and unknown material properties of the 3D printed PEEK inhibited a proper material allocation for the simulation. This limitation does not hinder the main purpose of the simulation which is to study the general design of the specimens for their intended application.

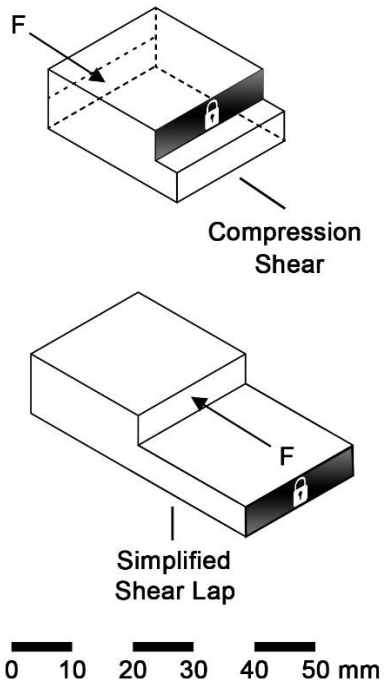

Figure 8.14 - Scaled diagram of model used for simulation. Fixed supports are annotated with a padlock and the force location and direction are represented by an arrow with 'F'.

8.3.2.6 Analysis of Crystallinity at Shear Failure Surface

The failure surface of CST specimens was analysed to evaluate its crystallinity. Three alternative techniques were used to study crystallinity namely DSC, Raman

spectroscopy and XRD. All techniques were used both on the failure surface and an amorphous version of each grade to ensure that the technique is reliable. Density crystallinity determination was not used on account of the micro-porosity related limitations of density measurement for MEX 3D printed specimens. The fracture surface was selected for characterisation as this is generally the weakest region in the specimen and therefore controls the overalls strength of the part. DSC is the only destructive technique used in which a small sample was taken from the fracture surface of select specimens. A representative fractured specimen was selected for each experimental parameter combination. The DSC test was carried out using a Mettler Toledo DSC 3+ (USA) operating in a nitrogen atmosphere with liquid nitrogen cooling. The sample weight was measured using an MYA 11.4Y Plus micro balance (RADWAG, Poland). The test was conducted starting from 30°C and heated to 400°C, at a heating rate of 10 K/min using three samples in each case. Apart from crystallinity, the result was used to determine the melting temperature (T_m) for each case. Crystallinity (X_c) was determined using Equation 8.7, where ΔH_m is the melting enthalpy, ΔH_{cc} is cold crystallisation enthalpy and $\Delta H_m^{100\%}$ is the melting enthalpy of an ideal PEEK crystal equal to 130 J/g **[416]**.

$$X_c = \frac{\Delta H_m - \Delta H_{cc}}{\Delta H_m^{100\%}}$$

Equation 8.7

The crystallinity determined using DSC is a bulk form of crystallinity as it uses a measurement of crystallinity averaged over all the sample used. Raman spectroscopy is a localised, surface technique and therefore the crystallinity measured is in effect only that of the spot location selected. To minimise related errors, 10 measurements were taken per processing condition. A Horiba XploRa Plus Smart Raman Microscopy (Japan) was used with a 785 nm laser, 50x objective, 50 µm slit, 500 µm hole, 1200 (750 nm) grating and a 50% filter. Raman spectra were recorded for all the fracture surfaces as well as the amorphous specimens, in each case taking two readings. All tests were conducted at standard room temperature and the Raman shift was calibrated using a silicon reference sample with a known peak.

The data collected from the Raman analysis was then processed using a custom python program in Jupyter Lab [417]. Each result was individually baseline corrected using asymmetric least square smoothing **[418]**, with a p value of 0.1, a λ of 1000 and 10 iterations. After smoothing, each curve was split into four ranges which are listed in Table

8.2. Each range was then deconvoluted in one or two gaussian curves, as listed in Table 8.2. by using non-linear least-squares minimization and curve-fitting (LMFIT) for Python [419]. The resulting fitted curves were then computed for area, peak location, and peak intensity. The peaks of interest were selected by following the studies conducted by Doumeng *et al.* [403] along with previous works such as those conducted by Agbenyega *et al.* and Stuart *et al.* amongst others [420–424].

Table 8.2 - Raman range split and number of deconvolutions

Wavenumber Range	Number of gaussian deconvolutions	Peaks of interest
1135 - 1160	1	1146
1580 – 1604	2	1590, 1596
1604 – 1625	1	1609
1630 – 1680	2	1649, 1643

The Raman shift at 1651 cm^{-1} was selected to determine the crystallinity, using Equation 8.8, where S_{1651} is the peak shift at 1651 cm^{-1}, as reported by Doumeng *et al.* The other indicator results were inadmissible due to insufficient spectral resolution.

$$X_c = 5765.2 - (3.4768)S_{1651}$$

Equation 8.8

The fractured surface of cleanly sheared specimens was analysed using XRD. The XRD of PEEK produces a broad peak usually denoting a mostly amorphous specimen. Within the 2θ testing range from 5° to 40°, a crystalline specimen has 4 principle peaks, at 18.7°, 20.7°, 22.7° and 28.8°, representing the (110), (111), (200) and (211) crystallographic planes [425, 426]. Another, less easily discernible peak resides at around 26°, representing the (112) plane but has a low intensity compared with the other peaks [425, 426] and can easily be drowned in noise. A Rigaku (Japan) Ultima IV Cu-Source XRD (λ = 1.54056 Å) was used to covert this range using an increment of 0.01° and a current intensity set to 40 mA. The specimen selected had an area of at least 10 mm by 10 mm of a clean sheared face that would allow for correct operation of the XRD system. Crystallinity (X_c) was calculated using Equation 8.9, where A_c is the area of crystalline peaks of diffraction and A_a is the area of amorphous peaks of diffraction [403].

$$X_c = \frac{A_c}{A_c + A_a}$$

Equation 8.9

The respective areas were determined using SciPy, Python package **[427]** with which the curves were fitted and deconvoluted into 12 gaussian curves. Subsequently the area under each curve was calculated and the curves representing the crystalline peaks were separated. This process was used to determine the crystallinity at the failure surface of clean sheared PEEK specimens.

All the previously mentioned techniques simply provided only a value for crystallinity. Often it is desirable to visualise the actual microstructure to properly understand what kind of crystal structure is being formed. MEX 3D printing has complex heat gradients which vary depending on the strategy used for path generation. These may generate not only diverse levels of crystallinity but also of crystallite size. To this end, scanning electron microscopy (SEM) (Zeiss Merlin Gemini, Germany) was used to study the topography, porosity and microstructure of the failure surface of CST specimens. Apart from crystal structure, with the use of SEM imaging, any micro- and macro-porosity present was imaged. Intra-layer failures i.e., those failures whose cracks go through the 3D printed layers instead of along them, would show micro-porosity as cracks tend to fail through the weakest regions. Specimens with interlayer failure i.e., in between the layers, should provide a clear view of the conventional macro-porosity. A representative sample from each study case was used for low magnification imaging using SEM on the fractured surface. Deeper within the fractured surface, a high magnification image was taken using 20 kV electron high tension with the aim of visualizing the microstructure at the shear failure surface of the 3D printed PEEK specimens. Each sample was gold coated to create a conductive surface, viewable under the SEM.

8.3.3 Results and Discussion

8.3.3.1 Tensile Strength

The stress at yield, modulus of elasticity and strain at break results are represented in Figure 8.15 along with the data sheet values which are marked as dashed lines. An analysis of statistically significant difference between means is listed in appendix 7, page 418. Results for all cases were found to be significantly lower than the datasheet values. The low modulus of elasticity achieved was higher than that achieved by Hu *et*

al. and Deng *et al*. both of which used a heated chamber **[256, 290]**. Other research groups achieved higher values with Arif *et al*. and Rinaldi *et al*. managing 3800 MPa and 3980 MPa respectively **[254, 260]**. Within the range of uncertainty of the results, there is no clear relationship between extruder temperature and all results.

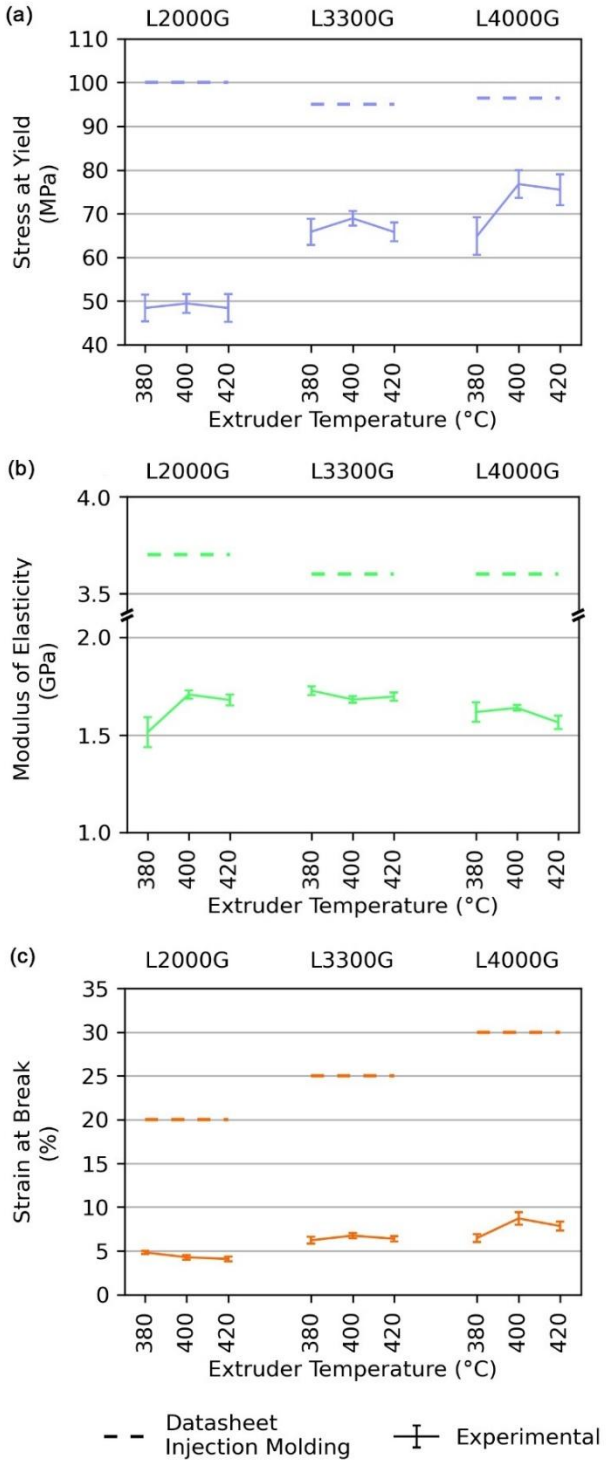

Figure 8.15 – Tensile testing results of stress at yield, modulus of elasticity and strain at break along with datasheet value represented as a dashed line (n=6).

Stress at yield was found to be higher for the higher molecular weight VESTAKEEP L3300G and L4000G compared with the L2000G grade. In contrast, the datasheet stress at yield, reported a 5% decrease in yield strength for VESTAKEEP L3300G and L4000G grades compared to VESTAKEEP L2000G. The experiment showed the average yield stress increased by 50% with increasing molecular weight. This trend is opposite that of the datasheet and therefore the cause behind the increase in stress at yield is related to the process i.e., additive manufacturing, rather than simply the grade being stronger. High molecular weight PEEK grades were found to create a better bond at room temperature than their lower molecular weight counterpart. To some extent, this result is counter to that of Xu *et al*. which found that increasing molecular weight at first increases the stress at yield but at higher molecular weights, the stress at yield would start to decrease. In the case of Xu *et al.*, the specimens were 3D printed using a 0.4 mm nozzle inside a heated chamber at 230°C with a heated bed at 300°C [268]. This leads to significantly different 3D printing thermal environment than as used in this study. Xu *et al* and Wang *et al*. also reported an increase in stress at yield between 380°C and 400°C something which was not observed in this study [257, 268]. The research team led by Wang *et al*. showed that increasing the nozzle size to 0.8 mm from 0.4 mm was shown to decrease the rate of increase in yield strength by increasing extruder temperature [257]. It is possible that when employing a 1 mm nozzle as done in this study, the benefits brought about by a higher extruder temperature are not substantial for XY plane 3D printing.

Most specimens failed closely after yielding, achieving rather low strains. The higher molecular weight VESTAKEEP L4000G extruded at 400°C achieved the highest strain at failure of 8.7%, whereas the lowest value was of 4.1% obtained by the lower molecular weight VESTAKEEP L2000G extruded at 420°C. Thus, both values are significantly lower compared to the data sheet value which is 25%, tested using injection molded specimens according to ISO 527-2 standard [232, 406, 407]. In most works published in literature, the strain at break achieved often surpassed the 10% strain mark, with yielding close to 5% strain [254, 256, 287]. The poor strain during tensile testing, shown in Figure 8.15 (c) of this study, may be attributed to the lack of a heated chamber. The importance of a heated chamber was demonstrated by Yang *et al*. when using 0.4 mm nozzle 3D printing [287]. This view is not supported by all available studies, for example Sikder *et al*. demonstrated that for both specimens printed at a relatively low chamber temperature of 25°C and 90°C, the strain achieved was at least 25% [273] which is higher

than that achieved in this study and in agreement with datasheet values. At 25°C chamber temperature, there are no possible, positive effects on the layer bond and therefore the higher strain results achieved are not process related. The reason behind the discrepancy is therefore cause by using specifically modified PEEK filament for AM.

An analysis of failure modes across different extrusion temperatures and material grades shows trends in failure types, as shown in Figure 8.16. The different failure types are shown in Figure 8.17. The higher extrusion temperature of 420°C generally failed with a straight cut and had a complete absence of delamination failures. In contrast, 380°C failed predominantly in delamination, either localized or throughout most of the specimen, demonstrating a weak layer bond strength. Among the material grades, L3300G demonstrated the best inter layer strength, with the vast majority of samples achieving clean cuts across all temperatures. L2000G, had high rates of localized delamination and clean cuts near the tabs, especially at lower temperatures. L4000G had a number of delamination failures at 380°C but none at higher temperatures. Overall, VESTAKEEP L3300G was observed to have the most occurrence of straight failures without delamination across all temperatures. Tab failures always occurred in a straight cut fashion and occurred at all temperatures. This indicates that failure probably occurred due to a deposition defect rather then due to weak layer bonding.

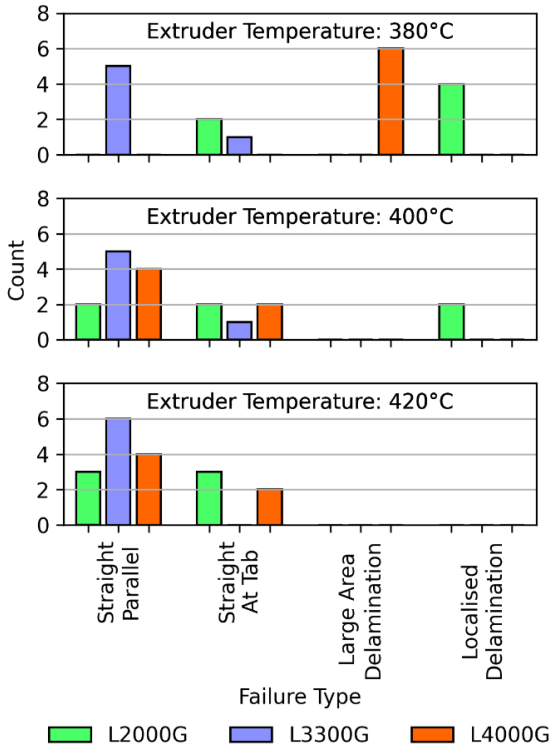

Figure 8.16 – Bar chart of failure type during tensile testing, for specimens 3D printed at 380°C, 400°C and 420°C extruder temperature using VESTAKEEP L2000G, L3300G and L4000G.

The only other works that studied the tensile properties of FGF printed PEEK were published by Tseng *et al*. and Curmi *et al*. The screw extruder used by Tseng *et al*. was significantly larger and more complex than that used in this study, involving multiple heating zones along with infrared chamber heating system **[155]**. This study's smaller and simpler setup achieved a higher stress at failure but poorer tensile modulus.

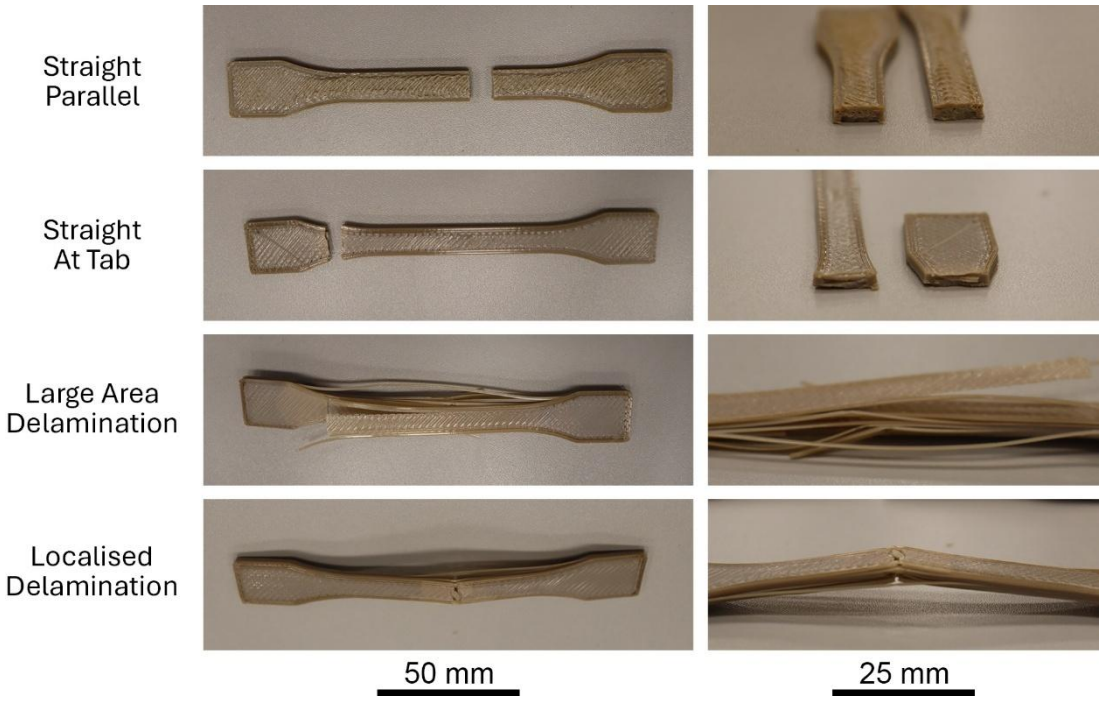

Figure 8.17 – PEEK tensile testing failure modes.

8.3.3.2 Shear Strength

8.3.3.2.1 Shear Lap Testing

The specimens tested in SLT failed in three principal ways i.e., in shear (S), tensile (T) or a mixed (M) mode, as illustrated in Figure 8.18 (a). All shear type failures always had a tensile component as instead of failing cleanly at the targeted shear plane, these tended to fail one layer beneath whilst breaking that layer from the rest in tensile, as shown in Figure 8.18 (b). The layer would be peeled off to some extent, thus indicating an undesired bending effect. Tensile failures occurred for specimens which had a greater shear strength at the target shear plane than tensile strength across the long tab. Some specimens even failed as a mixture of both whereby instead of a single shear plane, the crack would cross several planes and then continue parallel with the planes.

The different failure modes made comparison across experimental conditions impossible. Load vs displacement curves by failure mode, irrespective of grade and

extrusion temperature, are shown in Figure 8.18 (c). The minimum, median and maximum load results demonstrated that the weakest specimens failed in a staggered manner, irrespective of failure type. The stronger the specimens, the smoother the curve indicating no independent layer failures. Which failure type would occur was found to be related with extrusion temperature, as may be seen in Figure 8.19. This indicated that the higher the extruder temperature, the higher the shear strength, leading to a tensile failure instead.

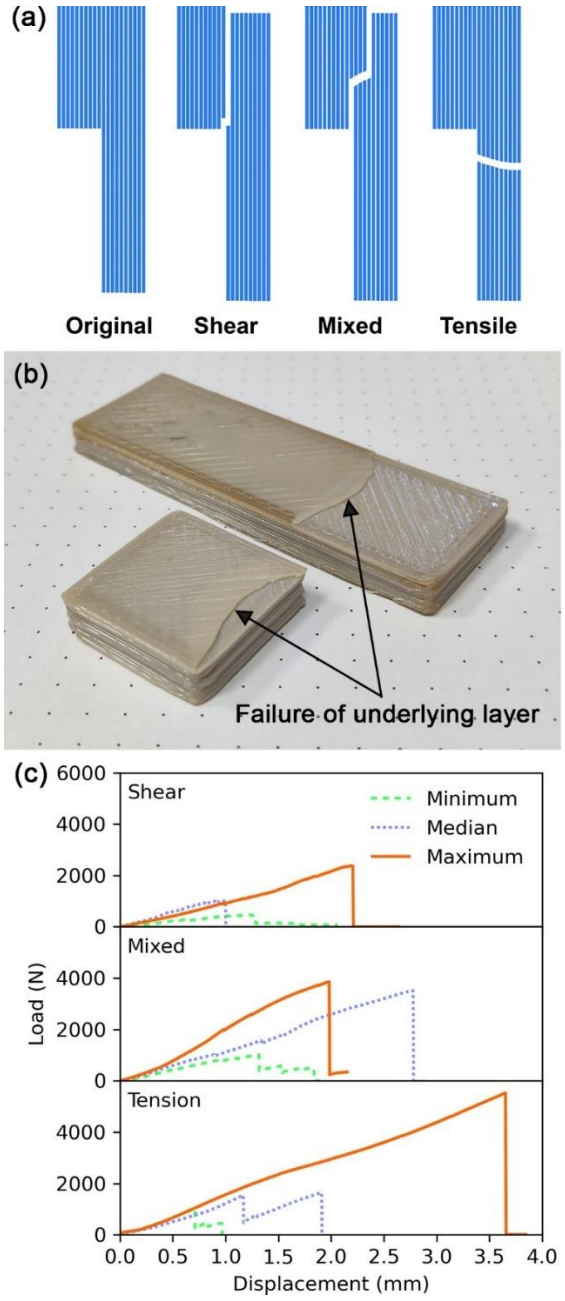

Figure 8.18 – (a) Illustration of modified shear lap testing failure modes and (b) shear type failure with underlayer breakage, background dots spaced equally by 5 mm. (c) Curves of minimum, median and maximum load achieved by modified shear lap testing for each failure type.

The results of the SLT demonstrate that despite the advantage of this testing technique when it comes to sample preparation, the actual results are rather poor. In view of this, compression shear testing was selected as a superior technique whilst maintaining simple specimen manufacturing. Simulation results confirmed this hypothesis.

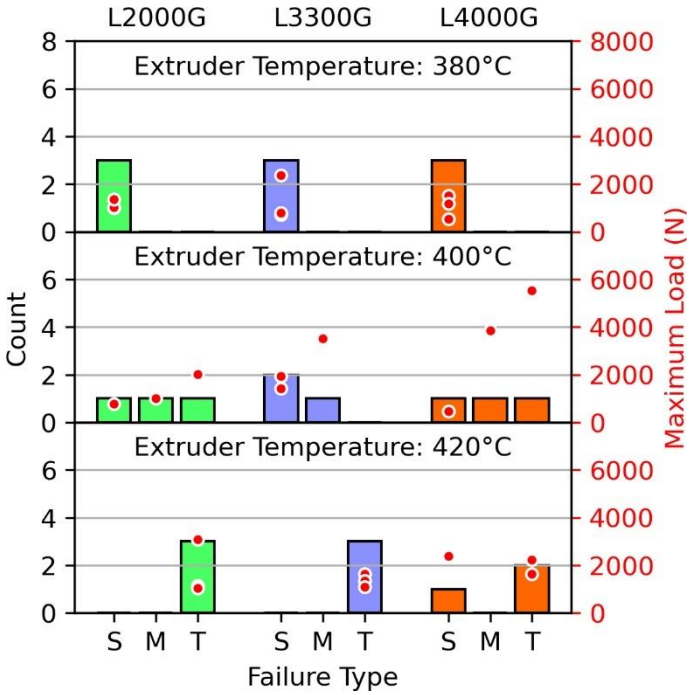

Figure 8.19 - Modified shear lap test, bar chart of failure type count per grade and extrusion temperature (n=3) denoted by S – shear, M – mixed and T – Tension, with overlaid discrete, maximum load results as scatter plot with (o) marker.

8.3.3.2.2 Simulation

The simulation results of Figure 8.20 indicated different shear and equivalent von-Mises stress distributions for all the specimens tested. In the case of SLT specimens, Figure 8.20 (a), the stress concentration at the top section of the tab, coincides with the undesired top layer delamination seen during experimentation, as shown in Figure 8.18 (b). The SLT simulation, shown in Figure 8.20 (b) demonstrated that the shear stress distributed occurs predominantly from one side only which is in contrast to that of CST, shown in Figure 8.20 (d) which occurs on both sides. These features highlight that the SLT is not adequate to study the shear strength due to its tendency to peel the specimen rather than cleave it. The shear stress distribution of CST specimens acted across the targeted plane as desired. Furthermore, equivalent the von-Mises stress distribution results of the CST specimen, shown in Figure 8.20 (c), did not show any apparent, critical bending moments and were therefore studied further through experimentation.

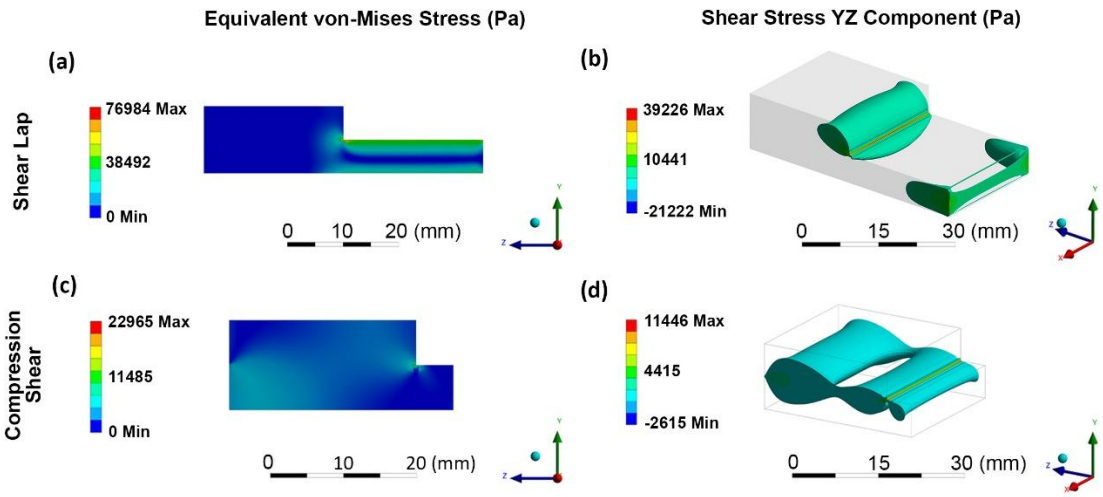

Figure 8.20 - Simulation results for shear lap: equivalent von-Mises (a) and shear stress YZ component (b), and compression shear: equivalent von-Mises (c) and shear stress YZ component (d).

8.3.3.2.3 Compression Shear Testing

A diverse number of failure modes were observed during compression shear testing, shown in Figure 8.21 (a). These failure modes can be split into two principal groups. Group 1 relates to those specimens which failed with clean shear i.e., the 3D printed faces were sheared off leaving little to no volume behind. This group is a combination of type 1 to type 5 failures. Often type 5 failures are difficult to assign as these can have notes from group 2 as well. The second group contains all those failure in which the crack front developed through multiple layers. These failures are comparable to bulk failure, where the crack growth preferentially propagates through voids rather than weakly bonded zones. Type 8 failures may be considered a mixture of both groups as the crack would start as a group 2 failure but then continuous off along a 3D printing plane. Splitting these failure modes in two groups is useful as the results were found to be related to the experimental testing parameter of extruder temperature. On the other hand, there was no relationship between failure type and PEEK grade.

The results of the bar chart in Figure 8.21 show a shifting trend from group 1 to group 2 failures with increasing extruder temperature. At an extruder temperature of 400°C, both groups of failures are prevalent. This shift in failure modes is supported by an increase in ultimate shear strength, as shown in the boxplot of Figure 8.22 and with the median curves of Figure 8.23. An analysis of statistically significant difference between means is listed in the appendix 7, page 418. It is therefore clear that group 2 failures are linked

with specimens which have achieved a superior layer bond strength, where the layer bond itself is no longer significantly weaker than the bulk of the specimen.

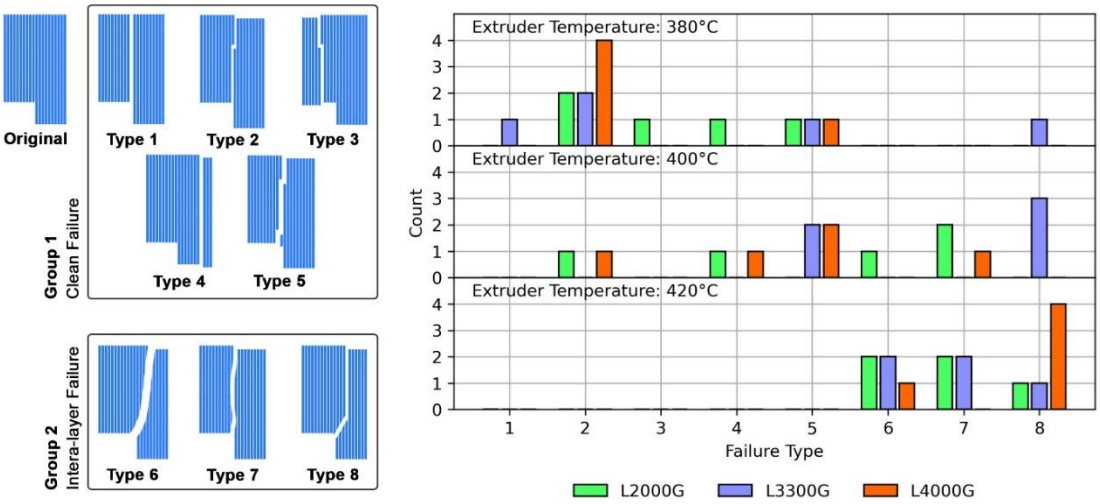

Figure 8.21 - Compression shear testing failure modes and bar chart of failure type per grade and extrusion temperature (n=5).

To achieve a stronger layer bond, extruder temperature is generally the most important factor. Higher molecular weight grades also led to a slight improvement in ultimate shear strength. The only instance which does not follow this trend is the result group of VESTAKEEP L4000G at 400°C which was weaker than the isothermal equivalent of VESTAKEEP L3300G. The largest change in ultimate shear strength was observed for VESTAKEEP L2000G. This grade recorded nearly 5 times increase in ultimate shear strength between specimens 3D printed at 380°C and 420°C, increasing from 3.10 ± 1.58 MPa to 15.08 ± 1.68 MPa. Each grade had an increase in ultimate shear strength with increasing extruder temperature. The difference in strength in between grades started to decrease as the extruder temperature was increased. This result indicates that the smaller molecular weight grades of PEEK are more temperature sensitive than the large molecular weight counterparts.

The tendency for lower molecular weight grades of PEEK to have a weaker ultimate shear strength at lower temperatures may be caused by the faster crystallisation rate of these grades **[405]**. The lower the molecular weight of PEEK, the greater the heat energy required to create a strong bond. This view is supported by the work of Shang *et al.* **[279]** which demonstrated that slowing down the crystallisation kinetics of PEEK led to an improved interlayer bond strength.

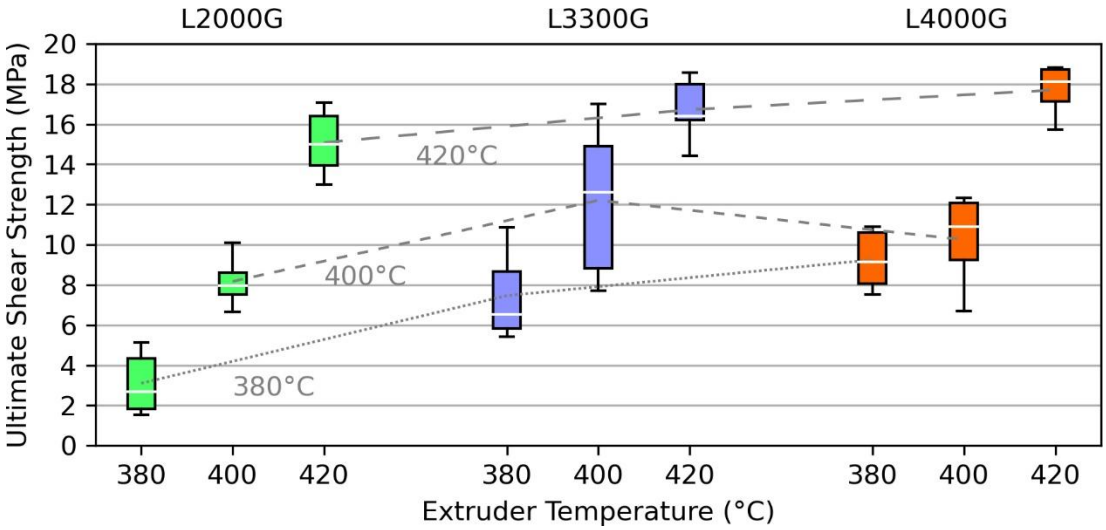

Figure 8.22 – Boxplot of ultimate shear strength of compression shear tested specimens with median marked with orange line. Dashed lines are isothermal trend lines for each extruder temperature, along average result (n=5).

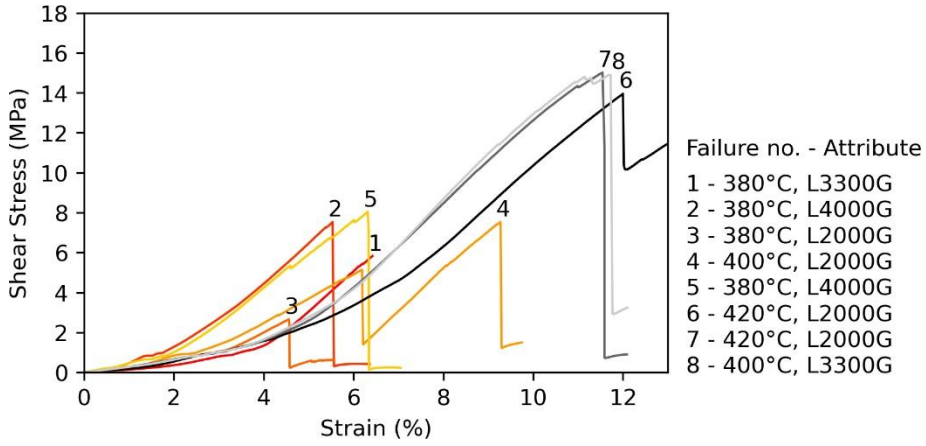

Figure 8.23 – Median curves of each shear testing failure mode, chosen from ordered list of curves, using maximum shear strength.

The shear testing results demonstrated that increasing extruder temperature and molecular weight led to increased shear strength. The poor shear strength of the low extruder temperature specimens led to a clean shear cut in between the 3D printed layer. All group 1 failures were sheared off cleanly producing surfaces as shown in Figure 8.24 (a) where the separate strands are easily resolved. Even for the rough surfaces of group 2 type failures, some sections were cleanly sheared, as shown in Figure 8.24 (b) which allowed for further magnification to view the crystalline microstructure as in Figure 8.24 (d).

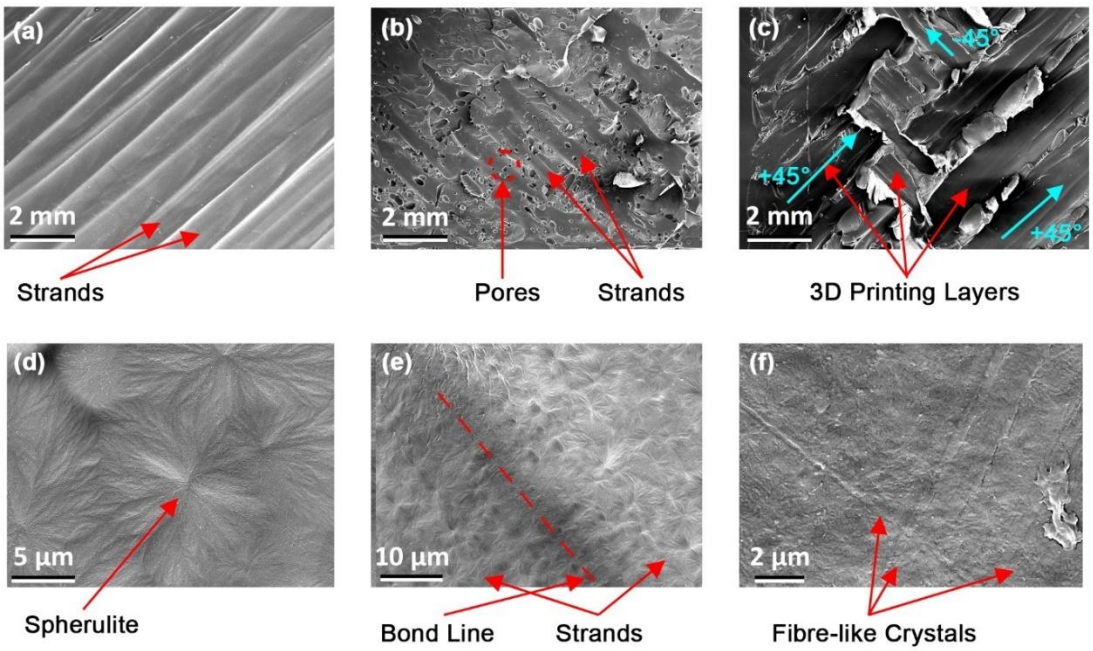

Figure 8.24 - Scanning electron microscopy micrographs of PEEK (a) strands at a clean fracture surface, type 2, (b) pores and strands at rough fractured surface, type 7, (c) multi-layer failure, type 5, (d) magnification of spherulite, (e) strand to strand bond line and (f) magnified fibre-like crystal.

The failure surfaces of group 1 and 2 are fundamentally different, as contrasted Figure 8.24 (a and b) showing the failure surfaces of VESTAKEEP L2000G, extruded at 380°C and at 420°C respectively. The first group was characterised by interlayer and inter-strand failure, the latter of which can be seen in the failure surface of VESTAKEEP L3300G, extruded at 380°C, shown in Figure 8.24 (c). In this later micrograph, the failure path moved in-between the 3D printed layers by selectively breaking the inter-strand bond. This is another indication that both the layer-to-layer bond and strand-to-strand bond are weak as a result of using a low extruder temperature especially with low molecular weight PEEK grades. Micrographs of group 2 failures, an example of which is shown in Figure 8.24 (b) demonstrated that the improved strength at higher extruder temperatures, changed the crack path from following the layer bond to following the voids in the part. The micrograph also shows the presence of pores not only in between strands but also inside the separate strands. Therefore, the extrudate may have some innate voids caused by insufficient compression in the extruder screw. Both intra- and inter-strand voids serve as crack propagation sites and decrease the overall strength of the specimens. This contributed towards the lower stress at yield and tensile modulus values compared to datasheet and literature.

The SEM micrographs allowed the observation of crystallinity both from the centre of the strand but also at the strand-to-strand bond, shown in Figure 8.24 (d and e) respectively. The observed microstructures were produced from the fractured surface of VESTAKEEP L2000G and VESTAKEEP L4000G respectively, extruded at 380°C. Magnifying the interface further then shown was not possible due to insufficient resolution. The interface region did not have a clear spherulite form as in the rest of the strands. This may be caused by the rapid cooling at the bond line which could inhibit spherulite formation. Apart from spherulites, possible fibre-like crystals were observed, as shown in Figure 8.24 (f), taken from VESTAKEEP L3300G, extruded at 380°C. These are similar to those observed by Wang *et al.*, when following a quench then anneal to crystallise process [428]. Such crystals formed with no clear trend in most specimens.

8.3.3.3 Crystallinity at Fracture Surface

SEM micrographs provided a view at the crystal structure present at the failure surface. This technique is limited to simply viewing the surface and did not provide any information on the actual crystallinity in that region. Each technique used, namely DSC, Raman Spectroscopy and XRD, has its own peculiarities leading to different crystallinity results. The crystallinity using DSC and Raman 1651 cm^{-1} shift for each experiment combination is shown in Figure 8.25. XRD results constituted of only single specimen measurements due to lack of viable specimens for XRD testing. XRD required a flat 1 cm^2 surface which could only be provided for by type 1 failures. Therefore, the results had limited usability and were shown in appendix 7, page 418.. DSC results indicated that the higher the molecular weight, the lower the crystallinity. This tendency was not reflected in either the Raman or XRD results. PEEK DSC crystallinity results are known to overestimate the actual specimen crystallinity [403]. PEEK recrystallises upon melting which is part of the reason why it has a high service temperature. This effect leads to an overestimation of the actual crystallinity in the specimen as the sample recrystallized even after the original crystal had melted, during the DSC test. In contrast XRD tends to underestimate the actual crystallinity [403]. Both DSC and Raman noted an increase in crystallinity with the extruder temperature increase for VESTAKEEP L2000G grade. The opposite effect was noted for both VESTAKEEP L3300G and L4000G grades. This discrepancy can be explained by observing the change in melting temperature, as recorded by DSC.

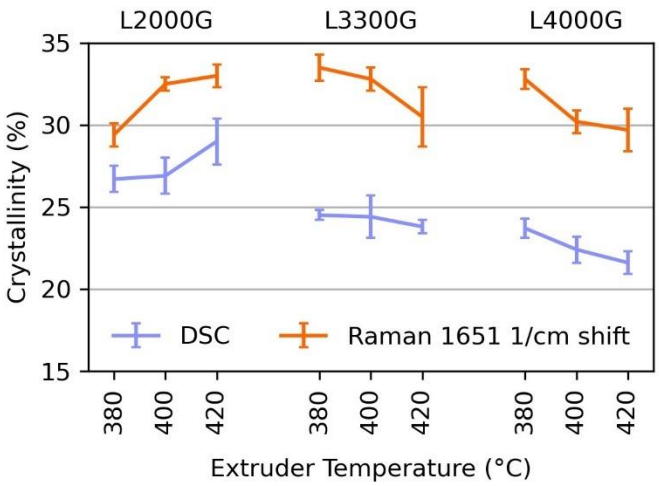

Figure 8.25 - Crystallinity of compression shear failure face using DSC (n=3) and Raman spectroscopy (n=10).

The DSC results, shown in Figure 8.26 (a), which were originally intended for crystallinity evaluation, highlighted an unexpected increase in melting temperature (T_m) with higher extruder temperatures. This result is illustrated in Figure 8.26 (b), where VESTAKEEP L2000G, L3300G and L4000G increased by 1°C, 2.5°C and 1.6°C respectively. The data sheet reported a melting temperature of 340°C for all three grades **[232, 406, 407]**. At high processing temperatures and long periods in the extruder, the risk of PEEK degradation increases. In FGF extruder systems, the melt residence time i.e., the period in which the molten material is kept in the barrel, is much higher than in filament systems. The exact time scale depends on the specific system design. The longer the screw and the larger the screw diameter, the longer is the heating zone and the slower is the screw speed, which results in a longer residence time. Filament systems usually have a much shorter melt zone and therefore do not usually suffer from similar issues.

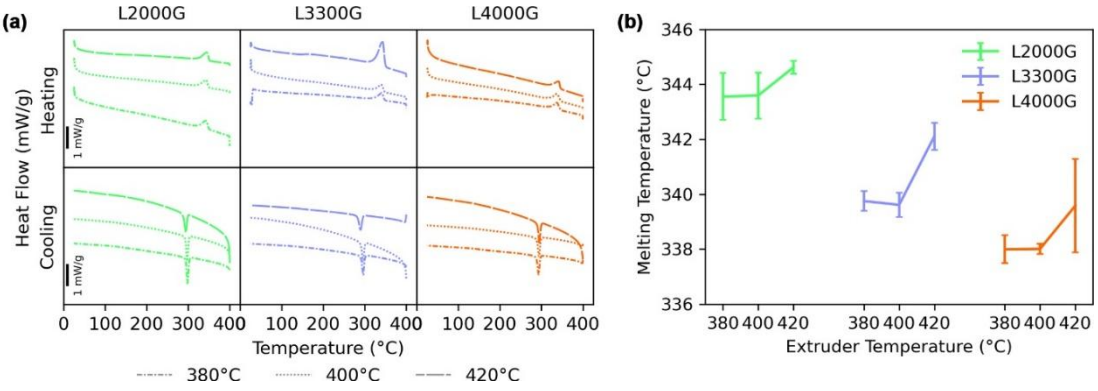

Figure 8.26 – Representative DSC results of VESTAKEEP L2000G, L3300G and L4000G, 3D printed at extruder temperature 380°C, 400°C and 420°C (a) and change in melt temperature of 3D printed PEEK parts at different extruder temperatures (n=3) (b).

Holding PEEK at high temperatures, between 400°C and 450°C, has been shown to cause oxidative cross-linking [429]. This process in turn decreases the crystallisation nucleation sites which decreases the crystallisation rate [430]. The decrease in crystallinity of L3300G and L4000G at higher extruder temperatures can be attributed to a decrease in a crystallisation rate. It is unclear what caused the discrepancy between these grades and the lower molecular weight VESTAKEEP L2000G, which reported an increase in crystallinity with an increase in extruder temperature.

With regard to melting temperature, the same study by Day *et al*. also reported its decrease with longer residence time [430], which goes against what is observed in this study. An increase in melting temperature can be attributed to a cross-linking reaction [431] or change in crystallite morphology [432] which would instead increase it. To evaluate whether a cross-linking reaction caused the change in melting temperature, further characterisation was conducted on the fracture surface. A Fourier transform infrared spectroscopy (FTIR) using attenuated total reflection (ATR) test was conducted to check for a change in absorbance at the 1100 cm^{-1} and 1730 cm^{-1} wavenumbers. These waves represent the C-O-C and C=O bonds respectively, which are created by oxidative cross-linking. The full method and result are shown in the appendix 7, page 418. In each case of PEEK grade and extruder temperature used, there was no difference compared to the respective, original granulate spectroscopy result. This demonstrated that no oxidative cross-linking occurred. In conclusion, the higher melting temperatures were probably caused by a change in crystalline morphology.

Comparing crystallinity with shear strength, no clear relations could be defined. The high crystallinity recorded can be the cause behind the low strain at break results obtained during tensile testing, as reported by Yang *et al*. [287]. It should be noted that the VESTAKEEP L2000G CST results had the most remarkable increase in shear strength with increased extruder temperature compared to other grades. It is also the only grade which demonstrated the expected increase in crystallinity with temperature.

8.3.4 Conclusion

The study further optimised the FGF 3D printing process by studying the effect of different grades of PEEK and various extrusion temperatures. Compression shear testing (CST) was found to be an improved method of studying interlayer bond strength over conventional, z-oriented tensile testing. It allowed for the study of representative infill

structures over relatively large surface areas with a simpler specimen production. CST indicated that the smaller molecular weight grades of PEEK are more temperature sensitive than the large molecular weight counterparts. Higher molecular weight PEEK grades processed at higher extruder temperatures, such as VESTAKEEP L4000G at 420°C, were found to produce the highest ultimate shear strength and thus the highest layer bond strength of 17.70 ± 0.58 MPa. A higher extruder temperature increased the ultimate shear strength of all PEEK grades. However, the lower molecular weight VESTAKEEP L2000G grade experienced the greatest increase of 5-fold the strength, from 3.10 ± 1.58 MPa to 15.08 ± 1.68 MPa.

DSC and Raman spectroscopy agreed that crystallinity at the fracture surface, increased with extruder temperature for the higher MVR VESTAKEEP L2000G but decreased for the other grades. At lower MVR, the crystallinity was found to decrease from 33% to 30% with increasing extruder temperatures, along with an increase in melting temperature, as measured by DSC. This behaviour was attributed to a change in crystalline morphology caused by the long residence time and high processing temperature of FGF.

Finally, tensile testing in the XY plane, demonstrated that this study's smaller and simpler FGF setup achieved a high stress at failure of 72.4 ± 3.7 MPa but poorer tensile modulus than the best available in literature. The use of a 1 mm nozzle and no heated chamber achieved better mechanical properties than a few studies that used 0.4 mm nozzle with a heated chamber [155, 256, 290] but was nonetheless weak compared to the best reported results. Extruder temperature did not affect mechanical properties whereas molecular weight had a strong relationship, increasing stress at failure by nearly 50% for the higher molecular weight grades.

8.4 Conclusion

This chapter established the potential of FGF systems as a viable alternative to FFF systems for 3D printing high-performance materials like PEEK. The findings demonstrate that careful calibration of extrusion parameters, particularly extrusion multiplier and temperature, is critical to achieving high-quality prints and mechanical performance. The optimization of interlayer bond strength through compression shear testing highlights the importance of molecular weight and processing conditions in enhancing part strength.

Higher molecular weight PEEK grades, processed at elevated temperatures, deliver superior layer adhesion and mechanical properties. Furthermore, the ability to achieve good results with a small scale FGF setup, provided a more affordable alternative to large scale FGF setups with their added complexity and high initial investment. In this manner FGF may be used for the fabrication of robust PEEK components in an affordable manner. Overall, these advancements position FGF systems as an adaptable solution for manufacturing products for demanding applications in aerospace, biomedical, and engineering fields.

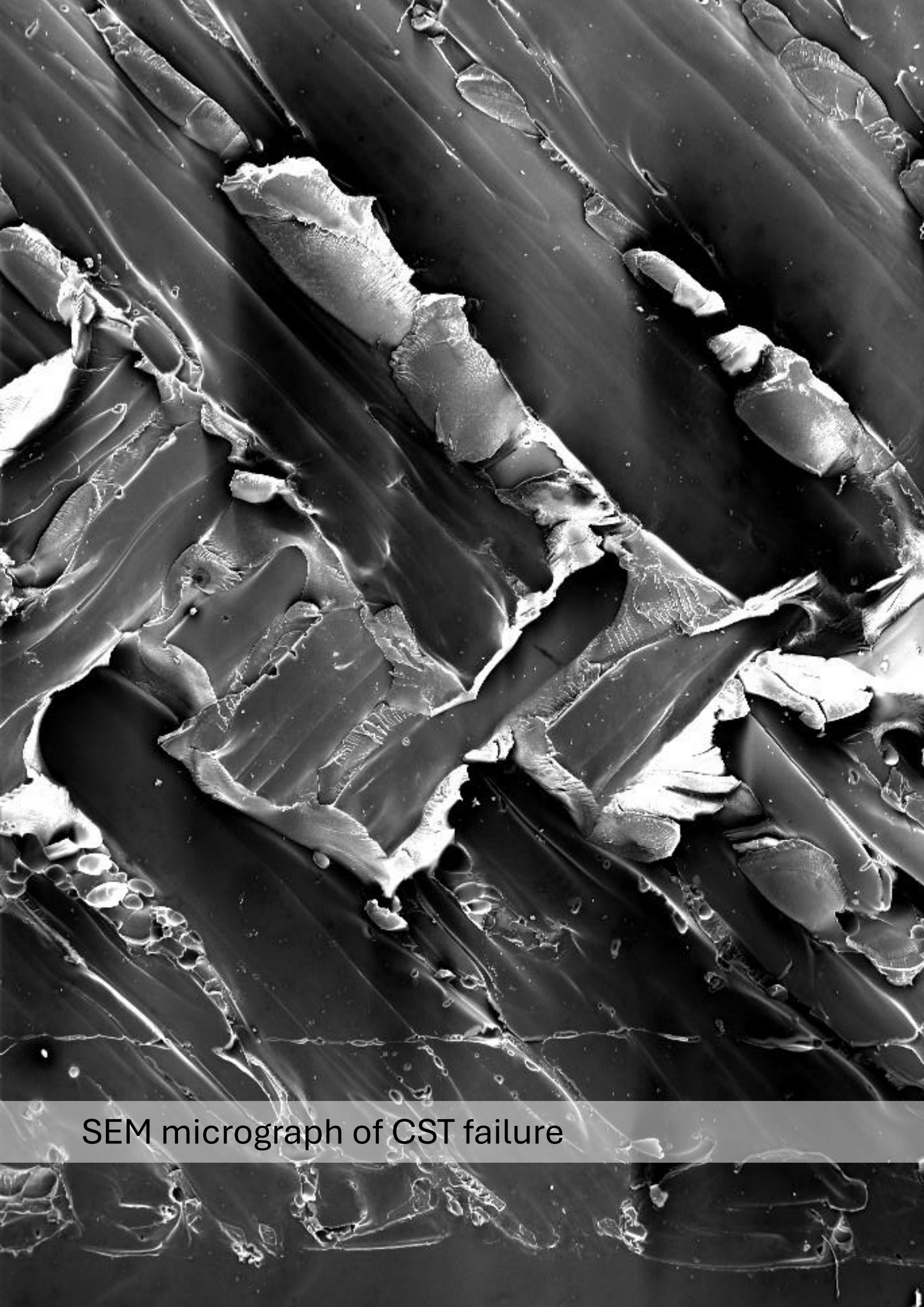

SEM micrograph of CST failure

9 Conclusions and Future Work

This chapter concludes the thesis and summarizes its contributions to the field. The research was motivated by the rapid growth of additive manufacturing and the limitations of fused filament fabrication (FFF), primarily its dependence on filament materials. Fused granulate fabrication (FGF) offers a cost-effective and material versatile alternative to FFF as it replaces filament with granulate feedstock as its raw material. Granulates are markedly cheaper and a wider range of materials are available in this format which may be used for FGF. Filament is fabricated from the same granulate during which process the material is degraded somewhat due to thermal loading. This is not an issue with FGF as it directly uses the granulate material. However, research on FGF is still limited, particularly in developing more accessible, small class extruders, which this thesis aimed to address.

The original aim was to develop a lightweight, simple, small scale, screw, granulate extrusion system for additive manufacturing and then apply that system to niche elastomeric and high-performance thermoplastic materials. The first step was to define the term 'small-scale' in the context of FGF extruders. A systematic literature review led to classification based on screw length and diameter. For small class extruders a screw length of less than 100 mm and a diameter greater than 7 mm was established as the acceptable range.

The review also highlighted research gaps across multiple FGF classes. This study focused solely on small class extruders. The scope of the study was limited to thermoplastics, including both elastomers and high-performance polymers. For elastomers, two types were extruded and 3D printed namely a hard elastomer, TPO, and a very soft one, TF3ZG0-LCNT. Two high-performance polymers were used namely, PEI which is predominantly amorphous and PEEK which is a semi-crystalline thermoplastic. The study emphasized low-cost, open-source solutions to develop an FGF extruder that could easily integrate with existing 3D printing motion systems. In this manner, the system developed would be more easily accessible to a wider audience and therefore its impact would be more substantial.

Three research gaps and their associated objectives guide d this work, each of which will be concluded in the following sections. In each case, the context of the text will focus on the extruder and the materials that were used with it.

9.1 Development of Small Scale FGF System

There is no existing small class FGF extruders capable of processing high performance thermoplastics as well as TPEs.

The objective linked with this first research gap was to develop a small, lightweight, granulate screw extruder which can extrude and 3D print using high temperature, high performance thermoplastics as well as TPEs. This study's contribution towards this research gap took the form of the extruder development outlined in chapter 4. This work achieved successful extrusion and 3D printing of the four materials originally set-out as part of the scope of the study namely TPO, TF3ZG0-LCNT, PEI and PEEK, as well as ABS. The latter is a conventional, commodity thermoplastic which is widely used as an FFF material.

A number of differences emerged between small-scale FGF and traditional large extruders. Initial analysis showed that small-scale FGF relies on conduction heating rather than viscous heating, making a powerful motor unnecessary. Instead, a lower-power motor reduces costs and weight but requires end-feeding to prevent pellet jamming. End feeding involves feeding the granule parallel with the screw axis, as opposed to side-feeding which is perpendicular. Side-feeding would cause pellets to get stuck between screw flight and barrel wall at the inlet, as the motor lacks the power to break them up.

The study also challenged common design practices, such as the length-to-diameter (L:D) ratio. Small-scale extruders use much lower ratios than the 20:1 or 30:1 which are typical L:D ratios in large industrial extruders. In this research, a 4.25:1 ratio screw with a 20 mm diameter was successfully used to extrude materials like ABS, TPO and PEEK, using Extruder deisgns 1 and 2. This suggests that some conventional rules for large extruders do not apply to small-scale systems. The successful use of a relatively large screw diameter hints at the potential for extruding irregular feedstock, such as reground thermoplastics even with small scale FGF.

Temperature control was another critical factor in extruder design. A cold feeding end was necessary for reliable solid conveying and pressure generation, especially with materials like TF3ZG0-LCNT which has a wide melting temperature range. Increasing the effective length of the cooling section and shortening the melting section prevented premature, undesired, pellet sticking. In contrast, TPO, with a narrower melting

temperature range, required less cooling. This discrepancy in melting behaviour was probably caused by difference in material chemistry whereby TPO is a homogenous, compatibilized alloy of polypropylene and EPDM rubber, whereas TF3ZG0-LCNT is assumed to be a blend of various materials.

The utilisation of AISI H13 tool steel, a high-temperature metallic material for the barrel, screw, and nozzle allowed for extrusion of high-performance thermoplastics. Additionally, the extruder's design was optimized for ease of handling and maintenance, which is when carrying out a screw warm push test. For instance, design elements were modified to prevent molten material ingress in threaded sections, reducing the risk of damage.

To handle the higher viscosity of high-performance thermoplastics, a 14 mm screw was developed, increasing theoretical processing force by 42.9% as opposed to the 20 mm screw and barrel system. This improvement in force increased throughput and enhanced printability. This was demonstrated when printing VESTAKEEP L4000G PEEK at a barrel temperature of 380°C. In this scenario using Extruder 3 (14 mm) required a lower extrusion multiplier in contrast with using Extruder 2 (20 mm).

This study also highlights the importance of extruder modularity to accommodate a range of thermoplastics. The developed extruder provides a cost-effective solution for small-scale FGF of high-performance thermoplastics and elastomers. When combined with a heated chamber 3D printer, it may allow users to produce parts with properties comparable to aluminium without the high costs of FFF PEEK or traditional machining practices. This advancement increases accessibility to applications such as load-bearing components, replacement parts, biomedical implants, and chemical-resistant objects, making additive manufacturing of high-performance materials more affordable and sustainable by using small scale FGF.

9.2 Determination and Optimisation of Process Parameters for FGF

Unknown processing parameter that are necessary to extrude and 3D print the materials selected using small-scale FGF extruders.

This research gap was addressed by the second objective which was to determine the optimal processing parameters for correct extrusion and 3D printing using the FGF system developed with the materials within the scope of the study.

TPO proved to be a good alternative to TPU, commonly used in FFF. No pre-drying was required due to its low measured water content saturation (cs) point of around 0.25%, compared to TPU's cs point of 2% [218]. TPO was successfully printed using both 1 mm and 0.4 mm nozzles, with barrel temperatures of 170°C, on a heated glass bed at 80°C and coated with Magigoo PP glue. The extrusion multipliers were 0.85 for the 1 mm nozzle and 5.5 for the 0.4 mm, indicating lower extrusion efficiency with the smaller nozzle. Tensile testing confirmed that the XY and YZ achieved the highest mechanical properties with superior stress at yield as well as stress and strain at break compared with the Z orientation. The best average stress at yield of 6.36 MPa was achieved when using the 0.4 mm nozzle and XY orientation, whereas the best average stress and strain at break of 13.8 MPa and 1300% respectively were reached by the specimens printed in the YZ orientation using the 1 mm nozzle. These results indicate that a 1 mm nozzle is best for mechanical properties at break whereas there is no clear distinction between stress at yield results for both nozzle sizes.

The other TPE 3D printed, TF3ZG0-LCNT required a longer cooling zone and shorter heating zone. This was necessary as TF3ZGO-LCNT is a blended TPE, which may cause its wide melting temperature range. Material characterisation tests revealed that a major component of the blend is polyamide (PA), which led to coating of the 70°C heated build plate with PA Magigoo adhesive. The optimal extrusion temperature ranged between 290°C and 310°C depending on the printing orientation. In the XY orientation, maximum strain exceeded 3365% at 300°C and 310°C. In contrast, the Z orientation which is the layer bond strength, improved at lower temperatures with strain at failure reaching 2328% ± 138 % at 290°C. This highlights the need to prioritize Z orientation strength for multiaxial strain applications.

The ease-of-use features implemented in Extruder 2 and later upgraded in Extruder 3, enabled the successful extrusion and 3D printing of PEI and PEEK. ULTEM 9085, a PEI grade, was relatively easy to 3D print, similar to TPO. With a 310°C extruder temperature and a 200°C build plate, the amorphous PEI could be successfully 3D printed with a 0.4 mm nozzle. A extrudate size enabled the attainment of better printing resolution which was necessary for production of injection moulding inserts. However, DMA Z orientation

specimens exhibited half the storage modulus of XY orientation specimens, indicating weakened layer bonding. This was attributed to the lack of heated chamber coupled with the use of a small nozzle diameter which led to weakening of the layer bond strength, lowering the overall part strength.

FGF of PEEK was markedly more challenging than that of PEI. Optimal PEEK extrusion required a smaller screw diameter, with a higher helix angle to generate sufficient pressure. Increased processing temperatures and higher molecular weight grades improved layer bond strength, with VESTAKEEP L4000G achieving 17.70 ± 0.58 MPa in shear strength at 420°C. The small molecular weight grade, VESTAKEEP L2000G, had the most significant 5-fold increased from 3.10 ± 1.58 MPa to 15.08 ± 1.68 MPa, brought about by increasing process temperature. Higher molecular weight PEEK also resulted in a 50% increase in tensile stress at failure, though tensile modulus was significantly lower compared to literature values. This process parameter optimisation exercised coupled with the material grade flexibility of FGF led to high mechanical properties despite the lack of a heated chamber.

In all extruder and material configurations, extrusion rate and screw speed did not correlate directly, necessitating non-linear adjustments. Throughout the study, 3D printing speeds were kept constant: 20 mm/s for PEEK and TF3ZG0-LCNT, and 30 mm/s for TPO and PEI. Slower speeds for PEEK and TF3ZG0-LCNT improved heat distribution and geometric accuracy, respectively, while higher speeds reduced printing time for TPO and PEI.

The study identified the key processing parameters for 3D printing the selected materials with small-scale FGF systems. These parameters provide a foundation for further optimization based on specific needs. While some advanced settings such as jerk or linear advance, were left at default, further tuning may be necessary for specific applications, such as load-bearing PEEK components with tight geometric tolerances. TF3ZG0-LCNT, in particular, requires more detailed research for printing larger objects due to its super soft nature which make it hard to maintain geometric tolerances.

In conclusion, this study provides a technique for desktop-scale 3D printing from pellets of elastomers and high-performance thermoplastics. The optimized parameters allow for novel production possibilities, simplifying prototyping and low-volume, customized fabrication processes for a wide range of users.

9.3 Quality and Application Evaluation

Unknown level of 3D printing quality achievable using small-scale FGF coupled with the materials selected.

The last research gap was addressed by the third objective which is to verify and validate the FGF system developed by producing case study parts of a specialized nature. Each of the materials studied has varying levels of prior research. ULTEM 9085 and PEEK are well-documented whereas TPO and TF3ZG0-LCNT are relatively novel with no significant studies, even with FFF. In view of this, a material-specific approach was undergone for TPEs and a more FGF centric evaluation was undergone for PEI and PEEK.

The TPO FGF process was validated by successfully 3D printing four complex geometries: a curly vase, a Benchy, a gyroid egg, and an orthotic insole. Each of these objects served a specific evaluation purpose. For instance, the successful printing of the curly vase demonstrated a continuous extrusion without unexpected blemishes or under extrusion events. The Benchy required retraction calibration to minimize stringing artefacts followed by the gyroid egg which represented a more challenging retraction test. Finally, an insole was produced successfully using the optimised TPO FGF process. In conclusion, TPO FGF was found to be a valid alternative for hard elastomer 3D printing, capable of high-quality production.

In contrast, the evaluation of TF3ZG0-LCNT focused on its ultra-soft properties, which enable unique capabilities but also limit printability. The key evaluation here was the material's stretchability and air-tightness. Biaxial strain tests on inflatables printed via FGF demonstrated significant stretchability, reaching a maximum strain of 590% before failure. Importantly, failures occurred consistently at the layer bond, indicating that even with a very soft TPE, layer bonding remained the weakest point. The material’s capability was further validated through the successful creation and testing of an elastomeric inflatable actuator, which gently manipulated a lightly loaded object, demonstrating practical applications for this material.

The evaluation of high-performance polymers, such as ULTEM 9085 and PEEK, required a focus on dimensional fidelity and surface roughness. ULTEM 9085 inserts for injection molding of cosmetic compounds revealed issues with surface roughness and dimensional warping, with deviations of ± 0.5 mm according to Chebyshev’s theorem at 95% range. The nature of 3 axis 3D printing left micro paths in the order of 10^{-1} mm which

caused a high surface roughness for flat, clamping surfaces and shallow slopes which could only be 3D printed as a series of terraces. This led to a lack of water-tightness which caused part flashing and undesired part anchorage. Despite these issues, the inserts were successfully used to produce 18 parts via injection molding prior to failure caused by a weak Z orientation.

Evaluation of PEEK focused on part strength, crystallinity, and surface roughness. While complex geometries were printed, the lack of uniform crystallinity, particularly in areas of rapid cooling, resulted in amorphous sections which were visibly semi-transparent. Crystallinity evaluation concluded that crystallinity increased with extruder temperature for high MVR grades but decreased for lower MVR grades. Apart from crystallisation, surface roughness was found to be consistent with previous FFF studies that used large nozzle diameters, confirming that the small scale FGF extrusion quality was acceptable for PEEK.

Addressing the research gap in FGF quality is a multifaceted challenge. For TPO, the results indicated that FGF can achieve or exceed the quality of FFF, particularly when compared to TPU. However, TF3ZG0-LCNT remains a poorly understood material, requiring further studies to enhance bond strength, minimize defects, and improve geometric fidelity for complex prints. These issues represent just a few of the questions raised by this research, leaving significant room for further exploration. The primary limitation for ULTEM 9085 and PEEK in FGF is the strength of the printed parts. While geometric accuracy is comparable to FFF, strength remains a concern. Future improvements could include incorporating a heated chamber, which would address both strength and geometric fidelity issues identified in this study.

The quality achieved by the FGF system developed was shown to be on par with that of FFF. In the case of TPEs the capabilities of FGF were found to be superior to those of FFF, introducing the capability to 3D print super soft TPE, otherwise impossible to do with FFF. The extrusion quality of high-performance thermoplastics was similar to that of FFF. Future enhancements in print quality will likely depend on improvements in motion systems and the introduction of heated chambers, which could unlock new levels of strength and geometric accuracy.

9.4 Impact and Limitations

The result of this work holds significance for additive manufacturing, particularly in expanding the capabilities of small-scale fused granulate fabrication. By demonstrating high-quality production across a wide range of materials including TPEs such as TPO and high-performance polymers such as PEEK and ULTEM 9085, this research enhanced the versatility and cost-efficiency of FGF systems. Compared to traditional FFF, FGF provided the added advantage of using granulate materials, reducing waste and material costs, which opens up advanced manufacturing to smaller enterprises.

This study also pioneered 3D printing of novel materials like TF3ZG0-LCNT, demonstrating their potential in specialized applications such as soft robotics. Additionally, it lays the groundwork for improving FGF processes through better control over extrusion temperatures, nozzle sizes, and screw speeds, all of which influence part quality. The findings suggest that future development of heated chambers and refined motion systems could significantly enhance both geometric fidelity and mechanical strength, particularly for high-performance polymers.

Industrially, the ability to print complex geometries with superior mechanical properties at lower costs opens new opportunities for customized, on-demand manufacturing in sectors such as automotive, aerospace, and healthcare. Moreover, this research contributes to sustainability by reducing material waste and aligning with the growing demand for more resource-efficient manufacturing processes.

This topical work contributed toward improving FGF in general which is one key solution towards the implementation of a circular economy to revalorise thermoplastic waste. Future developments in small scale FGF may even enable a domestic approach to such a circular economy. This research work contributed on a national level towards three R&I thematic areas specifically sustainable use of resources for climate change mitigation and adaptation, smart manufacturing and future digital technologies. On a European level it aligned with the European green deal and Waste Framework Directive 2008/98/EC. On a global level, it also promotes the United Nations goals, specifically 9 and 12 dealing with improving sustainability of production processes and reduction and revalorisation of waste.

Despite the fruitful impact of this study, key challenges remain. A major limitation is the motion system, especially for high-performance polymers, as the lack of a heated

chamber impacts strength and accuracy. Additionally, the extruder, though compact for FGF, is bulkier and heavier than FFF counterparts, requiring special motion systems to handle the added weight. FGF also lags behind FFF in ease of use. Filament-based systems are simpler, while FGF involves handling molten pellets, which can be messy and require skilled operators for cleaning and maintenance. High-performance polymers like PEEK are especially difficult to clean due to their viscous nature and high temperatures required. Calibration in FGF is also more complex due to its non-volumetric nature, making it harder than FFF, especially at varying speeds. These challenges, including more demanding operation and maintenance, make FGF less accessible and user-friendly than traditional filament-based systems, despite its potential for material versatility and cost savings.

These beneficial impacts brought about by the technology when contrasted with the remaining limitations of small scale FGF suggest that further development is necessary. A number of key research areas related with FGF will be outlined in the next section in order to improve the technology.

9.5 Future Work

In line with the scope, research gaps, and objectives of this study, future research should focus on improving the theoretical understanding of small-scale FGF through the development of models that take into account factors such as screw curvature, solid bed speed, and gravitational effects, in the context of short screws. Further reduction of extruder weight is also important to simplify motion systems, reducing complexity, cost and enhancing the interfacing of FGF technology to existing FFF systems. Enhancing energy efficiency is another key area, where the goal is to reduce heater and cooler power consumption without sacrificing temperature control, while improving thermal insulation to maintain consistent extrusion quality. Additionally, expanding the use of TF3ZG0-LCNT for super soft 3D printing should involve exploring more complex geometries, as well as potential applications in damping, biomedical devices, moulding, and training equipment, making it a versatile material able to provide novel solutions to multiple fields.

Beyond the scope of this study, more general areas for future work involve addressing broader industry and social needs. One promising avenue is the use of regrind waste materials for direct 3D printing, which would provide a viable consumer-level solution

for promoting a circular economy of thermoplastics, reducing material costs, and minimizing environmental impact. Further development of small-scale FGF extruders that can handle reinforced, high-performance thermoplastics efficiently, such as those with fibres or fillers, would open up new industrial applications. Another critical challenge is minimizing drooling in low-viscosity thermoplastics, which is essential for improving print quality. Integrating small-scale FGF extruders with heated chamber systems would enhance both the mechanical strength and geometric accuracy of 3D printed parts, especially when working with high-performance thermoplastics such as PEI and polyether ketones (PEK). Additionally, enhancing surface quality, particularly for applications like watertight and detailed surface finish injection moulding inserts, could be achieved by integrating a 5-axis motion system. This approach would significantly improve mould precision, especially for complex and curved surfaces, ensuring better fidelity and functionality in the final parts. Lastly, investigating the extrudability of composite materials with the developed system and optimizing it for high-viscosity, reinforced materials would expand the range of materials that can be effectively processed by small-scale FGF systems.

Finally, it is important to emphasise the field of additive manufacturing and even specifically that of FGF is still growing at a rapid rate. There are numerous research gaps available of which this chapter has only mentioned the most obvious and those that stem out directly from this work. The impact of FGF technology can already be felt in the world of manufacturing, prototyping, repair, maintenance and general products, at a consumer and domestic level. With the aid of future development, it can become an even more integral part of industry and society, fulfilling its large potential. Its unique benefits that were discussed throughout the text, make further development worthwhile.

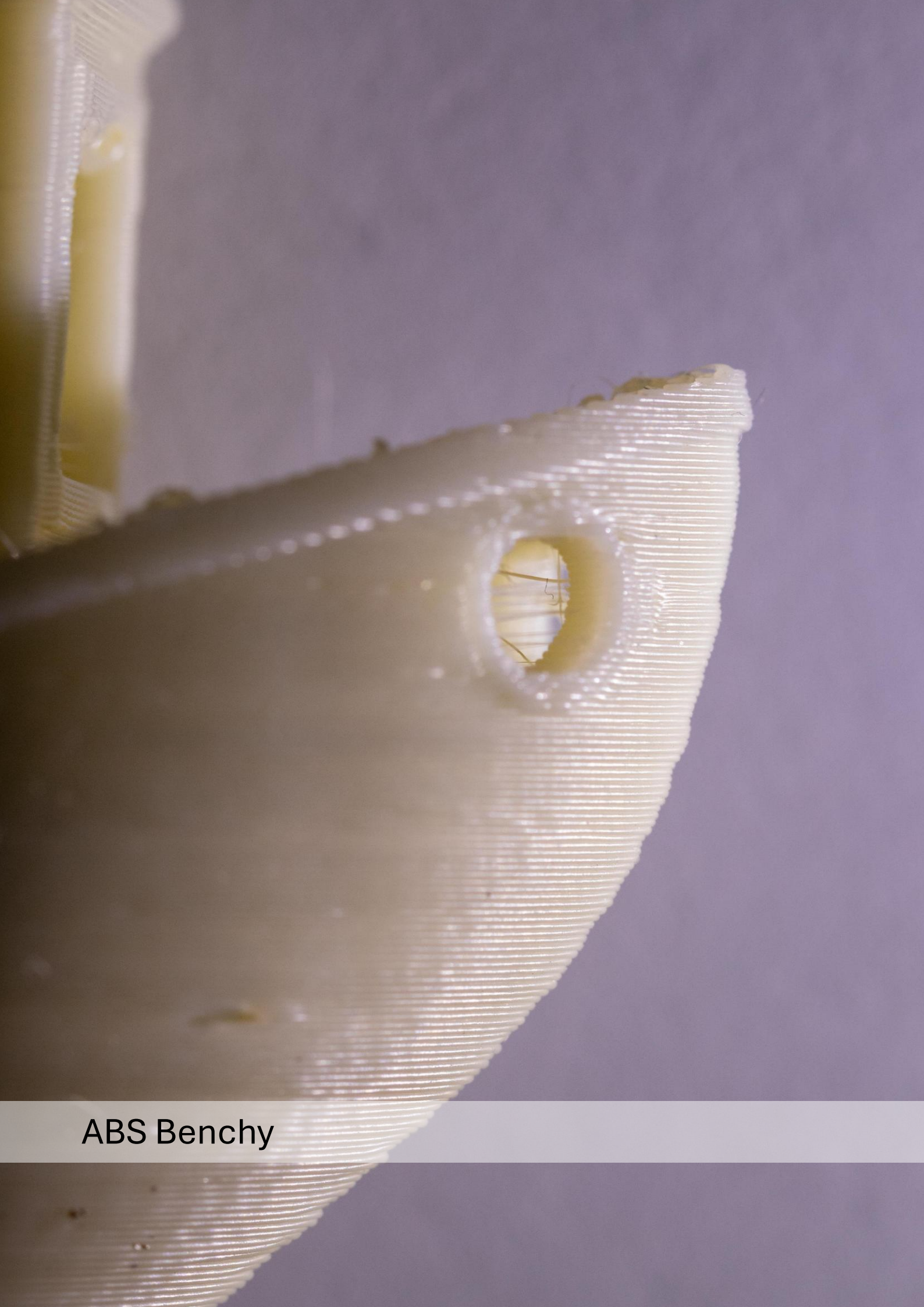

ABS Benchy

References

1. ISO/ASTM 52900:2021(en), Additive manufacturing — General principles — Fundamentals and vocabulary

2. Singh S, Ramakrishna S (2017) Biomedical applications of additive manufacturing: Present and future. Current Opinion in Biomedical Engineering 2:105–115. https://doi.org/10.1016/j.cobme.2017.05.006

3. Blakey-Milner B, Gradl P, Snedden G, et al (2021) Metal additive manufacturing in aerospace: A review. Materials & Design 209:110008. https://doi.org/10.1016/j.matdes.2021.110008

4. 3D Printing Market Size, Share | Forecast Analysis Report, 2032. https://www.fortunebusinessinsights.com/industry-reports/3d-printing-market-101902. Accessed 5 Nov 2024

5. Tan L, Zhu W, Zhou K (2020) Recent Progress on Polymer Materials for Additive Manufacturing. Advanced Functional Materials. https://doi.org/10.1002/ADFM.202003062

6. El Magri A, Vanaei S, Vaudreuil S (2021) An overview on the influence of process parameters through the characteristic of 3D-printed PEEK and PEI parts. High Performance Polymers 33:862–880. https://doi.org/10.1177/09540083211009961

7. Pagac M, Hajnys J, Ma Q-P, et al (2021) A Review of Vat Photopolymerization Technology: Materials, Applications, Challenges, and Future Trends of 3D Printing. Polymers 13:598. https://doi.org/10.3390/polym13040598

8. Al Rashid A, Ahmed W, Khalid MY, Koç M (2021) Vat photopolymerization of polymers and polymer composites: Processes and applications. Additive Manufacturing 47:102279. https://doi.org/10.1016/j.addma.2021.102279

9. Morici E, Dintcheva NT (2022) Recycling of Thermoset Materials and Thermoset-Based Composites: Challenge and Opportunity. Polymers 14:4153. https://doi.org/10.3390/polym14194153

10. (2021) The European Green Deal - European Commission. https://commission.europa.eu/strategy-and-policy/priorities-2019-2024/european-green-deal_en. Accessed 6 Nov 2024

11. THE 17 GOALS | Sustainable Development. https://sdgs.un.org/goals. Accessed 8 Mar 2024

12. Salmi M, Ituarte IF, Chekurov S, Huotilainen E (2016) Effect of build orientation in 3D printing production for material extrusion, material jetting, binder jetting, sheet object lamination, vat photopolymerisation, and powder bed fusion. International Journal of Collaborative Enterprise 5:218–231. https://doi.org/10.1504/IJCENT.2016.082334

13. Francis JN, Banerjee I, Chugh A, Singh J (2022) Additive manufacturing of polyetheretherketone and its composites: A review. Polymer Composites 43:5802–5819. https://doi.org/10.1002/pc.26961

14. Bain ED (2019) Polymer Powder Bed Fusion Additive Manufacturing: Recent Developments in Materials, Processes, and Applications. In: Polymer-Based Additive Manufacturing: Recent Developments. American Chemical Society, pp 7–36

15. Zhang Q, Davis AY, Black MS (2022) Emissions and Chemical Exposure Potentials from Stereolithography Vat Polymerization 3D Printing and Post-processing Units. ACS Chem Health Saf 29:184–191. https://doi.org/10.1021/acs.chas.2c00002

16. Jiang Z, Diggle B, Tan ML, et al (2020) Extrusion 3D Printing of Polymeric Materials with Advanced Properties. Advanced Science 7:2001379. https://doi.org/10.1002/advs.202001379

17. Rauwendaal C (2014) Polymer extrusion, 5th ed. Hanser Publications

18. Liao C-C, Li W-K, Su Y-H (2024) Influence of heated temperatures on PCM melting characteristics in a pneumatic-based extrusion system of fused deposition modeling: Experimental and numerical studies. Applied Thermal Engineering 124787. https://doi.org/10.1016/j.applthermaleng.2024.124787

19. Liu F, Hinduja S, Bartolo P (2017) Design, Fabrication and Initial Evaluation of a Novel Hybrid System for Tissue Engineering Applications. Procedia CIRP 65:213–218. https://doi.org/10.1016/j.procir.2017.04.030

20. Tadmor Z, Gogos CG (2006) Principles of Polymer Processing, 2nd Edition | Wiley, 2nd ed. Wiley-Interscience

21. Justino Netto JM, Idogava HT, Frezzatto Santos LE, et al (2021) Screw-assisted 3D printing with granulated materials: a systematic review. Int J Adv Manuf Technol 115:2711–2727. https://doi.org/10.1007/s00170-021-07365-z

22. Bellini A (2002) Fused deposition of ceramics: a comprehensive experimental, analytical and computational study of material behavior, fabrication process and equipment design. PhD Thesis, Drexel University

23. Bellini A, Shor L, Guceri S (2005) New developments in fused deposition modeling of ceramics. RAPID PROTOTYPING JOURNAL 11:214–220

24. Fico D, Rizzo D, Casciaro R, Esposito Corcione C (2022) A Review of Polymer-Based Materials for Fused Filament Fabrication (FFF): Focus on Sustainability and Recycled Materials. Polymers 14:465. https://doi.org/10.3390/polym14030465

25. Alexandre A, Cruz Sanchez FA, Boudaoud H, et al (2020) Mechanical Properties of Direct Waste Printing of Polylactic Acid with Universal Pellets Extruder: Comparison to Fused Filament Fabrication on Open-Source Desktop Three-Dimensional Printers. 3D Printing and Additive Manufacturing 7:237–247. https://doi.org/10.1089/3dp.2019.0195

26. (2024) Definition of ELASTIC. https://www.merriam-webster.com/dictionary/elastic. Accessed 8 Nov 2024

27. Desai SM, Sonawane RY, More AP (2023) Thermoplastic polyurethane for three-dimensional printing applications: A review. Polymers for Advanced Technologies 34:2061–2082. https://doi.org/10.1002/pat.6041

28. Awasthi P, Banerjee SS (2021) Fused deposition modeling of thermoplastic elastomeric materials: Challenges and opportunities. Additive Manufacturing 46:102177. https://doi.org/10.1016/j.addma.2021.102177

29. Drobny JG (2014) Handbook of Thermoplastic Elastomers, 2nd ed. Elsevier B.V.

30. Hailat M, Xiao HX, Frisch KC (2000) Studies on the Modification of Thermoplastic Polyolefins (TPOs)—Part I. Effect of Various Modifiers on the Adhesion of a Two-Component (2K) Polyurethane Coating to the Modified TPOs. Journal of Elastomers & Plastics 32:194–210. https://doi.org/10.1177/009524430003200302

31. Kraiburg TPE THERMOLAST® S TF3ZGOLCNT Thermoplastic Elastomer (FC/S Series). https://www.matweb.com/search/DataSheet.aspx?MatGUID=a1abff60cee5493888499d176c9f4f74. Accessed 16 Jan 2024

32. Das A, Chatham CA, Fallon JJ, et al (2020) Current understanding and challenges in high temperature additive manufacturing of engineering thermoplastic polymers. Additive manufacturing. https://doi.org/10.1016/J.ADDMA.2020.101218

33. Global Industrial Automation & Process Control Research Team at Frost & Sullivan (2022) Global Additive Manufacturing Growth Opportunities. Frost & Sullivan

34. Additive Manufacturing Market Size & Share | Growth Trends 2036. https://www.researchnester.com/reports/additive-manufacturing-market/5009. Accessed 13 Sep 2024

35. Fused Deposition Modeling (FDM) 3D Printing Market Analysis | Size. In: Global Market Estimates Research & Consultants. https://www.globalmarketestimates.com/market-report/fused-deposition-modeling-fdm-3d-printing-market-3944. Accessed 11 Nov 2024

36. Fused Granulate Fabrication (FGF) 3D Printer Market, Report Size, Worth, Revenue, Growth, Industry Value, Share 2024. In: Valuates Reports. https://reports.valuates.com/market-reports/QYRE-Auto-1P17325/global-fused-granulate-fabrication-fgf-3d-printer. Accessed 11 Nov 2024

37. Khondoker MAH, Sameoto D (2019) Direct coupling of fixed screw extruders using flexible heated hoses for FDM printing of extremely soft thermoplastic elastomers. Prog Addit Manuf 4:197–209. https://doi.org/10.1007/s40964-019-00088-4

38. Bernhardt EC, McKelvey JM (1958) Polymer Processing – New Engineering Specialty, 35th ed

39. Tadmor Z, Klein I (1978) Engineering Principles of Plasticating Extrusion. Krieger

40. Spalding MA, Dooley J, Hyun KS, Plastics D (1999) The Effect of Flight Radii Size on The Performance of Single-Screw Extruders. SPE ANTEC Tech Papers

41. Maddock B. H (1959) A Visual Analysis of Flow and Mixing in Extruder Screws. SPE J 15:383–389

42. Menges G, Klenk K (1967) Melting and plasticating of unplasticized PVC powder in the screw extruder. Kunststoffe 57:598–603

43. Lindt JT (1976) A dynamic melting model for a single-screw extruder. Polymer Engineering & Science 16:284–291. https://doi.org/10.1002/pen.760160411

44. Pricci A, De Tullio MD, Percoco G (2023) Modeling of extrusion-based additive manufacturing for pelletized thermoplastics: Analytical relationships between process parameters and extrusion outcomes. CIRP Journal of Manufacturing Science and Technology 41:239–258. https://doi.org/10.1016/j.cirpj.2022.11.020

45. Broyer E, Tadmor Z (1972) Solids conveying in screw extruders part I: A modified isothermal model. Polymer Engineering & Science 12:12–24. https://doi.org/10.1002/pen.760120103

46. Tadmor Z, Broyer E (1972) Solids conveying in screw extruders part II: Non isothermal model. Polymer Engineering & Science 12:378–386. https://doi.org/10.1002/pen.760120510

47. Tadmor Z, Duvdevani I, Klein I (1967) Melting in plasticating extuders theory and experiments. Polymer Engineering & Science 7:198–217. https://doi.org/10.1002/pen.760070313

48. Mount III EM, Chung CI (1978) Melting behavior of solid polymers on a metal surface at processing conditions. Polymer Engineering & Science 18:711–720. https://doi.org/10.1002/pen.760180906

49. Altınkaynak A, Gupta M, Spalding MA, Crabtree SL (2011) Melting in a Single Screw Extruder: Experiments and 3D Finite Element Simulations. International Polymer Processing 26:182–196. https://doi.org/10.3139/217.2419

50. Trippe J, Schöppner V (2017) Investigation of the influence of material and pellet shape on the dissipation in the solids conveying zone of single-screw extruders based on the discrete element method (DEM). AIP Conference Proceedings 1914:080002. https://doi.org/10.1063/1.5016742

51. La Gala A, Fiorio R, Erkoç M, et al (2020) Theoretical Evaluation of the Melting Efficiency for the Single-Screw Micro-Extrusion Process: The Case of 3D Printing of ABS. Processes 8:1522. https://doi.org/10.3390/pr8111522

52. Rauwendaal C (1983) TWO-STAGE EXTRUDER SCREWS. In: Conference Proceedings. Society of Plastics Engineers, p 186

53. Cong L, Gupta M (2008) Simulation of distributive and dispersive mixing in a co-rotating twin-screw extruder. pp 300–304

54. Injection Molding Static Mixing Nozzle (Type SMN) - StaMixCo Static Mixer Products & Technology. https://www.stamixco-usa.com/injection-molding-mixing. Accessed 5 Sep 2024

55. Screw Elements. In: CPM Extrusion Group. https://cpmextrusiongroup.com/components/screw-elements/. Accessed 5 Sep 2024

56. 2020-03-newsletter - Newsletters & Downloads - Leistritz Extrusion Technology. https://extruders.leistritz.com/en/newsletter/newsletter-overview/2020-12-newsletter. Accessed 5 Sep 2024

57. Page MJ, McKenzie JE, Bossuyt PM, et al (2021) The PRISMA 2020 statement: an updated guideline for reporting systematic reviews. BMJ 372:n71. https://doi.org/10.1136/bmj.n71

58. van Eck NJ, Waltman L (2010) Software survey: VOSviewer, a computer program for bibliometric mapping. Scientometrics 84:523–538. https://doi.org/10.1007/s11192-009-0146-3

59. VOSviewer - Visualizing scientific landscapes. In: VOSviewer. https://www.vosviewer.com//. Accessed 21 Mar 2024

60. Byard DJ, Woern AL, Oakley RB, et al (2019) Green fab lab applications of large-area waste polymer-based additive manufacturing. Additive Manufacturing 27:515–525. https://doi.org/10.1016/j.addma.2019.03.006

61. Romani A, Levi M, Pearce JM (2023) Recycled polycarbonate and polycarbonate/acrylonitrile butadiene styrene feedstocks for circular economy product applications with fused granular fabrication-based additive manufacturing. Sustainable Materials and Technologies 38:e00730. https://doi.org/10.1016/j.susmat.2023.e00730

62. Hu Z, He J, Chen W, et al (2024) High-performance carbon fiber reinforced polyether-ether-ketone composite pellets 3D-Printed via screw-extrusion additive manufacturing. Composites Science and Technology 246:110362. https://doi.org/10.1016/j.compscitech.2023.110362

63. Geoffroy L, Samyn F, Jimenez M, Bourbigot S (2019) Additive manufacturing of fire-retardant ethylene-vinyl acetate. POLYMERS FOR ADVANCED TECHNOLOGIES 30:1878–1890

64. Liu F, Vyas C, Poologasundarampillai G, et al (2018) Structural Evolution of PCL during Melt Extrusion 3D Printing. MACROMOLECULAR MATERIALS AND ENGINEERING 303

65. Liu F, Vyas C, Poologasundarampillai G, et al (2018) Process-Driven Microstructure Control in Melt-Extrusion-Based 3D Printing for Tailorable Mechanical Properties in a Polycaprolactone Filament. MACROMOLECULAR MATERIALS AND ENGINEERING 303

66. Liu F, Hinduja S, Bartolo P (2017) Design, fabrication and initial evaluation of a novel hybrid system for tissue engineering applications. 3RD CIRP CONFERENCE ON BIOMANUFACTURING 65:213–218

67. Liu F, Wang W, Mirihanage W, et al (2018) A plasma-assisted bioextrusion system for tissue engineering. CIRP ANNALS-MANUFACTURING TECHNOLOGY 67:229–232

68. Liu F, Hinduja S, Bartolo P (2018) User interface tool for a novel plasma-assisted bio-additive extrusion system. RAPID PROTOTYPING JOURNAL 24:368–378

69. Liu F, Wang W, Hinduja S, Bártolo PJ (2018) Hybrid Additive Manufacturing System for Zonal Plasma-Treated Scaffolds. 3D Printing and Additive Manufacturing 5:205–213. https://doi.org/10.1089/3dp.2018.0056

70. Stratasys FDM - Trademark Status & Document Retrieval - 1663961. https://tsdr.uspto.gov/#caseNumber=74133656&caseSearchType=US_APPLICATION&caseType=DEFAULT&searchType=statusSearch. Accessed 27 Mar 2024

71. Kumar N, Jain PK, Tandon P, Pandey PM 3D PRINTING OF FLEXIBLE PARTS USING EVA MATERIAL

72. Kumar N, Jain PK, Tandon P, Pandey PM (2018) Additive manufacturing of flexible electrically conductive polymer composites via CNC-assisted fused layer modeling process. J Braz Soc Mech Sci Eng 40:175. https://doi.org/10.1007/s40430-018-1116-6

73. Kumar N, Jain PK, Tandon P, Pandey PM (2018) Extrusion-based additive manufacturing process for producing flexible parts. J Braz Soc Mech Sci Eng 40:143. https://doi.org/10.1007/s40430-018-1068-x

74. Kumar N, Jain PK, Tandon P, Pandey PM (2018) Investigation on the effects of process parameters in CNC assisted pellet based fused layer modeling process. JOURNAL OF MANUFACTURING PROCESSES 35:428–436

75. Kumar N, Jain PK, Tandon P, Pandey PM (2018) The effect of process parameters on tensile behavior of 3D printed flexible parts of ethylene vinyl acetate (EVA). JOURNAL OF MANUFACTURING PROCESSES 35:317–326

76. Kumar N, Kumar Jain P (2021) Analysing the influence of raster angle, layer thickness and infill rate on the compressive behaviour of EVA through CNC-assisted fused layer modelling process. Proceedings of the Institution of Mechanical Engineers, Part C: Journal of Mechanical Engineering Science 235:1731–1740. https://doi.org/10.1177/0954406219889076

77. Georgopoulou A, Egloff L, Vanderborght B, Clemens F (2021) A Sensorized Soft Pneumatic Actuator Fabricated with Extrusion-Based Additive Manufacturing. Actuators 10:102. https://doi.org/10.3390/act10050102

78. Tian J, Zhang R, Wu Y, Xue P (2021) Additive manufacturing of wood flour/polyhydroxyalkanoates (PHA) fully bio-based composites based on micro-screw extrusion system. Materials & Design 199:109418. https://doi.org/10.1016/j.matdes.2020.109418

79. Tian J, Zhang R, Yang J, et al (2021) Additive Manufacturing of Wood Flour/PHA Composites Using Micro-Screw Extrusion: Effect of Device and Process Parameters on Performance. Polymers 13:1107. https://doi.org/10.3390/polym13071107

80. Carne RH, Alade AA, Orji BO, et al (2023) A screw extrusion-based system for additive manufacturing of wood: Sodium silicate thermoset composites. Advances

in Mechanical Engineering 15:16878132231210373. https://doi.org/10.1177/16878132231210373

81. Immonen K, Willberg-Keyriläinen P, Ropponen J, et al (2021) Thermoplastic Cellulose-Based Compound for Additive Manufacturing. Molecules 26:1701. https://doi.org/10.3390/molecules26061701

82. Wang W, Caetano G, Ambler W, et al (2016) Enhancing the Hydrophilicity and Cell Attachment of 3D Printed PCL/Graphene Scaffolds for Bone Tissue Engineering. Materials 9:992. https://doi.org/10.3390/ma9120992

83. Wang Z, Xu P, Zhou K, et al (2023) Flexural property characterization and structure analysis of graphene-reinforced polyphenylene sulfide prepared via low-cost pellet-based material extrusion additive manufacturing. Polymer Engineering & Science 63:3382–3397. https://doi.org/10.1002/pen.26453

84. Yu W, Hu Z, Zhang Y, et al (2023) Compatibilizing Biodegradable Poly(lactic acid)/polybutylene adipate-co-terephthalate Blends via Reactive Graphene Oxide for Screw-Based 3D Printing. Polymers 15:3992. https://doi.org/10.3390/polym15193992

85. Barbosa TV, Dernowsek JA, Tobar RJR, et al (2022) Fabrication, morphological, mechanical and biological performance of 3D printed poly(ϵ-caprolactone)/bioglass composite scaffolds for bone tissue engineering applications. Biomed Mater 17:055014. https://doi.org/10.1088/1748-605X/ac88ad

86. Bergaliyeva S, Sales DL, Jiménez Cabello JM, et al (2023) Thermal and Mechanical Properties of Reprocessed Polylactide/Titanium Dioxide Nanocomposites for Material Extrusion Additive Manufacturing. Polymers 15:3458. https://doi.org/10.3390/polym15163458

87. Wang Z, Zhang Q, Yue Y, et al (2019) 3D printed graphene/polydimethylsiloxane composite for stretchable strain sensor with tunable sensitivity. Nanotechnology 30:345501. https://doi.org/10.1088/1361-6528/ab1287

88. Lu S, Zhang B, Niu J, et al (2024) Effect of fiber content on mechanical properties of carbon fiber-reinforced polyether-ether-ketone composites prepared using screw extrusion-based online mixing 3D printing. Additive Manufacturing 80:103976. https://doi.org/10.1016/j.addma.2024.103976

89. Liu T, Tian X, Zhang Y, et al (2020) High-pressure interfacial impregnation by micro-screw in-situ extrusion for 3D printed continuous carbon fiber reinforced nylon composites. COMPOSITES PART A-APPLIED SCIENCE AND MANUFACTURING 130

90. Canessa E, Baruzzo M, Fonda C (2017) Study of Moineau-based pumps for the volumetric extrusion of pellets. ADDITIVE MANUFACTURING 17:143–150

91. (2020) MAHOR - V4 pellet extruder. In: mahor·xyz. https://mahor.xyz/producto/v4-pellet-extruder/. Accessed 27 Mar 2024

92. Tumaker | Integral Solutions in 3D Technology. In: Tumaker. https://tumaker.com/en/. Accessed 27 Mar 2024

93. Silveira ZC, De Freitas MS, Inforçatti Neto P, et al (2013) Study of the Technical Feasibility and Design of a Mini Head Screw Extruder Applied to Filament Deposition in Desktop 3-D Printer. KEM 572:151–154. https://doi.org/10.4028/www.scientific.net/KEM.572.151

94. Trejo EM, Jimenez X, Billah KMM, et al (2020) Compressive deformation analysis of large area pellet -fed material extrusion 3D printed parts in relation to in situ thermal imaging *. ADDITIVE MANUFACTURING 33

95. Billah KMM, Lorenzana FAR, Martinez NL, et al (2020) Thermomechanical characterization of short carbon fiber and short glass fiber-reinforced ABS used in large format additive manufacturing. ADDITIVE MANUFACTURING 35

96. Copenhaver K, Smith T, Armstrong K, et al (2023) Recyclability of additively manufactured bio-based composites. Composites Part B: Engineering 255:110617. https://doi.org/10.1016/j.compositesb.2023.110617

97. Korey M, Rencheck ML, Tekinalp H, et al (2023) Recycling polymer composite granulate/regrind using big area additive manufacturing. Composites Part B: Engineering 256:110652. https://doi.org/10.1016/j.compositesb.2023.110652

98. Pappas JM, Thakur AR, Leu MC, Dong X (2021) A parametric study and characterization of additively manufactured continuous carbon fiber reinforced composites for high-speed 3D printing. Int J Adv Manuf Technol 113:2137–2151. https://doi.org/10.1007/s00170-021-06723-1

99. Xiangyang D, John P, Aditya T (2021) Large-Scale Additive Manufacturing of High Strength Fiber-Reinforced Polymer Composites. In: SAMPE neXus 2021. NA SAMPE

100. Original Prusa MK4 3D Printer kit | Original Prusa 3D printers directly from Josef Prusa. In: Prusa3D by Josef Prusa. https://www.prusa3d.com/product/original-prusa-mk4-kit-2/#description. Accessed 28 Mar 2024

101. 3D Printers. In: Bambu Lab EU. https://eu.store.bambulab.com/en-mt/collections/3d-printer. Accessed 28 Mar 2024

102. Drotman D, Diagne M, Bitmead R, Krstic M (2016) Control-Oriented Energy-Based Modeling of a Screw Extruder Used for 3D Printing. In: Volume 2: Mechatronics; Mechatronics and Controls in Advanced Manufacturing; Modeling and Control of Automotive Systems and Combustion Engines; Modeling and Validation; Motion and Vibration Control Applications; Multi-Agent and Networked Systems; Path Planning and Motion Control; Robot Manipulators; Sensors and Actuators; Tracking Control Systems; Uncertain Systems and Robustness; Unmanned, Ground and Surface Robotics; Vehicle Dynamic Controls; Vehicle Dynamics and Traffic Control. American Society of Mechanical Engineers, Minneapolis, Minnesota, USA, p V002T21A002

103. Paramatti M, Romani A, Pugliese G, Levi M (2024) PLA Feedstock Filled with Spent Coffee Grounds for New Product Applications with Large-Format Material Extrusion Additive Manufacturing. ACS Omega

104. Suranaree University of Technology, Pitayachaval P, Baothong T, Suranaree University of Technology (2022) An Effect of Screw Extrusion Parameters On a

Pottery Model Forming by A Clay Printing Machine. IJIE 14:. https://doi.org/10.30880/ijie.2022.14.06.004

105. Liu X, Chi B, Jiao Z, et al (2017) A large-scale double-stage-screw 3D printer for fused deposition of plastic pellets. https://doi.org/10.1002/APP.45147

106. Mi D, Zhang J, Zhou X, et al (2023) Direct 3D Printing of Recycled PET/PP Granules by Shear Screw Extrusion. Polymers. https://doi.org/10.3390/POLYM15244620

107. Boyle BM, Xiong PT, Mensch TE, et al (2019) 3D printing using powder melt extrusion. Additive manufacturing. https://doi.org/10.1016/J.ADDMA.2019.100811

108. Samiul B, Ahmed K, Saito A, et al (2018) Development of Multi-Material 3D Printer. ECS Trans 88:449–453. https://doi.org/10.1149/08801.0449ecst

109. Products | FABRX. https://www.fabrx.co.uk/products. Accessed 4 Apr 2024

110. Aguilar-de-Leyva Á, Linares V, Domínguez-Robles J, et al (2023) Extrusion-based technologies for 3D printing: a comparative study of the processability of thermoplastic polyurethane-based formulations. Pharmaceutical Development and Technology 28:939–947. https://doi.org/10.1080/10837450.2023.2274945

111. Silveira ZDC, Freitas MSD, Neto PI, et al (2014) Design development and functional validation of an interchangeable head based on mini screw extrusion applied in an experimental desktop 3-D printer. IJRAPIDM 4:49. https://doi.org/10.1504/IJRAPIDM.2014.062037

112. Dávila J, Freitas MS, Neto P, et al (2016) Fabrication of PCL/β-TCP scaffolds by 3D mini-screw extrusion printing. https://doi.org/10.1002/APP.43031

113. Chiaroni AB, Silveira Z de C (2019) Experimental and numerical evaluation of the temperature profile of a modular extrusion head applied to an experimental 3D printer. The International Journal of Advanced Manufacturing Technology. https://doi.org/10.1007/S00170-019-03859-Z

114. Phung LX, Ngo NV, Nguyen HQ, et al (2023) Performance evaluation of different 3D printing techniques for PCL-based scaffold fabrication. In: Proceedings of the 2023 13th International Conference on Biomedical Engineering and Technology. ACM, Tokyo Japan, pp 198–203

115. Nguyen TK, Le BT, Nguyen MTH, et al (2023) Development of a novel direct powder screw extruder for 3D scaffold printing of PCL-based composites. Int J Adv Manuf Technol 128:3161–3182. https://doi.org/10.1007/s00170-023-12076-8

116. Zhou Z, Salaoru I, Morris P, Gibbons GJ (2018) Additive manufacturing of heat-sensitive polymer melt using a pellet-fed material extrusion. Additive Manufacturing 24:552–559. https://doi.org/10.1016/j.addma.2018.10.040

117. Justino Netto JM, Sarout AI, Santos ALG, et al (2022) Design and validation of an innovative 3D printer containing a co-rotating twin screw extrusion unit. Additive Manufacturing 59:103192. https://doi.org/10.1016/j.addma.2022.103192

118. Netto JMJ, Silveira ZC (2018) Design of an Innovative Three-Dimensional Print Head Based on Twin-Screw Extrusion. Journal of Mechanical Design. https://doi.org/10.1115/1.4041175

119. Fontana L, Giubilini A, Arrigo R, et al (2022) Characterization of 3D Printed Polylactic Acid by Fused Granular Fabrication through Printing Accuracy, Porosity, Thermal and Mechanical Analyses. Polymers 14:3530. https://doi.org/10.3390/polym14173530

120. Mosquera A, Andrade P, Cobos C, et al (2022) Redesign of a 3D Low Cost Filament Printer, Adapting it to a Pellet Extruder for New Material Assays. Macromolecular Symposia 404:2100323. https://doi.org/10.1002/masy.202100323

121. Drossel W-G, Ihlemann J, Landgraf R, et al (2020) Basic Research for Additive Manufacturing of Rubber. Polymers 12:2266. https://doi.org/10.3390/polym12102266

122. Alvarez Gómez M, Moreno Nieto D, Moreno Sánchez D, et al (2023) Additive Manufacturing of Thermoplastic Polyurethane-Cork Composites for Material Extrusion Technologies. Polymers 15:3291. https://doi.org/10.3390/polym15153291

123. Samaro A, Shaqour B, Goudarzi NM, et al (2021) Can filaments, pellets and powder be used as feedstock to produce highly drug-loaded ethylene-vinyl acetate 3D printed tablets using extrusion-based additive manufacturing? Int J Pharm 607:120922. https://doi.org/10.1016/j.ijpharm.2021.120922

124. Georgopoulou A, Clemens F (2022) Pellet-based fused deposition modeling for the development of soft compliant robotic grippers with integrated sensing elements. Flex Print Electron 7:025010. https://doi.org/10.1088/2058-8585/ac6f34

125. Liu H, Gong K, Portela A, et al (2023) Granule-based material extrusion is comparable to filament-based material extrusion in terms of mechanical performances of printed PLA parts: A comprehensive investigation. Additive Manufacturing 75:103744. https://doi.org/10.1016/j.addma.2023.103744

126. Pagés-Llobet A, Espinach FX, Julián F, et al (2023) Effect of Extruder Type in the Interface of PLA Layers in FDM Printers: Filament Extruder Versus Direct Pellet Extruder. Polymers 15:2019. https://doi.org/10.3390/polym15092019

127. Ivorra-Martinez J, Peydro MÁ, Gomez-Caturla J, et al (2023) The effects of processing parameters on mechanical properties of 3D-printed polyhydroxyalkanoates parts. Virtual and Physical Prototyping 18:e2164734. https://doi.org/10.1080/17452759.2022.2164734

128. Martinez-Orozco L, León N, Cailloux J, et al (2022) EcoBlends'up: PLA/BioPA blends composites, microfibrillated "in situ" through additive manufacturing. Theoretical and Applied Fracture Mechanics 118:103255. https://doi.org/10.1016/j.tafmec.2022.103255

129. Whyman S, Arif KM, Potgieter J (2018) Design and development of an extrusion system for 3D printing biopolymer pellets. INTERNATIONAL JOURNAL OF ADVANCED MANUFACTURING TECHNOLOGY 96:3417–3428

130. Patel A, Krishnanand, Taufik M (2022) Design and Analysis Studies in Pellet Extrusion Additive Manufacturing Processes. In: Deepak BBVL, Parhi DRK, Biswal BB, Jena PC (eds) Applications of Computational Methods in Manufacturing and Product Design. Springer Nature Singapore, Singapore, pp 351–359

131. Harris M, Potgieter J, Ray S, et al (2020) Polylactic acid and high-density polyethylene blend: Characterization and application in additive manufacturing. Journal of Applied Polymer Science 137:49602. https://doi.org/10.1002/app.49602

132. Wang F, Shor L, Darling A, et al (2004) Precision extruding deposition and characterization of cellular poly-ε-caprolactone tissue scaffolds. Rapid Prototyping Journal 10:42–49. https://doi.org/10.1108/13552540410512525

133. Kumar N, Jain PK, Tandon P, Pandey PM (2019) Toolpath Generation for Additive Manufacturing Using CNC Milling Machine. In: Kumar LJ, Pandey PM, Wimpenny DI (eds) 3D Printing and Additive Manufacturing Technologies. Springer Singapore, Singapore, pp 73–82

134. Bajpai A, Jain PK (2024) Investigation on using graphite filler for 3D printing of flexible electrically conductive polymer by extrusion-based additive manufacturing. Polymer Engineering & Sci 64:328–338. https://doi.org/10.1002/pen.26550

135. Kumar N, Jain PK, Tandon P, Pandey PM (2019) Investigations on the melt flow behaviour of aluminium filled ABS polymer composite for the extrusion-based additive manufacturing process. INTERNATIONAL JOURNAL OF MATERIALS & PRODUCT TECHNOLOGY 59:194–211

136. Kumar N, Jain PK, Tandon P, Mohan Pandey P (2018) Experimental investigations on suitability of polypropylene (PP) and ethylene vinyl acetate (EVA) in additive manufacturing. Materials Today: Proceedings 5:4118–4127. https://doi.org/10.1016/j.matpr.2017.11.672

137. Mittal YG, Kamble P, Gote G, et al (2023) A novel analytical model for screw extrusion of thermoplastic ABS with emphasis on additive manufacturing. Manufacturing Letters 35:652–657. https://doi.org/10.1016/j.mfglet.2023.08.054

138. Singamneni S, Warnakula A, Smith DA, Le Guen MJ (2019) Biopolymer Alternatives in Pellet Form for 3D Printing by Extrusion. 3D PRINTING AND ADDITIVE MANUFACTURING 6:217–226

139. Singamneni S, Behera MP, Truong D, et al (2021) Direct extrusion 3D printing for a softer PLA-based bio-polymer composite in pellet form. Journal of Materials Research and Technology 15:936–949. https://doi.org/10.1016/j.jmrt.2021.08.044

140. Hertle S, Kleffel T, Woerz A, Drummer D (2020) Production of polymer-metal hybrids using extrusion-based additive manufacturing and electrochemically treated aluminum. ADDITIVE MANUFACTURING 33

141. La Gala A, Fiorio R, Ceretti DVA, et al (2021) A Combined Experimental and Modeling Study for Pellet-Fed Extrusion-Based Additive Manufacturing to Evaluate the Impact of the Melting Efficiency. Materials 14:5566. https://doi.org/10.3390/ma14195566

142. Ceretti DVA, Marien YW, Edeleva M, et al (2022) Thermal and Thermal-Oxidative Molecular Degradation of Polystyrene and Acrylonitrile Butadiene Styrene during 3D Printing Starting from Filaments and Pellets. Sustainability 14:15488. https://doi.org/10.3390/su142315488

143. Khondoker MAH (2019) Development of a Multi-material Extruder System to 3D Print Hard Thermoplastics, Soft Elastomers and Liquid Metals. University of Alberta

144. Large Format Pellet Extruder FF- Pellet 600+. In: Impresoras 3D Fused Form. https://fusedformcorp.com/en/large-format-pellet-extruder-ff-pellet-600/. Accessed 5 Apr 2024

145. Mazzei Capote GA, Montoya-Ospina MC, Liu Z, et al (2022) Compounding a High-Permittivity Thermoplastic Material and Its Applicability in Manufacturing of Microwave Photonic Crystals. Materials 15:2492. https://doi.org/10.3390/ma15072492

146. MDPH2 - Pellet Head Extruder – Massive Dimension. https://massivedimension.com/products/mdphe-v1-pellet-head-extruder-system. Accessed 9 Apr 2024

147. Woern AL, Byard DJ, Oakley RB, et al (2018) Fused Particle Fabrication 3-D Printing: Recycled Materials' Optimization and Mechanical Properties. MATERIALS 11

148. Reich MJ, Woern AL, Tanikella NG, Pearce JM (2019) Mechanical Properties and Applications of Recycled Polycarbonate Particle Material Extrusion-Based Additive Manufacturing. MATERIALS 12

149. Little HA, Tanikella NG, J. Reich M, et al (2020) Towards Distributed Recycling with Additive Manufacturing of PET Flake Feedstocks. MATERIALS 13

150. Suescun Gonzalez C, Cruz Sanchez FA, Boudaoud H, et al Multi-material distributed recycling via material extrusion: recycled high density polyethylene and poly (ethylene terephthalate) mixture. Polymer Engineering & Science n/a: https://doi.org/10.1002/pen.26643

151. Schmidt L, Schricker K, Bergmann JP, et al (2019) Characterization of a granulate-based strand deposition process in the FLM-method for definition of material-dependent process strategies. RAPID PROTOTYPING JOURNAL 25:104–116

152. Brackett J, Yan Y, Cauthen D, et al (2019) Development of functionally graded material capabilities in large-scale extrusion deposition additive manufacturing. pp 1793–1803

153. Yeole P, Hassen AA, Kim S, et al (2020) Mechanical Characterization of High-Temperature Carbon Fiber-Polyphenylene Sulfide Composites for Large Area Extrusion Deposition Additive Manufacturing. ADDITIVE MANUFACTURING 34

154. Curmi A, Rochman A (2023) Miniaturized fused granulate fabrication of polyether ether ketone (PEEK). Prog Addit Manuf. https://doi.org/10.1007/s40964-023-00518-4

155. Tseng JW, Liu CY, Yen YK, et al (2018) Screw extrusion-based additive manufacturing of PEEK. Materials and Design 140:209–221. https://doi.org/10.1016/j.matdes.2017.11.032

156. Curmi A, Rochman A, Buhagiar J (2024) Influence of polyether ether ketone (PEEK) viscosity on interlayer shear strength in screw extrusion additive manufacturing. Additive Manufacturing 84:104086. https://doi.org/10.1016/j.addma.2024.104086

157. Barera G, Pegoretti A (2023) Screw Extrusion Additive Manufacturing of Carbon Fiber Reinforced PA6 Tools. https://doi.org/10.1007/S11665-023-08238-0

158. Wang Z, Liu R, Sparks T, Liou F (2016) Large-Scale Deposition System by an Industrial Robot (I): Design of Fused Pellet Modeling System and Extrusion Process Analysis. 3D Printing and Additive Manufacturing 3:39–47. https://doi.org/10.1089/3dp.2015.0029

159. Rattan RS, Nauta N, Romani A, Pearce JM (2023) Hangprinter for large scale additive manufacturing using fused particle fabrication with recycled plastic and continuous feeding. HardwareX 13:e00401. https://doi.org/10.1016/j.ohx.2023.e00401

160. Ludvigsen T Hangprinter - Cable Driven RepRap. https://hangprinter.org. Accessed 12 Apr 2024

161. Ludvigsen T (2024) tobbelobb/hp-mark

162. Li X, He J, Hu Z, et al (2022) High strength carbon-fiber reinforced polyamide 6 composites additively manufactured by screw-based extrusion. Composites Science and Technology 229:109707. https://doi.org/10.1016/j.compscitech.2022.109707

163. Direct3D – Pellet Extrusion. https://www.direct3d.it/. Accessed 16 Apr 2024

164. Piocreat G5Pro Industrial Pellets 3D printer - Piocreat. https://www.piocreat3d.com/product/g5pro-industrial-pellets-3d-printer.html. Accessed 16 Apr 2024

165. Brinter | 3D Bioprinted Human Biomods. In: Brinter. https://brinter.com/. Accessed 16 Apr 2024

166. 3D Cultures – Biofabrication Technologies. https://3dcultures.com/. Accessed 16 Apr 2024

167. REGENHU | Bioprinting for Tissue Models, Oral Dose Formulation and Drug Discovery. In: REGENHU. https://www.regenhu.com/. Accessed 17 Apr 2024

168. Daniele R, Armoni D, Dul S, Alessandro P (2023) From Nautical Waste to Additive Manufacturing: Sustainable Recycling of High-Density Polyethylene for 3D Printing Applications. Journal of Composites Science. https://doi.org/10.3390/JCS7080320

169. Wang W, Caetano GF, Chiang W-H, et al (2016) Morphological, mechanical and biological assessment of PCL/pristine graphene scaffolds for bone regeneration. Int J Bioprint 2:. https://doi.org/10.18063/IJB.2016.02.009

170. Huang B, Vyas C, Byun JJ, et al (2020) Aligned multi-walled carbon nanotubes with nanohydroxyapatite in a 3D printed polycaprolactone scaffold stimulates osteogenic differentiation. MATERIALS SCIENCE AND ENGINEERING C-MATERIALS FOR BIOLOGICAL APPLICATIONS 108

171. Huang B, Aslan E, Jiang Z, et al (2020) Engineered dual-scale poly (ε-caprolactone) scaffolds using 3D printing and rotational electrospinning for bone tissue regeneration. Additive Manufacturing 36:101452. https://doi.org/10.1016/j.addma.2020.101452

172. Lee JE, Sun Y-C, Lees I, Naguib HE (2024) Additive manufacturing of hybrid piezoelectric/magnetic self-sensing actuator using pellet extrusion and immersion precipitation with statistical modelling optimization. Composites Science and Technology 247:110393. https://doi.org/10.1016/j.compscitech.2023.110393

173. Pollen AM | Pellet Additive Manufacturing. https://www.pollen.am/index.html. Accessed 16 Apr 2024

174. AMBIT™ XTRUDE. In: Hybrid Manufacturing Technologies. https://hybridmanutech.com/portfolio/ambit-extrude/. Accessed 16 Apr 2024

175. Cosine AM1 3d Printer. In: Large Scale 3D Printing - Cosine. https://www.cosineadditive.com/en/am1. Accessed 16 Apr 2024

176. Yousfi M, Belhadj A, Lamnawar K, Maazouz A (2021) 3D printing of PLA and PMMA multilayered model polymers: an innovative approach for a better-controlled pellet multi-extrusion process. ESAFORM 2021. https://doi.org/10.25518/esaform21.1024

177. Andreu XL, Chenal J-M, Maazouz A, Lamnawar K (2023) Functionally Graded Multilayer Composites Based on Poly(D,L lactide)/Bioactive Fillers Fabricated by a 3D Direct Pellet Printing Multi-Extrusion Process. ACS Appl Polym Mater 5:236–246. https://doi.org/10.1021/acsapm.2c01475

178. Gradwohl M, Chai F, Payen J, et al (2021) Effects of Two Melt Extrusion Based Additive Manufacturing Technologies and Common Sterilization Methods on the Properties of a Medical Grade PLGA Copolymer. Polymers 13:572. https://doi.org/10.3390/polym13040572

179. Rigon D, Florian F, Ricotta M, et al (2021) Fatigue behaviour of 3D printed virgin and recycled short-glass-fiber-reinforced and mineral-filled polypropylene. Procedia Structural Integrity 34:199–204. https://doi.org/10.1016/j.prostr.2021.12.029

180. Spitaels L, Olabarri NA, Bossu J, et al (2024) Tool wear for finishing milling of green thermoplastic-ceramic composites fabricated with pellet AM. Procedia CIRP 121:97–102. https://doi.org/10.1016/j.procir.2023.09.235

181. Montoya-Ospina MC, Zeng J, Tan X, Osswald TA (2023) Material Extrusion Additive Manufacturing with Polyethylene Vitrimers. Polymers 15:1332. https://doi.org/10.3390/polym15061332

182. Northrup N, Weaver JM, George AR (2022) Durability of Vacuum Infusion Tooling Produced from Fused Granular Fabrication Additive Manufacturing. 3D Printing and Additive Manufacturing 3dp.2022.0130. https://doi.org/10.1089/3dp.2022.0130

183. Moreno Nieto D, Casal Lopez V, Ignacio Molina S (2018) Large-format polymeric pellet-based additive manufacturing for the naval industry. ADDITIVE MANUFACTURING 23:79–85

184. Sánchez DM, De La Mata M, Delgado FJ, et al (2020) Development of carbon fiber acrylonitrile styrene acrylate composite for large format additive manufacturing. Materials & Design 191:108577. https://doi.org/10.1016/j.matdes.2020.108577

185. Castelló-Pedrero P, García-Gascón C, García-Manrique JA (2024) Multiscale numerical modeling of large-format additive manufacturing processes using carbon fiber reinforced polymer for digital twin applications. Int J Mater Form 17:15. https://doi.org/10.1007/s12289-024-01811-5

186. Industrial 3D printer FGF Super Discovery 3D Printer. In: Discovery 3D Printers. https://discovery3dprinter.com/en/super-discovery-3d-printer-2/. Accessed 30 Sep 2024

187. Romani A, Perusin L, Ciurnelli M, Levi M (2024) Characterization of PLA feedstock after multiple recycling processes for large-format material extrusion additive manufacturing. Materials Today Sustainability 25:100636. https://doi.org/10.1016/j.mtsust.2023.100636

188. Winter K, Wilfert J, Häupler B, et al (2022) Large Scale 3D Printing: Influence of Fillers on Warp Deformation and on Mechanical Properties of Printed Polypropylene Components. Macro Materials & Eng 307:2100528. https://doi.org/10.1002/mame.202100528

189. Austermann J, Kuscera R, Wipperfürth J, et al (2023) Influence of material modification and fillers on the dimensional stability and warpage of polypropylene in screw-extrusion-based large area additive manufacturing. Polymer Engineering & Sci 63:1598–1612. https://doi.org/10.1002/pen.26309

190. Sayah N, Smith DE (2022) Effect of Process Parameters on Void Distribution, Volume Fraction, and Sphericity within the Bead Microstructure of Large-Area Additive Manufacturing Polymer Composites. Polymers 14:5107. https://doi.org/10.3390/polym14235107

191. Lengauer W, Duretek I, Fuerst M, et al (2019) Fabrication and properties of extrusion-based 3D-printed hardmetal and cermet components. INTERNATIONAL JOURNAL OF REFRACTORY METALS & HARD MATERIALS 82:141–149

192. Labus Zlatanovic D, Hildebrand J, Bergmann JP (2023) The study of screw extrusion-based additive manufacturing of eco-friendly aliphatic polyketone. Journal of Materials Research and Technology 25:4125–4138. https://doi.org/10.1016/j.jmrt.2023.06.223

193. Leschok M, Reiter L, Dillenburger B (2023) Large-scale hollow-core 3D printing (HC3DP): A polymer 3D printing technology for large-scale ultralightweight components. Additive Manufacturing 78:103874. https://doi.org/10.1016/j.addma.2023.103874

194. Mondal S, Katzschmann R, Clemens F (2023) Magnetorheological behavior of thermoplastic elastomeric honeycomb structures fabricated by additive manufacturing. Composites Part B: Engineering 252:110498. https://doi.org/10.1016/j.compositesb.2023.110498

195. Brooks BJ, Arif KM, Dirven S, Potgieter J (2017) Robot-assisted 3D printing of biopolymer thin shells. INTERNATIONAL JOURNAL OF ADVANCED MANUFACTURING TECHNOLOGY 89:957–968

196. Wang C, Zhang L, Fang Y, Sun W (2021) Design, Characterization, and 3D Printing of Cardiovascular Stents with Zero Poisson's Ratio in Longitudinal Deformation. Engineering 7:979–990. https://doi.org/10.1016/j.eng.2020.02.013

197. Reddy BV, Reddy NV, Ghosh A (2007) Fused deposition modelling using direct extrusion. Virtual and Physical Prototyping 2:51–60. https://doi.org/10.1080/17452750701336486

198. Akbari S, Johansson J, Johansson E, et al (2022) Large-Scale Robot-Based Polymer and Composite Additive Manufacturing: Failure Modes and Thermal Simulation. Polymers 14:1731. https://doi.org/10.3390/polym14091731

199. Krčma M, Paloušek D (2022) Comparison of the effects of multiaxis printing strategies on large-scale 3D printed surface quality, accuracy, and strength. Int J Adv Manuf Technol 119:7109–7120. https://doi.org/10.1007/s00170-022-08685-4

200. Romeijn T, Behrens M, Paul G, Wei D (2022) Instantaneous and long-term mechanical properties of Polyethylene Terephthalate Glycol (PETG) additively manufactured by pellet-based material extrusion. Additive Manufacturing 59:103145. https://doi.org/10.1016/j.addma.2022.103145

201. Duran MM, Moro G, Zhang Y, Islam A (2023) 3D printing of silicone and polyurethane elastomers for medical device application: A review. Advances in Industrial and Manufacturing Engineering 7:100125. https://doi.org/10.1016/j.aime.2023.100125

202. Banerjee SS, Burbine S, Kodihalli Shivaprakash N, Mead J (2019) 3D-Printable PP/SEBS Thermoplastic Elastomeric Blends: Preparation and Properties. Polymers 11:347. https://doi.org/10.3390/polym11020347

203. Dorigato A, Rigotti D, Pegoretti A (2018) Thermoplastic Polyurethane Blends With Thermal Energy Storage/Release Capability. Front Mater 5:. https://doi.org/10.3389/fmats.2018.00058

204. Korger M, Glogowsky A, Sanduloff S, et al (2020) Testing thermoplastic elastomers selected as flexible three-dimensional printing materials for functional garment and technical textile applications. Journal of Engineered Fibers and Fabrics 15:1558925020924599. https://doi.org/10.1177/1558925020924599

205. Unkovskiy A, Spintzyk S, Brom J, et al (2018) Direct 3D printing of silicone facial prostheses: A preliminary experience in digital workflow. The Journal of Prosthetic Dentistry 120:303–308. https://doi.org/10.1016/j.prosdent.2017.11.007

206. Wang J, McMullen C, Yao P, et al (2017) 3D-printed peristaltic microfluidic systems fabricated from thermoplastic elastomer. Microfluid Nanofluid 21:105. https://doi.org/10.1007/s10404-017-1939-y

207. Ma Z, Lin J, Xu X, et al (2019) Design and 3D printing of adjustable modulus porous structures for customized diabetic foot insoles. International Journal of Lightweight Materials and Manufacture 2:57–63. https://doi.org/10.1016/j.ijlmm.2018.10.003

208. Gorissen B, Reynaerts D, Konishi S, et al (2017) Elastic Inflatable Actuators for Soft Robotic Applications. Advanced Materials 29:1604977. https://doi.org/10.1002/adma.201604977

209. De Greef A, Lambert P, Delchambre A (2009) Towards flexible medical instruments: Review of flexible fluidic actuators. Precision Engineering 33:311–321. https://doi.org/10.1016/j.precisioneng.2008.10.004

210. Saadi M a. SR, Maguire A, Pottackal NT, et al (2022) Direct Ink Writing: A 3D Printing Technology for Diverse Materials. Advanced Materials 34:2108855. https://doi.org/10.1002/adma.202108855

211. Loterie D, Delrot P, Moser C (2020) High-resolution tomographic volumetric additive manufacturing. Nat Commun 11:852. https://doi.org/10.1038/s41467-020-14630-4

212. Loterie D, Delrot P, Moser C (2018) Volumetric 3D printing of elastomers by tomographic back-projections

213. Zanchin G, Leone G (2021) Polyolefin thermoplastic elastomers from polymerization catalysis: Advantages, pitfalls and future challenges. Progress in Polymer Science 113:101342. https://doi.org/10.1016/j.progpolymsci.2020.101342

214. Akkapeddi MK (2003) Commercial Polymer Blends. In: Utracki LA (ed) Polymer Blends Handbook. Springer Netherlands, Dordrecht, pp 1023–1115

215. Laoutid F, Lafqir S, Toncheva A, Dubois P (2021) Valorization of Recycled Tire Rubber for 3D Printing of ABS- and TPO-Based Composites. Materials 14:. https://doi.org/10.3390/ma14195889

216. Lv Q, Peng Z, Meng Y, et al (2022) Three-Dimensional Printing to Fabricate Graphene-Modified Polyolefin Elastomer Flexible Composites with Tailorable Porous Structures for Electromagnetic Interference Shielding and Thermal Management Application. Ind Eng Chem Res 61:16733–16746. https://doi.org/10.1021/acs.iecr.2c03086

217. Adrover-Monserrat B, Llumà J, Jerez-Mesa R, Travieso-Rodriguez JA (2023) Mechanical characterization of thermoplastic elastomers based on olefin processed through material extrusion. Int J Adv Manuf Technol 127:323–333. https://doi.org/10.1007/s00170-023-11523-w

218. Bruère VM, Lion A, Holtmannspötter J, Johlitz M (2022) Under-extrusion challenges for elastic filaments: the influence of moisture on additive manufacturing. Prog Addit Manuf 7:445–452. https://doi.org/10.1007/s40964-022-00300-y

219. Adflex X100G - Technical Datasheet. In: LyondellBasell. https://www.lyondellbasell.com/en/polymers/p/Adflex-X-100-G/cec1080a-3998-4cb1-85bd-616155008e33. Accessed 15 Dec 2023

220. Elastollan® (TPU) - the thermoplastic polyurethane of BASF. https://plastics-rubber.basf.com/emea/en/performance_polymers/products/elastollan.html. Accessed 15 Dec 2023

221. Massey LK (2002) Permeability Properties of Plastics and Elastomers A Guide to Packaging and Barrier Materials, 2nd ed. Elsevier B.V.

222. Pracella M (2017) 7 - Blends and Alloys. In: Jasso-Gastinel CF, Kenny JM (eds) Modification of Polymer Properties. William Andrew Publishing, pp 155–184

223. Ryntz RA (2000) Paintable, surface-damage resistant reactor grade thermoplastic olefin (TPO)

224. Wallin TJ, Pikul J, Shepherd RF (2018) 3D printing of soft robotic systems. Nat Rev Mater 3:84–100. https://doi.org/10.1038/s41578-018-0002-2

225. Xavier MS, Tawk CD, Zolfagharian A, et al (2022) Soft Pneumatic Actuators: A Review of Design, Fabrication, Modeling, Sensing, Control and Applications. IEEE Access 10:59442–59485. https://doi.org/10.1109/ACCESS.2022.3179589

226. Sun J-Y, Zhao X, Illeperuma WRK, et al (2012) Highly stretchable and tough hydrogels. Nature 489:133–136. https://doi.org/10.1038/nature11409

227. Wang Y, Yin R, Jin L, et al (2023) 3D-Printed Photoresponsive Liquid Crystal Elastomer Composites for Free-Form Actuation. Advanced Functional Materials 33:2210614. https://doi.org/10.1002/adfm.202210614

228. Cheng J, Wang R, Sun Z, et al (2022) Centrifugal multimaterial 3D printing of multifunctional heterogeneous objects. Nat Commun 13:7931. https://doi.org/10.1038/s41467-022-35622-6

229. Sylvie Beland (2012) High Performance Thermoplastic Resins and Their Composites, 1st ed. Elsevier

230. Strong AB (1993) High performance and engineering thermoplastic composites. Lancaster, Pa. : Technomic Pub. Co.

231. Chueca de Bruijn A, Gómez-Gras G, Pérez MA (2020) Mechanical study on the impact of an effective solvent support-removal methodology for FDM Ultem 9085 parts. Polymer Testing 85:106433. https://doi.org/10.1016/j.polymertesting.2020.106433

232. CAMPUS® Datasheet VESTAKEEP®4000 G - PEEK Evonik Operations GmbH

233. Sabic ULTEM™ RESIN 9085 Global Technical Data Sheet

234. Zanjanijam AR, Major I, Lyons JG, et al (2020) Fused Filament Fabrication of PEEK: A Review of Process-Structure-Property Relationships. Polymers 12:1665. https://doi.org/10.3390/polym12081665

235. Chuang KC, Grady JE, Draper RD, et al (2015) Additive Manufacturing and Characterization of Ultem Polymers and Composites. Dallas, TX

236. Zaldivar RJ, Witkin DB, McLouth T, et al (2017) Influence of processing and orientation print effects on the mechanical and thermal behavior of 3D-Printed ULTEM® 9085 Material. Additive Manufacturing 13:71–80. https://doi.org/10.1016/j.addma.2016.11.007

237. Byberg KI, Gebisa AW, Lemu HG (2018) Mechanical properties of ULTEM 9085 material processed by fused deposition modeling. Polymer Testing 72:335–347. https://doi.org/10.1016/j.polymertesting.2018.10.040

238. Fischer M, Schöppner V (2017) Fatigue Behavior of FDM Parts Manufactured with Ultem 9085. JOM 69:563–568. https://doi.org/10.1007/s11837-016-2197-2

239. Bagsik A, Schöppner V, Klemp E (2010) FDM part quality manufactured with Ultem* 9085. In: 14th international scientific conference on polymeric materials. pp 307–315

240. Taylor G, Wang X, Mason L, et al (2018) Flexural behavior of additively manufactured Ultem 1010: experiment and simulation. Rapid Prototyping Journal 24:1003–1011. https://doi.org/10.1108/RPJ-02-2018-0037

241. Taylor G, Anandan S, Murphy D, et al (2019) Fracture toughness of additively manufactured ULTEM 1010. Virtual and Physical Prototyping 14:277–283. https://doi.org/10.1080/17452759.2018.1558494

242. Han P, Tofangchi A, Deshpande A, et al (2019) An approach to improve interface healing in FFF-3D printed Ultem 1010 using laser pre-deposition heating. Procedia Manufacturing 34:672–677. https://doi.org/10.1016/j.promfg.2019.06.195

243. Ajinjeru C, Kishore V, Chen X, et al (2021) Rheological survey of carbon fiber-reinforced high-temperature thermoplastics for big area additive manufacturing tooling applications: Journal of Thermoplastic Composite Materials. https://doi.org/10.1177/0892705719873941

244. Polyakov I, Vaganov G, Yudin V, et al (2018) Investigation of properties of nanocomposite polyimide samples obtained by fused deposition modeling. Mechanics of Composite Materials 54:33–40

245. Kaynan O, Yildiz A, Bozkurt YE, et al (2019) Development of Multifunctional CNTs Reinforced PEI Filaments for Fused Deposition Modeling. In: AIAA Scitech 2019 Forum. American Institute of Aeronautics and Astronautics

246. Blanco I, Cicala G, Ognibene G, et al (2018) Thermal properties of polyetherimide/polycarbonate blends for advanced applications. Polymer

Degradation and Stability 154:234–238. https://doi.org/10.1016/j.polymdegradstab.2018.06.011

247. Crass A (2022) Ultem® Use in Aerospace Applications. In: Performance Plastics. https://performanceplastics.com/blog/ultem-use-in-aerospace-applications/. Accessed 12 Sep 2024

248. Fabrizio M, Strano M, Farioli D, Giberti H (2022) Extrusion Additive Manufacturing of PEI Pellets. Journal of Manufacturing and Materials Processing 6:157. https://doi.org/10.3390/jmmp6060157

249. Giberti H, Strano M, Annoni M (2016) An innovative machine for Fused Deposition Modeling of metals and advanced ceramics. MATEC Web of Conferences 43:03003. https://doi.org/10.1051/matecconf/20164303003

250. Biron M (2013) 4 - Detailed Accounts of Thermoplastic Resins. In: Biron M (ed) Thermoplastics and Thermoplastic Composites (Second Edition). William Andrew Publishing, pp 189–714

251. Dua R, Rashad Z, Spears J, et al (2021) Applications of 3D-Printed PEEK via Fused Filament Fabrication: A Systematic Review. Polymers 13:4046. https://doi.org/10.3390/polym13224046

252. Kurtz SM (2012) Chapter 1 - An Overview of PEEK Biomaterials. In: Kurtz SM (ed) PEEK Biomaterials Handbook. William Andrew Publishing, Oxford, pp 1–7

253. Rezvani Ghomi E, Eshkalak SK, Singh S, et al (2021) Fused filament printing of specialized biomedical devices: a state-of-the art review of technological feasibilities with PEEK. RPJ 27:592–616. https://doi.org/10.1108/RPJ-06-2020-0139

254. Arif MF, Kumar S, Varadarajan KM, Cantwell WJ (2018) Performance of biocompatible PEEK processed by fused deposition additive manufacturing. Materials & Design 146:249–259. https://doi.org/10.1016/j.matdes.2018.03.015

255. Abdullah F, Okuyama K, Morimitsu A, Yamagata N (2020) Effects of Thermal Cycle and Ultraviolet Radiation on 3D Printed Carbon Fiber/Polyether Ether Ketone Ablator. Aerospace 7:95. https://doi.org/10.3390/aerospace7070095

256. Deng X, Zeng Z, Peng B, et al (2018) Mechanical Properties Optimization of Poly-Ether-Ether-Ketone via Fused Deposition Modeling. Materials 11:216. https://doi.org/10.3390/ma11020216

257. Wang P, Zou B, Xiao H, et al (2019) Effects of printing parameters of fused deposition modeling on mechanical properties, surface quality, and microstructure of PEEK. Journal of Materials Processing Technology 271:62–74. https://doi.org/10.1016/j.jmatprotec.2019.03.016

258. Wu W, Geng P, Li G, et al (2015) Influence of layer thickness and raster angle on the mechanical properties of 3D-printed PEEK and a comparative mechanical study between PEEK and ABS. Materials 8:5834–5846. https://doi.org/10.3390/ma8095271

259. Valentan B, Kadivnik Z, Brajlih T, et al (2013) Processing Poly(Ether Etherketone) on a 3D Printer for Thermoplastic Modelling. Materiali in tehnologije

260. Rinaldi M, Ghidini T, Cecchini F, et al (2018) Additive layer manufacturing of poly (ether ether ketone) via FDM. Composites Part B: Engineering 145:162–172. https://doi.org/10.1016/j.compositesb.2018.03.029

261. Ding S, Zou B, Wang P, Ding H (2019) Effects of nozzle temperature and building orientation on mechanical properties and microstructure of PEEK and PEI printed by 3D-FDM. Polymer Testing 78:105948. https://doi.org/10.1016/j.polymertesting.2019.105948

262. Qu H, Zhang W, Li Z, et al (2022) Influence of Thermal Processing Conditions on Mechanical and Material Properties of 3D Printed Thin-Structures Using PEEK Material. Int J Precis Eng Manuf 23:689–699. https://doi.org/10.1007/s12541-022-00650-1

263. Challa BT, Gummadi SK, Elhattab K, et al (2022) In-house processing of 3D printable polyetheretherketone (PEEK) filaments and the effect of fused deposition modeling parameters on 3D-printed PEEK structures. Int J Adv Manuf Technol 121:1675–1688. https://doi.org/10.1007/s00170-022-09360-4

264. Li Y, Lou Y (2020) Tensile and Bending Strength Improvements in PEEK Parts Using Fused Deposition Modelling 3D Printing Considering Multi-Factor Coupling. Polymers 12:2497. https://doi.org/10.3390/polym12112497

265. Vidakis N, Petousis M, Mountakis N, Karapidakis E (2023) Box-Behnken modeling to quantify the impact of control parameters on the energy and tensile efficiency of PEEK in MEX 3D-printing. Heliyon 9:e18363. https://doi.org/10.1016/j.heliyon.2023.e18363

266. El Magri A, Vaudreuil S, Ben Ayad A, et al (2023) Effect of printing parameters on tensile, thermal and structural properties of 3D -printed poly (ether ketone ketone) PEKK material using fused deposition modeling. J of Applied Polymer Sci 140:e54078. https://doi.org/10.1002/app.54078

267. El Magri A, El Mabrouk K, Vaudreuil S, et al (2020) Optimization of printing parameters for improvement of mechanical and thermal performances of 3D printed poly(ether ether ketone) parts. J of Applied Polymer Sci 137:49087. https://doi.org/10.1002/app.49087

268. Xu Q, Shang Y, Jiang Z, et al (2021) Effect of molecular weight on mechanical properties and microstructure of 3D printed poly(ether ether ketone). Polymer International 70:1065–1072. https://doi.org/10.1002/pi.6166

269. Zhao D, Li T, Zhang H, et al (2021) Effects of processing parameters and annealing on the mechanical properties of polyether ether ketone(PEEK) via fused deposition modeling(FDM). In: 2021 3rd International Academic Exchange Conference on Science and Technology Innovation (IAECST). IEEE, Guangzhou, China, pp 1020–1026

270. Zarean P, Malgaroli P, Zarean P, et al (2023) Effect of Printing Parameters on Mechanical Performance of Material-Extrusion 3D-Printed PEEK Specimens at the Point-of-Care. Applied Sciences 13:1230. https://doi.org/10.3390/app13031230

271. Mohamed T, Barhoumi N, Lamnawar K, et al (2021) Optimization of fused deposition modeling process parameters using the Taguchi method to improve the tensile properties of 3D-printed polyether ether ketone. Proceedings of the Institution of Mechanical Engineers, Part L: Journal of Materials: Design and Applications 235:2565–2573. https://doi.org/10.1177/14644207211017572

272. Jiang C-P, Cheng Y-C, Lin H-W, et al (2022) Optimization of FDM 3D printing parameters for high strength PEEK using the Taguchi method and experimental validation. RPJ 28:1260–1271. https://doi.org/10.1108/RPJ-07-2021-0166

273. Sikder P, Challa BT, Gummadi SK (2022) A comprehensive analysis on the processing-structure-property relationships of FDM-based 3-D printed polyetheretherketone (PEEK) structures. Materialia 22:101427. https://doi.org/10.1016/j.mtla.2022.101427

274. Timoumi M, Barhoumi N, Znaidi A, et al (2022) Mechanical behavior of 3D-printed PEEK and its application for personalized orbital implants with various infill patterns and densities. Journal of the Mechanical Behavior of Biomedical Materials 136:105534. https://doi.org/10.1016/j.jmbbm.2022.105534

275. Rendas P, Figueiredo L, Geraldo M, et al (2023) Improvement of tensile and flexural properties of 3D printed PEEK through the increase of interfacial adhesion. Journal of Manufacturing Processes 93:260–274. https://doi.org/10.1016/j.jmapro.2023.03.024

276. Pulipaka A, Gide KM, Beheshti A, Bagheri ZS (2023) Effect of 3D printing process parameters on surface and mechanical properties of FFF-printed PEEK. Journal of Manufacturing Processes 85:368–386. https://doi.org/10.1016/j.jmapro.2022.11.057

277. Berretta S, Davies R, Shyng YT, et al (2017) Fused Deposition Modelling of high temperature polymers: Exploring CNT PEEK composites. Polymer Testing 63:251–262. https://doi.org/10.1016/j.polymertesting.2017.08.024

278. Pigliaru L, Rinaldi M, Ciccacci L, et al (2020) 3D printing of high performance polymer-bonded PEEK-NdFeB magnetic composite materials. Functional Composite Mater 1:4. https://doi.org/10.1186/s42252-020-00006-w

279. Shang Y, Xu Q, Jiang B, et al (2022) Slowing crystallization to enhance interlayer strength of 3D printed poly (ether ether ketone) parts by molecular design. Additive Manufacturing 59:103104. https://doi.org/10.1016/j.addma.2022.103104

280. Xu Q, Xu W, Yang Y, et al (2022) Enhanced interlayer strength in 3D printed poly (ether ether ketone) parts. Additive Manufacturing 55:102852. https://doi.org/10.1016/j.addma.2022.102852

281. Diouf-Lewis A, Farahani RD, Iervolino F, et al (2022) Design and characterization of carbon fiber-reinforced PEEK/PEI blends for Fused Filament Fabrication additive

manufacturing. Materials Today Communications 31:103445. https://doi.org/10.1016/j.mtcomm.2022.103445

282. Wang P, Zou B, Ding S, et al (2021) Effects of FDM-3D printing parameters on mechanical properties and microstructure of CF/PEEK and GF/PEEK. Chinese Journal of Aeronautics 34:236–246. https://doi.org/10.1016/j.cja.2020.05.040

283. Ai J-R, Li S, Vogt BD (2022) Increased strength in carbon-poly(ether ether ketone) composites from material extrusion with rapid microwave post processing. Additive Manufacturing 60:103209. https://doi.org/10.1016/j.addma.2022.103209

284. van de Werken N, Koirala P, Ghorbani J, et al (2021) Investigating the hot isostatic pressing of an additively manufactured continuous carbon fiber reinforced PEEK composite. Additive Manufacturing 37:101634. https://doi.org/10.1016/j.addma.2020.101634

285. Zhen H, Zhao B, Quan L, Fu J (2023) Effect of 3D Printing Process Parameters and Heat Treatment Conditions on the Mechanical Properties and Microstructure of PEEK Parts. Polymers 15:2209. https://doi.org/10.3390/polym15092209

286. Chen W, Zhang X, Tan D, et al (2022) Improvement in Mechanical Properties of 3D-Printed PEEK Structure by Nonsolvent Vapor Annealing. Macromol Rapid Commun 43:2100874. https://doi.org/10.1002/marc.202100874

287. Yang C, Tian X, Li D, et al (2017) Influence of thermal processing conditions in 3D printing on the crystallinity and mechanical properties of PEEK material. Journal of Materials Processing Technology 248:1–7. https://doi.org/10.1016/j.jmatprotec.2017.04.027

288. Mrówka M, Machoczek T, Jureczko P, et al (2021) Mechanical, Chemical, and Processing Properties of Specimens Manufactured from Poly-Ether-Ether-Ketone (PEEK) Using 3D Printing. Materials 14:2717. https://doi.org/10.3390/ma14112717

289. Wu W, Xin J, Hu B, et al (2023) Achieving injection molding interlayer strength via powder assisted hot isostatic pressing in material extrusion polyetheretherketone. Additive Manufacturing 74:103735. https://doi.org/10.1016/j.addma.2023.103735

290. Hu B, Duan X, Xing Z, et al (2019) Improved design of fused deposition modeling equipment for 3D printing of high-performance PEEK parts. Mechanics of Materials 137:103139. https://doi.org/10.1016/j.mechmat.2019.103139

291. Han P, Tofangchi A, Zhang S, et al (2020) Effect of in-process laser interface heating on strength isotropy of extrusion-based additively manufactured PEEK. Procedia Manufacturing 48:737–742. https://doi.org/10.1016/j.promfg.2020.05.107

292. Liu T, Zhang M, Kang Y, et al (2023) Material extrusion 3D printing of polyether ether ketone in vacuum environment: Heat dissipation mechanism and performance. Additive Manufacturing 62:103390. https://doi.org/10.1016/j.addma.2023.103390

293. Velisaris CN, Seferis JC (1986) Crystallization kinetics of polyetheretherketone (peek) matrices. Polymer Engineering & Science 26:1574–1581

294. Wu WZ, Geng P, Zhao J, et al (2014) Manufacture and thermal deformation analysis of semicrystalline polymer polyether ether ketone by 3D printing. Materials Research Innovations 18:S5-12-S5-16. https://doi.org/10.1179/1432891714Z.000000000898

295. Rodgers MBL, I. VJ (2020) SEMI-CRYSTALLINE BUILD MATERIALS

296. #3DBenchy. In: #3DBenchy. https://www.3dbenchy.com/. Accessed 15 Dec 2023

297. Official CR-10S: 300*300*400mm/Filament Sensor/Dual Z-axis. https://www.creality3dofficial.com/products/official-creality-cr-10s-3d-printer. Accessed 1 Oct 2024

298. 3D printers | Original Prusa 3D printers directly from Josef Prusa. In: Prusa3D by Josef Prusa. https://www.prusa3d.com/category/3d-printers/. Accessed 1 Oct 2024

299. V6 Hemera XS Direct Kit. In: E3D. https://e3d-online.com/products/hemera-xs-direct-kit. Accessed 1 Oct 2024

300. 123-3D.nl - 3D-printers | kits | parts | filament. In: 123-3D.nl. https://www.123-3d.nl. Accessed 1 Oct 2024

301. Nema 17 Bipolar 1.8deg 79Ncm(111.896oz.in) 2.3A 42x42x67mm 4 Wires - 17HS26-2304S | StepperOnline. https://www.omc-stepperonline.com/nema-17-bipolar-1-8deg-79ncm-111-896oz-in-2-3a-42x42x67mm-4-wires-17hs26-2304s. Accessed 4 Oct 2024

302. Nema 17 Stepper Motor L=39mm Gear Ratio 20:1 High Precision Planetary Gearbox - 17HS15-0404S-HG20 | StepperOnline. https://www.omc-stepperonline.com/nema-17-stepper-motor-l-39mm-gear-ratio-20-1-high-precision-planetary-gearbox-17hs15-0404s-hg20. Accessed 4 Oct 2024

303. Otai J (2023) Strength and hardness of 4140 steel at different temperatures. In: Special steel china supplier-OTAI Special Steel. https://www.otaisteel.com/strength-and-hardness-of-4140-steel/. Accessed 5 Oct 2024

304. ASM International Handbook Committee (1990) ASM handbook. Volume 1, Properties and selection: irons, steels, and high-performance alloys, 10th ed. ASM International, Materials Park, OH

305. Brandes EA, Brook GB (1992) Smithells Metals Reference Book. Elsevier B.V.

306. A global ABS solutions provider. https://www.elix-polymers.com/product-file/2/p2h-at. Accessed 12 Jun 2025

307. Acrylonitrile Butadiene Styrene (ABS) | Trinseo. https://www.trinseo.com/solutions/acrylonitrile-butadiene-styrene. Accessed 12 Jun 2025

308. NatureWorks | Home. https://www.natureworksllc.com/. Accessed 12 Jun 2025

309. Bex GJ, Six W, De Keyzer J, et al (2019) Two-component injection moulding of thermoplastics with thermoset rubbers: The effect of the mould temperature distribution. AIP Conference Proceedings 2055:080002. https://doi.org/10.1063/1.5084876

310. Lendvai L, Rigotti D (2023) Thermal and thermomechanical properties of boron nitride-filled acrylonitrile butadiene styrene (ABS) composites. Acta Technica Jaurinensis 16:123–128. https://doi.org/10.14513/actatechjaur.00706

311. Holman J (2009) Heat Transfer, 10th edition. McGraw-Hill Education, Boston

312. NF-A4x20 PWM. https://noctua.at/en/products/fan/nf-a12x15-pwm-176. Accessed 15 Oct 2024

313. Spoerk M, Gonzalez-Gutierrez J, Sapkota J, et al (2018) Effect of the printing bed temperature on the adhesion of parts produced by fused filament fabrication. Plastics, Rubber and Composites 47:17–24. https://doi.org/10.1080/14658011.2017.1399531

314. Thingiverse.com Ten Easter Eggshells by DaveMakesStuff. https://www.thingiverse.com/thing:5316996. Accessed 15 Dec 2023

315. Lee C-Y, Liu C-Y (2019) The influence of forced-air cooling on a 3D printed PLA part manufactured by fused filament fabrication. Additive Manufacturing 25:196–203. https://doi.org/10.1016/j.addma.2018.11.012

316. León-Calero M, Reyburn Valés SC, Marcos-Fernández Á, Rodríguez-Hernandez J (2021) 3D Printing of Thermoplastic Elastomers: Role of the Chemical Composition and Printing Parameters in the Production of Parts with Controlled Energy Absorption and Damping Capacity. Polymers 13:. https://doi.org/10.3390/polym13203551

317. Rigotti D, Dorigato A, Pegoretti A (2018) 3D printable thermoplastic polyurethane blends with thermal energy storage/release capabilities. Materials Today Communications 15:228–235. https://doi.org/10.1016/j.mtcomm.2018.03.009

318. Arifvianto B, Iman TN, Prayoga BT, et al (2021) Tensile properties of the FFF-processed thermoplastic polyurethane (TPU) elastomer. Int J Adv Manuf Technol 117:1709–1719. https://doi.org/10.1007/s00170-021-07712-0

319. Beloshenko V, Beygelzimer Y, Chishko V, et al (2021) Mechanical Properties of Flexible TPU-Based 3D Printed Lattice Structures: Role of Lattice Cut Direction and Architecture. Polymers 13:2986. https://doi.org/10.3390/polym13172986

320. Kabir S, Kim H, Lee S (2020) Physical property of 3D-printed sinusoidal pattern using shape memory TPU filament. Textile Research Journal 90:2399–2410. https://doi.org/10.1177/0040517520919750

321. Max volumetric speed | Prusa Knowledge Base. https://help.prusa3d.com/article/max-volumetric-speed_127176. Accessed 15 Dec 2023

322. (2020) The Plastics Group of America. Polifil® TPO – Thermoplastic Polyolefin (Filled and Unfilled) - Processing Guide. https://plasticsgroup.com/wp-content/uploads/2020/07/processing_guide_tpo.pdf. Accessed 1 Oct 2022

323. Gordelier TJ, Thies PR, Turner L, Johanning L (2019) Optimising the FDM additive manufacturing process to achieve maximum tensile strength: a state-of-the-art review. Rapid Prototyping Journal 25:953–971. https://doi.org/10.1108/RPJ-07-2018-0183

324. Zhang S-U, Han J, Kang H-W (2017) Temperature-dependent mechanical properties of ABS parts fabricated by fused deposition modeling and vapor smoothing. Int J Precis Eng Manuf 18:763–769. https://doi.org/10.1007/s12541-017-0091-7

325. Torrado AR, Shemelya CM, English JD, et al (2015) Characterizing the effect of additives to ABS on the mechanical property anisotropy of specimens fabricated by material extrusion 3D printing. Additive Manufacturing 6:16–29. https://doi.org/10.1016/j.addma.2015.02.001

326. Haryńska A, Carayon I, Kosmela P, et al (2020) Processing of Polyester-Urethane Filament and Characterization of FFF 3D Printed Elastic Porous Structures with Potential in Cancellous Bone Tissue Engineering. Materials 13:. https://doi.org/10.3390/ma13194457

327. Jung YS, Woo J, Lee E, et al (2022) Synthesis and properties of bio-based thermoplastic poly(ether urethane) for soft actuators. J Polym Res 29:521. https://doi.org/10.1007/s10965-022-03375-x

328. Maldonado MP, Pinto GM, Costa LC, Fechine GJM (2022) Enhanced thermally conductive TPU/graphene filaments for 3D printing produced by melt compounding. Journal of Applied Polymer Science 139:e52405. https://doi.org/10.1002/app.52405

329. Samadikhoshkho Z, Zareinia K, Janabi-Sharifi F (2019) A Brief Review on Robotic Grippers Classifications. In: 2019 IEEE Canadian Conference of Electrical and Computer Engineering (CCECE). IEEE, Edmonton, AB, Canada, pp 1–4

330. Mandlekar N, Joshi M, Butola BS (2022) A review on specialty elastomers based potential inflatable structures and applications. Advanced Industrial and Engineering Polymer Research 5:33–45. https://doi.org/10.1016/j.aiepr.2021.05.004

331. Schenk M, Viquerat AD, Seffen KA, Guest SD (2014) Review of Inflatable Booms for Deployable Space Structures: Packing and Rigidization. Journal of Spacecraft and Rockets 51:762–778. https://doi.org/10.2514/1.A32598

332. Rus D, Tolley MT (2015) Design, fabrication and control of soft robots. Nature 521:467–475. https://doi.org/10.1038/nature14543

333. Tawk C, Spinks GM, In Het Panhuis M, Alici G (2019) 3D Printable Linear Soft Vacuum Actuators: Their Modeling, Performance Quantification and Application in Soft Robotic Systems. IEEE/ASME Trans Mechatron 24:2118–2129. https://doi.org/10.1109/TMECH.2019.2933027

334. Keong BAW, Hua RYC (2018) A Novel Fold-Based Design Approach toward Printable Soft Robotics Using Flexible 3D Printing Materials. Advanced Materials Technologies 3:1700172. https://doi.org/10.1002/admt.201700172

335. Rosalia L, Ang BW-K, Yeow RC-H (2018) Geometry-Based Customization of Bending Modalities for 3D-Printed Soft Pneumatic Actuators. IEEE Robot Autom Lett 3:3489–3496. https://doi.org/10.1109/LRA.2018.2853640

336. Demir KG, Zhang Z, Yang J, Gu GX (2020) Computational and Experimental Design Exploration of 3D-Printed Soft Pneumatic Actuators. Advanced Intelligent Systems 2:2000013. https://doi.org/10.1002/aisy.202000013

337. Tawk C, In Het Panhuis M, Spinks GM, Alici G (2018) Bioinspired 3D Printable Soft Vacuum Actuators for Locomotion Robots, Grippers and Artificial Muscles. Soft Robotics 5:685–694. https://doi.org/10.1089/soro.2018.0021

338. Xavier MS, Tawk CD, Yong YK, Fleming AJ (2021) 3D-printed omnidirectional soft pneumatic actuators: Design, modeling and characterization. Sensors and Actuators A: Physical 332:113199. https://doi.org/10.1016/j.sna.2021.113199

339. Anver HMCM, Mutlu R, Alici G (2017) 3D printing of a thin-wall soft and monolithic gripper using fused filament fabrication. In: 2017 IEEE International Conference on Advanced Intelligent Mechatronics (AIM). IEEE, Munich, Germany, pp 442–447

340. Herianto, Irawan W, Ritonga AS, Prastowo A (2019) Design and fabrication in the loop of soft pneumatic actuators using fused deposition modelling. Sensors and Actuators A: Physical 298:111556. https://doi.org/10.1016/j.sna.2019.111556

341. Scharff RBN, Wu J, Geraedts JMP, Wang CCL (2019) Reducing Out-of-Plane Deformation of Soft Robotic Actuators for Stable Grasping. In: 2019 2nd IEEE International Conference on Soft Robotics (RoboSoft). IEEE, Seoul, Korea (South), pp 265–270

342. NinjaFlex 3D Printer Filament (85A). In: NinjaTek. https://ninjatek.com/shop/ninjaflex/. Accessed 30 Jan 2024

343. TPU Filament Filaflex 82A, Flexible Filament for 3D Printing. In: Recreus. https://recreus.com/gb/filaments/9-684-filaflex-82a.html. Accessed 30 Jan 2024

344. eFlex（TPU-87A）. In: https://www.esun3d.com/. https://~^(?<subdomain>.+)\\.esun3d\\.com$:443/eflex-tpu-87a-product/. Accessed 30 Jan 2024

345. S series TPU 95A. In: UltiMaker. https://ultimaker.com/materials/s-series-tpu-95a/. Accessed 30 Jan 2024

346. ISO 37:2017 Rubber, vulcanized or thermoplastic - Determination of tensile stress-strain properties

347. ISO 62:2008 Plastics - Determination of water absorption

348. Blandino J, Sterling J, Baginski F, et al (2004) Optical Strain Measurement of an Inflated Cylinder Using Photgrammetry with Application to Scientific Balloons. In: 45th AIAA/ASME/ASCE/AHS/ASC Structures, Structural Dynamics & Materials Conference. American Institute of Aeronautics and Astronautics, Palm Springs, California

349. Yang K, Natherson RA, Yoder CD, Roth S (2021) A Comparison of Two Non-Contact Strain Measurement Techniques with Applications to Scientific Balloons

350. Bustos C, Herrera CG, Celentano D, et al (2016) Numerical Simulation and Experimental Validation of the Inflation Test of Latex Balloons. Lat Am j solids struct 13:2657–2678. https://doi.org/10.1590/1679-78252622

351. Socrates G, Socrates G (2001) Infrared and Raman characteristic group frequencies: tables and charts, 3rd ed. Wiley, Chichester ; New York

352. Boubakri A, Elleuch K, Guermazi N, Ayedi HF (2009) Investigations on hygrothermal aging of thermoplastic polyurethane material. Materials & Design 30:3958–3965. https://doi.org/10.1016/j.matdes.2009.05.038

353. Gibson I (2005) Rapid Prototyping: a Tool for Product Development. Computer-Aided Design and Applications 2:785–793. https://doi.org/10.1080/16864360.2005.10738342

354. Shelton TE, Willburn ZA, Hartsfield CR, et al (2020) Effects of thermal process parameters on mechanical interlayer strength for additively manufactured Ultem 9085. Polymer Testing 81:106255. https://doi.org/10.1016/j.polymertesting.2019.106255

355. Davoudinejad A, Khosravani MR, Pedersen DB, Tosello G (2020) Influence of thermal ageing on the fracture and lifetime of additively manufactured mold inserts. Engineering Failure Analysis 115:104694. https://doi.org/10.1016/j.engfailanal.2020.104694

356. Davoudinejad A, Bayat M, Pedersen DB, et al (2019) Experimental investigation and thermo-mechanical modelling for tool life evaluation of photopolymer additively manufactured mould inserts in different injection moulding conditions. Int J Adv Manuf Technol 102:403–420. https://doi.org/10.1007/s00170-018-3163-7

357. Moritz VF, Bezerra GSN, Hopkins Jnr M, et al (2022) Heat Dissipation Plays Critical Role for Longevity of Polymer-Based 3D-Printed Inserts for Plastics Injection Moulding. JMMP 6:117. https://doi.org/10.3390/jmmp6050117

358. Mischkot M, Davoudinejad A, Charalambis A, et al (2017) Dimensional accuracy of Acrylonitrile Butadiene Styrene injection molded parts produced in a pilot production with an additively manufactured insert. In: 33rd Annual Meeting of the Polymer Processing Society (PPS33)

359. Dizon JRC, Valino AD, Souza LR, et al (2020) 3D Printed Injection Molds Using Various 3D Printing Technologies. MSF 1005:150–156. https://doi.org/10.4028/www.scientific.net/MSF.1005.150

360. Walsh E, Ter Horst JH, Markl D (2021) Development of 3D printed rapid tooling for micro-injection moulding. Chemical Engineering Science 235:116498. https://doi.org/10.1016/j.ces.2021.116498

361. Dempsey D, McDonald S, Masato D, Barry C (2020) Characterization of Stereolithography Printed Soft Tooling for Micro Injection Molding. Micromachines 11:819. https://doi.org/10.3390/mi11090819

362. A. Vella, Arif, Rochman, Pierre, Vella (2023) Rapid tooling development for low volume injection molding of cosmetic compacts. Material Research Forum 207–216. https://doi.org/10.21741/9781644902479-23

363. Rodzeń K, Harkin-Jones E, Wegrzyn M, et al (2021) Improvement of the layer-layer adhesion in FFF 3D printed PEEK/carbon fibre composites. Composites Part A: Applied Science and Manufacturing 149:106532. https://doi.org/10.1016/j.compositesa.2021.106532

364. Altaf K, Rani AMA, Ahmad F, Ahmad J Enhanced polymer rapid tooling for metal injection moulding process. In: Pro-AM Conference Papers. Nanyang Technological University

365. Altaf K, Qayyum J, Rani A, et al (2018) Performance Analysis of Enhanced 3D Printed Polymer Molds for Metal Injection Molding Process. Metals 8:433. https://doi.org/10.3390/met8060433

366. Boros R, Kannan Rajamani P, Kovacs JG (2019) Combination of 3D printing and injection molding: Overmolding and overprinting. Express Polym Lett 13:889–897. https://doi.org/10.3144/expresspolymlett.2019.77

367. Gohn AM, Brown D, Mendis G, et al (2022) Mold inserts for injection molding prototype applications fabricated via material extrusion additive manufacturing. Additive Manufacturing 51:102595. https://doi.org/10.1016/j.addma.2022.102595

368. Zink B, Kovács NK, Kovács JG (2019) Thermal analysis based method development for novel rapid tooling applications. International Communications in Heat and Mass Transfer 108:104297. https://doi.org/10.1016/j.icheatmasstransfer.2019.104297

369. Tomori T, Melkote S, Kotnis M (2004) Injection mold performance of machined ceramic filled epoxy tooling boards. Journal of Materials Processing Technology 145:126–133. https://doi.org/10.1016/S0924-0136(03)00881-1

370. Sá Ribeiro A, Hopkinson N, Henrique Ahrens C (2004) Thermal effects on stereolithography tools during injection moulding. Rapid Prototyping Journal 10:176–180. https://doi.org/10.1108/13552540410538996

371. Zhang Y, Moon SK (2021) The Effect of Annealing on Additive Manufactured ULTEM™ 9085 Mechanical Properties. Materials 14:2907. https://doi.org/10.3390/ma14112907

372. Farioli D, Strano M, Vangosa FB, et al (2021) Rapid tooling for injection molding inserts. ESAFORM 2021. https://doi.org/10.25518/esaform21.4186

373. Roozenburg NFM, Eekels J (1995) Product Design: Fundamentals and Methods. Wiley, Chichester

374. Bagalkot A, Pons D, Symons D, Clucas D (2021) Analysis of Raised Feature Failures on 3D Printed Injection Moulds. Polymers 13:1541. https://doi.org/10.3390/polym13101541

375. Ćwikła G, Grabowik C, Kalinowski K, et al (2017) The influence of printing parameters on selected mechanical properties of FDM/FFF 3D-printed parts. IOP Conf Ser: Mater Sci Eng 227:012033. https://doi.org/10.1088/1757-899X/227/1/012033

376. (2023) CloudCompare (version 2.13) [GPL software].

377. Li H, Taylor G, Bheemreddy V, et al (2015) Modeling and characterization of fused deposition modeling tooling for vacuum assisted resin transfer molding process. Additive Manufacturing 7:64–72. https://doi.org/10.1016/j.addma.2015.02.003

378. Manufacture of Fused Deposition Modeling Joints using ULTEM 9085

379. LyondellBasel (2023) Moplen HP501L Technical Data Sheet

380. PEI 9085 Pellets | Filament2Print. https://filament2print.com/gb/pellets-and-coloring/1308-pei-9085-pellets.html. Accessed 23 Jan 2024

381. PEI Ultem 9085 Filament. In: 3D4Makers.com | 3D Printing Filament. https://www.3d4makers.com/products/pei-ultem-9085-filament. Accessed 23 Jan 2024

382. Grey Resin. In: Formlabs. https://formlabs.com/eu/store/materials/grey-resin/. Accessed 23 Jan 2024

383. High Temp Resin. In: Formlabs. https://formlabs.com/eu/store/materials/high-temp-resin/. Accessed 23 Jan 2024

384. Kazmer DO (2016) Venting. In: Injection Mold Design Engineering. Carl Hanser Verlag GmbH & Co. KG, pp 227–242

385. Lerma Valero JR (2020) CHAPTER 2 - Thermodynamic Behavior of Plastics: PVT Graphs. In: Lerma Valero JR (ed) Plastics Injection Molding. Hanser, pp 25–34

386. Lerma Valero JR (2020) CHAPTER 25 - Defects in Injection Molded Parts. In: Lerma Valero JR (ed) Plastics Injection Molding. Hanser, pp 328–344

387. Wu XL, Huang WM, Ding Z, et al (2014) Characterization of the thermoresponsive shape-memory effect in poly(ether ether ketone) (PEEK). J Appl Polym Sci 131:n/a-n/a. https://doi.org/10.1002/app.39844

388. Triminì V, Varetti S, Percoco G, et al (2023) Evaluation of the influence of process parameters on crystallinity and tensile strength of 3D printed PEEK parts. Proceedings of the Institution of Mechanical Engineers, Part C: Journal of Mechanical Engineering Science. https://doi.org/10.1177/09544062231198784

389. Curmi A, Rochman A (2022) From Theory to Practice: Development and Calibration of Micro Pellet Extruder for Additive Manufacturing. Key Engineering Materials 926:34–45. https://doi.org/10.4028/p-b22a9a

390. Wang P, Zou B, Ding S (2019) Modeling of surface roughness based on heat transfer considering diffusion among deposition filaments for FDM 3D printing heat-resistant resin. Applied Thermal Engineering 161:. https://doi.org/10.1016/j.applthermaleng.2019.114064

391. Alsoufi MS, El-Sayed A, Elsayed AE (2017) How Surface Roughness Performance of Printed Parts Manufactured by Desktop FDM 3D Printer with PLA+ is Influenced by Measuring Direction. American Journal of Mechanical Engineering 5:211–222. https://doi.org/10.12691/ajme-5-5-4

392. Li Y, Linke BS, Voet H, et al (2017) Cost, sustainability and surface roughness quality – A comprehensive analysis of products made with personal 3D printers. CIRP Journal of Manufacturing Science and Technology 16:1–11. https://doi.org/10.1016/j.cirpj.2016.10.001

393. Barreno-Avila AF, Monar-Naranjo M, Barreno-Avila EM (2021) Fusion deposition modeling (FDM) 3D printing parameters correlation: An analysis of different polymers surface roughness. IOP Conference Series: Materials Science and Engineering 1173:012071. https://doi.org/10.1088/1757-899x/1173/1/012071

394. Rajat J, Nauriyal S, Khas KS Effects of Process Parameters on Surface Roughness, Dimensional Accuracy and Printing Time in 3D Printing. In: Advances in Production and Industrial Engineering. pp 187–197

395. Collinson DW, Windheim N von, Gall K, Brinson LC (2022) Direct evidence of interfacial crystallization preventing weld formation during fused filament fabrication of poly(ether ether ketone). Additive Manufacturing 51:. https://doi.org/10.1016/j.addma.2022.102604

396. Zhou H, Cheng X, Jiang X, et al (2023) Study of the interlayer bonding strength for combined printing and milling of polyetheretherketone. J of Applied Polymer Sci 140:e53773. https://doi.org/10.1002/app.53773

397. Luo M, Tian X, Shang J, et al (2020) Bi-scale interfacial bond behaviors of CCF/PEEK composites by plasma-laser cooperatively assisted 3D printing process. Composites Part A: Applied Science and Manufacturing 131:105812. https://doi.org/10.1016/j.compositesa.2020.105812

398. Luo M, Tian X, Zhu W, Li D (2018) Controllable interlayer shear strength and crystallinity of PEEK components by laser-assisted material extrusion. J Mater Res 33:1632–1641. https://doi.org/10.1557/jmr.2018.131

399. Basgul C, Yu T, MacDonald DW, et al (2018) Structure–property relationships for 3D-printed PEEK intervertebral lumbar cages produced using fused filament fabrication. J Mater Res 33:2040–2051. https://doi.org/10.1557/jmr.2018.178

400. Luo M, Tian X, Shang J, et al (2019) Impregnation and interlayer bonding behaviours of 3D-printed continuous carbon-fiber-reinforced poly-ether-ether-

ketone composites. Composites Part A: Applied Science and Manufacturing 121:130–138. https://doi.org/10.1016/j.compositesa.2019.03.020

401. Wang P, Zou B (2022) Improvement of Heat Treatment Process on Mechanical Properties of FDM 3D-Printed Short- and Continuous-Fiber-Reinforced PEEK Composites. Coatings 12:827. https://doi.org/10.3390/coatings12060827

402. Yang D, Cao Y, Zhang Z, et al (2021) Effects of crystallinity control on mechanical properties of 3D-printed short-carbon-fiber-reinforced polyether ether ketone composites. Polymer Testing 97:107149. https://doi.org/10.1016/j.polymertesting.2021.107149

403. Doumeng M, Makhlouf L, Berthet F, et al (2021) A comparative study of the crystallinity of polyetheretherketone by using density, DSC, XRD, and Raman spectroscopy techniques. Polymer Testing 93:106878. https://doi.org/10.1016/j.polymertesting.2020.106878

404. Pu J, McIlroy C, Jones A, Ashcroft I (2021) Understanding mechanical properties in fused filament fabrication of polyether ether ketone. Additive Manufacturing 37:101673. https://doi.org/10.1016/j.addma.2020.101673

405. Chivers R (1994) The effect of molecular weight and crystallinity on the mechanical properties of injection moulded poly(aryl-ether-ether-ketone) resin. Polymer 35:110–116. https://doi.org/10.1016/0032-3861(94)90057-4

406. CAMPUS® Datasheet VESTAKEEP®2000 G - PEEK Evonik Operations GmbH

407. CAMPUS® Datasheet VESTAKEEP®3300 G - PEEK Evonik Operations GmbH

408. International Standards Organisation ISO 527-2:2012 - Plastics — Determination of tensile properties — Part 2: Test conditions for moulding and extrusion plastics

409. Moetazedian A, Budisuharto AS, Silberschmidt VV, Gleadall A (2021) CONVEX (CONtinuously Varied EXtrusion): A new scale of design for additive manufacturing. Additive Manufacturing 37:101576. https://doi.org/10.1016/j.addma.2020.101576

410. Schneider K, Lauke B, Beckert W (2001) Compression Shear Test (CST) – A Convenient Apparatus for the Estimation of Apparent Shear Strength of Composite Materials. Applied Composite Materials 8:43–62. https://link.springer.com/article/10.1023/A:1008919114960

411. (2023) Standard Test Method for Determining Strength of Adhesively Bonded Rigid Plastic Lap-Shear Joints in Shear by Tension Loading

412. (2021) Standard Test Method for Strength Properties of Adhesive Bonds in Shear by Compression Loading

413. (2021) Standard Test Method for Shear Properties of Composite Materials by the V-Notched Beam Method

414. (2022) Standard Test Method for Short-Beam Strength of Polymer Matrix Composite Materials and Their Laminates

415. (2020) Standard Test Method for Facesheet Properties of Sandwich Constructions by Long Beam Flexure

416. Blundell DJ, Osborn BN (1983) The morphology of poly(aryl-ether-ether-ketone). Polymer 24:953–958. https://doi.org/10.1016/0032-3861(83)90144-1

417. Kluyver T, Ragan-Kelley B, P&#233, et al (2016) Jupyter Notebooks – a publishing format for reproducible computational workflows. In: Positioning and Power in Academic Publishing: Players, Agents and Agendas. IOS Press, pp 87–90

418. Eilers P, Boelens H (2005) Baseline Correction with Asymmetric Least Squares Smoothing. Unpublished Manuscript

419. Matt Newville, Dan Allan Non-Linear Least-Squares Minimization and Curve-Fitting for Python — Non-Linear Least-Squares Minimization and Curve-Fitting for Python

420. Ellis G, Naffakh M, Marco C, Hendra PJ (1997) Fourier transform Raman spectroscopy in the study of technological polymers Part 1: poly(aryl ether ketones), their composites and blends. Spectrochimica Acta Part A: Molecular and Biomolecular Spectroscopy 53:2279–2294. https://doi.org/10.1016/S1386-1425(97)00168-6

421. Louden JD (1986) Crystallinity in poly(aryl-ether ketone) films studied by Raman spectroscopy. Polym commun (Guildf) 27:82–84

422. Agbenyega JK, Ellis G, Hendra PJ, et al (1990) Applications of Fourier Transform Raman spectroscopy in the synthetic polymer field. Spectrochimica Acta Part A: Molecular Spectroscopy 46:197–216. https://doi.org/10.1016/0584-8539(90)80090-L

423. Briscoe BJ, Stuart BH, Thomas PS, Williams DR (1991) A comparison of thermal- and solvent-induced relaxation of poly(ether ether ketone) using Fourier transform Raman spectroscopy. Spectrochimica Acta Part A: Molecular Spectroscopy 47:1299–1303. https://doi.org/10.1016/0584-8539(91)80219-9

424. Stuart BH, Briscoe BJ (1994) A Fourier transform Raman spectroscopy study of poly (ether ether ketone)/polytetrafluoroethylene (PEEK/PTFE) blends. Spectrochimica Acta Part A: Molecular Spectroscopy 50:2005–2009. https://doi.org/10.1016/0584-8539(94)80212-2

425. Dawson PC, Blundell DJ (1980) X-ray data for poly(aryl ether ketones). Polymer 21:577–578. https://doi.org/10.1016/0032-3861(80)90228-1

426. Hay JN, Langford JI, Lloyd JR (1989) Variation in unit cell parameters of aromatic polymers with crystallization temperature. Polymer 30:489–493. https://doi.org/10.1016/0032-3861(89)90019-0

427. Virtanen P, Gommers R, Oliphant TE, et al (2020) SciPy 1.0: Fundamental Algorithms for Scientific Computing in Python. Nature Methods 17:261–272. https://doi.org/10.1038/s41592-019-0686-2

428. Wang Y, Chen B, Evans KE, Ghita O (2016) Novel fibre-like crystals in thin films of Poly Ether Ether Ketone (PEEK). Materials Letters 184:112–118. https://doi.org/10.1016/j.matlet.2016.08.024

429. Chan C-M, Venkatraman S (1986) Crosslinking of poly(arylene ether ketone)s 1. Rheological behavior of the melt and mechanical properties of cured resin. J Appl Polym Sci 32:5933–5943. https://doi.org/10.1002/app.1986.070320722

430. Day M, Suprunchuk T, Cooney JD, Wiles DM (1988) Thermal degradation of poly(aryl-ether–ether-ketone) (PEEK): A differential scanning calorimetry study. J Appl Polym Sci 36:1097–1106. https://doi.org/10.1002/app.1988.070360510

431. Beyler CL, Hirschler MM (2016) Thermal Decomposition of Polymers. In: SFPE Handbook of Fire Protection Engineering, 1st ed. Springer New York

432. Lee Y, Porter RS (1988) Effects of thermal history on crystallization of poly(ether ether ketone) (PEEK). Macromolecules 21:2770–2776. https://doi.org/10.1021/ma00187a022

433. Magnoni P, Rebaioli L, Fassi I, et al (2017) Robotic AM system for plastic materials: tuning and on-line adjustment of process parameters. 27TH INTERNATIONAL CONFERENCE ON FLEXIBLE AUTOMATION AND INTELLIGENT MANUFACTURING, FAIM2017 11:346–354

434. Goyanes A, Allahham N, Trenfield SJ, et al (2019) Direct powder extrusion 3D printing: Fabrication of drug products using a novel single-step process. INTERNATIONAL JOURNAL OF PHARMACEUTICS 567

435. Rebaioli L, Magnoni P, Fassi I, et al (2019) Process parameters tuning and online re-slicing for robotized additive manufacturing of big plastic objects. ROBOTICS AND COMPUTER-INTEGRATED MANUFACTURING 55:55–64

436. Rigon D, Ricotta M, Ardengo G, Meneghetti G (2021) Static mechanical properties of virgin and recycled short glass fiber-reinforced polypropylene produced by pellet additive manufacturing. Fatigue Fract Eng Mat Struct 44:2554–2569. https://doi.org/10.1111/ffe.13517

437. Ramirez MA, Barocio E, Tsai J-T, Pipes RB (2022) Temperature-Dependent Mechanical Properties of Additive Manufactured Carbon Fiber Reinforced Polyethersulfone. Appl Compos Mater 29:2293–2319. https://doi.org/10.1007/s10443-022-10063-y

438. Do QD, Nguyen DK, Van Nguyen T, et al (2023) Effect of Printing Parameters on Characteristics of PCL Scaffold Fabricated by Direct Powder Extrusion. In: Nguyen DC, Vu NP, Long BT, et al (eds) Advances in Engineering Research and Application. Springer International Publishing, Cham, pp 455–461

439. Mercado Rivera FJ, Rojas Arciniegas AJ, Rios Narvaez DA (2023) A comparison between large-format 3D printing and conventional fused filament fabrication. Advances in Materials and Processing Technologies 1–16. https://doi.org/10.1080/2374068X.2023.2226919

440. Kalle J, Joni K, Alexander S, Juhani O (2023) Potential and Challenges of Fused Granular Fabrication in Patternmaking. Inter Metalcast 17:2469–2476. https://doi.org/10.1007/s40962-023-00989-9

441. Hirsch P, Scholz S, Borowitza B, et al (2024) Processing and Analysis of Hybrid Fiber-Reinforced Polyamide Composite Structures Made by Fused Granular Fabrication and Automated Tape Laying. JMMP 8:25. https://doi.org/10.3390/jmmp8010025

Appendix 1

Systematic Literature Review Articles

Ref.	Article Title	Publication Year	Material	Filler and Additives	Screw length [mm]	Screw diameter [mm]	Design	Extruder Type	Nozzle [mm]
[132]	Precision extruding deposition and characterization of cellular poly-ε-caprolactone tissue scaffolds	2004	PCL;	No	150	20	Single screw extruder (SSE)	Custom	0.3
[197]	Fused deposition modelling using direct extrusion	2007	ABS;	No	N/A	N/A	Single screw extruder (SSE)	Custom	0.55
[111]	Design development and functional validation of an interchangeable head based on mini screw extrusion applied in an experimental desktop 3-D printer	2014	PCL;	Bioglass;	150	7	Single screw extruder (SSE)	Fab@CTI	0.4
[93]	Study of the technical feasibility and design of a mini head screw extruder applied to filament deposition in desktop 3-D printer	2014	N/A	N/A	150	7	Single screw extruder (SSE)	Fab@CTI	N/A
[169]	Morphological, mechanical and biological assessment of PCL/pristine graphene scaffolds for bone regeneration	2016	PCL;	Graphene;	N/A	N/A	Single screw extruder (SSE)	3D Discovery	0.3

[102]	Control-oriented energy-based modeling of a screw extruder used for 3D printing	2016	PLA;	No	50	6	Single screw extruder (SSE)	Custom	0.2 - 0.4
[158]	Large-scale deposition system by an Industrial Robot (I): Design of fused pellet modeling system and extrusion process analysis	2016	N/A	N/A	508	50.8	Single screw extruder (SSE)	Custom	N/A
[112]	Fabrication of PCL/β-TCP scaffolds by 3D mini-screw extrusion printing	2016	PCL;	b-TCP	150	7	Single screw extruder (SSE)	Fab@CTI	0.4
[82]	Enhancing the Hydrophilicity and Cell Attachment of 3D Printed PCL/Graphene Scaffolds for Bone Tissue Engineering	2016	PCL;	Graphene;	N/A	N/A	SSE, pre-heated material	Liu	0.5
[105]	A large-scale double-stage-screw 3D printer for fused deposition of plastic pellets	2017	ABS;	Glass Fibre;	500	25	SSE, double stage	Custom	4
[195]	Robot-assisted 3D printing of biopolymer thin shells	2017	Biopolyesters;	No	N/A	N/A	Single screw extruder (SSE)	Custom	3.2
[90]	Study of Moineau-based pumps for the volumetric extrusion of pellets	2017	PLA; PET;	No	N/A	N/A	Moineau pump	Custom	N/A
[433]	Robotic AM System for Plastic Materials: Tuning and	2017	PLA;	No	N/A	N/A	Single screw	Lorenzo	2

	On-line Adjustment of Process Parameters						extruder (SSE)		
[71]	3D PRINTING OF FLEXIBLE PARTS USING EVA MATERIAL	2018	EVA;	No	162	20	SSE, no compression	CNC EVA	N/A
[72]	Additive manufacturing of flexible electrically conductive polymer composites via CNC-assisted fused layer modeling process	2018	EVA;	Graphite	162	20	SSE, no compression	CNC EVA	0.8
[136]	Experimental investigations on suitability of polypropylene (PP) and ethylene vinyl acetate (EVA) in additive manufacturing	2018	ABS; EVA; PP;	No	162	20	SSE, no compression	CNC EVA	N/A
[73]	Extrusion-based additive manufacturing process for producing flexible parts	2018	EVA;	No	162	20	SSE, no compression	CNC EVA	0.8
[74]	Investigation on the effects of process parameters in CNC assisted pellet based fused layer modeling process	2018	EVA;	No	162	20	SSE, no compression	CNC EVA	0.8
[75]	The effect of process parameters on tensile behavior of 3D printed flexible parts of ethylene vinyl acetate (EVA)	2018	EVA;	No	162	20	SSE, no compression	CNC EVA	0.8

[133]	Toolpath generation for additive manufacturing using CNC milling machine	2018	N/A	N/A	162	20	SSE, no compression	CNC EVA	N/A
[116]	Additive manufacturing of heat-sensitive polymer melt using a pellet-fed material extrusion	2018	PVOH;	No	206	12	Single screw extruder (SSE)	Custom	N/A
[155]	Screw extrusion-based additive manufacturing of PEEK	2018	PEEK;	Short Carbon Fibre	280	14	SSE, static	Custom	0.3; 0.4;
[108]	Development of multi-material 3D printer	2018	PMMA;	CNT;	N/A	4	SSE, no compression	Custom	0.4; 0.5; 0.6; 0.8;
[67]	A plasma-assisted bioextrusion system for tissue engineering	2018	PCL;	No	N/A	N/A	SSE, pre-heated material	Liu	0.5
[69]	Hybrid Additive Manufacturing System for Zonal Plasma-Treated Scaffolds	2018	PCL;	No	N/A	N/A	SSE, pre-heated material	Liu	0.5
[65]	Process-Driven Microstructure Control in Melt-Extrusion-Based 3D Printing for Tailorable Mechanical Properties in a Polycaprolactone Filament	2018	PCL;	No	N/A	N/A	SSE, pre-heated material	Liu	0.5
[68]	User interface tool for a novel plasma-assisted bio-additive extrusion system	2018	PCL;	No	N/A	N/A	SSE, pre-heated material	Liu	0.5

[118]	Design of an Innovative Three-Dimensional Print Head Based on Twin-Screw Extrusion	2018	N/A	No	132	12	Twin screw extruder	Netto	N/A
[147]	Fused particle fabrication 3-D printing: Recycled materials' optimization and mechanical properties	2018	PLA; rPP; rABS; rPET;	No	256	16	Single screw extruder (SSE)	Pearce	1.2
[183]	Large-format polymeric pellet-based additive manufacturing for the naval industry	2018	ABS; PLA; PETG;	Glass Fibre; Flame Retardant;	N/A	N/A	Single screw extruder (SSE)	Super Discovery 3D Granza	5
[129]	Design and development of an extrusion system for 3D printing biopolymer pellets	2018	PLA;	N/A	90	15	SSE, no compression	Whyman	0.8; 1.5;
[107]	3D printing using powder melt extrusion	2019	PLA; HIPS; ABS;	No	58	6	Single screw extruder (SSE)	Custom	0.4
[135]	Investigations on the melt flow behaviour of aluminium filled ABS polymer composite for the extrusion-based additive manufacturing process	2019	ABS;	Aluminum Powder;	162	20	SSE, no compression	CNC EVA	N/A
[138]	Biopolymer Alternatives in Pellet Form for 3D Printing by Extrusion	2019	PLA; PBAT;	No	125	14	Single screw extruder (SSE)	Custom	0.5; 1.0; 1.5; 2.0;

[37]	Direct coupling of fixed screw extruders using flexible heated hoses for FDM printing of extremely soft thermoplastic elastomers	2019	SEBS; MM3520 shape memory polymer (SMP);	No	180	15.5	Flexible Hose	Custom	0.5
[151]	Characterization of a granulate-based strand deposition process in the FLM-method for definition of material-dependent process strategies	2019	ABS; PLA;	No	320	14	Single screw extruder (SSE)	Custom	3
[191]	Fabrication and properties of extrusion-based 3D-printed hardmetal and cermet components	2019	TPE;	Cermet;	N/A	N/A	Single screw extruder (SSE)	ExAM 255	0.3
[113]	Experimental and numerical evaluation of the temperature profile of a modular extrusion head applied to an experimental 3D printer	2019	PCL;	No	150	7	Single screw extruder (SSE)	Fab@CTI	0.8
[434]	Direct powder extrusion 3D printing: Fabrication of drug products using a novel single-step process	2019	HPC;	Itraconazole Drug;	N/A	N/A	Single screw extruder (SSE)	FabRx	0.8
[435]	Process parameters tuning and online re-slicing for robotized additive	2019	PLA; ABS;	No	N/A	N/A	Single screw extruder (SSE)	Lorenzo	2

	manufacturing of big plastic objects								
[152]	Development of functionally graded material capabilities in large-scale extrusion deposition additive manufacturing	2019	ABS;	Carbon Fibre;	N/A	N/A	Single screw extruder (SSE)	Manufacturing Demonstration Facility's (MDF)	10.16
[63]	Additive manufacturing of fire-retardant ethylene-vinyl acetate	2019	EVA;	Aluminum TriHydroxyde (ATH)	N/A	N/A	Single screw extruder (SSE)	PAM Series P (Pollen AM)	0.4
[60]	Green fab lab applications of large-area waste polymer-based additive manufacturing	2019	rABS; rPP;	No	256	16	Single screw extruder (SSE)	Pearce	1.75
[148]	Mechanical properties and applications of recycled polycarbonate particle material extrusion-based additive manufacturing	2019	rPC;	No	256	16	Single screw extruder (SSE)	Pearce	1.2
[170]	Aligned multi-walled carbon nanotubes with nanohydroxyapatite in a 3D printed polycaprolactone scaffold stimulates osteogenic differentiation	2020	PCL;	No	N/A	N/A	Single screw extruder (SSE)	3D Discovery	0.3
[171]	Engineered dual-scale poly (ε-caprolactone) scaffolds using 3D printing and	2020	PCL;	No	N/A	N/A	Single screw	3D Discovery	0.3

	rotational electrospinning for bone tissue regeneration						extruder (SSE)		
[94]	Compressive deformation analysis of large area pellet-fed material extrusion 3D printed parts in relation to in situ thermal imaging	2020	ABS;	Carbon Fibre;	320	30	Single screw extruder (SSE)	BAAM-100 Cincinatti	7.62
[95]	Thermomechanical characterization of short carbon fiber and short glass fiber-reinforced ABS used in large format additive manufacturing	2020	ABS;	Carbon Fibre; Glass Fibre;	320	30	Single screw extruder (SSE)	BAAM-100 Cincinatti	7.62
[89]	High-pressure interfacial impregnation by micro-screw in-situ extrusion for 3D printed continuous carbon fiber reinforced nylon composites	2020	Nylon;	Carbon Fibre	96	8	SSE, static, interfacial impregrnation	Custom	0.4
[140]	Production of polymer-metal hybrids using extrusion-based additive manufacturing and electrochemically treated aluminum	2020	PP;	No	160	16	Single screw extruder (SSE)	Custom	2
[153]	Mechanical Characterization of High-Temperature Carbon Fiber-Polyphenylene Sulfide Composites for Large Area	2020	PPS;	Carbon Fibre;	N/A	N/A	Single screw extruder (SSE)	Custom	10.116

	Extrusion Deposition Additive Manufacturing								
[51]	Theoretical Evaluation of the Melting Efficiency for the Single-Screw Micro-Extrusion Process: The Case of 3D Printing of ABS	2020	ABS;	No	193	28 - 16	SSE, static, cone	La Gala	N/A
[121]	Basic Research for Additive Manufacturing of Rubber	2020	Natural rubber; Nitrile-butadine (NBR); EPDM;	No	50	8	Single screw extruder (SSE)	Mahor	0.4
[25]	Mechanical Properties of Direct Waste Printing of Polylactic Acid with Universal Pellets Extruder: Comparison to Fused Filament Fabrication on Open-Source Desktop Three-Dimensional Printers	2020	PLA; rPLA;	No	50	8	Single screw extruder (SSE)	Mahor	0.8
[149]	Towards Distributed Recycling with Additive Manufacturing of PET Flake Feedstocks	2020	rPET;	No	256	16	Single screw extruder (SSE)	Pearce	1.75
[184]	Development of carbon fiber acrylonitrile styrene acrylate composite for large format additive manufacturing	2020	ASA;	Carbon Fibre;	N/A	N/A	Single screw extruder (SSE)	Super Discovery 3D Granza	5

[131]	Polylactic acid and high-density polyethylene blend: Characterization and application in additive manufacturing	2020	PLA;	HDPE; PE-g-MAH	90	15	SSE, no compression	Whyman	1.5
[81]	Thermoplastic Cellulose-Based Compound for Additive Manufacturing	2021	Cellulose acetate propionate (CAP); Thermoplastic cellulose (CP);	Cellulose fibre	N/A	N/A	Single screw extruder (SSE)	Brinter	0.8
[76]	Analysing the influence of raster angle, layer thickness and infill rate on the compressive behaviour of EVA through CNC-assisted fused layer modelling process	2021	EVA;	No	162	20	SSE, no compression	CNC EVA	0.8
[139]	Direct extrusion 3D printing for a softer PLA-based bio-polymer composite in pellet form	2021	PLA;	PBAT	125	14	Single screw extruder (SSE)	Custom	N/A
[196]	Design, Characterization, and 3D Printing of Cardiovascular Stents with Zero Poisson's Ratio in Longitudinal Deformation	2021	PCL;	No	N/A	N/A	Single screw extruder (SSE)	Custom	0.25

[141]	A Combined Experimental and Modeling Study for Pellet-Fed Extrusion-Based Additive Manufacturing to Evaluate the Impact of the Melting Efficiency	2021	ABS; PLA; SEBS;	No	193	28 - 16	SSE, static, cone	La Gala	0.8; 1.5;
[123]	Can filaments, pellets and powder be used as feedstock to produce highly drug-loaded ethylene-vinyl acetate 3D printed tablets using extrusion-based additive manufacturing?	2021	EVA;	Metoprolol tartrate (MPT)	50	8	Single screw extruder (SSE)	Mahor	N/A
[98]	A parametric study and characterization of additively manufactured continuous carbon fiber reinforced composites for high-speed 3D printing	2021	PLA;	Carbon Fibre;	254	28	Single screw extruder (SSE)	MDPH2 Massive Dimension	4
[99]	Large-scale additive manufacturing of high strength fiber-reinforced polymer composites	2021	PLA;	Carbon Fibre;	254	28	Single screw extruder (SSE)	MDPH2 Massive Dimension	4
[176]	3D printing of PLA and PMMA multilayered model polymers: An innovative approach for a better-controlled pellet multi-extrusion process	2021	PMMA; PLA;	N/A	N/A	N/A	Single screw extruder (SSE)	PAM Series P (Pollen AM)	0.6

[178]	Effects of Two Melt Extrusion Based Additive Manufacturing Technologies and Common Sterilization Methods on the Properties of a Medical Grade PLGA Copolymer	2021	Poly(lactic-co-glycolic) Acid (PLGA);	No	N/A	N/A	Single screw extruder (SSE)	PAM Series P (Pollen AM)	0.4
[179]	Fatigue behaviour of 3D printed virgin and recycled short-glass-fiber-reinforced and mineral-filled polypropylene	2021	rPP;	Glass Fibre	N/A	N/A	Single screw extruder (SSE)	PAM Series P (Pollen AM)	0.6
[436]	Static mechanical properties of virgin and recycled short glass fiber-reinforced polypropylene produced by pellet additive manufacturing	2021	vPP; rPP;	Glass Fibre	N/A	N/A	Single screw extruder (SSE)	PAM Series P (Pollen AM)	0.6
[79]	Additive Manufacturing of Wood Flour/PHA Composites Using Micro-Screw Extrusion: Effect of Device and Process Parameters on Performance	2021	Polyhydroxyalkanoates (PHA);	Wood;	156	6	Single screw extruder (SSE)	Tian	0.5; 0.8; 1; 1.5;
[78]	Additive manufacturing of wood flour/polyhydroxyalkanoates (PHA) fully bio-based composites based on micro-screw extrusion system	2021	Polyhydroxyalkanoates (PHA);	Wood;	156	6	Single screw extruder (SSE)	Tian	N/A

[77]	A Sensorized Soft Pneumatic Actuator Fabricated with Extrusion-Based Additive Manufacturing	2021	Styrene-ethylene-butylene-styrene triblock copolymer (TPS);	No	50	8	Single screw extruder (SSE)	Tumaker	0.4
[182]	Durability of Vacuum Infusion Tooling Produced from Fused Granular Fabrication Additive Manufacturing	2022	ABS;	Glass Fibre;	N/A	N/A	Single screw extruder (SSE)	Ambit Extruder	3
[437]	Temperature-Dependent Mechanical Properties of Additive Manufactured Carbon Fiber Reinforced Polyethersulfone	2022	PESU;	Carbon Fibre;	N/A	N/A	Single screw extruder (SSE)	CAMRI	4
[104]	An Effect of Screw Extrusion Parameters On a Pottery Model Forming by A Clay Printing Machine	2022	Clay;	No	75	16	Single screw extruder (SSE)	Custom	5; 6; 7;
[199]	Comparison of the effects of multiaxis printing strategies on large-scale 3D printed surface quality, accuracy, and strength	2022	PP;	Glass Fibre;	N/A	30	Single screw extruder (SSE)	Custom	5
[200]	Instantaneous and long-term mechanical properties of Polyethylene Terephthalate Glycol (PETG) additively	2022	PETG;	No	N/A	N/A	Single screw extruder (SSE)	Custom	5

	manufactured by pellet-based material extrusion								
[188]	Large Scale 3D Printing: Influence of Fillers on Warp Deformation and on Mechanical Properties of Printed Polypropylene Components	2022	PP;	Glass Fibre;	N/A	17	Single screw extruder (SSE)	Delta Wasp 3MT	3
[85]	Fabrication, morphological, mechanical and biological performance of 3D printed poly(ε-caprolactone)/bioglass composite scaffolds for bone tissue engineering applications	2022	PCL;	Bioglass;	150	7	Single screw extruder (SSE)	Fab@CTI	0.4
[145]	Compounding a High-Permittivity Thermoplastic Material and Its Applicability in Manufacturing of Microwave Photonic Crystals	2022	ABS;	BaTiO3/dibutyl phthalate/octyl gallate composite	200	N/A	Single screw extruder (SSE)	Fused Form–FF600+ single-screw extruder 3D printer	N/A
[198]	Large-Scale Robot-Based Polymer and Composite Additive Manufacturing: Failure Modes and Thermal Simulation	2022	ABS; PP;	Glass Fibre; Cellulose Fibre;	N/A	N/A	Single screw extruder (SSE)	IBRAM	4

[142]	Thermal and Thermal-Oxidative Molecular Degradation of Polystyrene and Acrylonitrile Butadiene Styrene during 3D Printing Starting from Filaments and Pellets	2022	ABS; PS;	No	193	28 - 16	SSE, static, cone	La Gala	0.8; 1.5;
[119]	Characterization of 3D Printed Polylactic Acid by Fused Granular Fabrication through Printing Accuracy, Porosity, Thermal and Mechanical Analyses	2022	PLA;	No	50	8	Single screw extruder (SSE)	Mahor	0.8
[120]	Redesign of a 3D Low Cost Filament Printer, Adapting it to a Pellet Extruder for New Material Assays	2022	PLA;	No	50	8	Single screw extruder (SSE)	Mahor	N/A
[117]	Design and validation of an innovative 3D printer containing a co-rotating twin screw extrusion unit	2022	PP;	No	132	12	Twin screw extruder	Netto	0.4; 0.6;
[177]	Functionally Graded Multilayer Composites Based on Poly(D,L lactide)/Bioactive Fillers Fabricated by a 3D Direct Pellet Printing Multi-Extrusion Process	2022	PLA;	Bioglass; Hydroxyapatite;	N/A	N/A	Single screw extruder (SSE)	PAM Series Lx (Pollen AM)	0.4

[190]	Effect of Process Parameters on Void Distribution, Volume Fraction, and Sphericity within the Bead Microstructure of Large-Area Additive Manufacturing Polymer Composites	2022	ABS;	Carbon Fibre;	N/A	N/A	Single screw extruder (SSE)	Strangpresse Model 19	3.17
[128]	EcoBlends'up: PLA/BioPA blends composites, microfibrillated in situ through additive manufacturing	2022	PLA;	PA	50	8	Single screw extruder (SSE)	Tumaker	0.8
[124]	Pellet-based fused deposition modeling for the development of soft compliant robotic grippers with integrated sensing elements	2022	Styrene-ethylene-butylene-styrene triblock copolymer (TPS);	No	50	8	Single screw extruder (SSE)	Tumaker	0.6
[130]	Design and Analysis Studies in Pellet Extrusion Additive Manufacturing Processes	2022	N/A	N/A	90	15	SSE, no compression	Whyman	1.5
[96]	Recyclability of additively manufactured bio-based composites	2023	PLA;	Wood;	320	30	Single screw extruder (SSE)	BAAM-100 Cincinatti	7.62
[97]	Recycling polymer composite granulate/regrind using big area additive manufacturing	2023	ABS;	Carbon Fibre;	320	30	Single screw extruder (SSE)	BAAM-100 Cincinatti	7.62

[157]	Screw Extrusion Additive Manufacturing of Carbon Fiber Reinforced PA6 Tools	2023	PA;	Carbon Fibre;	400	20	Single screw extruder (SSE)	CMS Kreator Ares	3
[181]	Material Extrusion Additive Manufacturing with Polyethylene Vitrimers	2023	HDPE-V;	No	N/A	N/A	Single screw extruder (SSE)	Cosine AM1	1
[83]	Flexural property characterization and structure analysis of graphene-reinforced polyphenylene sulfide prepared via low-cost pellet-based material extrusion additive manufacturing	2023	Polyphenylene sulfide (PPS);	Graphene;	N/A	N/A	Single screw extruder (SSE)	Creality G5	1.5
[438]	Effect of Printing Parameters on Characteristics of PCL Scaffold Fabricated by Direct Powder Extrusion	2023	PCL;	No	55	8	Single screw extruder (SSE)	Custom	0.3
[137]	A Novel Analytical Model for Screw Extrusion of Thermoplastic ABS with Emphasis on Additive Manufacturing	2023	ABS;	No	150	16	SSE, no compression	Custom	1
[106]	Direct 3D Printing of Recycled PET/PP Granules by Shear Screw Extrusion	2023	rPET; rPP;	No	240	16	Single screw extruder (SSE)	Custom	0.3

[80]	A screw extrusion-based system for additive manufacturing of wood: Sodium silicate thermoset composites	2023	Sodium Silicate;	Wood;	420	35	Flexible Hose	Custom	N/A
[84]	Compatibilizing Biodegradable Poly(lactic acid)/polybutylene adipate-co-terephthalate Blends via Reactive Graphene Oxide for Screw-Based 3D Printing	2023	PLA/PBAT;	PVGO blend nanocomposites;	N/A	N/A	Single screw extruder (SSE)	Custom	0.4
[194]	Magnetorheological behavior of thermoplastic elastomeric honeycomb structures fabricated by additive manufacturing	2023	SEBS;	Carbonyl iron powder (CIP)	N/A	N/A	Single screw extruder (SSE)	Custom	N/A
[168]	From Nautical Waste to Additive Manufacturing: Sustainable Recycling of High-Density Polyethylene for 3D Printing Applications	2023	HDPE;	Glass Fibre	N/A	N/A	Single screw extruder (SSE)	Direct3D	1
[192]	The study of screw extrusion-based additive manufacturing of eco-friendly aliphatic polyketone	2023	Aliphatic polyketone;	No	N/A	N/A	Single screw extruder (SSE)	ExOn10 from Herz GmbH, Germany	4
[110]	Extrusion-based technologies for 3D printing: a comparative study of the processability of	2023	TPU;	Anhydrous theophylline (AT)	N/A	N/A	Single screw extruder (SSE)	FabRx	0.8

	thermoplastic polyurethane-based formulations								
[439]	A comparison between large-format 3D printing and conventional fused filament fabrication	2023	ABS; PP;	Wood;	222	14	Single screw extruder (SSE)	Felfil Evo	3
[159]	Hangprinter for large scale additive manufacturing using fused particle fabrication with recycled plastic and continuous feeding	2023	PLA;	No	260	15.875	SSE, no compression	Hang Printer	3
[122]	Additive Manufacturing of Thermoplastic Polyurethane-Cork Composites for Material Extrusion Technologies	2023	TPU;	Cork Powder;	50	8	Single screw extruder (SSE)	Mahor	0.8
[125]	Granule-based material extrusion is comparable to filament-based material extrusion in terms of mechanical performances of printed PLA parts: A comprehensive investigation	2023	PLA;	No	50	8	Single screw extruder (SSE)	Mahor	0.4
[44]	Modeling of extrusion-based additive manufacturing for pelletized thermoplastics: Analytical relationships between process parameters and extrusion outcomes	2023	N/A	N/A	N/A	N/A	Unknown	N/A	N/A

[440]	Potential and Challenges of Fused Granular Fabrication in Patternmaking	2023	PLA;	Cellulose Fibre;	N/A	N/A	Single screw extruder (SSE)	N/A	8
[61]	Recycled polycarbonate and polycarbonate/acrylonitrile butadiene styrene feedstocks for circular economy product applications with fused granular fabrication-based additive manufacturing	2023	rPC; rPC/ABS;	No	256	16	Single screw extruder (SSE)	Pearce	0.8
[115]	Development of a novel direct powder screw extruder for 3D scaffold printing of PCL-based composites	2023	PCL;	PEG;	70	10	SSE, nozzle heating	Phung	0.4
[114]	Performance evaluation of different 3D printing techniques for PCL-based scaffold fabrication	2023	PCL;	No	70	10	SSE, nozzle heating	Phung	0.4
[193]	Large-scale hollow-core 3D printing (HC3DP): A polymer 3D printing technology for large-scale ultralightweight components	2023	PETG; PLA; COC; PP;	No	N/A	N/A	Single screw extruder (SSE)	SAEKI Robotics	4 - 6;
[86]	Thermal and Mechanical Properties of Reprocessed Polylactide/Titanium Dioxide Nanocomposites for	2023	PLA; rPLA;	Titanium (IV) Nanopowder;	N/A	N/A	Single screw extruder (SSE)	Super Discovery 3D Granza	2

	Material Extrusion Additive Manufacturing								
[126]	Effect of Extruder Type in the Interface of PLA Layers in FDM Printers: Filament Extruder Versus Direct Pellet Extruder	2023	PLA;	No	50	8	Single screw extruder (SSE)	Tumaker	0.8
[127]	The effects of processing parameters on mechanical properties of 3D-printed polyhydroxyalkanoates parts	2023	Polyhydroxyalkanoates (PHA);	No	50	8	Single screw extruder (SSE)	Tumaker	0.8
[189]	Influence of material modification and fillers on the dimensional stability and warpage of polypropylene in screw-extrusion-based large area additive manufacturing	2023	PP;	Talc; Hollow Glass Beads; Glass Fibre;	N/A	16	Single screw extruder (SSE)	Yizumi	1.5
[172]	Additive manufacturing of hybrid piezoelectric/magnetic self-sensing actuator using pellet extrusion and immersion precipitation with statistical modelling optimization	2024	Piezoelectric polyvinylidene fluoride;	Iron (II, III) ovide; Single walled carbon nanotubes;	N/A	N/A	Single screw extruder (SSE)	3D Cultures	N/A
[134]	Investigation on using graphite filler for 3D printing of flexible electrically conductive polymer by extrusion-based additive manufacturing	2024	EVA;	Graphite	162	20	SSE, no compression	CNC EVA	0.4

[88]	Effect of fiber content on mechanical properties of carbon fiber-reinforced polyether-ether-ketone composites prepared using screw extrusion-based online mixing 3D printing	2024	PEEK;	Carbon Fibre;	144	16	SSE, double stage	Custom	1
[62]	High-performance carbon fiber reinforced polyether-ether-ketone composite pellets 3D-Printed via screw-extrusion additive manufacturing	2024	PEEK;	Carbon Fibre	360	18	SSE, static	Custom	3
[187]	Characterization of PLA feedstock after multiple recycling processes for large-format material extrusion additive manufacturing	2024	rPLA:	No	N/A	17	Single screw extruder (SSE)	Delta Wasp 3MT	3
[103]	PLA Feedstock Filled with Spent Coffee Grounds for New Product Applications with Large-Format Material Extrusion Additive Manufacturing	2024	PLA;	Coffee;	N/A	17	Single screw extruder (SSE)	Delta Wasp 3MT	3
[441]	Processing and Analysis of Hybrid Fiber-Reinforced Polyamide Composite Structures Made by Fused	2024	Nylon; rNylon;	Glass Fibre; Carbon Fibre;	N/A	N/A	Single screw extruder (SSE)	N/A	1; 1.5; 3; 6;

	Granular Fabrication and Automated Tape Laying								
[180]	Tool wear for finishing milling of green thermoplastic-ceramic composites fabricated with pellet AM	2024	PA;	Zirconia	N/A	N/A	Single screw extruder (SSE)	PAM Series Lx (Pollen AM)	1
[150]	Multi-material distributed recycling via material extrusion: recycled high density polyethylene and poly (ethylene terephthalate) mixture	2024	rPET; PET;	No	256	16	Single screw extruder (SSE)	Pearce	1.75
[185]	Multiscale numerical modeling of large-format additive manufacturing processes using carbon fiber reinforced polymer for digital twin applications	2024	ABS;	Carbon Fibre;	N/A	N/A	Single screw extruder (SSE)	Super Discovery 3D Granza	2

Appendix 2

Extruder Development 1 Engineering Drawings

01.0

Drawing number

Sub-drawing number

Same assembly or component

Document type Notation		Created by Albert Curmi 28/10/2024		
Title Drawing Numbering System		DWG No. 00.0		
General tolerance ±0.1 mm	Material N/A	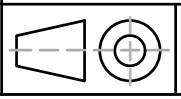	Scale N/A	Sheet 1/15

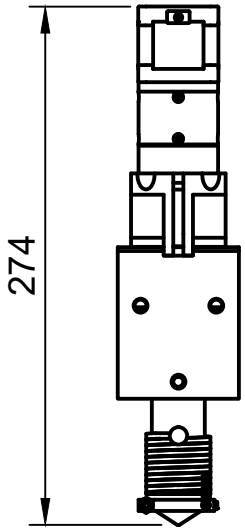

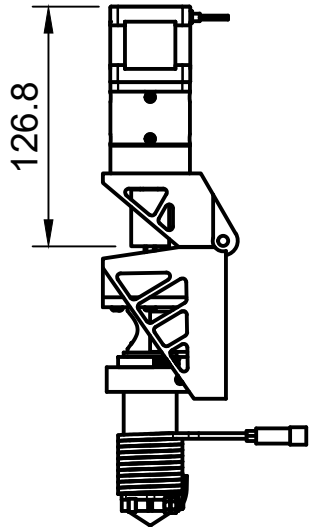

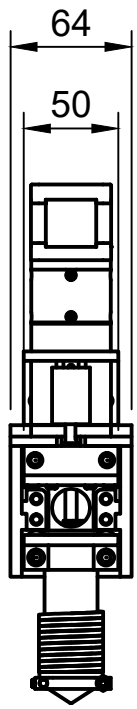

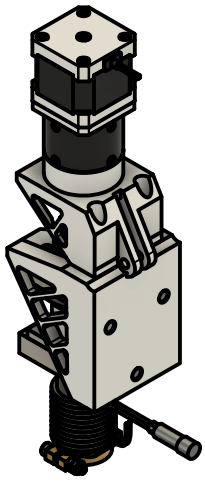

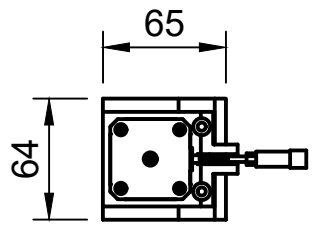

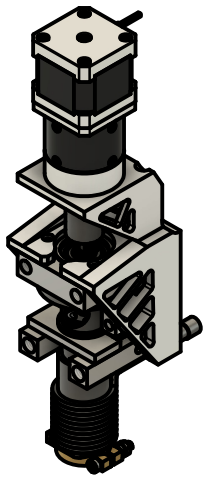

Document type Assembly Drawing		Created by Albert Curmi 28/10/2024		
Title Extruder 1 General Dimensions		DWG No. 01.0		
General tolerance ±0.1 mm	Material N/A		Scale 1:4	Sheet 2/15

(1:2)

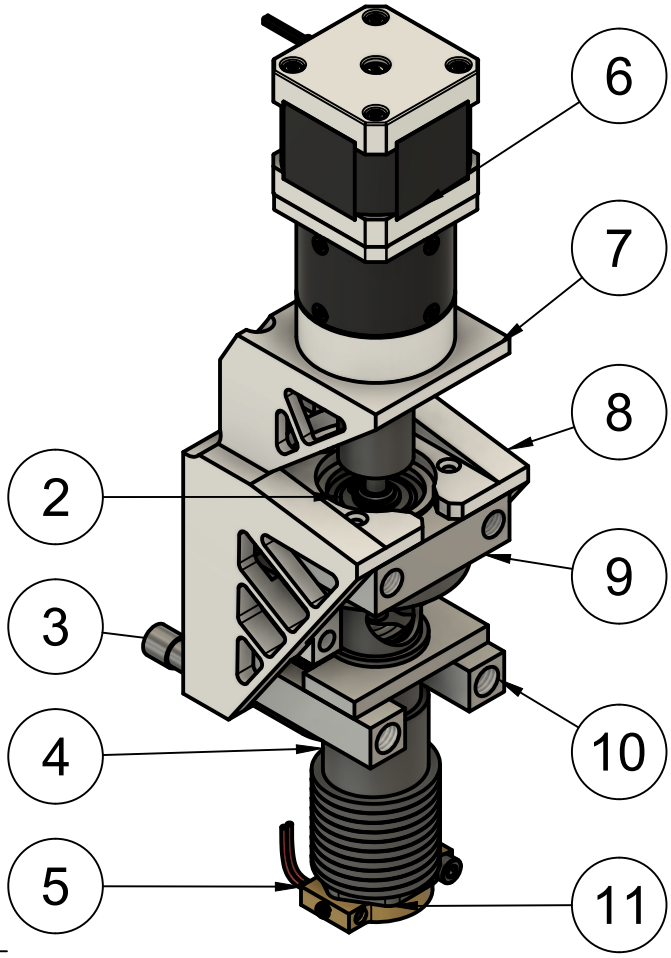

Parts List		
Item	Part Name	Material
1	Fastners Assembly	Steel
2	Extrusion Screw Assembly	N/A
3	Coil Heater	N/A
4	Heater Barrel	H13 Tool Steel
5	Temperature Sensor Assembly	
6	17HS15-0404S-H G30 v1	N/A
7	Vertical Motor Assembly	
8	Anterior Support	ABS Plastic
9	Bearing Block	Aluminum 2014-T4
10	Bottom Cooling Zone Assembly	
11	Nozzle	H13 Tool Steel

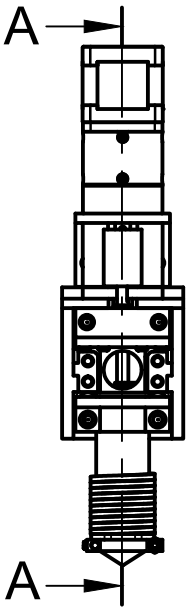

A-A (1:4)

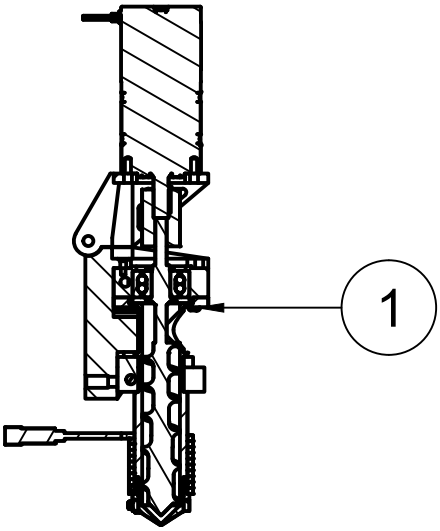

Document type: Assembly Drawing		Created by: Albert Curmi		28/10/2024
Title: Extruder 1 Sub-assemblies		DWG No.: 01.1		
General tolerance: ±0.1 mm	Material: ----		Scale: 1:4	Sheet: 3/15

Parts List		
Item	Part Name	Material
1	Screw 1	H13 Tool Steel
2	Circlip	Steel
3	Double Row Bearing, OD 30 mm, ID 10 mm, H 14 mm	N/A

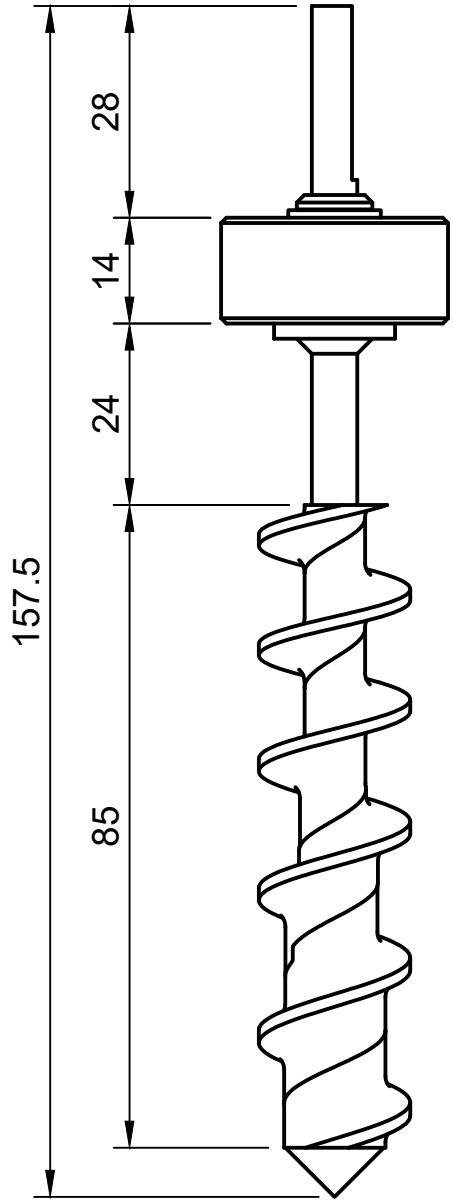

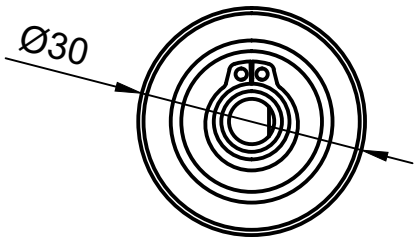

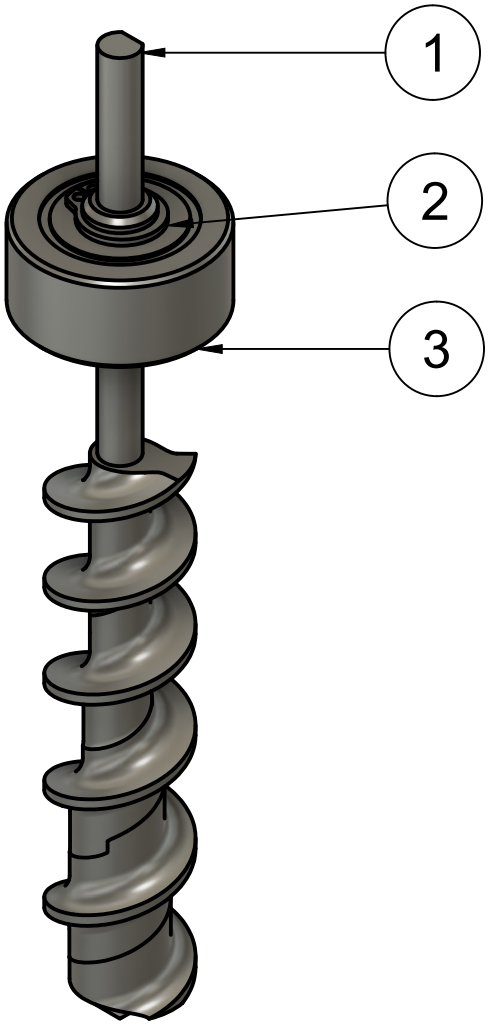

Document type: Assembly Drawing		Created by: Albert Curmi		28/10/2024
Title: Extrusion Screw Assembly		DWG No.: 02.0		
General tolerance: ±0.1 mm	Material: N/A		Scale: 1:1	Sheet: 4/15

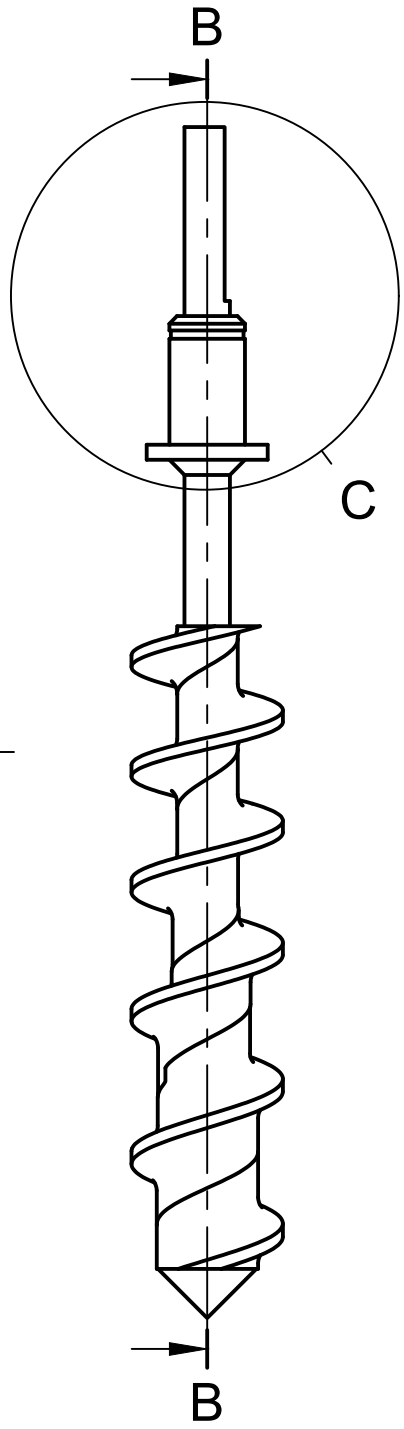

B-B (1:1)

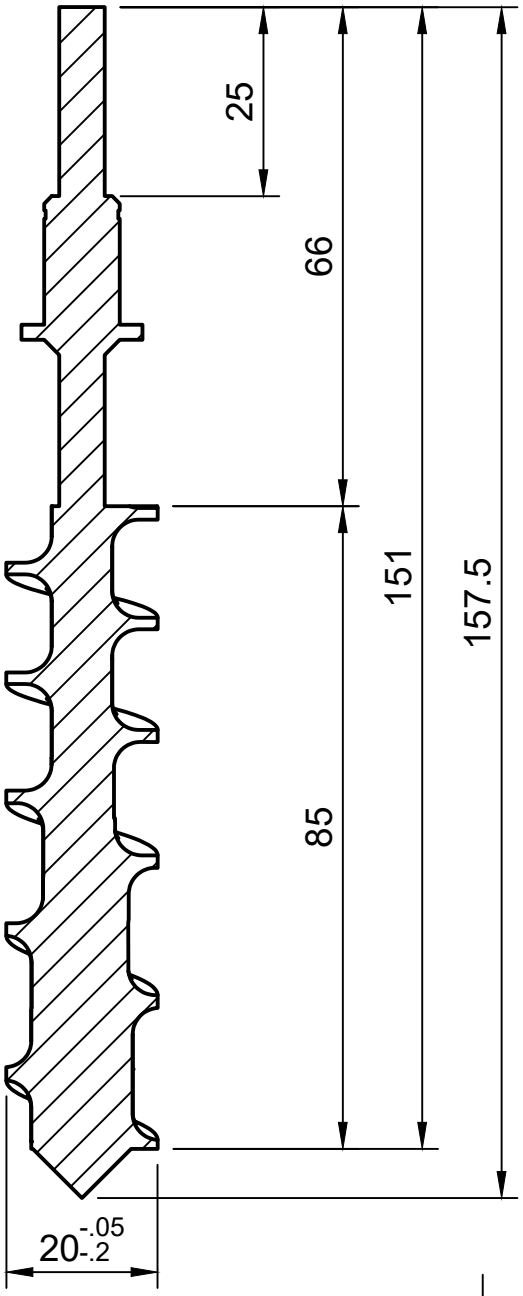

C (2:1)

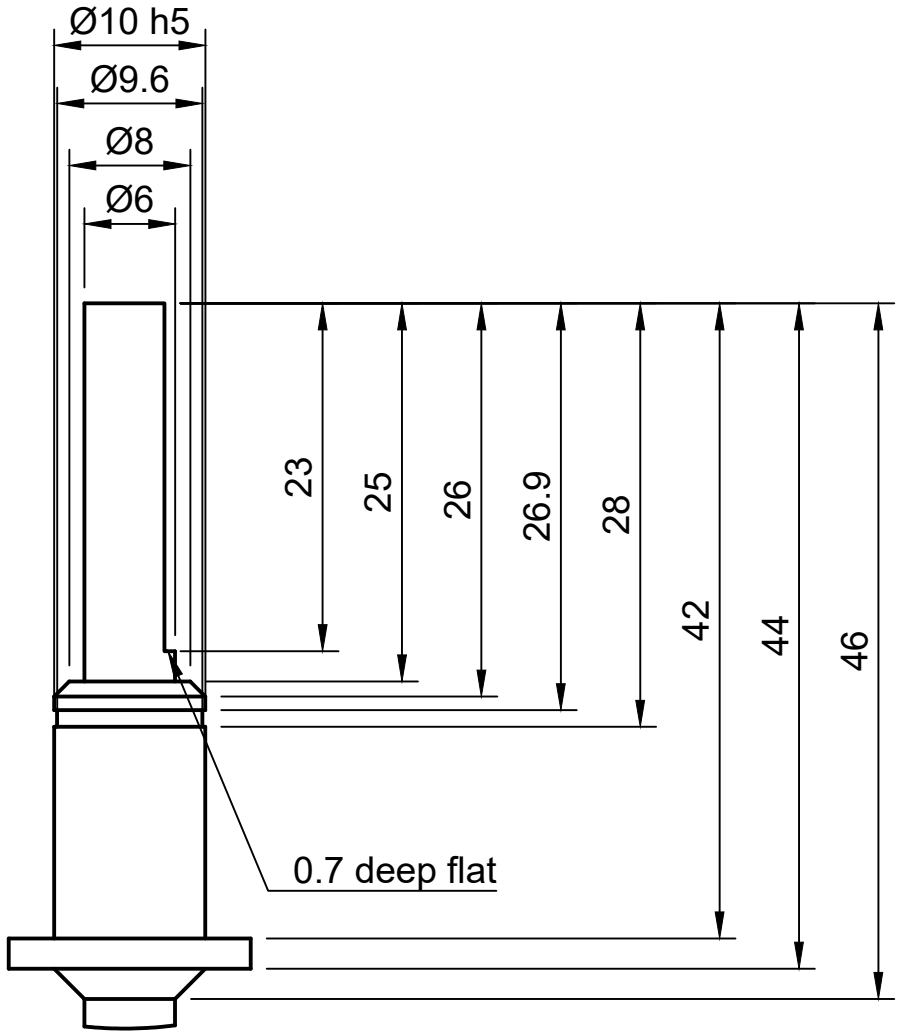

Document type: Part Drawing			Created by: Albert Curmi	28/10/2024
Title: Screw 1			DWG No.: 03.0	
General tolerance: ±0.1 mm	Material: H13 Tool Steel		Scale: 1:1	Sheet: 5/15

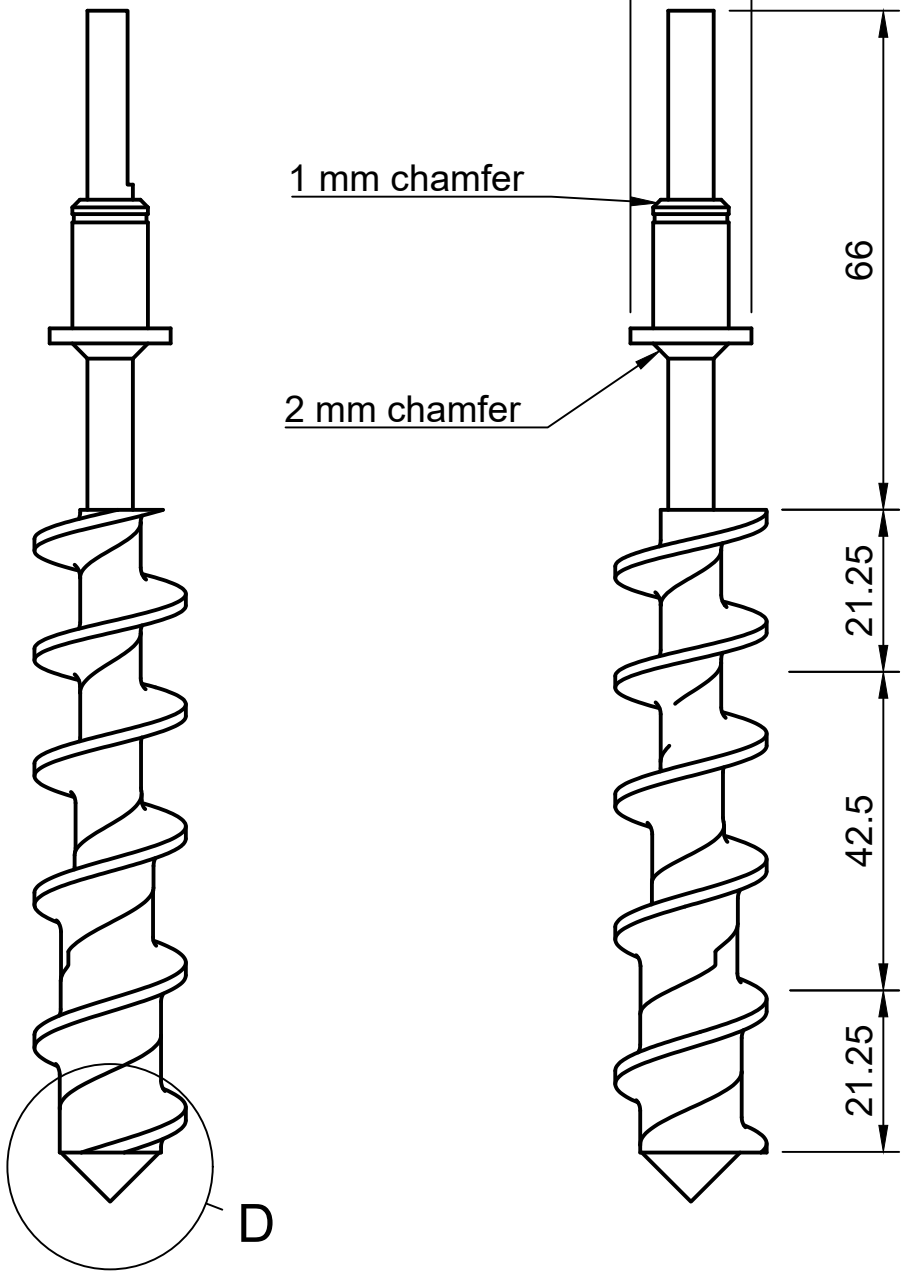

D (4)

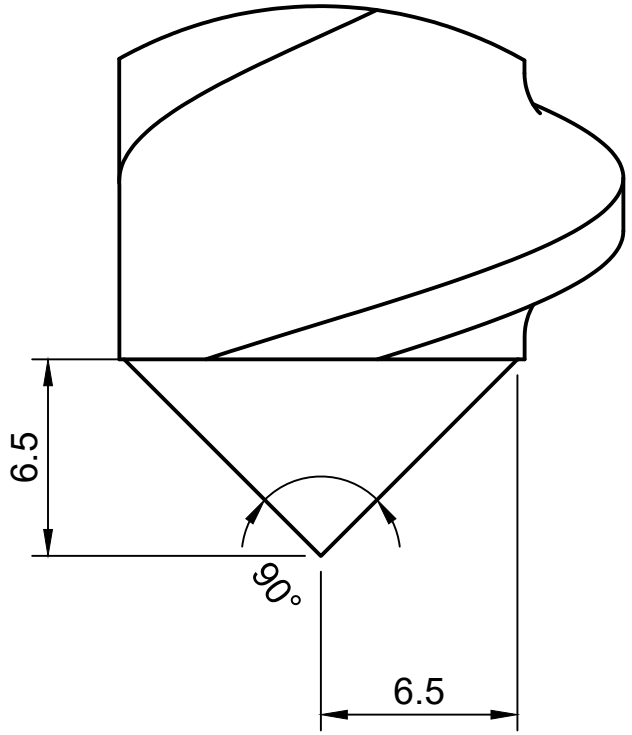

Document type: Part Drawing		Created by: Albert Curmi 28/10/2024		
Title: Screw 1		DWG No.: 03.1		
General tolerance: ±0.1 mm	Material: H13 Tool Steel		Scale: 1:1	Sheet: 6/15

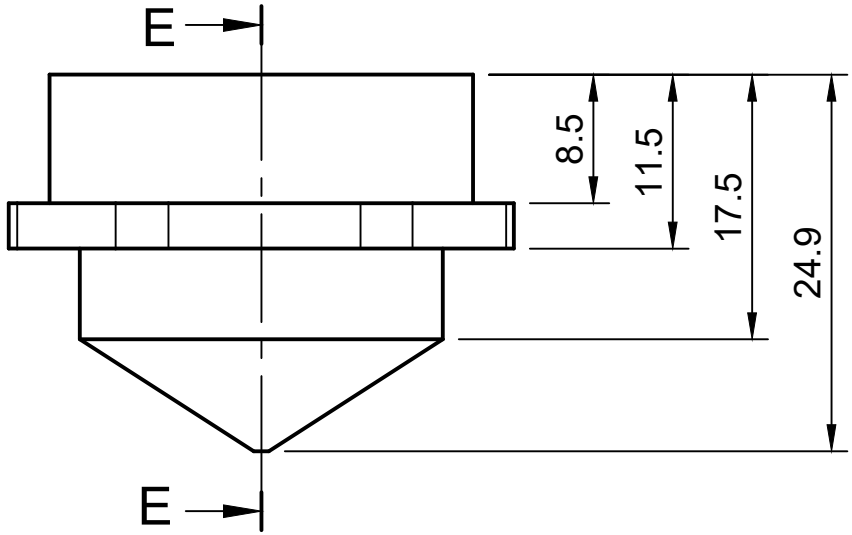

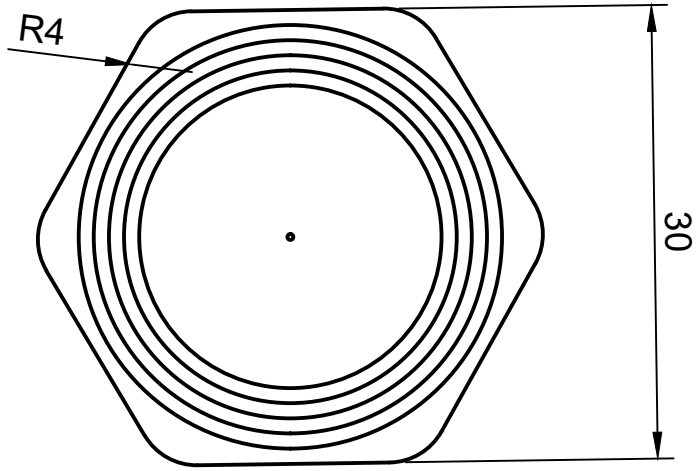

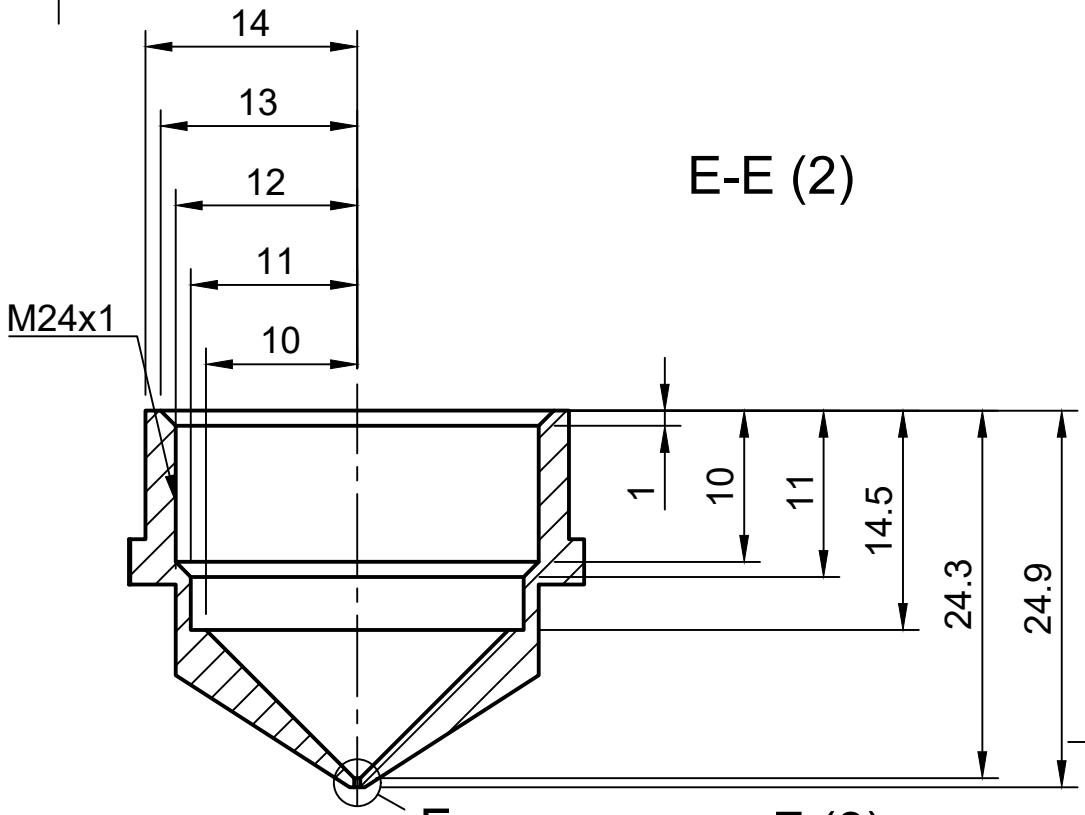

E-E (2)

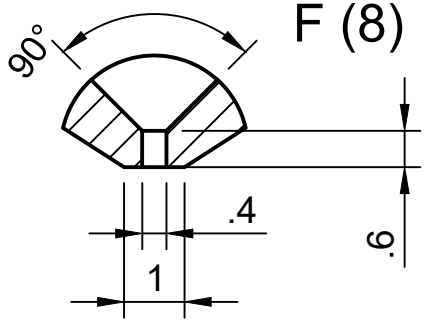

F (8)

Document type: Part Drawing		Created by: Albert Curmi 28/10/2024		
Title: Nozzle		DWG No.: 04.0		
General tolerance: ±0.1 mm	Material: H13 Tool Steel		Scale: 2:1	Sheet: 7/15

Parts List			
Item	Qty	Part Name	Material
1	1	Temeperature Sensor Block	Brass
2	1	PT 100	Steel
3	1	M4, 4 mm, grub screw	Steel
4	2	M4 nut	Steel
5	1	M4, 25 mm	Steel

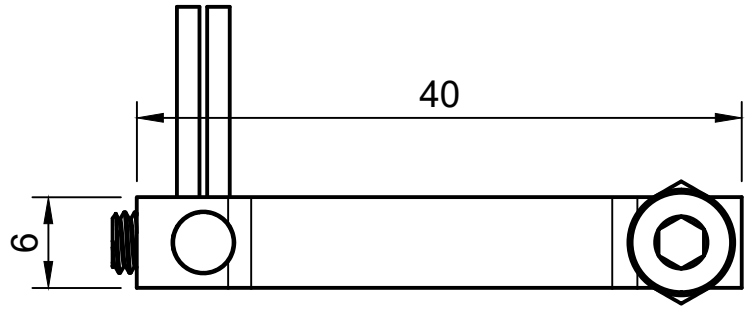

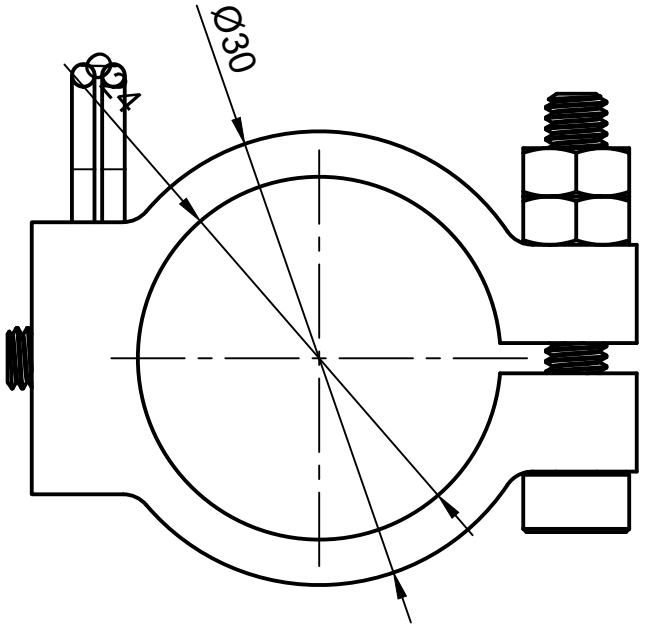

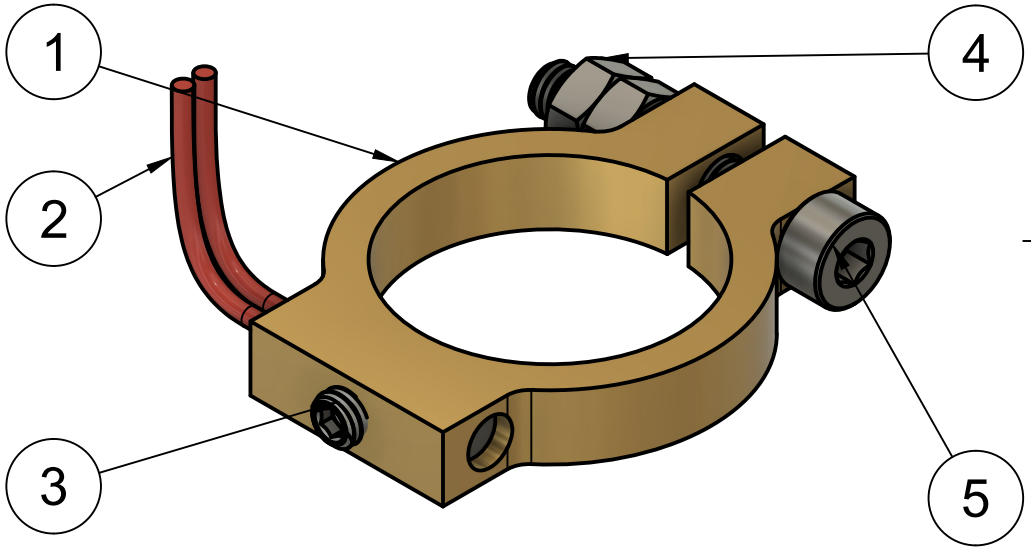

Document type: Assembly Drawing		Created by: Albert Curmi		28/10/2024
Title: Temperature Sensor Assembly		DWG No.: 05.0		
General tolerance: ±0.1 mm	Material: N/A		Scale: 2:1	Sheet: 8/15

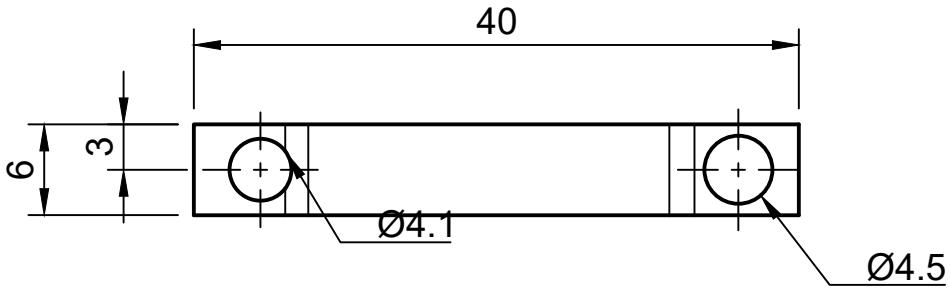

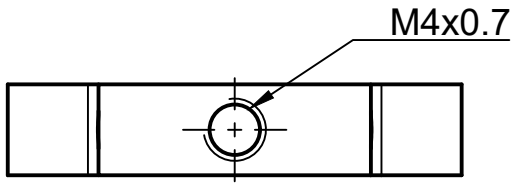

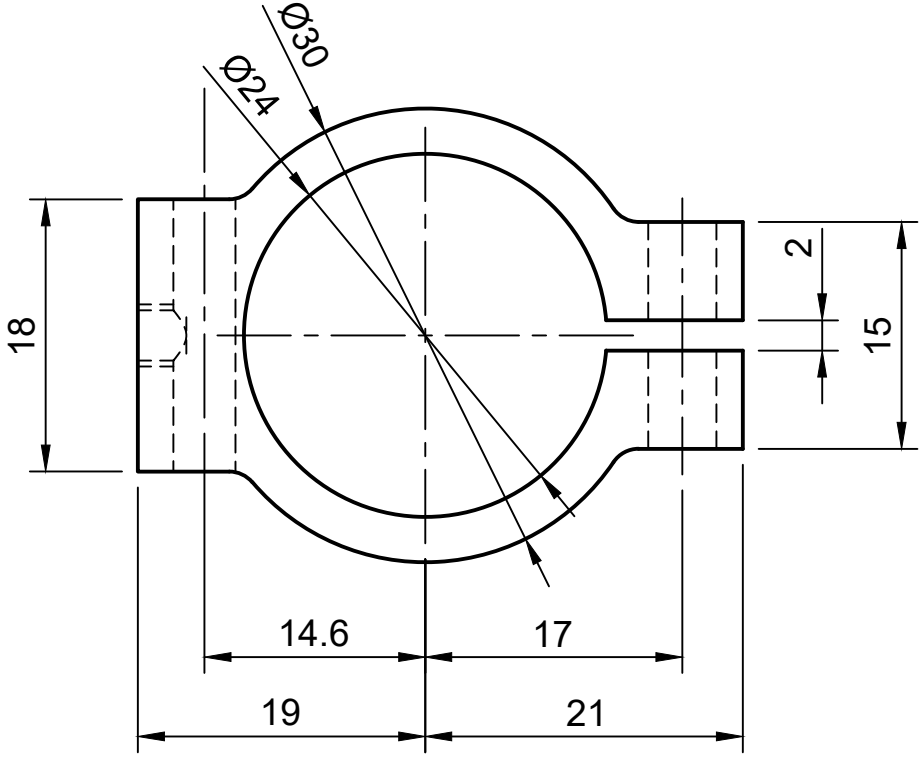

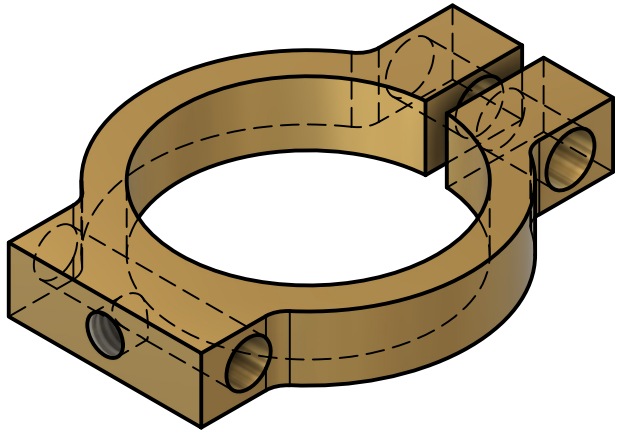

Document type: Part Drawing		Created by: Albert Curmi		28/10/2024
Title: Temperature Sensor Block		DWG No.: 06.0		
General tolerance: ±0.1 mm	Material: Brass		Scale: 2:1	Sheet: 9/15

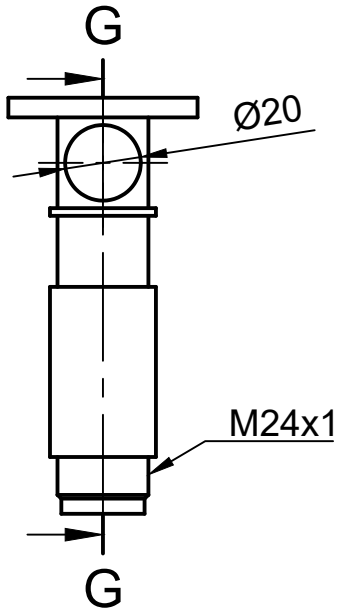

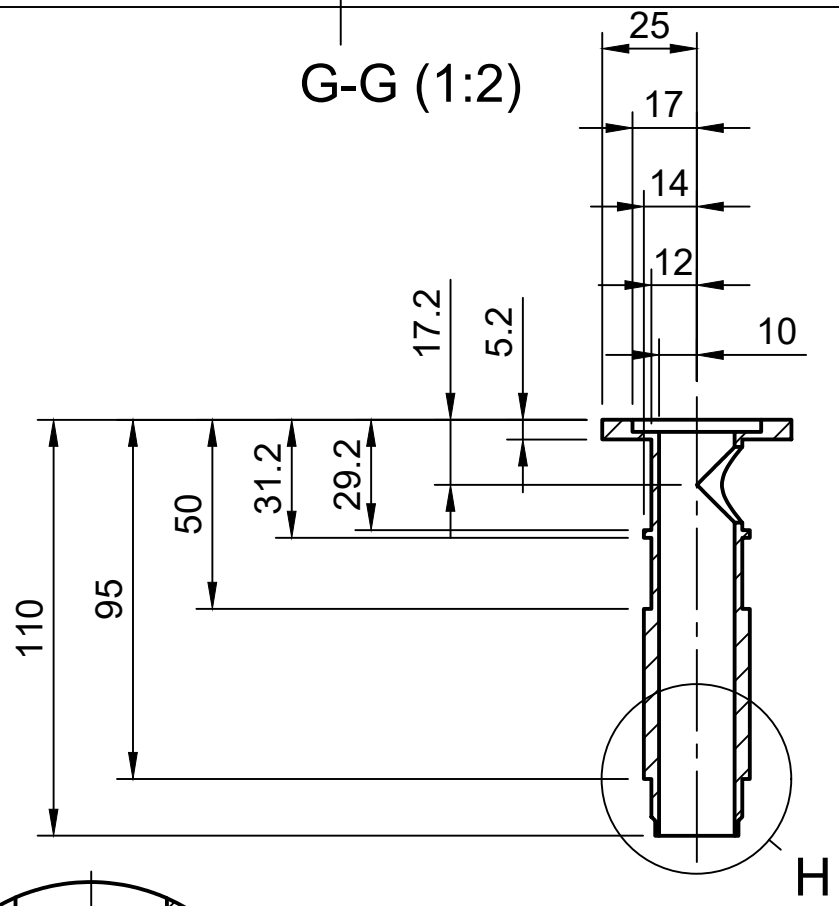

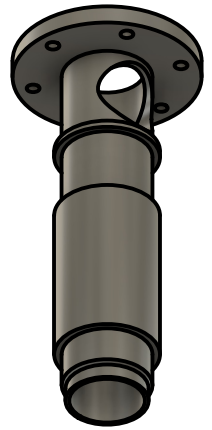

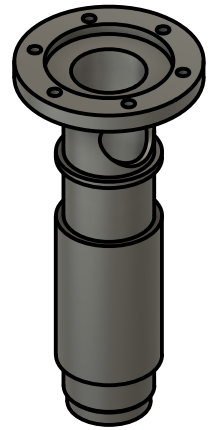

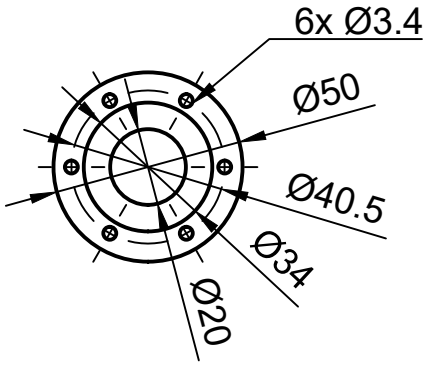

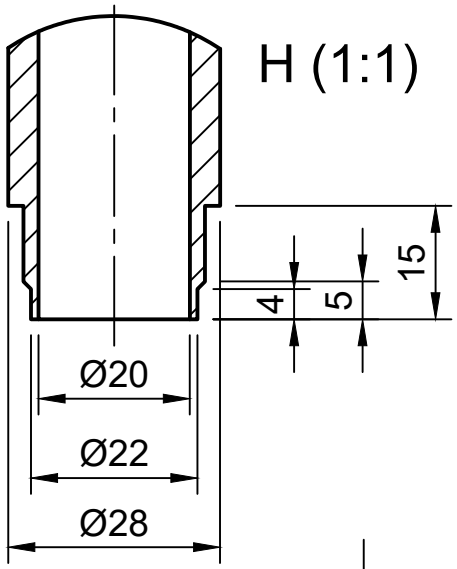

Document type: Part Drawing			Created by: Albert Curmi	28/10/2024
Title: Heater Barrel			DWG No.: 07.0	
General tolerance: ±0.1 mm	Material: H13 Tool Steel		Scale: 1:2	Sheet: 10/15

Parts List			
Item	Qty	Part Name	Material
1	2	M3 x 25	Steel
2	1	Holder	Aluminum 2014-T4
3	1	Bottom Cooling Block	Aluminum 2014-T4

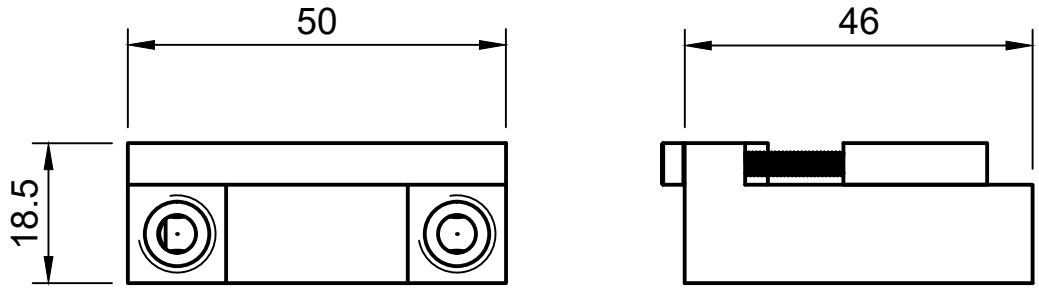

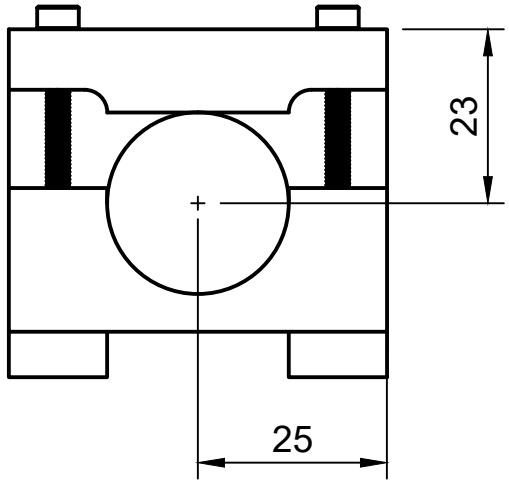

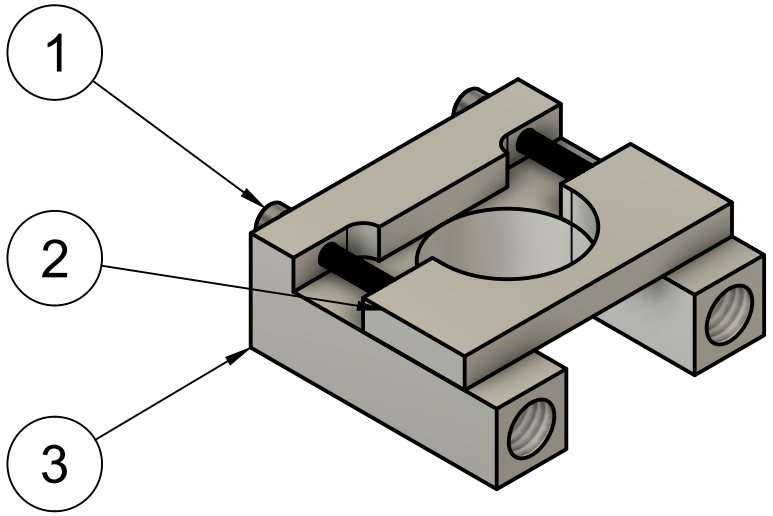

Document type: Assembly Drawing		Created by: Albert Curmi		28/10/2024
Title: Bottom Cooling Zone Assembly		DWG No.: 08.0		
General tolerance: ±0.1 mm	Material: N/A		Scale: 1:1	Sheet: 11/15

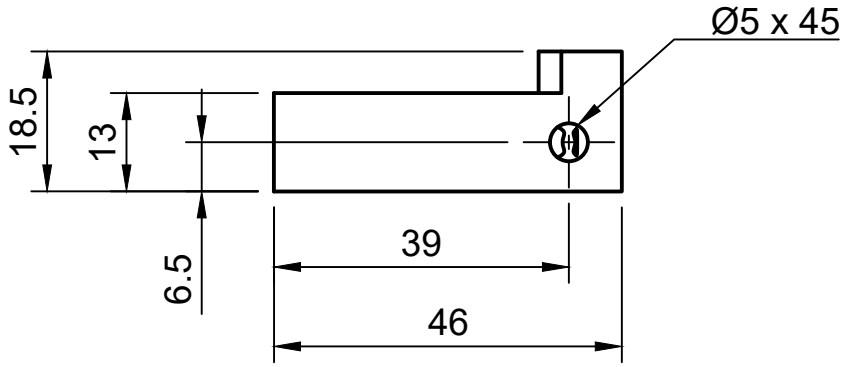

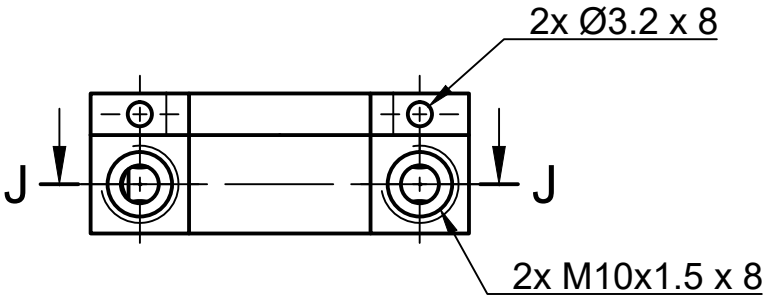

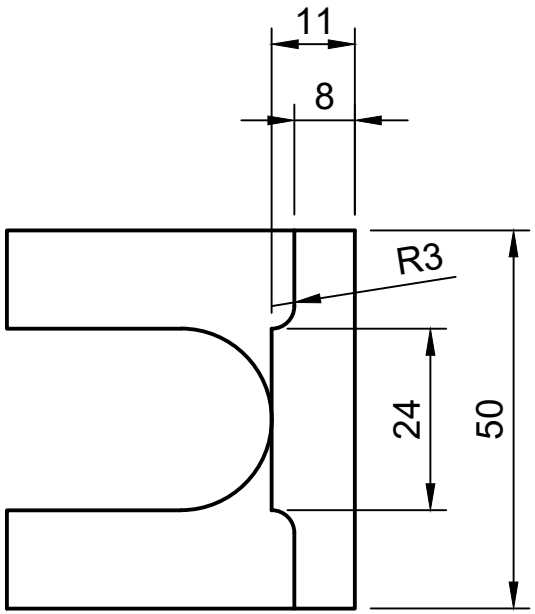

J-J (1)

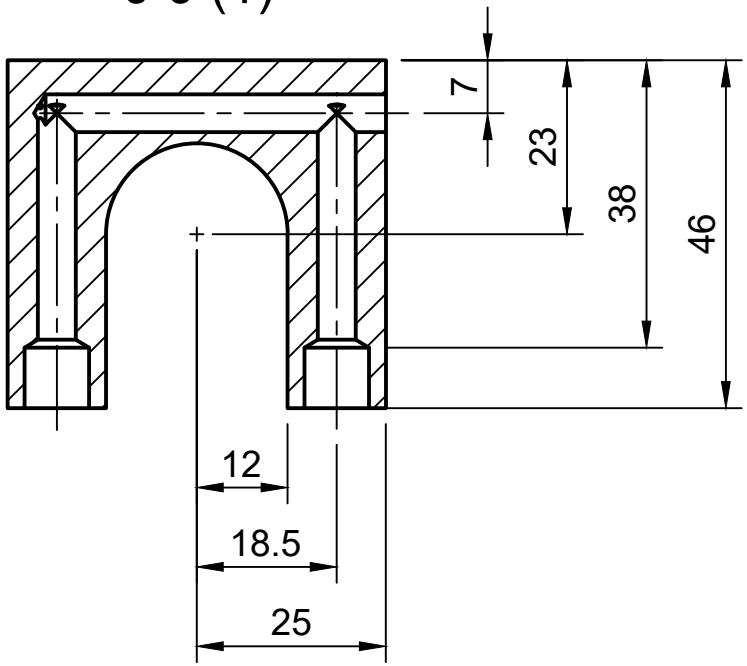

Document type: Part Drawing		Created by: Albert Curmi 28/10/2024		
Title: Bottom Cooling Block		DWG No.: 09.0		
General tolerance: ±0.1 mm	Material: Aluminum 2014-T4		Scale: 1:1	Sheet: 12/15

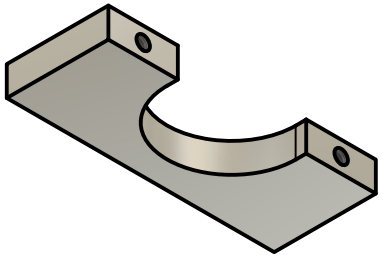

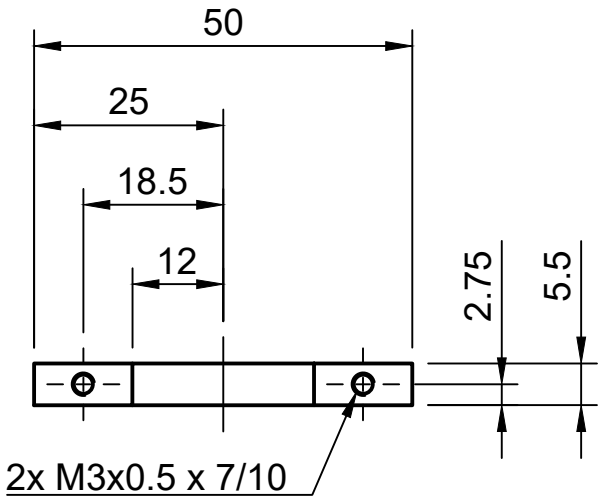

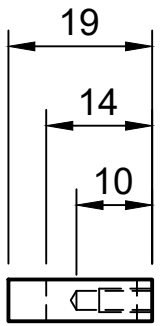

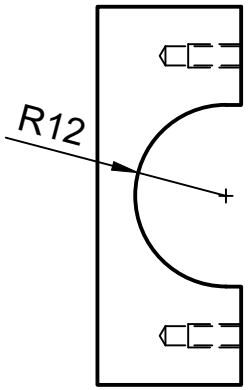

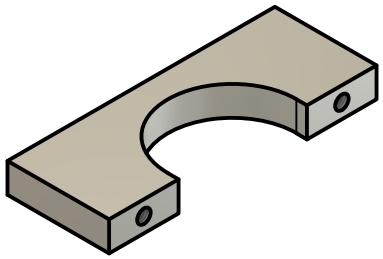

Document type: Part Drawing		Created by: Albert Curmi		28/10/2024
Title: Holder		DWG No.: 10.0		
General tolerance: ±0.1 mm	Material: Aluminum 2014-T4		Scale: 1:1	Sheet: 13/15

K-K (1)

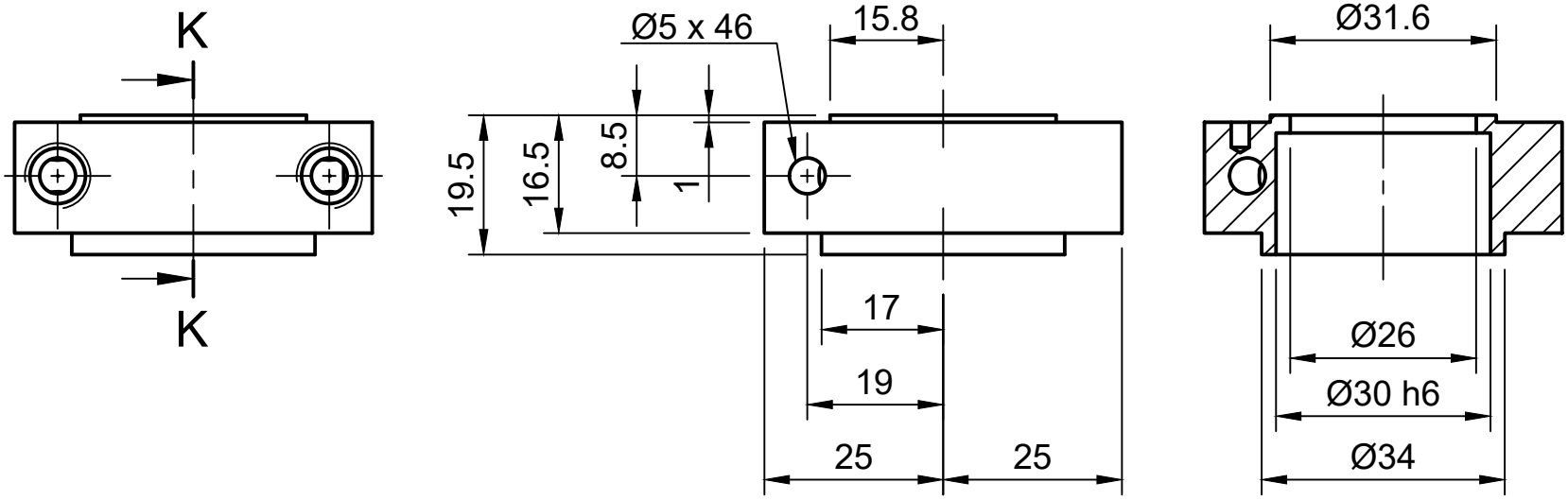

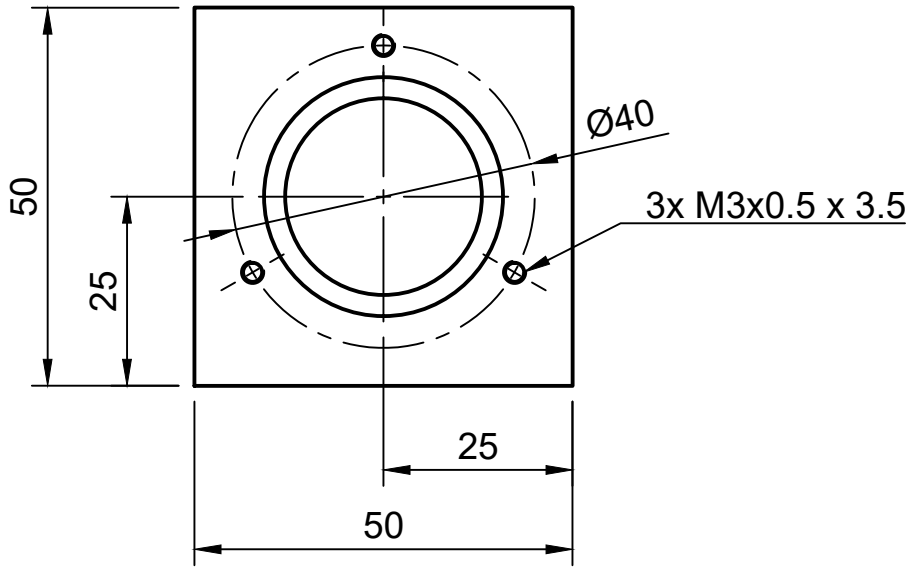

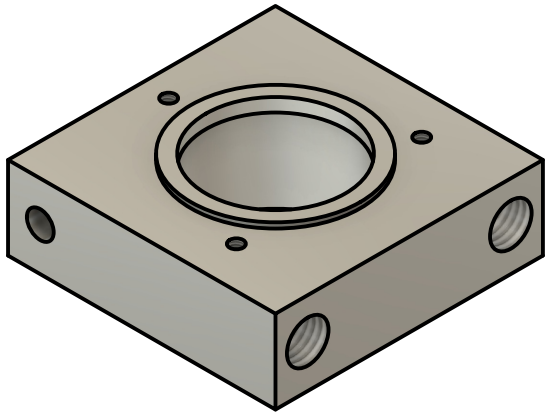

Document type: Part Drawing		Created by: Albert Curmi 28/10/2024		
Title: Bearing Block		DWG No.: 11.0		
General tolerance: ±0.1 mm	Material: Aluminum 2014-T4		Scale: 1:1	Sheet: 14/15

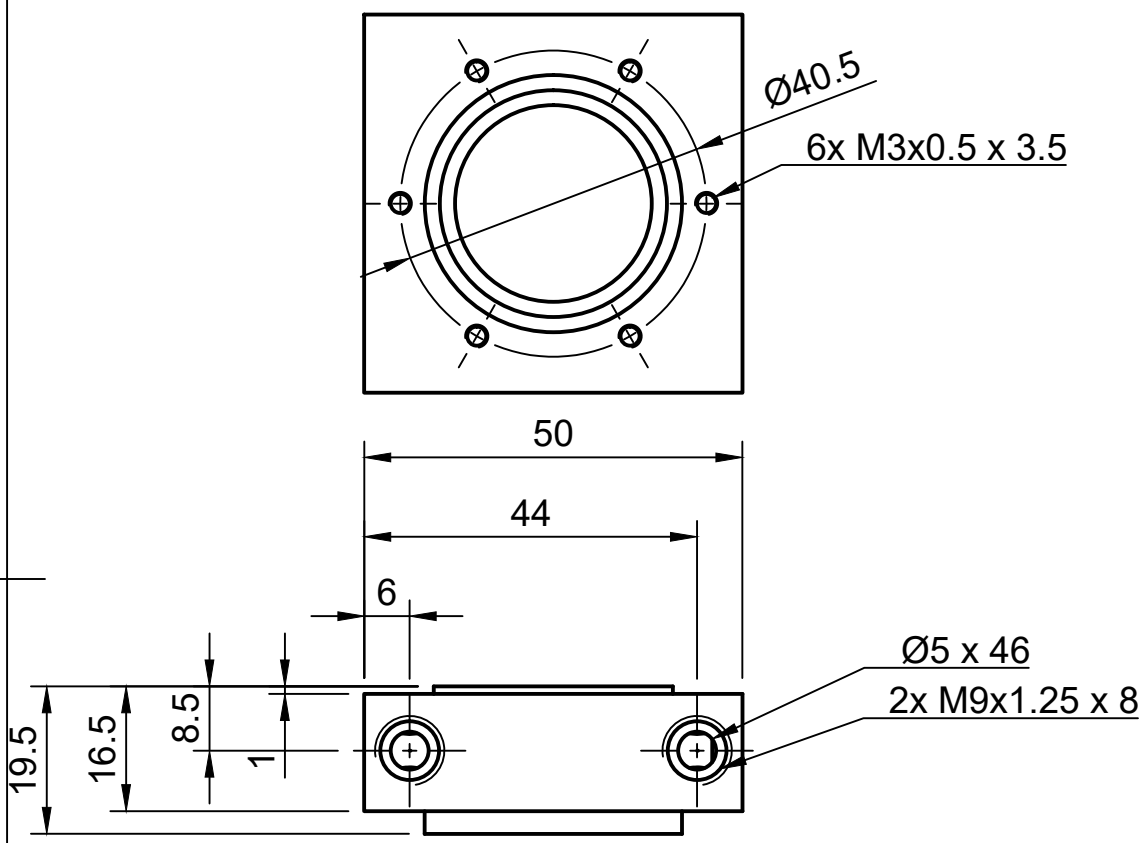

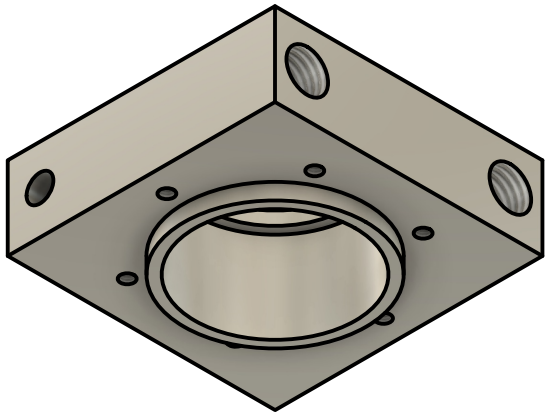

Document type: Part Drawing		Created by: Albert Curmi 28/10/2024		
Title: Bearing Block		DWG No.: 11.1		
General tolerance: ±0.1 mm	Material: Aluminum 2014-T4		Scale: 1:1	Sheet: 15/15

Appendix 3

Extruder Development 2 Engineering Drawings

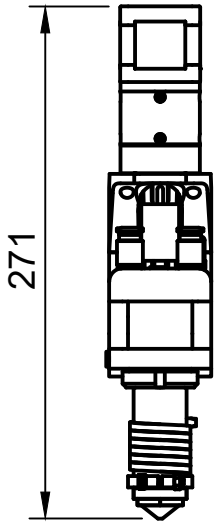

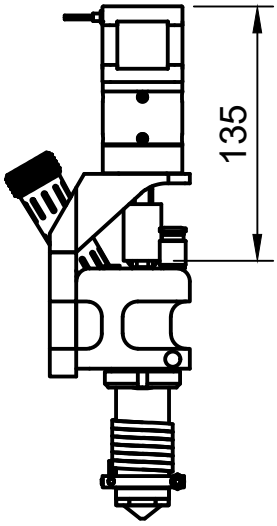

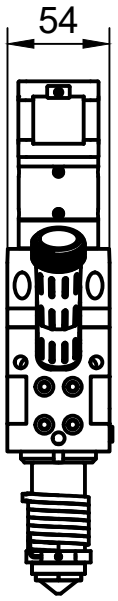

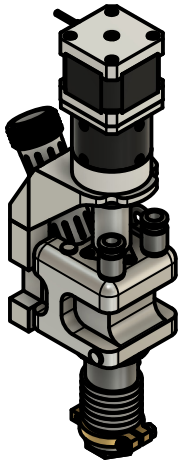

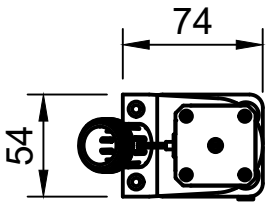

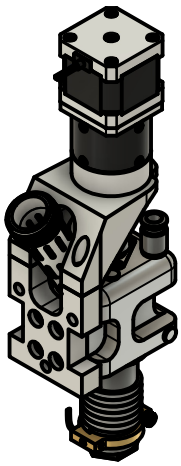

Document type Assembly Drawing		Created by Albert Curmi 29/10/2024		
Title Extruder 2 General Dimensions		DWG No. 01.0		
General tolerance ±0.1 mm	Material N/A		Scale 1:4	Sheet 1/16

(1:2)

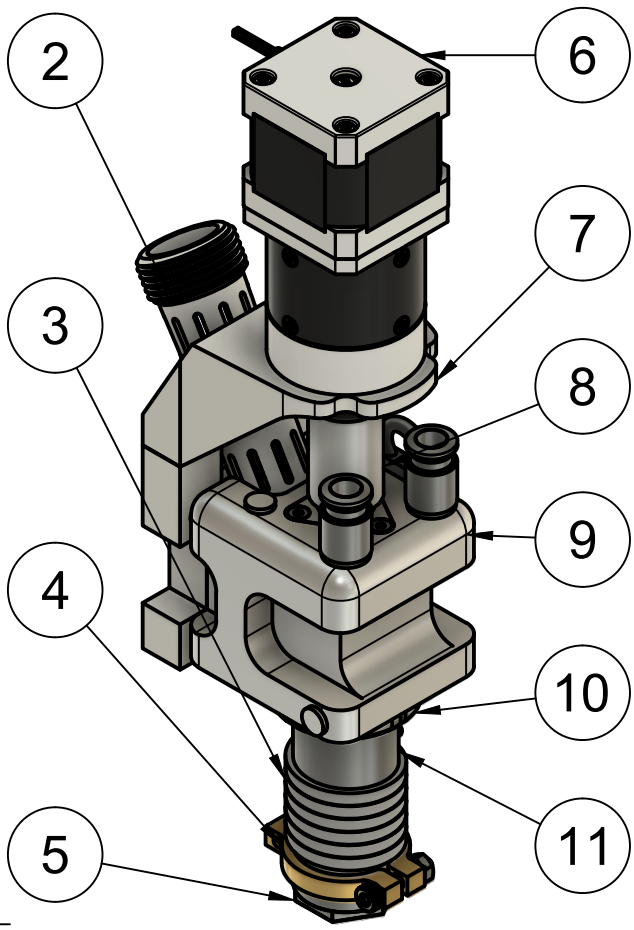

Parts List		
Item	Part Name	Material
1	Screw Assembly	
2	Pellet Feeder	ABS Plastic
3	Coil Heater	Steel
4	Temperature Sensor Block Barrel	
5	Nozzle	H13 tool steel
6	17HS15-1684S-HG30 v1	N/A
7	Mount CR-10	ABS Plastic
8	Drive Train	Aluminum 2014-T4
9	Feeding End	
10	Locking Nut	Steel
11	Heated Barrel	H13 tool steel

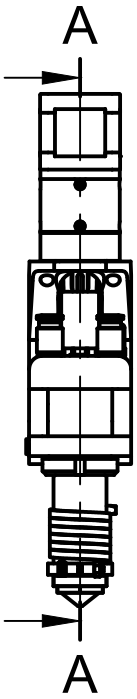

A-A (1:4)

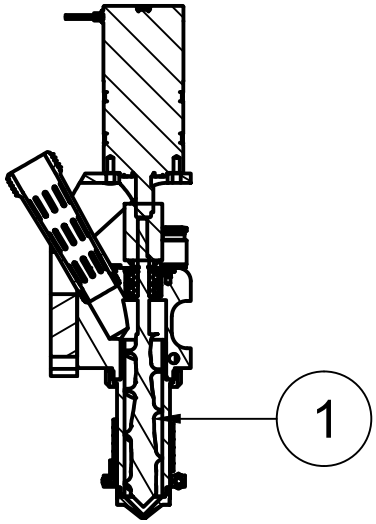

Document type: Assembly Drawing		Created by: Albert Curmi		29/10/2024
Title: Extruder 2 General Dimensions		DWG No.: 01.1		
General tolerance: ±0.1 mm	Material: N/A		Scale: 1:4	Sheet: 2/16

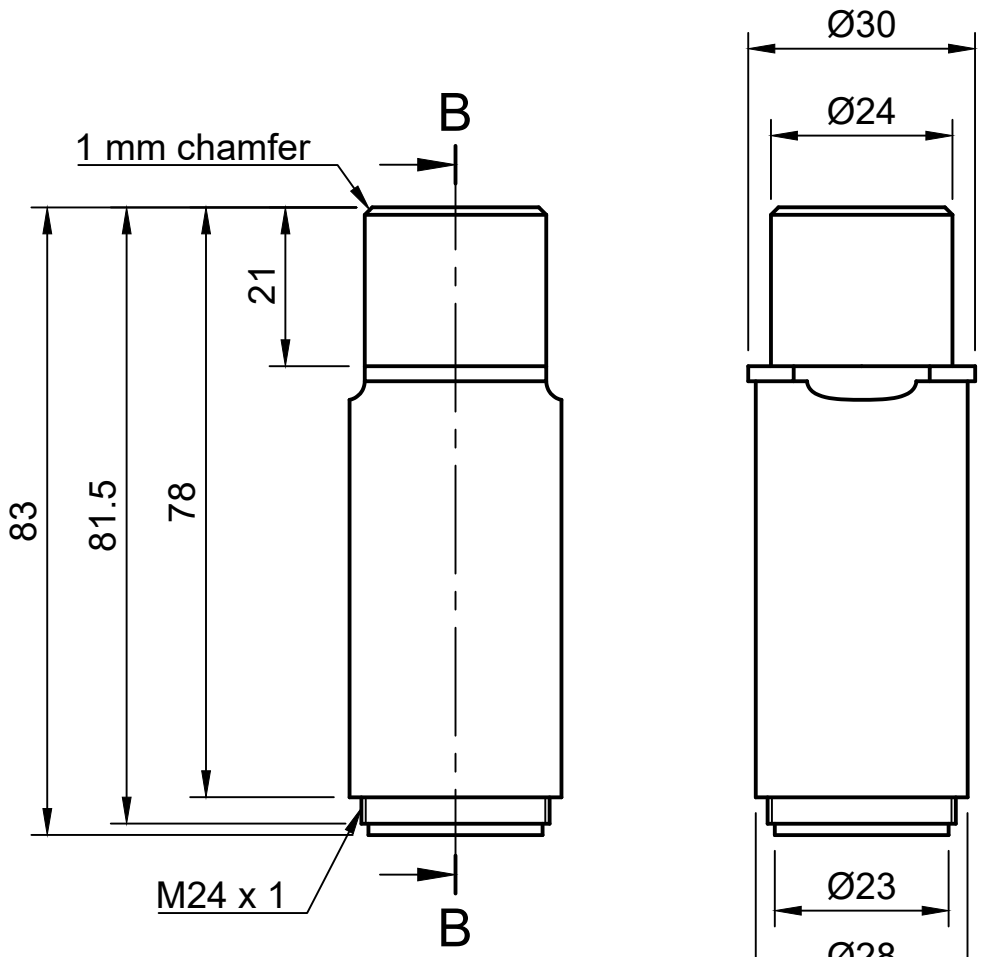

B-B (1:1)

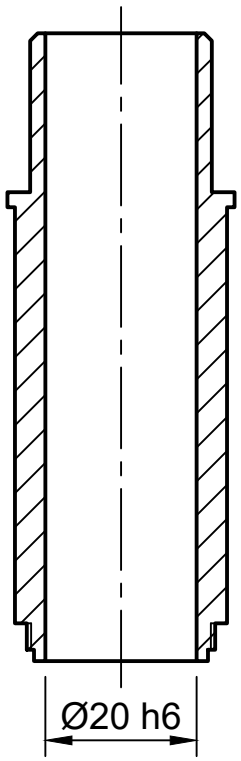

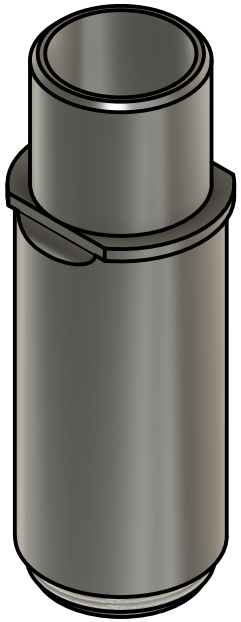

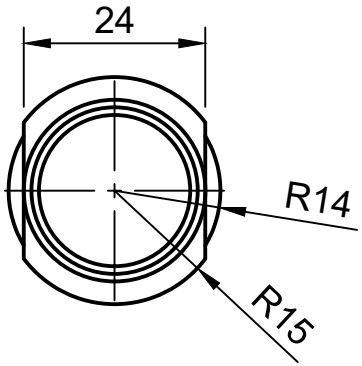

Document type: Part Drawing		Created by: Albert Curmi 29/10/2024		
Title: Heated Barrel		DWG No.: 02.0		
General tolerance: ±0.1 mm	Material: H13 tool steel		Scale: 1:1	Sheet: 3/16

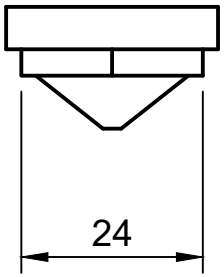

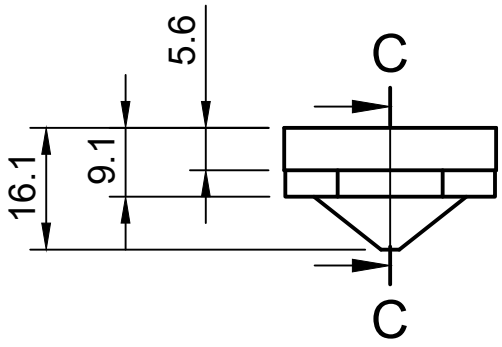

C-C (1)

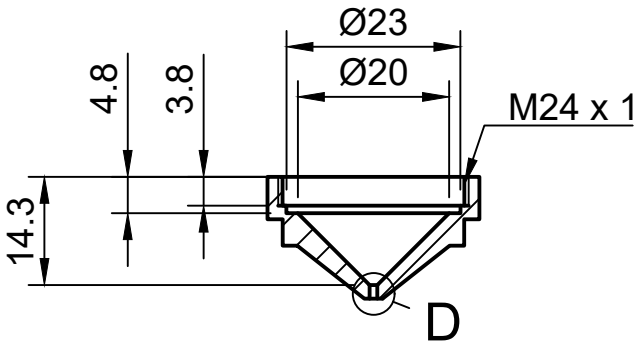

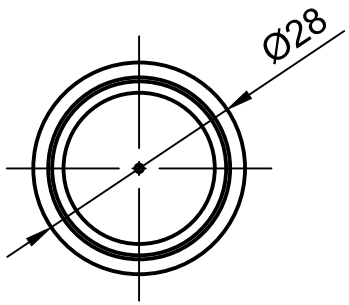

D (8)

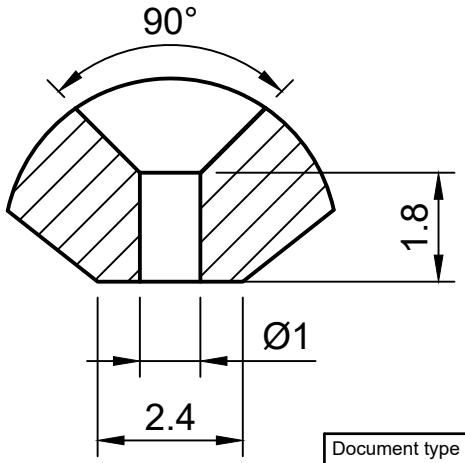

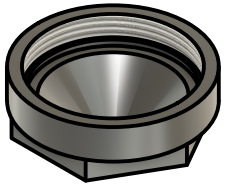

Document type: Part Drawing		Created by: Albert Curmi		29/10/2024
Title: Nozzle 1 mm		DWG No.: 03.0		
General tolerance: ±0.1 mm	Material: H13 tool steel		Scale: 1:1	Sheet: 4/16

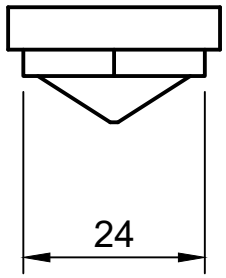

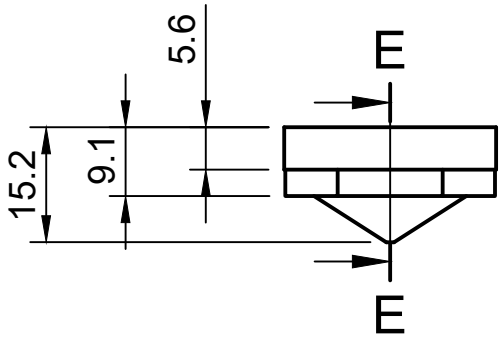

E-E (1)

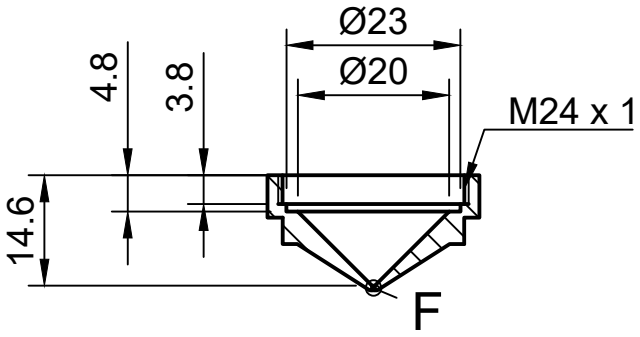

F (16)

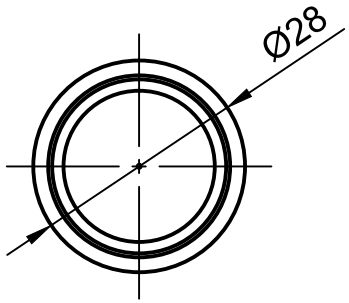

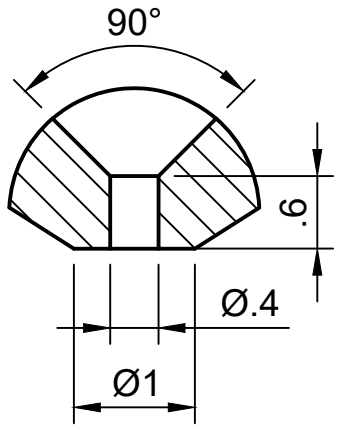

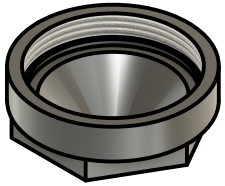

Document type: Part Drawing		Created by: Albert Curmi 29/10/2024		
Title: Nozzle 0.4 mm		DWG No.: 04.0		
General tolerance: ±0.1 mm	Material: H13 tool steel		Scale: 1:1	Sheet: 5/16

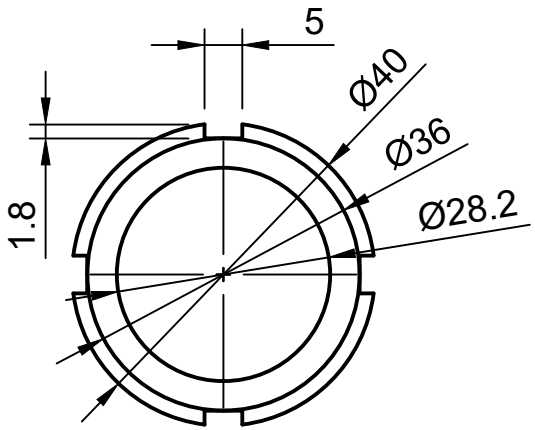

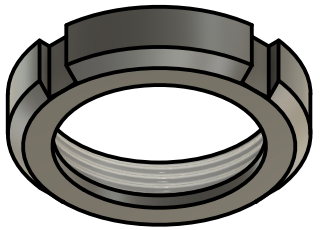

G-G (1)

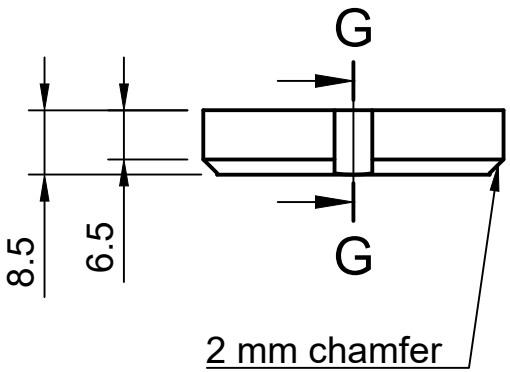

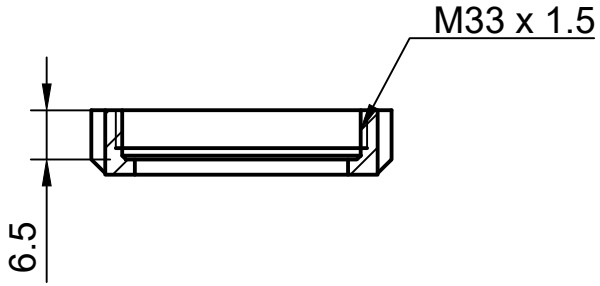

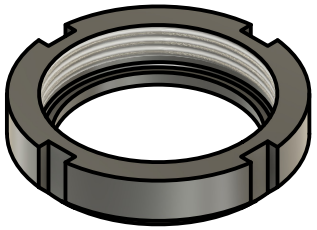

Document type: Part Drawing		Created by: Albert Curmi 29/10/2024		
Title: Locking Nut		DWG No.: 05.0		
General tolerance: ±0.1 mm	Material: Steel		Scale: 1:1	Sheet: 6/16

Parts List			
Item	Qty	Part Name	Material
1	1	Screw 2	H13 tool steel
2	1	6-8 mm e-clip	Steel
3	1	Circlip Spacer	Brass
4	1	Bearing Spacer	Brass
5	2	SKF_626-2Z	

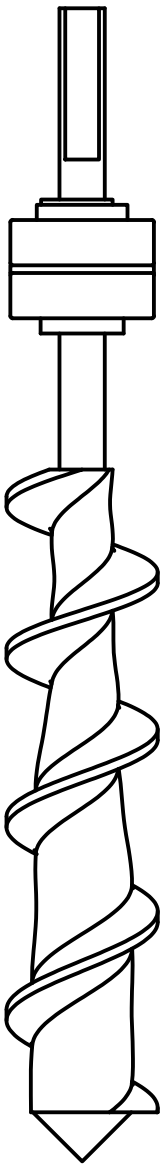

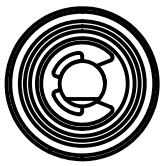

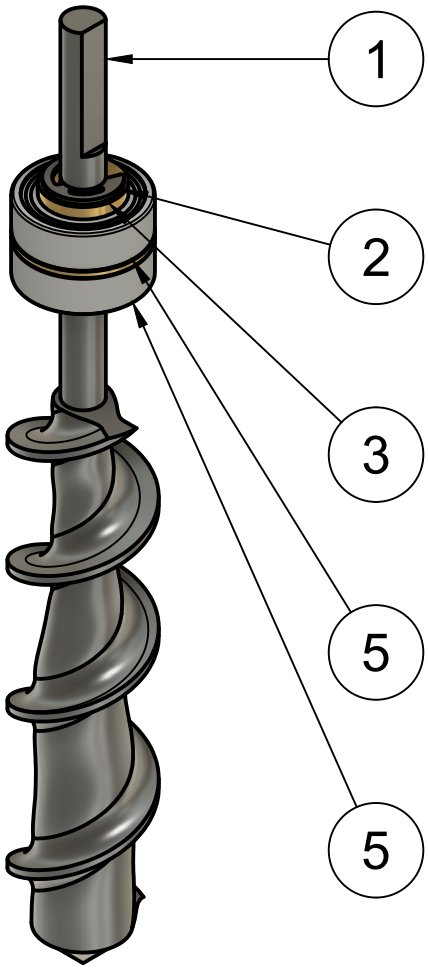

Document type: Assembly Drawing		Created by: Albert Curmi		29/10/2024
Title: Screw Assembly		DWG No.: 06.0		
General tolerance: ±0.1 mm	Material: N/A		Scale: 1:1	Sheet: 7/16

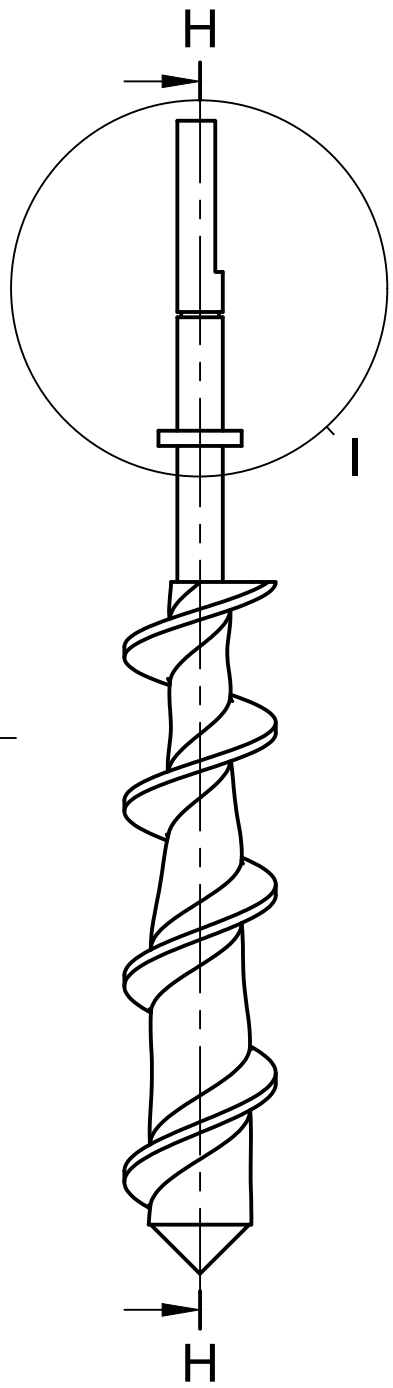

H-H (1)

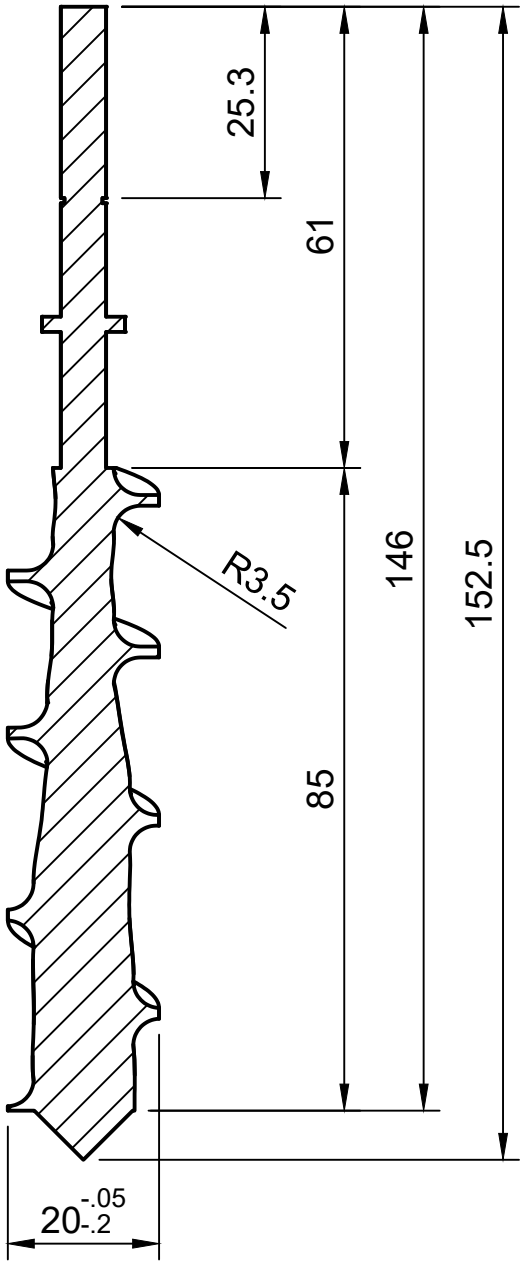

I (2:1)

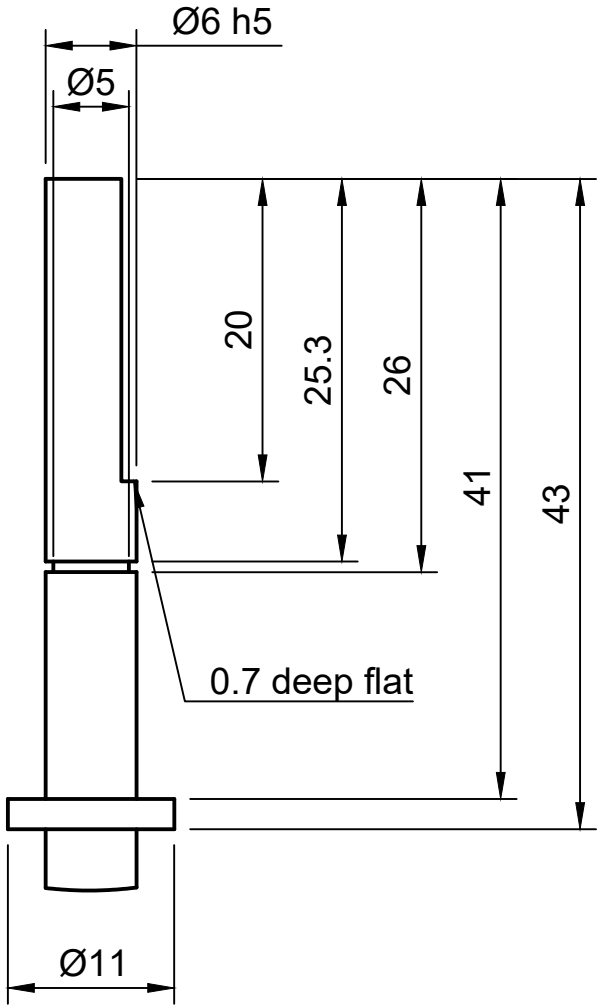

Document type: Part Drawing			Created by: Albert Curmi	29/10/2024
Title: Screw 2			DWG No.: 07.0	
General tolerance: ±0.1 mm	Material: H13 tool steel		Scale: 1:1	Sheet: 8/16

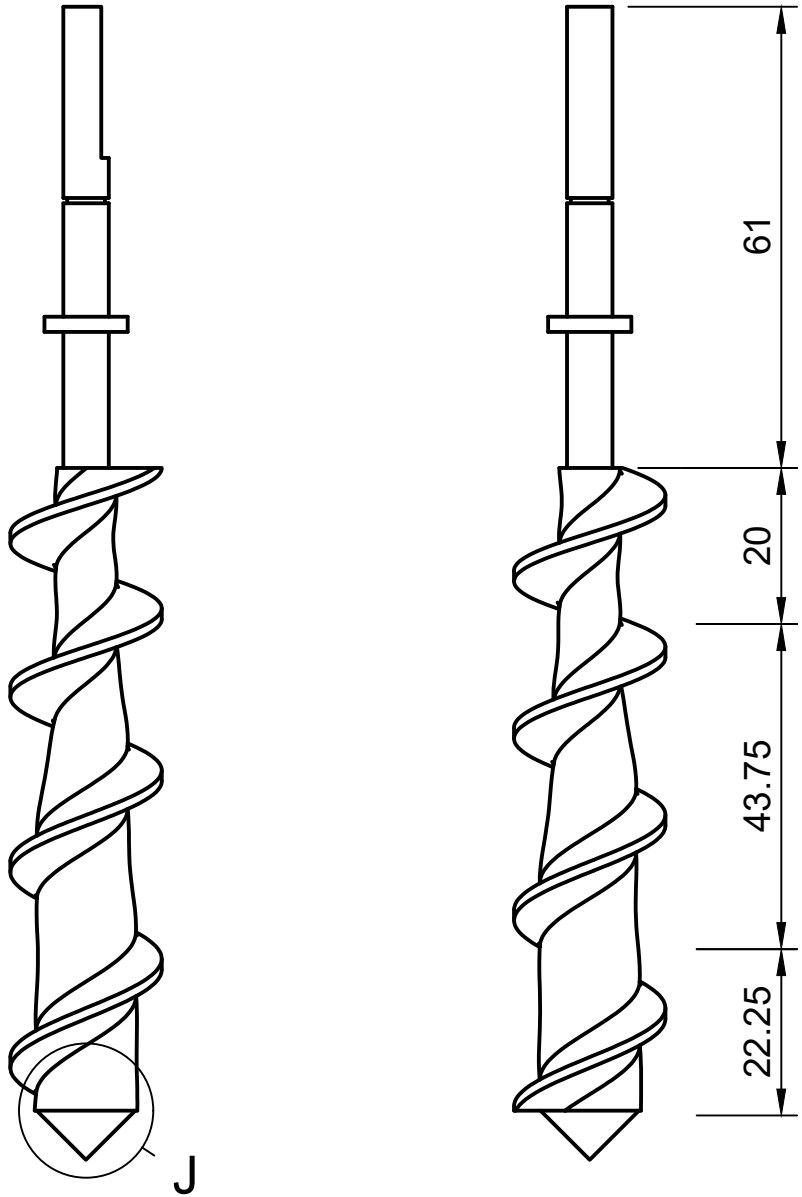

J (4)

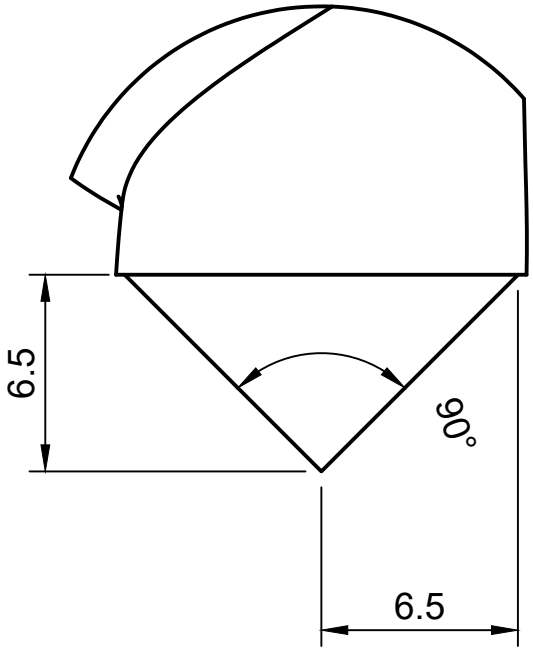

Document type: Part Drawing		Created by: Albert Curmi 29/10/2024		
Title: Screw 2		DWG No.: 07.1		
General tolerance: ±0.1 mm	Material: H13 tool steel		Scale: 1:1	Sheet: 9/16

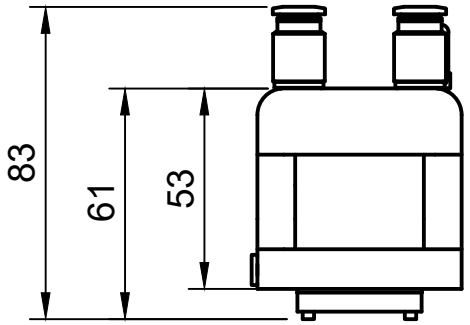

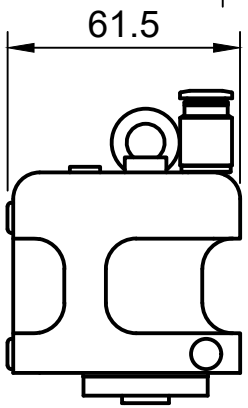

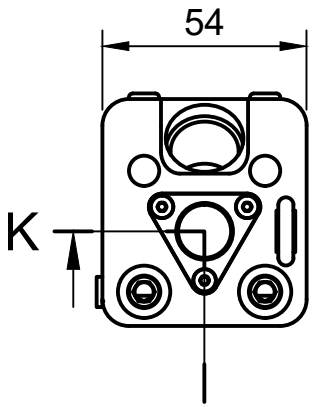

K-K (1:2)

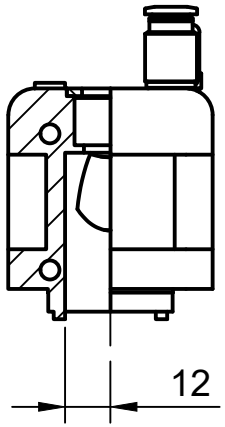

Parts List			
Item	Qty	Part Name	Material
1	1	Screws	Steel
2	1	Water Plugs	Aluminum 2014-T4
3	2	186109_QS-G1_8-8-I v1	Steel
4	1	M4 Eye Bolt	Steel
5	1	Feeding Block	Aluminum 2014-T4
6	1	Bearing Lid	Aluminum 2014-T4

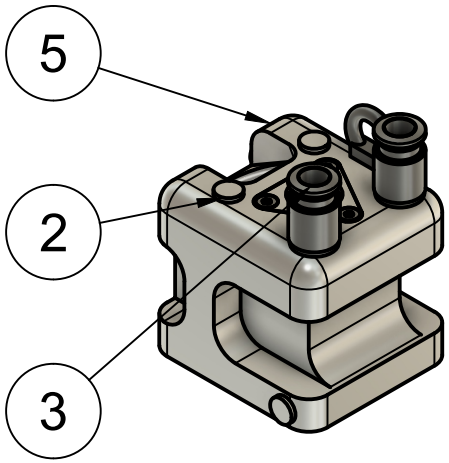

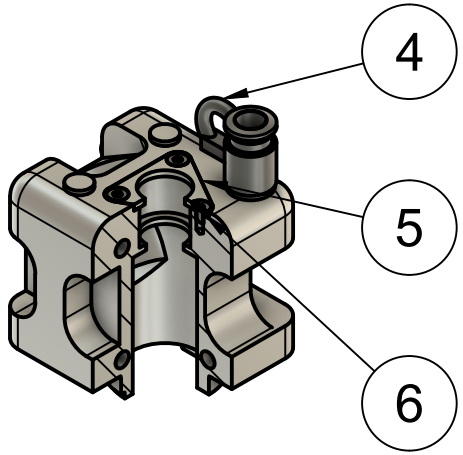

Document type: Assembly Drawing		Created by: Albert Curmi		29/10/2024
Title: Feeding End		DWG No.: 08.0		
General tolerance: ±0.1 mm	Material: N/A		Scale: 1:2	Sheet: 10/16

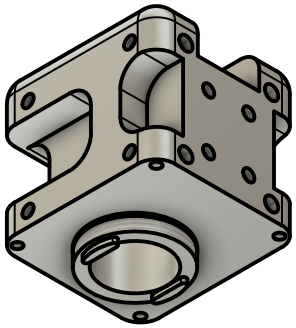

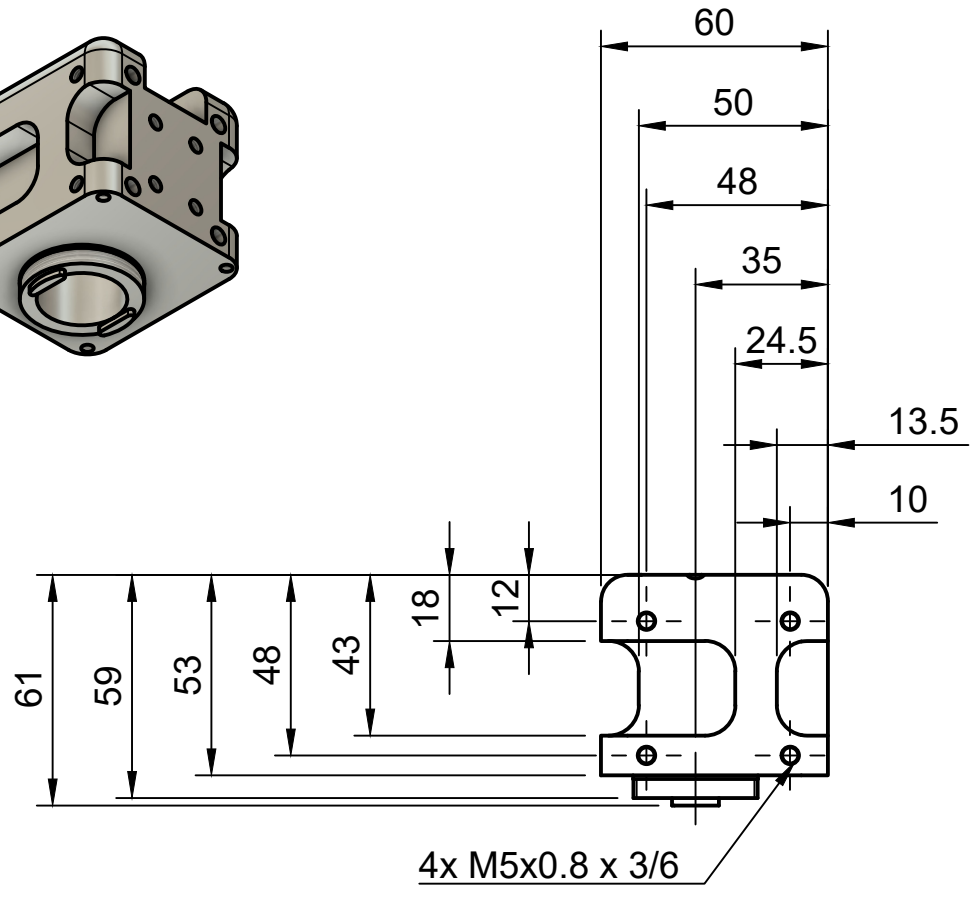

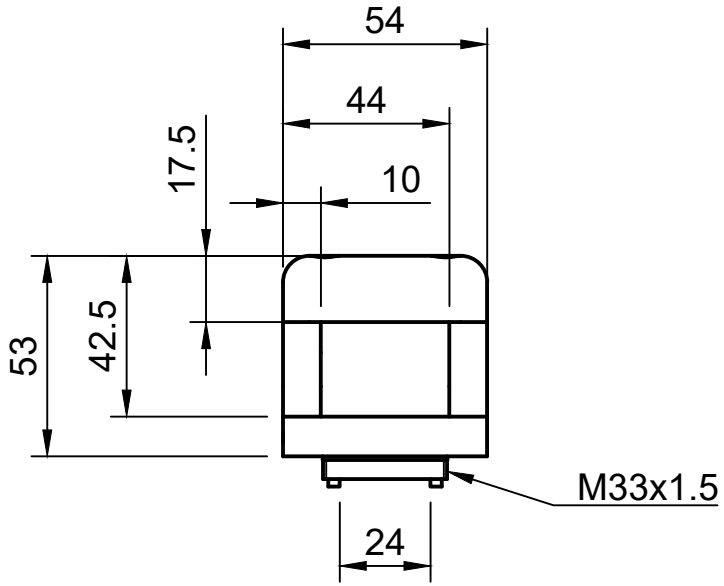

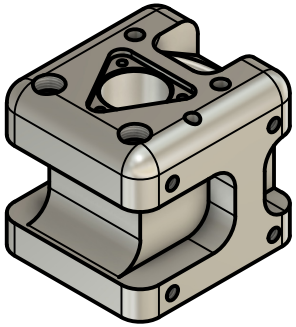

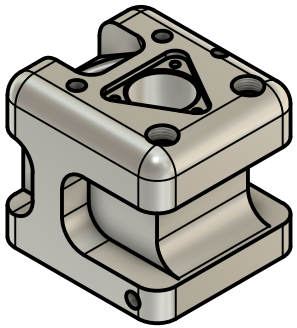

Document type: Part Drawing		Created by: Albert Curmi 29/10/2024		
Title: Feeding Block		DWG No.: 09.0		
General tolerance: ±0.1 mm	Material: Aluminum 2014-T4		Scale: 1:2	Sheet: 11/16

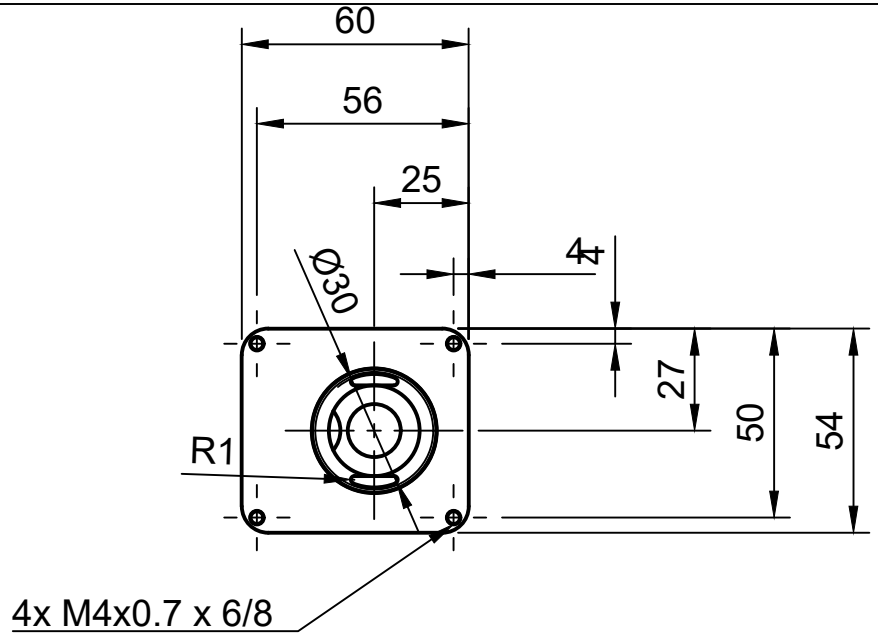

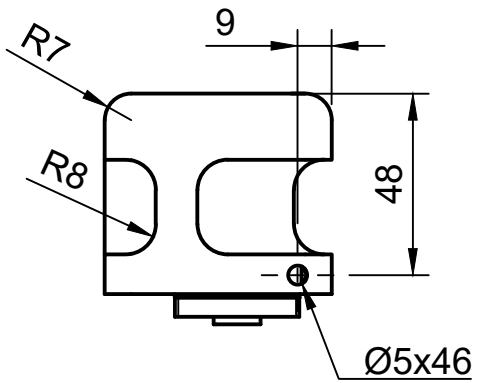

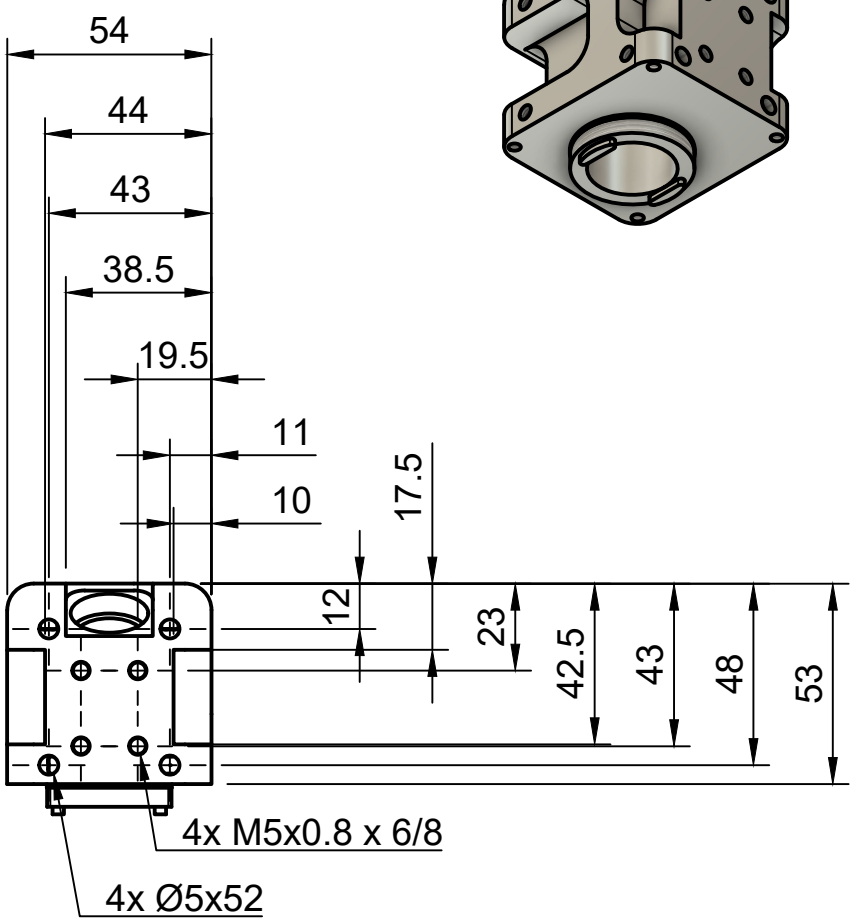

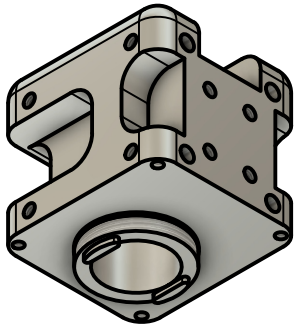

Document type: Part Drawing		Created by: Albert Curmi 29/10/2024		
Title: Feeding Block		DWG No.: 09.1		
General tolerance: ±0.1 mm	Material: Aluminum 2014-T4		Scale: 1:2	Sheet: 12/16

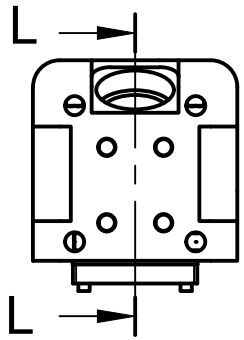

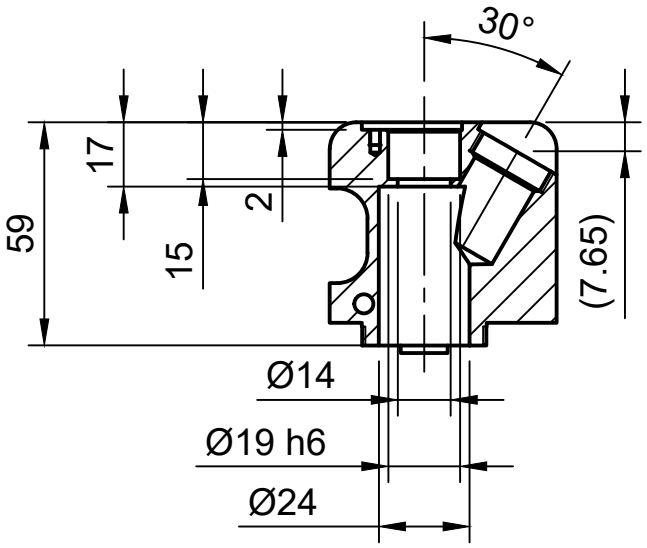

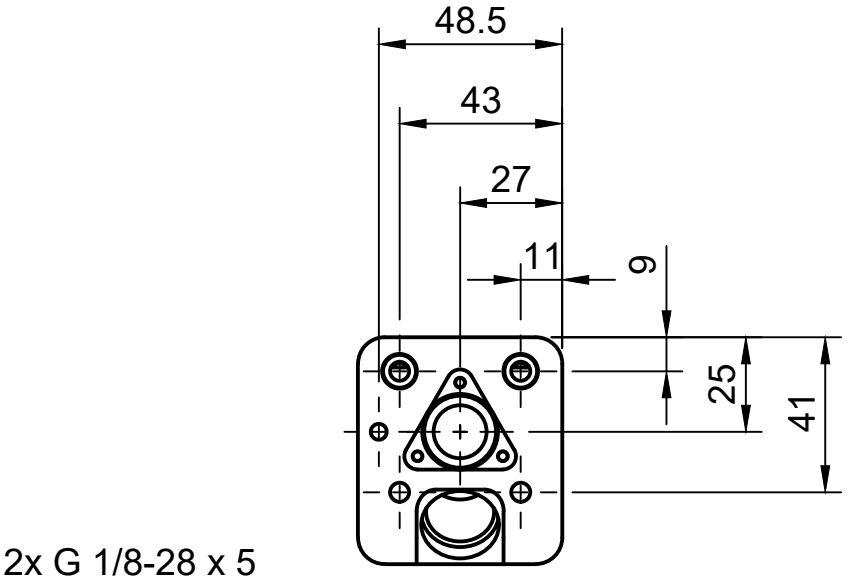

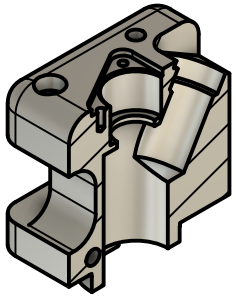

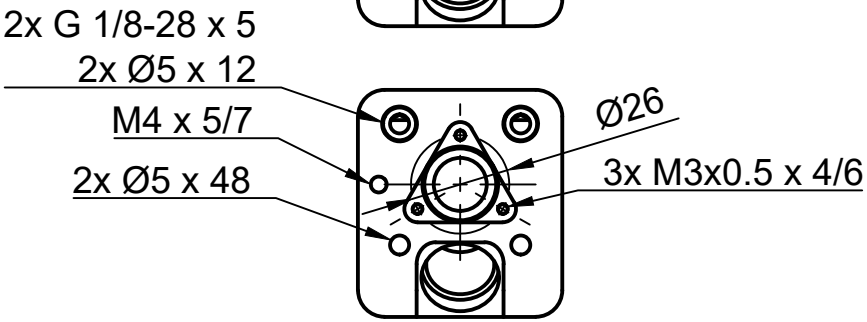

Document type: Part Drawing			Created by: Albert Curmi	29/10/2024
Title: Feeding Block			DWG No.: 09.2	
General tolerance: ±0.1 mm	Material: Aluminum 2014-T4		Scale: 1:2	Sheet: 13/16

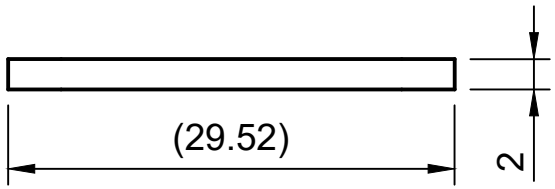

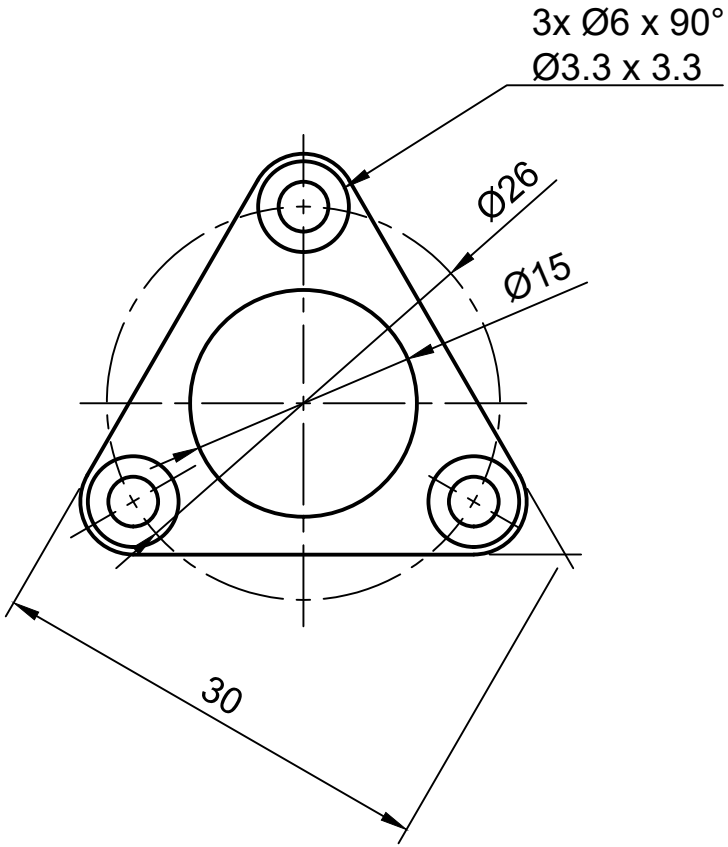

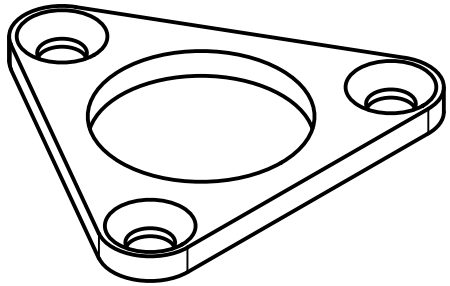

Document type: Part Drawing			Created by: Albert Curmi	29/10/2024
Title: Bearing Lid			DWG No.: 10.0	
General tolerance: ±0.1 mm	Material: Aluminum 2014-T4		Scale: 2:1	Sheet: 14/16

Parts List	
Item	Part Name
1	PT 100
2	M3 X 4 mm
3	M4 Nut
4	M4 X 20 mm
5	Brass Ring Barrel

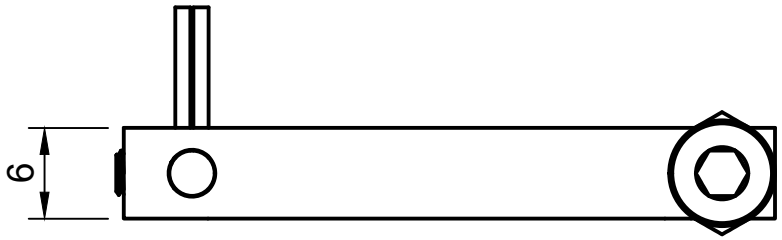

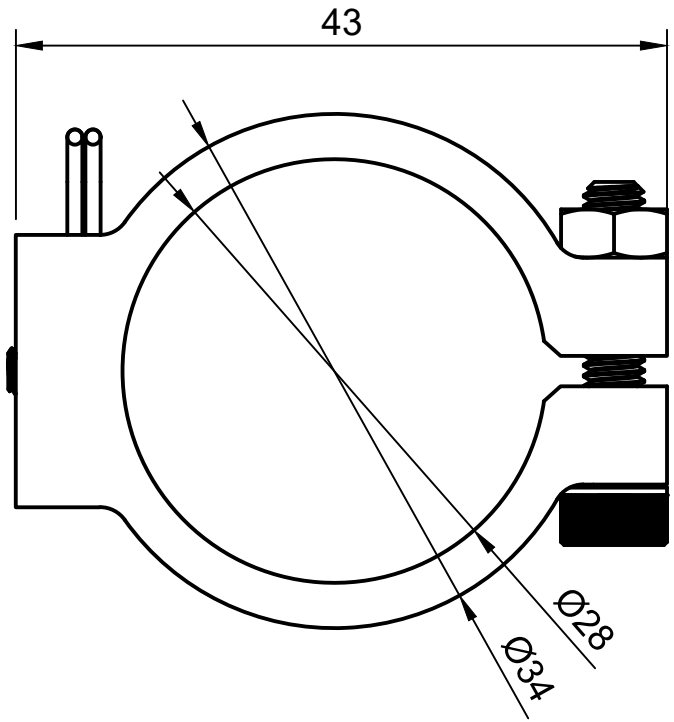

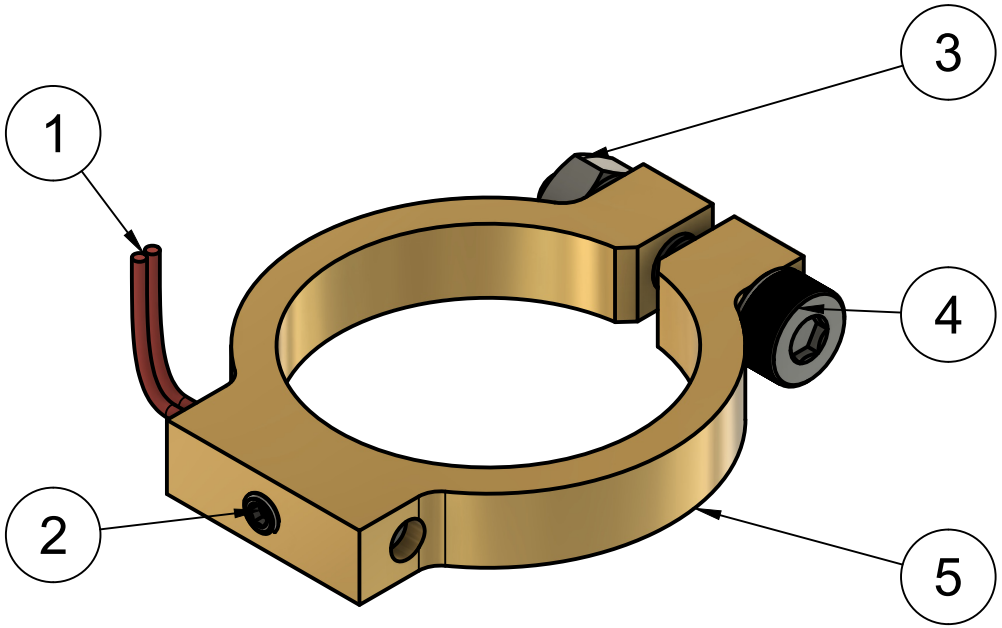

Document type: Assembly Drawing		Created by: Albert Curmi		29/10/2024
Title: Temperature Sensor Assembly		DWG No.: 11.0		
General tolerance: ±0.1 mm	Material: N/A		Scale: 2:1	Sheet: 15/16

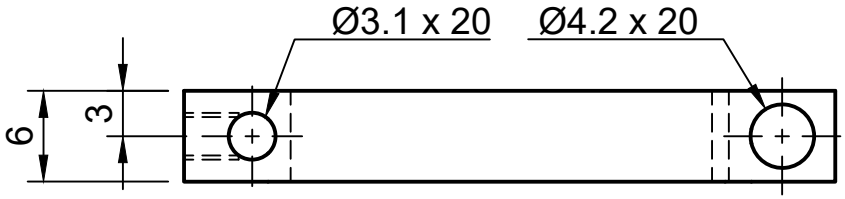

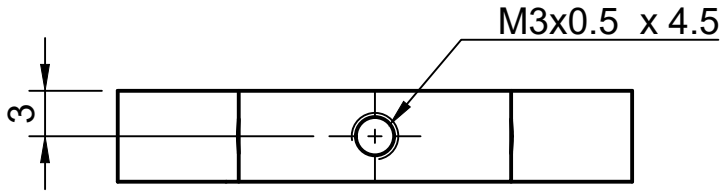

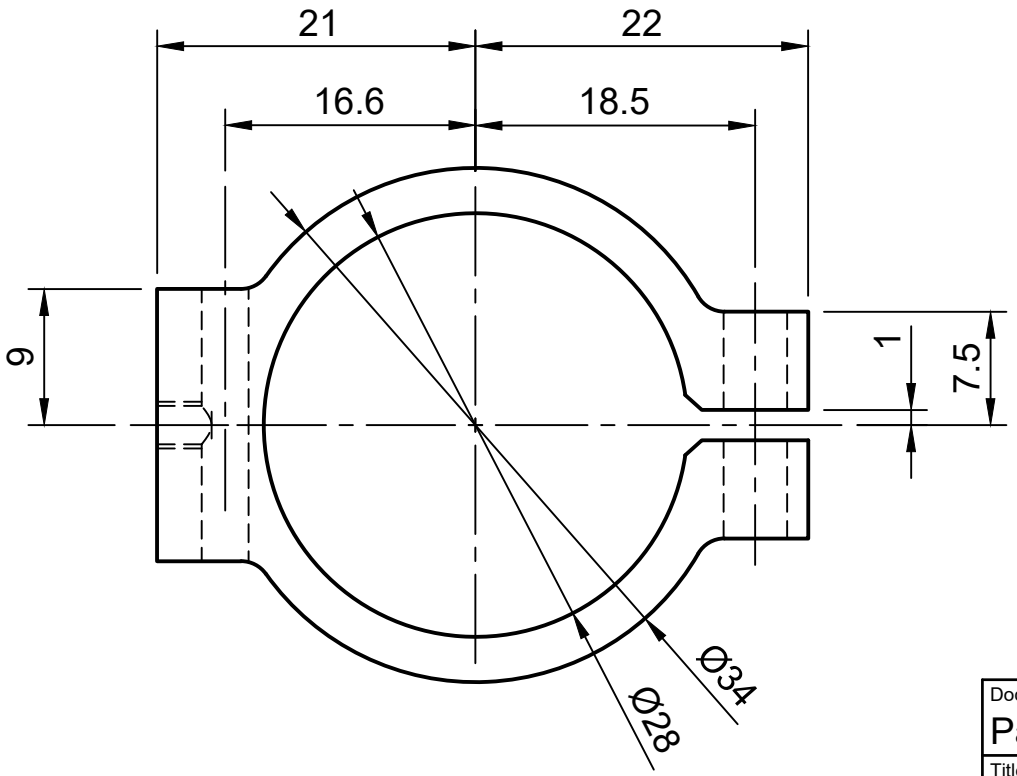

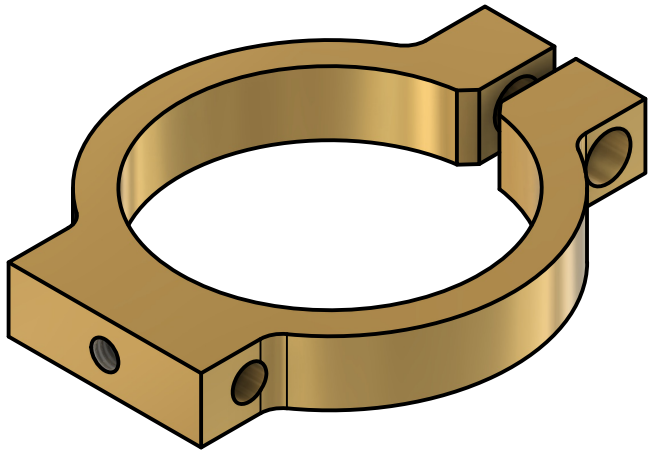

Document type: Part Drawing		Created by: Albert Curmi 29/10/2024		
Title: Brass Ring Barrel		DWG No.: 12.0		
General tolerance: ±0.1 mm	Material: Brass		Scale: 2:1	Sheet: 16/16

Appendix 4

Extruder Development 3 Engineering Drawings

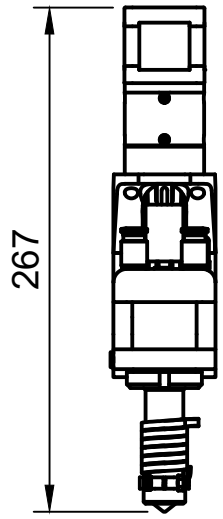

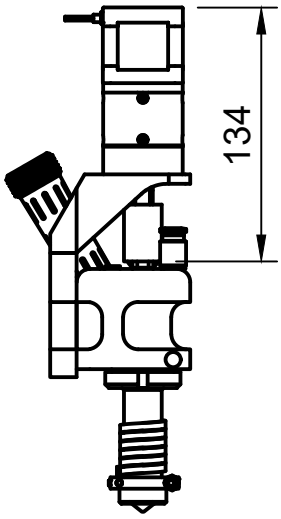

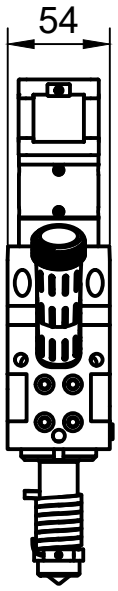

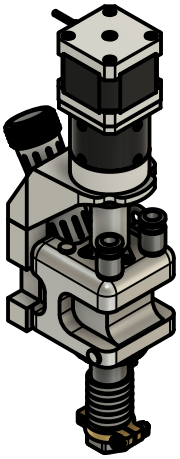

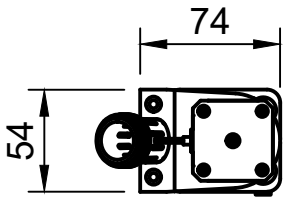

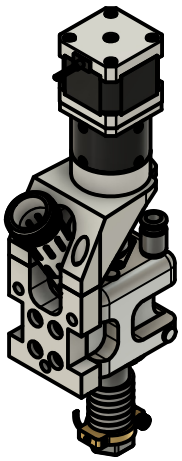

Document type Assembly Drawing		Created by Albert Curmi 29/10/2024		
Title Extruder 3 General Dimensions		DWG No. 01.0		
General tolerance ±0.1 mm	Material N/A		Scale 1:4	Sheet 1/9

(1:2)

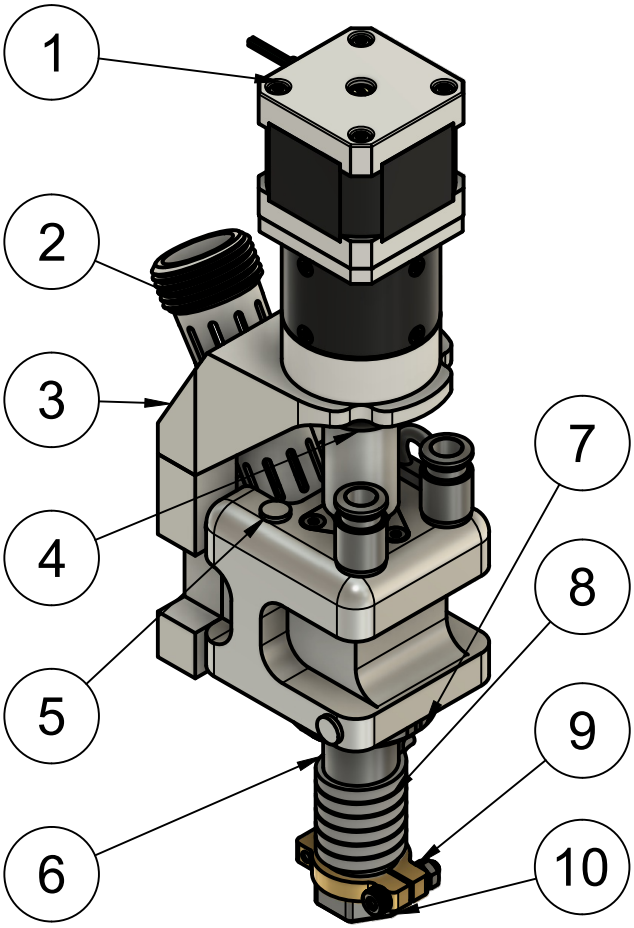

Parts List		
Item	Part Name	Material
1	17HS15-1684S-H G30 v1	N/A
2	Pellet Feeder	ABS Plastic
3	Mount CR-10	ABS Plastic
4	Drive Train	Aluminum 2014-T4
5	Feeding End	
6	Heated Barrel	H13 tool steel
7	Locking Nut	Steel
8	Coil Heater	N/A
9	Temperature Sensor	
10	Nozzle	H13 tool steel
11	Screw Assembly	

A-A (1:4)

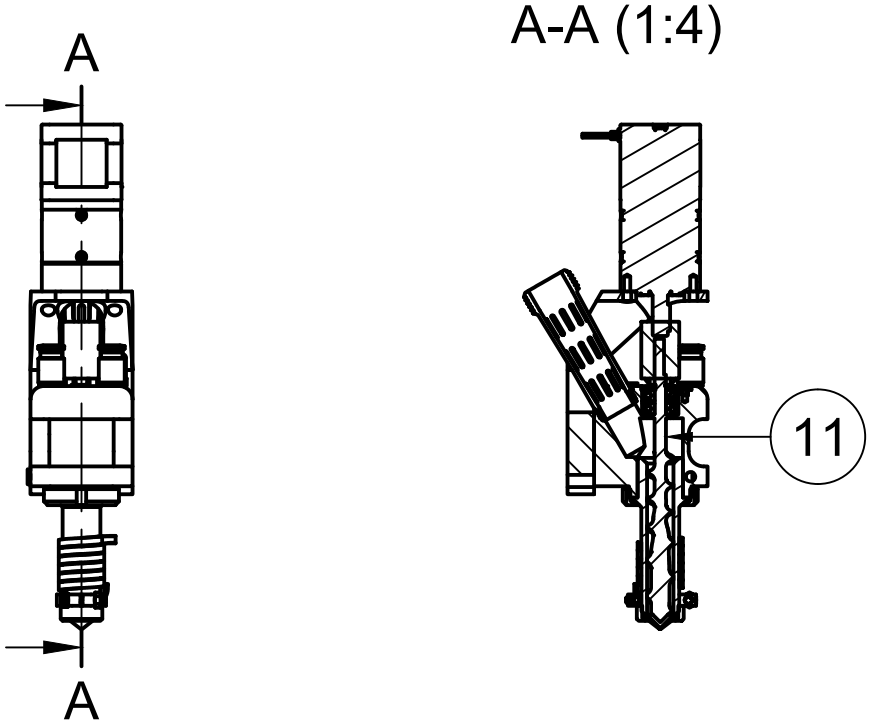

Document type Assembly Drawing		Created by Albert Curmi 29/10/2024		
Title Extruder 3 Sub-assemblies		DWG No. 01.1		
General tolerance ±0.1 mm	Material N/A		Scale 1:4	Sheet 2/9

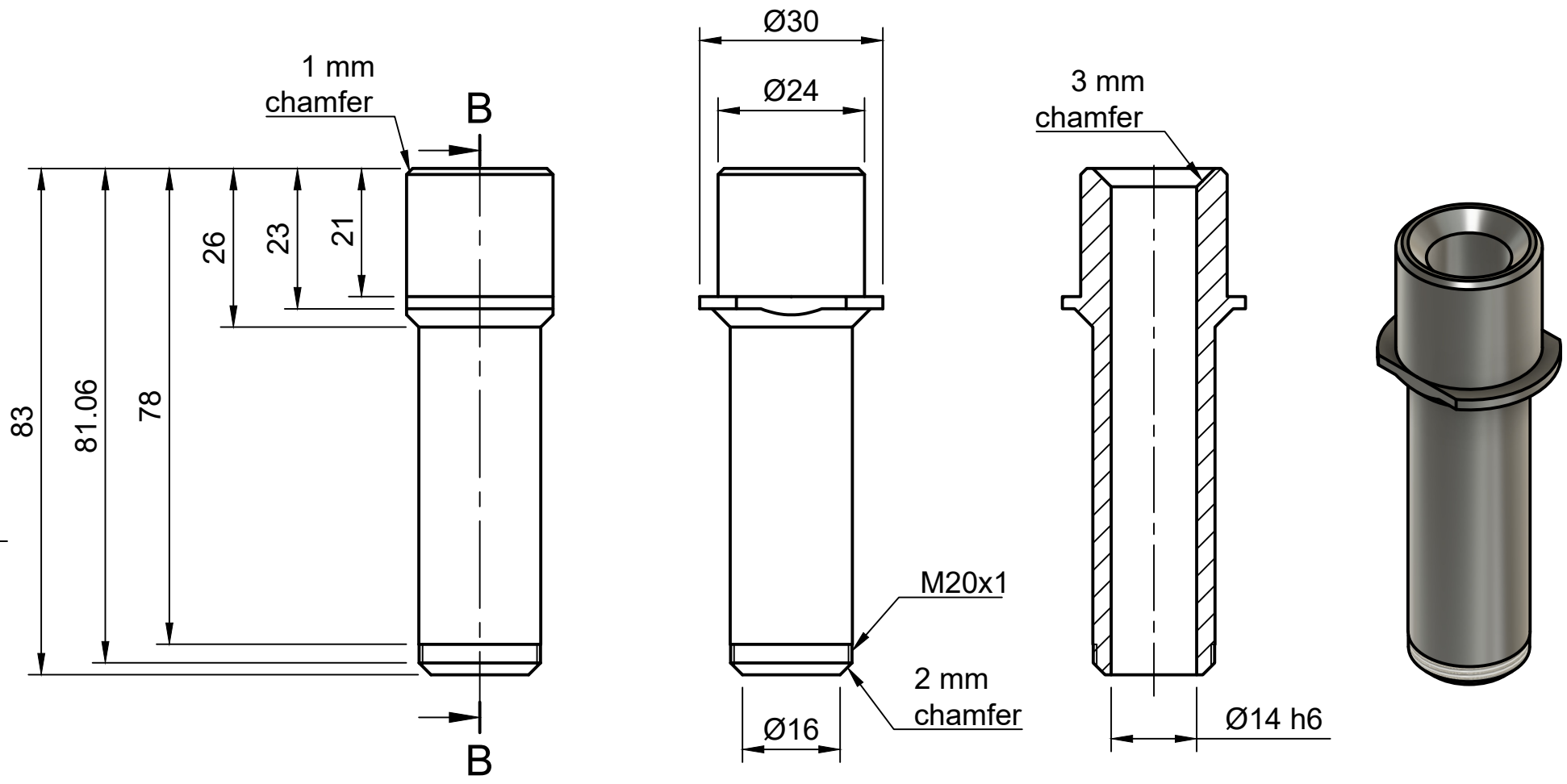

Document type: Part Drawing		Created by: Albert Curmi		29/10/2024
Title: Heated Barrel		DWG No.: 02.0		
General tolerance: ±0.1 mm	Material: H13 tool steel		Scale: 1:1	Sheet: 3/9

Parts List		
Item	Part Name	Material
1	Nozzle cap 0.4 mm	H13 tool steel
2	Nozzle Locking Nut	H13 tool steel

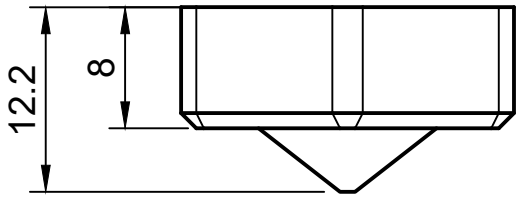

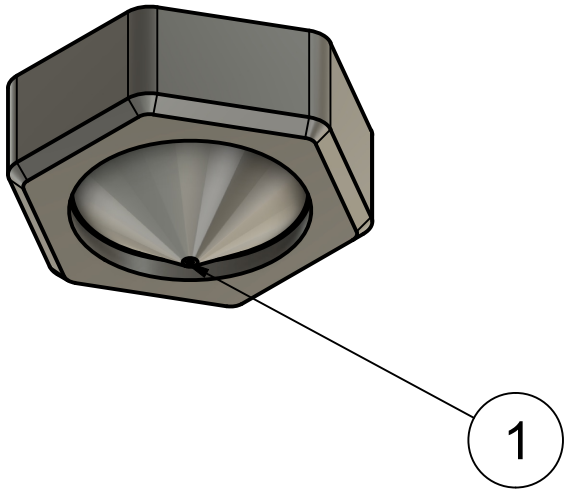

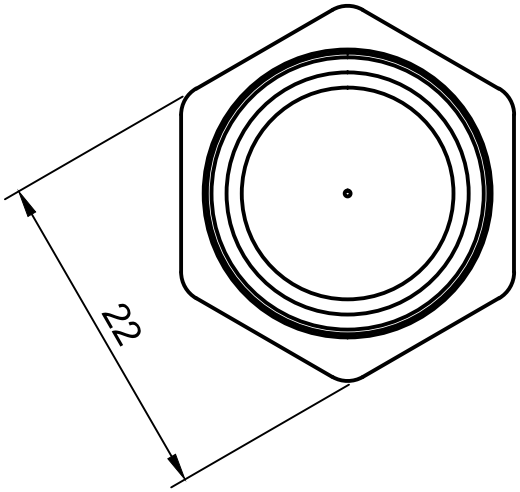

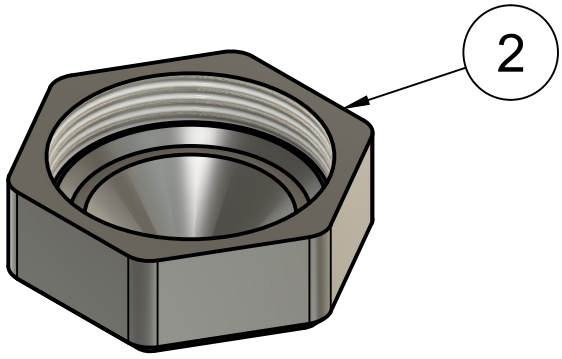

Document type: Assembly Drawing		Created by: Albert Curmi 29/10/2024		
Title: Nozzle		DWG No.: 03.0		
General tolerance: ±0.1 mm	Material: H13 tool steel		Scale: 2:1	Sheet: 4/9

D (16)

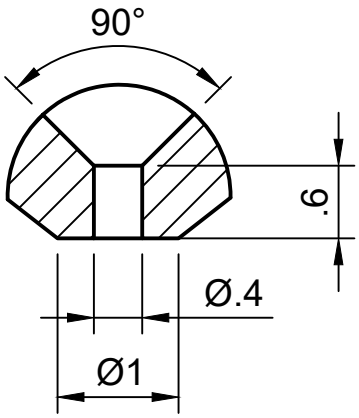

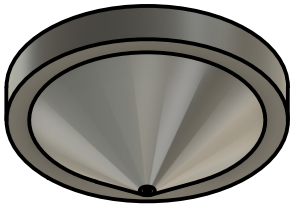

C-C (2)

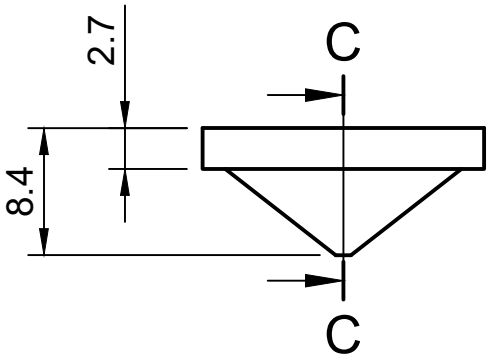

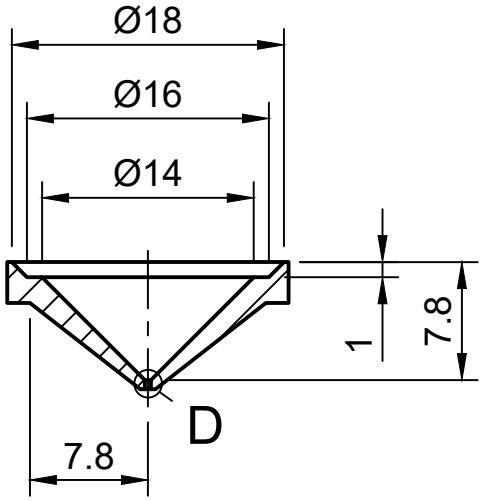

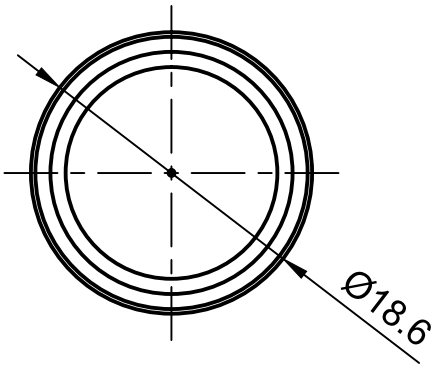

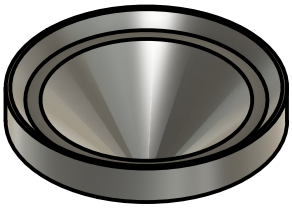

Document type: Part Drawing		Created by: Albert Curmi		29/10/2024
Title: Nozzle Cap 0.4 mm		DWG No.: 04.0		
General tolerance: ±0.1 mm	Material: H13 tool steel		Scale: 2:1	Sheet: 5/9

F (16)

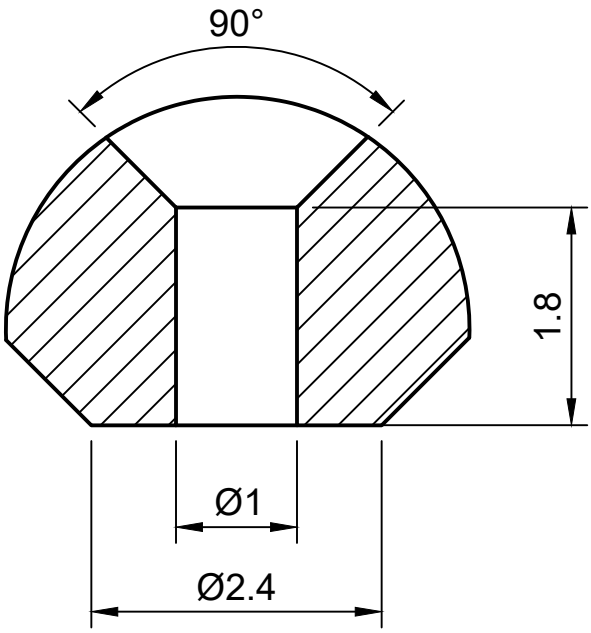

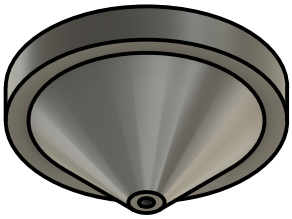

E-E (2)

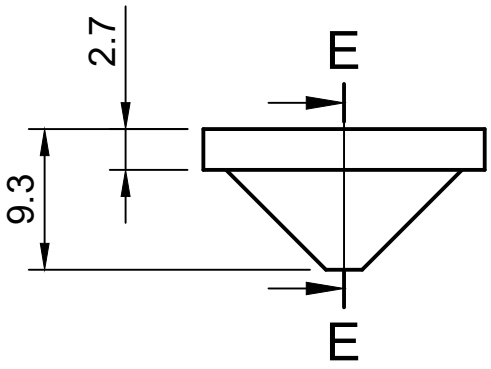

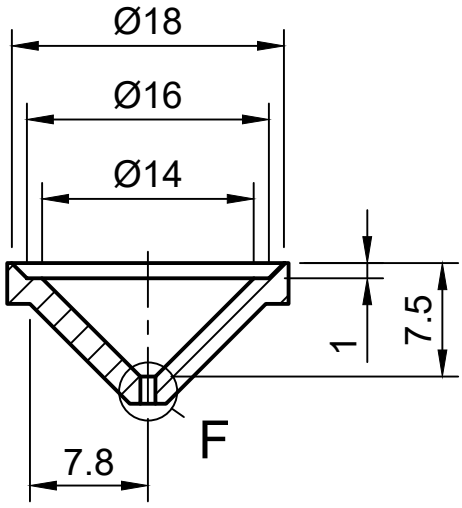

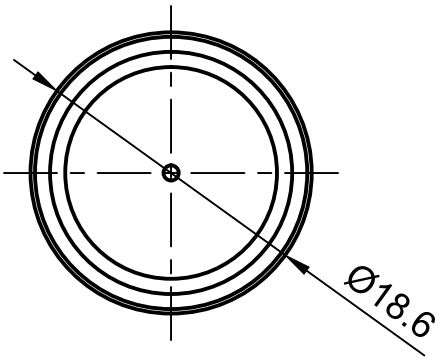

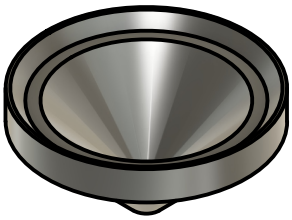

Document type Part Drawing		Created by Albert Curmi 29/10/2024		
Title Nozzle Cap 1 mm		DWG No. 05.0		
General tolerance ±0.1 mm	Material H13 tool steel		Scale 2:1	Sheet 6/9

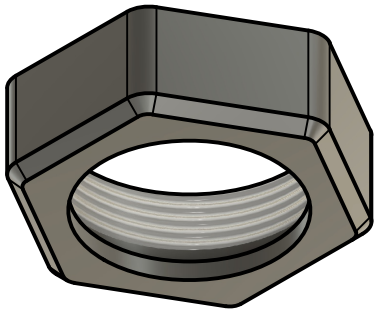

G-G (2)

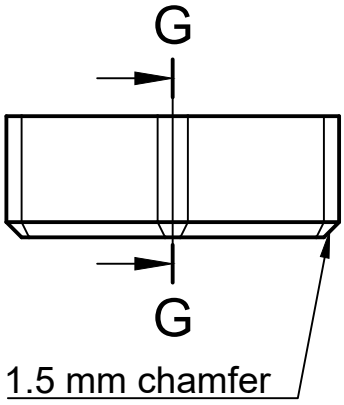

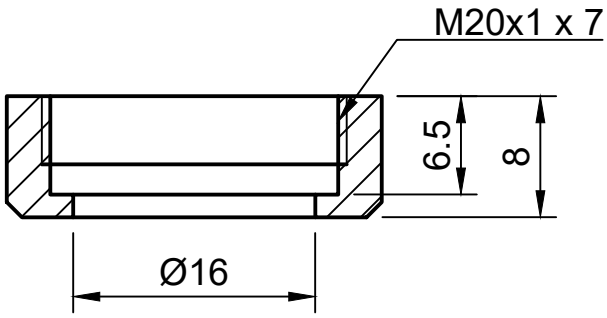

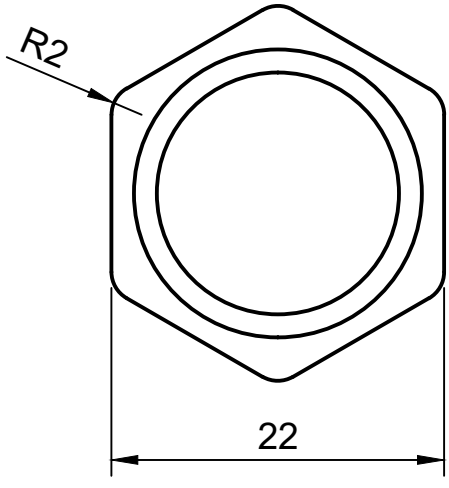

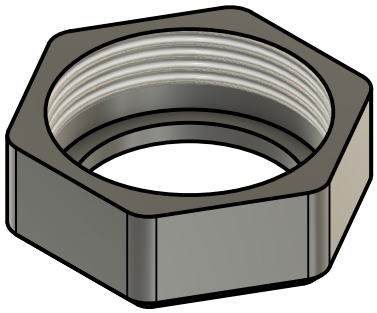

Document type: Part Drawing		Created by: Albert Curmi 29/10/2024		
Title: Nozzle Locking Nut		DWG No.: 06.0		
General tolerance: ±0.1 mm	Material: H13 tool steel		Scale: 2:1	Sheet: 7/9

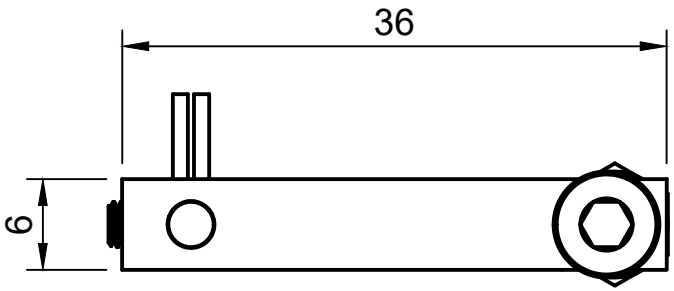

Parts List		
Item	Part Name	Material
1	PT 100	Steel
2	Temperature Sensor Block	Brass
3	M3 X 4 mm	Steel
4	M4 Nut	Steel
5	M4 X 20 mm	Steel

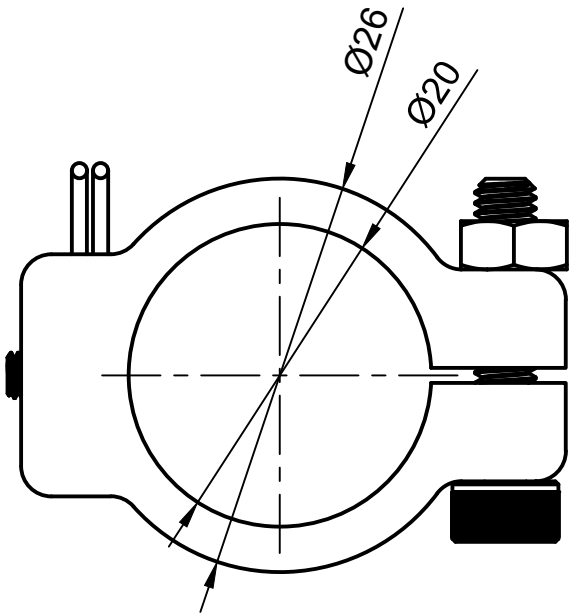

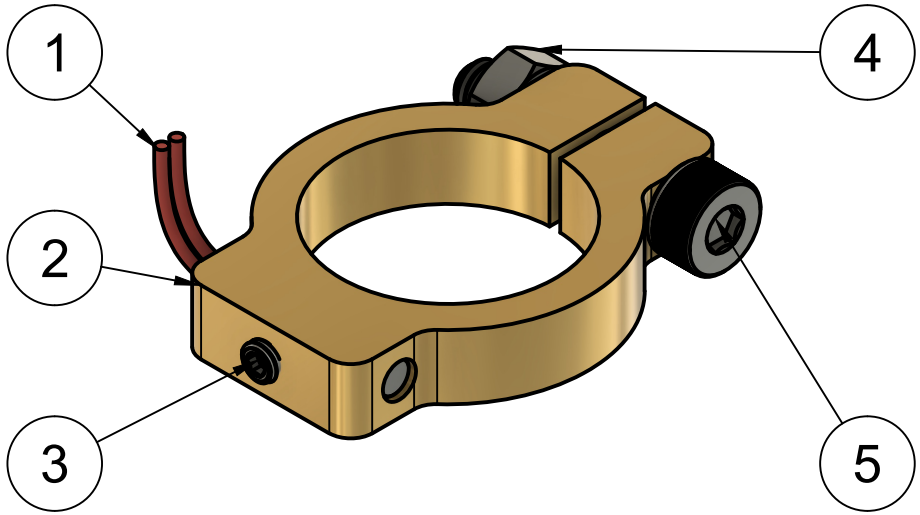

Document type: Assembly Drawing		Created by: Albert Curmi		29/10/2024
Title: Temperature Sensor		DWG No.: 07.0		
General tolerance: ±0.1 mm	Material: N/A		Scale: 2:1	Sheet: 8/9

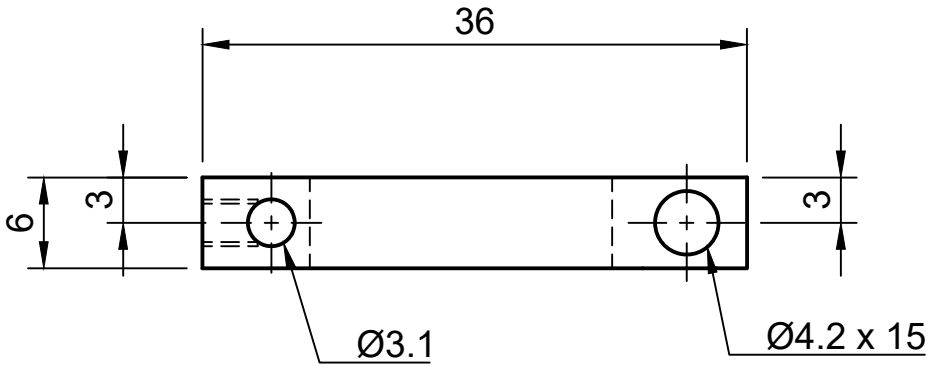

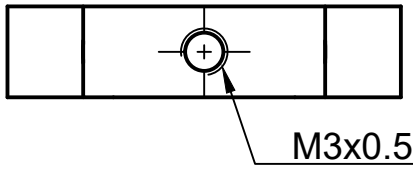

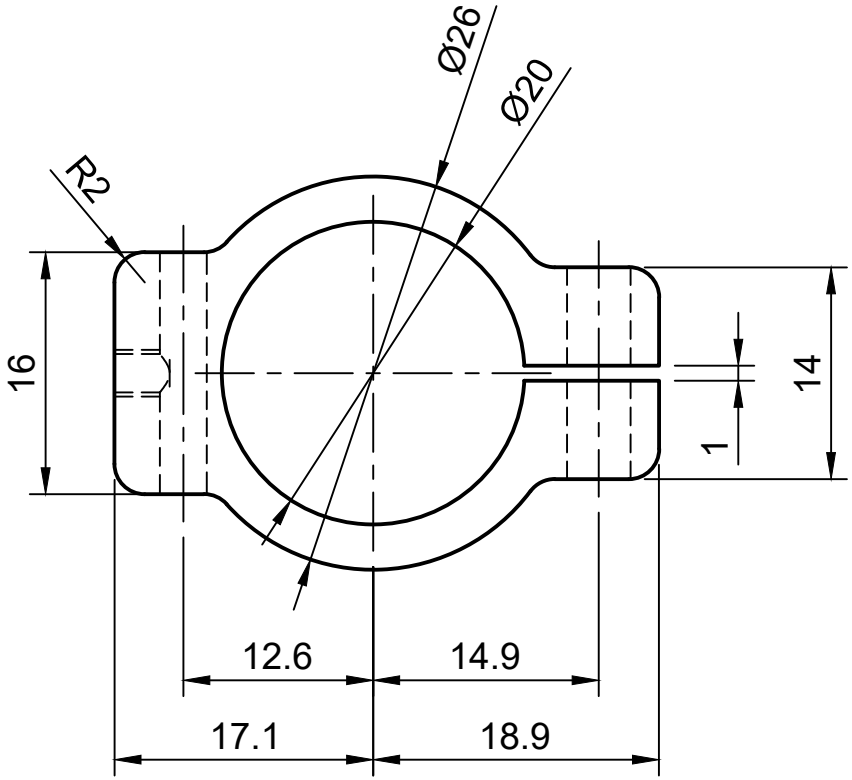

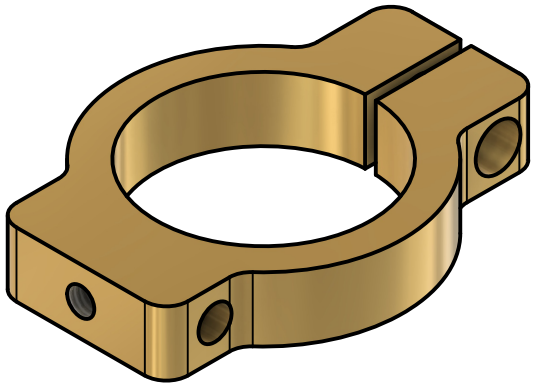

Document type: Part Drawing		Created by: Albert Curmi		29/10/2024
Title: Temperature Sensor Block		DWG No.: 08.0		
General tolerance: ±0.1 mm	Material: Brass		Scale: 2:1	Sheet: 9/9

Appendix 5

Extruder Development 4 Engineering Drawings

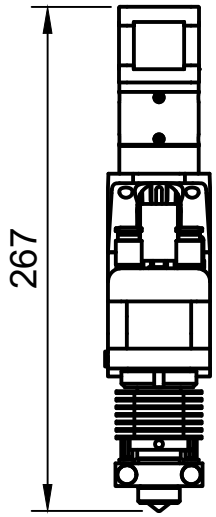

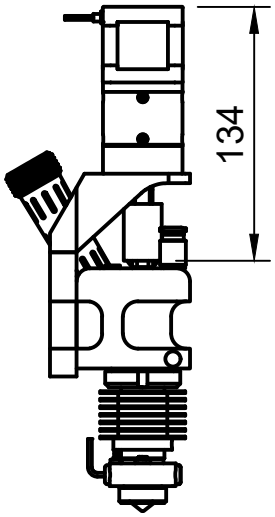

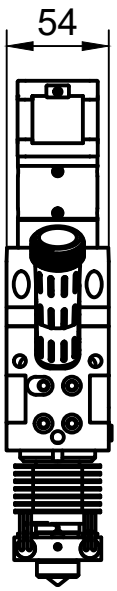

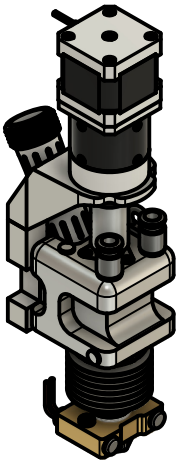

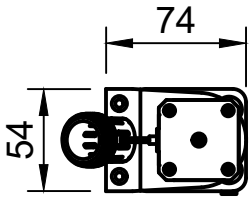

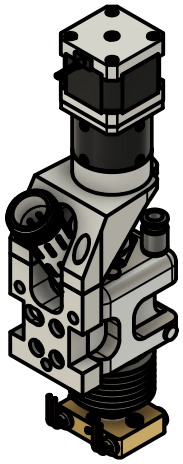

Document type: Assembly Drawing		Created by: Albert Curmi 30/10/2024		
Title: Extruder 4 General Dimensions		DWG No.: 01.0		
General tolerance: ±0.1 mm	Material: N/A		Scale: 1:4	Sheet: 1/6

(1:2)

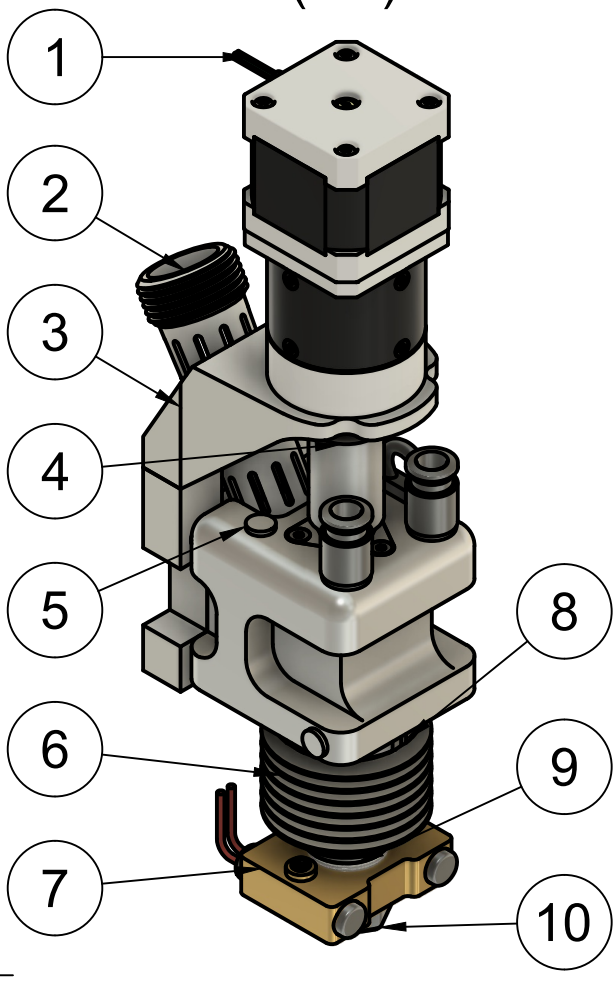

Parts List		
Item	Part Name	Material
1	17HS15-1684S-H G30	N/A
2	Pellet Feeder	ABS Plastic
3	Mount CR-10	ABS Plastic
4	Drive Train	Aluminum 2014-T4
5	Feeding End	
6	Lower Heat Exchanger	Aluminum 2014-T4
7	Threaded Heater	
8	Locking Nut	Steel
9	Heated Barrel	H13 tool steel
10	Nozzle	H13 tool steel
11	Screw Assembly	

A

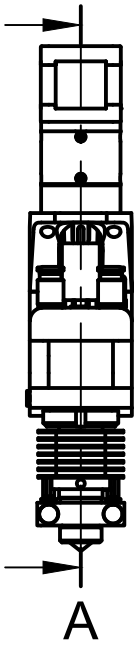

A

A-A (1:4)

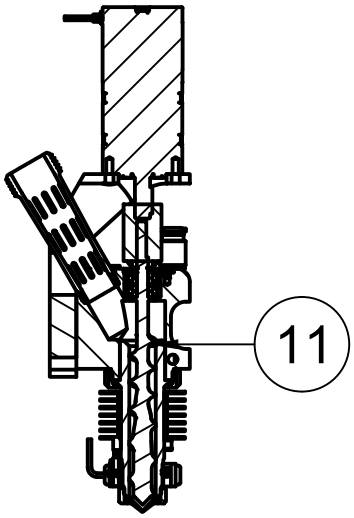

Document type Assembly Drawing		Created by Albert Curmi 30/10/2024		
Title Extruder 4 Sub-assemblies		DWG No. 01.1		
General tolerance ±0.1 mm	Material N/A		Scale 1:4	Sheet 2/6

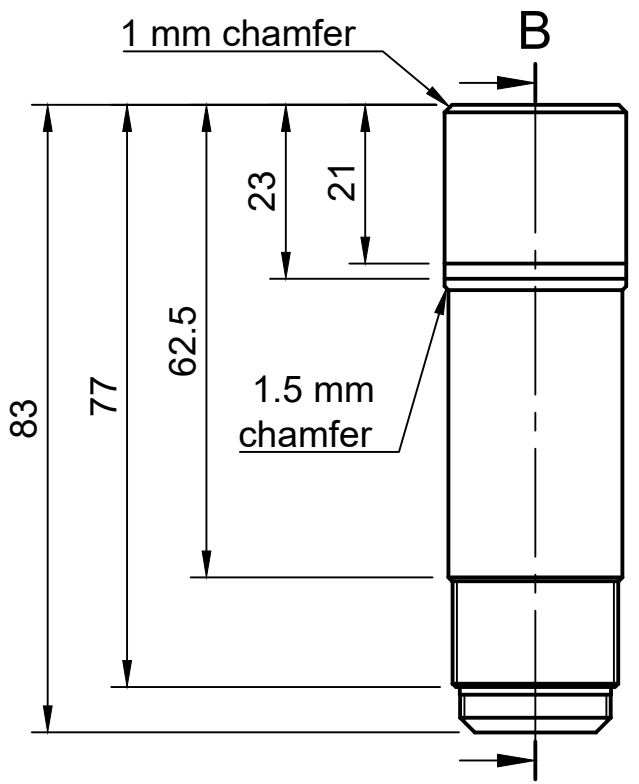

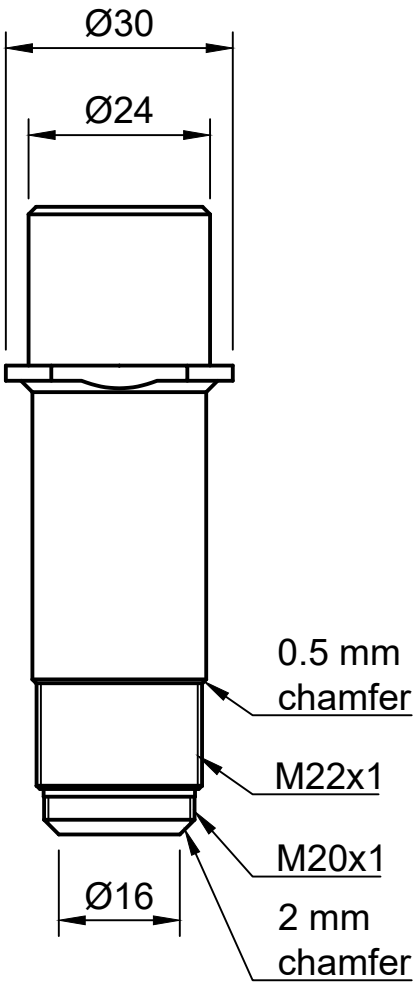

B-B (1:1)

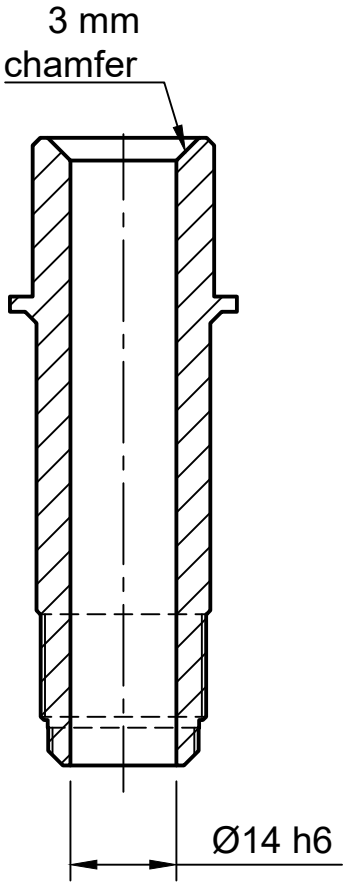

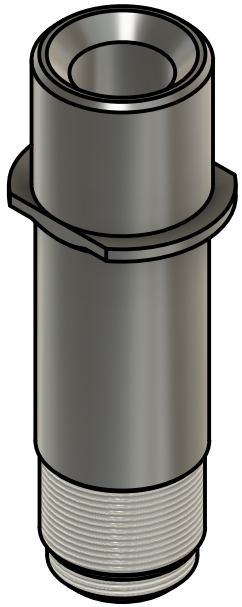

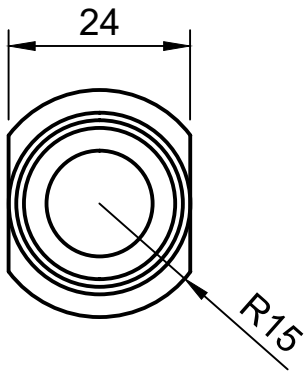

Document type: Part Drawing		Created by: Albert Curmi 30/10/2024		
Title: Heated Barrel		DWG No.: 02.0		
General tolerance: ±0.1 mm	Material: H13 tool steel		Scale: 1:1	Sheet: 3/6

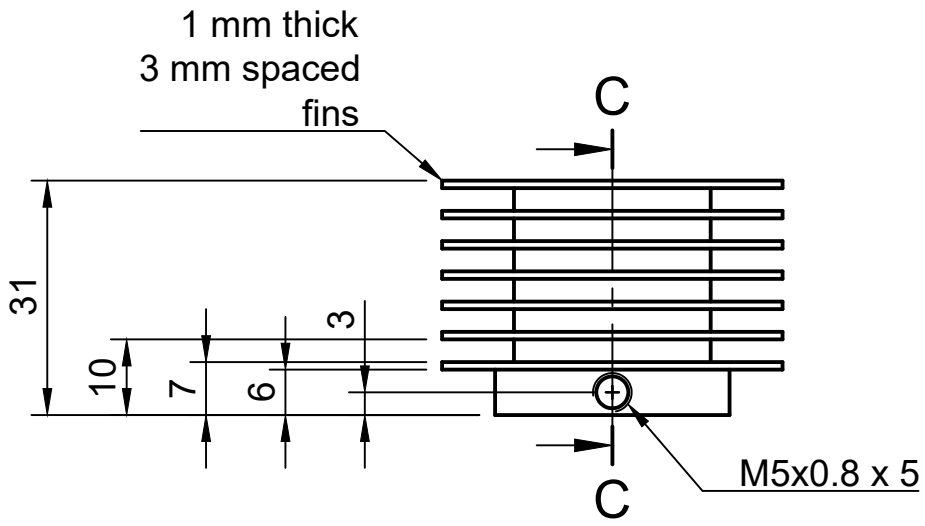

C-C (1:1)

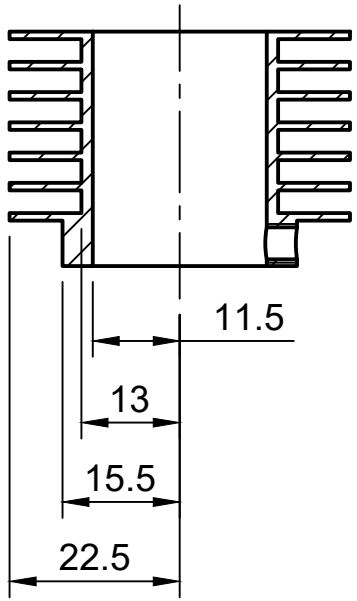

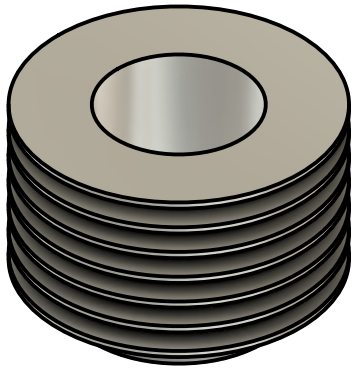

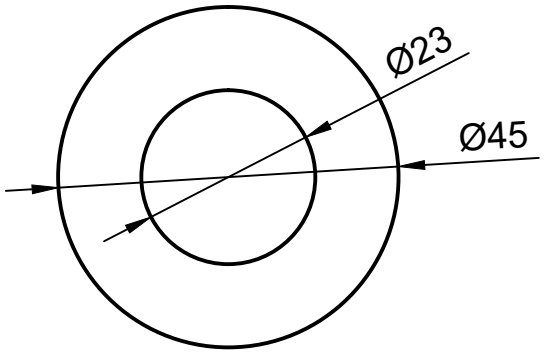

Document type: Part Drawing		Created by: Albert Curmi		30/10/2024
Title: Lower Heat Exchanger		DWG No.: 03.0		
General tolerance: ±0.1 mm	Material: Aluminum 2014-T4		Scale: 1:1	Sheet: 4/6

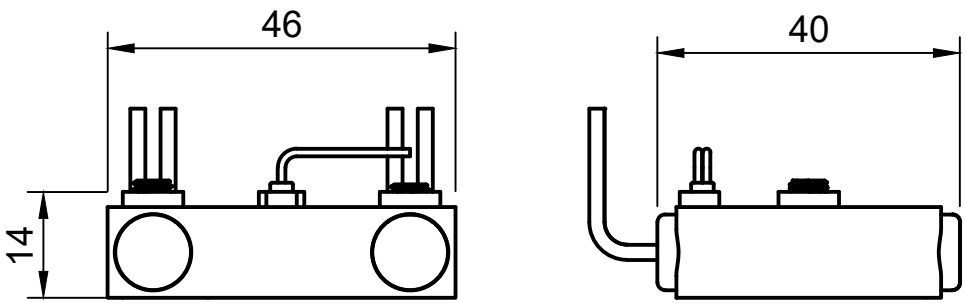

Parts List			
Item	Qty	Part Name	Material
1	1	M3 x 5 mm Set Screw	Steel
2	2	Cartridge 10 x 40 mm	Steel
3	2	M5 x 4 mm Set Screw	Steel
4	1	Thread Heater Block	Brass
5	1	PT 100	Steel

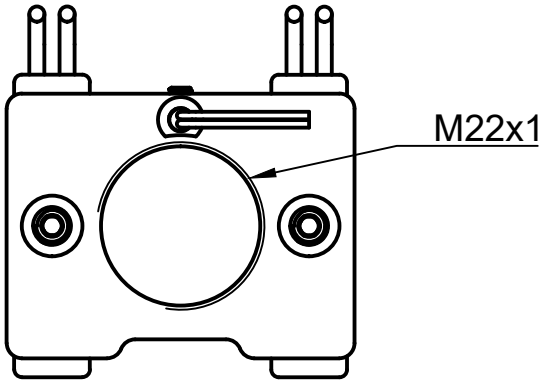

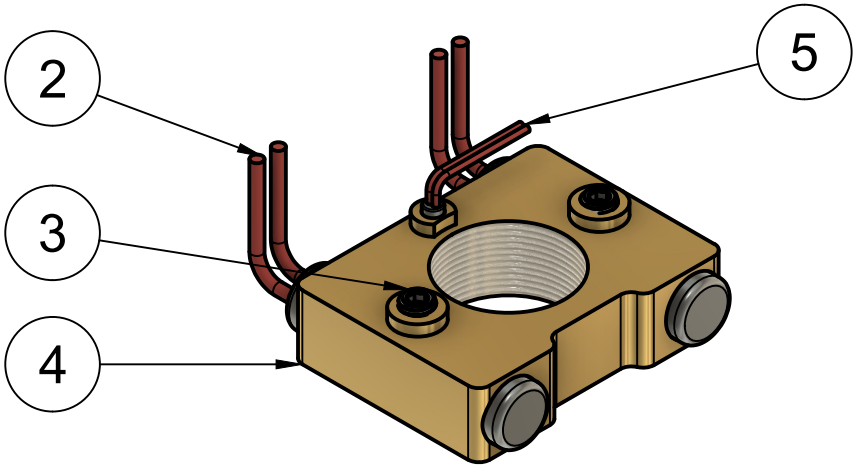

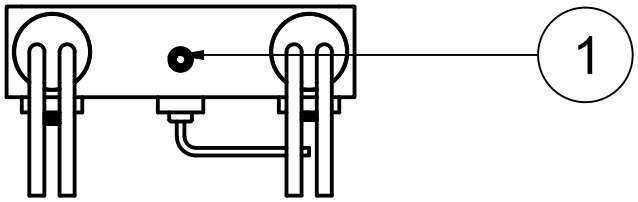

Document type: Assembly Drawing		Created by: Albert Curmi		30/10/2024
Title: Threaded Heater		DWG No.: 04.0		
General tolerance: ±0.1 mm	Material: N/A		Scale: 1:1	Sheet: 5/6

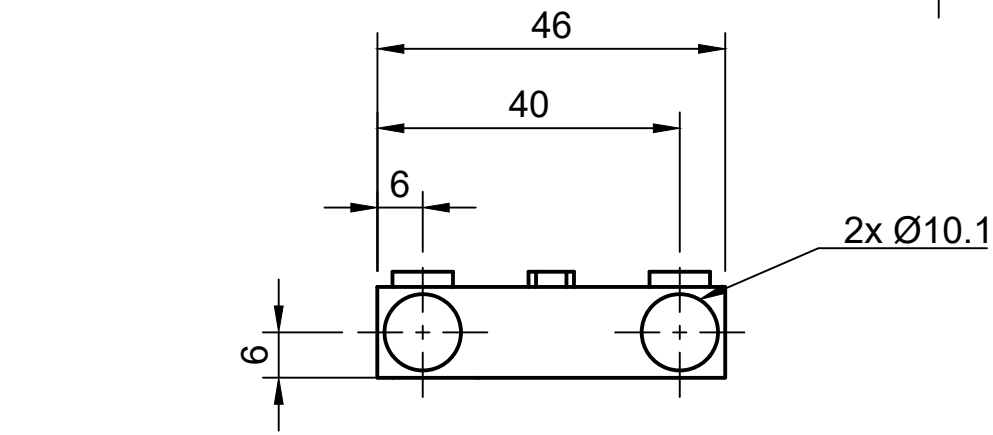

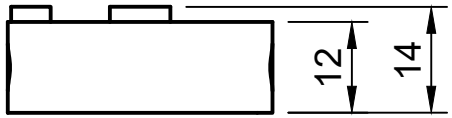

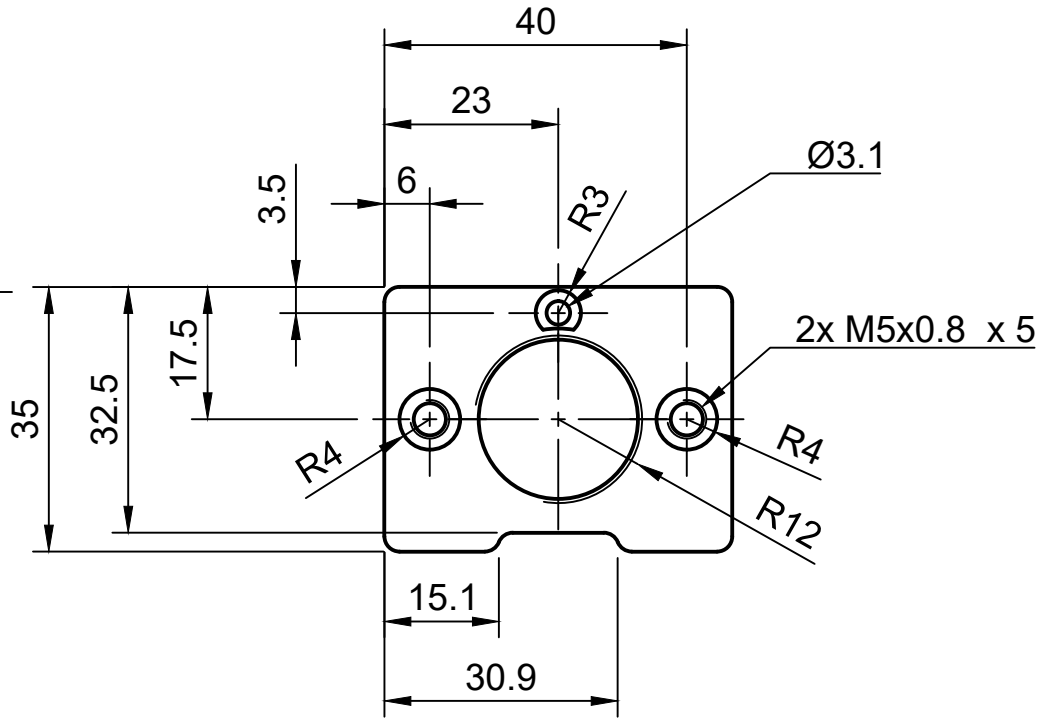

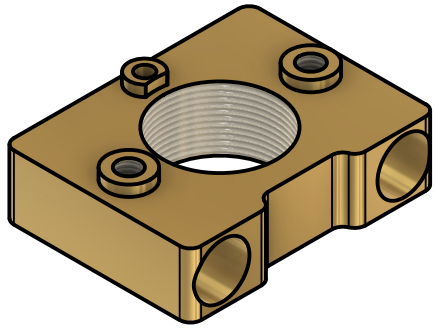

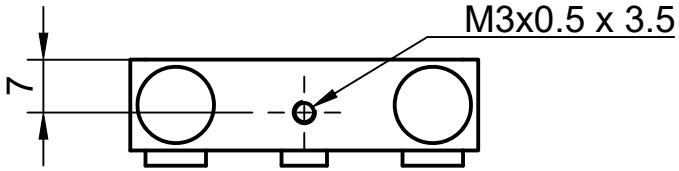

Document type: Part Drawing		Created by: Albert Curmi 30/10/2024		
Title: Threaded Heater Block		DWG No.: 05.0		
General tolerance: ±0.1 mm	Material: Brass		Scale: 1:1	Sheet: 6/6

Appendix 6

Inflatable Volume Determination Script

Volume Determination from Video

```
# import required libraries
import cv2
import numpy as np
import os
import matplotlib.pyplot as plt
import math
import csv
import time


# This code is based on 20231115 - Contourer


def imgResize(img, resize):
    scale_percent = resize  # percent of original size
    width = int(img.shape[1] * scale_percent / 100)
    height = int(img.shape[0] * scale_percent / 100)
    dim = (width, height)

    # resize image
    return cv2.resize(img, dim, interpolation=cv2.INTER_AREA)


# load the input images
baseImg = cv2.imread('start.jpg')

# Set scale
s = cv2.selectROI("Select a scale cube of 10 mm", baseImg)
mm2perpixel = 100 / (s[3] * s[2])
cv2.destroyWindow("Select a scale cube of 10 mm")
mmperpixel = 10 / ((s[3] + s[2]) / 2)
print(mm2perpixel)

f = open("scale.txt", "w")
f.write(str(mm2perpixel) + " mm2 / pixel2\n" + str(s[2]) + " pixel / 10
mm\n" + str(s[3]) + " pixel / 10 mm")
f.close()

# Crop image to actual usable space
baseImgRS = imgResize(baseImg, 25)
# Select ROI
r = cv2.selectROI("Select the Area", baseImgRS)
# Crop image
crpdBaseImg = baseImg[int(r[1] * 4):int((r[1] + r[3]) * 4), int(r[0] *
4):int((r[0] + r[2]) * 4)]
cv2.destroyWindow("Select the Area")
# Select the region of interest
```

```
roi = cv2.selectROI("Select the Region of Interest",
imgResize(crpdBaseImg, 25))
cv2.destroyWindow("Select the Region of Interest")

# Removing unwanted regions
removeRoi = cv2.selectROI("Select region for removal",
imgResize(crpdBaseImg, 25))
cv2.destroyWindow("Select region for removal")

path = "Images/"
img_list = os.listdir(path)
contourList = []
areaList = []
radiusList = []
lengthList = []
volumeList = []

imgStep = 1

for imgNow in range(1, len(img_list), imgStep):
    img2 = cv2.imread('Images/' + img_list[imgNow])
    crpdImg = img2[int(r[1] * 4):int((r[1] + r[3]) * 4), int(r[0] *
4):int((r[0] + r[2]) * 4)]

    # Center point of ROI
    cROI = [int((roi[0] * 4) + ((roi[2] * 4) / 2)), int((roi[1] * 4) +
((roi[3] * 4) / 2))]

    # Subtract from base images
    subtracted = cv2.subtract(crpdBaseImg, crpdImg)
    # Convert to greyscale
    greySubtracted = cv2.cvtColor(subtracted, cv2.COLOR_BGR2GRAY)
    # Set threshold for a clearer results
    thresh = cv2.threshold(greySubtracted, 5, 255,
cv2.THRESH_BINARY)[1]
    # Create a kernel (i.e. a small matrix)
    kernel = np.ones((5, 5), np.uint8)
    # Use the kernel to perform morphological opening
    thresh = cv2.morphologyEx(thresh, cv2.MORPH_OPEN, kernel)
    #cv2.imshow('Threshold', imgResize(thresh, 25))

    # Black out undesired region
    thresh = cv2.rectangle(
        thresh,
        ((removeRoi[0]*4), (removeRoi[1]*4)),
        ((removeRoi[0]*4) + (removeRoi[2]*4), (removeRoi[1]*4) +
(removeRoi[3]*4)),
        (0, 0, 0),
```

```
        -1
    )

    contours, hierarchy = cv2.findContours(thresh, cv2.RETR_TREE,
cv2.CHAIN_APPROX_SIMPLE)
    im2 = cv2.drawContours(thresh, contours, -1, (255, 255, 0), 8)
    contours, hierarchy = cv2.findContours(im2, cv2.RETR_TREE,
cv2.CHAIN_APPROX_SIMPLE)

    # find the biggest contour (c) by the area
    contours = sorted(contours, key=cv2.contourArea)[-3:]
    dis = 100000
    selectCon = []
    for c in contours[-2:]:
        x, y, w, h = cv2.boundingRect(c)
        x0 = cROI[0] * 4
        y0 = cROI[1] * 4
        x1 = (x + (w/2)) * 4
        y1 = (y + (h/2)) * 4

        if math.dist([x0,y0], [x1,y1]) < dis:
            dis = math.dist([x0,y0], [x1,y1])
            selectCon = c

    selectCon = contours[-1]

    x, y, w, h = cv2.boundingRect(selectCon)

    # draw the biggest contour (c) in green
    image_rgb = cv2.cvtColor(im2, cv2.COLOR_GRAY2RGB)
    im = cv2.rectangle(image_rgb, (x, y), (x + w, y + h), (0, 255, 0),
10)

    # Calculating Area
    contourList.append(selectCon)
    areaList.append(cv2.contourArea(selectCon) * mm2perpixel)

    # Finding Oval
    ellipse = cv2.fitEllipse(selectCon)
    radius = (ellipse[1][0] / 2) * mmperpixel
    length = (ellipse[1][1]) * mmperpixel
    volume = (math.pi * radius * radius * (length - (2 * radius))) +
((4 * math.pi * radius * radius * radius) / 3)
    radiusList.append(radius)
    lengthList.append(length)
    volumeList.append(volume)

# Saving Data
```

```
with open('Area.csv', 'w', newline='') as f:
    writer = csv.writer(f)
    writer.writerows(
        zip(np.multiply(np.array(range(1, len(img_list),imgStep)),
1/30),
            areaList,
            radiusList,
            lengthList,
            volumeList)
    )

cv2.waitKey(0)
cv2.destroyAllWindows()
```

Data Processing and Visualisation

```
# import required libraries
import matplotlib.pyplot as plt
import pandas as pd
import numpy as np
import math
from sklearn.linear_model import LinearRegression
from sklearn.preprocessing import PolynomialFeatures
import peakutils


# Hex Point to Point / Length
# Large - 14.198 mm  / 54 mm
# Medium - 11.888 mm / 53 mm
# Small - 9.579 mm   / 52 mm

# Square Side to Side / Length
# Large - 12 mm      / 54 mm
# Medium - 10 mm     / 53 mm
# Small - 8 mm       / 52 mm

def fitter(x, y, degree=1):
    poly = PolynomialFeatures(degree=degree, include_bias=False)
    poly_features = poly.fit_transform(x.reshape(-1, 1))
    poly_reg_model = LinearRegression()
    model = poly_reg_model.fit(poly_features, y)
    y_predicted = poly_reg_model.predict(poly_features)

    return model, y_predicted


df = pd.read_csv('Area.csv', header=None)
df.columns = ["Frames", "Area", "Radius", "Length", "Volume"]

fig, ax = plt.subplots(nrows=3, ncols=2, figsize=(10, 10))

# Radius with Time
ax[1, 0].plot(df["Frames"], df["Radius"], label="Original")
ax[1, 0].set_xlabel("Time (s)")
ax[1, 0].set_ylabel("Radius (mm)")

# Trying to filter out the spikes and inconsistencies
yF = df["Radius"].rolling(10).median()
ax[1, 0].plot(df["Frames"], yF, label="Filtered")

x = np.array(df["Frames"])[10:-10]
y = np.nan_to_num(np.array(yF))[10:-10]
model, radiusFit = fitter(x=x, y=y, degree=1)
```

```
ax[1, 0].plot(x, radiusFit, c='r', label="Fitted")

# Length with Time
length = np.add(np.array(df["Length"]), -np.multiply(2, df["Radius"]))
ax[1, 1].plot(df["Frames"], length, label="Original")
ax[1, 1].set_xlabel("Time (s)")
ax[1, 1].set_ylabel("Length (mm)")

# Trying to filter out the spikes and inconsistencies
yF = length.rolling(10).median()
ax[1, 1].plot(df["Frames"], yF, label="Filtered")

x = np.array(df["Frames"])[10:-10]
y = np.nan_to_num(np.array(yF))[10:-10]
model, LengthFit = fitter(x=x, y=y, degree=2)
ax[1, 1].plot(x, LengthFit, color='r', label="Fitted")

# Volume with Time
ax[0, 1].plot(df["Frames"], df["Volume"], label="Original")
ax[0, 1].set_xlabel("Time (s)")
ax[0, 1].set_ylabel("Volume (mm³)")

# Trying to filter out the spikes and inconsistencies
yF = df["Volume"].rolling(10).median()
ax[0, 1].plot(df["Frames"], yF, label="Filtered")

x = np.array(df["Frames"])[10:-10]
y = np.nan_to_num(np.array(yF))[10:-10]
model, yFit = fitter(x=x, y=y, degree=1)
literFlow = round(model.coef_[0] * 60 / 1000000, 2)
print("Volume increase of: " + str(literFlow) + " l/min")
ax[0, 1].plot(x, yFit, c='r', label="Fitted - " + str(round(literFlow,
2)) + " l/min")

# Reprocessing the data using the corrected radius
x = np.array(df["Frames"])[10:-10]
r = radiusFit
l = LengthFit  # Length is already reduced by radius

r2 = []
r2.append(r[0])
Rv = 5 / literFlow  # Experiment was set using a flow rate of 5 l/min
# Rv = Rv * 1.07

for i in range(0, len(x) - 1):
    # Simplified dv/dt method
    # r22 = (Rv * (r[i]/r2[-1]) * (r[i+1] - r[i])) + r2[-1]
```

```
    # Complete dv/dt method but with dh/dt abs to remove numerical
error
    dhdt = abs((l[i + 1] - l[i]) / (x[i + 1] - x[i]))
    r22 = (((Rv * r[i] * (r[i + 1] - r[i]) * (dhdt + (2 * r[i]))) /
            (r2[-1] * (dhdt + (2 * r2[-1])))) +
           r2[-1]
           )

    #dr1 = r[i + 1] - r[1]
    #dh1 = l[i + 1] - l[1]
    #B = (2 * r[i] * l[i] * dr1) + (r[i] * r[i] * dh1) + (4 * r[i] *
r[i] * dr1)
    #r22 = r2[i] + (((Rv * B) - (dh1 * r2[i] * r2[i]))/((2 * r2[i] *
l[i]) + (4 * r2[i] * r2[i])))
    r2.append(r22)

h = np.add(l, np.multiply(r, 2))
l2 = np.add(h, - np.multiply(r2, 2))
new_volume = np.add(
    np.multiply(np.multiply(r2, r2), l2) * math.pi,
    np.multiply(np.multiply(r2, r2), r2) * ((4 * math.pi) / 3)
)

x = np.array(df["Frames"])[10:-10]
y = np.nan_to_num(np.array(new_volume))
model, y_predicted = fitter(x=x, y=y, degree=1)
newLiterFlow = round(model.coef_[0] * 60 / 1000000, 2)
print("New volume increase of: " + str(newLiterFlow) + " l/min")

ax[0, 1].plot(x, new_volume, label="Corrected - " +
str(round(newLiterFlow, 2)) + " l/min", c='k')
ax[0, 1].legend()

# Corrected Radius
ax[1, 0].plot(x, r2, c='k', label="Corrected")
ax[1, 0].legend()

# Corrected Length
ax[1, 1].plot(x, l2, c='k', label="Corrected")
ax[1, 1].legend()

# Area with Time
ax[0, 0].plot(df["Frames"], df["Area"], label="Contour")
ax[0, 0].set_xlabel("Time (s)")
ax[0, 0].set_ylabel("Area (mm²)")

# Original slot area
```

```
areaSlot = np.add(np.multiply(np.multiply(r, r), math.pi),
np.multiply(np.add(r, r), l))
ax[0, 0].plot(x, areaSlot, label="Stadium Original")

# Corrected slot area
areaSlot = np.add(np.multiply(np.multiply(r2, r2), math.pi),
np.multiply(np.add(r2, r2), l2))
ax[0, 0].plot(x, areaSlot, label="Stadium Corrected")

ax[0, 0].legend()

# Perimetric Strain with Time
perimeter = np.multiply(np.array(df["Radius"]), 2 * math.pi)
perimeter0 = 2 * math.pi * 4
perimtericStrain = perimeter - perimeter0
perimtericStrain = np.multiply(perimtericStrain, 100 / perimeter0)
ax[2, 0].plot(df["Frames"], perimtericStrain, label="Original")
ax[2, 0].set_xlabel("Time (s)")
ax[2, 0].set_ylabel("Perimetric Strain (%)")

x = np.array(df["Frames"][10:-10])
y = perimtericStrain[10:-10]
model, y_predicted = fitter(x=x, y=y, degree=1)
ax[2, 0].plot(x, y_predicted, label="Original Fit - " +
str(round(model.coef_[0], 2)) + " /s")

# Corrected Perimetric Strain with Time
x = np.array(df["Frames"][10:-10])
perimeter = np.multiply(r2, 2 * math.pi)
perimeter0 = 2 * math.pi * 4
perimtericStrain = perimeter - perimeter0
perimtericStrain = np.multiply(perimtericStrain, 100 / perimeter0)
y = perimtericStrain

model, y_predicted = fitter(x=x, y=y, degree=1)
ax[2, 0].plot(x, y, color='k', label="Corrected - " +
str(round(model.coef_[0], 2)) + " /s")
ax[2, 0].legend()

# Longitudinal Strain with Time
longitude = np.add(df["Length"], - np.multiply(df["Radius"], 2))
longitude0 = 52 - 10
longitudeStrainT = longitude - longitude0
longitudeStrain = np.multiply(longitudeStrainT, 100 / longitude0)
ax[2, 1].plot(df["Frames"], longitudeStrain, label="Original")
ax[2, 1].set_xlabel("Time (s)")
ax[2, 1].set_ylabel("Longitudinal Strain (%)")
```

```
x = np.array(df["Frames"][10:-10])
y = longitudeStrain[10:-10]
model, y_predicted = fitter(x=x, y=y, degree=2)
ax[2, 1].plot(x, y_predicted,
              label="Original Fit - " + str(round(model.coef_[0], 2)) +
", " + str(round(model.coef_[1], 2)))

longitude = l2
longitude0 = 52 - 10
longitudeStrainT = longitude - longitude0
longitudeStrain = np.multiply(longitudeStrainT, 100 / longitude0)
model, yFit = fitter(x=x, y=longitudeStrain, degree=2)
ax[2, 1].plot(x, longitudeStrain, color='k',
              label="Corrected - " + str(round(model.coef_[0], 2)) + ",
" + str(round(model.coef_[1], 2))
              )
ax[2, 1].legend()

plt.tight_layout()
plt.savefig("Out/Results.png")
plt.show()
plt.close()
```

Appendix 7

Tensile statistical analysis

Analysis of possibility of cross-linking

X-ray diffraction (XRD) crystallinity analysis

Statistical Analysis of Results

The tensile testing statistical analysis results are shown in Table 1. The Shapiro-Wilk normality tested indicated that all groups are normally distributed except for stress at yield, VESTAKEEP L4000G, 400°C group and modulus of elasticity, VESTAKEEP L2000G, 420°C group. Given that only these two instances broke the normality assumption, the one-way ANOVA test was deemed sufficient for this case. The test confirmed the hypothesis that not all means were statistically different but did not define which specifically. The Tukey post-hoc analysis produced this result, where those means with a significance lower the 0.05 are deemed statistically significant differences with a 95% confidence.

Table 1 – Tensile testing Tukey analysis with underline and red results signifying a 95% confidence, statistically significant difference in means.

Stress at Yield										
		L2000G			*L3300G*			*L4000G*		
		380	*400*	*420*	*380*	*400*	*420*	*380*	*400*	*420*
L2000G	*380*									
	400	1.000								
	420	1.000	1.000							
L3300G	*380*	0.005	0.009	0.005						
	400	0.000	0.001	0.000	0.998					
	420	0.005	0.010	0.005	1.000	0.998				
L4000G	*380*	0.009	0.018	0.009	1.000	0.988	1.000			
	400	0.000	0.000	0.000	0.227	0.649	0.222	0.142		
	420	0.000	0.000	0.000	0.379	0.824	0.372	0.255	1.000	
Modulus of Elasticity										
L2000G	*380*									
	400	0.015								
	420	0.063	1.000							
L3300G	*380*	0.005	1.000	0.991						
	400	0.056	1.000	1.000	0.993					
	420	0.027	1.000	1.000	1.000	1.000				
L4000G	*380*	0.563	0.732	0.957	0.487	0.946	0.842			
	400	0.311	0.924	0.997	0.752	0.996	0.971	1.000		
	420	0.986	0.169	0.433	0.073	0.405	0.251	0.984	0.886	
Strain at Break										
L2000G	*380*									
	400	0.987								
	420	0.923	1.000							

	380	0.280	0.033	0.013					
L3300G	*400*	0.036	0.002	0.001	0.990				
	420	0.157	0.015	0.005	1.000	0.999			
	380	0.113	0.009	0.003	1.000	1.000	1.000		
L4000G	*400*	0.000	0.000	0.000	0.002	0.029	0.005	0.008	
	420	0.000	0.000	0.000	0.123	0.589	0.227	0.300	0.836

The compression shear testing results were also analysed, with the results listed in Table 2. The Shapiro-Wilk normality test indicated that all groups were normally distributed and therefore the one-way ANOVA test qualified completely. As in the case of the tensile test results, the Tukey post-hoc for the CST results are presented with a 95% confidence.

Table 2 - Compression shear testing, ultimate shear strength Tukey with underline and red results signifying a 95% confidence, statistically significant difference in means.

		L2000G			*L3300G*			*L4000G*		
		380	*400*	*420*	*380*	*400*	*420*	*380*	*400*	*420*
	380									
L2000G	*400*	0.014								
	420	0.000	0.000							
	380	0.052	1.000	0.000						
L3300G	*400*	0.000	0.092	0.451	0.026					
	420	0.000	0.000	0.944	0.000	0.040				
	380	0.001	0.996	0.003	0.911	0.413	0.000			
L4000G	*400*	0.000	0.820	0.021	0.495	0.859	0.001	0.998		
	420	0.000	0.000	0.573	0.000	0.006	0.998	0.000	0.000	

Investigating Possibility of Crosslinking During 3D Printing

The increase in melt temperature recorded by differential scanning calorimetry (DSC) results, shown in Figure 8.26 (b) of the main text can be caused by a cross-linking event [1] or by a change in crystalline morphology [2]. To narrow down the cause behind the increase in melting temperature, a Fourier transform infrared spectroscopy (FTIR) using attenuated total reflection (ATR) test was conducted. FTIR ATR was conducted on the compression shear testing (CST) specimen fracture surface. The same CST specimens used with the DSC analysis were sampled for the FTIR ATR test. The purpose of this test was to evaluate the presence or increase of C=O and C-O-C bonds, which are caused by oxidative crosslinking [3]. FTIR ATR analysis was carried out on an IRAffinity-1, by Shimadzu (Kyoto, Japan), set in transmittance measurement mode with 20 scans taken per sample at a resolution of 4 cm-1. Three repeats were conducted for each test. FTIR ATR was also conducted on PEEK granulates of the 3 grades for comparison. All the results were subsequently compared with emphasis on the 1100 cm-1 and 1730 cm-1 wavenumbers. These waves represent the C-O-C and C=O bonds respectively.

The results of the test are shown in Figure 1, with a spectral range of 1000 cm-1 to 2000 cm-1. In each case of PEEK grade and extruder temperature used, there was no difference compared to the respective, original granulate spectroscopy result. The lack of any peak formation at 1100 cm-1 and 1730 cm-1 as compared with the granulate demonstrated that no oxidative cross-linking occurred. This in turn leads to the conclusion that the melting temperature increase was caused by a change in crystalline morphology.

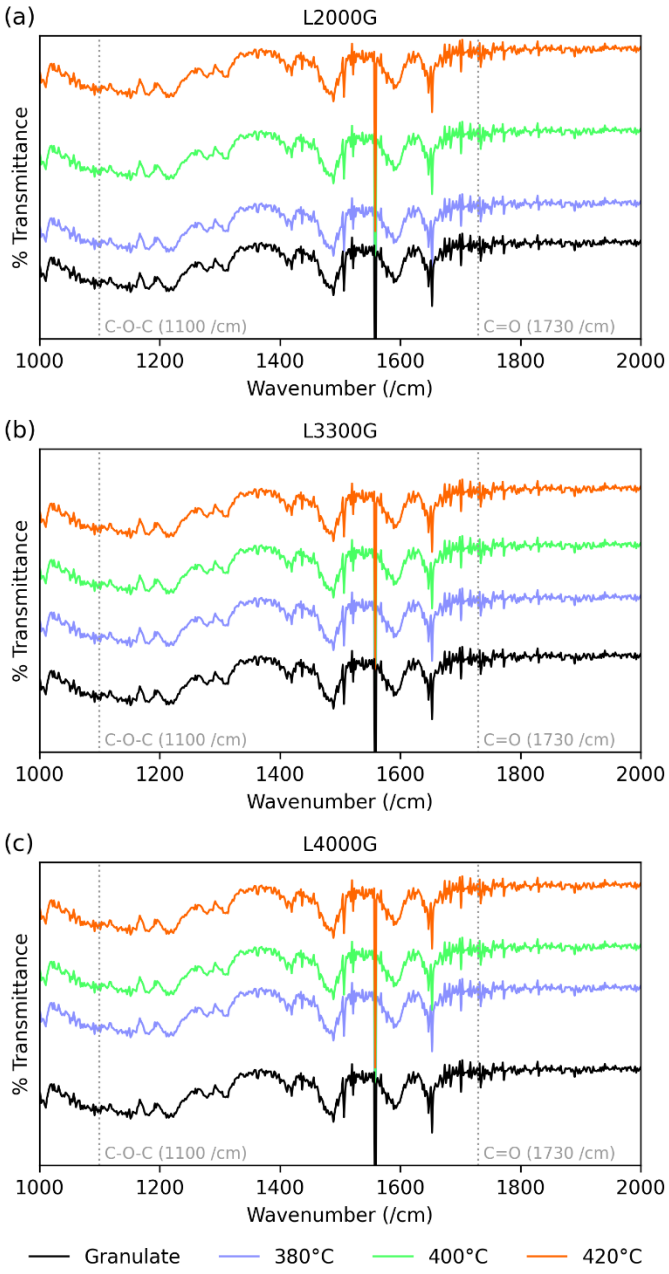

Figure 1 - FTIR ATR representative results for VESTAKEEP L2000G, L3300G and L4000G, for granulates and CST specimens 3D printed at 380°C, 400°C and 420°C.

X-ray Diffraction Analysis (XRD) Crystallinity

The XRD results are shown in Figure 2. There is no clear trend in the result and due to the lack of repeats, the validity of the result is uncertain. It was not possible to take multiple readings due to the specimen geometry required. XRD requires a flat surface with at least a 1 cm sided square for testing. Such a surface could only be provided by group 1, type 1 specimens and therefore there was a limited number of available specimens. XRD results were overall lower than DSC and Raman results, as predicted by literature [4].

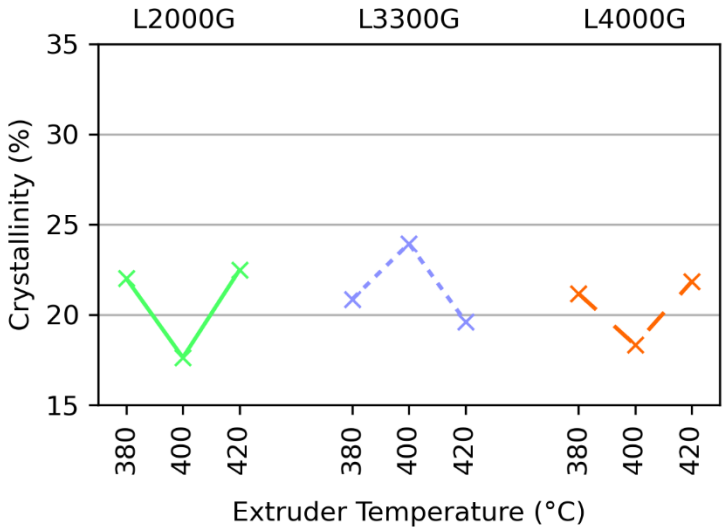

Figure 2 - Crystallinity of compression shear failure face using XRD.

References

1. Beyler CL, Hirschler MM. Thermal Decomposition of Polymers. In: SFPE Handbook of Fire Protection Engineering. 1st ed. Springer New York; 2016.

2. Lee Y, Porter RS. Effects of thermal history on crystallization of poly(ether ether ketone) (PEEK). Macromolecules. 1988 Sep;21(9):2770–6.

3. Yang L, Ohki Y, Hirai N, Hanada S. Aging of poly(ether ether ketone) by heat and gamma rays — Its degradation mechanism and effects on mechanical, dielectric and thermal properties. Polymer Degradation and Stability. 2017 Aug 1;142:117–28.

4. Doumeng M, Makhlouf L, Berthet F, Marsan O, Delbé K, Denape J, et al. A comparative study of the crystallinity of polyetheretherketone by using density, DSC, XRD, and Raman spectroscopy techniques. Polymer Testing. 2021 Jan;93:106878.